CITY UNIVERSITY
LONDON

Heart Rate Variability analysis in patients undergoing local anaesthesia

A thesis submitted to the graduate faculty in partial fulfilment
of the requirements for the degree of Doctor of Philosophy
in Biomedical Engineering and Physics

Kamran Shafqat

School of Engineering and Mathematical Sciences
Electronic, Electrical and Information Engineering

City University London

Feb 2010

Abstract

The analysis of Heart Rate Variability (HRV), the beat to beat fluctuation in the heart rate, is a non-invasive technique with a main aim in gaining information about the autonomic neural regulation of the heart. Assessment of HRV has been shown to aid clinical diagnosis and intervention strategies. However, there are quite a few conflicting reports on HRV that perhaps impede its use as a reliable clinical tool. The complex nature of different mechanisms that affect the HRV and the large number of signal processing techniques that have been used for HRV analysis are the contributing factors of these conflicting results. The aim of this study was to investigate for the first time the effect of HRV during Brachial plexus block (local anaesthesia), applied using the axillary approach. The hypothesis was that, such investigation will enable the detection of possible changes in the dynamics of the cardiovascular system due to the intravenous introduction of anaesthetic drugs during local anaesthesia. For this purpose advanced HRV signals processing techniques were developed and evaluated on data collected before and after the application of the Brachial plexus block from fourteen patients undergoing local anaesthesia. Signal processing techniques for R-wave detection, signal representation, ectopic beat detection and detrending were first developed and validated with the help of simulated signals and physiological signals from Physionet data base. After the validation stage these methods were then used to analyse the data from the locally anaesthetised patients.

The ECG R-wave peak detection was carried out using the wavelet transform with first derivative of Gaussian smoothing function as the mother wavelet. The algorithm achieved accuracy and sensitivity of over 90%. The heart timing signal was used for the HRV signal representation and also for the correction of missing and/or ectopic beats. The results obtained from the ectopic beat correction algorithm showed that the algorithm managed to significantly reduce the error caused by missing and/or ectopic beats. Detrending of the HRV signal was carried out using the wavelet packet analysis algorithm which was specifically developed for this study. The respiration signal was also estima-

ted from the ECG signal using the ECG Derived Respiration (EDR) technique. In order to take better account of slow respiration rates and/or irregular respiratory patterns in the HRV analysis, a new method for the estimation of the variable boundaries associated with the LF and the HF band of the HRV signal was implemented. This method relies on the frequency contents of both the HRV signal and the respiration signal and uses the cross-spectrum between these two signals to obtain the boundaries related to the HF band of the signal. The boundaries related to the LF band were defined using the HRV signal spectrum alone. The boundary estimation technique was applicable in all the spectral analysis methods that were used in this study.

After the pre-processing steps the clinical data was analysed using frequency and time-frequency analysis methods to obtain the parameters related to the HRV signals. Initially spectral analysis was carried out using the traditional non-parametric (Welch's periodogram) and parametric (Autoregressive modelling) methods. Statistical analysis of the parameters obtained from both the non-parametric and the parametric methods showed significant decrease in the LF/HF ratio values within an hour of application of the block in nine out of fourteen patients. In order to overcome the inability of these methods to deal with non-stationary, time-frequency analysis techniques were used to further analyse the HRV signals. The three time-frequency analysis methods used were the Continuous Wavelet Transform (CWT), the Wigner-Ville Distribution (SPWVD) and the Empirical Mode Decomposition (EMD). The analysis of the parameters estimated from these three techniques on the clinical data showed that the CWT and the EMD techniques have performed equivalently, meaning that both these methods have detected significant decrease in thirteen out of fourteen patients for the ratio values after the application of the anaesthetic block. The presence of interference terms has caused the degradation in the performance of the SPWVD method and due to this reason it was only able to detect significant changes in the $^{LF}/_{HF}$ ratio values in ten of the fourteen patients. The results suggest that due to anxiety and/or adrenaline present in the local anaesthetic mixture, the $^{LF}/_{HF}$ ratio values showed a transient increase shortly after the application of the block. After this transient increase the ratio values decreased considerably and remained low as compared to the values before the application of the block. This decrease could represent the shift of the sympathovagal balance towards parasympathetic predominance and/or inhabitation of sympathetic activity due to local anaesthesia. The use of time-frequency analysis such as EMD and CWT could provide useful information about the changes caused in the dynamics of the cardiovascular system when a local anaesthetic drug is administered in a patient.

Dedicated to my grandparents

Acknowledgements

I would like express my gratitude to Dr. P. A. Kyriacou and Dr. S. K. Pal for providing me the opportunity to this research. I would also like to thanks Dr. P. Weller and Dr. P. Liatsis for the useful discussions and the guidance they provided throughout my research. I would also like to acknowledge Dr. S. Kumari for her assistance in the clinical trials.

I would like to say a especial thanks to my family and my wife for their uncompromising support and understanding during my study.

Finally, I would like to thank my friends Mr. V. O . Rybnok and Miss. M. Hickey who made it possible for me to survive the lab environment and help me in every aspect of my research.

Contents

City, University of London
Northampton Square
London
EC1V 0HB
United Kingdom

T +44 (0)20 7040 5060

THE FOLLOWING PARTS OF THIS THESIS HAVE BEEN REDACTED FOR COPYRIGHT REASONS:

List of Figures

List of Tables

Abbreviations

F_N number of peaks missed, page 55

F_P Noise detected as peaks, page 55

T_P Correctly identified peaks, page 55

ht Heart Timing signal, page 98

AHHS Amplitude Hilbert-Haung Spectrum, page 218

AIC Akaike Information Criterion, page 91

AP Auto-Regressive, page 29

ARMA AutoregressiveMovingaverage, page 89

ASA American Society of Anesthesiologists, page 42

AV Atrioventricular node, page 9

BIC Bayesian Information Criterion, page 91

bmp beats per minutes, page 13

CAT Criterian Autoregressive transfer, page 91

CF Center Frequency, page 145

CRM Cardiac Rhythm Management, page 11

CWD Choi-Williams distribution, page 191

CWT Continuous Wavelet Transform, page 63

DNA Deoxyribonucleic acid, page 63

DSTFT Discrete Short Time Fourier Transform, page 62

DWT Discrete Wavelet Transform, page 63

ECG Electrocardiogram, page 6

EGM Endocardial electrogram, page 11

EMD Empircal Mode Decomposition, page 210

EMG Electromyograph, page 44

FIR Finite Impulse Response, page 45

FPE Final Prediction Error, page 91

FS Fourier series, page 60

FT Fourier Transform, page 60

FWT Fast Wavelet Transform, page 68

HP Heart Period, page 98

HR Heart Rate, page 6

HRV Heart Rate Variability, page 6

HT Hilbert Transform, page 163

IBI Interbeat Interval, page 44

ICF Instantaneous Center Frequency, page 164

IF instantenous frequency, page 162

IMF Intrinsic Mode Function, page 213

IP instantenous power, page 162

IPFM Integral Pulse Frequency Modulation, page 95

LDF Laser Doppler Flowmetry, page 253

MA Moving average, page 89

MDL Minimum Descripition Length, page 91

MNE Mean Normalized Error, page 109

NAHT Normalised Amplitude Hilbert Transfor, page 218

NSR Normal Sinus Rhythm , page 55

PRT pneumatic respiration transducer, page 136

PSD Power Spectral Density, page 28

PWVD pseudo Wigner-Ville distribution, page 187

RMS Root Mean Square, page 62

SA Sinoatrial node, page 9

SDSE Standard Deviation Spectral Extension, page 145

SNR Signal-to-Noise Ratio, page 45

SPA Smoothness Prior Approach, page 120

SPWVD smoothed-pseudo Wigner-Ville distribution, page 189

STFT Short Time Fourier Transform, page 61

TFD Time-Frequency Distribution, page 162

WSS Wide Sense Stationary, page 86

WT Wavelet Transform, page 62

WVD Wigner-Ville Distribution , page 184

1 Thesis outline

Heart rate variability is the term used to define the beat-to-beat fluctuation in the heart rate. Short term and long term variations in the heart rate are known to have different physiological origins and the magnitude of these variations has been shown to be indicative of the autonomic state of a patient [1]. Assessment of heart rate variability has been shown to aid clinical diagnosis and intervention strategies. In this work a systematic approach for the frequency domain analysis of heart rate variability is presented. Important aspects such as errors introduced by the signal representation, effect of ectopic beats on the power spectrum of the signal and the effect of trend removal techniques are discussed. By utilising the information regarding these important issues, the heart rate variability signal from a group of patients undergoing local anaesthesia were analysed. The purpose for studying the signals from this group of patients was to investigate the effect of local anaesthetic drugs on heart rate variability parameters. A brief summary of each of the chapters in this report follows:

Chapter 2 provides fundamental anatomical and physiological information about the cardiovascular and the autonomic nervous system, which is essential for better understanding and interpretation of heart rate variability. This chapter also introduces the electrocardiograph signal associated with the heart contractions and presents the effect of some of the heart diseases on this signal.

Chapter 3 provides basic information regarding the different regulators of the heart rate related to the autonomic nervous system. Inter and intra-patient factors affecting the variability of the heart rate are discussed. The most commonly used methods for the analysis of the heart rate variability will be presented alongside some of the clinical applications. Some of the difficulties when using these methods of analysis will also be underlined.

Chapter 4 This chapter provides a brief introduction of local anaesthesia and Brachial plexus block, the regional nerve blockage technique applied to the patients selected

in this study.

Chapter 5 Detection of the ECG R-wave is the first step in heart rate variability studies. This chapter describes the implementation of an algorithm which uses digital filtering technique and an adaptive threshold for the detection of the R-wave. The implemented algorithm was tested extensively using simulated and real ECG data. The simulated signals were used to check the performance of the implemented algorithm in the presence of varying levels of different kind of artefacts usually present in the typical ECG recordings. The validation on real ECG signals was carried out by using signals from Physionet data bank and also ECG signals recorded from the patients undergoing local anaesthesia which were included in this study.

Chapter 6 This chapter presents another algorithm for the detection of the ECG R-wave based on wavelet analysis. A brief introduction of the wavelet analysis and its application in the field of ECG analysis is presented in this chapter. After the introduction of the wavelet analysis the implementation aspects of the ECG characterisation algorithm and the validation results obtained by analysing the simulated and real ECG signals are also discussed in this chapter. This algorithm was validated using the same sets of signals which were used for the validation of the first algorithm presented in previous chapter.

Chapter 7 presents the fundamental ideas and the properties of the parametric (Autoregressive) and the non-parametric (Welch's periodogram) methods of spectral analysis. These are the two most basic and commonly used methods employed for the frequency domain analysis of the Heart Rate variability (HRV) signals. In this study these two techniques have been used not only to estimate the frequency domain parameters associated with the HRV signals but also to validate the results obtained from different steps (signal representation, beat correction and detrending) involved in the HRV analysis.

Chapter 8 This chapter discusses the issues of HRV signal representation and resampling of the irregular time series and are discussed in this chapter. Using the results from simulated signal study the effectiveness of heart timing (*ht*) representation in HRV analysis is presented. A method of correction for ectopic/missing beats is also discussed and validated in this chapter. Again with the help of simulated signals the effect of ectopic/missing beats and finite data length on the HRV frequency domain analysis is shown in this chapter. Using the results obtained in this chapter along with the information provided in the previous chapter the setup for the frequency domain analysis of the HRV signals using parametric and non-parametric parame-

ters is establish. This setup is then used for the study of heart rate variability signals from patients under local anaesthesia.

Chapter 9 describes the two algorithms implemented in this study for detrending the HRV signals. One of these algorithms is based on Smoothness Prior Approach while the other algorithm uses wavelet packet analysis for detrending the signals. After describing the theory and the technical details related to the implementation of the two algorithms the performance of both of these algorithms were tested using simulated and real HRV signals. .

Chapter 10 In order to define the respiration related band of the HRV signal more accurately the respiration signal was estimated. The implementation details and the validation results obtained for the ECG Derived Respiration (EDR) algorithm which was used for estimating the respiration signal for the ECG signals are presented in this chapter. This algorithm estimates the direction of the mean cardiac electrical axis using the area of QRS complexes to obtained a measurement of respiration signal from the ECG signal. The algorithm was validated using data sets from Physionet which included ECG and respiration measurements. The implemented algorithm was used to obtain the estimate of the respiration signal from the ECG signal. This estimated signal was then compared with the respiration measurement data included in these data sets.

Chapter 11 After pre-processing (ECG R-wave detection, HRV signal representation, ectopic beat correction and detrending) the HRV signals obtained from the locally anaesthetised patients included in this study were analysed in the frequency domain using different techniques. This chapter presents the results obtained by analysis of the HRV signals using nonparametric (Welch's periodogram) and parametric (Autoregressive modelling) methods. The parameters of the HRV signals (low to high frequency power ratio, total power, low and high frequency power in normalised and absolute units and high and low frequency values) were calculated using five minute segments of the data. In order to detected changes in the parameter values due to the introduction of the local anaesthetic drug in the patients the parameter values obtained before the application of the block were compared with the values obtained after the application of the block. Statistical tests (Wilcoxon, signed rank test) were performed to check if there was any statistical significant difference in the HRV parameters before and after the block.

Chapter 12 In this chapter the results obtained by analysing the same HRV signal from the locally anaesthetised patients using a continuous wavelet transform are presen-

ted. This technique was used as it can provide the time-frequency distribution of the signal which might reveal more information about the dynamical changes occurring in the signal. The ability of the continuous wavelet transform for tracking changes in the amplitude and frequency of the signal were validated using simulated signals. The results from this study provided the setup which was then used for the analysis of the HRV signal from the locally anaesthetised patients. The parameters related to the HRV analysis were calculated this time using the time-frequency distribution obtained from the continuous wavelet transform. After estimating the parameters values, statistical tests were carried out to check for significant differences in the values before and after the application of the anaesthetic drug.

Chapter 13 In this chapter, two other quadratic distributions from Cohen's class (Smoothed-pseudo Wigner-Ville distribution and Choi-Williams distribution) were tested for their feasibility for the analysis of the HRV signals. This chapter provides a brief introduction to the general theory of quadratic distributions for time-frequency analysis. The performance of these two distributions was tested using simulated signals. The results from this analysis indicated better performance of the Smoothed-pseudo Wigner-Ville distribution when compared with the Choi-Williams distribution in estimating the power related to the different bands of the HRV signals. The simulated signals study helped in validating the setup used for the analysis of the real HRV signals. On the basis of the results obtained from the simulated signals study the HRV signal from the locally anaesthetised patients were also analysed using the Smoothed-pseudo Wigner-Ville distribution. Using the time-frequency representation obtained from the Smoothed-pseudo Wigner-Ville distribution the HRV parameters were calculated and statistical tests were performed to check for significant differences in the parameter values before and after the application of the anaesthetic drug.

Chapter 14 In this chapter time-frequency analysis approach of Empirical Mode Decomposition (EMD) was used for the analysis of the HRV signals obtained from the locally anaesthetised patients. EMD is a data driven adaptive method in which the basis is calculated directly from the data. This ability of driving a basis set directly from the data instead of using fixed predefined basis as used by other techniques allows EMD to provide more compact and meaningful representation of the signals especially in the case of non-stationary and non-linear signals. A brief description of the technique and its application is presented in this chapter. After the introduction a step wise systematic approach was used to analyse the simulated signals using the EMD approach. The results from the simulated signals study not only

provided evidence of the ability of the EMD analysis to track transient changes in the characteristics of the signal but it also helped in validating the set for the EMD analysis which was then used to analyse the HRV signal obtained from the locally anaesthetised patients. Similarly to the previous cases, after obtaining the time-frequency distribution of the HRV signals using the EMD technique the parameters related to the HRV signals were calculated. Finally statistical tests were performed to compare the HRV parameters values obtained from the data before the application of the block to the parameters values after the application of the block.

Chapter 15 In this chapter general discussion and comparison of the results and the signal processing techniques used for the analysis is presented. The parametric, non-parametric and time-frequency analysis methods used in this study are compared with relevant studies presented in the literature. The method proposed in this study for the estimation of the boundaries related to the LF and the HF band of the signal is also compared with other methods that have been used for boundary estimation. Finally, some of the studies relevant to the changes occurring in cardiovascular dynamics due the application of the anaesthetic block are presented. The results presented in these studies are compared with the results obtained during this work.

Chapter 16 This chapter gives an overall summary and provides final conclusions from this study. Recommendations for future work are also discussed.

2

Anatomy and physiology: cardiovascular and autonomic nervous system

2.1. Introduction

Over the last 20 years there has been a widespread interest in the study of variabilities in cardiovascular activity, such as Heart Rate (HR), arterial blood pressure, stroke volume and the shape of the Electrocardiogram (ECG) wave complexes. It is typical for these signals to fluctuate on a beat-to-beat basis around their mean value. The beat to beat fluctuation in the HR is known as the Heart Rate Variability (HRV). These are associated with the autonomic neural regulation of the heart. The monitoring of the fluctuations observed in HR provides information concerning its autonomic regulation and disturbances. In certain circumstances, the evaluation of HRV has been shown to provide an indication of cardiovascular health [1]. To better understand HRV and its interpretation, knowledge of the cardiovascular and the autonomic nervous system is fundamental.

This chapter provides a brief overview of the anatomy and the physiology of the human heart. The main characteristics of the ECG (a record of the bio-potentials associated with the contractions of the heart muscle) are also discussed. Furthermore this chapter discusses the most commonly encountered heart diseases and their effect on ECGs.

2.2. Cardiovascular system

The cardiovascular system is made up of the heart and its associated vasculature. Together they make an extensive network that carries blood to every part of the body. The flow of blood is maintained by the heart and its beating activity. The cardiovascular system is controlled by the autonomic nervous system and regulated by the need of the body. Numerous control mechanisms help to regulate and integrate the diverse functions and component parts of the cardiovascular system to supply blood to specific body areas according to the need. The list of functions of the cardiovascular system is large, but its main function is maintaining the homeostasis of the body [2].

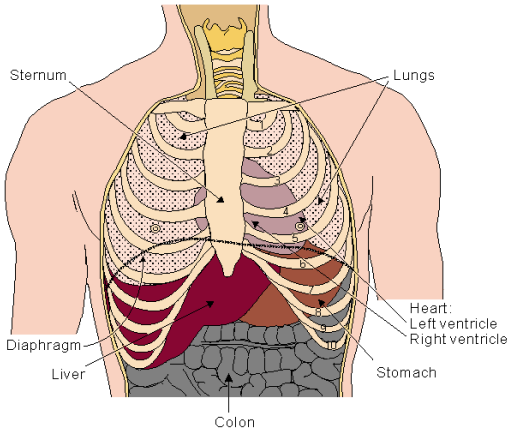

Fig. 2.1: Location of the heart in the thorax. It is bounded by the diaphragm, lungs, oesophagus, descending aorta, and sternum [3]

2.2.1. The anatomy and function of the human heart

The main organ of the cardiovascular system is the heart. It is responsible for the circulation of the blood according to the needs of the body. The heart is located in the thorax posterior to the sternum and costal cartilages and rests on the superior surface of the diaphragm (Fig. 2.1). The heart has a broad base at the top and tapers to a pointed tip known as the apex at the bottom. It is situated at an angle under the sternum so that its base lies predominantly to the right of the apex and to the left of the sternum. The size of the heart is no larger than one's own fist.

The heart is enclosed in a fibrous sac called the pericardium. The walls of the heart are primarily composed of cardiac-muscle called the myocardium. The myocardium contracts and relaxes in a coordinated manner when an electrical stimulus is applied. The heart's function is to pump blood around the body, through the arterial system to enable the transport of vital nutrients and oxygen. There are three main types of blood vessels, namely arteries which carry the oxygenated blood from the heart to the various part of the body, the veins which carry deoxygenated blood from the various parts of the body back to the heart, and the capillaries which join the arteries and the veins and are the site for the gaseous and chemical exchange between the various cells and the blood [2].

Like all other muscles, the heart receives its oxygen and nutrients from arteries known as coronary arteries. The two major coronary arteries branch off the aorta, and then divide into many smaller arteries that lie in the heart muscle and feed the heart [4]. A blockage of these vessels often leads to a heart attack. . In fact, coronary heart disease has been shown to be the leading cause of death in developed countries [5]. Myocardial Infarction (MI), heart failure, angina, and sudden death can all occur from the blockages which occur in the coronary arteries. Following an MI, the conventional treatment is to inject a "clot-busting" decoagulating agent in order to remove the blockage. However, often the heart has already suffered much damage and muscle-tissue loss leading to an

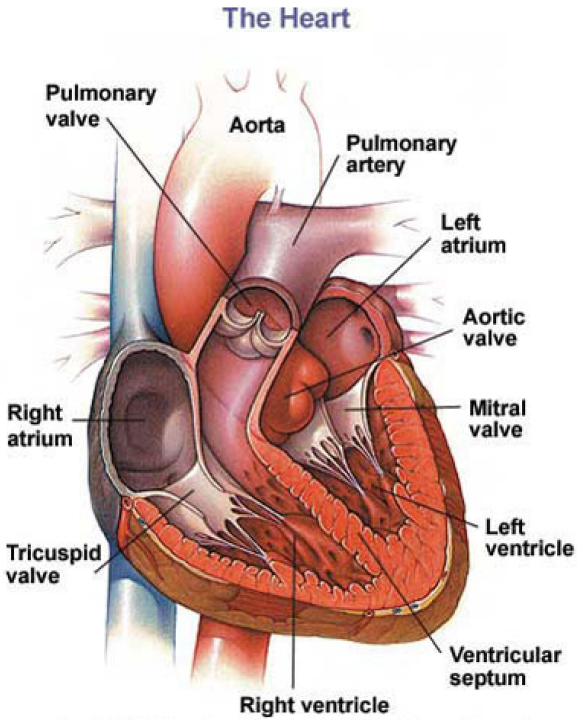

Fig. 2.2: Correctional view of the heart showing its chamber [6]

increased likelihood of re-infarction [1].

The heart, illustrated in Fig. 2.2 is divided into two functional halves, each half containing two chambers: an atrium and a ventricle. The heart also contains four unidirectional valves.

- The right AV (Tricuspid) valve, between right atrium and ventricle.
- The left AV (Mitral) valve, between left atrium and ventricle.
- The pulmonary semilunar valve, between the right ventricle and left pulmonary artery and
- The aortic semilunar valve, between the left ventricle and the aorta.

The right atrium receives blood from the head and the torso via the superior vena cava, and from the abdomen and legs from the inferior vena cava (see Fig. 2.2). From the right atrium, the blood is passed into the right ventricle from where it is pumped to the pulmonary artery and on to the lungs. From the lungs, the oxygenated blood returns through the pulmonary veins to the left atrium and the left ventricle, and is then pumped out again to the body through the aorta. The pumping of the heart is caused by alternating contractions and relaxations of the myocardium (the heart beat). Valves between the atria and the ventricles, as well as between the ventricles and the arteries, maintain unidirectional blood flow. These valves and the septum separate the two halves of the heart to prevent the mixing of blood from the two sides. This separation is important because the

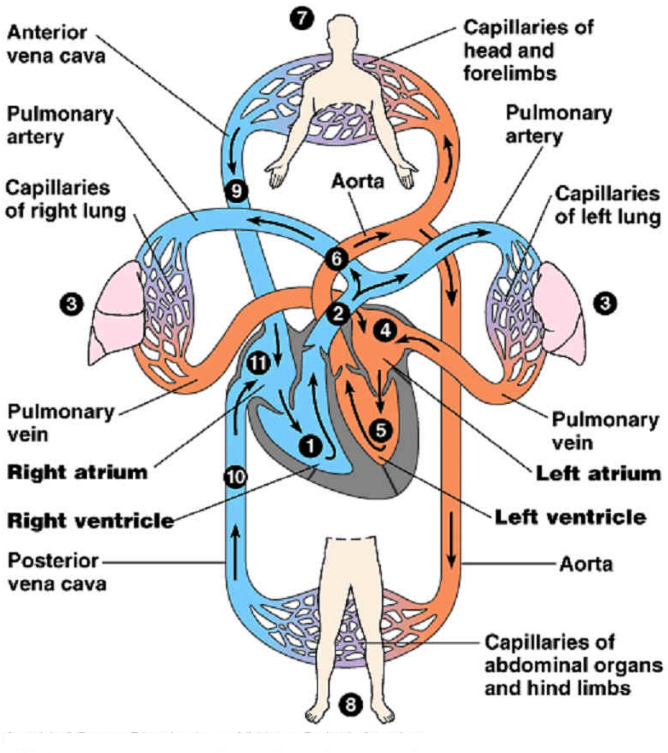

Fig. 2.3: Systemic and Pulmonary network [8]

right half of the heart is receiving and pumping deoxygenated blood while the left side of the heart receives and pumps oxygenated blood [7].

The blood travels continuously through the circulatory system to and from the heart through two separate vascular (blood vessel) loops, both originating and terminating at the heart. The pulmonary circulation consists of a closed loop of vessels carrying blood between the heart and the lungs, whereas the systemic circulation consists of a closed loop of vessels carrying blood between the heart and other organs.

Blood returning from the systemic circulation enters the right atrium through the vena cava and the deoxygenated blood returning from the body tissues enters the right atrium. From the lungs, after the gas exchange, the blood returns to the left atrium. The blood from the left atrium flows into the left ventricle and eventually into the aorta that supplies the oxygenated blood to all parts of the body. This is called the systemic circulation. The systemic and pulmonary circulation is shown in Fig. 2.3.

2.3. The conduction path

The cardiac cycle is normally initiated by an electrical impulse that originates from the sinoatrial (SA) node, which is located at the junction of the superior vena cava and the right atrium. From the SA node three specialised branches or pathways emerge and terminate at the atrioventricular (AV) node. These nodes are named the anterior, the middle and the posterior internodal tracts [9]. Another tract also emerges from the SA

Fig. 2.4: The conducting system of the heart [10]

node and leads into the left atrium. This tract is called the Bachman's bundle and forms an interatrial passage. An impulse passes from the SA node through the specialised tracts in the atria to activate first the right atrium and then the left atrium. The passage of the impulse is delayed once it has reached the AV node and continues into the various tracts emerging out of the AV node (see Fig. 2.4) [9]. These tracts are as follows:

1. Bundle of His
2. the right bundle branch
3. the left bundle branch and
4. the Purkinje Network

The right bundle branches lie along the right side of the interventricular septum to the apex of the right ventricular before it gives off significant branches. The left common bundle block crosses to the left side of the septum and splits into the anterior division and the posterior division. Each branch of this conduction system of the heart contributes its own signal to the overall measurable signal. The branches are composed of representative cells that are also anatomically different. All these cells are electrically excitable and exhibit their own characteristic action potential [9].

2.4. The electrocardiogram (ECG) signal

Normally, the HR is controlled by the autonomic nervous system. However, both the SA and the AV nodes and the Purkinje fibres may initialise impulses spontaneously. The spontaneous HR varies in these cells from 70 beats per minute for the SA node, to approximately 30 beats per minute for the Purkinje fibres. In this way, a block of the impulse does not prevent basic ventricular activity.

The impulse initiating the heart beat is transmitted as a change in electrical potential of the cell membranes along the propagation path. All myocardial cells exhibit a potential difference across the cell membrane which is due to a difference in ion balance between the exterior and the interior of the cell. Muscular cells, as well as some other cells such as nerve cells, possess the ability of being excitable, i.e. transmitting an impulse [11].

Deviations in the cell membrane permeability may cause a change in the membrane potential. The result is an inward flow of positively charged potassium ions. As a result, the cell becomes neutral or slightly positively charged, i.e. it is depolarised. A fraction of a second later, the cell resumes its usual negative potential again, i.e. it is repolarised. From the onset of the depolarisation phase and extending into the repolarisation phase, a refractory period prevents the cell from initiating a new depolarisation phase. The entire event is referred to as an action potential and is caused by electrical stimulation or a change in chemical concentration. The depolarisation corresponds to the contraction phase, while repolarisation corresponds to the relaxation phase [11].

The electrical impulse, initiating depolarisation and repolarisation of the heart, propagates with the help of flowing ions. The ion flow, in turn, causes currents in the surrounding tissue due to the resistivity of the body [11]. These currents are measurable either invasively by the Endocardial electrogram (EGM), or on the body surface by the ECG. The EGM is measured endocardially by inserting an electrode through the vein system to either the right atrium or the right ventricle. For implantation purposes, the EGM is recorded in the right chambers of the heart since this is the low pressure side of the cardiovascular system. The electrode insertion is usually related to permanent placement for use, e.g. by implantable Cardiac Rhythm Management (CRM) devices, thus implying the need for a surgical procedure. As mentioned before (see section 2.3), each branch of the conduction system contributes to the resultant signal. Hence, the ECG is in effect a vector sum of composite signals. The building blocks of the common ECG signal are shown in Fig. 2.5. The ECG is measured by using surface electrodes in different configurations. Details of such configurations will be described in section 2.4.1.

A typical ECG waveform comprises of an initial P-wave, followed by the main 'QRS' complex and then a trailing T-wave (see Fig. 2.6). These waves are defined as follows:

P-wave: The low voltage fluctuation caused by the depolarisation of the atria prior to contraction. The atria contain very little muscle and thus the voltage change is quite small with typical amplitude of 0.25 millivolts.

QRS complex: The largest-amplitude portion of the ECG caused by the ventricular depolarisation. The time during which ventricular contraction occurs is referred to as systole. Although atrial repolarisation occurs simultaneously, it is not seen due to

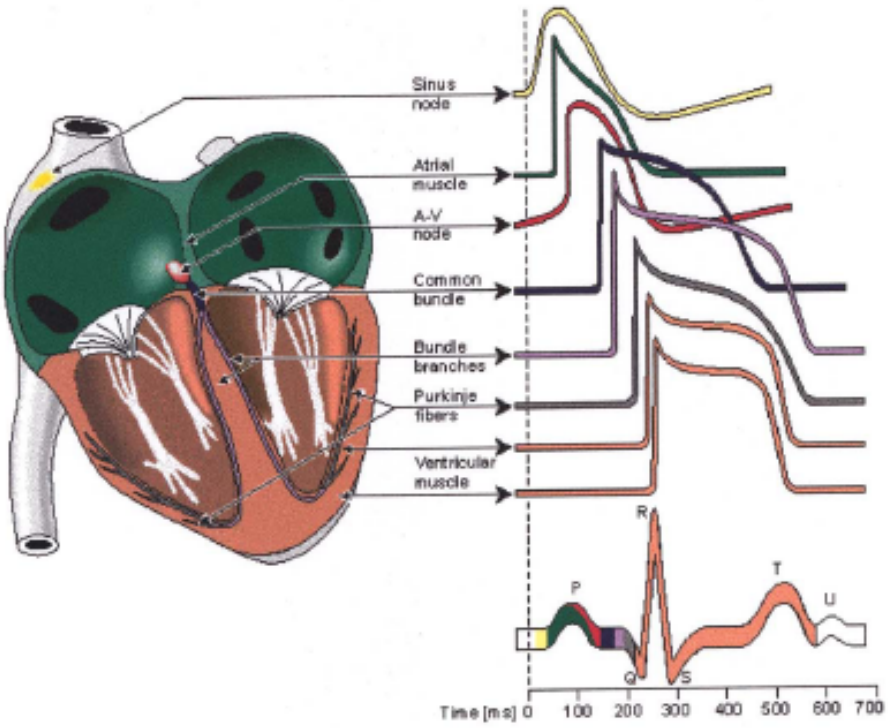

Fig. 2.5: Representative electrical activity from various regions of the heart [12]

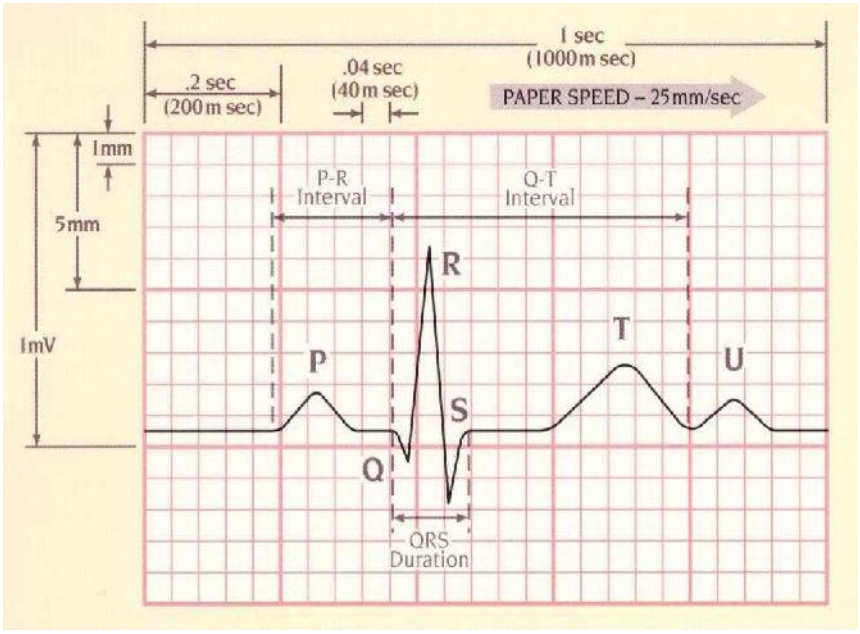

Fig. 2.6: Amplitude and time intervals in the ECG [13]. The atrial depolarisation is reflected by the P wave, the ventricular depolarisation by the QRS complex, and the ventricular repolarisation by the T wave. The atrial repolarisation is simultaneous with the ventricular depolarisation and is therefore hidden within the QRS complex

the low amplitude of the signal generated by this process. The typical amplitude of the R wave is about 1.6 millivolts.

T-wave: Caused by ventricular repolarisation. The T wave has typical amplitude of 0.1 to 0.5 millivolts.

The duration of the P wave is usually about 0.08 to 0.1 seconds. The period of time

Fig. 2.7: ECG 12-lead standard configuration. The red circles with numbers show the position of leads V_1, V_2, ..., V_6 [15]

from the onset of the P wave to the beginning of the QRS is termed as the PR interval and normally ranges from 0.12 to 0.20 seconds [14]. The duration of the QRS complex is normally 0.06 to 0.1 seconds indicating that ventricular depolarisation normally occurs very rapidly. The isoelectric period (ST segment) following the QRS is the time at which the entire ventricle is depolarised and roughly corresponds to the plateau phase of the ventricular action potential. The ST segment duration is about 0.05 to 0.15 seconds. The duration of the QT segments, the interval from the start of the Q wave to the end of the T wave, is 0.35 to 0.40 seconds. The RR interval is used to measure HR.

The time average Heart Rate (HR_{60}) is usually calculated by counting the number of beats in a 60 second time period. The instantaneous HR, $HR_{inst.}$ is $\frac{60}{RR}$ where RR is the time between successive R-peaks (an RR interval). HR_{60} can vary between 30 and 220 beats per minute (bpm) and although the instantaneous HR can be as high as 300 bpm, this is not sustainable for more than a few beats without serious problems manifesting themselves.

2.4.1. ECG lead configurations

The standard 12-lead ECG is today the most common lead system for recording from the body surface: six electrodes are positioned over the chest (V_1, V_2, ..., V_6), and three electrodes on the extremities, i.e. both arms and the left leg, see Fig. 2.7. The remaining three extremity leads are derived as linear combinations of the recorded extremity leads. Lead I, II and III are also called the bipolar limb leads, these were first introduced by Einthoven and are derived from the electrodes placed on the limbs [16].

Lead I : Left Arm and Right Arm

Lead II : Left Leg and Right Arm

Lead III : Left leg and Left Arm

Other leads can be divided into unipolar limb lead (aVR, $aVL and aVF$) and unipolar chest leads V_1 to V_6. Leads V_1 to V_6 form a transversal plane, and also provide more local cardiac information due to their closer distance to the heart, while the extremity leads form a frontal plane with more global information. Usually one or two leads are routinely monitored in clinical setting. Typically, lead II and lead V_5 are chosen since they offer the most useful information in the context of medical diagnosis [17]. Lead II represents an electrical activity vector from the centre point (close to heart) to the left leg. While lead V_5 represents the vector from electrode position V_5 to the heart.

2.5. Cardiac disease

Heart disease can generally be classified into two categories, ischaemia and arrhythmias. Usually ischaemic heart disease is related to insufficient blood supply to the heart muscle itself, due to blocks in the coronary arteries. While, arrhythmias involve deviation in rhythm from the normal resting HR, which is usually 60 to 100 bpm and initiated by the SA node. The two types of diseases may be related, e.g. ischaemic heart disease may cause certain types of arrhythmias [7].

2.5.1. Myocardial ischaemia

Ischaemic heart disease is one of the most common causes of death in the industrialised world; as many as half of the deaths in North America and Europe are related to this group of diseases [7]. A diet, including large amounts of cholesterol combined with smoking, are contributing risk factors to ischaemic heart disease.

Ischaemic heart disease is caused by insufficient blood supply to the heart itself. Being a muscle, the heart must be supplied with oxygen in order to function; this is taken care of by the coronary arteries and their ramifications. In more or less all adults, areas of thickening, denoted atherosclerotic plaques, slowly develop in the arteries. In many individuals, these plaques never cause any symptoms, while in others they may obstruct the coronary arteries. The obstruction may lead to difficulties in supplying the heart with sufficient amount of blood during exercise or mental stress. Medically, myocardial ischaemia is identified in the following ways [18]:

1. Anginal discomfort

2. ST-segment deviation on the ECG (see Fig. 2.8)

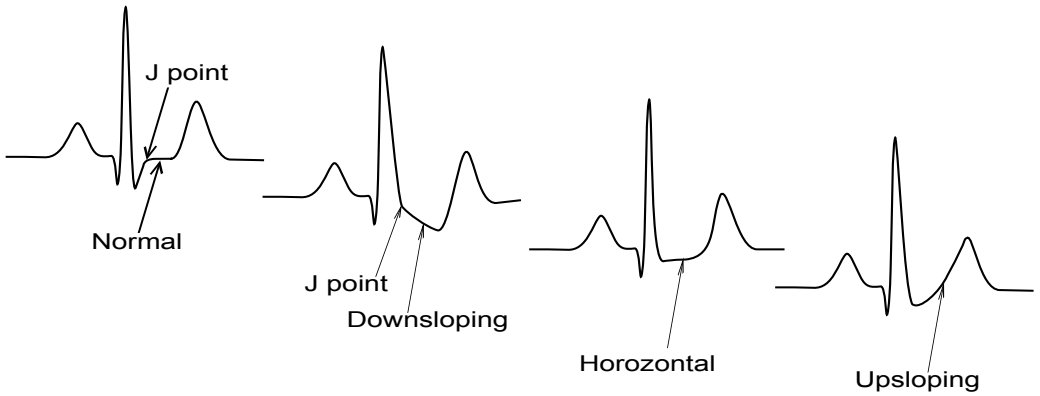

Fig. 2.8: S-T depression in the ECG of the Heart

3. Reduced uptake of thallium 201 or technetium 99 in myocardial perfusion images or

4. Regional or global impairment of the ventricular function

Usually, an S-T depression is associated with myocardial ischaemia when the S-T segment is 0.1 mV or more below the isoelectric line at the J point [18] (see Fig. 2.8).

2.5.2. Cardiac arrhythmias

Based on HR, cardiac arrhythmias can be divided into two types:

- Bradycardia and
- Tachycardia

Bradycardia occurs when the HR goes below 60 bpm, while, the HR above 100 bpm results in tachycardia. A fit individual may very well have a resting HR of less than 60 bpm, and most people have a rate exceeding 100 bpm during exercise. However, a too slow or too fast HR may also be associated with arrhythmic activity, which degrades the cardiac function.

Bradyarrhythmias appear if the natural pacemaker of the heart, the SA node, ceases to pace, paces too slowly, or a block in the conduction path appears. In the last case, "back up" pacemakers take over from the SA node. The effect is a decreased HR which only allows for less strenuous activities and is usually associated with dizziness, fainting or fatigue. Also in this case, the morphology of the ECG signal can change considerably. These beats are usually termed as the ectopic beats. Although non-sinus beats can arise from any region of the heart an ectopic beat is usually classified as atrial, AV junctional or ventricular. Several studies [1, 19, 20, 21] have shown that increased number of ectopic beats can be indicative of poor recovery after a traumatic event or denote the onset of potentially fatal arrhythmia.

Tachyarrhythmias constitute a heterogeneous group of diseases which appear when the depolarisation wave re-enters into an area just recently excited. Non-SA node pacemakers may also appear and interfere with the normal conduction path. In severe tachyarrhythmias, such as flutter and fibrillation, one or more re-entry loops are formed which constantly excite parts of the cardiac muscle.

Supraventricular tachyarrhythmias, originating above the ventricles, reduce the ability of the atria to fill the ventricles with blood, but are usually not immediately life threatening. Due to the decreased heart function, discomfort such as fatigue or palpitations are common. Atrial tachycardias may affect the ventricles such that the AV node propagates the tachyarrhythmia, causing a rapid ventricular response which in turn degrades ventricular function. A secondary effect of severe atrial tachycardias, such as sustained atrial fibrillation, is that blood clots can form if the atria quiver instead of contracting normally. A stroke results when a blood clot lodges in an artery of the brain.

Ventricular tachyarrhythmias are, as the name suggests, initialised in the ventricles. Since the ventricular depolarisation in these arrhythmias does not follow the normal propagation path, the result is a decreased or completely ceased ventricular function, which, in turn, affects the whole cardiovascular function. Ventricular flutter and fibrillation constitute the most severe conditions which, unless treated, lead to death within a few minutes [11].

2.6. Discussion and conclusions

In this chapter a brief overview of the anatomy and the physiology of the heart was presented. The characteristics of the ECG signal, which represents the electrical activity of the heart, was discussed. The most commonly occurring heart diseases and their effect on the electrical activity of the heart was also presented. Building on the basis of the fundamental ideas presented in this chapter, the next chapter will discuss the autonomic nervous system control of the heart. The basic ideas and clinical applications of the HRV (variation of the HR due to ANS control), the conceptual basis of this research, will also be presented in the next chapter.

3

Physiology of beat-to-beat Heart Rate and Heart Rate Variability

3.1. Introduction

The mean heart rate HR_{60} varies on an intra-patient basis (depending upon activity) and on an inter-patient basis (depending on their cardiovascular fitness). However, the instantaneous RR interval or beat-to-beat (instantaneous) heart rate HR_{inst} also varies around the mean (HR_{60}). Figure 3.1 illustrates how the HR_{inst} typically varies for a normal subject at rest over approximately 60 seconds. In this case, the mean heart rate HR_{60} calculated from the HR values shown in Fig. 3.1 (c) is 79 bpm, whereas the instantaneous heart rate HR_{inst} is changing throughout the one minute interval. The maximum value of HR_{inst} is 85 bpm occurring around 12 seconds while, the minimum value is 73 bpm at around 30 seconds. This phenomenon of the heart rate rising and falling on different time scales is known as Heart Rate Variability (HRV). Although the irregularity of the beat-to-beat intervals of a human heart was first noted in the early 1600's [1], its physiological importance was not appreciated until 1965 when Hon and Lee [22] noted that foetal distress was preceded by changes in the pattern of beat-to-beat intervals before any

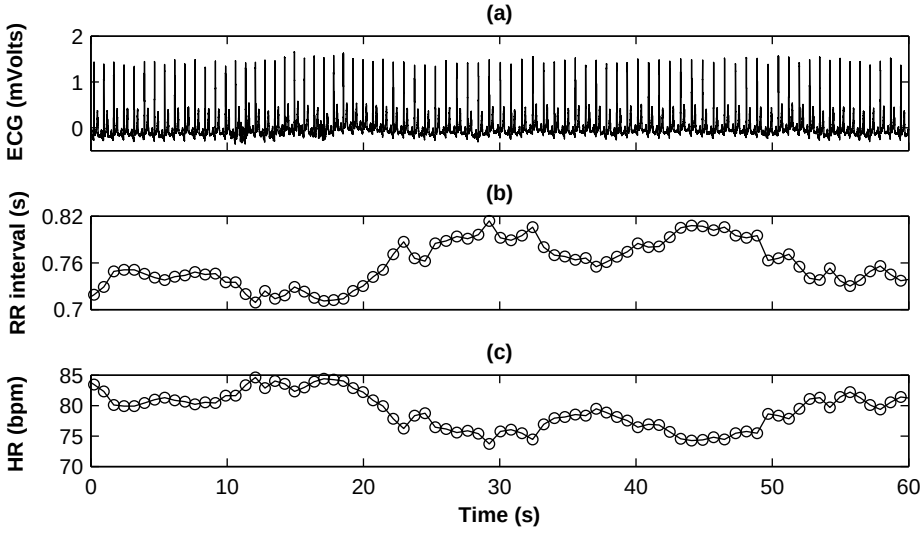

Fig. 3.1: (a) A one minute ECG signal of a normal subject in resting condition; (b) RR interval; (c) instantaneous or beat to beat heart rate HR_{inst}

significant change in the baseline heart rate. Since then many different indices and techniques have been proposed and tested on a great variety of patient groups with varying degrees of success [1]. This chapter describes the regulators of the HR and HRV and also provides an overview of some of the most commonly used HRV analysis techniques.

3.2. The autonomic nervous system and the sympathovagal balance

The brain, via the CNS, regulates two motor systems, the voluntary motor system (muscular control of the limbs, body and head) and the involuntary motor system or ANS. The ANS regulates the internal organs, including the heart, digestive tract, lungs, bladder and blood vessels. It should be noted, however, that it is possible to exert voluntary control over internal organs, e.g. by deliberately over breathing.

The ANS is divided into two opposing branches, the sympathetic and the parasympathetic nervous systems, which exert opposing effects on most organs. The sympathetic system is generally excitatory whereas the parasympathetic system is inhibitory. The sympathetic system acts to increase heart rate, arterial tone, cardiac output, respiration rate, a decrease in the digestive system and dilates the pupils. The parasympathetic system, also known as the vagal system regulates conservative processes and is usually activated when the body is relaxed or asleep. This system is responsible for decreasing heart rate, cardiac output, respiration, increase in the digestive system activity and constriction of the pupil. Animals lacking a healthy sympathetic nervous system find it difficult to deal with physical and mental stress. The complicated interaction between the sympathetic and parasympathetic branches of the ANS and the overall effect that they have on the autoregulation of the cardiovascular system and the autonomic tone has become known as the *sympathovagal balance* [1].

In the sympathetic system (the left side of Fig. 3.2) the spinal cord neurons innervate an adjacent series of ganglia. Neurons from these ganglia innervate the internal organs. In the parasympathetic system (right side of Fig. 3.2), motor neurons from the brain stem innervate ganglia found in the internal organs themselves which in turn innervate the organ in which they are found. The parasympathetic axons from the brain stem extend to the internal organs in various cranial nerves, particularly the vagal nerve (vagus). This nerve, which fans out over a significant portion of the interior lung wall lining is the dominant path for parasympathetic stimulation. For this reason, parasympathetic action is often referred to as vagal nerve activity [1].

The sympathetic and parasympathetic nervous system ganglia are not simply relay stations and their internal synaptic interactions are not well understood. However, it is well established [24] that the neurons of the parasympathetic ganglia release acetylcholine at

Fig. 3.2: Organisation of the autonomic nervous system. The sympathetic system (left) is stimulated by stressful situations, increases HR, cardiac output, blood flow to the muscles and inhibits digestive activity. Stimulation of the parasympathetic branch of the ANS (right) leads to increased digestive activity, and depresses BP, HR, and cardiac output [23]

their terminals whereas norepinephrine (or noradrenalin) is released from the terminals of the sympathetic ganglia. Internal organ regulation is consequently achieved by administering chemical blockers of these agents and norepinephrine is therefore currently used as the clinical standard for measuring the level of sympathetic nerve traffic to the human heart.

Note that the stimulatory frequencies of the branches of the nervous system are much higher than the resultant frequency of the cardiac cycle (HR_{inst}). The vagal and sympathetic simulations do not have a direct effect on the sinoatrial node but change the sensitivity of this region of the heart (in a competing fashion). When the varying levels of stimulation cross a certain threshold, the sinoatrial node is activated. Heart cells have two types of neuromodulatory receptors, one for acetylcholine and one for norepinephrine corresponding to the parasympathetic and sympathetic nervous systems respectively. Their receptors in turn interact with inhibitory or excitatory proteins which, through a series of chemical exchanges, decrease or increase the calcium (Ca^{2+}) in the heart cell membrane and inhibits or stimulates HR and the strength of contraction [25].

The heart's intrinsic pacemaker (the sinoatrial node) causes a HR of around 100 to 120 bpm in the absence of any neurohormonal (nervous and hormonal) influence. However, for a healthy heart with no conduction block, the variation of the heart rate is a manifestation of both the antagonistic effects of the parasympathetic and the sympathetic nerves through changes in acetylcholine and norepinephrine levels, and a resting healthy

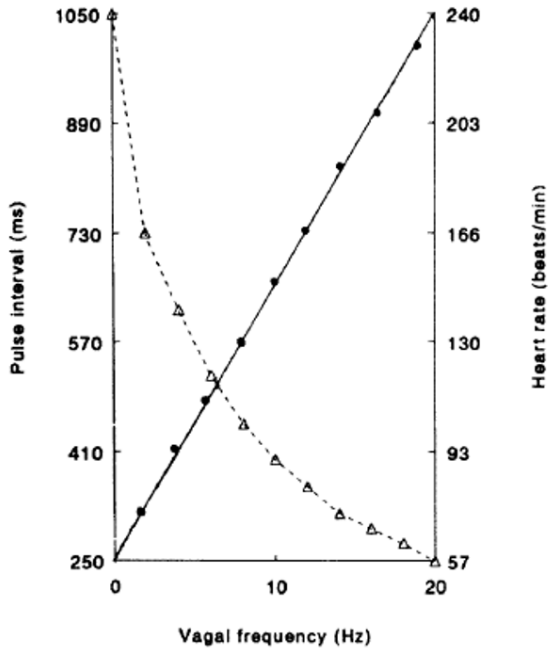

Fig. 3.3: Chronotropic RR interval (-.-) and HR_{inst} (-▷-) responses to graded efferent vagal stimulation (from Malik [1]). Note that the increase in RR interval is proportional to the increase in vagal stimulatory frequency

human is likely to have a heart rate of around 70 to 80 bpm. During rest both autonomic divisions (the sympathetic and parasympathetic) are thought to be tonically active (i.e. they have a minimum baseline activity) with the parasympathetic (vagal) effects achieving dominance [25]. Each set of motor neurons that forms these two nerve divisions interact in a highly complex manner and the modulation of HR cannot simply be interpreted as a linear sum of two opposing effects: a tachycardic response (i.e. increase in HR) from the sympathetic branch of the ANS and a bradycardic response (a slowing of the HR) from the parasympathetic branch, since they act over different time scales. The parasympathetic response is almost immediate (with only a 400 ms latency period) and short lasting, whereas following the onset of sympathetic stimulation there is a delay of up to 5 seconds followed by a steady increase in HR for the next 20 to 30 seconds [26]. Sympathetic activity augmentation is the body's principal method for increasing the HR above the intrinsic level generated by the sinoatrial node to the maximum possible (from about 110 to 200 bpm).

Furthermore, while increased frequency of vagal nerve stimulation tends to slow the beat-to-beat heart rate, HR_{inst} (see Fig. 3.3) and increased frequency of signalling in the sympathetic nerves tends to increase HR_{inst}, at stimulatory frequencies close to that of the sinoatrial node, the cardiac pacemaker can synchronise with the vagal impulses and small increases in vagal frequency may actually cause the HR_{inst} to increase instead. That is, an increase in the frequency of vagal stimulation can cause an almost immediate increase in heart rate, the opposite of the normal response [1].

3.2.1. Reflexes controlling heart rate and its variability

The vagal and sympathetic centres are simultaneously stimulated by many different receptors in the cardiovascular and central nervous systems. These receptors, in general, have either a tachycardic or bradycardic effect on the heart rate. The following summary of HR-modulating response mechanisms is taken from Hainsworth *et. al*. [26]:

Bradycardic Reflexes

- **Baroreceptors** are situated in the adventitia (membranous structure covering the organ) of some arteries and cause increases in vagal and decreases in sympathetic activity. Increases in blood pressure will stretch these vessels and cause a rapid increase in baroreceptor discharge frequency. However, this frequency then rapidly falls to a moderate (but still elevated) level. The receptors quickly reset to change their operating range if a change in pressure continues although chronic resetting can occur over a period of many months. These receptors modulate HR on a beat-to-beat basis through parasympathetic stimulation and over a much longer period through sympathetic nerve stimulation.

- **Carotid chemoreceptors** Stimulation by noradrenalin leads to slowing HR and increases in the rate and depth of respiration. The direct effect on HR changes may be masked by the effect of respiration.

- **Coronary chemoreflex** A slowing of the HR, mainly stimulated by increases in ventricular pressure - thought to be present only in MI patients.

- **Lung hyperinflation** Abnormally large increases in lung volume may stimulate certain pulmonary nerves which innervate the bronchi and lungs and may be stimulated during hyperinflation of the lungs.

- I**ndirect respiratory cardiovascular changes** Pulmonary congestion, embolisms or Intra-Venous (IV) injections of CNS depressants will also cause a bradycardic response.

Tachycardic Reflexes

- **Metabaroreceptors** Situated in the muscle and stimulated by metabolites produced during exercise. Unlike the baroreceptors they do not respond to stretching or pressure.

- **Atrial receptors** Stimulated mainly by stretching from increases in atrial volume with a frequency proportional to the atrial pressure.

- **Aortic chemoreceptors** Stimulation leads to an increase in HR and in the rate and depth of respiration.

- **Muscle receptors** Effort in the muscle groups associated with the cardiovascular system will innervate the heart through stimulation of receptors sited in particular muscles.

- **Lung inflation (moderate pressures)** stimulates airway stretch receptors attached to the myelinated nerves.

- **Baroreflex** Receptors in the arterial and vascular systems sense changes in tension through being stretched by the pressure changes. A decrease in tension (from a drop in BP for example) causes the heart to beat more often and more forcefully while a BP increase produces a bradycardic response.

3.3. Factors influencing heart rate and its variability

Apart from the autonomic regulation of the heart via the sympathetic and parasympathetic motor neurones, the average heart rate HR_{60} and the instantaneous heart rate HR_{inst} are controlled by a variety of other factors.

3.3.1. Intra-patient factors

The following is a list of known changes that can occur for most humans from either internal stimuli or exogenous interventions.

- **Respiratory Sinus Arrhythmia (RSA):** This phenomenon, initially documented by Hales in 1733 [27], is the acceleration of HR_{inst} on inspiration, and its deceleration on expiration. The magnitude of the effect is highly variable (or non-existent in some older or infirm subjects) and tends to be larger the slower and deeper the breathing [1].

  RSA is mainly mediated through changes in efferent vagal activity and its magnitude, and is claimed to provide an index of the level of vagal activity to the heart [28]. RSA is partly influenced by the physical action of the lungs and the cardiac filling volume from the variations in intrathoracic pressure. However, RSA can be observed in the absence of breathing and therefore the mechanism is partly due to a CNS effect [1]. Furthermore, changes in HR similar to those caused by RSA have also been observed in denervated hearts (heart physically disconnected from the CNS by a medical procedure) and this is thought to be related to increased stretching of the sinus node caused by inspiratory increases in venous return [29].

- **Cardiac Output (stroke volume$\times$HR) changes:** At rest, changes in HR between about 80 and 150 bpm have little effect on cardiac output because the increase in HR is compensated for by the decrease in stroke volume. Below about 50 bpm stroke volume tends to be fixed and so cardiac output falls with HR.

- **Valsalva Maneuver:** A respiratory procedure which is thought to provide a rough guide to the integrity of the autonomic neural pathways involved [1]. The sub-

ject takes a deep breath followed by a maximal expiratory effort against a closed glottis. This generates an intra-thoracic pressure of around 100 mmHg which is transmitted to the intra-thoracic and abdominal blood vessels. Initially, pulmonary arterial pressure increases but venous return from outside this region is impaired so the cardiac output falls and BP decreases. The resulting baroreceptor activity causes a rising HR and vascular resistance together with the restoration of mean arterial pressure. On removal of the obstruction, venous return is initially enhanced causing a marked overshoot of BP and baroreflex-mediated bradycardia. Patients suffering from autonomic neuropathy show a sustained fall in pressure during the procedure with little or no compensatory tachycardia or a following BP overshoot and bradycardia.

- **Decreases in Venous Return:** A decrease in the amount of blood returning to the heart can be caused by haemorrhage and postural stress (causing blood pooling). Cardiac filling pressures are consequently reduced (hypovolaemia) and the intravascular volume moves towards the peripheral veins. This normally causes a HR increase in the short term.

- **The Baroreflex and the vasovagal reaction:** The Baroreflex uses arterial and vascular mechanical stretch receptors to adjust the HR if the BP changes. When venous return decreases, BP remains constant or slightly increases while vascular resistance and HR increase. However, despite these increases in vascular resistance and HR this is not enough to compensate for the falling BP from a decreased return in blood volume. Finally if the venous return is too low there may be an abrupt fall in BP and loss of consciousness accompanied by a decrease in vascular resistance and HR. This is known as the vasovagal reaction.

- **Exercise:** This immediately induces an increase in HR through a CNS mediated vagal withdrawal. Metabaroreceptors within the muscle also become stimulated to increase HR further through increased sympathetic activity which vaso-constricts the non-exercising muscles and splanchnic (soft internal organ) circulation. Receptors involved in lung inflation and possibly baroreceptor inhibition also contribute to the process. Less fit, aged or extremely youthful hearts have a lower HR maximum and a higher resting HR. Training increases the amount of cardiac muscle and stroke volume to produce a higher maximum and lower resting HR.

- **Thermoregulation:** Peripheral and core body temperature are controlled by both internal and external factors. This may affect peripheral resistance, the resistance to blood flow in the peripheral blood vessels.

- **Embolisms:** When a small blood vessel is obstructed by fragments of material carried by the blood flow the result is often a tachycardic response as well as the destruction of the organ (in whole or part) that is supplied by this vessel.

- **Intra-venous (IV) injections:** Stimulatory or inhibitory chemicals can be intravenously injected to increase or reduce HR.

- **Circadian Rhythms:** These are defined to be variations in biological activity that appear to have a natural cycle of between 23 and 27 hours, but are often locked into the 24-hour day-night cycle [30] (due to light exposure). The most prominent 24-hour physiological variation in humans is that of the fall in blood pressure and HR for a normal subject while asleep. The factors which affect this variation include the health of a patient's ANS, circulating and local hormones, level of patient awareness and the strength of the heart itself [31].

3.3.2. Inter-patient factors

Although it is possible to expect certain differences in baseline (resting) HR and HRV depending on the type of patient, there are multiple factors that contribute to these differences. It is therefore difficult to categorise or assess patients without using demographic data. The major factors that lead to inter-patient differences in HR and HRV (independently of the intra-patient factors presented in section 3.3.1) are:

- **Genetics and family history:** Although family history can be an important risk factor for cardiovascular disease [32], relatively little is known about the nature of specific genetic risk factors. Research into this area is beginning to grow and some researchers [33] are attempting to identify and characterise genes responsible for inherited disorders in the hope that this information will also provide some insight into common forms of cardiovascular disease.

- **Sex:** The depression of HRV with age tends to be more marked in males and post-menopausal women, supporting the idea that oestrogen provides some form of protection against coronary heart disease [34]. Furthermore, Barrett-Conner *et. al*. [32] found that a positive family history of heart attacks was only independently predictive of death in men and not (pre-menopausal) women.

- **Age:** HRV is lower in the old and very young although this may be masked by the subject's sex and overall level of fitness [34].

- **Medical condition and level of fitness:** High cholesterol levels tend to be associated with lower HRV [34].

3.4. Quantifying HRV

Short term and long term variations in HR are known to have different physiological origins and the magnitude of these variations has been shown to be indicative of the autonomic state of a patient [1]. Over the last 20 years, much effort has been put into quantifying these variations with a view to making clinically useful assessments of patient welfare [19]. This section provides an overview of the metrics (and their relevance to autonomic function) which has been found to be the most useful.

3.4.1. HRV metrics from the RR tachogram

HRV metrics are calculated from an analysis of the RR tachogram; the time series of RR intervals. It is important to note that this is an unusual time series in that both axes are time intervals, one being related to the other. Furthermore, since the variability in HR occurs on a beat-to-beat basis, the time series is inherently unevenly spaced along the horizontal axis. Figure 3.1 (b) illustrates this concept; each circle indicates the location of a beat in time (along the horizontal axis). The horizontal distance between each point (time stamp) is different for each adjacent pair, with the difference recorded on the vertical axis.

There are many ways of assessing HRV and a comprehensive list of metrics investigated since the 1960's are detailed by Malik *et. al* [19]. They can be broken down into three basic categories:

- Geometrical indices.
- Statistical indices and
- Frequency domain metrics.

3.4.1.1. Geometric indices

HRV indices that are generally referred to as geometric (in contrast to time-series methods), attempt to quantify the shape of the histogram of the RR tachogram. According to Malik [1] there are three basic approaches:

1. some measurement of the geometrical form of the histogram is made (e.g. the baseline width or the height of the sample density) and the HRV measure is derived from this number or,
2. the geometrical pattern is approximated by a mathematically defined shape and the HRV measures are derived from the shape parameters, or
3. the general pattern of the geometrical form is classified into one of several predefined categories and the HRV metric is derived on a category specific basis.

The following list of indices is recommended by the Task Force of the European Society of Cardiology and the North American Society of Pacing Electrophysiology [19] and is accepted as the standard for HRV measurement:

- **HRV triangular index (or HRV index):** Total number of all NN (normal-to-normal), intervals formed from the RR tachogram by excluding non-sinus beats, divided by the maximal height of the histogram of all NN intervals measured on a discrete scale with bins of $\frac{1}{f_s}$ seconds, where f_s is the sample rate of the ECG recording.
- **TINN (ms):** Triangular Interpolation of the histogram of the NN intervals. This is calculated by approximating the NN interval distribution to an isosceles triangle and measuring the width of the unequal side (the base).
- **Differential index (ms):** Difference between the widths of the histogram of differences between adjacent NN intervals (hist[δNN(t)]) measured at selected heights.
- **Logarithmic index:** Coefficient, κ of the negative exponential curve $Ae^{-\kappa d}$, which is the best approximation of the histogram of absolute differences between adjacent NN intervals where $d = [|\delta NN(t)|]$ and A is an arbitrary scaling factor. Estimation is usually done by fitting to the log of the distribution. The higher the value of κ, the tighter the distribution and the lower the overall variability.

These methods tend to be relatively insensitive to outliers and are therefore considered to be robust to artefacts and computational errors in the RR tachogram derivation. However, they are sampling frequency and recording length dependent. Furthermore, they do not deal well with multi-modal distributions (often caused by sudden shifts in the baseline HR), concentrating on the dominant peak in the histogram and underestimating the overall HRV. For this reason they tend to be used only on very stable patients with little change in baseline HR over well-defined periods (usually 24 hrs).

3.4.1.2. Statistical indices

Statistical HRV indices are calculated on a beat-to-beat basis and are based on Euclidean root-mean-square (rms) metrics. They are therefore, sensitive to outliers and more suited to hand-edited data (which is usually short term due to the labour-intensive nature of such work). Time series indices are generally broken down into two broad categories [35]:

1. Variables directly derived from the beat-to-beat intervals, such as the mean HR and the standard deviation (SD) for the entire record.
2. Variables based on the differences between adjacent cycles, such as the proportion of differences between adjacent cycles that exceed an arbitrary limit.

The following indices are recommended by the Task Force of the European Society of Cardiology and the North American Society of Pacing Electrophysiology [19]:

- **SDNN (ms):** Standard deviation of all NN intervals (also known as SDRR) usually over 24 hours.
- **SDANN (ms):** Standard deviation of the averages of NN intervals in all 5-minute segments of the entire (24-hour) recording.
- **RMSSD (ms):** The square root of the mean of the sum of the squares of differences between adjacent NN intervals.
- **SDNN index (ms):** Mean of the standard deviations of all NN intervals for all 5-minute segments of the entire (24-hour) recording.
- **SDSD (ms):** Standard deviation of differences between adjacent NN intervals.
- **NN50 (count):** Number of pairs of adjacent NN intervals differing by more than 50 ms in the entire recording; three variants are possible - counting all such NN intervals pairs, counting only pairs in which the first interval is longer, and counting only pairs in which the second interval is longer.
- **pNN50 (%):** Percentage of adjacent NN differing by more than 50 ms over an entire 24-hour ECG recording.

Many variations of these indices have been investigated with varying degrees of success. For instance, Griffin and Moorman [36] showed that neonatal sepsis is associated with a reduced baseline HR variability coupled with short-lived decelerations of HR and consequently the mean and SD of such distributions are often similar to those calculated from the ECG of normal (healthy) neonates. However, Griffin and Moorman found that the observed decelerations significantly altered the third moment of the distribution of one hour RR interval segments. Therefore, measuring this skewness allowed the differentiation between septic neonates and normal neonates up to 24hrs before diagnosis of sepsis in the degenerating group. It should be noted however, that the robustness of higher order moments in the context of HRV has yet to be demonstrated.

3.4.1.3. Frequency domain metrics

Heart rate changes occur on a wide range of time scales; sympathetic changes stimulated by exercise cause an immediate increase in HR resulting in a lower long term baseline HR and increased HRV over a period of weeks and months. Similarly, a sudden increase in blood pressure (due to an embolism for example) will lead to a sudden semi-permanent

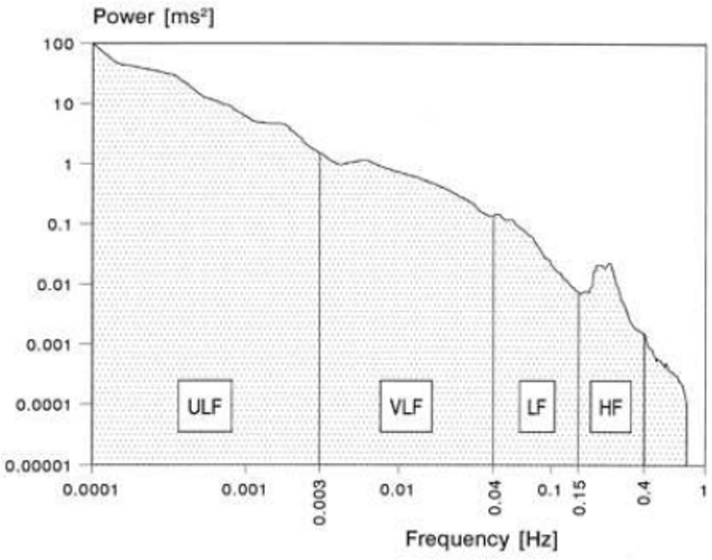

Fig. 3.4: Typical FFT of RR intervals over 24hr [19]. Note that the Meyer waves are masked by the power spectral dominance of the VLF and ULF contributions

increase in HR. However, over many months the baroreceptors will reset their operating range to cause a drop in baseline HR and BP. In order to better understand the contributing factors to HRV and the time scales over which they affect the heart it is useful to consider the RR time series (or tachogram) in the frequency domain.

Components in the long term Power spectral analysis was first introduced into HRV analysis in 1981 by Akselrod *et. al.* [37]. Since then many authors have applied a variety of power spectral estimation techniques. In order to facilitate inter-study comparisons, the frequency spectrum of an RR interval tachogram has been split (by definition) into four frequency bands:

- Ultra Low Frequency (ULF) 0.000 Hz$\geq$ULF$\leq$0.0003 Hz
- Very Low Frequency (VLF) 0.0003 Hz$\geq$VLF$\leq$0.04 Hz
- Low Frequency (LF) 0.04 Hz$\geq$LF$\leq$0.15 Hz
- High Frequency (HF) 0.15 Hz$\geq$HF$\leq$0.4 Hz

Figure 3.4 shows a typical 24-hour Power Spectral Density (PSD) with the above bands marked (using logarithmic scales on axes). Over such a period, frequencies below 0.04 Hz (VLF and ULF) become dominant.

The motivation for splitting the spectrum into these frequency bands lies in the belief that the distinct biological regulatory mechanisms that contribute to HRV act at frequencies that are confined (approximately) within these bands. Fluctuations below 0.04 Hz in the VLF and ULF bands are thought to be due to long-term regulatory mechanisms such as the thermoregulatory system, the reninangiotensin system (related to blood pressure

and other chemical regulatory factors) and other harmonalumoral factors [38]. In 1998 Taylor *et. al.* [39] showed that the VLF fluctuations appear to depend primarily on the parasympathetic outflow. In 1999 Serrador *et. al.* [40] demonstrated that the ULF band appears to be dominated by contributions from physical activity and that HRV in this band tends to increase during exercise. They therefore, assert that any study that assesses HRV using data (even partially) from this frequency band should always include an indication of physical activity patterns.

Components in the short term It is generally accepted in the clinical community that the HF band is a measure of the parasympathetic outflow [38]. However, the physiological interpretation of the LF band is more controversial and although sympathetic and parasympathetic mechanisms can operate at these frequencies many authors ascribe fluctuations in the LF band to sympathetic activation only [41].

Consider Fig. 3.5 where Auto-Regressive (AR), discussed in section 7.3.2, analysis has been used to generate the PSD of a 10 minute RR tachogram. We are only interested in the region below 0.4 Hz since the respiratory modulation frequency is the highest component of the HRV signal and this is rarely above 20 respiration per minute (rpm) (about 0.33 Hz). Two distinctive peaks are usually observed in the PSD, the lower frequency (around 0.1 Hz) being referred to as Meyer waves and the higher frequency component (around 0.25 Hz) being attributed to respiration effects.

The $\frac{LF}{HF}$ ratio and sympathovagal balance Rhythms within the HF band, synchronous with the respiration rate, are due to the intra-thoracic pressure changes and mechanical variations caused by the action of breathing. The high frequency peak (above 0.15 Hz) is mediated almost exclusively by fluctuations of the vagal-cardiac nerve activity [41] and is generally accepted as a marker of parasympathetic activity [42]. The peak around 0.1 Hz corresponding to the Meyer waves is mostly mediated by fluctuations of sympathetic nerve activity. Although sympathetic and parasympathetic mechanisms are involved in the LF band, an increase in LF power has always been observed as a consequence of sympathetic activation such as rest-tilt manoeuvres, mental stress, haemorrhage, and coronary occlusion [38]. An increase in LF power is therefore accepted as a marker of sympathetic activation by many authors [43].

Since physiological interventions produce reciprocal changes of sympathetic and vagal outflows (over a limited range of arterial pressure; however, some physiological interventions provoke parallel changes [41]) it has been suggested [27, 41, 44] that the balance between these opposing neural regulatory mechanisms can be quantified by the ratio of the power in the LF to the power in the HF band ($^{LF}/_{HF}$) which is then taken as a measure

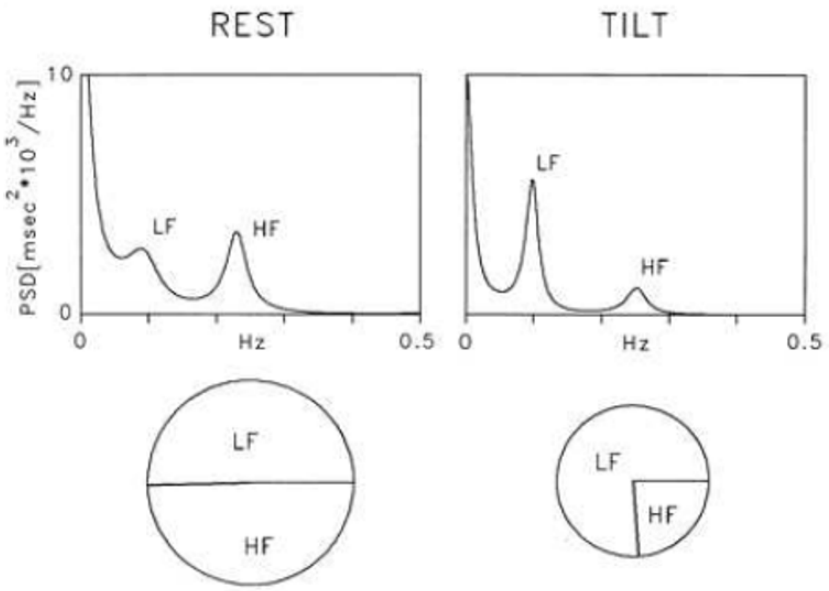

Fig. 3.5: AR spectral analysis (model order 12, 10 minute window) of an RR tachogram in a healthy subject at rest and during 90^o head-up tilt. At rest, two major components of similar power are detectable at low frequencies (LF) and high frequencies (HF). During tilt, the LF component becomes dominant, but as total variance is reduced, the absolute power of LF appears unchanged compared with that at rest. Normalisation leads to predominant LF and smaller HF components, which express the alteration of spectral components due to tilt. The pie charts show the relative contributions from each band together with the absolute power of the two components represented by the area [19]

of the sympathovagal balance. Although this metric is generally thought to quantify the relative contributions of the two branches of the CNS, this idea remains a topic of much debate amongst clinicians. However, there is a consensus that this is a useful model for clinical applications [45].

For instance, clinical studies [46, 47] have presented evidence that the $^{LF}/_{HF}$ ratio is the best indicator of post-MI mortality up to one year from discharge, although Valkama *et. al.* [47] showed that only changes in the HF band are relevant for assessment of post-MI convalescence. However, there are two problems with the use of the sympathovagal balance for studying cardiac problem related patients. First, their norepinephrine levels may not change or they may decrease (rather than the usual increase for healthy subjects) when sitting upright, thus confusing any averages taken over an extended period. Second, these patients may have unusually high levels of muscle sympathetic nerve activity and norepinephrine levels with low SD of RR intervals and a low $^{LF}/_{HF}$ ratio [41]. The measure must therefore be considered on a patient specific basis. In fact sympathovagal balance is only considered to be useful in patients with less advanced stages of heart failure, with little guidance as to which exact criteria identify such patients [41].

Eckberg points out that normalised 0.1 Hz RR interval spectral power changes bear

no significant relation to baseline levels or baroreflex-mediated changes to sympathetic nerve activity (as measured by changes in myocardial norepinephrine) [41]. Furthermore, although there is a quantitative relation between respiratory frequency RR interval (HF) spectral power and vagal-cardiac nerve activity, moderate changes of this activity away from the baseline do not alter this HF power. Conversely, large changes of HF RR interval spectral power provoked by respiratory changes may not reflect changes of vagal-cardiac activity. Therefore any analysis must take into account the respiratory changes that occur during the period under analysis. It has therefore been suggested that power in the HF band is too problematical to measure in most circumstances and that frequency domain measures should concentrate on the lower end of the spectrum. Signorini *et. al*. [48] claim that only the contributions below 0.1 Hz help define the differences between pathological and non-pathological conditions. These results have been corroborated by the work of Teich *et. al*. [49] in a study to determine which HRV indices proved the most able to differentiate between pathological cases. They found that the indices which were best able to differentiate between pathological and normal clinical states all relied on a variability calculation equivalent to computing the PSD in the LF range. However, it is clear that the power in the HF band does carry information about the beat-to-beat variability of the heart and its ability to function in a healthy manner. For example, La Rovere *et. al*. [50] and McClements [51] have shown that the HF as well as the LF metrics may be useful in long term prediction of post-MI. Furthermore, the wealth of clinical studies that have presented evidence for the $^{LF}/_{HF}$ ratio being an excellent indicator of recovery [19, 46] and even the HF band alone [47], illustrates that it would be unwise to discount the HF metric completely at this stage.

The majority of the literature in the field of HRV analysis has demonstrated that frequency domain metrics, rather than time series or geometric metrics, are the most useful indices for assessing patient welfare and differentiating between patient groups [19]. This thesis will therefore concentrate on frequency domain metrics. Furthermore, the origin of long term HRV metrics is unclear and estimates of them may be influenced by factors as diverse as local conditions (e.g. temperature) [1] and quality of sleep [52]. However, short term metrics have been shown to be capable of assessing neurological activity [1, 19] and therefore may have a clinical interpretation as well as be more amenable to controlled experimentation. The scope of this thesis is thus further narrowed to include studies on only the short term (LF and HF) HRV metrics.

3.5. The clinical utility of Heart Rate Variability

HRV is probably a less straightforward measure of autonomic system activity than plasma catecholamine concentration, baroreflex sensitivity measured by response to phenylephrine response, or sympathetic activity as measured through microneurography (a technique for measuring electrical signals from human peripheral nerves using a tungsten microelectrode). However, there exists a consensus [1] that HRV does give a useful quantification of ANS activity.

Recently Nolan *et. al*. [53] have pointed out that Chronic Heart Failure (CHF) is associated with autonomic dysfunction, which can be quantified by measuring HRV. They showed that a reduction in HRV identifies patients at high risk of death and that HRV is a better predictor of death due to progressive heart failure than other conventional clinical measurements, such as elevated BP, the cardiothoracic ratio, the ratio of the maximal transverse diameter of the cardiac silhouette to the distance between the internal margins of the ribs at the level of the right hemidiaphragm, left ventricular end-diastolic diameter and the presence of non-sustained ventricular tachycardia. Their results show that high-risk subgroups can be identified by HRV and elected as candidates for additional therapy.

3.6. Standard terminology

When using time-domain indices, it was recommended [19] that at least two of the following four measures are used: SDNN and HRV triangular index for an estimate of overall (long term) HRV, SDANN for an estimate of the long-term components of HRV and RMSSD. The choice should be specific to the type of medical condition being considered and the type of data that it is possible to collect. Furthermore it is inappropriate to compare time domain measures, especially for long term recordings that are derived from ECGs of different time lengths. For frequency domain measures the number of samples used for the calculation, the size and type of spectral window used and the method of calculating the power in respect of the window should be reported to allow inter-study comparisons [19]. Furthermore, when using parametric methods, the type of model, the number of samples, the central frequency for each component and the model order should be quoted. Reporting statistics to test the reliability of the model (such as the prediction error whiteness test for goodness of the fit and the optimal order test to check the suitability of the model order used) is also important.

3.7. Measurement standards

For long duration recordings (usually in the time domain) the Task Force recommends at least 18 hours for long term HRV analysis. However, Haaksma *et. al*. [54] performed an in-depth study of the influence of different time segments on HRV and found that at least 20 hours of data were required for time domain variables or total power in frequency analysis. The Task Force recommends avoiding the use of frequencies below LF in the PSD for HRV assessments as the major constituent of VLF is the non harmonic component which is strongly affected by algorithms for baseline or trend removal. The Task Force also recommends that if the LF and HF are normalised by TP (the total power minus the VLF and ULF contributions) then both the values for the absolute and normalised calculations should be recorded. Furthermore, it should be noted that components of HRV provide a measure of the degree of autonomic modulation rather than the level of autonomic tone: the averages of the modulations do not represent an average level of tone. There is, therefore, a great deal of inter-patient variation. Other significant recommendations include:

- ECG sampling rates between 250 Hz and 500 Hz
- Careful checks to ensure baseline or trend removal does not affect the frequencies of interest
- Use of an accepted and accurate fiducial point detector to identify a stable and noise-independent beat location
- Use of appropriate interpolation techniques, especially in the presence of artefact or ectopic beats
- Careful thought as to whether the artefact and ectopic rejection criteria cause a bias in analysing the data that is not discarded
- Reporting the relative number and relative duration of RR intervals that were omitted and interpolated
- Reporting the type of interpolation algorithm and frequency of resampling
- Frequency domain methods to be preferred to time domain methods for short term recordings. The recording should be at least 10 times the lower frequency bound of the investigated component.
- Short term HRV assessment to be carried out on 5-minute segments, 24-hour indices recommended to assess intervention therapies.

- Environmental variables to be controlled as much as possible during long-term ECG recordings (nature of physical activity as well as mental and emotional state)
- Consideration of whether it is appropriate to compare HRV across patient groups and
- Simple automatic editors of RR sequences (such as static timing thresholds) not to be used since they are known to have undesirable effects leading to potentially serious errors.

Sampling rates In the same year that Malik *et. al*. published the recommendations, Aboud and Barnea [55] showed that a sampling frequency of 128 Hz is sufficient, in patients with normal HRV levels, to give a large enough signal to noise ratio in the RR tachogram. However, for patients with significantly lower levels of variability (such as heart transplant patients) they found that a sampling rate of at least 1000 Hz is required.

3.8. Clinical applications of HRV

HRV assessment is considered by the task force on HRV Standards [19] as useful in the following clinical conditions:

- Assessment of risk after acute MI - Depressed HRV is a powerful predictor of mortality and of arrhythmic complications. The predictive value of HRV is independent of other factors established for post-infarction risk stratification (such as depressed Left Ventricular Ejection Fraction (LVEF). and increased ventricular ectopic activity) [1, 56].
- Prediction of mortality - For prediction of all-cause mortality, HRV is similar to that of LVEF [19, 57].
- Prediction of arrhythmic events - HRV is superior to LVEF in predicting arrhythmic events such as sudden cardiac death or ventricular tachycardia [19, 57].
- Assessment of Myocardial Dysfunction - Most patients with a very advanced phase of the disease and a drastic reduction in HRV show little or no LF component, despite clinical signs of sympathetic activation. Therefore, in conditions characterised by a marked and unopposed persistent sympathetic excitation, the sinus node seems greatly to diminish its responsiveness to neural inputs.
- Assessment of outcome after cardiac transplantation - post-operative HRV is highly depressed [58, 59, 60]. In 1995 Bernardi *et. al*. [61] conducted a large study to measure HRV in response to carotid baroreceptor stimulation in 26 heart transplant

recipients at 2 to 63 months after transplantation and found no evidence for return of parasympathetic control of heart rate during this period.

- Assessment of Diabetic Neuropathy - A reduction in the time domain parameters of HRV not only carries a negative prognostic value but also precedes the clinical expression of autonomic neuropathy.

- Tetraplegia patients (patients with chronic complete high cervical spinal cord lesions that have intact efferent vagal and sympathetic neural pathways directed to the sinus node) represent a unique clinical model to evaluate the contribution of supraspinal mechanisms in determining the sympathetic activity responsible for LF oscillations of HRV since spinal sympathetic neurons are deprived of modulatory control and in particular of baroreflex supraspinal inhibitory inputs.

In 1996 Malik *et. al*. [19] produced a summary of selected studies investigating the clinical value of HRV in cardiological diseases other than those reported above. They also point out that there are several well reported intervention strategies that lead to changes in a patient's HRV, namely,

- $\beta-$**blockade:** $\beta-$blockers cause modest increases in HRV, although they prevent the normal rise in the LF component observed in the morning hours. In conscious post-MI dogs, $\beta-$blockers do not modify HRV. Importantly, $\beta-$blockade increases HRV in the animals destined to be at low risk for lethal arrhythmias post-MI.

- **Anti-arrhythmic drugs:** These tend to decrease HRV.

- **Scopolamine:** Low dose muscarinic receptor blockers markedly increase HRV indicating an increase in vagal activity. However, the efficacy during long term treatment with this drug is not known.

- **Thrombolysis:** HRV is higher 90 minutes after thrombolysis in patients with patency of the infarct related artery. The difference is not evident in a 24 hour assessment.

- **Exercise Training:** Exercise training over a reasonable period of time significantly increases HRV and regular exercise is thought to modify the autonomic balance. Exercise can also accelerate the recovery of the physiological sympathovagal interaction, as shown in post-MI patients.

3.9. The problem of HRV measurement and repeatability

Although commercial systems for HRV measurement and assessment are available, no existing techniques are considered to be accurate or meaningful enough by clinicians to

provide robust measures of patient welfare and outcome prediction [1]. The following points highlight the main reasons for this:

1. In 1993 the FDA stopped approving HRV monitors because they felt the there was no consensus on the usefulness or applicability of HRV measurements [62]. Furthermore there was a lack of methods or studies to attest to the accuracy and validity of the methodologies of the commercial manufacturers.

2. Pre-processing methods for the RR time series tend to be arbitrary and adhoc. Data is selected based on its usefulness for the study and lack of artefact. Therefore the techniques are rarely transferable to other studies.

3. Long term HRV metrics include beat-to-beat variations as well as definite shifts in the overall heart rate. A shift into tachycardia or bradycardia will lead to a rise in the contribution to the HRV measure employed, yet the intrinsic variability may be quite low. Detrending techniques are often employed to remove such shifts, yet these changes are part of the overall HRV.

4. The non-linear and non-stationary nature of HRV leads to abrupt changes in the signal so that HRV metrics are highly susceptible to outliers and artefacts. The complex variations of the RR intervals are due to many interacting stimuli on many different time scales with different magnitudes. It is difficult to choose the window over which to assess HRV and an appropriate weighting for each scale (or contribution). For example, is a small change in the parasympathetic control more relevant than a slightly larger change in the sympathetic control?

5. Drugs are continually administered to an ITU patient and dominate the changes in HRV, seriously affecting the clinical utility of such measures.

6. The problem of inter-patient comparability - Due to significant inter-patient variation within similar groups it is difficult to ascribe definite values of HRV metrics to delineate pathology from normal behaviour.

3.10. Discussion and conclusions

In this chapter the regulation of heart rate from different branches of ANS was discussed. The fundamental ideas and the most commonly used measurement techniques of HRV were briefly presented. Appropriate clinical applications and some of the results obtained with different HRV analysis technique were also presented.

The information provided in these introductory chapters will provide the basis for the chapters to follow where the focus will be to explore systematically approaches for the

frequency domain analysis of heart rate variability. Issues such as error introduced by the signal representation, effect of ectopic beats on the power spectrum of the signal and the effect of trend removal techniques will be evaluated using simulated and real data. Knowledge gained from such approaches will serve as tools in the HRV analysis from a group of patients undergoing local anaesthesia.

The data that will be used for the HRV analysis in this study were taken from a group of patients undergoing local anaesthesia. Before discussing the steps involved in HRV analysis (ECG characterisation, ectopic beat detection, signal representation etc.) a brief introduction in local anaesthesia will be given in the next chapter. Also, the details of the study protocol and the methodology will be described.

4 Local anaesthesia

4.1. Introduction

Local anaesthesia is an anaesthetic technique that reversibly inhibits the propagation of signals along nerves. When it is used on specific nerve pathways, effects such as analgesia (loss of pain sensation) and paralysis (loss of muscle power) can be achieved. Depending on their structure, the different nerves show varying susceptibility to the effects of anaesthesia. Local anaesthetic drugs act mainly by inhibiting sodium influx through sodium-specific ion channels in the neuronal cell membrane, in particular the so-called voltage-gated sodium channels. When the influx of sodium is interrupted, an action potential cannot arise and signal conduction is inhibited [63]. There are various drugs available that could be used as local anaesthetic agents. At present some of the most commonly used local anaesthetic agents in clinical practise include Prilocaine, Lidocaine, Mepivacaine, Bupivacaine and Lignocaine.

4.2. Side effects

At their respective toxic plasma levels, all local anaesthetics can have side effects on the cardiovascular or central nervous systems. The higher the plasma levels and the quicker the rate of increase, the more pronounced are the symptoms [63].

4.2.1. Central nervous system complications

Central nervous system toxicity may cause generalised seizure and/or central respiratory paralysis. The warning sign for this includes restlessness, metallic taste, muscle twitches, slurred speech and tinnitus. High toxic levels could also be reached very rapidly, usually in case of an intravascular injection, resulting in a primary generalised seizure or coma without any warning [63].

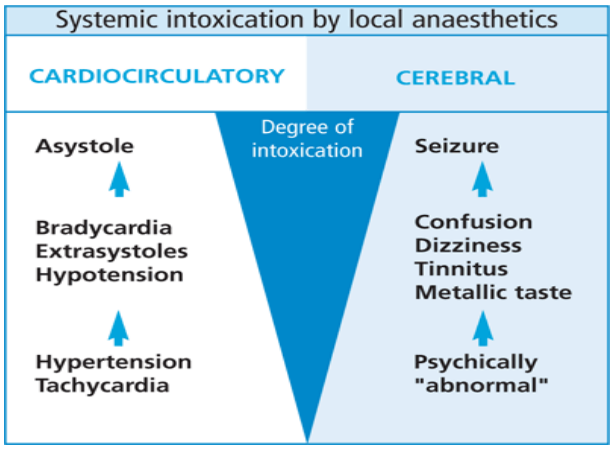

Fig. 4.1: Symptoms shown by central nervous system and cardiovascular system with increasing level of local anaesthetic intoxication [64]

4.2.2. Cardiovascular complications

The conductive system of the heart is quite sensitive to the action of local anaesthetics. Complications of the cardiovascular system may include disturbances of pacemaker activity, excitability and conduction: bradycardia, signs of A-V block, arrhythmia, asystoles, negative inotropia, decreased cardiac output, and hypotension [63]. Usually, the central nervous system shows symptoms of toxicity before complications with the cardiovascular system when the blood plasma level of local anaesthetic increases.

The only exception is Bupivacaine, which can cause cardiac arrhythmias without any signs of central nervous system toxicity. This Bupivacaine cardiotoxicity is caused by a dose-dependent depression of ATP synthesis. Most patients recover from central nervous system intoxication without any major problems if appropriate measures are taken immediately. Cardiovascular complications on the other hand may have serious consequences. Therefore, the symptoms of intoxication of the central nervous system and specially the cardiovascular system should be strictly monitored to ensure safe administration of local anaesthetics. With increasing level of plasma intoxication different symptoms can occur in the cardiovascular and the central nervous system and this is shown in Fig. 4.1.

Other side effects which are not very common include allergic reaction and methemoglobinemia [65]. Methemoglobinaemia can occur while using Prilocaine and as it reduces the amount of haemoglobin that is available for oxygen transport, this side effect is potentially life-threatening. Therefore, dose limits for Prilocaine should be strictly observed.

4.3. Brachial Plexus block

Brachial plexus block is a local anaesthetic technique applied to patients having surgical procedures on their forearms, wrist or hands. In this research project we have studied patients undergoing such procedures using this anaesthetic technique.

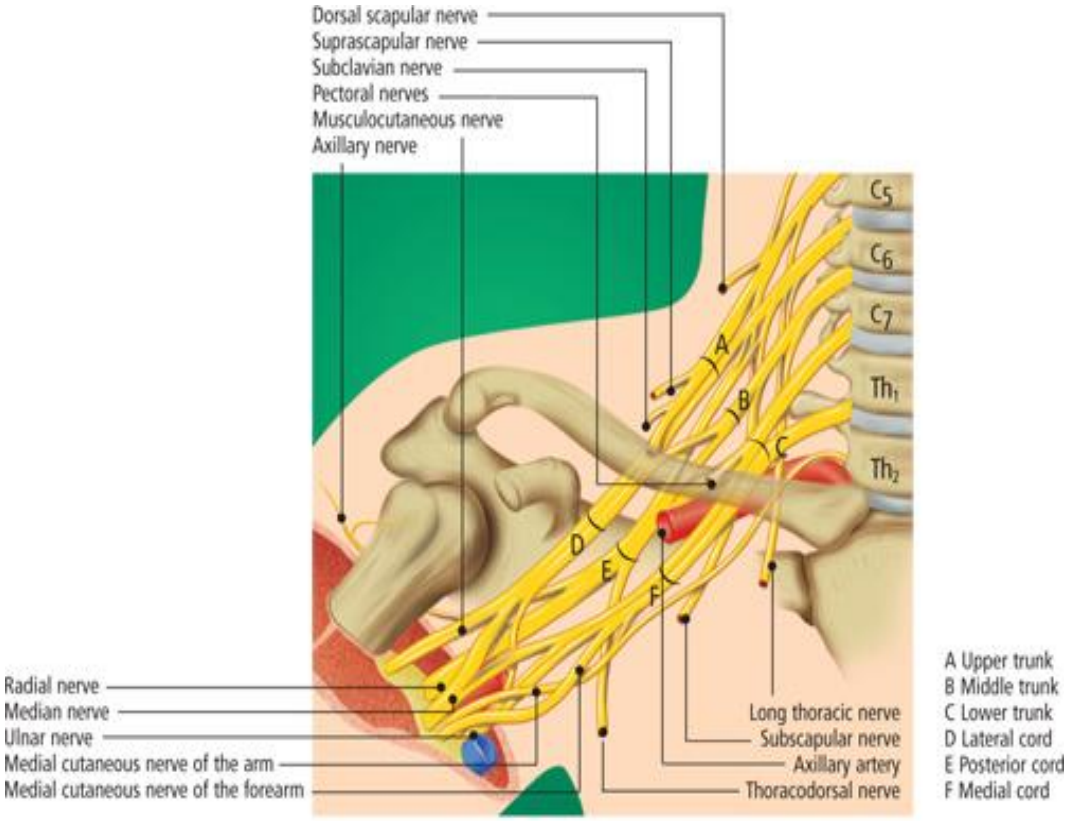

Fig. 4.2: Anatomy of Brachial plexus [64]

To anaesthetise the arm, local anaesthesia was applied in close proximity of the nerve fibre arrangement called Brachial plexus, in the axilla (armpit region). The process of injecting local anaesthetic is called regional nerve blockade or more simply, a nerve block, and it is a common procedure in anaesthesia.

The brachial plexus is formed from the ventral roots *C5* to *Th1*, with small additions from *C4* and *Th2* (see Fig. 4.2). The 5^{th} and 6^{th} cervical nerves unite to form the upper trunk, which continues on to become the major component of the lateral cord. The ventral root of the 7^{th}cervical nerve becomes the middle trunk and together with portions of the upper and lower trunk continues on to become the posterior cord. Ultimately, the 8th cervical nerve and the 1st thoracic nerve unite to form the lower trunk, which together with portions of the middle trunk becomes the medial cord [64].

The brachial plexus passes through the posterior scalenus gap relatively close to the surface between the scalenus anterior and scalenus medius muscles. A short distance away, it leaves the suprascapular nerve, which primarily supplies the shoulder joint, exiting from the upper trunk to the dorsal [64]. The trunks subsequently divide to form the individual cords just above the clavicle (see Fig. 4.2).

The axillary artery is encased together with the cords in a common sheath which runs beneath the clavicle in the direction of the axilla. This neurovascular sheath should run from the deep cervical fascia to the axilla. Before reaching the axilla, the plexus divides

Fig. 4.3: Different approaches used for Brachial plexus block [66]

into the following nerves:

- Musculocutaneous nerve from the lateral cord
- Median nerve from the lateral and medial cords
- Ulnar nerve from the medial cord and
- Radial, axillary and circumflex humeri nerves from the posterior cord.

Depending on the site of surgery four different approaches of brachial plexus can be used, these include interscalene approach, supraclavicular approach, vertical approach and axillary approach as shown in Fig. 4.3.

In general the interscalene approach is used for proximal surgery, including the shoulder; the supraclavicular route is used for upper arm, elbow and radial aspect of the midforearm; and the axillary approach is used for hand, wrist and lower forearm surgery.

In this study, axillary approach was used because of its suitability for the surgical procedure, simplicity and relatively few side effects. For this technique the puncture site is located slightly above the axillary artery, at the highest point in the axilla and slightly beneath the pectoralis major muscle which borders the axilla to the ventral. On successful completion of the block, the arm is fully anaesthetised and ready for surgery after onset of about 10 to 15 minutes. The main complication from this block is the possibility of

haematoma formation as a result of arterial puncture. Also, high upper arm tourniquet may be poorly tolerated because the medial upper arm is supplied by the intercostobrachialis nerves (*Th2*) and the lateral upper arm by the axillary nerve (which is usually not blocked). Frequent gaps in the area of the musculocutaneous nerve and the radial nerve are another disadvantage. These technique-related weaknesses can be compensated by carrying out secondary peripheral blocks of isolated nerves.

4.4. Subjects and protocol

After obtaining approval from the Local Research Ethics Committee and informed written consent, fourteen ASA (American Society of Anesthesiologists; scale 1 to 5, with 5 the most critically ill patients) I and II patients (7 males and 7 females) mean age 50.6 ± 20.7 years and mean weight 67 ± 15.3 Kg undergoing elective general surgery under local anaesthesia were recruited to the study. The study was observational and patients' surgical, anaesthetic and monitoring management were as per routine. Patients with known cardiovascular and respiratory problems and those suffering from diabetes were excluded from the study. All the patients were null by mouth twelve hours before the operation. One of the patients included in the study (patient # 12) was categorised as anxious by medical staff before the start of the procedure. All patients were haemodynamically stable and well oxygenated.

In all cases the axillary approach (see section 4.3) was used for the brachial plexus block. A combination of 30 ml of 1% Lignocaine and 29 ml of 0.5 Bupivacaine with 1:200000 part Adrenaline was used as anaesthetic agent.

An AS/3 Anaesthesia Monitor (Datex-Engstrom, Helsinki, Finland) was used to collect lead II ECG signals from the patients. The ECG signal was digitised at 1 kHz sampling frequency using a PCMCIA 6024E 12-bit data acquisition card (National Instruments Corporation, Austin, Texas). Prior to the acquisition of ECG signals the patient was asked to lie on the bed silently during the monitoring. In order to avoid any excess mental activity the patients were asked not to listen to music or use any kind of reading material during the study. The monitoring of ECG signals started in the ward approximately thirty minutes before the application of the block. The monitoring continued while the patients were moved to the anaesthetic room approximately fifteen minutes before the application of the block so that baseline readings were not affected by movement. After the application of the block the patients were moved in the adjacent recovery room where they stayed there for at least thirty minutes or until the time of the surgery. In very few cases the recording of the ECG signal was stopped when the patients were moved to the operating theatre. The ECG monitoring continued during the surgery in the operating

Table 4.1.: Details of patients included in the study of HRV during local anaesthesia

Pat. #	Gender Female (F)/male (M)	Age (years)	Weight (kg)	Type of operation	Illness/specific condition
1	F	73	66.8	Fasciotomy left palm	non smoker
2	F	21	63.0	Exploration bone graft right hand	non smoker
3	M	25	58.0	Exploration of laceration web space left hand	non smoker
4	F	37	70.5	Thumb tip reconstruction	non smoker
5	F	53	51.3	Ligament transfer	non smoker
6	M	59	79.3	Dermofasciectomy left plam	smoker 12-15 cigarettes a day
7	F	72	85.7	Right carpal tunnel decompression	smoker 20 cigarettes a day
8	F	22	46.8	Exploration of laceration right palm	non smoker
9	M	67	87.1	Fasciotomy and z-plasty left hand	non smoker
10	M	21	54.4	Debridement laceration right hand, removal of foreign body, skin graft	non smoker
11	M	62	48.9	Tendon repair left hand	non smoker
12	F	69	80.8	Joint replacement fingers right hand	non smoker
13	M	72	83.0	Dermofasciectomy right hand and skin graft	non smoker
14	M	52	81.8	Excision rheumatoid nodule left elbow	non smoker

theatre and ended approximately thirty minutes after the end of surgery. In the operating theatre during the surgery the patients were given extra sedative (Midazolam, 2 mg) if required. Table 4.1 provides more details for all patients recruited in this study.

5

Development of R-wave detection algorithm using digital filter algorithm

5.1. Introduction

The starting point in any HRV study involves the extraction of Interbeat Interval (IBI) information from the ECG signal. The time interval between consecutive heart beats is customarily measured in the ECG signal from the beginning of a QRS complex to the beginning of the next QRS complex. But in practice due to a noisy environment and low amplitude ECG signal sometimes it is difficult to locate this reference (fiducial) point, therefore the R-wave peak, which has a bigger amplitude and better frequency resolution, is used as the reference point. Defining the time of occurrence of two consecutive R-waves as $r_i(t)$ and $r_{i+1}(t)$, i = 1, ... , N, the expression $x(t)= r_{i+1}(t)-r_i(t)$ is obtained for a time period in milliseconds or seconds. This $x(t)$ is called the RR interval time series or the tachogram as presented in Fig. 5.1.

As the purpose of the measurement is to study the variability in the RR interval, the algorithms for the detection of the R-wave should be able to take into account the physiological variability of the QRS complexes and also the presence of various types of noise that can be present in the ECG signal. Noise sources include electromyograph (EMG) noise, motion artefact, power-line interference, baseline wander, and T waves with high

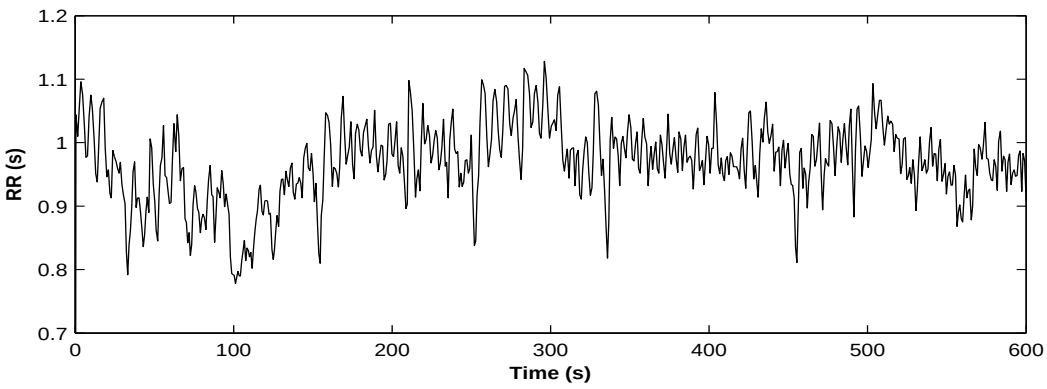

Fig. 5.1: RR interval time series (tachogram)

frequency characteristics similar to QRS complexes. It is also important to keep the deviation from the exact location of the R-wave minimum. The algorithm developed to detect the R-wave peaks of the ECG signals acquired from the locally anaesthetised patients in real time is discussed in the following section.

5.2. Implementation of R-wave detection algorithm using a digital filter

In order to reduce the influence of the artefacts, improve the Signal-to-Noise Ratio (SNR) and maximise the QRS energy, a digital bandpass Finite Impulse Response (FIR) filter with a passband approximately 5-15 Hz [67, 68, 69], which can be represented mathematically as shown in Eq. 5.1, was used.

$$y(n) = \sum_{k=0}^{N-1} h(k)x(n-k) \tag{5.1}$$

Where $h(k)$ is the impulse response of the filter and $x(n-k)$ represent the data samples. The FIR filter was used because of its linear phase characteristics. The filter was implemented using the optimal (Equiripple) design method, as these filters meet the given arbitrary specifications with a minimum filter order [70]. The filter and the peak detection algorithm was implemented in *Matlab 6.5* environment using the available filter design and signal processing toolboxes. At the sampling rate of 1000 Hz the filter turned out to be a type 1 (positive symmetry) 151 tap filter and achieved at least 20 dB attenuation in both the stopbands. The delay caused by this filtering process turned out to be 75 samples i.e. 0.075 seconds. The response of the filter is shown in Fig. 5.2.

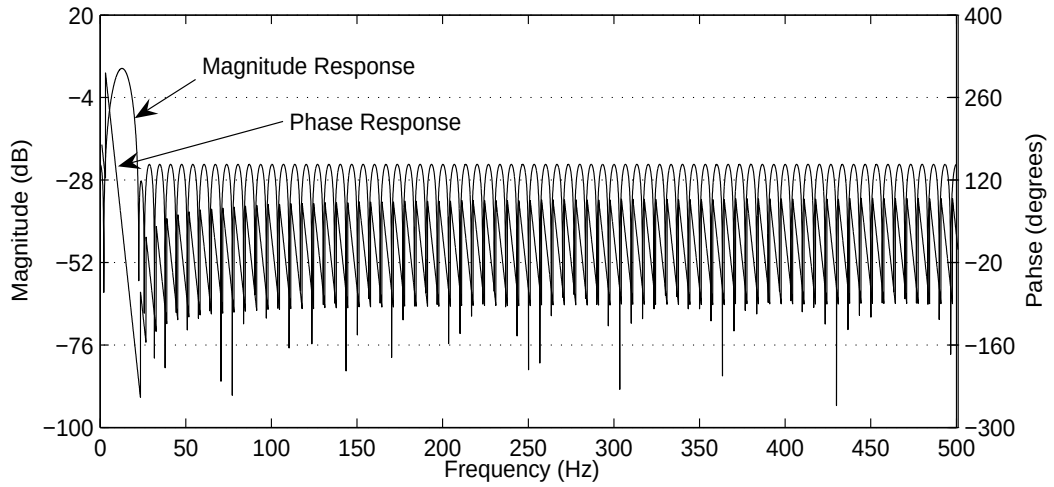

Fig. 5.2: Magnitude and Phase response of the bandpass filter used for QRS enhancement

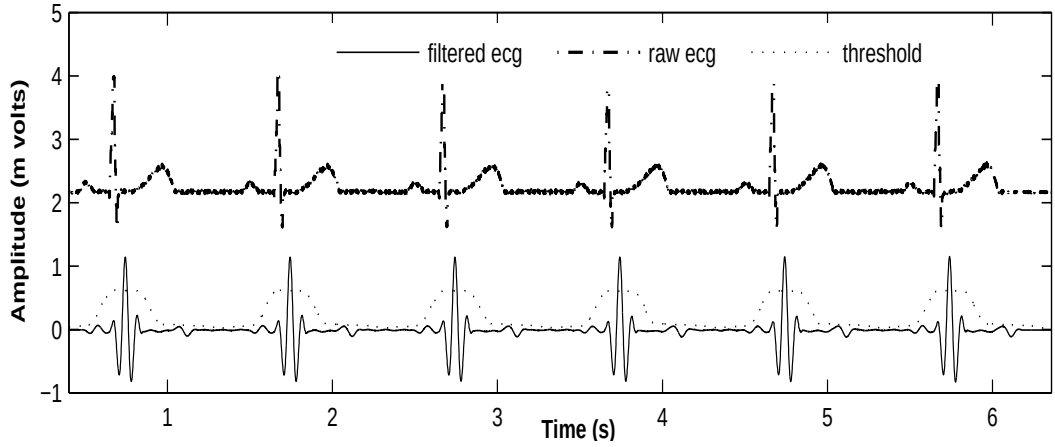

Fig. 5.3: Simulated ECG signal, filtered signal and threshold used for QRS detection

5.2.1. Adaptive threshold

After filtering the ECG signal a threshold was built to detect the QRS complexes by convolving the absolute value of the filtered signal with a square window of 300 samples and multiplying it by a constant (0.00615). This constant was found empirically to give the best detection results in the simulated and volunteers ECG signals. A simulated ECG signal along with the filtered signal and the threshold obtained using the above explained procedure is shown in Fig. 5.3.

The filtered signal clearly indicated that except the QRS complex, the other parts of the ECG signal are suppressed to avoid false peak detection. The peak of each wave in the filtered ECG signal corresponds to the R-wave peak of the QRS complex in the raw ECG signal. Therefore the R-wave is detected by first finding the region of the filtered ECG signal that is above the threshold and then looking for the maximum value in this region. The exact position of the R-wave peak in the raw ECG is obtained by subtracting 75 ms from the location of the peak detected in the filtered signal; subtraction is done to compensate for the delay caused by the filter.

Since the human normal heart rate is not expected to increase more than 150 bpm in resting condition, and in order to avoid detection of high amplitude T wave and other noise peaks as R-wave, a refectory period of 400 ms has been used after a valid R-wave was found. An average of the amplitude of the last three detected R-waves was also maintained and a peak was considered a valid R-wave if its amplitude was bigger than 0.2 and smaller than 2.5 of the average amplitude. This restriction reassures that very large peaks, caused by sudden movement, and very small peaks are not mistakenly identified as normal QRS peaks even if the ECG signal crosses the threshold at these positions. Figure 5.4 presents the results obtained by processing an artefact free simulated ECG signal. This ECG signal consists of 36 heart beats with heart rate varying from 30 to 120 bmp.

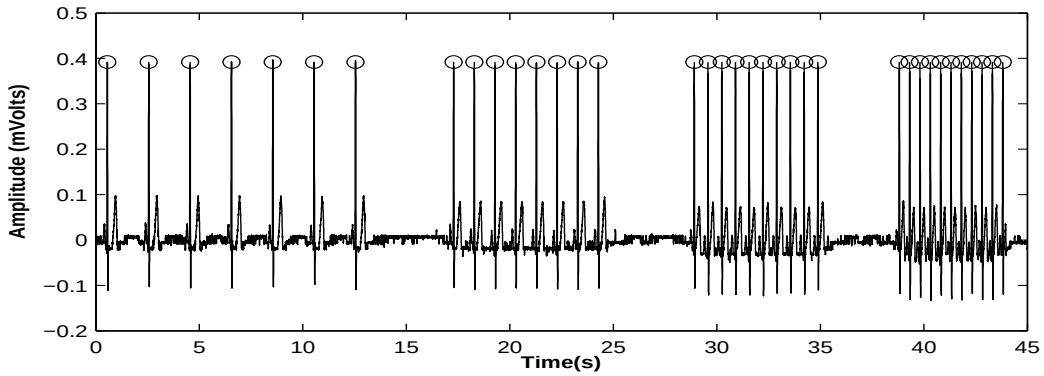

Fig. 5.4: Result of QRS detection in clean simulated ECG signal with HR changing from 30 to 120 bmp

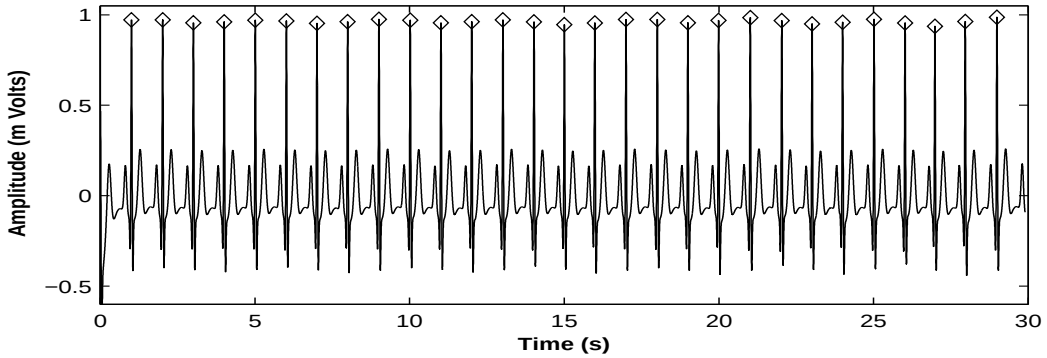

Fig. 5.5: Simulated ECG signal with exact peaks location

5.3. Algorithm evaluation in the presence of simulated artefacts

In order to test the performance of the peak detection algorithm in the presence of varying level of artefact commonly encountered in the ECG recordings a simulated ECG signal was generated using the model proposed by McSharr and Clifford [71]. This differential model allows the generation of an ECG signal with known heart rate and location of the peaks. The knowledge of the exact location of the R-wave was important to calculate the error caused by different artefacts in peak detection. The generated ECG signal with the exact location of the R-wave peaks is shown in Fig. 5.5. This simulated ECG signal was then corrupted by different types of artefacts to produce corrupted ECG signals at varying SNR levels (10, 5, 3 and 0 dB). These artefacts can be divided into two major categories.

1. random artefacts
    - White Noise (WN)
    - Colour Noise (CN)
2. artefacts mimicking the contamination generally present in the physiological signal (e.g. breathing artefacts, muscle movement, electrode movement and combination of all these).

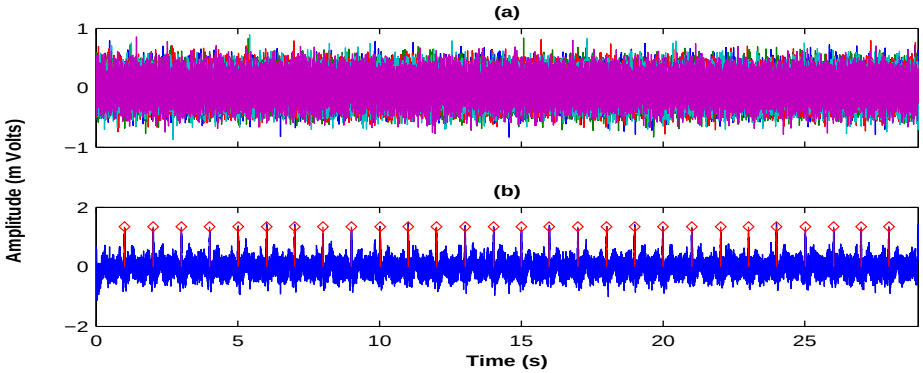

Fig. 5.6: (a) Five samples of white noise at SNR level of zero dB; (b) Peak detection results in one ECG signal corrupted at SNR level of zero dB (Digital filter algorithm)

The signals simulating the physiological artefacts were generated using the time varying AR modelling technique as described by Sameni *et. al.* [72]. In this case, the model parameters were trained on ECG artefacts from MIT-BIH non-stress test database (NSTDB) [73].

In order to take into account the random nature of the artefacts each simulated signal was generated five times for a particular SNR level. After peak detection in each of the corrupted signals the following parameters were recorded to evaluate the performance of the algorithm:

1. the number of missed peaks
2. noise detected as peaks
3. mean difference between the peak location, detected in the corrupted signals, and the actual peak location for each of the five runs for each type of noise at a particular SNR level.
4. maximum difference in the peak location and
5. mean of the five mean differences mentioned in point 3

The results obtained from this simulated study will be presented in the following sections.

5.3.1. White Noise (WN)

White noise is a random signal (or process) with a flat power spectral density. In other words, the signal's power spectral density has equal power in any band, at any centre frequency having a given bandwidth. White noise is considered analogous to white light which contains all frequencies [74]. The five samples of white noise generated at SNR level of zero dB and the peak detection results in one of the corrupted ECG signals at this SNR level is shown in Fig. 5.6. In the case of white noise there were no missed peaks and

Table 5.1.: Parameters obtained from the peak detection results of ECG signals corrupted by white noise at varying SNR levels

White Noise results			
SNR	mean difference MD (samples)	max. difference (samples)	mean of MD (samples)
10	1.02, 0.89, 1.04, 0.089, 0.86	2, 2, 3, 3, 2	0.96
5	0.93, 1.07, 0.93, 1.04, 0.75	2, 3, 2, 3, 3	0.94
3	1.21, 1.18, 1.18, 1.04, 0.75	3, 3, 3, 3, 3	1.07
0	1.21, 1.21, 0.89, 0.96, 1.04	3, 4, 3, 3, 3	1.06

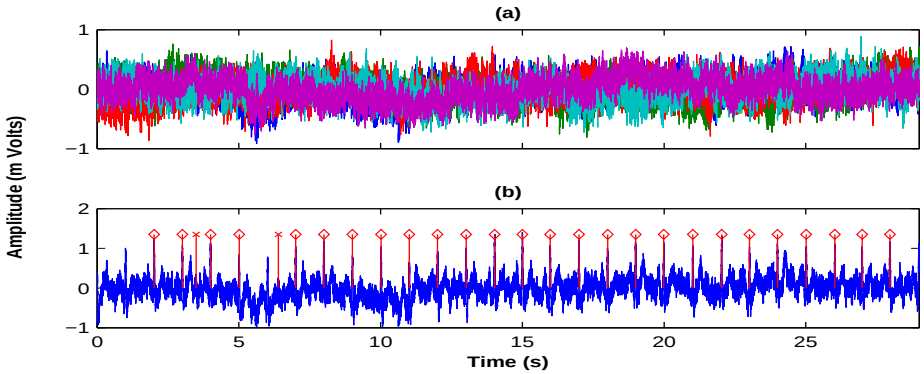

Fig. 5.7: (a) Five samples of colour noise ($\beta = 1.0$) at SNR level of zero dB; (b) Peak detection result in ECG signal corrupted by one of the colour noise samples shown in part (a) (Digital filter algorithm)

no noise was detected as a peak in any of the five signals that were analysed at different SNR levels.

The other parameters calculated from the peak detection results of ECGs corrupted by white noise at varying SNR levels are presented in table 5.1.

5.3.2. Colour Noise (CN)

Even though noise is a random signal, it can have characteristic statistical properties. Spectral density (power distribution in the frequency spectrum) is such a property, which can be used to distinguish different types of noise. This classification by spectral density is given as "colour" terminology, with different types named after different colours, and is common in different disciplines where noise is an important factor (like acoustics, electrical engineering, and physics). Many of these definitions assume a signal with components at all frequencies, with a spectral density per unit of bandwidth proportional to $\frac{1}{f^\beta}$. For instance, white noise is flat, with $\beta = 0$, while brown has $\beta = 2$ [75].

In this study three different values of β (1.0, 1.5 and 2) were used for each SNR level.

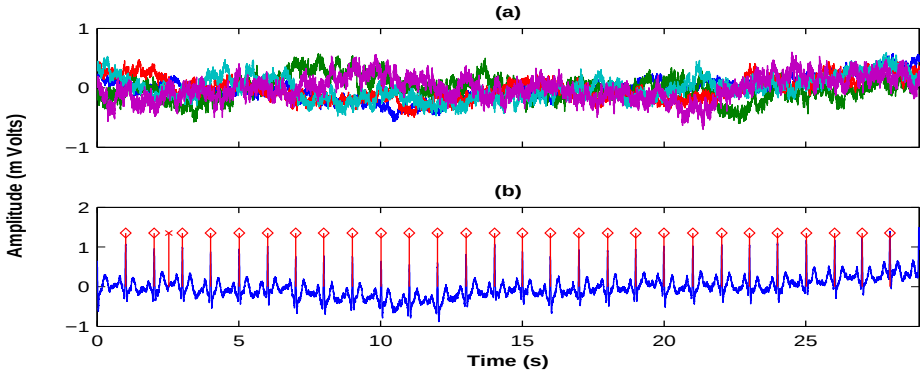

Fig. 5.8: (a) Five samples of colour noise ($\beta = 1.5$) at SNR level of zero dB; (b) Peak detection results in ECG signal corrupted by one of the colour noise samples shown in part (a) (Digital filter algorithm)

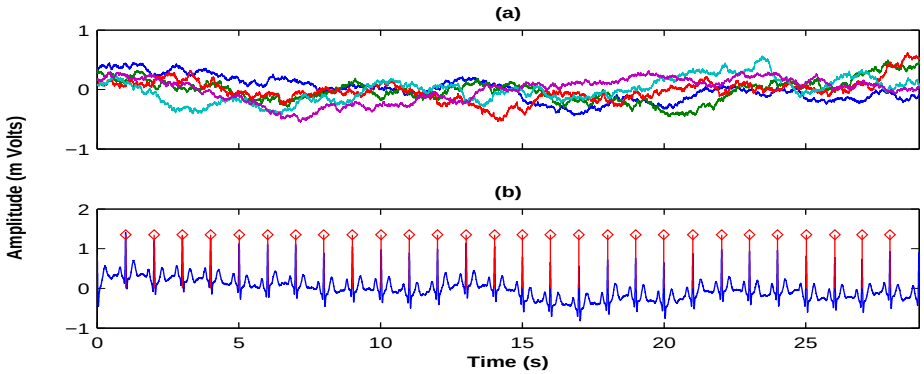

Fig. 5.9: (a) Five samples of colour noise ($\beta = 2.0$) at SNR level of zero dB; (b) Peak detection results in ECG signal corrupted by one of the colour noise samples shown in part (a) (Digital filter algorithm)

The result of peak detection in one of the corrupted ECG signals and the noise samples at SNR level of zero dB for each β value are presented in Fig. 5.7, 5.8 and 5.9.

In the case of colour noise there were few missed peaks and noise detected as peaks in the case of $\beta = 1$ and $\beta = 1.5$. The results of peaks for the ECG signal corrupted by colour noise at varying SNR level are summarised in table 5.2.

5.3.3. Baseline Wander/breathing artefact (BW)

As mentioned before, the signals simulating the physiological artefacts, breathing, muscle, electrode movement and signal representing a combination of all these (combined artefact, see section 5.3.6), were generated using the time varying AR modelling technique as described by Sameni *et. al.* [72]. Five sets of breathing artefacts were again generated at SNR levels of 10, 5, 3 and 0 dB. The five simulated breathing artefacts and peak detection results in one of the corrupted ECG signals at SNR = 0 dB is shown in Fig. 5.10.

For the breathing artefact the algorithm did not miss any peaks at the studied SNR levels. Also no noise peaks were detected. The mean difference and other results obtained from analysing the ECG signals corrupted by breathing artefact at different SNR levels are presented in table 5.3.

Table 5.2.: Parameters obtained from the peak detection results of ECG signals corrupted by coloured noise at varying SNR levels

SNR	correct peaks detected	missed peaks	noise Peaks	mean difference MD (samples)	max. diff. (samples)	mean of MD (samples)
Colour noise results $\beta = 1$						
10	28, 28, 28, 28, 28	0, 0, 0, 0, 0	0, 0, 0, 0, 0	0.75, 0.75, 0.86, 0.71, 0.75	2, 2, 2, 2, 2	0.76
5	28, 28, 28, 28, 28	0, 0, 0, 0, 0	1, 1, 3, 0, 1	1.32, 1.0, 0.93, 1.07, 0.96	3, 2, 2, 3, 3	1.06
3	28, 28, 28, 28, 28	0, 0, 0, 0, 0	0, 0, 0, 0, 1	1.04, 1.32, 1.14, 1.14, 1.36	3, 4, 2, 3, 4	1.20
0	26, 25, 27, 25, 28	2, 3, 1, 3, 0	2, 2, 4, 1, 2	1.18, 1.07, 1.32, 1.18, 1.43	4, 4, 4, 4, 3	1.24
Colour noise results $\beta = 1.5$						
10	28, 28, 28, 28, 28	0, 0, 0, 0, 0	0, 0, 0, 0, 0	0.86, 0.82, 0.79, 0.93, 0.79	2, 2, 2, 2, 2	0.84
5	28, 28, 28, 28, 28	0, 0, 0, 0, 0	0, 0, 0, 0, 0	0.82, 0.82, 0.89, 0.68, 0.79	2, 2, 2, 2, 2	0.80
3	28, 28, 28, 28, 28	0, 0, 0, 0, 0	0, 0, 0, 0, 0	0.82, 0.89, 0.71, 0.89, 0.71	2, 2, 1, 2, 2	0.81
0	28, 28, 28, 28, 28	0, 0, 0, 0, 0	1, 1, 0 , 0, 0	0.71, 0.82, 0.79, 0.89, 1	2, 2, 2, 2, 3	0.84
Colour noise results $\beta = 2.0$						
10	28, 28, 28, 28, 28	0, 0, 0, 0, 0	0, 0, 0, 0, 0	0.89, 0.89, 0.89, 0.82, 0.93	2, 2, 2, 2, 2	0.86
5	28, 28, 28, 28, 28	0, 0, 0, 0, 0	0, 0, 0, 0, 0	0.79, 0.82, 0.79, 0.93, 0.86	2, 2, 2, 2, 2	0.84
3	28, 28, 28, 28, 28	0, 0, 0, 0, 0	0, 0, 0, 0, 0	0.82, 0.89, 0.79, 0.86, 0.89	2, 2, 1, 2, 2	0.85
0	28, 28, 28, 28, 28	0, 0, 0, 0, 0	1, 1, 0 , 0, 0	0.86, 0.89, 0.68, 0.79, 0.89	2, 2, 2, 2, 2	0.82

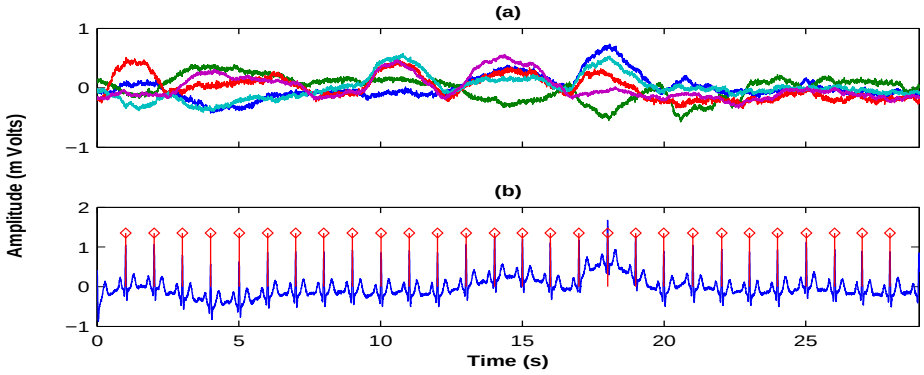

Fig. 5.10: (a) Five sets of simulated breathing artefacts at SNR level of zero dB; (b) Peak detection result in ECG signal corrupted by breathing artefact at SNR level of zero dB (Digital filter algorithm)

Table 5.3.: Parameters obtained from the peak detection results of ECG signals corrupted by breathing artefact at varying SNR levels

Breathing artefact results			
SNR	mean difference MD (samples)	max. difference (samples)	mean of MD (samples)
10	0.96, 0.93, 0.93, 0.89, 0.86	2, 2, 2, 2, 2	0.91
5	0.96, 0.93, 0.86, 0.82, 0.86	2, 2, 2, 2, 2	0.89
3	0.96, 0.93, 0.86, 0.79, 0.86	2, 2, 2, 2, 2	0.88
0	1.0, 0.93, 0.86, 0.82, 0.79	2, 2, 2, 2, 2	0.80

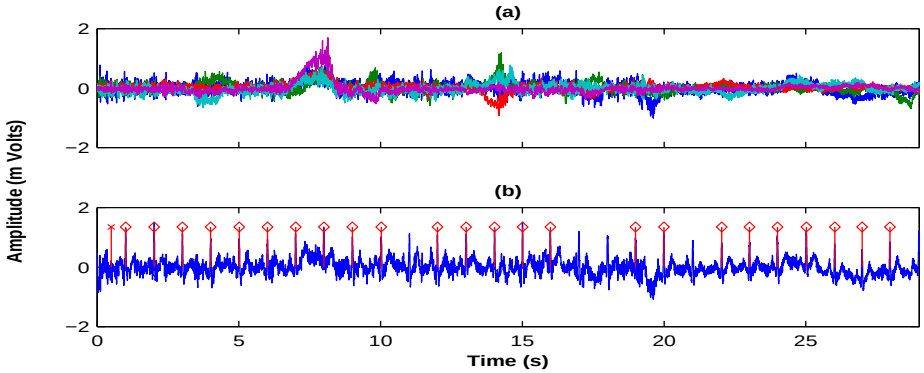

Fig. 5.11: (a) Five sets of simulated muscle artefacts at SNR level of zero dB; (b) Peak detection result in ECG signal corrupted by muscle artefact at SNR level of zero dB (Digital filter algorithm)

5.3.4. Muscle Artefact (MA)

The five simulated muscle artefacts generated at 0 dB SNR level along with the peak detection result in one of the corrupted ECG signals is presented in Fig. 5.11. From the peak detection result shown in Fig. 5.11 (b) it can be seen that the algorithm has missed four original ECG peaks and it has also detected one false peak (noise detected as a peak). The parameters calculated from the peak detection analysis of ECG corrupted by muscle artefacts at different SNR levels are summarised in table 5.4.

5.3.5. Electrode Movement Artefact (EMA)

The artefact introduced by electrode movement was also simulated at the four different SNR levels. The five signals representing the electrode movement and the peak detection result in one of the corrupted ECG signals at SNR level of zero dB is shown in Fig. 5.12 (a) and 5.12 (b) respectively. In the case of electrode movement, the peak detection algorithm did not miss any peaks and there was no noise detected as peaks at any of the SNR levels used in the simulated study. The parameters calculated from the peak detection analysis of the ECG signals corrupted by electrode movement artefact are presented in table 5.5.

Table 5.4.: Parameters obtained from the peak detection results of ECG signals corrupted by muscle artefact at varying SNR levels

Muscle artefact results						
SNR	correct peaks detected	missed peaks	noise peaks	mean difference MD (samples)	max. difference (samples)	mean of MD (samples)
10	28, 28, 28, 28, 28	0, 0, 0, 0, 0	0, 0, 0, 0, 0	0.89, 0.89, 0.93, 0.75, 0.82	2, 2, 2, 2, 2	0.86
5	27, 28, 28, 28, 28	1, 0, 0, 0, 0	1, 0, 1, 0, 0	0.86, 0.89, 0.89, 0.61, 0.75	3, 2, 2, 2, 2	0.8
3	25, 28, 28, 28 28	3, 0, 0, 0, 0	1, 0, 1, 2, 0	1.0, 0.89, 0.96, 0.64, 0.79	4, 2, 2, 2, 2	0.86
0	24, 27, 28, 27, 28	4, 1, 0, 1, 0	1, 0, 2, 2, 0	1.14, 1.0, 1.0, 0.70, 0.82	6, 3, 2, 2, 2	0.93

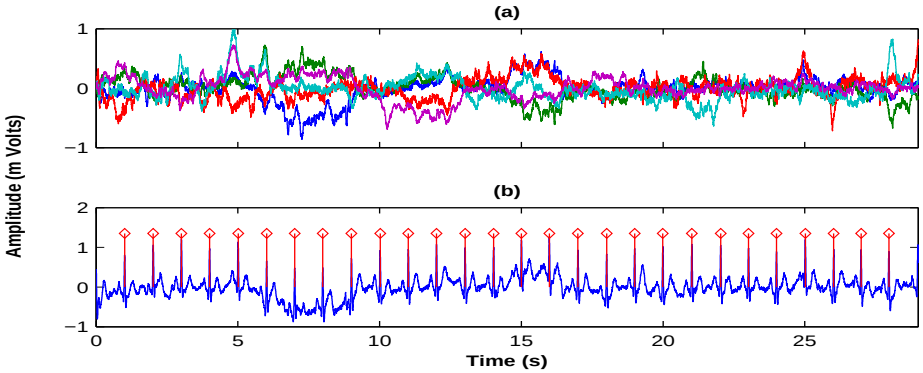

Fig. 5.12: (a) Five sets of simulated electrode movement artefacts at SNR level of zero dB; (b) Peak detection results in ECG signal corrupted by electrode movement artefact at SNR level of zero dB (Digital filter algorithm)

Table 5.5.: Parameters obtained from the peak detection results of ECG signals corrupted by electrode movement artefact at varying SNR levels

Electrode movement artefact results			
SNR	mean difference MD (samples)	max. difference (samples)	mean of MD (samples)
10	0.89, 0.89, 0.86, 0.86, 0.82	2, 2, 2, 1, 1	0.86
5	0.76, 0.75, 0.89, 0.85, 0.82	2, 1, 2, 2, 1	0.82
3	0.78, 0.79, 0.93, 0.82, 0.86	2, 2, 2, 2, 2	0.84
0	0.79, 0.86, 1.0, 0.86, 0.78	2, 2, 3, 2, 2	0.86

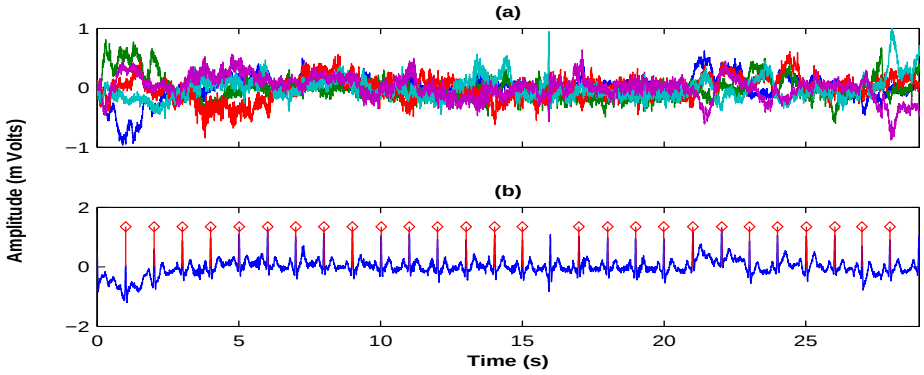

Fig. 5.13: (a) Five set of simulated combined artefacts at SNR level of zero dB; (b) peak detection results in ECG signal corrupted by electrode movement artefact at SNR level of zero dB (Digital filter algorithm)

Table 5.6.: Parameters obtained from the peak detection results of ECG signals corrupted by combined artefact at varying SNR levels

combined artefact results						
SNR	correct peaks detected	missed peaks	noise peaks	mean difference MD (samples)	max. difference (samples)	mean of MD (samples)
10	28, 28, 28, 28, 28	0, 0, 0, 0, 0	0, 0, 0, 0, 0	0.86, 0.756 0.82, 0.82, 1.0	2, 2, 2, 2, 2	0.85
5	28, 28, 27, 28, 28	0, 0, 1, 0, 0	0, 0, 0, 0, 0	0.86, 0.79, 0.81, 0.75, 0.89	2, 2, 2, 2, 2	0.82
3	28, 28, 27, 28, 28	0, 0, 1, 0, 0	0, 0, 0, 0, 0	0.89, 0.75, 0.74, 0.75, 1.0	3, 2, 2, 2, 3	0.83
0	27, 28, 28, 28, 27	1, 0, 0, 0, 1	0, 0, 0, 0, 0	0.93, 0.79, 0.81, 0.64, 1.11	3, 2, 2, 2, 4	0.86

5.3.6. Combined artefact

In the previous sections the performance of the peak detection algorithm was tested in the presence of different physiological artefacts at varying SNR levels individually but in reality the signals are usually corrupted by a combination of all these artefacts. Therefore, another simulated signal which was a combination of breathing, electrode movement and muscle artefact was also considered in this study. The five artefact signals and results of peak detection in one of the corrupted ECG signals are shown in Fig. 5.13 (a) and 5.13 (b) respectively. The parameters calculated using the result of peak detection in ECG signals corrupted by combined artefact at different SNR level is presented in table 5.6.

This simulated study gave an indication of the performance of the peak detection algorithm implemented using digital filter and adaptive thresholding technique. The performance of the algorithm was most affected by the presence of muscle artefact. The maximum number of peaks that the algorithm has missed was four and this was in the

case when the ECG signal was corrupted with muscle artefact at a SNR level of zero dB. The most number of false positives, noise detected as peaks, was four which occurred in the case for signals corrupted by colour noise ($\beta = 1.5$) again at SNR level of zero dB. For almost all the noise cases, the mean difference (MD) and mean of MD showed a gradual increase as the SNR level decreases.

Following this study, the performance of the peak detection algorithm was evaluated both offline and online on real ECG data, and this will be the subject of the next sections.

5.4. Off-line evaluation of the digital filter peak detection algorithm evaluation on real data

The developed peak detection algorithm was also tested using an ECG data set of normal patients from the Normal Sinus Rhythm (NSR) database available at (`http://www.physionet.org/physiobank/database/nsrdb/`). These signals were digitised at 128 Hz and a segment of fifteen minutes from each record was analysed. In order to use these signals the data were first resampled to 1000 Hz. For each record the following quantities were estimated:

- Correctly identified peaks (T_p), the annotations generated by the algorithm agreed with the annotation present in the database record. Two events are held to be simultaneous (by the ANSI standards [35]) if they occur within $\pm$150 ms of each other.
- Noise detected as peaks (F_P), beats identified by the algorithm when the clinician has not scored one and
- Peaks missed (F_N), beats missed by the algorithm when the clinician has scored one as indicated by the database record were used to calculate the sensitivity and the accuracy of the algorithm, described in sections 5.2 and 5.2.1, using Eq. 5.2 and Eq 5.3 respectively. The results for the QRS detection for these signals are summarised in table 5.7.

$$\%\text{Sensitivity} = \frac{T_P}{T_P + F_N} \tag{5.2}$$

$$\%\text{Accuracy} = \frac{T_p}{T_p + F_P} \tag{5.3}$$

The data sets 19090, 19140 and 19830 showed large amount of error. This was due to the fact that all these signals contain sawtooth wave like pulses in the beginning as shown is Fig. 5.14. This artefact has caused the average of R peaks to be inaccurate resulting in a lot of false detection. The same artefact has also caused the algorithm to completely

Table 5.7.: QRS detection results for samples from Normal Sinus Rhythm database using digital filter algorithm

Sr. No	Name of sample	Total no. of Peaks	no. of Peak missed (F_N)	no.of noise det. as peaks (F_P)	no. of correctly det. peaks (T_P)	% Sensitivity	% Accuracy
1	16265	875	1	4	874	99.88	99.43
2	16272	575	5	2	570	99.13	99.65
3	16420	785	3	1	782	99.62	99.87
4	16539	725	1	3	724	99.86	99.58
5	16773	689	4	3	685	99.42	99.56
6	16786	628	2	0	626	99.68	100
7	17052	714	3	2	711	99.57	99.72
8	17453	707	4	2	703	99.43	99.72
9	18177	912	3	5	909	99.67	99.45
10	18184	751	5	2	746	99.33	99.73
11	16273	772	1	3	771	99.87	99.61
12	16483	770	1	2	769	99.87	99.74
13	16795	575	3	4	574	99.82	99.82
14	19088	733	5	2	728	99.32	99.72
15	19090	742	19	66	723	97.43	91.63
16	19140	782	1	59	781	99.87	92.97
17	19830	876	1	14	875	99.88	98.42
18	19093	546	3	4	543	99.45	99.26

fail in detecting the R-waves correctly in the data set 19093. When these signals were processed again after removing the noisy part (sawtooth pulses) at the beginning of the data set then the algorithm worked accurately achieving an overall sensitivity of 99.63% and accuracy of 99.66% .

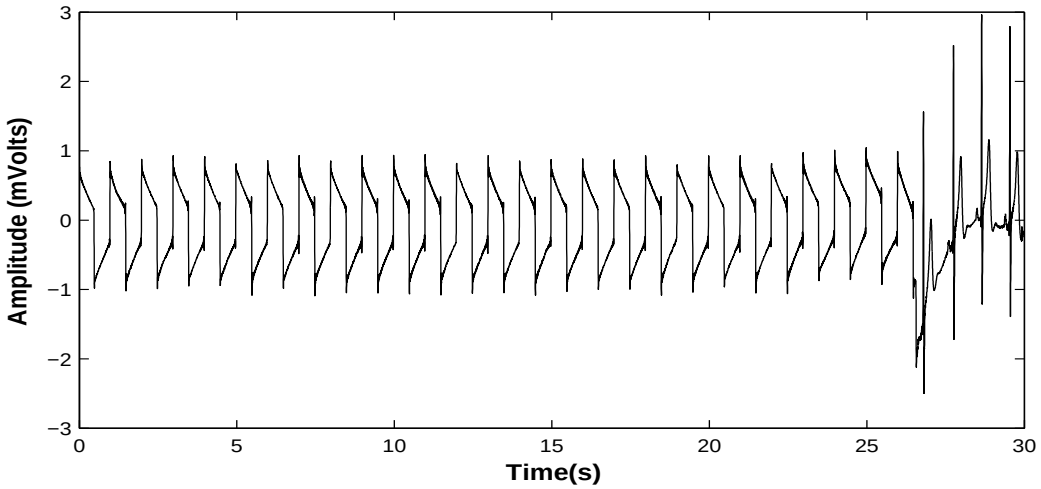

Fig. 5.14: Artefact at the beginning of 19093 data set in the Normal Sinus Rhythm database. Similar artefact has caused error in detection in the data sets 19090, 19140 and 19830

5.5. On-line evaluation of the digital filter peak detection algorithm on real data

The algorithm was also evaluated on-line in six healthy volunteers in normal resting conditions and in four out of the fourteen locally anaesthetised patients recruited for this study. The six volunteers included in the study have no know cardiovascular problems and have mean age 26 ± 2 years, mean weight 65.4 ± 6.3 Kg. The on-line evaluation of the algorithm on the healthy volunteers was performed in the biomedical engineering research laboratory at City University where the volunteers were connected to a Lead II ECG monitor (Cardioline Delta 60 Plus, Milan, Italy). Similarly the evaluation of the four patients took place at Broomfield Hospital, Chelmsford, Essex where the patients were connected to a Lead II ECG monitor (Datex-Engstrom, Helsinki, Finland). The patients details are presented previously in section 4.4.

The ECG signals from both volunteers and patients were digitised at 1000 Hz using a National Instrument PCMCIA 6024E card. About 17788 heart beats from the healthy volunteers were analysed. The algorithm missed only four QRS complexes in these signals. A few examples are shown in Fig. 5.15. The results obtained by analysing the ECG data from the four patients undergoing local anaesthesia are summarised in table 5.8. In total 64815 beats were analysed and the algorithm achieved an overall accuracy of 99.84% and sensitivity of 99.83%. Figure 5.16 presents three examples from these data sets.

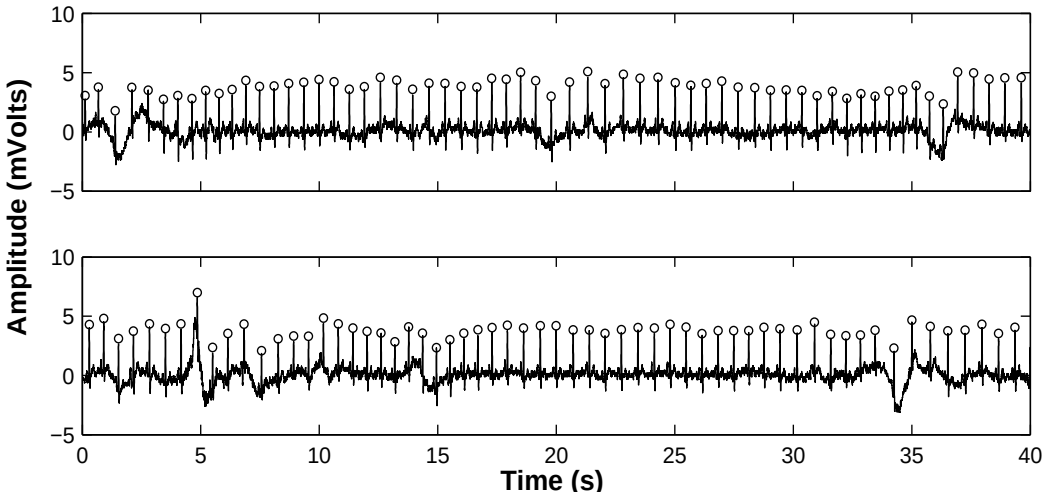

Fig. 5.15: QRS detection examples in healthy volunteers using the digital filter algorithm

Table 5.8.: QRS detection results from the locally anaesthetised patients (n=4) using the digital filter algorithm

Data No.	Total no. of Peaks	no. of Peak missed (F_N)	no.of noise det. as peaks (F_P)	no. of correctly det. peaks (T_P)	% Sensitivity	% Accuracy
1	13079	20	12	13689	99.63	99.90
2	15625	21	23	15604	99.80	99.68
3	11977	6	19	11971	99.96	99.88
4	23504	18	13	23486	99.94	99.94
					Avg.= 99.83	Avg.= 99.84

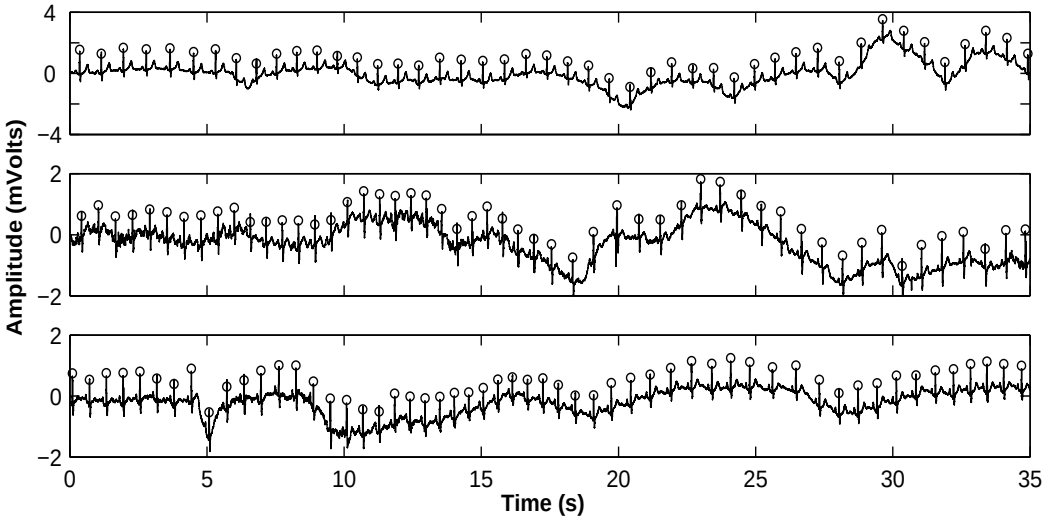

Fig. 5.16: QRS detection examples in anaesthetised patients using the digital filter algorithm

5.6. Discussion and conclusions

In this chapter the implementation of an ECG R-wave detector based on the digital filter technique was described. The implemented algorithm was tested extensively both offline and online. The offline evaluation was performed using simulated ECG signals (see section 5.3) which were corrupted by varying levels of different artefacts generally present in ECG recordings and also by using signals from the NSR database (see section 5.4) available from *Physionet*. The online analysis was carried out on six healthy volunteers in normal resting conditions and four patients undergoing local anaesthetic procedure. The results indicated that even though the algorithm has performed satisfactorily in most cases, the presence of artefacts with high frequency spread (see Fig. 5.14) could cause the algorithm to completely fail.

In order to address these issues another algorithm for the detection of the ECG R-wave was implemented. This algorithm was implemented using the wavelet transform. The next chapter will provide a brief introduction of wavelet analysis before presenting the details about the implementation of the algorithm and results obtained from the analysis of real and simulated ECG data.

6

Development of R-wave detection algorithm using Wavelet Transform

In the previous chapter an R-wave detection algorithm based on digital filtering technique was presented. The performance of this algorithm was not satisfactory when the ECG signals were corrupted by artefacts having broad frequency distribution. To deal with this issue another R-wave detection algorithm using wavelet transform was developed. Before describing the implementation of the algorithm a brief introduction to the theory of wavelet analysis will be presented in the next section.

6.1. Introduction to classical frequency domain analysis methods

Fourier technique is the most commonly used classical method of analysing signals in frequency domain. In this case, a periodic signal could be represented by a Fourier series (FS) as shown in Eq. 6.1.

$$x(t) = \sum_{k=-\infty}^{\infty} a_k e^{jk\omega_0 t} = \sum_{k=-1}^{1} a_k e^{jk\left(\frac{2\pi}{T}\right)t} \tag{6.1}$$

$$a_k = \frac{1}{T}\int_0^T x(t) a_k e^{jk\omega_0 t} dt \tag{6.2}$$

Where ω_0 is the fundamental frequency of the signal. Equation. 6.1 is referred to as the synthesis equation and Eq. 6.2 is known as the analysis equation. The set of coefficients $\{a_k\}$ are often called the Fourier series coefficients.

For aperiodic signal, as the period becomes infinite the frequency components form a continuum and the FS sum becomes an integral. The resulting spectrum of coefficients in this representation is called Fourier transform (FT) (Eq. 6.3) and the synthesis integral itself that uses these coefficients to represent the signal as a linear combination of complex exponentials is called inverse FT and is given in Eq. 6.4.

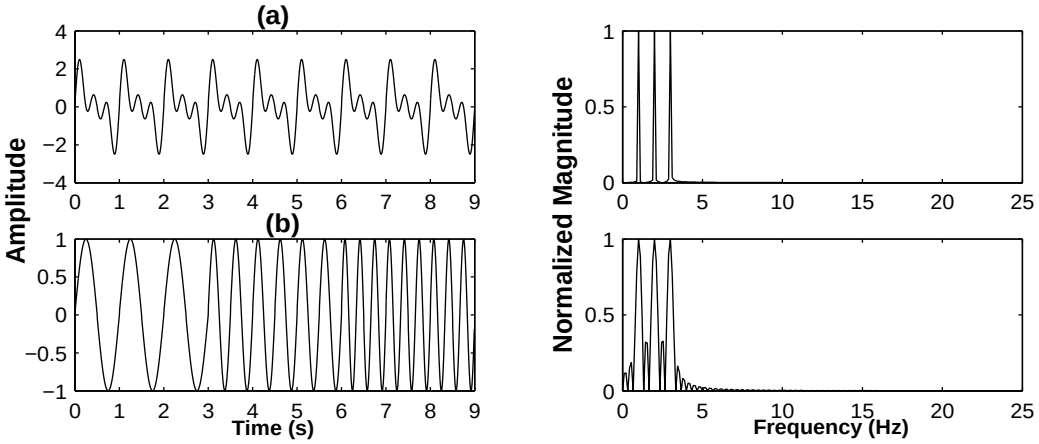

Fig. 6.1: Example of FFT of (a) stationary (b) non-stationary signal

$$X(j\omega) = \frac{1}{2\pi} \int_{-\infty}^{\infty} x(t) e^{-j\omega t} dt \tag{6.3}$$

$$x(t) = \frac{1}{2\pi} \int_{-\infty}^{\infty} X(j\omega) e^{j\omega t} dt \tag{6.4}$$

Now by examining Eq. 6.3 it can be seen that the frequency components appearing in the signal at different time instances will affect the magnitude part equally, as the integration is carried out from minus infinity to plus infinity. Thus it contains only globally average information and might obscure the transient features of the signal. Because of this reason without the inclusion of the phase response the magnitude FT alone is not suitable for analysis of non-stationary signals (signals in which frequency changes with time). For instance Fig. 6.1 highlight this effect. The first part of the figure shows a composite signal consisting of three frequencies (1, 2 and 3 Hz) with its FT on the right side. This FT representation is quite similar to the one given on the right side of part b of the figure, even thought in this case the signal is non-stationary (Fig. 6.1 left side) and its frequency is changing from 1 Hz to 3 Hz with time.

In order to obtain two dimensional time-frequency representation of a signal the FT was modified. In 1946 physicist Dennis Gabor suggested performing FT analysis on small segments of the signal that could be considered stationary. This modified FT is known as the Short Time Fourier Transform (STFT). The signal is split into smaller segments using a window function. This window is moved incrementally along the signal to produce a series of spectral analysis, each of which is located at a particular point in time. STFT is presented in Eq. 6.5.

$$STFT\ X(\omega)(t', f) = \int_{t} [x(t)\, \omega(t - t')] e^{-j2\pi f} dt \tag{6.5}$$

From Eq. 6.5 it is clear that the STFT is nothing but the FT of the signal multiplied by a window function. Similarly the discrete version of the STFT is known as the Discrete Short Time Fourier transform (DSTFT) [76, 77]. The DSTFT and the inverse transforms are shown in Eq. 6.6 and Eq. 6.7 respectively.

$$Forward\ DSTFT \qquad X[n,k] = \sum_{l=0}^{M} x[n+l]w(l)e^{\frac{-j2\pi lk}{N}} \tag{6.6}$$

$$Reverse\ DSTFT \qquad x[n+l] = \frac{1}{N\,w[l]} \sum X[n,k]e^{\frac{-j2\pi lk}{N}} \tag{6.7}$$

The frequency resolution of the DSTFT can be related to the bandwidth of the window sequence. Taking the Root Mean Square (RMS) as a measure of the bandwidth Δf the frequency resolution can be written as

$$\Delta f = \left[\sum_{k=0}^{N-1} k^2 \frac{|G[Lk]|^2}{\sum_{k=0}^{N-1}|G[k]|^2}\right]^{1/2} \tag{6.8}$$

where $G[k]$ is the DFT of the window function. The time resolution (spread in time) Δt can similarly be written as

$$\Delta t = \left[\sum n^2|g[n]|^2 / \sum_{n}|g[n]|^2\right]^{1/2} \tag{6.9}$$

From this discussion the trade-off between time and frequency resolution is obvious because as the window size increases the frequency resolution increases but the time resolution decreases. In the same way, by decreasing the window length the time resolution could be increased but this would result in loss of frequency resolution. The resolution in time and frequency cannot be arbitrarily small because the "duration-bandwidth" product $\Delta t.\Delta f$ of any signal is bounded from below by Eq. 6.10. This equation is referred as the Heisenberg-Gabor uncertainty principle.

$$Time - bandwidth\ product = \Delta t.\Delta f \geq \frac{1}{4\pi} \tag{6.10}$$

The main drawback of STFT is the use of fixed time and frequency resolution throughout the signal, it averages the components that fall inside the window but cannot capture those components that last longer than the window itself.

This is where the Wavelet Transform (WT) excels. Its ability to examine the signal simultaneously both in time and frequency is quite different from the traditional STFT. Unlike FT which uses sinusoids as basis functions, which are not localised in space, wavelets expand the signal in terms of functions which are localised both in time and

frequency. These functions are obtained by scaling and translating a signal called the mother wavelet. This allows the capture of short duration (high frequency) and long duration (low frequency) information simultaneously. Hence, the method is particularly useful for the analysis of transient, aperiodic and other non-stationary signal features. Another key advantage of the wavelet technique is the variety of wavelet functions available thus allowing the most appropriate to be chosen for a specific application. WT analysis has now been applied to a variety of biomedical signals such as EMG, ECG, clinical sounds respiratory pattern, blood pressure and Deoxyribonucleic acid (DNA) sequences [78, 79, 80, 81, 82, 83].

6.2. Wavelet analysis

Depending on the way the WT is applied it can be split into two main groups

1. Continuous Wavelet Transform (CWT)
2. Discrete Wavelet Transform (DWT)

6.2.1. Continuous Wavelet Transform (CWT)

The CWT is defined as

$$CWT(a,b) = \frac{1}{\sqrt{a}} \int_{-\infty}^{\infty} s(t)\psi^*(\frac{t-b}{a})dt \tag{6.11}$$

Where a and b are the scaling and translation factor respectively [84].

The wavelet measures the frequency contents of the signal by a dilated and translated version of ψ (see Eq. 6.12), which is called the mother wavelet.

$$\psi_{a,b} = \frac{1}{\sqrt{a}}\psi(\frac{t-b}{a}) \tag{6.12}$$

The parameter a determines the centre frequency of the function $\psi(a^{-1}(t-b))$ and the parameter b indicates the time shifting (translation). The difference between STFT and CWT can be seen by comparing the time frequency tilling of the two methods (Fig. 6.2).

The tilling of the STFT, shown in Fig. 6.2 is linear (fixed) and this is because the signal's time frequency is measured using a time shifted and frequency modulated single prototype function. On the other hand the time frequency resolution of the elementary function used to analyse the signal in wavelet analysis changes with the scaling factor a providing a logarithmic tilling. At small values of a (scaling factor) the time resolution is good but the frequency resolution is poor, whereas at high frequencies (i.e. large a

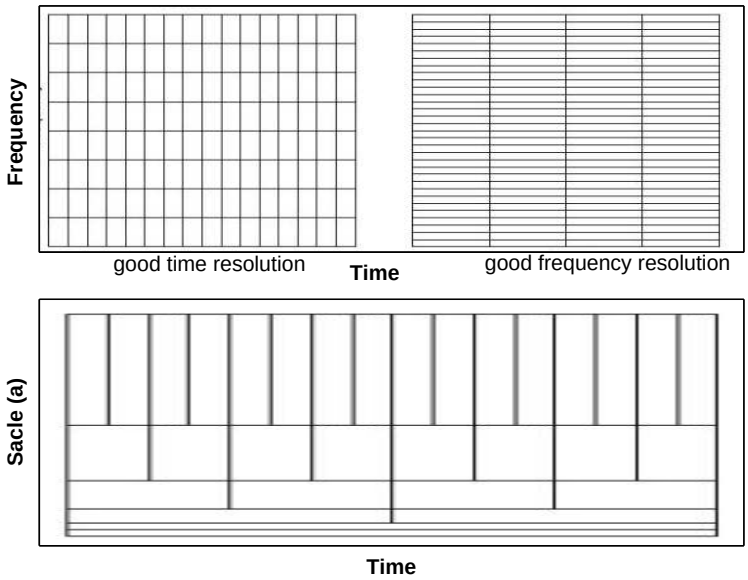

Fig. 6.2: Time-Frequency tilling of (a) STFT and (b) WT

values) the opposite is true. However, the product of time-frequency resolution remains constant which implies that the WT also obeys the uncertainty principle (Eq. 6.10).

In order to be classified as a wavelet a function must satisfy certain mathematical criteria. These criteria are:

1. It must have finite energy
$$E = \int |\psi(t)|^2 dt < \infty \tag{6.13}$$

2. If $\hat{\Psi}(f)$ is the Fourier transform of $\psi(t)$ i.e.
$$\hat{\Psi}(f) = \int_{-\infty}^{\infty} \psi(t)\, e^{-i(2\pi f)t}\, dt \tag{6.14}$$
then the following condition must hold
$$C_g = \int_0^{\infty} \frac{|\psi(t)|^2}{f}\, df \; < \infty \tag{6.15}$$
This implies that $\psi(t)$ must have zero mean, or in other words the wavelet has no zero frequency component $\hat{\Psi}(0) = 0$. Equation 6.15 is known as the admissibility condition and C_g is called the admissibility constant. The value of C_g depends on the wavelet used.

3. For complex wavelet, the FT must be real and vanishes for negative frequencies.

Analogous to the spectrogram the energy density surface of the STFT, the square of the

WT is commonly called the scalogram (given in Eq. 6.16)

$$SCAL(a,b) = |CWT(a,b)|^2 \tag{6.16}$$

The relative contribution to the total energy contained within the signal at a specific scale a is given by the scale dependent energy distribution as given by Eq. 6.17.

$$E(a) = \frac{1}{C_g} \int_{-\infty}^{\infty} |CWT(a,b)|^2 \, db \tag{6.17}$$

In order to compare the wavelet energy spectrum of a signal to its Fourier energy spectrum the wavelet scale a must be converted to the characteristic frequency of the wavelet such as spectral peak frequency, central frequency or passband centre. The spectral components are inversely proportional to the dilation i.e. $f \propto \frac{1}{a}$. The frequency associated with a wavelet at arbitrary scale a is presented in Eq. 6.18.

$$f = \frac{f_c}{a} \tag{6.18}$$

Where f_c is the characteristic frequency of the mother wavelet and f is the representative frequency for the wavelet at scale a. The original signal may be reconstructed using inverse CWT given in Eq. 6.19.

$$x(t) = \frac{1}{C_g} \int_{-\infty}^{\infty} \int_{0}^{\infty} T(a,b)\psi_{a,b}(t) \, \frac{dadb}{a^2} \tag{6.19}$$

In practise a fine discretisation of the CWT is computed where usually the b location is discretised at the sampling interval and a scale is discretised logarithmically. A vast amount of information is contained within this redundant representation of the CWT.

6.2.2. Discrete Wavelet Transform (DWT)

The issue of redundancy and also the lack of analytical solution for the wavelet function used in CWT has led to the development of Discrete Wavelet transform (DWT) to take full advantage of wavelet transforms.

In order to remove redundancy the WT given in Eq. 6.12 is modified as

$$\psi_{m,n} = \frac{1}{\sqrt{a_0^m}} \, \psi\left(\frac{t - nb_0a_0^m}{a_0^m}\right) \tag{6.20}$$

where m and n control the wavelet translation and dilation respectively; a_0 is a specified dilation step parameter set at a value greater than 1 and b_0 is the location parameter

which must be greater than zero [85]. The most efficient and commonly used logarithmic scaling of both dilation and translation step is known as dyadic grid arrangement. This arrangement lends itself nicely to the construction of orthonormal basis (they are orthogonal to each other and have unit energy). Using $a_0 = 2$ and $b_0 = 1$ in Eq. 6.20 the wavelet can be written compactly as shown in Eq. 6.21.

$$\psi_{m,n} = 2^{-\frac{m}{2}} \psi(2^{-m}t - n) \tag{6.21}$$

For the wavelet to be orthogonal to its translation and dilation the condition given in Eq. 6.22 must be satisfied

$$\int \psi_{j,k}(t)\, \psi^*_{m,n}(t)\, dt = \begin{cases} 1 & if\ j = m\ \&\ k = n \\ 0 & otherwise \end{cases} \tag{6.22}$$

The DWT of a signal using dyadic grid can then be written as shown in Eq. 6.23.

$$T_{m,n} = \int_{\infty}^{\infty} x(t)\, \psi_{m,n}(t)\, dt \tag{6.23}$$

When the DWT is used to transform a continuous signal, the result will be a series of wavelet coefficients and it is referred to as the wavelet series decomposition. The necessary and sufficient condition for the reconstruction of the original signal from such a decomposition is that the energy of the wavelet coefficients must lie between two positive bounds [85]

$$A \left\| f \right\|^2 \leq \sum_{j,k} \left| \langle f, \psi_{j,k} \rangle \right|^2 \leq B \left\| f \right\|^2 \tag{6.24}$$

where $A \left\| f \right\|^2$ is the energy of $f(t)$, $A \succ 0$ and $B \prec \infty$ and A and B are independent of $f(t)$.

When Eq. 6.24 is satisfied the family of basis function $\psi_{j,k}$ with $j, k \in \mathbb{Z}$ is referred to as a frame, with frame bound A and B. When $A = B$ the frame is tight and discrete wavelet behaves exactly like an orthonormal basis. When $A \neq B$ exact reconstruction is still possible at the expanse of dual frame. When dual frames are used for DWT the decomposition wavelet is different from the reconstruction wavelet. In this case the two sets of wavelet functions should satisfy the bi-orthogonality condition given in Eq. 6.25.

$$\left\langle \psi_{j,k}(t), \tilde{\psi}_{m,n}(t) \right\rangle = \int \psi_{j,k}(t)\, \tilde{\psi}_{m,n}(t)\, dt = \begin{cases} 1 & if\ j = m\ \&\ k = n \\ 0 & if\ j \neq m\ \&\ k \neq n \end{cases} \tag{6.25}$$

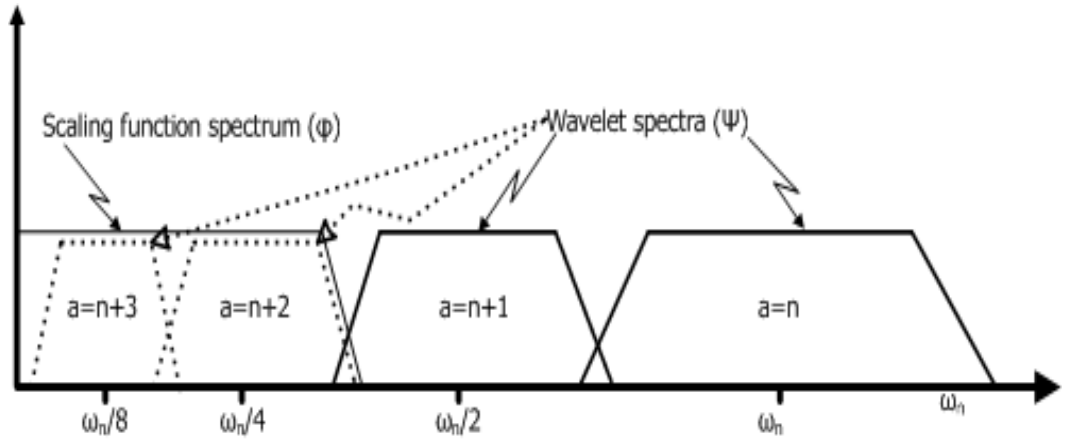

Fig. 6.3: Use of scaling function φ to cover the low frequency part of the signal

The disadvantage of removing the redundancy is that the DWT is no longer shift invariant, which means that DWT of a signal and DWT of a shifted version of the same signal are not simply shifted versions of each other.

6.2.2.1. Scaling function

In order to cover the signal spectrum all the way down to zero another function called the scaling function, introduced by Mallat [86], is associated with the wavelet. Sometimes, the scaling function also referred to as the averaging filter. From Fig. 6.3 it can be seen that the scaling function covers the spectrum of a signal from zero to a certain frequency (i.e. scale). Without the scaling function an infinite number of wavelets would be required to cover this part of spectrum.

The scaling function has the same form as the wavelet and is shown mathematically in Eq. 6.26.

$$\phi_{m,n} = 2^{-\frac{m}{2}} \phi(2^{-m}t - n) \tag{6.26}$$

where $\phi_{0,0}(t) = \varphi(t)$ is also known as the father wavelet. The scaling function is orthogonal to its translation, but not to its dilation [87]. Signal approximation can be produced by convolving it with the scaling function (see Eq. 6.27).

$$S_{m,n} = \int_{\infty}^{\infty} x(t)\, \phi_{m,n}(t)\, dt \tag{6.27}$$

The approximation coefficients given in Eq. 6.27 are simply weighted averages of the continuous signal factor by $2^{m/2}$. The approximation coefficients at a specific scale m are collectively known as the discrete approximation at that scale. The signal $x(t)$ can be represented using a combined series expansion using both the approximation coefficient and the wavelet (details) coefficients as given in Eq. 6.28. This equation indicates that the original continuous signal is expressed as a linear combination of approximation of itself

at an arbitrary scale m_0 and signal details from scale $-\infty$ to m_0.

$$x(t) = \sum_{n=-\infty}^{\infty} S_{m_0,n}\, \phi_{m_0,n}(t) + \sum_{m=-\infty}^{m_0} \sum_{n=-\infty}^{\infty} T_{m,n} \psi_{m,n}(t) \tag{6.28}$$

The signal detail at scale m can be written as (Eq. 6.29)

$$d_m(t) = \sum_{n=-\infty}^{\infty} T_{m,n} \psi_{m,n}(t) \tag{6.29}$$

then Eq. 6.28 can be simplified as presented in Eq. 6.30.

$$x(t) = x_{m_0}(t) + \sum_{m=-\infty}^{m_0} d_m(t) \tag{6.30}$$

Using Eq. 6.30 it could be shown that

$$x_{m-1}(t) = x_m(t) + d_m(t) \tag{6.31}$$

Equation 6.31 indicates that by adding the signal detail at an arbitrary scale m to the approximation at that scale, gives the signal approximation at the next smaller scale $m-1$ (smaller scale means increase resolution). This is called multiresolution representation [86].

6.2.2.2. Fast Wavelet Transform

The approximation coefficients at scale $m+1$ can be generated using the scaling coefficients at the previous scale (see Eq. 6.32).

$$S_{m+1,n} = \frac{1}{\sqrt{2}} \sum_k c_k\, S_{m,2n+k} = \frac{1}{\sqrt{2}} \sum_k c_{k-2n}\, S_{m,k} \tag{6.32}$$

Similarly the wavelet coefficients can be found from the approximation coefficients at the previous scale (see Eq. 6.33). Using Eq. 6.32 the approximation coefficient at scale $m+1$ can be obtained by approximating the coefficient at the previous scale. Similarly the wavelet coefficients can be calculated using the approximation coefficients b_k as (see Eq. 6.33).

$$T_{m+1,n} = \frac{1}{\sqrt{2}} \sum_k b_k\, S_{m,2n+k} = \frac{1}{\sqrt{2}} \sum_k b_{k-2n}\, S_{m,k} \tag{6.33}$$

where $b_k = (-1)^k c_{1-k}$.

Now if the approximation coefficient $S_{m_0,n}$ is known then by repeated application of Eq. 6.32 and Eq. 6.33 the approximation and details wavelet coefficients can be generated for all the scales larger than m_0. These calculations can be done even without the knowledge of the underlying continuous signal $x(t)$. The decomposition algorithm is the

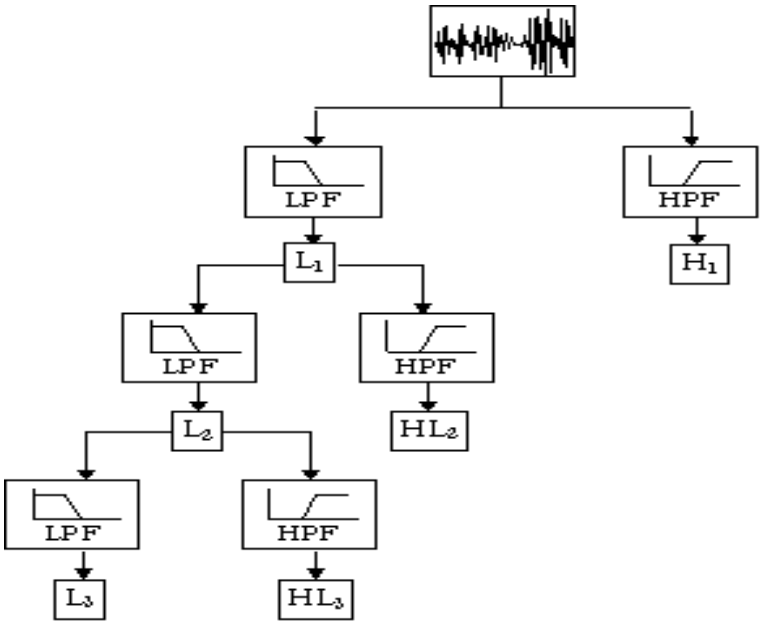

Fig. 6.4: DWT filter bank implementation

first half of the Fast Wavelet Transform (FWT) algorithm, which allows the calculation of the coefficients as discussed above rather than using the convolution equation given in Eq. 6.23. Equation 6.32 and 6.33 perform highpass and lowpass filtering respectively of the input signal (i.e. $S_{m,2+k}$) to get the output ($S_{m+1,n}$ and $T_{m+1,n}$). The vector containing sequences $\frac{1}{\sqrt{2}}\,c_k$ and $\frac{1}{\sqrt{2}}\,b_k$ represents the lowpass and highpass filter respectively. These filter coefficients determine the wavelet used. Coefficients of many wavelets and wavelet properties are discussed in [85]. Going in the opposite direction $S_{m,n}$ can also be reconstructed using S_{m+1} and T_{m+1} as shown in Eq. 6.34.

$$S_{m,n} = \frac{1}{\sqrt{2}} \sum c_{n-2k}\, S_{m+1,k} + \frac{1}{\sqrt{2}} \sum b_{n-2k}\, T_{m+1,k} \tag{6.34}$$

In Eq. 6.34 k and n are used as location index at scale $m+1$ and m respectively. The reconstruction formula is the second half of the multiresolution algorithm. Full derivation of Eq. 6.34 can be found in [88].

Finally, as mentioned before, Eq. 6.32 and Eq. 6.33 perform the highpass and lowpass filter; therefore the wavelet transform could be implemented using a constant Q-filter bank [86] as shown in Fig. 6.4.

6.3. Implementation of ECG characterisation algorithm

The algorithm for R-wave detection implemented in this work is based on the algorithm presented by Sahambi *et. al*. [89]. The wavelet used for the characterisation of the ECG signal is the first derivative of the Gaussian smoothing function.

The wavelet is real and infinitely differentiable. The smoothing function with the cor-

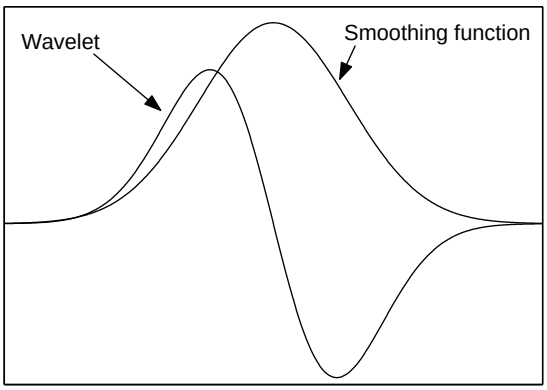

Fig. 6.5: Wavelet and Gaussian smoothing function used for ECG characterisation

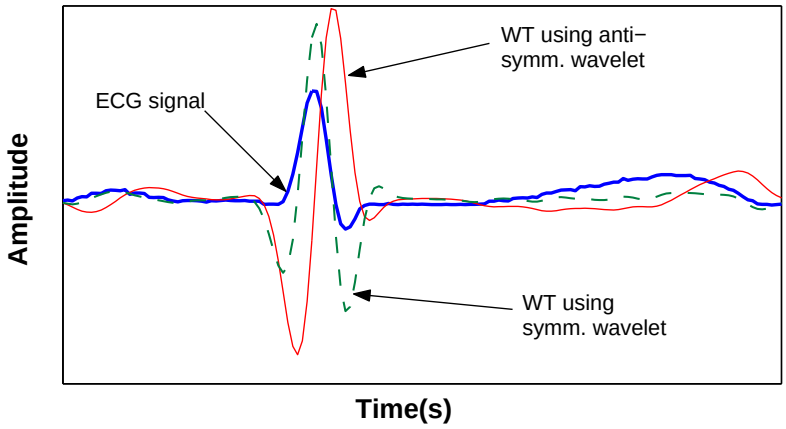

Fig. 6.6: ECG wavelet transform using anti-symmetric and symmetric wavelet

responding wavelet is shown in Fig. 6.5. Mallet has showed in his work that if the wavelet is the n^{th} derivative of a smoothing function $\theta(x)$ (a function which has the impulse response of a low pass filter) then the wavelet transform of a function $f(t)$ is directly proportional to the n^{th} derivative of $f(x)$ smoothed by $\theta_a(x)$. The wavelet at scale a can be written as shown in Eq. 6.35.

$$W_a f(x) = f * (a^n \frac{d^n \theta_a}{dx^n})(x) = a^n \frac{d^n}{dx^n}(f * \theta_a)(x) \tag{6.35}$$

where $\theta_a(x)$ is the dilation of $\theta(x)$ by a factor a defined as $\theta_a(x) = (1/a)\theta(x/a)$. Equation 6.35 means that the zero crossings of the $W_a f(x)$ corresponds to the inflection points of $f * \theta_a(x)$. A similar proof is presented by Sahambi *et. al.* [90] for the wavelet used in ECG characterisation.

The wavelet shown in Fig. 6.5 is anti-symmetric. In this case the peaks of the signal correspond to the zero crossing in the wavelet transform. In the case of symmetric wavelet (for instant, second derivative of Gaussian function, also known as the Mexican hat wavelet) the peaks will correspond to maxima points in the wavelet. This fact is shown in Fig. 6.6.

The algorithm for the detection of peaks is based on searching for modulus maxima of

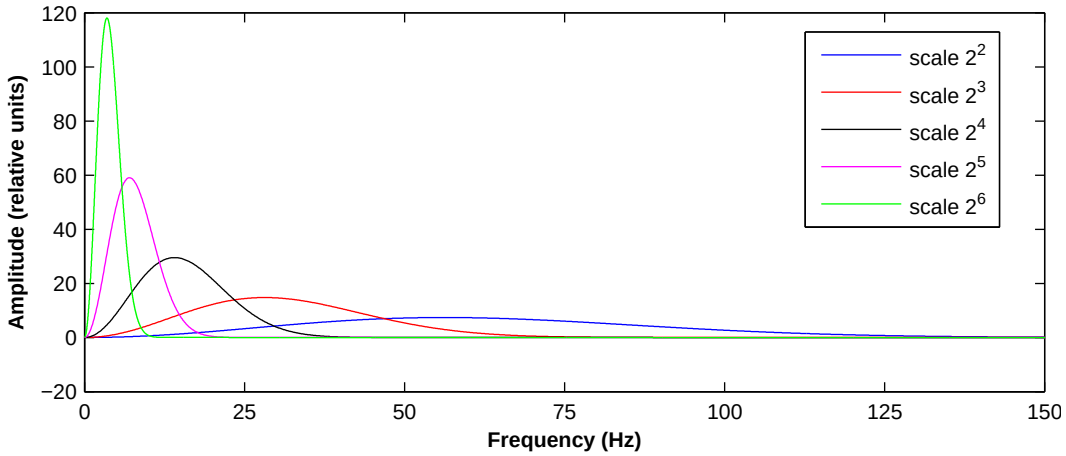

Fig. 6.7: The Fourier Transform (FT) of wavelet at scale 2^2, 2^3, 2^4, $2^5$and 2^6 (sampling rate = 1000 Hz)

Table 6.1.: Passband of wavelet filters at scale 2^2, 2^3, 2^4, $2^5$and 2^6

Scale	Lower 3 dB frequency (Hz)	Upper 3 dB frequency (Hz)
2^2	34.7	81.0
2^3	17.3	40.5
2^4	8.7	20.3
2^5	4.3	10.2
2^6	2.2	5.1

the wavelet transform at different scales. The magnitude of the Fourier transforms for scales 2^2, 2^3, 2^4, $2^5$and 2^6 of the wavelet at the sampling rate of 1000 Hz is presented in Fig. 6.7 and the wavelet passband are shown in table 6.1.

6.3.1. R-wave and QRS onset/offset detection

By looking at the passband given in table 6.1 and Fig. 6.7 it can be observed that most of the QRS energy will be between scales 2^4 and 2^5. The energy of motion artefact and baseline wander (i.e. noise) increases in scales larger than 2^5. Therefore, scales 2^2, 2^3, 2^4 and 2^5 are chosen for ECG characterisation. Some simulated signals representing different parts of the ECG signal, artefact and ECG corrupted by powerline interface and baseline drift along with the WT at the four chosen scales are shown in Fig. 6.8.

From Fig. 6.8 it can be seen that the (a) QRS complex produces a pair of minima-maxima in WT at different scales and the R-wave position can be found by locating the zero crossing between this pair of minima-maxima. Similarly the figure also shows that

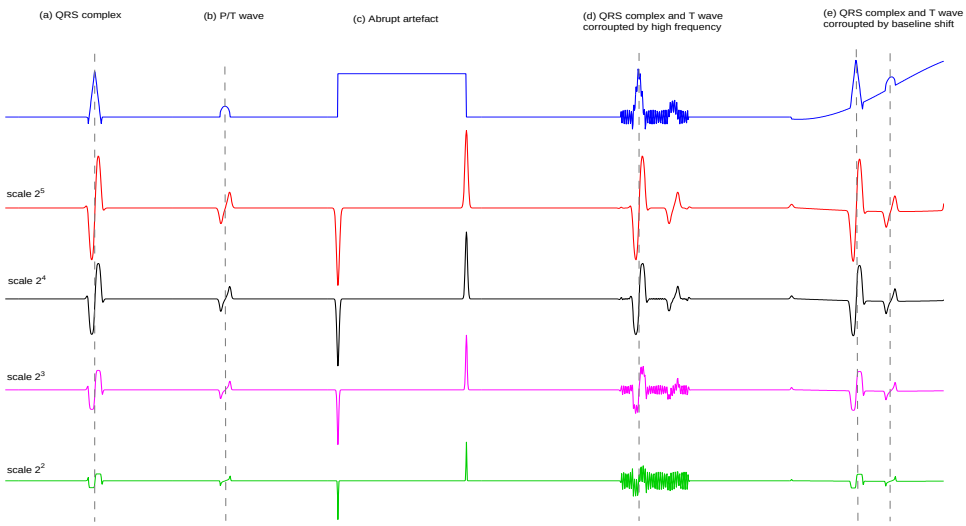

Fig. 6.8: WT of simulated ECG signal (inspired by [91])

artefacts like (c), abrupt shift artefact, produces isolated extremas that can be easily distinguished from those created by ECG signal. If the signal is corrupted by high frequency noise (d) the first two scales (i.e. 2^2 and 2^3) will be most affected, while the higher scales are not affected by this kind of noise. At sampling rate of 1 kHz baseline wandering will have significant effect only in scales higher than 2^5.

The R-wave detection is done by searching for the modulus maxima (minima-maxima) pair that crosses the threshold Th_m $\{m= 2, 3, 4, 5\}$. The search is carried out first at the largest scale (i.e. m=5) and then at the smaller scale. This is done to save computation power as the largest scale is less affected by the high frequency noise and have less number of modulus maxima. After calculating the position of modulus maxima at scale 2^5 the analysis is done at scale 2^4 in the neighbourhood of this position. If more than one modulus maxima passes the threshold then the largest one is noted. If no modulus maxima exist then this position is not considered further. In this way the search is continued till the finest scale (i.e. 2^2) and the zero crossings between the minima-maxima pair corresponds to the location of the R-wave. The thresholds are updated each time an R-wave is detected using Eq. 6.36.

$$Th_m = \left[\frac{\left(\frac{7}{8}\right) Th_m + \left(\frac{1}{8}\right) max \left\langle \left| Wf(2^m, n_m^{min}) \right|, \left| Wf(2^m, n_m^{max}) \right| \right\rangle}{2.5} \right] \tag{6.36}$$

where $\left|Wf(2^m, n_m^{min})\right|$and $\left|Wf(2^m, n_m^{max})\right|$ represent the absolute values of the minimum and maximum at scale m corresponding to a valid QRS complex.

An accumulated average of four estimated threshold values is maintained. In the pre-

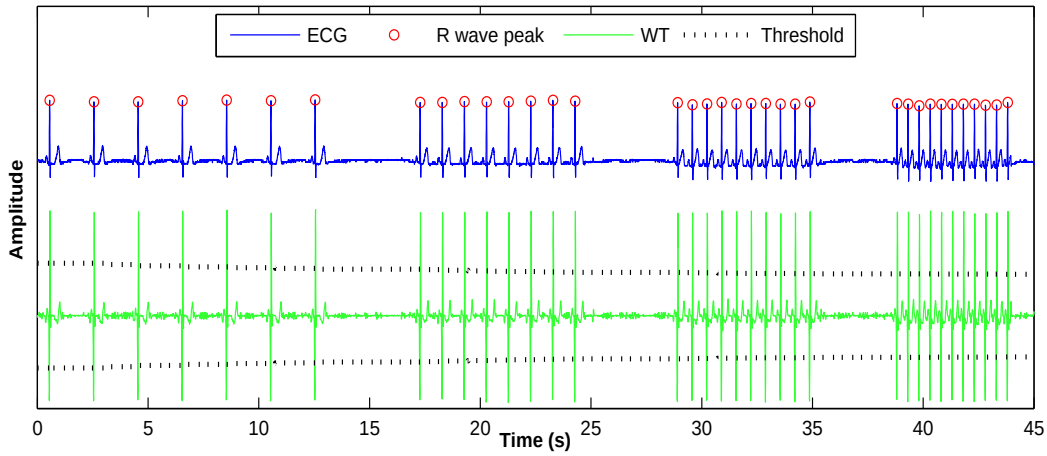

Fig. 6.9: Result of QRS detection in simulated ECG signal. The WT transform of the signal at scale 2^5 and the threshold at this scale

sence of an artefact in the signal, if the threshold value becomes too small (less than 0.3 of the average) or too large (more than 3 times the average) then the new threshold is set to half the value of the average. The result of processing the simulated ECG signal of Fig. 5.4 along with the WT at scale 2^5 and the threshold used for this scale is presented in Fig. 6.9.

As shown in Fig. 6.9 the R-wave corresponds to a minima maxima pair. But in the case of ectopic beats or in the presence of noise, two or more modulus maxima can occur of which only one is useful. For this reason, each time a group of three extremas is analysed to see if any two of them represents a valid QRS complex. The comparison starts by checking the sign of the first extrema. If it's positive then this point is discarded. If this point is a minimum then the sign of the second extrema is checked if it is negative then the first extrema is discarded (as two consecutive modulus maxima having the same sign could not represent a valid QRS complex). If the second modulus maxima is positive then the distance between the first two points is calculated if they are more than 50 ms apart then they cannot be from the same QRS complex and are discarded. If they are less than 50 ms apart then the third modulus maxima is taken into consideration. If the time interval between the second and third extrema is more than 50 ms then the first two points forms a QRS complex and the third extrema is stored to be used in the next set of modulus maximas. But if the distance between second and third point is less than 50 ms then the sign of third one is considered. If it is positive then the first and third point form a QRS complex, otherwise, if the third point is negative then it is discarded and the first two modulus maxima are used to detect the R-wave peak. The result obtained with this modulus maxima pruning algorithm when the simulated ECG signal given in Fig. 5.4 and 6.9 was corrupted by abrupt shift noise is presented in Fig. 6.10. In this figure some of the artefact peaks have crossed the threshold but by analysing the modulus maxima in a group of three as described above the detection of the R wave is still quite accurate.

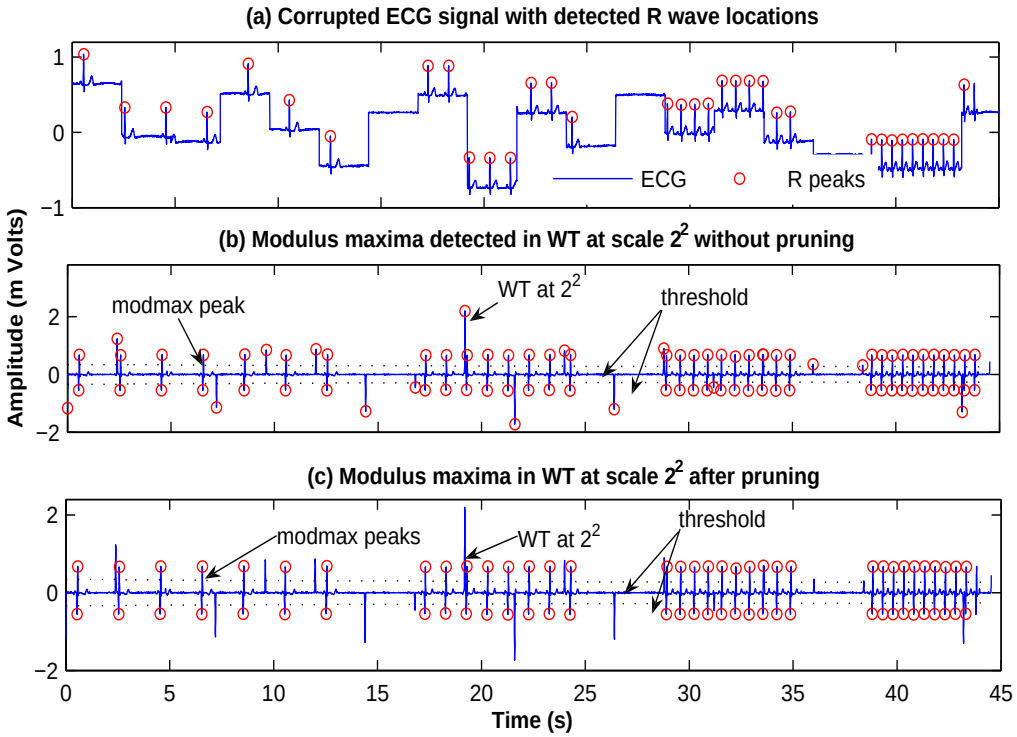

Fig. 6.10: Modulus maxima pruning result

6.4. Algorithm evaluation in presence of simulated artefacts

The performance of this peak detection algorithm implemented using the wavelet technique was also evaluated in the presence of simulated artefacts. The protocol of the study and the artefacts used to corrupt the ECG signal were exactly the same as described in section 5.3. The signals simulating the artefacts were generated using the time varying AR modelling technique as described by Sameni *et. al.* [72]. The results obtained from peak detection analysis of ECG signals corrupted by various artefacts will be presented in the following sections.

6.4.1. White Noise (WN)

The five white noise samples and the result of peak detection in one of the corrupted ECG signals at SNR level of zero dB is shown in Fig. 6.11. As before (see section 5.3.1) the wavelet peak detection algorithm also did not miss any peaks or detect any false peaks in all the ECG signals corrupted at various SNR levels by white noise. The mean difference in the peak location (MD), maximum difference in the peak location and mean of MD are presented in table 6.2.

By comparing the values of parameters presented in table 6.2 with the values presented in table 5.1, it can be seen that the values obtained for the wavelet detection algorithm are constantly lower for each of the SNR levels which indicates that this algorithm has caused less error in the detection of peak location due to the presence of white noise.

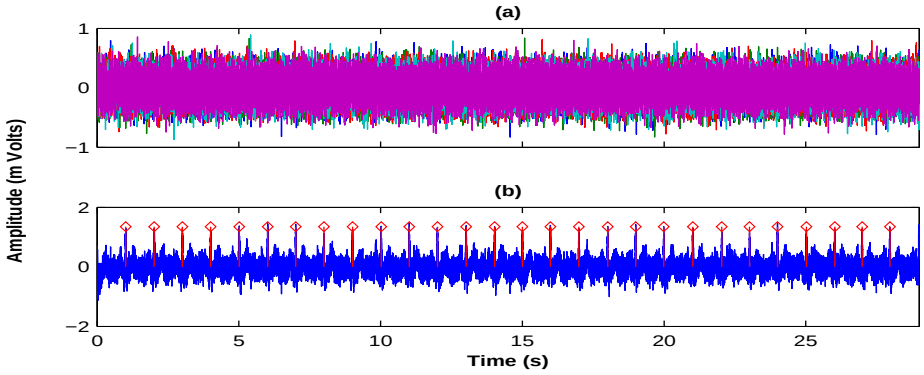

Fig. 6.11: (a) Five samples of white noise at SNR level of zero dB; (b) Peak detection result in one ECG signal corrupted at SNR level of zero dB (WT algorithm)

Table 6.2.: Parameters obtained from the peak detection results of ECG signals corrupted by white noise at varying SNR levels (WT algorithm)

Whit Noise results			
SNR	mean difference MD (samples)	max. difference (samples)	mean of MD (samples)
10	0.64, 0.788, 0.82, 0.68, 0.57	2, 2, 3, 3, 2	0.7
5	0.71, 0.78, 0.64, 0.78, 0.86	2, 1, 2, 2, 2	0.76
3	0.82, 0.64, 0.81, 1.0, 0.57	2, 2, 2, 2, 2	0.77
0	0.68, 0.89, 0.88, 0.96, 0.74	1, 3, 2, 2, 2	0.83

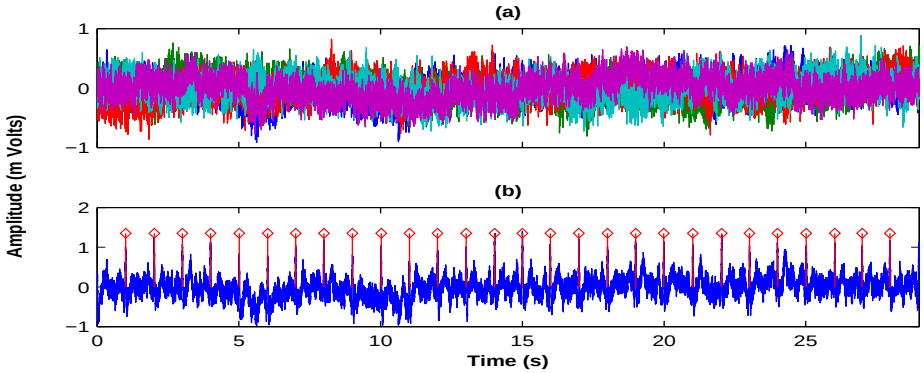

Fig. 6.12: (a) Five samples of colour noise ($\beta = 1.0$) at SNR level of zero dB; (b) Peak detection result in ECG signal corrupted by one of the colour noise samples shown in part (a) (WT algorithm)

6.4.2. Colour Noise (CN)

In case of the colour noise, the peak detection analysis was carried out again at the SNR levels of 10, 5, 3 and 0 using the same β values (1, 1.5 and 2) as mentioned in section 5.3.2. The artefacts corresponding to the three β values at SNR level of zero dB and the result of peak detection in one of the corrupted ECG signals at this SNR level for the three cases ($\beta = 1.0, 1.5, 2.0$) is presented in Fig. 6.12, 6.13 and 6.14 respectively.

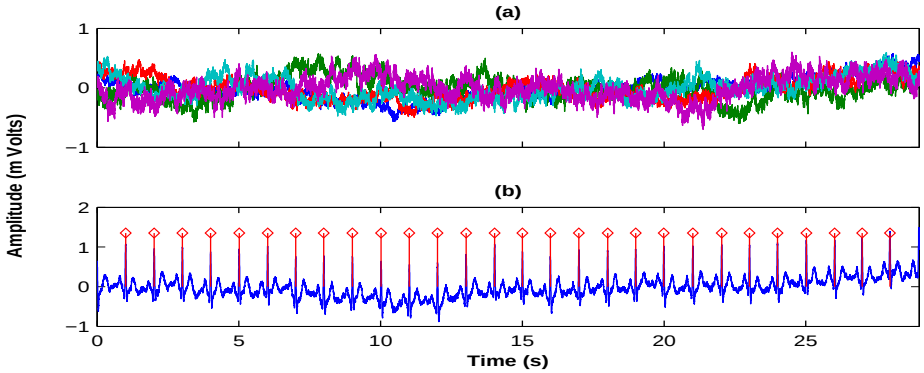

Fig. 6.13: (a) Five samples of colour noise ($\beta = 1.5$) at SNR level of zero dB; (b) Peak detection results in ECG signal corrupted by one of the colour noise samples shown in part (a) (WT algorithm)

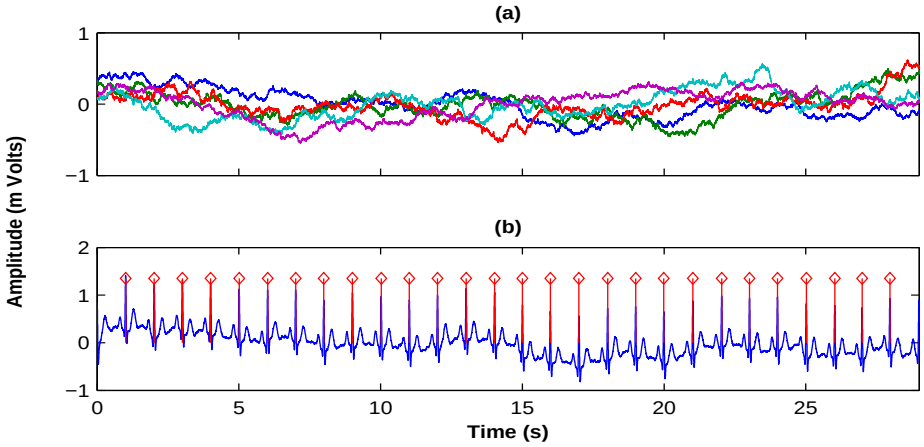

Fig. 6.14: (a) Five samples of colour noise ($\beta = 2.0$) at SNR level of zero dB; (b) Peak detection results in ECG signal corrupted by one of the colour noise samples shown in part (a) (WT algorithm)

The wavelet algorithm missed one peak in two trails of colour noise ($\beta = 1$) at SNR of zero. Apart from that there were no missed and false peaks in the ECGs corrupted by various colour noises at the SNR levels used in this simulated study. The parameters calculated from the peak detection analysis of corrupted ECG signals are presented in table 6.3. By comparing the parameters from table 6.3 to the parameters shown in table 5.2, which are obtained when the same data was analysed using the digital filter peak detection algorithm, it can be seen that the peak locations are detected more accurately by the wavelet algorithm as compared to the digital filter algorithm in the presence of different types of colour noise.

6.4.3. Baseline Wander/breathing artefact (BW)

The same ECG signals that were previously corrupted by breathing artefacts (see section 6.15) were analysed using the wavelet algorithm. The five simulated breathing artefacts are shown in Fig. 6.15 (a) whereas, part (b) of the same figure shows the result of peak detection in a corrupted ECG signal at SNR level of zero dB.

Table 6.3.: Parameters obtained from the peak detection results of ECG signals corrupted by colour noise at varying SNR levels (WT algorithm)

SNR	Mean Difference MD (samples)	max. diff. (samples)	mean of MD (samples)
Colour noise results $\beta = 1$			
10	0.57, 0.75, 0.82, 0.64, 0.78	2, 1, 2, 2, 2	0.71
5	1.04, 0.93, 1.04, 0.75, 0.89	3, 2, 2, 3, 2	0.93
3	0.86, 1.44, 0.82, 0.93, 1.11	2, 4, 3, 3, 4	1.00
0	1.12, 0.92, 1.22, 1.282 1.04	3, 2, 4, 4, 3	1.11
Colour noise results $\beta = 1.5$			
10	0.75, 0.79, 0.82, 0.71, 0.71	2, 1, 1, 1, 1	0.75
5	0.68, 0.71, 0.82, 0.57, 0.96	2, 2, 2, 1, 2	0.75
3	0.68, 0.68, 0.57, 0.79, 0.57	2, 1, 1, 2, 2	0.66
0	0.71, 0.75, 0.75, 0.71, 1.18	2, 2, 2, 2, 3	0.82
Colour noise results $\beta = 2.0$			
10	0.75, 0.75, 0.75, 0.75, 0.78	1, 1, 1, 2, 1	0.75
5	0.75, 0.75, 0.68, 0.75, 0.68	1, 1, 1, 1, 1	0.72
3	0.68, 0.86, 0.82, 0.75, 0.64	1, 1, 2, 1, 1	0.75
0	0.71, 0.61, 0.61, 0.68, 0.71	2, 2, 1, 1, 1	0.66

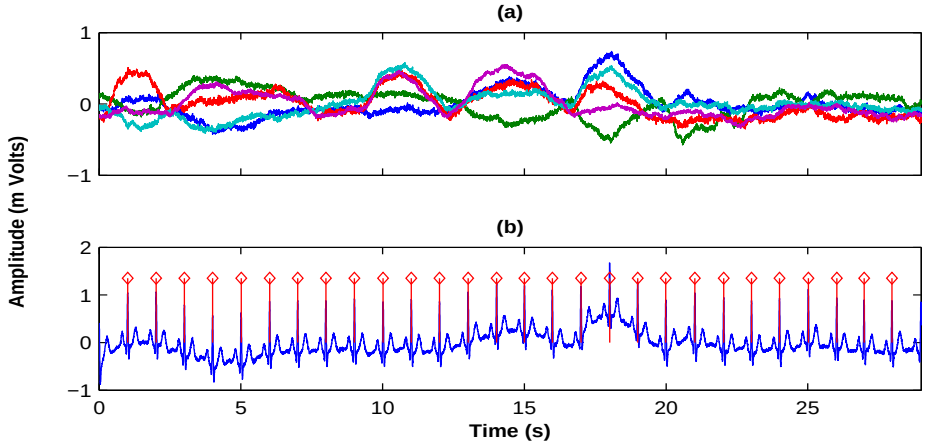

Fig. 6.15: (a) Five sets of simulated breathing artefacts at SNR level of zero dB; (b) Peak detection result in ECG signal corrupted by breathing artefact at SNR level of zero dB (WT algorithm)

Table 6.4.: Parameters obtained from the peak detection results of ECG signals corrupted by breathing artefact at varying SNR levels (WT algorithm)

Breathing artefact results			
SNR	mean difference MD (samples)	max. difference (samples)	mean of MD (samples)
10	0.75, 0.79, 0.79, 0.64, 0.71	1, 1, 1, 1, 1	0.74
5	0.75, 0.82, 0.75, 0.64, 0.71	1, 1, 1, 1, 1	0.74
3	0.71, 0.79, 0.68, 0.61, 0.64	1, 1, 1, 1, 1	0.69
0	0.71, 0.79, 0.71, 0.64, 0.67	2, 2, 2, 2, 2	0.74

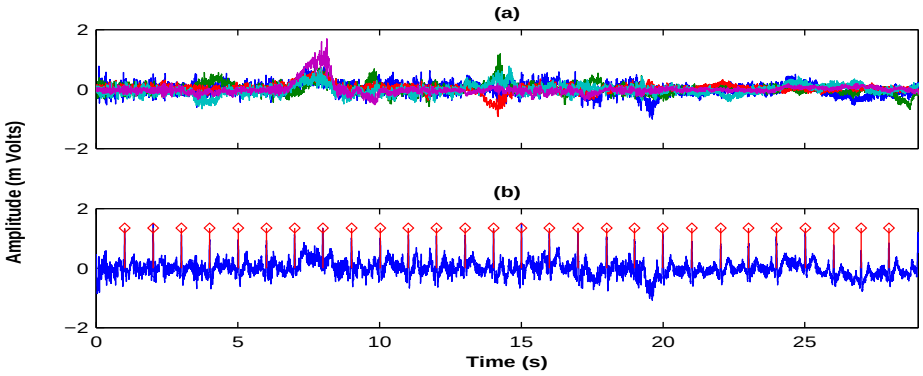

Fig. 6.16: (a) Five sets of simulated muscle artefacts at SNR level of zero dB; (b) Peak detection result in ECG signal corrupted by muscle artefact at SNR level of zero dB (WT algorithm)

As in the case of the previous peak detection algorithm, the wavelet algorithm also did not miss any peaks or detect any false peaks in any signal at the considered SNR levels. The parameters obtained from the peak detection analysis are summarised in table 6.4.

By comparing the results of table 6.4 and table 5.3 it can be seen that less error is caused by the breathing artefact when the peak detection is carried out using the wavelet algorithm.

6.4.4. Muscle Artefact (MA)

The five simulated muscle artefacts generated at 0 dB SNR level along with the peak detection result in one of the corrupted ECG signals is presented in Fig. 6.16. In the case of ECG signals corrupted by muscle movement artefact the algorithm did not detect any false peaks at various SNR levels. However, in two runs at SNR level of zero dB the algorithm did miss one peak. The parameters calculated from the peak detection analysis of ECG corrupted by muscle artefacts at different SNR levels are summarised in table 6.5.

By comparing the results obtained from the ECG signals corrupted by muscle artefact

Table 6.5.: Parameters obtained from the peak detection results of ECG signals corrupted by muscle artefact at varying SNR levels (WT algorithm)

Muscle artefact results			
SNR	mean difference MD (samples)	max. difference (samples)	mean of MD (samples)
10	0.75, 0.75, 0.86, 0.64, 0.68	2, 1, 1, 1, 1	0.74
5	0.74, 0.86, 0.82, 0.68, 0.75	3, 2, 2, 1, 2	0.77
3	0.89, 0.86, 0.89, 0.85,0.78	4, 2, 2, 2, 2	0.85
0	1.14, 1.0, 1.0, 0.70, 0.82	6, 3, 2, 2, 2	0.93

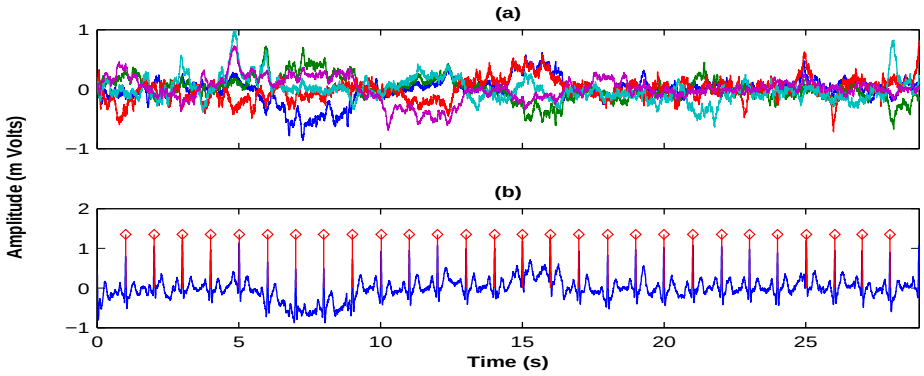

Fig. 6.17: (a) Five sets of simulated electrode movement artefacts at SNR level of zero dB; (b) Peak detection result in ECG signal corrupted by electrode movement artefact at SNR level of zero dB (WT algorithm)

when the peak detection was done using the digital filter (see section 5.3.4) with the results obtained when using the wavelet algorithm it can be seen that the wavelet algorithm has missed only two peaks at SNR level of zero dB and there are no false positives. The digital filter algorithm has missed peaks and detected false positives at all SNR levels except at SNR of 10 dB (see table 5.4). The error in the peak location due to the presence of noise is also less in the wavelet algorithm case compared to the digital filter algorithm case.

6.4.5. Electrode Movement Artefact (EMA)

The ECG signals corrupted by electrode movement artefact that were used previously in section 5.3.5 were again analysed here using the wavelet peak detection algorithm. The artefact samples and a peak detection result at SNR level of zero dB are presented in Fig. 6.17. In the case of electrode movement, the peak detection algorithm did not miss any peaks and there was no noise detected as peaks at any of the SNR levels used in the simulated study. The parameters calculated from the peak detection analysis of the ECG

Table 6.6.: Parameters obtained from the peak detection results of ECG signals corrupted by electrode movement artefact at varying SNR levels (WT algorithm)

Electrode movement artefact results			
SNR	mean difference MD (samples)	max. difference (samples)	mean of MD (samples)
10	0.89, 0.89, 0.86, 0.86, 0.82	2, 2, 2, 1, 1	0.86
5	0.76, 0.75, 0.89, 0.85, 0.82	2, 1, 2, 2, 1	0.82
3	0.78, 0.79, 0.93, 0.82, 0.86	2, 2, 2, 2, 2	0.84
0	0.79, 0.86, 1.0, 0.86, 0.78	2, 2, 3, 2, 2	0.86

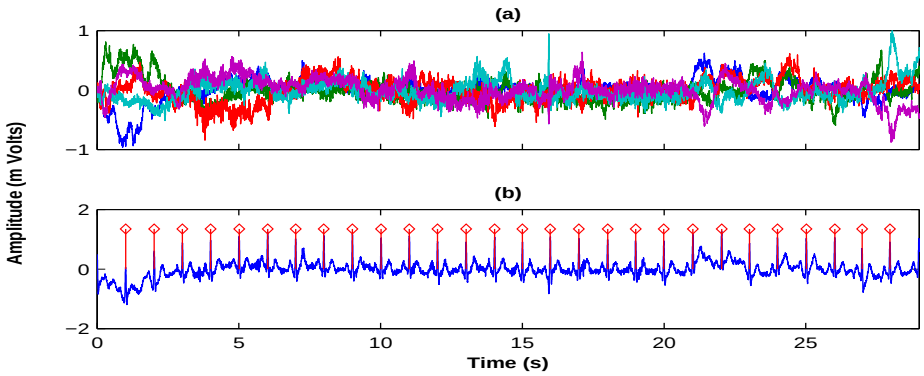

Fig. 6.18: (a) Five sets of simulated combined artefacts at SNR level of zero dB; (b) Peak detection result in ECG signal corrupted by electrode movement artefact at SNR level of zero dB (WT algorithm)

signals corrupted by electrode movement artefact are presented in table 6.6. The peak detection algorithm implemented using the wavelet algorithm caused less error than the digital filter algorithm in the location of the detected peaks in the presence of electrode movement artefacts.

6.4.6. Combined artefact

The last type of simulated artefact that was used for the evaluation of the peak detection algorithm was the combination of breathing, electrode movement and muscle artefact. The simulated signals that corrupted the ECG signal at various SNR levels used with the WT algorithm were the same as the ones used with the digital filter algorithm described in section 5.3.6. The five artefact signals at SNR level of zero dB are presented in Fig. 6.18 (a). The result obtained from peak detection when the ECG signal was corrupted by one of the artefacts shown in Fig. 6.18 (a) is shown in Fig. 6.18 (b). Similar to the other artefact cases the parameters were again calculated from the results of peak detection of ECG signals corrupted by combined artefact at different SNR level. These parameters are presented in table 6.7.

Table 6.7.: Parameters obtained from the peak detection results of ECG signals corrupted by combined artefact at varying SNR levels (WT algorithm)

Combined noise artefact results						
SNR	correct peaks detected	missed peaks	noise peaks	mean difference MD (samples)	max. difference (samples)	mean of MD (samples)
10	28, 28, 28, 28, 28	0, 0, 0, 0, 0	0, 0, 0, 0, 0	0.75, 0.68, 0.71, 0.64, 0.71	1, 1, 1, 1, 1	0.70
5	28, 28, 28, 28, 28	0, 0, 0, 0, 0	0, 0, 0, 0, 0	0.82, 0.68, 0.67, 0.57, 0.75	2, 2, 2, 1, 2	0.70
3	28, 28, 28, 28, 27	0, 0, 0, 0, 1	0, 0, 0, 0, 0	0.71, 0.71, 0.71, 0.57, 0.63	2, 2, 2, 2, 2	0.67
0	28, 28, 27, 28, 27	0, 0, 1, 0, 0	0, 0, 0, 0, 0	0.67, 0.71, 0.79, 0.68, 0.70	2, 3, 3, 2, 2	0.71

By comparing the results presented here with the results presented in section 5.3, where the same artefacts were used for the evaluation of the performance of the peak detection algorithm which was based on digital filtering technique, it can be seen that the wavelet peak detection algorithm has performed better. This algorithm when compared with the digital filtering peak detection algorithm has produced fewer errors, by missing less numbers of original peaks and by detecting less false positives. Also, the differences between the known peak locations of the simulated ECG signal (see Fig. 5.5) and the peak locations obtained by analysing the corrupted ECG signals were smaller in the case of the wavelet peak detection algorithm compared to the difference obtained when the digital filter technique was used for peak detection. This was true for almost all of the artefacts and the SNR levels that were considered in the simulated study.

To further compare the two developed peak detection algorithms, the wavelet algorithm will be further evaluated off-line using real ECG signals (as in section 5.4), and on-line as described in section 5.5. This evaluation of the WT algorithm and the results will be presented in the next section.

6.5. Off-line evaluation of the wavelet peak detection algorithm evaluation on real data

The developed WT peak detection algorithm was also tested using an ECG data set of normal patients from the Normal Sinus Rhythm (NSR) database available at (`http://www.physionet.org/physiobank/database/nsrdb/`). The same data (see section 5.4) as the ones used to evaluate the digital filtering algorithm were also used for the

Table 6.8.: QRS detection result for samples from Normal Sinus Rhythm database using wavelet algorithm

Sr. No	Name of sample	Total no. of Peaks	no. of Peak missed (F_N)	no.of noise det. as peaks (F_P)	no. of correctly det. peaks (T_P)	% Sensitivity	% Accuracy
1	16265	875	0	0	875	100	100
2	16272	575	2	3	573	99.13	99.65
3	16420	785	3	1	782	99.62	99.87
4	16539	725	1	1	724	99.86	99.58
5	16773	689	0	0	689	100	100
6	16786	628	1	0	627	99.84	100
7	17052	714	0	0	714	100	100
8	17453	707	0	0	707	100	100
9	18177	912	0	0	912	100	100
10	18184	751	4	0	747	99.46	100
11	16273	772	1	1	771	99.87	99.87
12	16483	770	1	0	769	99.87	100
13	16795	575	1	1	574	99.82	99.82
14	19088	733	0	0	733	100	100
15	19090	742	0	0	742	100	100
16	19140	782	0	0	782	100	100
17	19830	876	0	0	876	100	100
18	19093	546	0	0	546	100	100

WT evaluation. The results for QRS detection employing this technique are summarised in table 6.8. The sensitivity and the accuracy for this algorithm was calculated again by using Eq. 5.2 and Eq. 5.3 respectively.

The data obtained from healthy volunteers and anaesthetised patients used in section 5.5 were also processed in order to make better comparison with the first algorithm. In the case of healthy volunteers, detection of 17788 beats resulted in zero false positives and zero false negatives. Results obtained by analysing four anaesthetic patients data, presented in table 5.8, with the wavelet algorithm are shown in table 6.9.

Table 6.9.: QRS detection result for anaesthetic patients data set using wavelet algorithm

Data No.	Total no. of Peaks	no. of Peak missed (F_N)	no.of noise det. as peaks (F_P)	no. of correctly det. peaks (T_P)	% Sensitivity	% Accuracy
1	13079	1	1	13078	99.99	99.99
2	15625	9	5	15624	99.85	99.92
3	11977	3	4	11974	99.98	99.97
4	23504	1	1	23503	99.99	99.99
					Avg.= 99.95	Avg.= 99.96

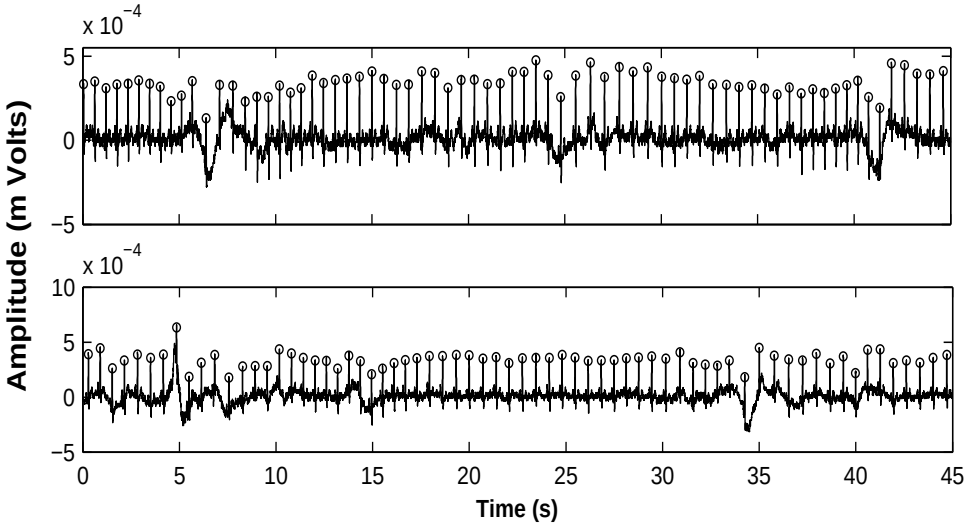

Fig. 6.19: QRS detection examples in healthy volunteers using wavelet algorithm

Further tests were done by using this algorithm online for the detection of the R-wave in anaesthetised patients using the same data acquisition setup as describe in section 5.5. Few examples of R-wave detection in healthy volunteers and anaesthetic patients are shown in Fig. 6.19 and Fig. 6.20 respectively.

By comparing the results of R-wave detection on the healthy volunteers data set it can be seen that the wavelet algorithm has achieved better accuracy (99.96%) and sensitivity (99.95%) when compared to the digital filter algorithm, which achieved an accuracy of 99.84% and sensitivity of 99.83% (see table 5.8 and table 6.9). Similarly by comparing the results given in table 6.8, using the wavelet technique, with the ones presented in table 5.7, for the digital filter algorithm, it can be seen that the wavelet algorithm has performed much better with data sets (1990,19140,19830 and 19093), where the first algo-

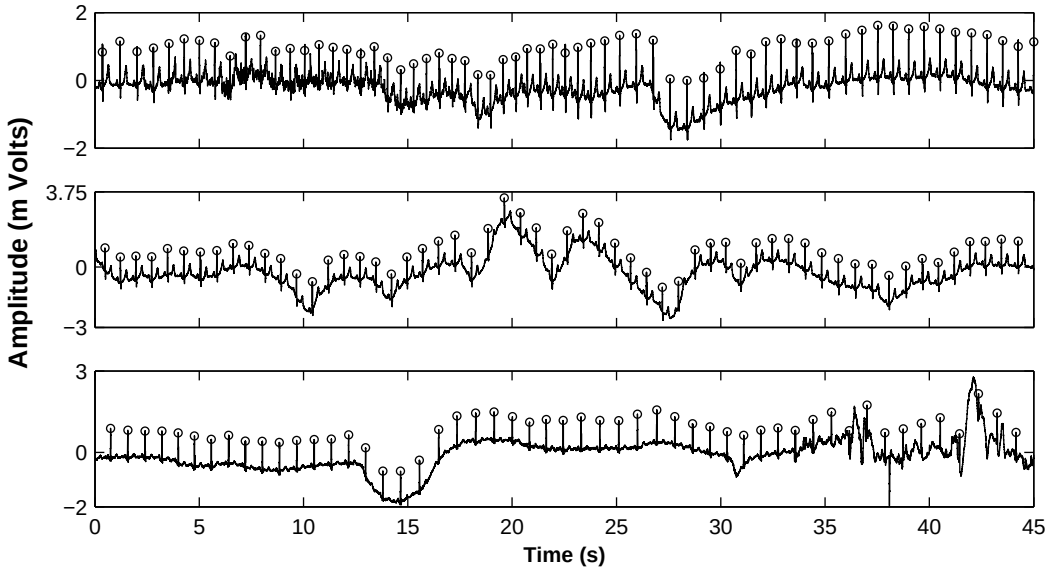

Fig. 6.20: QRS detection examples in anaesthetic patients using Wavelet algorithm

rithm detected a large number of false peaks due to the artefact at the beginning of the data (see Fig. 5.14). In this data set the wavelet algorithm achieved an accuracy of 99.93% and sensitivity of 99.86%.

6.6. Summary

Similar to the case of the ECG R-wave detector implemented using the digital filter discussed in chapter 5, the R-wave detector implemented using WT was also extensively tested offline by making use of the simulated signals that closely mimic the physiological artefacts which generally contaminate the ECG signals (see section 6.4). The algorithm was also validated on real ECG signals from the NSR database (the results from this analysis are presented in table 6.8). In order to compare the WT based detector with the detector based on the digital filter the data from healthy volunteers and locally anaesthetised patients, which were previously analysed using the digital filter detector were also processed using the WT based algorithm for peak detection. The WT algorithm achieved achieved accuracy and sensitivity of more than 99%.

6.7. Conclusions from ECG R-wave detection

Signal processing techniques for QRS detection has been a research topic for more than 30 years. With the progress of computer technology more complex and advance signal processing techniques have been applied for QRS detection. A comprehensive review of the different methods used for QRS detection has been presented by Köhler *et. al.* [92]. Neural networks, genetic algorithms, wavelet transforms, filter banks, digital filters as

well as heuristic methods mostly based on nonlinear transforms are some of the methods that have been used for R-wave detection. Many of these algorithms shared the same analysis steps. These steps can be divided into preprocessing or feature extraction stage including linear and nonlinear filter and a decision stage including peak detection and decision logic [92]. The performances of these algorithms are validated against standard ECG databases or subset of these databases; some of these are available from *Physionet*. Köhler *et. al.* [92] have categorised the algorithms base on their performance (sensitivity and accuracy) and computational requirements. Algorithms in the high performance category have sensitivity and accuracy of more than 99%. The two algorithms developed in the study have shown similar results in analysis of the real ECG signals acquired from the locally anaesthetised patients and the NSR database taken from *Physionet*.

Even though in most cases both algorithms have achieved accuracy and sensitivity of more than 99%, the WT algorithm is preferred because of its reliability in the presence of high level of artefacts with wide frequency characteristics. The inability of the first algorithm (digital filter based algorithm) to deal with such artefacts has caused the algorithm to identify a lot of false positives. Due to this fact the digital filter R-wave detector has shown poor performance in a few signals from the NSR database that contained a sawtooth wave like artefact at the beginning of the signal (see Fig. 5.14). The wavelet algorithm could distinguish QRS complexes from various type of artefacts that usually contaminate the ECG signals by utilising information from four different wavelet scales which represent information from different frequency bands. The digital filter algorithm on the other hand relies on a single filtered signal for peak detection which decreases the accuracy of this algorithm in the presence of artefact with wide frequency spread. Another advantage of the wavelet technique is that it could be easily used to obtain a full ECG characterisation which would allow detection of ectopic beats. However, the better performance of the wavelet peak detection algorithm comes at a price of high computational requirement. In their review Köhler *et. al.* [92] have mentioned other algorithms, based on techniques such as filter banks, vectorcardiogram and zero crossing counts, which have achieved similar performance with significantly less computational requirement. In future these algorithms could be tried for more optimal online implementation of ECG R-wave detection.

In the current work, because of the better overall performance achieved by the WT peak detection algorithm, it has been decided that in further analysis this algorithm will be the preferred R-wave detection algorithm. After the R-wave detection the next step in HRV analysis requires the detection and correction of ectopic beats and formation of a time series representing the beat to beat variation of the heart rate. The following chapter will discuss these steps.

7 Introduction: Spectral Analysis

7.1. Introduction

Apart from the frequency domain analysis of HRV, spectral analysis techniques will be employed in this work to show the effectiveness of the methods that will be used for signal representation; ectopic beat correction and detrending of the HRV signals. This chapter presents an introduction of the commonly used spectral analysis techniques.

A number of frequency domain HRV measures have been used as standard in cardiology both for the purpose of physiological and clinical interpretation and for diagnostic purposes. The use of frequency domain analysis in different clinical applications has been reviewed by Singh *et. al.* [93]. Power Spectral Density (PSD) analysis is the natural tool to examine the variability of cardiovascular signal, as it allows the estimation of location and strength of major components which contribute to the signal variance. Mathematically PSD of a Wide Sense Stationary (WSS) signal can be written as the DTFT of the autocorrelation sequence (see Eq. 7.1).

$$P_{xx}(e^{j\omega}) = \sum_{m=-\infty}^{m=\infty} r_{xx}[m]e^{-jm\omega} \tag{7.1}$$

where $r_x(k)$ is the autocorrelation sequence shown in Eq. 7.2.

$$r_{xx}[m] = E\left\{x[n+m]\, x^{\star}[m]\right\} \tag{7.2}$$

and $E\{x\}$ represents the mean or expected value of x.

The use of power spectral analysis was first introduced in the study of HRV in the 1980s [37, 94, 95, 96]. Since then spectral analysis has gained increasing attention and a variety of techniques have been proposed to accurately identify the rhythms hidden in the HRV signals. The most commonly used methods for estimation of PSD can be generally classified as non-parametric (FFT based) and parametric methods. The basic difference in these algorithms is in the way in which the autocorrelation function of the

signal is estimated to obtain the PSD. Both the parametric and the non-parametric methods that will be used in this study are described in the following sections.

7.2. Application of non-parametric methods for the estimation of PSD

As shown in Eq. 7.1 in order to calculate the true value of PSD the autocorrelation sequence of the signal has to be calculated but, as in most practical applications data is measured over a finite interval, suppose $n = 0, 1, ..., N-1$, therefore only an estimate of the autocorrelation sequence can be obtained as shown in Eq. 7.3 [97].

$$\hat{r}_{xx}[m] = \frac{1}{N-|m|} \sum_{n=0}^{N-|m|-1} x^*[n+|m|]\, x(n) \qquad ; \quad -(N-1) \leq m \leq N-1 \tag{7.3}$$

Using this estimate of the autocorrelation sequence (see Eq. 7.3) the estimation of power spectrum can be written as shown in Eq. 7.4.

$$\hat{P}(f) = T \sum_{m=-L}^{L} \hat{r}_{xx}[m] e^{(-j2\pi f m T)} \tag{7.4}$$

where T is the sampling period.
This is one of the basic non-parametric methods for estimating the power spectrum and is known as the periodogram, first introduced by Schuster in 1898 in the study of periodicities in sunspot numbers [98]. The periodogram can also be written in terms of the finite length signal x_N as shown in Eq. 7.5.

$$\hat{P}_{per}(f) = \frac{T}{N} \left| \sum_{n=0}^{N-1} x[n] exp(-j2\pi f n T) \right|^2 \tag{7.5}$$

In Eq. 7.5 the data is considered to be windowed using a rectangular window.

Unfortunately, the power spectrum, estimated using the periodogram ($\hat{P}_{per}$) method is not consistent (i.e. it is a biased estimate and its variance does not go to zero as data length N approaches infinity). Windowing the data has major effect on the performance of the periodogram. The sharp transition of the rectangular window causes large ripples (side lobe) in the spectrum which might mask the smaller signal components. This behaviour is called *Gibbs phenomenon*.

In order to improve the performance of the periodogram different methods has been used. One of the commonly used methods is Welch's method. In this case, the periodogram is modified in two ways. Firstly, the data is split into overlapping segments. Secondly, instead of a rectangular window, different functions with smoother transition

to zero are used to window each segment of data. This is done in order to reduce the *Gibbs phenomenon*. The smoother transition of the window function reduces the side lobe level but also increases spectral smoothing. After windowing, the periodogram of each segment is calculated and averaged. If data x of length N is divided into P sequences each of length D and each sequence is offsetted by S points, then the sample spectrum of the p^{th} segment can be written as shown in Eq. 7.6 [97].

$$\tilde{P}_{xx}^{(p)}(f) = \frac{1}{UDT}\left|X^{(p)}(f)\right|^2 \tag{7.6}$$

where $X^{(p)}(f)$ is the DFT of the p^{th} segment of the data and U is the discrete time window energy defined as (see Eq. 7.7).

$$U = T\sum_{n=0}^{L-1} w^2[n] \tag{7.7}$$

The fact or U is used so that the periodogram will be an asymptotically unbiased estimate of power spectrum, where the expectation value approaches to the theoretical value of the power spectrum as N approaches infinity.

The average of the windowed segment periodogram yields the Welch's periodogram estimate (see Eq. 7.8).

$$\hat{P}_{Wxx}(f) = \frac{1}{P}\sum_{p=0}^{P-1} \tilde{P}_{xx}^{(p)}(f) \tag{7.8}$$

The variance of the Welch's periodogram is roughly inversely proportional to the number of segments, represented above as P. Therefore, by dividing the original signal into more segments provides a better result. Usually an overlap of 50% to 75% is used. By increasing the overlap further does not provide significant improvement. The resolution of the periodogram depends on the window used and is generally defined as the 3 dB bandwidth of the data window.

Considering two sequences $x[n]$ and $y[n]$ each of length N which are again divided into P sequences each of length D, the cross-spectrum of the p^{th} segment can be written as shown in Eq. 7.9.

$$\tilde{P}_{xy}^{(p)}(f) = \frac{1}{UDT}\, X^{(p)}(f)\left[Y^{(p)}(f)\right]^* \tag{7.9}$$

The final periodogram is again obtained by averaging over the segmented periodograms as shown in Eq. 7.10.

$$\hat{P}_{Wxy}(f) = \frac{1}{P}\sum_{p=0}^{P-1} \tilde{P}_{xy}^{(p)}(f) \tag{7.10}$$

7.3. Application of parametric methods for the PSD estimation

7.3.1. Introduction

The basic limitation of non-parametric methods for spectral analysis is the inherent assumption that autocorrelation estimate $r_{xx}[m]$ is zero for lag m larger that the data length N. This assumption severely limits the frequency resolution and the quality of power spectrum estimate that is achieved. Another assumption is that data is assumed to be periodic with period N. Both these assumptions are quite unrealistic.

The parametric method of spectral analysis does not require these assumptions. This method extrapolates the values of autocorrelation for lag larger than the data length. This extrapolation is done by constructing a model, using prior information about the data, which approximate the process that generated the observed data. Such model will make a more realistic assumption about the data outside the window. Thus, the need of the window function can be eliminated along with their distorting impact. The PSD spectrum can then be calculated using the model parameters. The degree of improvement in resolution and spectral fidelity, if any, is determined by the appropriateness of the selected model and the ability to fit the measured data or autocorrelation sequence with a few model parameters.

The parametric approach to spectral estimation involves the following three steps:

1. An appropriate model is selected to represent the measured data.
2. Model parameters are estimated and
3. The estimated parameters of the model are used to calculate the PSD spectrum.

7.3.2. Autoregressive Spectral estimation

A special class of models driven by a white noise process and possessing rational system function includes the Autoregressive (AR), Moving average (MA) and Autoregressive-moving average (ARMA). The output process of this class of model has power spectral density that is totally described in terms of model parameters and the variance of the white noise process. These parametric methods model the signal as the output of a linear system characterised by a rational system function of the form as shown in Eq. 7.11.

$$H(z) = \frac{B(z)}{A(z)} = \frac{\sum_{k=0}^{q} b_k z^{-k}}{1 + \sum_{k=1}^{p} a_k z^{-k}} \tag{7.11}$$

The corresponding difference equation is (see Eq. 7.12)

$$x[n] = -\sum_{k=1}^{p} a_k x[n-k] + \sum_{k=0}^{q} b_k w[n-k] \tag{7.12}$$

where $w[n]$ is the output sequence to the system and the observed data $x[n]$ represent the output sequence. In this case the power density of spectrum of the data can be written as shown in Eq. 7.13.

$$P_x(f) = T\,\sigma_w^2 \frac{|B(f)|^2}{|A(f)|^2} \tag{7.13}$$

Of all the models, AR is the most widely used because of its suitability to represent the spectra with narrow peaks. The AR model results in very simple linear equations for AR parameters. The power spectral density using AR model can be written as (see Eq. 7.14) [97].

$$P_x(f) = \frac{T\,\sigma_w^2}{|A(f)|^2} \tag{7.14}$$

where σ_w^2 is the variance (i.e. $\sigma_w^2 = E[|w[n]|^2]$).

A p^{th} order autoregressive process consisting of m channels can be written as shown in Eq. 7.15

$$\boldsymbol{x}[n] = -\sum_{k=1}^{p} \boldsymbol{A}[k]\boldsymbol{x}[n-k] - \boldsymbol{u}[n] \tag{7.15}$$

In this case $\boldsymbol{A}[k]$ are the $m \times m$ autoregressive parameter matrix and $\boldsymbol{u}[n]$ is an $m \times 1$ vector representing the input driving noise process. The z-transform for the system can be written as shown in Eq. 7.16.

$$\boldsymbol{P}_{AR}(z) = \boldsymbol{A}^{-1}(z)\boldsymbol{P}_w\boldsymbol{A}^{-H}(1/z^*) \tag{7.16}$$

and the multichannel PSD function can be written as shown in Eq. 7.17 [97].

$$\boldsymbol{P}_{AR}(f) = T\,\left[\underline{\boldsymbol{a}_p}\,\underline{\boldsymbol{e}_p^H}(f)\right]^{-1}\boldsymbol{P}_w\left[\underline{\boldsymbol{e}_p}(f)\,\underline{\boldsymbol{a}_p^H}\right]^{-1} \tag{7.17}$$

Whereas in Eq. 7.17

$$\underline{\boldsymbol{e}_p}(f) = [\boldsymbol{I}_m \quad exp(j2\pi fT)\boldsymbol{I}_m \;\ldots\; exp(j2\pi fpT)\boldsymbol{I}_m]$$

$$\underline{\boldsymbol{a}_p} = [\boldsymbol{I} \quad \boldsymbol{A}[1] \;\ldots\; \boldsymbol{A}[p]]$$

and $\boldsymbol{P}_w$ is the input covariance matrix and superscript H is used to indicate Hermitian transpose operation. The diagonal entries of matirx $\boldsymbol{P}_{AR}(f)$ will have the auto-spectrum terms while the other terms of the matrix will represent the cross-spectrum between the signals.

There are various methods available for the estimation of parameters of the single and multichannel autoregressive models. Further details regarding parameter estimation can

be found in Marple's book [97]. Basselli *et. al.* [99] have also provided a good introduction of multichannel autoregressive spectral analysis and its application in HRV studies.

7.3.2.1. Model order selection

As mentioned before the choice of appropriate model order plays an important role in parametric spectral analysis. If the model order it too low then the resultant spectrum will be smoothed and will have poor resolution. If, on the other hand, the model order is too high, then the spectrum may contain spurious peaks. There are several criteria for selecting model order. Some of the more commonly used criterion include *Final Prediction Error* (FPE) and *Akaike Information Criterion* (AIC) proposed by Akaike [100, 101], *Minimum Description Length* (MDL) put forward by Rissanen [102], *Bayesian Information Criterion* (BIC) [103, 104, 105] and *Criterion Autoregressive transfer* (CAT) proposed by Parzen [106]. Mathematically these criteria can be written as shown in Eq. 7.18.

$$\begin{aligned} FPE(p) &= \hat{\sigma}_{wp}^2 \left(\frac{N+p+1}{N-p-1}\right) \\ AIC(p) &= ln\hat{\sigma}_{wp}^2 + 2p/N \\ MDL(p) &= N\, ln\hat{\sigma}_{wp}^2 + p\, lnN \\ CAT(p) &= (\frac{1}{N}\sum_{k=1}^{p}\frac{1}{\bar{\sigma}_{wk}^2}) - \frac{1}{\hat{\sigma}_{wp}^2} \\ BIC[p] &= N\, ln\hat{\sigma}_{wp}^2 - (N-p)\, ln(1-\frac{p}{N}) + p\, ln(N) + p\, ln\left[\frac{1}{p}\left(\frac{\sigma_x^2}{\hat{\sigma}_{wp}^2}-1\right)\right] \end{aligned} \tag{7.18}$$

where

$$\bar{\sigma}_{wk}^2 = \frac{N}{N-k}\hat{\sigma}_{wp}^2$$

and σ_x^2 is the variance of the output signal.

Similarly the multichannel version of AIC and FPE can be written as shown in Eq. 7.19 and Eq. 7.20 respectively [99].

$$AIC_{mc}(p) = N\, ln\left[\det(\boldsymbol{P})\right] + 2L^2 p \tag{7.19}$$

$$FPE = \left(\frac{N+Lp+1}{N-Lp-1}\right)\det(\boldsymbol{P}) \tag{7.20}$$

In Eq. 7.19 and Eq. 7.20 N represent the total length of the data, L represents the number of total channels and $\boldsymbol{P}$ is the mean value of the forward and backward linear prediction error matrices.

Various experimental results have shown that the model criteria do not provide definitive results [107]. Recently the suitability of these criteria was studied for the HRV signals [108, 109] with contrasting results. Boardman *et. al.* [108] analysed data in segment of 128 samples with sampling frequency of 4 Hz and compared FPE, AIC, MDL and CAT their results showed that all the four criteria underestimate the model order. As a consequence, they suggested the use of model order 16 for the HRV studies. Carvalho *et. al.* [109] studied the suitability of the above four criteria as well as BIC using signal segments of 15 seconds to 300 seconds at sampling frequencies of 2 Hz and 4 Hz.

According to their result FPE, AIC and CAT criteria tends to overestimate the AR model order and perform poorly for the HRV signals. The other two criteria MDL and BIC both underestimate the order but present better option as order selection criteria. This study suggests that for AR spectral analysis of HRV signal at 4 Hz a model order between 15 and 20 should be used for the data segment of 15 seconds to 300 seconds.

Accordingly, in our study an AR model with model order 16 was used for spectral analysis of HT signals (f_s= 4 Hz) obtained from the data of the anaesthetised patients.

7.4. Discussion and conclusions

In this chapter the basic idea of the Welch's periodogram (non-parametric) and the AR modelling (parametric) method of spectral analysis was introduced. These two basic techniques will be used in the following chapters to verify the results obtained from various steps involved in the HRV analysis (signals representation, ectopic beat correction and detrending of the HRV signals). Finally, the HRV signals obtained from the data from the anaesthetised patients included in this study will be analysed using these basic spectral techniques, before making use of the more sophisticated techniques for frequency domain analysis for the HRV signals.

8

Tachogram resampling and Ectopic beat correction

8.1. Introduction

The R-wave detection in the ECG signal is followed by the construction of the tachogram signal (see Fig. 5.1) as mentioned in section 5.1. By using the R wave location the heart rate in bpm can also be obtained as $60/(r_{i+1} - r_i)$. As the tachogram values are calculated at the beat occurrence time, therefore this signal and the heart rate signal, calculated from it, both are unevenly sampled. Since the non-parametric (Fourier based) and parametric methods of frequency analysis require the data to be evenly sampled, the tachogram has to be resampled. Interpolation techniques usually used for resampling the heart rate data can cause problems in HRV parameter estimation.

This chapter discusses the methods used for interpolation and HRV signal representation. After obtaining the HRV presentation the effect of ectopic and/or missing beats on the frequency analysis of the HRV signals is presented and the method used for correction of the ectopic and/or missing beats is described.

8.2. Linear and Spline Interpolation

Interpolation of irregularly spaced data such as HR can cause non-linear affects and can be seen as a time-variant filter that acts with different frequency response as a function of the space between interpolated samples [110]. Thus, the spectrum obtained by the interpolated data is filtered with a time-variant filter. The filter response can be estimated by the spectrum of the impulsive response, which is obtained by interpolating a unitary impulse at time $t = 0$, preceded and followed by zeros regularly spaced at T_0. Since the beat to beat heart period changes, the filtering effect changes and becomes time varying. The impulsive response for linear and cubic spline interpolation is shown in Fig. 8.1. Similarly the filter responses obtained for different interpolation schemes are presented in Fig. 8.2. From the filter responses the cutoff frequency for the linear interpolation is $0.36/T_0$ Hz when the interpolating factor is two and goes to $0.32/T_0$ Hz when the

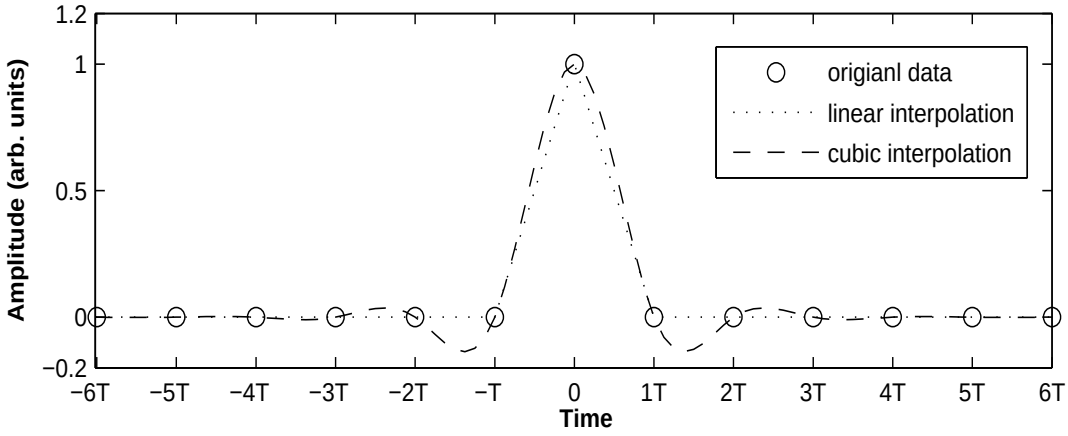

Fig. 8.1: Impulsive response, linear and cubic spline interpolation with interpolation order 16

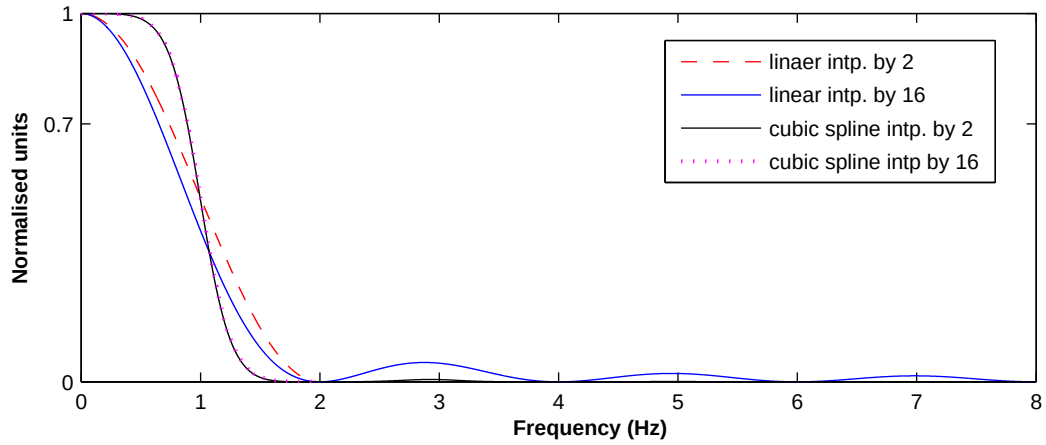

Fig. 8.2: Frequency response, linear interpolation (intp.) and cubic spline of order two and sixteen (T_0=0.5)

interpolating factor increases to sixteen or higher. The number of data values added between two original data values by interpolation is equal to interpolating factor minus one e.g. interpolating by a factor of two adds one value between original data values. The cutoff frequency for the cubic spline interpolation is $0.44/T_0$ Hz and has negligible dependence on the interpolating factor, a fact represented by the closeness of cubic spline filter response for interpolating factor of two and sixteen (see Fig. 8.2). Similarly the cutoff frequency of fourteenth order spline is $0.48/T_0$ [110]. Because the cutoff frequency is relative to $1/T_0$, in absolute frequency terms, the filtering effect will be more significant at low heart rate values. Another problem with cubic interpolation is that it could create unacceptable oscillations when one RR interval is unusually longer than its predecessor. In order to avoid these problems Berger *et. al.* suggested a simple and efficient algorithm, which drives the heart rate signal from the ECG at a constant sampling rate so that no further interpolation is required [111].

8.3. Heart rate signal using Berger algorithm

Hyndman and Mohan first suggested the Integral Pulse Frequency Modulation (IPFM) model as a functional description of the sinoatrial node [112]. It still remains a useful model for the mechanism by which the ANS modulates the heart rate. An IPFM model is a device that integrates its input signal until the result of this integration reaches a preset threshold, at which point the device sends out a pulse, which represents a heartbeat, resets the integrator to zeros and start the integration process again [111]. The operation of IPFM can be expressed mathematically as shown in Eq. 8.1.

$$T = \int_{t_k}^{t_k+1} (1 + m(t))\, dt \tag{8.1}$$

where T is the integrator's threshold value, which is equal to the duration of each RR interval where there is no autonomic modulation of SA node's intrinsic firing rate. The input signal is $s(t) = 1 + m(t)$, where all the autonomic influences are lumped together in this model and are represented by $m(t)$. The signal $m(t)$ is supposed to be causal and bandlimited with negligible power spectral density over 0.4 Hz. The RR interval decreases with an increase in $m(t)$, so that the instantaneous heart rate varies in proportion to $s(t)$ and t_k represents the time of the k^{th} R-wave. The continuous form generalisation of the IPFM model can be written as shown in Eq. 8.2.

$$x = \int_{0}^{t(x)} \frac{1 + m(\tau)}{T}\, d\tau \tag{8.2}$$

where $t(x)$ is a continuous function that solves the model equation and whose values at $x = k = 1, 2, ..., N$ $(t(k) = t_k)$ are the k^{th} beat occurrence time .

The first step in estimating the evenly spaced (in time) heart rate signal is the choice of sampling frequency. This frequency is chosen independently, without regards to the mean heart rate or the sampling rate of the ECG signal. The heart rate value at each sample point is obtained by defining a local window that extends from the previous sample to the next sample. The number of RR intervals that lies inside this window, including fractions, is noted and the heart rate is calculated as given in Eq. 8.3.

$$hr_i = f_r.n_i/2 \tag{8.3}$$

where f_r is the sampling rate of the resulting heart rate signal and n_i is the number of RR intervals inside the local window centred at the i^{th} sample point. The process of calculating the RR interval inside a window is depicted in Fig. 8.3.

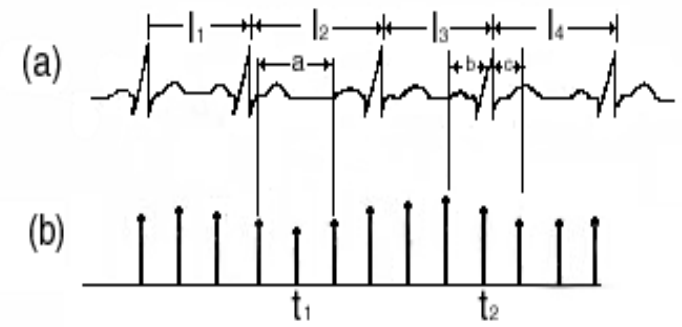

Fig. 8.3: Berger *et. al.* algorithm. (a) A segment of an ECG (electrocardiogram) signal; (b) The heart rate samples corresponding to the ECG signal in (a), determined using Berger *et. al.* algorithm. The fraction (often less than unity) of RR intervals within the local window centred at t_1 is a/I_2, and at t_2 is $b/I_3 + c/I_4$. The value of the heart rate at each sample point is taken to be the number of intervals that fell within the local window centred at that point divided by the width of the window. This calculation is performed at each point in (b), *i.e.* four more times between t_1 and t_2 [111]

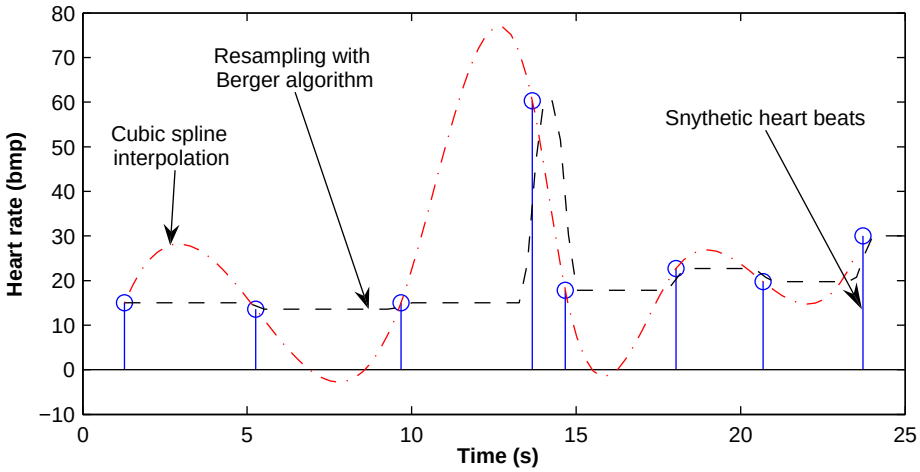

Fig. 8.4: Synthetic heart rate; Equidistance heart rate signal obtained by cubic spline interpolation and Berger *et. al.* algorithm

As mentioned before, the cubic spline could produce unacceptable oscillations if one RR interval is unusually longer than the previous interval. Therefore, an artificial RR series with large variations in RR interval was created to see the error caused by these oscillations, and also to compare the result obtained by using cubic spline interpolation with heart rate signal obtained using Berger's algorithm.

The results obtained by both methods and the actual heart rate at each beat positions are shown in Fig. 8.4. In both cases the sampling frequency was 4 Hz. It can be clearly seen that in this case the oscillations due to cubic spline will cause the heart rate signal to deviate considerably from the actual value. In fact the heart rate could even acquire negative values (see Fig. 8.4 red line), something which is physiologically impossible. Ebden's work [113], also presented the errors produced by the cubic spline interpolation on a patient data with four seconds of asystole.

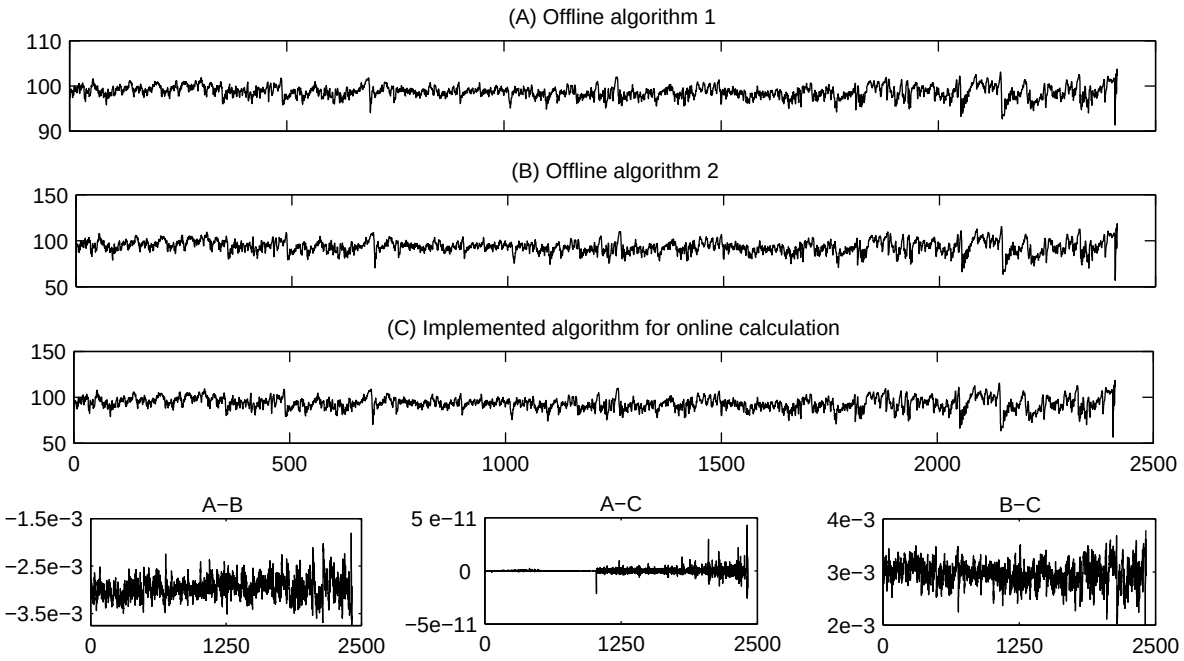

Fig. 8.5: Comparison results between two offline implementations of Berger *et. al.* algorithm with the version implemented for online calculation

An important observation in regards to the use of this algorithm online (real time) is the fact that the heart rate values will have a delay because of their dependency on near future events in the ECG signal. A modified version of the algorithm, considering the requirements of online processing, was implemented. This algorithm was tested for verification of the results with the two other versions of the algorithm that were available on the web [114, 115]. Both these algorithms were implemented to work offline. The results of the comparison between these three algorithms are shown in Fig. 8.5.

In sections 8.2 and 8.3 two different approaches that are use to obtain evenly sampled HRV signals were discussed. Despite the lowpass filtering effect caused by linear and spline interpolation, the cubic spline interpolation is routinely used in HRV studies. As mentioned before, large variations in the tachogram can cause unacceptable errors when cubic spline is used for the generation of evenly spaced HRV time series. Therefore, in such a case either the Berger *et. al.* algorithm or higher order spline should be used. In the case where the heart rate is not too low and does not have large variations the cubic spline interpolation can be used to get acceptable results.

8.4. Ectopic and missing beat correction

In addition to the SA node, other latent pacemakers exist throughout the heart. Normal regular conduction of the electrical impulse from the SA node and the refectory period of the cells reject any electrical impulses except those coming from the SA node.

However, some of the additional pacemakers, in certain cases, interpose additional pacemaker impulses that generate ectopic beats. These ectopic beats are usually manifested as premature beats followed by a longer than normal heart period interval up to the next normal beat due to the compensatory delay [116]. In addition to ectopic beats, QRS mis-detection can cause a similar effect to that of the ectopic beats in the HRV analysis. The time domain signal associated with the HRV exhibits a sharp transient at the ectopic beat, making it unsuitable particularly in the Power Spectral Density (PSD) estimate of the HRV. It has been shown previously [117] that the area of the low frequency (LF) component of HRV spectrum in normal subjects can increase up to 89% if the analysis signal has 4% of ectopic beats. The same amount of ectopic beats also cause an increase of up to 402% in the area of high frequency (HF) component of HRV [117].

Depending on the focus of the ectopic beat it may or may not reset the normal activity of the SA node. When the focus of the ectopic beat is in the ventricle, the activity of the SA node is not resetted which results in a missed normal beat inhibited by the ectopic beat, followed by a normal beat placed at the same position as if the ectopic beat has not occurred. Consequently when the ectopic beat is rejected the period between two adjacent normal beats is approximately twice than the mean heart rate. In this case the reconstruction of the missing beat with the insertion of an intermediate beats offers an approach that results in minimal disturbance of the final PSD estimate. Unfortunately when the location of the ectopic beat focus is superventricular (focus is in the atria or the AV node) its electrical activity is able to reset the SA node activity, resulting in a shortened period between two consecutive normal beats. This period is noticeably smaller than twice the mean heart period. The simplest solution of including an intermediate beat and shifting the remaining beats will not work because both these procedures substantially distort the PSD estimation of HRV [116].

8.4.1. Ectopic beat detection and correction algorithm

In order to deal with the effect of ectopic beats a recently introduced time domain HRV signal, the heart timing signal (*ht*) was used. The use of this signal makes it possible to recover an unbiased estimate of modulating signal $m(t)$ (see Eq. 8.1) and avoid the lowpass filtering effect generated when analysing heart rate or Heart Period (HP) [110]. In the absence of ectopic beats the *ht* signal can be estimated by rewriting Eq. 8.1 as shown in Eq. 8.4.

$$k = \int_0^{t_k} \frac{1 + m(t)}{T}\, dt \tag{8.4}$$

where k is an integer that represents the number of the k^{th} beat and t_k is the occurrence of the k^{th} beat [110].

Using Eq. 8.4 the *ht* signal can be written as shown in Eq. 8.5.

$$ht(t_k) = kT - t_k = \int_0^{t_k} m(\tau)\, d\tau \tag{8.5}$$

Each $ht(t_k)$ reflects the deviation of the position of each beat from the mean RR interval. In the frequency domain the relationship between $m(t)$ and $ht(t)$ can be written as given in Eq. 8.6.

$$H(j\omega) = \frac{M(\omega)}{j\omega} \tag{8.6}$$

The criteria for the detection of the ectopic beats using the *ht* signal depends on the beats location and is based on the fact that instantaneous Heart Rate (instHR) is bandlimited since the SA node modulation is also bandlimited according to the IPFM model. Therefore, it is possible to impose a threshold (U) on the estimate of the derivative of instHR, as given in Eq. 8.7, to classify the beats as anomalies if the derivative passes the threshold.

$$\widehat{instHR}_k = 2\left|\frac{\hat{t_{k-1}} - 2t_k + t_{k+1}}{(t_{k-1} - t_k)(t_{k-1} - t_{k+1})(t_k - t_{k+1})}\right| \tag{8.7}$$

and the threshold is defined as $U = min(4.3 \cdot \sigma_{\widehat{instHR}_k}, 0.5)$ where, $\sigma_{\widehat{instHR}_k}$ is the standard deviation of $\widehat{instHR}_k$.

If the threshold is passed at some time instant t_k it means the either one of the two beats, at time instances t_k or t_{k+1}, is incorrect or both represent anomalies. To determine which beat is anomalous Eq. 8.7 is calculated six more times and compared with the threshold after making the following changes

1. By removing the beat at time location t_k.
2. By removing the beat at time location t_{k+1}.
3. By inserting an intermediate beat between t_{k-1} and t_k.
4. By inserting an intermediate beat between t_k and t_{k+1}.
5. By moving t_k to the intermediate position between t_{k-1} and t_{k+1}
6. By moving t_{k+1} to the intermediate position between t_k and t_{k+2}.

If the derivative estimate becomes lower than the threshold by removing a beat then it means a FP (false positive) at the beat location. If the condition is satisfied by insertion of a beat then that represents a FN (false negative) and lastly, if the condition is met by moving the beat from the original location it usually indicates ectopic beat at that location. If the condition is not met by any of the six situations then the process is extended by considering possible consecutive FP, FN or ectopic beats and so the process continues

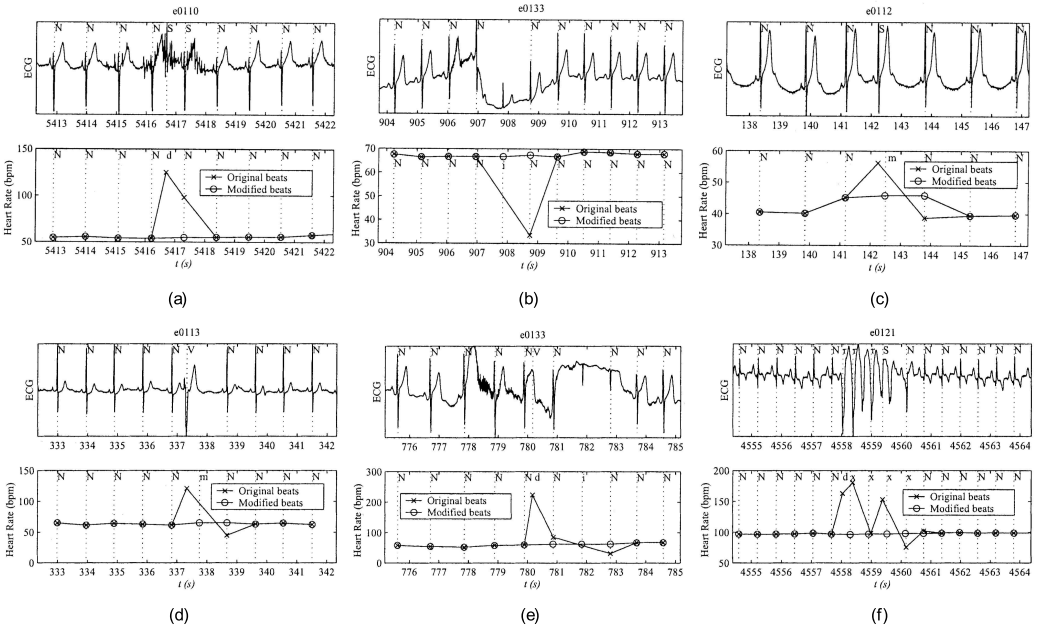

Fig. 8.6: Different kinds of anomalies in the ESDB database. Upper panel represents the ECG with the originally annotated beat classification. Lower panel shows the original heart rate and the modified one indicating which action has been carried out. (a) FP deletion. (b) FN insertion. (c) Superventricular ectopic beat moving. (d) Ventricular ectopic beat moving. (e) Deletion and insertion in one-step double correction. (f) Multiple insertion of evenly spaced beats [116]

until the derivative becomes smaller than the threshold by involving one more beat in each step. The results of beat correction in a few signals, representing different kind of anomalies, from ESDB database [116] are shown in Fig. 8.6. Each part of Fig. 8.6 shows the ECG signal, the original and the modified heart rate indicating the type of correction that has been carried out. Note that these new corrected beats locations are used as an estimate to classify the anomalies and will not be introduced directly into the HRV analysis.

As mentioned before the ectopic beat may reset the activity of the SA node. This results in a phase shifted series of normal beats following the ectopic beat. If the k_e^{th} beat is considered as ectopic then the location of the beats preceding the ectopic beat can be given as $t_k = t(k)$ where $k < k_e$ and the beats after the ectopic beat can be written as $t_k = t(k + 1 + s)$ with $k > k_e$. The premature resetting of the integration occurs at $t(k_e - 1 + s)$ and s is an unknown real quantity $(s \leq 1)$ corresponding to the value reached by the integral at the resetting time $t(k_e - 1 + s)$. It is important to note that the SA node resetting time $t(k_e - 1 + s)$ is different from the ectopic beat occurrence time, because the propagation mechanism of the ectopic impulse may be somewhat different to the normal beat and then, the instant of the SA node reset $(t(k_e - 1 + s))$ will not be the same as the one associated with the ectopic beat position, typically from a QRS detector [116]. The time occurrences of the ectopic beats have no relation to the SA node and are not used in this method of correction. The signal x of Eq. 8.2 generated

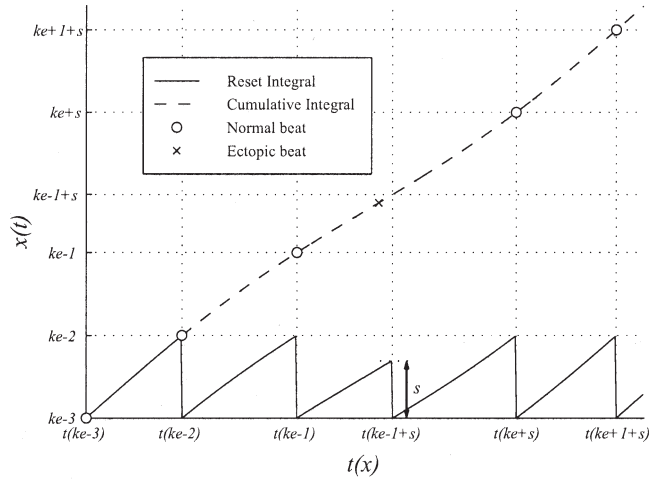

Fig. 8.7: Beat occurrence time generation in presence ectopic beat from the integral of the IPFM model [116]

by the IPFM model (dashed line) is shown in Fig. 8.7. The solid line represent the same curve but it resets when the integral reaches the threshold. The normal threshold is one but the ectopic beat prematurely reset the integral at s. This causes the beats after the ectopic beats to have an additional unknown delay s.

Using this interpretation of the ectopic beats the *ht* signal values before and after an ectopic beat, occurring at k_e, in a series of N beats can be calculated as shown in Eq. 8.8.

$$\begin{aligned} ht(t_k) &= ht(t(k)) = kT - t_k \\ &= kT - t_k \qquad\qquad for\, k < k_e \\ ht(t_k) &= ht(t(k-1+s)) \\ &= (k-1+s)T - t(k-1+s), \quad for\, k > k_e \end{aligned} \tag{8.8}$$

If there are more than one ectopic beat then the parameter s for each ectopic beat and the correct T has to be calculated to obtain the *ht* signal accurately. The value of the parameter s is related to the type of the anomaly. A value of less than one indicates the occurrence of superventricular ectopic beat. Similarly $s > 1$ means that several consecutive normal beats were missed due to ectopic beats or FP and $s = 1$ usually indicates the occurrence of either a FN or a ventricular ectopic beat [116].

In order to estimate the value of s, first the HP signal is calculated ($hp(t_k) = t_k - t_{k-1}$) at all the positions except those involving the ectopic beats. The HP signal before the ectopic beat is calculated as $hp(t(k)) = t(k) - t(k-1)$ with $k < k_e$ and for the beats after the ectopic beat its value is calculated as $hp(t(k-1+s)) = t(k-1+s) - t(k+s-2)$ with $k > k_e + 1$. Using the HP values at the beat location time, the equispaced HP signal ($\widehat{hp}$) could be estimated using higher order spline or Berger's algorithm. From this signal, the

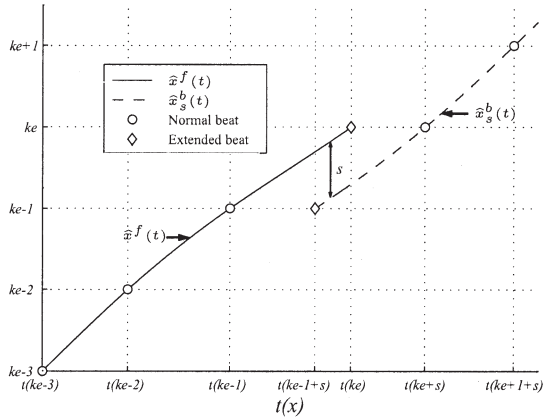

Fig. 8.8: Forward and backward extended beat occurrence times and the interpolated continuous curves can be calculated from the known normal beats. Note that the offset of the backward extended curve is s after the ectopic beat. Circles represent the previously known beat occurrence times and diamonds represent the forward and backward calculated beat occurrence times [110]

virtual beat times $t(k_e - n + s)$, being the hypothetical n^{th} normal beat positions, can be estimated by backward extending the signal starting from the first normal beat $(t(k_e + s))$ after the ectopic beat location (see Eq. 8.9).

$$t(k_e - n + s) = t(k_e - n + 1 - s) - \widehat{hp}(t(k_e - n + 1 + s)) \tag{8.9}$$

Equation. 8.9 is evaluated for $n = 1$ up to $t(k_e - n + s) < t(k_e - 1)$. At this point, the backward extended beat sequence is overlapped in time with the existing beat sequence previous to the ectopic beat as shown in Fig. 8.8. Similarly the forward extend signal $(\hat{x}^f(t))$ is obtained using the beat locations before the ectopic beat (see Fig. 8.8). After the calculation of the forward and backward signal the vertical distance between them is calculated to estimate s using Eq. 8.10.

$$\hat{s} = \frac{1}{t(k_e) - t(k_e - 1 + s)} \int_{t(k_e - 1 + s)}^{t(k_e)} (\hat{x}^f(t) - \hat{x}^b_s(t))\, dt \tag{8.10}$$

This process must be repeated once for each ectopic beat to obtain the corresponding $\hat{s}$ value.

With $\hat{s}$ values estimated for each ectopic beat, the mean heart rate T, which in absence of ectopic beats is calculated as $T = t(N)/N$ (total number of beats are $N + 1$). In the presence of ectopic beats the T value has to be adjusted to take into account the fact that with ectopic beats the effective number of beats will be $N + 1 + \sum_j \hat{s}_j$ where $\sum_j \hat{s}_j$ is the sum of all the jumps at each j^{th} ectopic beat and that the last beat time is $t_N = (t(N + \sum_j \hat{s}_j) \neq t(N)$ [116]. With this information, T can be calculated as shown in Eq. 8.11.

$$T = \frac{t_N}{N + \sum_j \hat{s_j}} \tag{8.11}$$

With $\hat{s}$ and T calculated, *ht* signal values in the presence of ectopic beats can be calculated at the beat times (t_k) using Eq. 8.8. This signal is then interpolated to obtain a continuous estimation of the *ht* signal.

8.5. Effect of ectopic beat on simulated signals

In this section the performance of the ectopic beat correction algorithm will be validated with the help simulated signals. The method will be tested using both the parametric and nonparametric spectral analysis method. After the validation with the simulated signals the results obtained with real HRV data will be presented in the next section.

8.5.1. Simulated signal results using non-parametric method

The performance of the non-parametric spectral analysis method and the effect of different representations of the signal on spectral analysis of HRV were assessed by simulated signals. The simulated signals were used as the modulating signal $m(t)$ (see Eq. 8.1) in the IPFM model to generate the beat locations with mean heart rate period T equal to one second. These beat locations were then used to generate the HR signal using Berger's algorithm (see section 8.3) and also equidistance samples of *ht* signal (see section 8.4) at 4 Hz sampling frequency. The first signal consists of a single frequency and can be mathematically written as (Eq. 8.12).

$$m(t) = 0.4 \cdot cos(2\pi \cdot 0.1 \cdot t) \tag{8.12}$$

The spectrum of the modulated signal and the spectrum obtained using the HR and the *ht* signals are shown in Fig. 8.9. For *ht* and HR signals the power spectrum was obtained after the mean of the signal was removed. From the result shown in Fig. 8.9 it can be seen that both the HR and *ht* signals could be used for accurately representing the modulating signal. But in practise the signal will consist of a range of frequencies in the region of 0 Hz to approximately 0.5 Hz, therefore the spectrum of HR and *ht* signals were also compared using another simulating signal which can be written as shown in Eq. 8.13.

$$m(t) = 0.1 \cdot cos(2\pi \cdot 0.1 \cdot t) + 0.1 \cdot cos(2\pi \cdot 0.25 \cdot t) \tag{8.13}$$

These frequencies were chosen to reflect the LF and HF components present in HRV. The mean heart period (T) was again fixed to one second. In order to avoid spectral

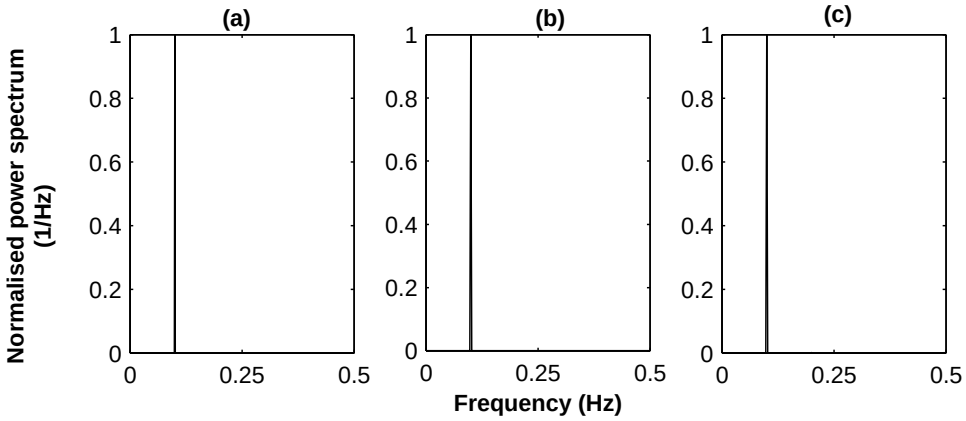

Fig. 8.9: Normalised Power spectrum (NPS); (a) simulated signal (see Eq. 8.12) used as a modulating part in IPFM model; (b) spectrum of *ht* signal; (c) spectrum of HR signal obtained using Berger algorithm

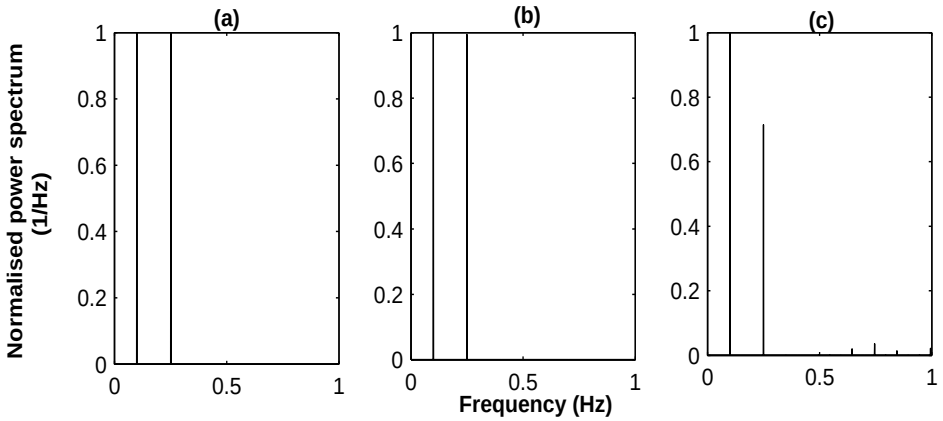

Fig. 8.10: Normalised Power spectrum (NPS); (a) simulated signal (see Eq. 8.13) used as a modulating part in IPFM model; (b) spectrum of *ht* signal; (c) spectrum of HR signal obtained using Berger algorithm

leakage in the power spectrum analysis, integer numbers of periods of both tones were analysed by taking exactly 1000 beats in the study. The results of the power spectrum of the modulating signal of Eq. 8.13 and the corresponding *ht* and HR signals are presented in Fig. 8.10. The results in Fig. 8.9 results showed that the HR signal obtained from Berger's algorithm was not able to provide accurate representation of the modulating signal. The power in the second component, at frequency of 0.25 Hz, of the modulating signal (see Eq. 8.13) is attenuated in the spectrum obtained using this signal. Also, the spectrum showed spurious peaks. Compared to this, the spectrum obtained using the *ht* signal shows no spurious peak and there is negligible attenuation in the magnitude of the second component. The magnitude of this component is 0.9947 instead of 1.

In order to see the effect of using shorter data segments with Welch's periodogram method, the spectrum was calculated using five minutes of the *ht* signal. For this case, the result of Fig. 8.10b were used as a gold standard and the performance of Welch's periodogram was evaluated using the following parameters:

- Location of the peaks

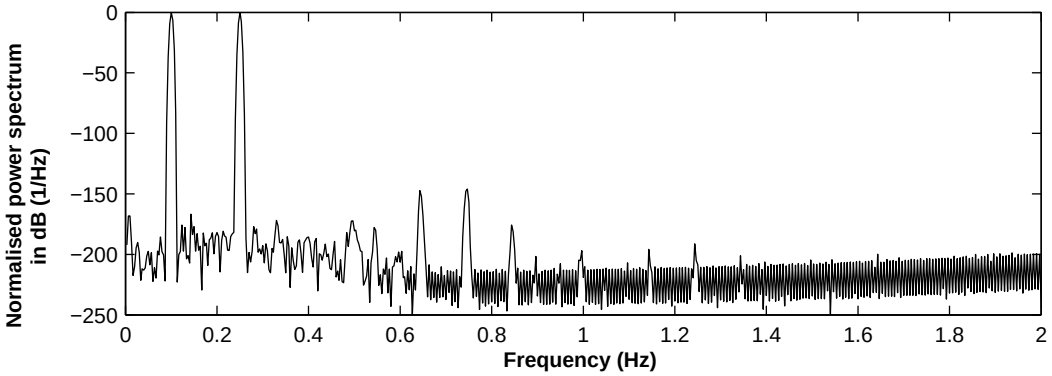

Fig. 8.11: Normalised Power Spectrum (NPS) obtained for the modulating signal of Eq. 8.13 with 5 minutes of data using Welch's periodogram method

Table 8.1.: Total powe (Pt), location of the frequency peak f_{peak}, 3 dB bandwidth (Δf_{3dB}), fraction of power in a $\pm$0.01 Hz band centred on the peak ($\frac{P_{peak}}{P_t}$%) and amplitude of the first sidelobe (P_{sl}) calculated using Fig. 8.11

Total signal Power (Pt)	f_{peak} (Hz)		Peak power (Ppeak) (dB)	$\frac{P_{peak}}{P_t}$	Δf_{3dB}	P_{sl} (dB)
2.9309	LF	0.1003	0.0	0.4986	0.003	-167
	HF	0.2501	-0.0855	0.4959	0.003	-175

- LF and HF peak height and $^{LF}/_{HF}$ ratio
- Peak width at 3 dB below each peak
- Fraction of power within $\pm$ 0.001 Hz of each peak and
- Power in the first sidelobe of each major peak (P_{sl})

The results obtained with Welch's periodogram using five minutes of data are presented in Fig. 8.11. In this case, five minutes of data at 4 Hz sampling rate resulted in using 1200 points for the evaluation of PSD. The data was windowed using a Hamming window of 600 points with 50% overlap. Using the result shown in Fig. 8.11 the metrics defined above were calculated and the results are presented in table 8.1. Results presented in table 8.1 show that the peak locations are detected quite accurately with a difference of 0.0003 Hz in the LF and 0.0001 Hz in the HF peak. The bandwidth is approximately 0.003 Hz and the first sidelobes after the main peaks are at -167 dB and -175 dB for the LF and HF peaks respectively. Figure 8.11 shows that the biggest spurious peak occurs at around 0.75 Hz which is approximately 140 dB below. The spectral leakage is also minimal as power within 0.01 Hz of the main peaks represents 49.86% and 49.59% of the total power for LF and HF respectively, which is quite close to the theoretical value of

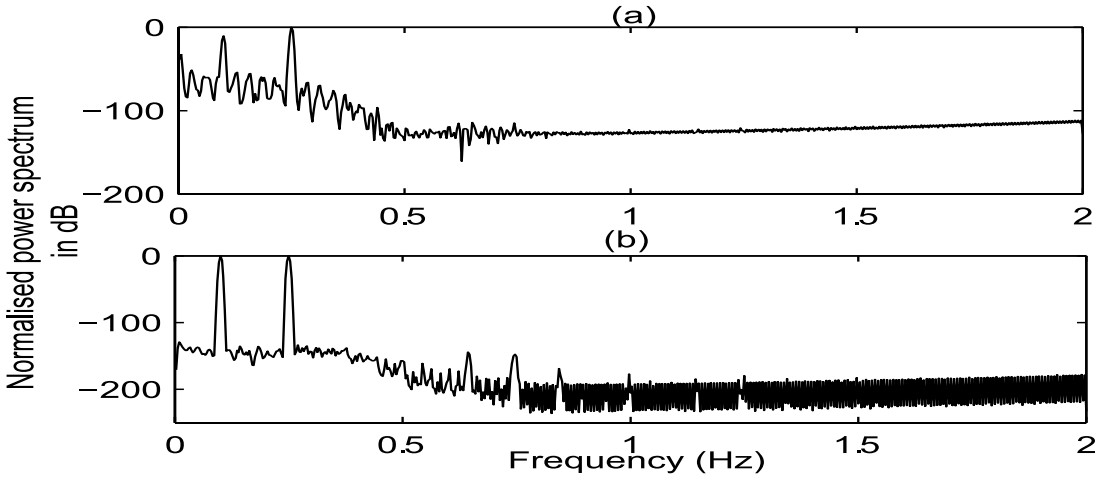

Fig. 8.12: Normalised Power Spectrum in one of the ten signals generated by removing five random beats from the beat sequence generated by modulating signal of Eq. 8.13; (a) spectrum before beat correction; (b) spectrum after beat correction

50%, expected for both the components.

The effect of ectopic and missing beats on the power spectrum of the signal was studied using the modulating signal presented in Eq. 8.13 and was used to generate the spectrum shown in Fig. 8.10 and Fig. 8.11. To evaluate the performance in the case of missing beats, five beats were randomly removed from the beat sequence generated by this modulating signal. In the second case again five beats were randomly chosen and they were moved forward by subtracting 0.2 seconds from their original positions. In each case (missing beat and beat repositioning) ten signals were generated.

For the missing beat case, the spectrum obtained before and after the beat correction for one of the generated signals, using the method explained in section 8.4.1, is shown in Fig. 8.12. The performance matrices used in table 8.1 were also calculated for each of the ten power spectra obtained after correcting for the missing beats and are presented in table 8.2.

In general the difference in LF peak location was 0.00031 Hz and for the HF peak the difference was 0.00011 Hz. The fraction of power in a ± 0.01 Hz band centred around the LF peak was 49.26% and for the band centred around the HF peak was 49.65%. There was a slight decrease in the power of the HF component, the peak value decreased from -0.0855 dB to -0.17 dB. The power in the LF component showed decrease only in two cases (first and last one see table 8.2), the average decrease was -0.016 dB. The first side-lobe P_{sl} (not shown in table 8.2) was approximately 135 dB below for both LF and HF components. The 3 dB bandwidth (Δf_{3dB}) for both the components remained unchanged at 0.003 Hz.

The spectrum obtained after beat correction in one of the ten signals for the beat movement case is shown in Fig. 8.13. The performance matrices calculated from the ten

Table 8.2.: Location of the frequency peaks, 3 dB bandwidth (Δf_{3dB}), fraction of power in a ± 0.01 Hz band centered on the peak ($\frac{P_{peak}}{P_t}$%) and amplitude of the first sidelobe (P_{sl}) calculated using spectrum generated after beat correction for missing beat

Sr. No	LF peak (Hz)	LF peak power P_{LF} (dB)	$\frac{P_{LF}}{P_{total}}$	HF peak (Hz)	HF peak powerP_{HF} (dB)	$\frac{P_{HF}}{P_{total}}$
1	0.10027	-0.0338	0.4940	0.2501	0.0	0.4970
2	0.10029	0.0	0.4995	0.2501	-0.0870	0.5026
3	0.10027	0.0	0.4953	0.2501	-0.1791	0.4983
4	0.1003	0.0	0.4986	0.2501	-0.1739	0.5017
5	0.10027	0.0	0.4959	0.2502	-0.2602	0.4889
6	0.10029	0.0	0.4936	0.2501	-0.1089	0.4966
7	0.10053	0.0	0.4758	0.2501	-0.5394	0.4788
8	0.10027	0.0	0.4954	0.2501	-0.0135	0.4984
9	0.10029	0.0	0.4936	0.2501	-0.3384	0.5057
10	0.10029	-0.1259	0.4943	0.2501	0.0	0.4973

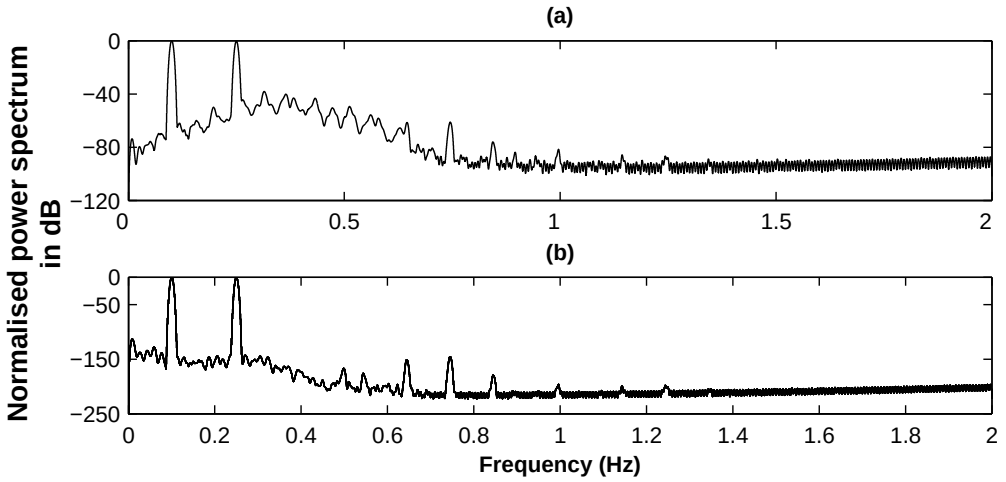

Fig. 8.13: Normalised spectrum in one of the ten signals generated by moving five random beats backward by 0.2 s from the beat sequence generated by modulating signal of Eq. 8.13; (a) spectrum before beat correction; (b) spectrum after beat correction

Table 8.3.: Location of the frequency peaks, 3 dB bandwidth (Δf_{3db}), fraction of power in a $\pm$0.01 Hz band centered on the peak ($\frac{P_{peak}}{P_t}$%) and amplitude of the first sidelobe (P_{sl}) calculated using spectrum generated after beat correction for moving beat case

Sr. No	LF peak (Hz)	LF peak power P_{LF} (dB)	$\frac{P_{LF}}{P_{total}}$	HF peak (Hz)	HF peak powerP_{HF} (dB)	$\frac{P_{HF}}{P_{total}}$
1	0.10030	0.0	0.4474	0.2501	-0.3897	0.4269
2	0.10029	0.0	0.4922	0.2501	-0.1261	0.4689
3	0.10027	0.0	0.4917	0.2501	-0.1947	0.4685
4	0.10027	0.0	0.4888	0.2501	-0.0799	0.4657
5	0.10027	0.0	0.4843	0.2502	-0.2509	0.4615
6	0.10033	0.0	0.4754	0.2501	-0.1991	0.4530
7	0.10029	0.0	0.4943	0.2501	-0.1692	0.4710
8	0.10027	0.0	0.4909	0.2501	-0.1842	0.4678
9	0.10029	0.0	0.4907	0.2501	-0.2499	0.4675
10	0.10029	0.0	0.4620	0.2501	-0.0221	0.4402

spectrums in this case is presented in table 8.3. In this case the difference in the LF peak location was 0.00029 Hz and for the HF peak the difference in peak location was 0.00012 Hz. The fraction of power in a $\pm$0.01 Hz band centred around the LF peak was 48.18% and for the band centred around the HF peak was 45.90%. The power in the LF component was not affected while the HF power decreased to -0.19 dB. The sidelobe for the LF and the HF components were approximately at -150 dB.

From the spectrum obtained without beat correction (see Fig. 8.13 (a)) it can be seen that error in the beat location has caused significant power increase especially in the HF region of the signal. The beat correction algorithm has significantly reduced the error in the power spectrum of the signal. The results obtained in this section showed that satisfactory spectra of 5 minutes of the signal (1200 points) can be obtained using the Welch's method with a Hamming window of 600 points with 50% overlap. Also, the simulations done by removing and moving five random beats from the beat sequence

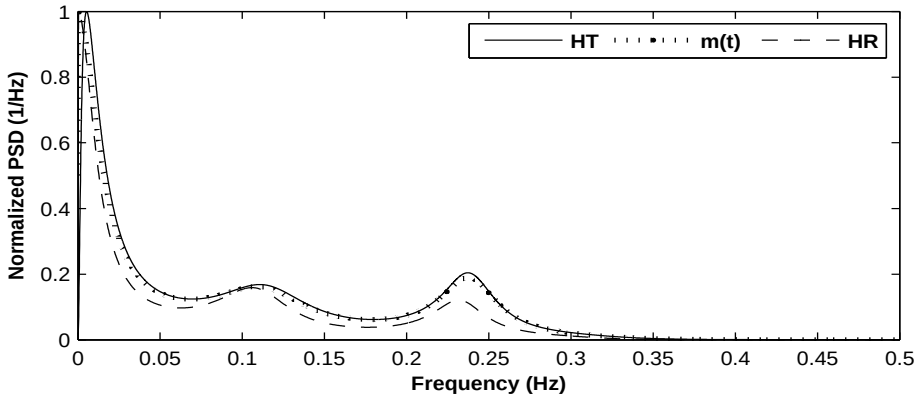

Fig. 8.14: Mean spectrum of $m(t)$ (see section 8.5.2), *ht* and HR signal obtained from twenty random realisation

generated by the modulating signal of Eq. 8.13 showed that the ectopic beat correction algorithm discussed in section 8.4.1 has managed to reduce the error in the spectra of the signals quite considerably. In the following chapter the same setup will be employed as one of the methods of power spectral analysis to study the HRV signals obtained from a group of patients undergoing local anaesthesia.

8.5.2. Simulated Signal Results using parametric method

To compare the effect of *ht* and HR signal representations on spectral analysis when using the parametric method, another simulated study was performed. In this case the beat locations were generated using $m(t)$ signal which was modelled using an AR model that approximately matches the PSD at supine rest [110]. The coefficients and the variance used for a sampling rate of 1 Hz were $a = [1 - 1.62651.8849 - 1.83271.297 - 0.77580.4133 - 0.2136]$ and $\sigma = 404 \times 10^{-6}$. The mean heart rate T was again taken to be equal to 1. Twenty random realisation of $N = 1024$ samples of $m[n]$ were generated using the AR model. Then the $m[n]$ sequences were interpolated obtaining $128.N$ samples by mean of zeros padding at its spectra. This operation keeps the spectrum and obtains enough samples to perform the numerical integration involved in the IPFM model [110]. Using the $m[n]$ values the cumulative integral of $(1 + m[n])/T$ was calculated and the beat occurrence time t_k was noted as the instants when this integral crosses $k = 1, 2 ... N$. After generating the peak time values the spectrum was obtained for the *ht* and the HR representation for each 20 cases using a 9^{th} order AR model. The mean spectrum of the $m(t)$ signal and the mean spectrum obtained using *ht* and HR signals are shown in Fig. 8.14. To see the global behaviour of each method (*ht* and HR) with frequency the Mean Normalised Error (MNE) defined in Eq. 8.14 was calculated.

$$MNE(f) = \frac{\sum_{i=1}^{20}(\widehat{PSD}_i(f) - PSD_i(f))}{\sum_{i=1}^{20}\widehat{PSD}_i(f)} \tag{8.14}$$

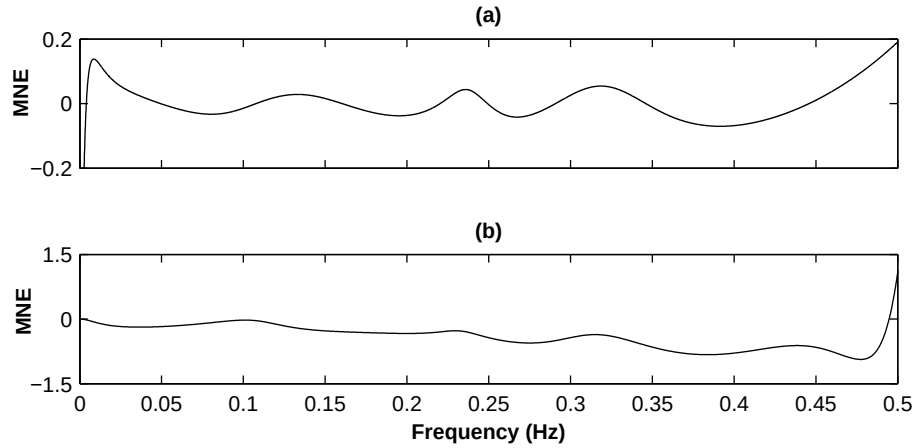

Fig. 8.15: Mean Normalised Error (MNE) (a) for the *ht* signal; (b) for the HR signal

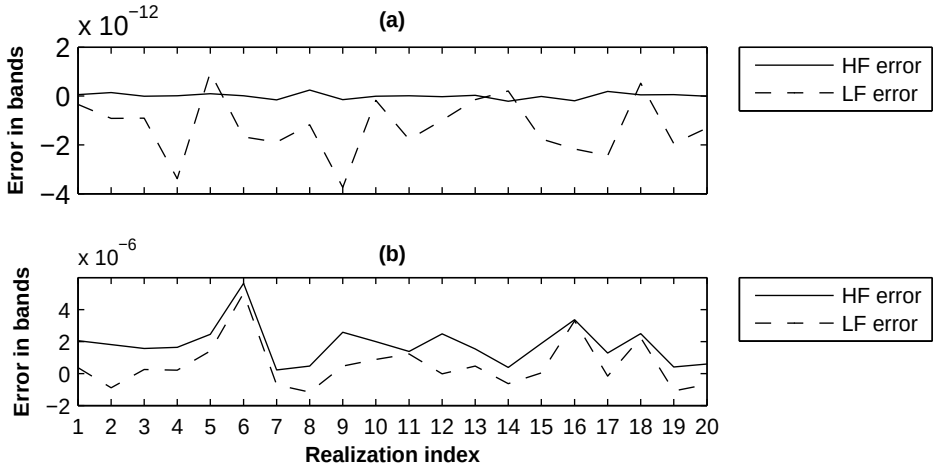

Fig. 8.16: Error in the LF and the HF bands calculated for the 20 realisation of $m(t)$ using (a) the *ht* spectrum and (b) the spectrum generate using HR signal

The results obtained for MNE for both the *ht* and HR signals are presented in Fig. 8.15. From the results shown in Fig. 8.15 it can be seen that the MNE of the *ht* signal is less than half of the error for the HR signal. The large error around *DC* component for the *ht* signal, Fig. 8.15 (a), is due to the removal of the linear trend. This is also the cause of the difference in the mean spectrum obtained from the *ht* signal and the mean spectrum of $m(t)$ (see Fig. 8.14). From Fig. 8.15 (b), HR signal representation case, it can be seen that the MNE increases with an increase in the frequency. This is due to the lowpass filter effect of Berger's algorithm.

An important aspect of frequency HRV analysis is the power in the VLF, the LF and the HF band. Since in this study only the LF and the HF bands are studied, the error in the power associated with these two bands was also calculated for each realisation. The error produced in the HF and the LF band by the *ht* and the HR spectrum are shown in Fig. 8.16. The results in Fig. 8.16 show that the error produced by the HR signal in both the LF and the HF band are significantly higher than the corresponding error produced by the *ht* representation.

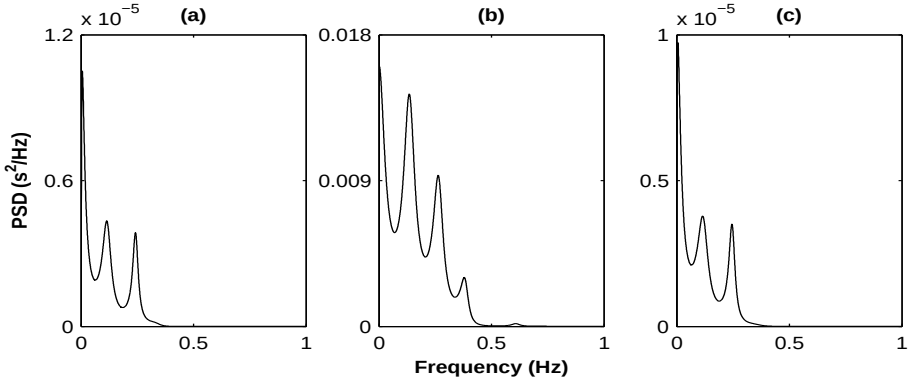

Fig. 8.17: Power spectrum; (a) original ($m(t)$) signal; (b) corrupted signal; (c) signal after beat correction. Signal was corrupted by removing five random beats

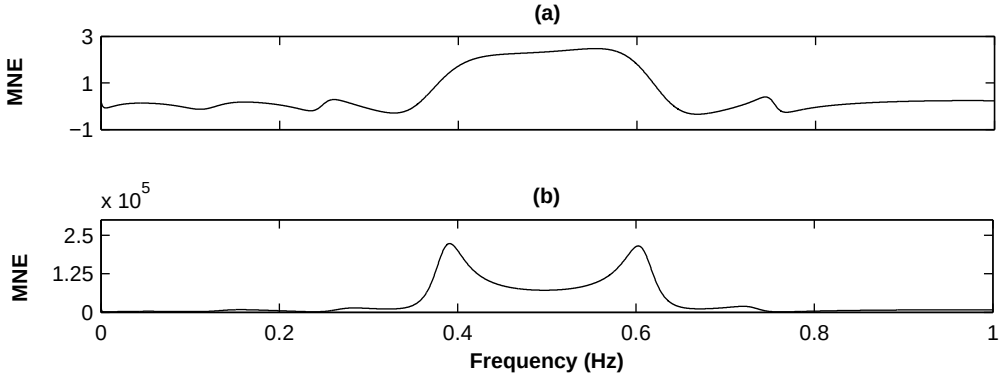

Fig. 8.18: MNE (a) after performing beat correction; (b) before beat correction. Signals are corrupted by removing five random beats

The effect of ectopic beat was studied by making use of the beat location generated by one of the twenty realisations of $m(t)$. As before (see section 8.5.1), the corrupted beat sequences were generated by removing five random beats from the original beat sequence and secondly, by selecting five random beats and moving them backwards by 0.2 s. For each test ten corrupted beat sequences were generated. The spectrum was calculated for each of the ten cases before and after the beat correction. The spectrum before and after beat correction in one of the ten corrupted signals, corrupted by removing beats from the original sequence, is presented in Fig. 8.17. As before the MNE and the error in the LF and the HF band was calculated. These results are presented in Fig. 8.18 and Fig. 8.19 respectively.

From the results shown in Fig. 8.18 and Fig. 8.19 it can be seen that the MNE and error in the LF and the HF band has increased, but the increase is significantly larger for the case when the spectrum analysis is done without the beat correction. These results were expected, as the spectrum generated without the beat correction (see Fig. 8.17) is quite different from the spectrum of the $m(t)$ signal which is used as a reference.

Similarly, the spectral result before and after beat correction in the case when the signal was corrupted by moving five random beats by 0.2 s is shown in Fig. 8.20. From the result presented in Fig. 8.20 it can be seen that if the corrupted beats are not corrected before

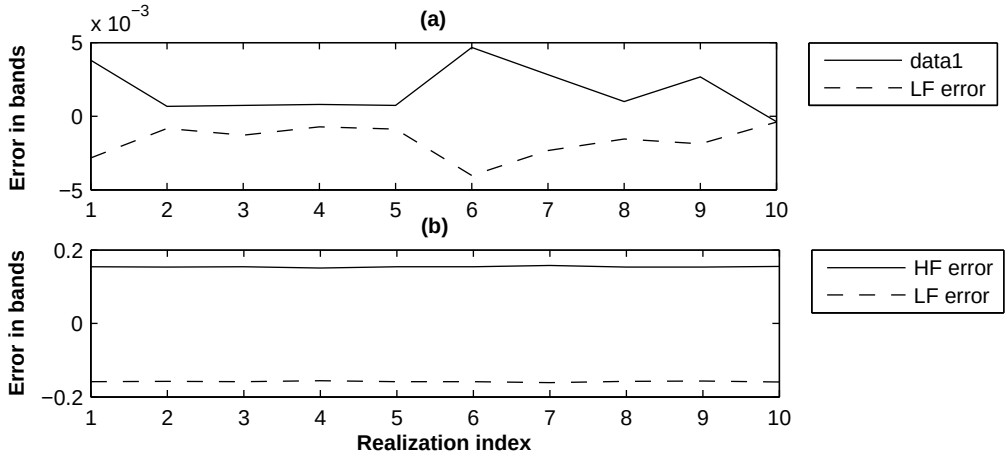

Fig. 8.19: Error in the LF and the HF band calculated for each of the ten signals generated by randomly removing five beats; (a) error in the bands after beat correction; (b) error in the bands before beat correction.

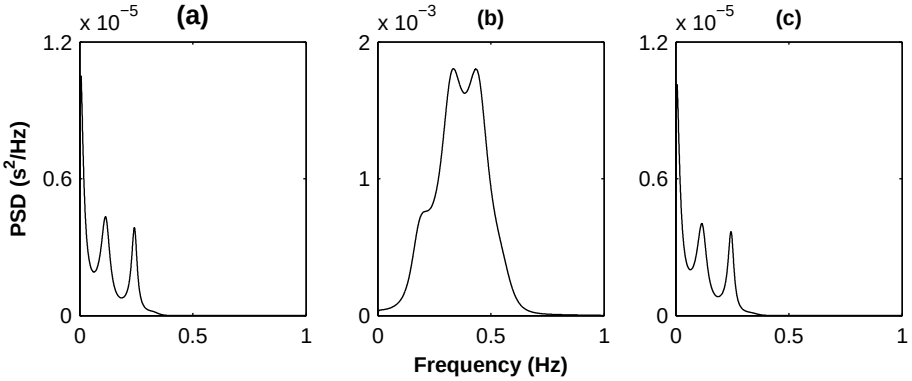

Fig. 8.20: Power spectrum; (a) original ($m(t)$) signal; (b) corrupted signal; (c) signal after beat correction. Signal was corrupted by moving five random beats by 0.2 s beats

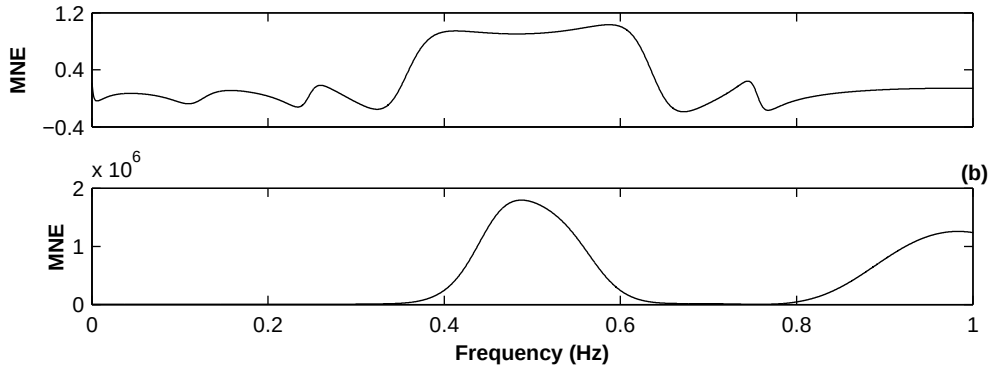

Fig. 8.21: MNE (a) after performing beat correction; (b) before beat correction. Signals are corrupted by moving five random beats by 0.2 s

spectral analysis the spectral components can change drastically producing enormous errors. These facts could be seen by comparing the MNE and error in the power of the LF and the HF bands calculated before and after beat correction and presented in Fig. 8.21 and Fig. 8.22 respectively.

Similar to the results presented in section 8.5.1 for the non-parametric spectral analysis the results presented in this section show that the *ht* signal provides better spectral results

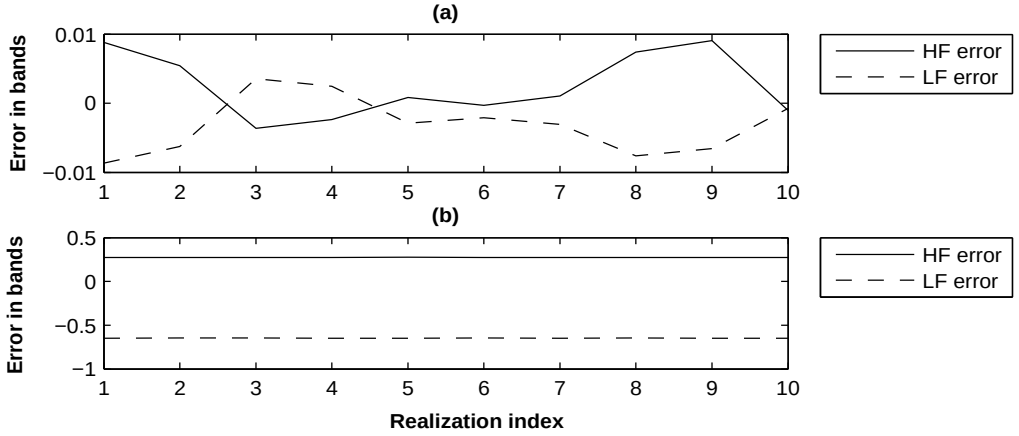

Fig. 8.22: Error in the LF and the HF band calculated for each of the ten signals generated by randomly moving five beats backward by 0.2 s; (a) error in the bands after beat correction; (b) error in the bands before beat correction

for the modulating signal in HRV analysis. The effectiveness of the ectopic beat correction algorithm is also evident from the various results obtained in this section.

8.6. Effect of ectopic beat on real HRV signal

The signals used in the simulated study were quite simple and they do not represent the complex dynamics often observed in real HRV data. From the theoretical point of view, it can be seen that different parameters such as changes in the amplitude and/or frequency of the signal and noise will affect the spectral analysis results. These signals were used so that error introduced by processing steps such as interpolation of the data, signal representation and ectopic beat correction could be quantified separately. In a way this provided an upper bound on the performance of the full analysis setup. The same setup was then used with a real HRV signal of five minute duration. This signal was taken from NSR database and annotations were checked so that all the beats included in the signal were considered normal ECG beats. As in this case the theoretical spectrum which should be considered as a reference was not available so the spectrum obtained

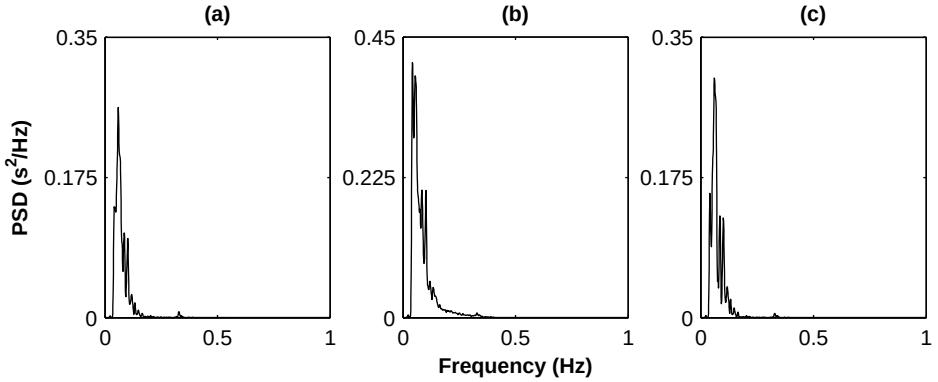

Fig. 8.23: Spectrum of the real HRV signal obtained using Welch's method (missing beat case); (a) spectrum of the original signal; (b) spectrum after removing five random beats from the signal; (c) spectrum after beat correction

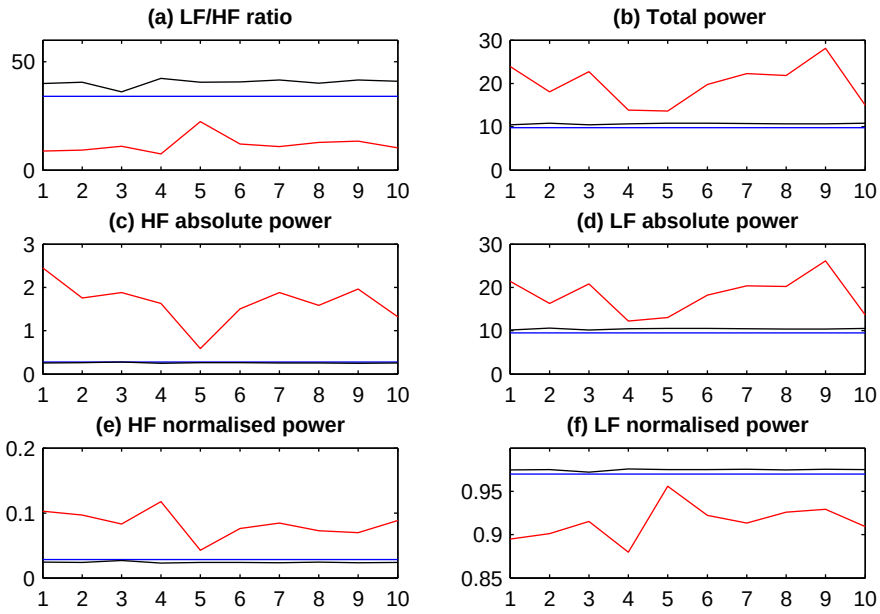

Fig. 8.24: Parameter estimated from the original signal (blue line), corrupted signal (red line) and signal after beat correction (black line). Signals are corrupted by removing five random beats from the original signal. The parameters are estimated from the spectrum obtained using Welch's method

from the original signal was taken as a reference for the beat correction algorithm. The signal was corrupted in the same way as the simulated signals. Two cases were studied, in the first case five beats were randomly removed from the original signal and analysis was carried out on the corrupted signal before and after beat correction. For the second case five beats were randomly selected and they were moved forward by 0.2 seconds. In each case (missing and moving beat) the analysis was repeated ten times. The spectral analysis was carried out using both the parametric and non-parametric method. The spectrums, using Welch's periodogram method, of the original signal and the corrupted signal before and after beat correction in the case of missing beats are shown in Fig. 8.23. In order to see the effect of the beat correction algorithm HRV, frequency domain parameters ($^{LF}/_{HF}$, total power, power in both the HF and LF band in absolute and normalised units) were estimated and are presented in Fig. 8.24.

In Fig. 8.24 the parameter values from the original signal, which is used as a reference, are presented in blue line. These values are constant in each of the ten cases as the reference signal remains the same. The figure also indicates that the values obtained after beat correction (black line) are quite close to the reference values (blue line) as compared to the values calculated from the corrupted signal without beat correction (red line). Similar results were obtained when the signal was corrupted by moving five random beats backward by 0.2 seconds. The spectrum and the parameter estimated in this case are presented in Fig. 8.25 and Fig. 8.26 respectively.

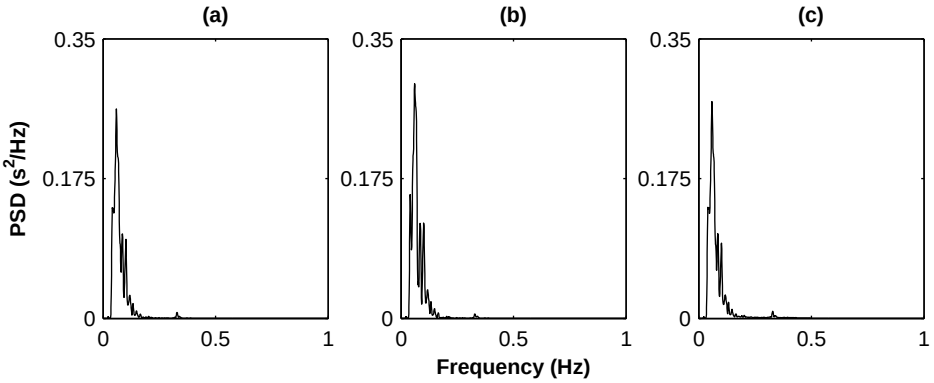

Fig. 8.25: Spectrum of the real HRV signal obtained using Welch's method (moving beat case); (a) spectrum of the original signal; (b) spectrum after moving five random beats from the signal; (c) spectrum after beat correction

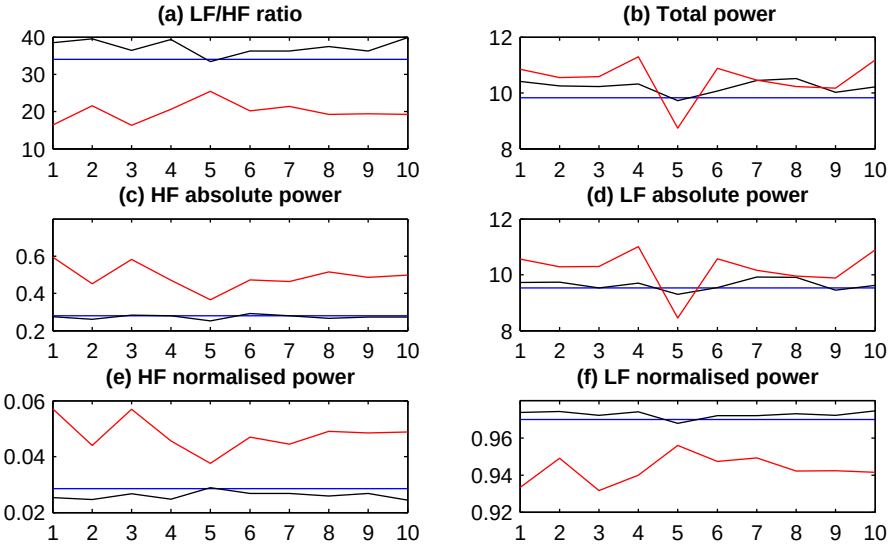

Fig. 8.26: Parameter estimated from the original signal (blue line), corrupted signal (red line) and signal after beat correction (black line). Signals are corrupted by moving five random beats from the original signal backward by 0.2 s. The parameters are estimated from the spectrum obtained using Welch's method

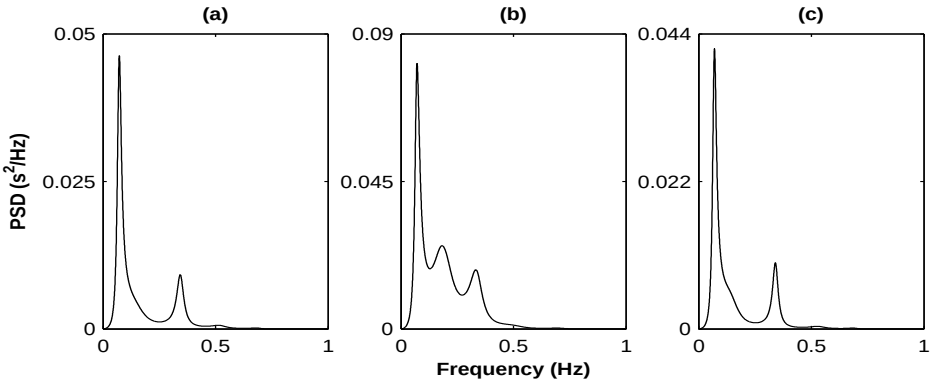

Fig. 8.27: Spectrum of the real HRV signal obtained using AR method (moving beat case); (a) spectrum of the original signal; (b) spectrum after moving five random beats from the signal; (c) spectrum after beat correction

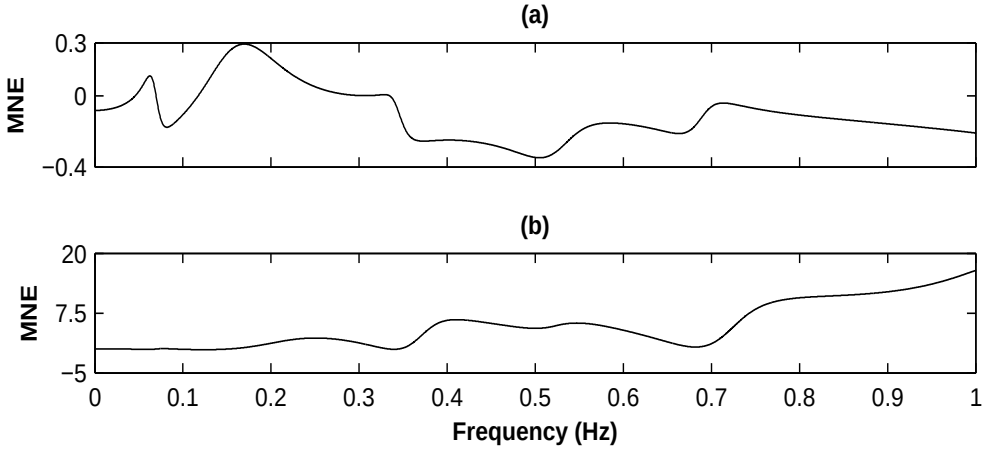

Fig. 8.28: MNE in real HRV signal (a) after performing beat correction; (b) before beat correction. Signals are corrupted by removing five random beats from the original signal

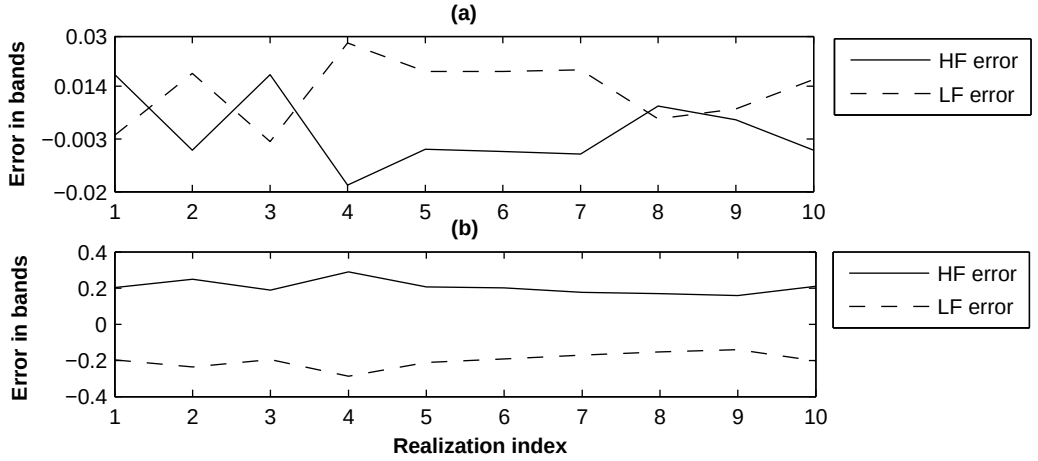

Fig. 8.29: Error in the LF and the HF band calculated for each of the ten signals generated by randomly removing five beats from the real HRV signal; (a) error in the bands after beat correction; (b) error in the bands before beat correction.

The effect of ectopic/missing beats on the spectral analysis of the real HRV data was also estimated using parametric (AR) technique. Similar to the previous cases the signal was corrupted by either removing five random beats and by selecting five random beats and moving them backwards by 0.2 seconds. For each case (missing/moving beats) ten signals were generated. The spectrum of the original signal and one of the ten corrupted signals, corrupted by removing beats, before and after beat correction is shown in Fig. 8.27. In this case the MNE (see Eq. 8.14) and error associated with the LF and the HF bands was estimated and presented in Fig. 8.28 and Fig. 8.29 respectively. By looking at the results presented in Fig. 8.28 and Fig. 8.29 it can be seen that in the case of real HRV signal, when the signal were corrupted by removing five random beats, the MNE and error associated with the LF and the HF band are approximately ten times smaller after beat correction, than their corresponding values before beat correction.

The spectrums obtained in the case when the signal was corrupted by moving five random beats by 0.2 seconds are shown in Fig. 8.30. MNE and the error associated with

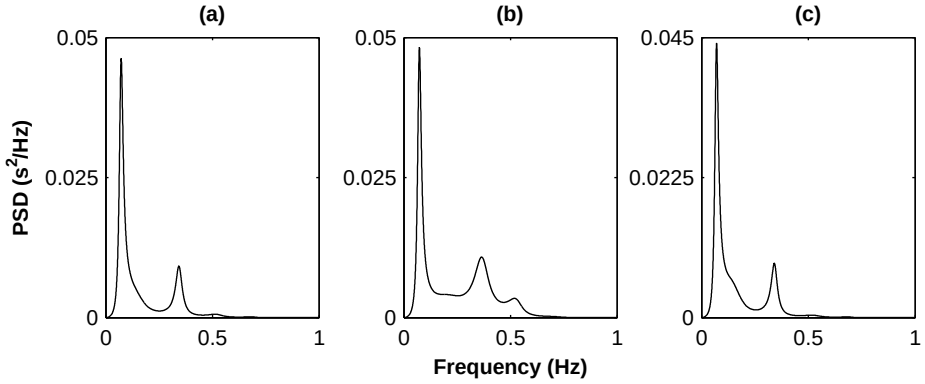

Fig. 8.30: Spectrum of the real HRV signal obtained using AR method (moving beat case); (a) spectrum of the original signal; (b) spectrum after moving five random beats from the signal; (c) spectrum after beat correction

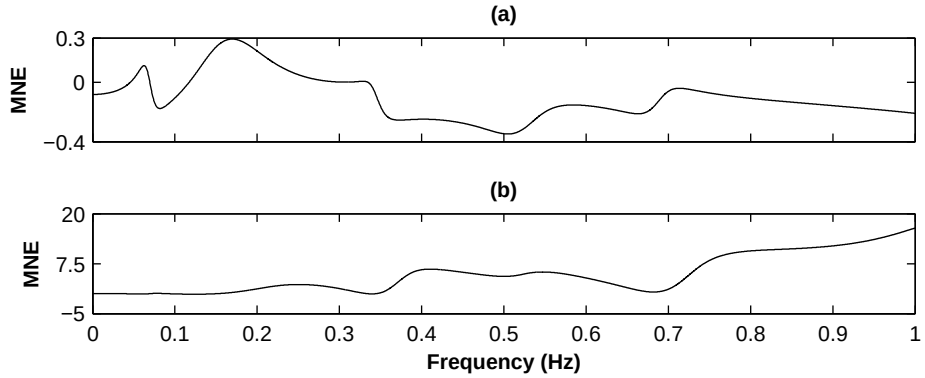

Fig. 8.31: MNE in real HRV signal (a) after performing beat correction; (b) before beat correction. Signals are corrupted by moving five random beats from the original signal backward by 0.2 s

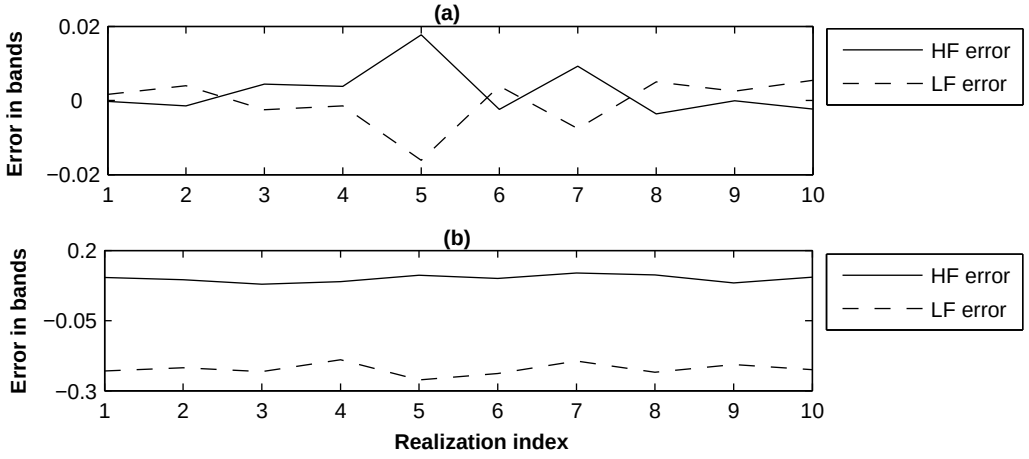

Fig. 8.32: Error in the LF and the HF band calculated for each of the ten signals generated by randomly moving five beats from the real HRV signal backward by 0.2 s; (a) error in the bands after beat correction; (b) error in the bands before beat correction.

the two bands were also calculated in this case and are presented in Fig. 8.31 and Fig. 8.32 respectively.

From the results presented in Fig. 8.31 and Fig. 8.32 it can be seen that the beat correction algorithm has also managed to reduce the error quite significantly in the case

when the real HRV signal was corrupted by moving five random beats backwards by 0.2 seconds.

8.7. Discussion and conclusions

The results in this chapter provide evidence of the feasibility of using the *ht* signal representation in HRV analysis. The performance of the non-parametric and parametric method of spectral analysis was studied using simulated signals. The effect of ectopic beats on the spectrum generated by both these methods has been shown. The results obtained from simulated signals (see sections 8.5.1 and 8.5.2) give clear indication of the importance of detection and correction for missing and/or ectopic beats. However, as the simulated signals used in this chapter were narrow band signals they did not represent the real HRV signals particularly well and only provided an upper bound on the performance of the beat correction algorithm. For this reason, beat correction tests were also carried out on real HRV signal (see section 8.6). The real signal was again corrupted by removing five random beats and also by moving five random beats by 0.2 seconds. The results obtained in the real HRV signal case also indicated that the beat correction algorithm has managed to significantly reduce the error caused by the missing and/or ectopic beats.

Using the results presented in this chapter the optimal setup for spectral analysis was established. In chapter 11 these arrangements will be used for the spectral analysis of the data obtained from patients undergoing elective surgery under local anaesthesia.

But before the spectral analysis can be carried out the signals need to be detrended. The techniques implemented and evaluated for detrending the HRV signals will be discussed in the next chapter.

9 Tachogram detrending

9.1. Introduction

Nonstationarities in the HRV signal can cause distortion in the time and frequency domain analysis. In particular these nonstationarities will distribute large amount of variance in the lowest frequency. In order to deal with this problem many researchers detrend the data prior to analysis. Detrending is usually based on first order [118, 119] or higher order [119, 120] polynomial model or by using successive-difference filters.

Linear detrending is done by fitting a linear regression to the data. This method removes the linear influence and transforms the data set into a series with a mean of zero. Linear detrending works well if the data has a linear or low order trend. Although these trends count for a significant portion of the variance, the residual series are seldom stationary. In case of successive difference filters the low frequency components are attenuated properly but this method also amplifies the high frequency components. The spectral densities are relatively accurate at frequency of one sixth of the sampling rate. Frequencies lower than one sixth of the sampling rate are greatly attenuated, however, for the frequencies above one sixth of the sampling rate the spectral densities are amplified [120] (see Fig. 9.1).

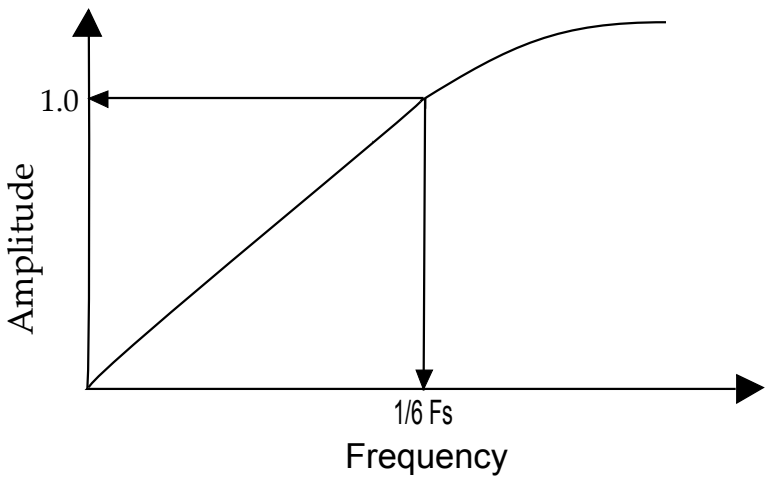

Fig. 9.1: Example of filter response for successive difference filter

Porges and Bohrer [120] presented a moving polynomial filter, which has been shown to remove the low frequency trends without distorting the high frequency components. This filter smoothes the data by conforming to the shifting level of baseline. When the smoothed baseline is removed from the original data set, the residual time series is free from the influence of the baseline and slow periodic activity. In this case the number of coefficients and the order of the polynomial is important. The order and duration of the polynomial are selected to bend into slow moving trends without distorting the frequency band of interest. For heart rate data, a cubic order polynomial with duration of 10.5 s is used for the adults and a cubic order polynomial with duration of 4.2 s is used for the signals for neonates. This algorithm is quite sensitive to the choice of polynomial order and the duration.

To avoid these issues another algorithm proposed by Tarvainen *et. al*. [121] was implemented as one of the approaches to detrend the HRV signal. This algorithm is based on the *Smoothness Prior Approach* (SPA). The main advantage of this algorithm lies in its simplicity, as the frequency response of the filter can be adjusted by a single parameter. The other method implemented for detrending was based on Wavelet Packet (WP) analysis.

The performance of both the detrending algorithms was first evaluated using simulated signals. The algorithms were then tested with the real data. The effect of detrending on the time domain analysis was studied using three parameters recommended in [19, 111] and also used in [122, 121] to see the detrending effect. These parameters include, standard deviation of all RR intervals (SDNN), the square root of the mean squared differences of successive RR intervals (RMSSD) and the relative amount of successive RR intervals differing more than 50 ms (pNN50). The simulated signals were used to clearly identify the differences in the performance of the two methods. Both the simulated signals consisted of three sine components corresponding to the Very Low Frequency (VLF), Low Frequency (LF) and High Frequency (HF) components of the HRV signal.

9.2. Detrending using Smoothness Prior Approach (SPA)

If the equispaced heart rate series is considered to consist of a nearly stationary component and a low frequency aperiodic trend then it could be represented as shown in Eq. 9.1.

$$z = z_{stationary} + z_{trend} \tag{9.1}$$

The trend component can be modelled with a linear observation model as (see Eq. 9.2).

$$z_{trend} = H\theta + v \tag{9.2}$$

Where $H \in \mathbb{R}^{(N-1)\times M}$ is the observation matrix, $\theta \in \mathbb{R}^M$ are the regression parameters, v is the observation error and $N = length(z) + 1$. The problem then reduces to finding the parameter by some fitting procedure so that the prediction $\hat{z}_{trend} = H\hat{\theta}$ can be used as the estimate of the trend. The estimate $\hat{\theta}$ is given by regularised least squares solution as shown in the Eq. 9.3 [121].

$$\hat{\theta}_\lambda = \arg\min_\theta \left\{ \|H\theta - z\|^2 + \lambda^2 \|D_d(H\theta)\|^2 \right\} \tag{9.3}$$

Where λ is the regularisation parameter and D_d indicates the discrete approximation of the d^{th}derivative operator. This is a modification of the ordinary least squares solution to the direction in which the side norm $\|D_d(H\theta)\|$ gets smaller. The solution to Eq. 9.3 can be expressed mathematically as shown in Eq. 9.4 [121].

$$\hat{\theta}_\lambda = (H^T H + \lambda^2 H^T D_d^T D_d H)^{-1} H^T z \tag{9.4}$$

Using Eq. 9.4 the trend component (z_{trend}) can be written as (see Eq. 9.5)

$$\hat{z}_{trend} = H\hat{\theta}_\lambda \tag{9.5}$$

As the regularisation part of Eq. 9.3 draws the solution toward the null space of the regularisation matrix D_d, D_2 (second order difference matrix) could be used for estimating the aperiodic trend of HR signal. The second order difference matrix $D_2 \in \mathbb{R}^{(N-3)\times(N-1)}$ can be written as shown in Eq. 9.6.

$$D_2 = \begin{pmatrix} 1 & -2 & 1 & 0 & \cdots & 0 \\ 0 & 1 & -2 & 1 & \ddots & \vdots \\ \vdots & \ddots & \ddots & \ddots & \ddots & 0 \\ 0 & \cdots & 0 & 1 & -2 & 1 \end{pmatrix} \tag{9.6}$$

In SPA method detrending is done by using second order difference matrix D_2 (see Eq. 9.6) and an identity matrix as the observation matrix, i.e. $H = I \in \mathbb{R}^{(N-1)\times(N-1)}$ [121]. Now using Eq. 9.1, 9.4 and 9.5 the detrended, nearly stationary HR signal can be written as shown in Eq. 9.7.

$$\hat{z}_{stationary} = z - H\hat{\theta} = (I - (I + \lambda^2 D_2^T D_2)^{-1})\, z \tag{9.7}$$

Equation 9.7 can be written as $\hat{z}_{stationary} = \mathcal{L}z$ where $\mathcal{L} = I - (I + \lambda^2 D_2^T D_2)^{-1}$ corresponds to a time varying finite-impulse response highpass filter.

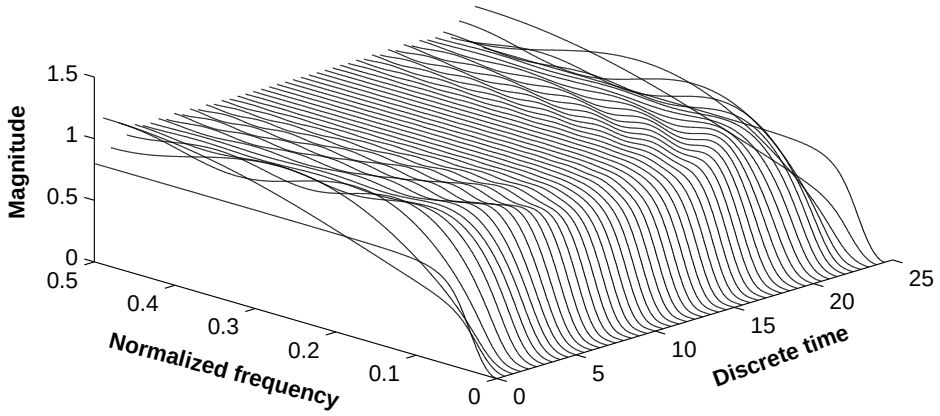

Fig. 9.2: Time varying frequency response of filter ($\mathcal{L}$) used in Smoothness Prior Approach (SPA) detrending ($N = 51$ and $\lambda = 10$)

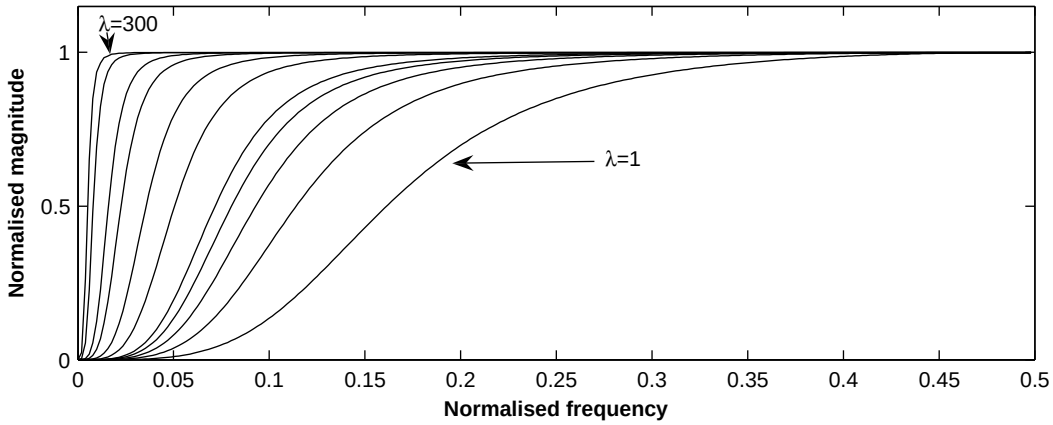

Fig. 9.3: Frequency response obtained from middle row of $\mathcal{L}$ for $\lambda = 1, 2, 10, 20, 50$ and 300 the corresponding cutoff frequencies are 0.215, 0.146, 0.064, 0.045, 0.029 and 0.012 times the sampling frequency

9.2.1. Detrending results using Smoothness Prior Approach (SPA)

The frequency response of the filter for each discrete time point can be obtained as the Fourier transform of its rows (see Fig. 9.2). From Fig. 9.2 it can be seen that the start and the end points of the data are handled differently. The filtering effect is attenuated at these points so that distortion is avoided. The Fourier transform of the middle row of $\mathcal{L}$ is used to calculate the cutoff frequency of the filter. The effect of the smoothing parameter λ on the frequency response of the filter is presented in Fig. 9.3. The cutoff frequency of the filter decreases as the λ value increases. This fact can be seen in Fig. 9.4, which presents the cutoff frequency plotted against λ values changing from 1 to 1000.

As mentioned before (see section 3.4.1.3) for short term HRV analysis ULF and VLF components do not reflect important information, therefore, the cutoff frequency of the detrending filter was chosen at $\lambda = 413$ giving a cutoff frequency of 0.0391 Hz, so that at the sampling rate of 4 Hz, used in this work for generating equidistance HRV signals, these components will be attenuated from the signal. The effect of this detrending me-

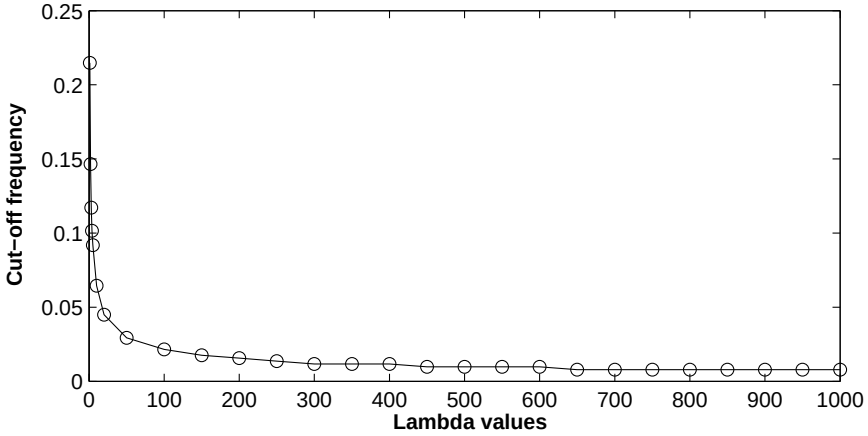

Fig. 9.4: Effect of changes in λ values on cutoff frequency of the filter. The cutoff values are presented with respect to normalised frequency

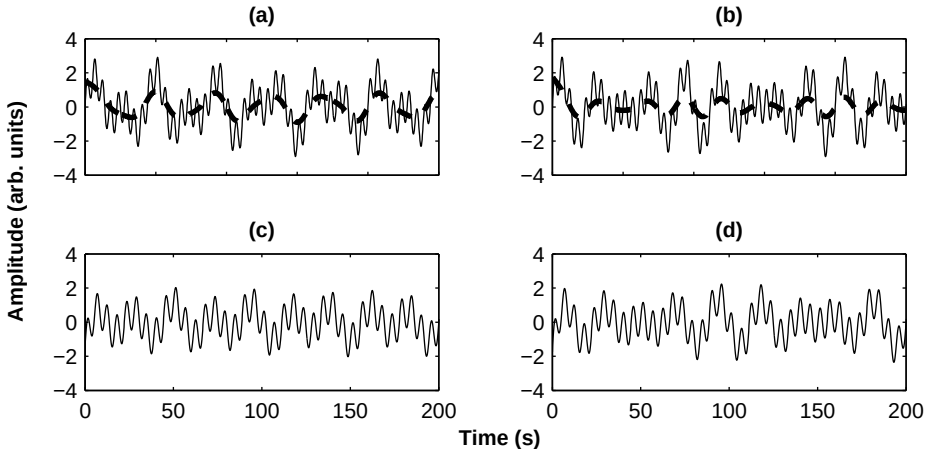

Fig. 9.5: Results of detrending the two simulated signals using SPA technique; (a) first simulated signal (thin solid line) and estimated trend (thick dashed line); (b) second simulated signal (thin solid line) and estimated trend (thick dashed line); (c) detrending result for first simulated signal; (d) detrending result for second simulated signal

thod was evaluated by applying it on two simulated signals. The first simulated signal consisted of three sine wave components of 0.025, 0.045 and 0.18 Hz and equal amplitudes. In the case of the second simulated signal the frequency corresponding to the slowest component was changed from 0.025 Hz to 0.035 Hz and the frequencies of the other two components remained the same. The frequencies were chosen so that each one represents the trend, LF and HF part of the HRV signal respectively. The results of detrending these two simulated signals using the SPA method are presented in Fig. 9.5. From the results shown in Fig. 9.5 (c) and 9.5 (d) it can be seen that the slow varying parts of the original signals have been attenuated to some extent. The changes caused by the detrending algorithm in the frequency components of the signals can be seen by looking at the normalised power spectrum of the signals before and after detrending (see Fig. 9.6). From the spectrum obtained after detrending the first simulated signal (see Fig. 9.6 c)) it can be seen that the magnitude of the trend signal with frequency 0.025 Hz has been re-

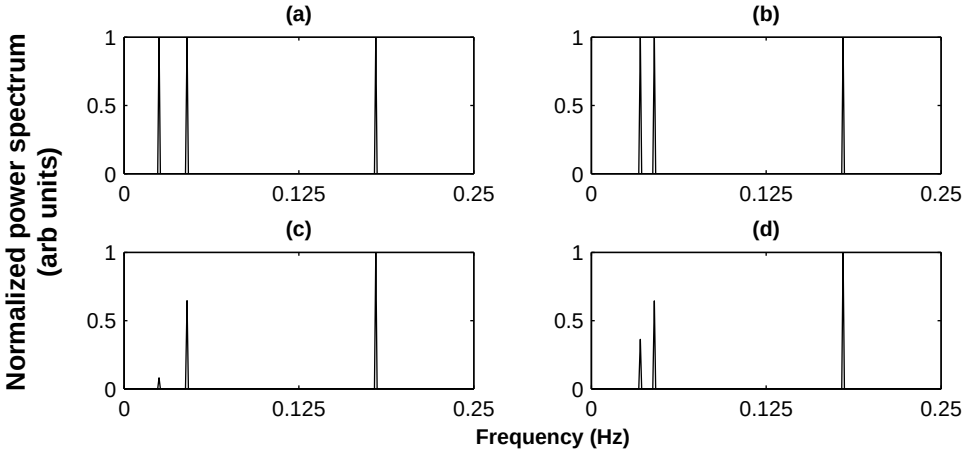

Fig. 9.6: Normalised power spectrum (NPS) of the original simulated signal 1 (a) and signal 2 (b), the spectrum of the signals after removing trend from signal 1 (c) and signal 2 (d) using smoothness prior approach

duced from unity to about 0.1. The filter has also attenuated the signal at 0.045 Hz from 1 to 0.65 approximately. In the case of the detrending result for the second simulated signal (see Fig. 9.6 (d)), the attenuation in the VLF part of the signal is comparable to the attenuation in the second component (around 0.045 Hz) of the signal. From the results shown in Fig. 9.5 (d) and Fig. 9.6 (d) it can be seen that the trend is not removed suitably from the second simulated signal. Also, due to the slow transition of the filter from the stopband to the passband the LF component of the signals is getting attenuated as well (see Fig. 9.6 (c) and 9.6 (d)).

The results obtained by detrending the real RR-interval time series from four different subjects are shown in Fig. 9.7. The thicker line in each plot in the top panel represents the estimated trend using the SPA method and the signals shown in the bottom panel represent the signals after the trend has been removed. The effect of detrending on the frequency contents of the signal can be seen by looking at the power spectrum of the original signal and the detrended signal given in Fig. 9.8. The spectra in Fig. 9.8 were obtained by using the non-parametric (Welch's periodogram) and the parametric (autoregressive (AR)) method of spectral analysis. For Welch's method a Hamming window of 600 data points with 50% overlapped was used while for the autoregressive spectrum a model order of 20 was used and the coefficients were calculated using the modified covariance method.

From the spectrum obtained using Welch's method (Fig. 9.8 top panel) it can be seen that the VLF component has been attenuated considerably with a slight change in the LF region of the signal. More prominent change can be seen by comparing the spectrum obtained using the AR method (Fig. 9.8 bottom panel) before and after detrending. In this case, before detrending the peak around 0.1 Hz cannot be distinguished clearly because of a strong VLF component.

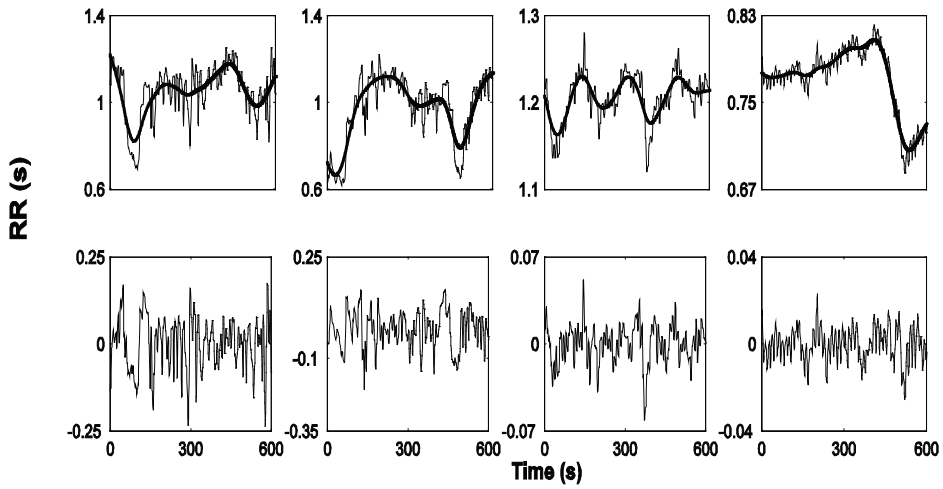

Fig. 9.7: Original RR-interval time series and the estimated trend (thick line) in the top panel, detrended signal, using smoothness prior approach (bottom panel)

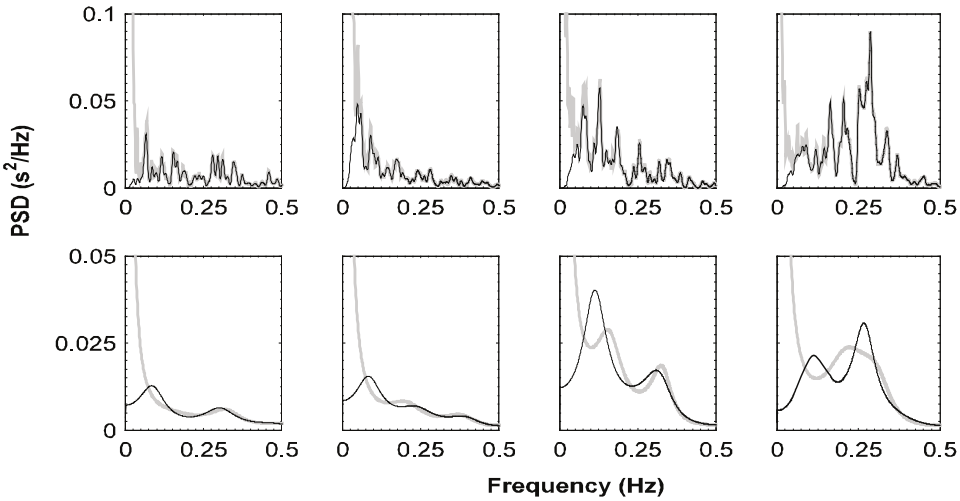

Fig. 9.8: PSD of the signal before (gray thick line) and after detrending (black thin line) using smoothness prior approach. Top row shows the result obtained using non-parametric (Welch's) method and bottom row shown the result obtained using 20th order AR model

After detrending, the peak in the LF region, around 0.1 Hz, is clearly visible and location wise is more comparable with the LF peak present in the spectrum obtained from Welch's periodogram method.

9.3. Detrending using Wavelet Packets

Although detrending the signal using the smoothness prior method discussed in section 9.2 has successfully attenuated the trend from the signal, this method has two main disadvantages. Firstly, it has caused some attenuation in the passband region of the signal (see Fig. 9.6), due to the slow transition of the lowpass filter. Secondly, in this method the filter ($\mathcal{L}$) grows with the length of the signal which makes it unsuitable for processing large HRV signals.

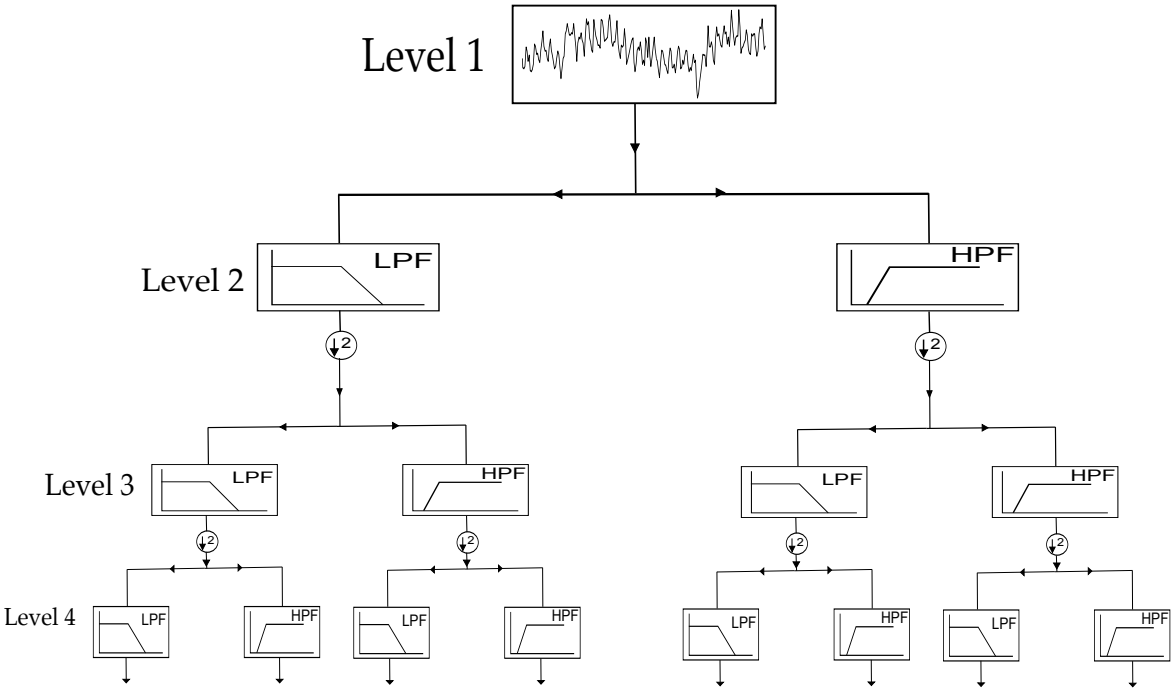

Fig. 9.9: Wavelet Packet transform of a signal to level 4

In order to address these issues another detrending algorithm was implemented using Wavelet Packets (WP) analysis. This algorithm is based on the technique mentioned in the work of Wiklund *et. al*. [122].

9.3.1. Wavelet Packets (WP) Analysis

Wavelet packet analysis is a generalisation of wavelet analysis offering a richer decomposition procedure by splitting not only the approximation (lowpass) part of the signal, as done in the case of DWT (see section 6.2.2 and Fig. 6.4), but also the detail (highpass) part of the signal. The original signal is considered to be at level 1 and the decomposition process is applied n times to get the WP transform at level $n+1$. The process of WP transform of a signal to level 4 is shown in Fig. 9.9. As a result of full WP decomposition of a signal to a certain level the filter bank structure becomes a full binary tree as shown in Fig. 9.9. A full decomposition to a level results in an evenly spaced frequency resolution, which is similar to the result obtained by the STFT algorithm. In general, a decomposition into level J requires a signal of length of at least 2^{J-1}. The upper and lower bound on the number of basis for such a decomposition can be written as shown in Eq. 9.8 [123].

$$2^{2^{j-2}} < A_j < 2^{2^j} \tag{9.8}$$

where $j = J - 1$.

The time-frequency plane tiling produce by the WP transform depends on the basis

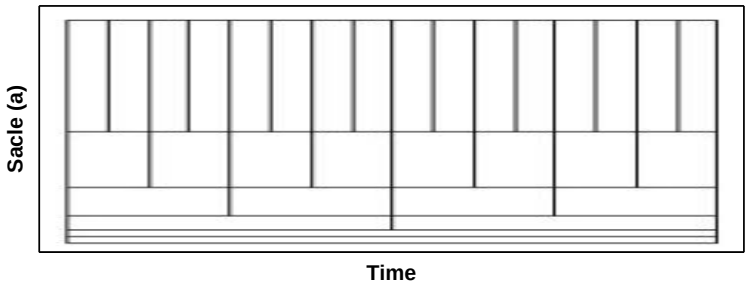

Fig. 9.10: Wavelet packet tiling in time-frequency plane

selected for the representation of the signal. Some examples of the possible tilings are shown in Fig. 9.10. The selection of the best basis for signal representation depends on the application. Some of the commonly used criteria for basis selection include thresholding and minimisation of entropy of the analysed signal. Entropy of the signal could be measured using different approaches such as, Shannon's entropy and l^p-Norm etc. It is important to note from Fig. 9.9 that the frequency order is not monotonically increasing. This is due to the fact that downsampling causes all the high pass part to be mirrored. Thus, in the next application of DWT to this part, the low and high frequency parts appear in reverse order. This frequency ordering is called filter bank ordering. The monotonically increasing frequency ordering (natural frequency ordering) could be obtained by interchanging the position of high and low frequency parts in every other application of the DWT step.

9.3.2. Detrending results using Wavelet Packet (WP) analysis

As mentioned previously in section 9.3 the algorithm for detrending is based on the work of Wiklund *et. al*. [122]. In this case the authors have sampled the HR signal at 2.4 Hz and detrending was done by calculating the DWT up to sixth scale using the Daubechies (db12) wavelet. To remove the trend, the wavelet coefficients at the lowest scale (i.e. 6) were replaced with zeros and the signal was reconstructed using the coefficients at the first five scales. At the sampling frequency of 2.4 Hz removing the coefficients at the sixth scale would result in removing the frequency components from 0-0.01875 Hz. But at 4 Hz sampling rate the frequency range represented by the sixth scale would be from 0 Hz to 0.03125 Hz approximately and further splitting this low part component will not be helpful in removing the signal below 0.04 Hz.

Due to these considerations the WP transform was applied for the detrending purpose as it allows the decomposition of the detail part of the transform. The basis used for the WP analysis is shown in Fig. 9.11. This basis was chosen according to the bandwidth of the resulting filters rather than using the usual methods used for the calculation of the best basis. The response of the resulting filters is shown in Fig. 9.12.

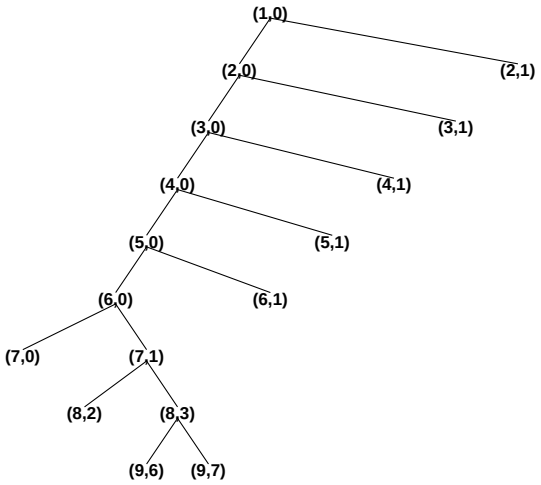

Fig. 9.11: WP tree used for detrending. The pair of number in the bracket at each node represents particular part of the decomposition. The first number in the pairs shows the level of the decomposition J and the possible values for the second number (n) are 0.....$2(J-1)-1$ except for $J=1$ which represent the original signal.

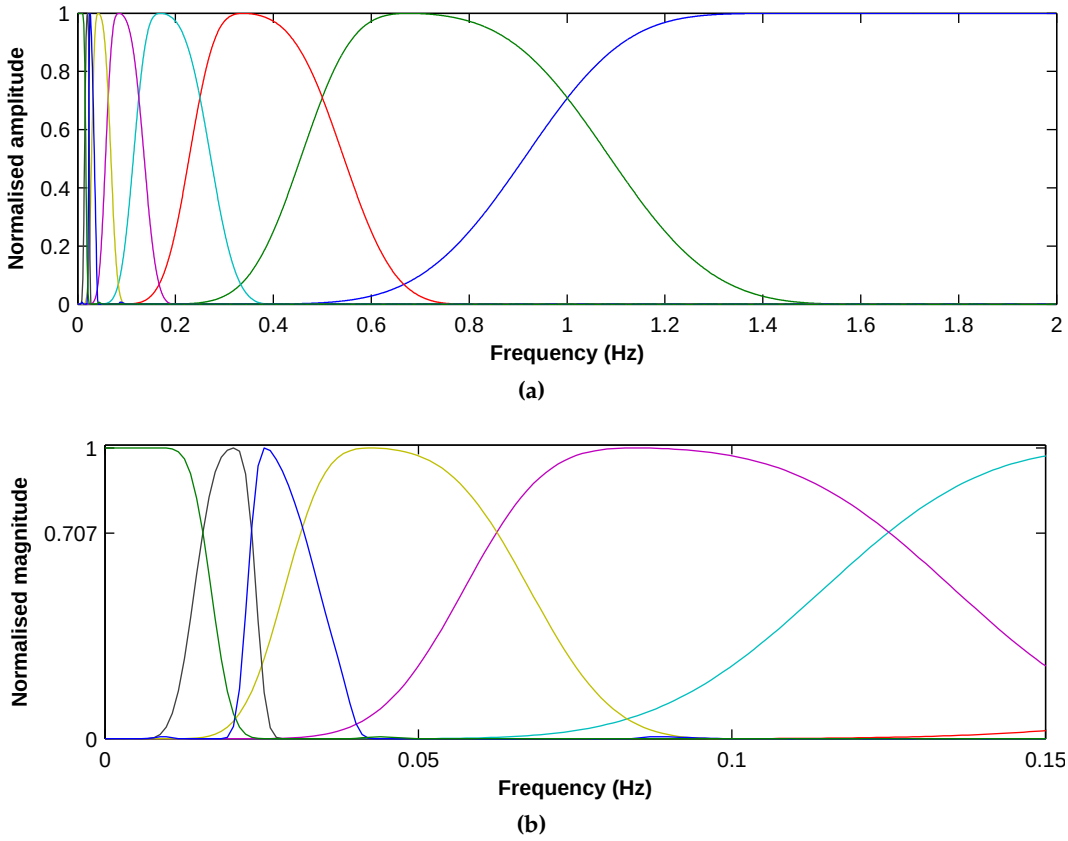

Fig. 9.12: Filter responses of the filters obtained by the basis shown in Fig. 9.11 for detrending using WP analysis, part a shows all the nine filter in the frequency range from 0 to 2 Hz and part b shows the same response with filters in the range of 0 to 0.15 Hz

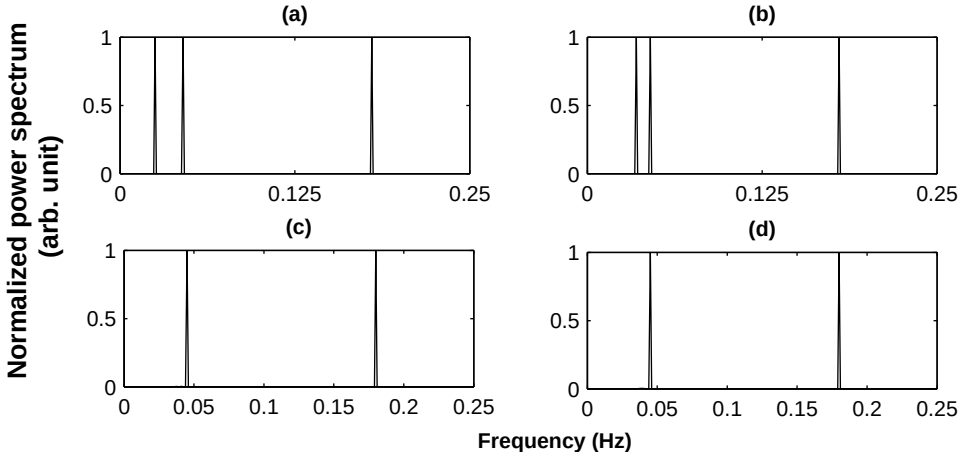

Fig. 9.13: Normalised power spectrum of the original simulated signal 1 (a) and signal 2 (b), the spectrum of the signals after removing trend from signal 1 (c) and signal 2 (d) using WP algorithm

Figure 9.12 shows that in this analysis seven bandpass filters, one low pass and one high-pass filter will be used. Using the information about the cutoff frequencies of these filters, the frequencies approximately from 0 to 0.039 Hz were attenuated by making the coefficients of the WP decomposition coming from the low pass filter and the first bandpass filter (from the left) present in Fig. 9.12 (b), zero and reconstructing the signal from the remaining coefficients. This low pass and bandpass filter represent nodes (7,0) and (9,6) of the basis shown in Fig. 9.11.

The simulated signals that were used for the evaluation of the detrending method using the SPA method (see Fig. 9.5) have also been used here to evaluate the WP algorithm for detrending. The results of the WP detrending approach are shown in Fig. 9.13. As before, the spectrum of the original signal was compared to see the effect of detrending on the signals. The spectrum of both the original signal and the detrended signals are shown in Fig. 9.13. By comparing Fig. 9.13 and Fig. 9.6 it can be seen the WP algorithm has not only attenuated the trend component of the signal more than the SPA method, but also it has not caused any significant reduction in the power of the other two components corresponding to the LF and the HF part of the HRV signal. The results obtained for the real RR-interval time series of the same four subjects previously used with the SPA method (see Fig. 9.7) are shown in Fig. 9.14. As before, the thicker line in each plot in the top panel represents the trend, this time estimated using WP algorithm, and the bottom panel shows the signals obtained after detrending. The spectrum of the original RR-interval time series and the detrended signals of Fig. 9.14 are shown in Fig. 9.15. As before, the peaks in the LF and HF regions can be visualised better in the detrended signal spectra as compared to the original spectra. Similar to Fig. 9.8 the spectra shown in the top panel of the Fig. 9.15 are obtained using Welch's method and those at the bottom panel are obtained using the AR modelling approach.

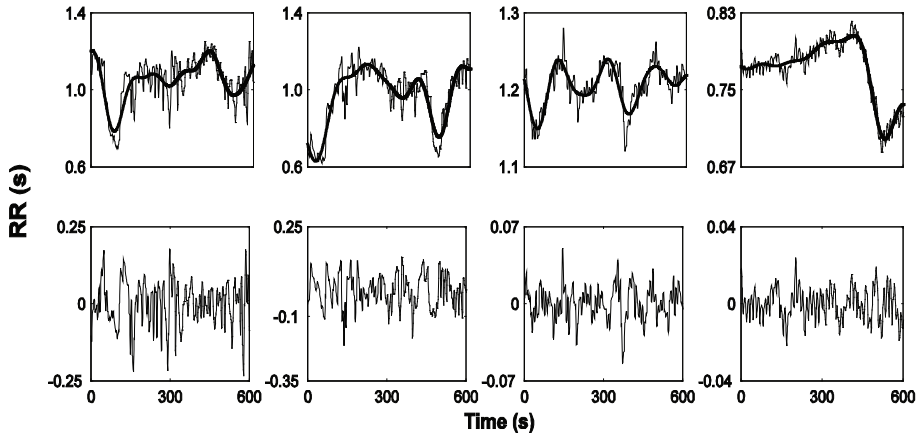

Fig. 9.14: Original RR-interval time series and the estimated trend (thick line) in the top panel, detrended signal, using WP method, (bottom panel). The RR interval time series are same as presented in Fig. 9.7

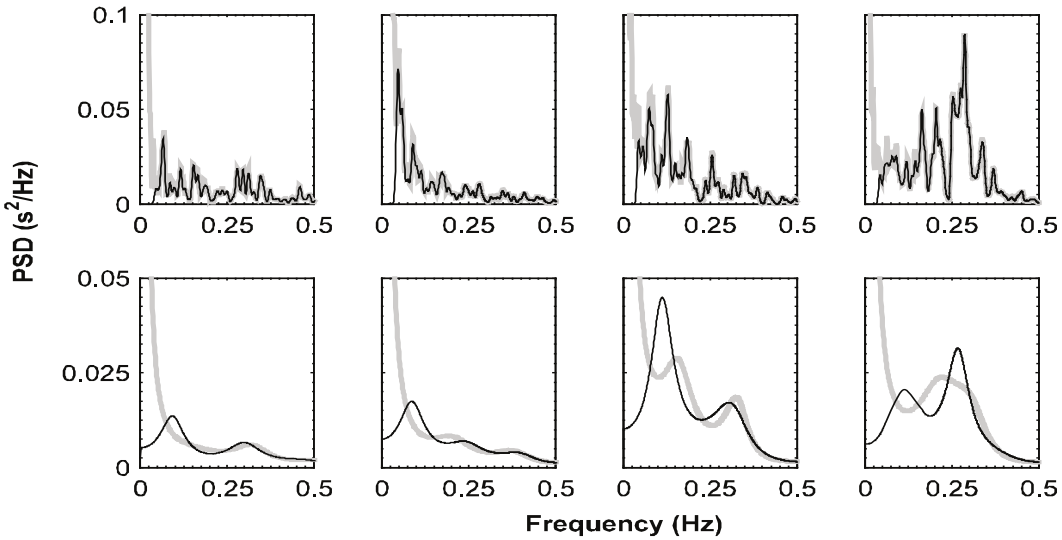

Fig. 9.15: PSD of the signal before (gray thick line) and after detrending (black thin line) using smoothness prior approach. Top row shows the result obtained using non-parametric (Welch's) method and bottom row shows the result obtained using 20th order AR model

By comparing the spectra shown in the top panel of Fig. 9.15 with those shown in the top panel of Fig. 9.8 it can be seen that the LF component of the signal is better preserved in the case of WP detrended signals. The preservation of the LF component of the signal can be seen more clearly in Fig. 9.16, where the spectrum (non-parametric) from one of the RR interval time series is presented along with the spectrum of the detrended signals obtained using the SPA and the WT methods.

9.4. Parameter comparison between two detrending techniques

The effect of both detrending procedures on the time domain indices are shown in table 9.1. From the indices shown in table 9.1 it can be seen that both the detrending techniques have affected SDNN, which describes the total variance of the signal the most.

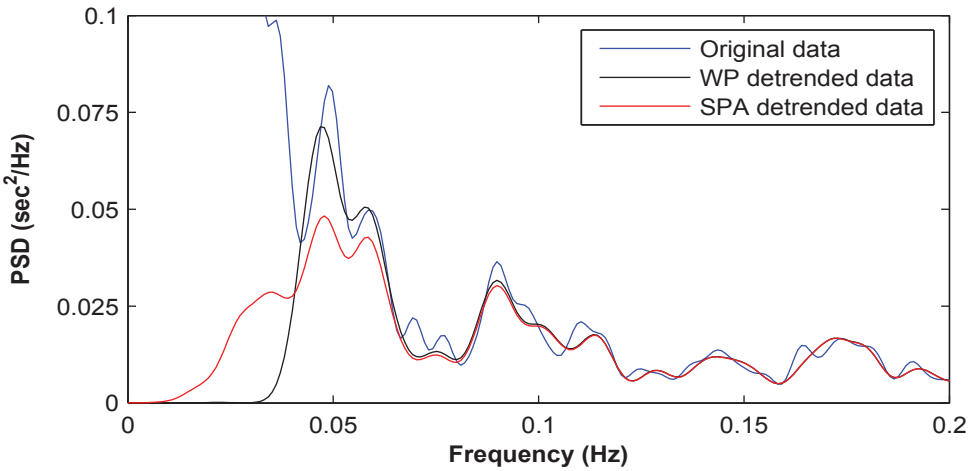

Fig. 9.16: PSD of the original RR interval time series before detrending (blue line); the WT detrended signal (black line) and the SPA detrended signal (red line). The cutoff frequency of both the methods is approximately 0.039 Hz. The poor performance of SPA method in terms of less attenuation in the stopband and reduction of power in the LF region due to slow transition of the filter is clearly evident

Table 9.1.: Effect of detrending techniques on three time domain parameters (SDNN, RMSSD and pNN50)

TIME DOMAIN PARAMETERS								
SDNN (ms)			RMSSD (ms)			pNN50 (%)		
Original	SPA	WP	Original	SPA	WP	Original	SPA	WP
122.540	60.168	60.453	26.448	26.319	26.346	8.451	8.133	8.224
152.460	78.518	78.890	32.712	32.662	32.685	8.224	8.042	8.151
102.680	56.215	56.319	25.696	25.644	25.655	4.543	4.498	4.453
67.649	35.696	35.393	12.734	12.668	12.683	0.545	0.545	0.545

For the other two indices (RMSSD and pNN50) the values obtained after the WP detrending are slightly better matched with the original values than the ones obtained by the SPA detrending method. Similarly, the effect of detrending on the frequency domain parameters is presented in table 9.2.

Again from the results presented in table 9.2 it can be seen that both the detrending methods have significantly affected the total power of the signal as expected. However, due to better attenuation achieved by the WP detrending algorithm the VLF power is less in all cases for this method compared to the VLF power calculated after detrending with the SPA method. Also, the power in the LF region (P-LF) is better matched with the original signal in the case of the WP detrending method. It should be noted that the values

Table 9.2.: Effect of detrending techniques on the frequency domain parameters. Total power (PT), Very Low Frequency power (P-VLF) (ms2), Low Frequency power (P-LF) (ms2), High Frequency power (P-HF) (ms2), Normalised Low Frequency power (P-Lfnorm) (n.u), Normalised High Frequency power (nu) and Ratio (P-LF/P-HF)

FREQUENCY DOMAIN PARAMETERS						
Original						
PT	P-VLF	P-LF	P-HF (ms2)	P-Lfnorm	P-HFnorm	Ratio
1346.1	1342.1	1.4	2.0	0.30	0.5	0.7
1008.9	1004.1	2.8	1.5	0.60	0.3	1.9
838.9	825.0	6.1	6.4	0.40	0.5	1.0
728.2	726.7	1.1	0.3	0.70	0.2	3.2
SPA						
PT	P-VLF	P-LF	P-HF	P-Lfnorm	P-Hfnorm	Ratio
3.72	0.09	1.07	1.95	0.30	0.54	0.55
4.71	0.45	2.25	1.46	0.53	0.34	1.54
13.52	0.15	5.67	6.30	0.42	0.47	0.90
1.34	0.15	0.80	0.30	0.67	0.25	2.71
WP						
PT	P-VLF	P-LF	P-HF	P-Lfnorm	P-Hfnorm	Ratio
3.72	0.01	1.16	1.95	0.31	0.53	0.59
4.61	0.03	2.58	1.46	0.56	0.32	1.76
13.61	0.03	5.87	6.31	0.43	0.46	0.93
1.23	0.01	0.83	0.30	0.68	0.24	2.81

obtained for both cases are slightly lower than the corresponding values in the original signal which is expected as in the case of original signal the slow varying trend will have affected all these values to some extend especially the values of the LF region. Statistical tests were not carried out on the time domain and frequency domain parameters estimated after detrending with the two implemented techniques as the changes in the SDNN,

total power and power in the VLF region of the signals is quite obvious (see table 9.1 and 9.2). While, other parameters do not show large changes compared to the parameters values in the original (signal before detrending), which is expected as the detrending method should not affect the signal in the LF or the HF frequency regions.

9.5. Discussion and conclusions

There are various techniques such as digital filters, Kalman filter [124], WT analysis [122] and Empirical Mode Decompositions [125], which have been used for detrending the HRV signals. Due to the lack of a generally accepted standard it is difficult to judge which method is the most suitable for detrending the HRV signal. Also, this makes it difficult to compare the results of detrending quantitatively on real HRV signals. In most studies presented in the literature, simulated signals have been used to show the effectiveness of the detrending techniques. But again due to the lack of fixed reference different kinds of simulated signals are used and mostly the results for the simulated signals and also for the real HRV signals are presented only in the time domain [124, 125]. This represents a major drawback as the full effect of the detrending technique can only be seen by analysing the results both in the time and the frequency domain.

In order to choose a detrending method, apart from its ability to remove the trend from the signal, other criteria such as simplicity of implementation, computational requirement should also be considered. As detrending is effectively a lowpass filtering procedure, digital filters present a simpler solution. The use of digital filters have the advantage that the cutoff frequency and to a certain extent the transition region of the filter could be adjusted quite precisely. If analysis is done offline and sufficient data is available then FIR filters could be used, but due to the large filter order (filter taps) these filters might not be suitable for online analysis. Infinite Impulse Response (IIR) filters generally have much smaller filter order than FIR filter and therefore they could be suitable for online analysis. But unlike the offline case, in online analysis it will be more difficult to deal with the phase distortion caused by the IIR filters. In this case, the IIR filter should either design in such a way that it causes acceptable distortion in the passband of the signal or the data could be passed through a phase correcting filter after detrending. But it should be kept in mind that it is not always possible to design an appropriate phase correcting filter. Therefore, in online application a trade-off has to be made when choosing the technique for detrending. IIR filters provide better control over the filter characteristics (cutoff, transition region) but causes phase distortion. If phase distortion is undesirable then techniques such as wavelet or wavelet packet analysis could be used. In this case phase distortion could be avoided but the filter characteristics could not be

adjusted manually and are restricted with the choice of the wavelet function. In this study two methods, one based on Wavelet Packet (WP) analysis and the other using *Smoothness Prior Approach* (SPA), were implemented for detrending. These methods were compared for their simplicity of implementation, computational requirement and their ability to remove trend from the signals.

In general, both detrending methods, WP and SPA, have been successful in removing the trend from the signal. The WP algorithm has the following advantages over the SPA method;

1. WP method is computationally more efficient than the SPA method, this becomes important when considering the real time implementation and also processing of long HR data.

2. WP method has caused less distortion in the detrended signal and

3. WP method has achieved better attenuation of the trend part of the signal than the SPA.

The results presented in this chapter clearly indicate the effect of slow varying trend on various indices used to study HRV signals. In order to reduce the error caused by these slow varying trends, the data must be detrended before further analysis could be carried out. For this purpose two different detrending techniques, one based on *Smoothness Prior Approach* (SPA) and another based on wavelet packet (WP) analysis were implemented. These techniques were validated and compared using simulated and real HRV data. The results suggest that the WP method is superior and therefore this method was used for detrending the data obtained from locally anaesthetised patients before further analysis.

10 Respiration signal estimation

10.1. Introduction

Despite clear evidence that the breathing characteristics markedly affect beat-to-beat cardiovascular variability [126, 127, 128, 129, 130], in the last five years approximately 15% published papers on HRV quoted in the Index Medicus have referenced respiration, and only 20% of these recognised the interaction between HRV and respiration [131]. In this study an effort was made to take respiration into account. As the direct measurements of respiratory signals were not possible from the locally anaesthetised patients, the ECG signal was used for the estimation of the respiration signal.

In order to estimate the respiration signal from the single lead ECG signal recorded from the locally anaesthetised patients the ECG Derived Respiration (EDR) technique proposed and clinically validated by Moody *et. al.* [132, 133] was used. This technique has also been used previously by others in different physiological studies [134, 135]. The algorithm was implemented in *Matlab* and validated using subset of the "Fantasia Database" available from *Physionet* [136]. In the following section the EDR algorithm will be discussed briefly and the validation results obtained from "Fantasia Database" will be presented before presenting the estimated respiration signals from the locally anaesthetised patients.

10.2. EDR algorithm description

The ECG signals recorded from the surface of the chest are influenced by motion of the heart with respect to the electrodes, and by changes in the electrical impedance of the thoracic cavity [132]. These physical influences of respiration result in amplitude variations in the observed ECG. In terms of the equivalent dipole model of cardiac electrical activity, respiration induces an apparent modulation in the direction of the mean cardiac electrical axis. The mean cardiac electrical axis often reflects the anatomic position of the heart in the chest. The modulation produced by the respiration in the direction of the

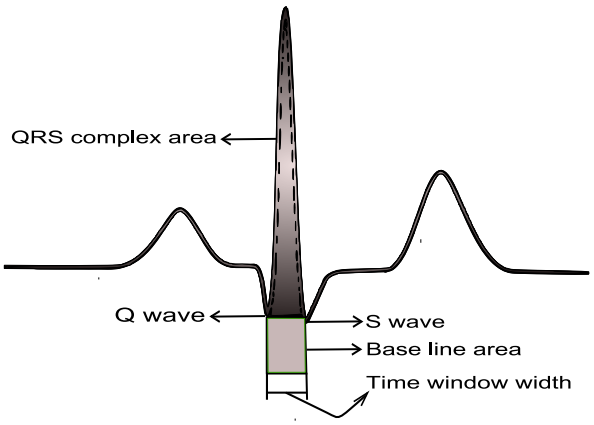

Fig. 10.1: Figure showing the calculation of the QRS complex and baseline area

mean cardiac electrical axis is independent from electrode motion artefacts which result from the mechanical deformation of the electrode/skin interface.

The earlier work in determining the direction of the electrical axis was carried out by Pellegrini [137] in order to create "virtual ECG leads" which would represent what would be obtained from electrodes fixed in position relative to the heart. With the hypothesis that the fluctuations in the axis direction measurements would reflect the physical influences of respiration on the ECG, Moody *et. al*. [132] presented a simplified technique to estimate the electrical axis direction from two-lead ECG signals. The basis of this method is that the mean cardiac vector changes during inhalation and exhalation due to the rotation of the heart in the chest. As a result of this rotation, the amplitude of each ECG lead changes. By using two orthogonal ECG leads the mean cardiac vector could be approximated in the plane defined by the two leads. The respiratory signals derived from these measurements were compared with simultaneously recorded measurements of chest circumference using a mercury strain gauge; later studies used pneumatic respiration transducer (PRT) measurements.

To obtain the direction of the electrical axis the baseline was removed from the ECG signal and then the area of each normal QRS complex was measured in each of the two leads of the ECG signal over a fixed window. The width of the window was determined during the learning phase of the algorithm. The window starts from the Q wave and ends at the S wave of the ECG signal. Since the window width is fixed, the area is proportional to the mean amplitude of the signal over the course of the window, hence to the projection of the mean cardiac electrical vector on the lead axis. The calculation of the QRS complex area and the baseline area can be seen in Fig. 10.1. Assuming that the leads are orthogonal, the arctangent of the ratio of the area measure in the two leads gave the angle of the mean axis with respect to one of the lead axes (see Fig. 10.2). Even if the leads are not orthogonal this will cause a systematic but harmless error in the axis direction estimation.

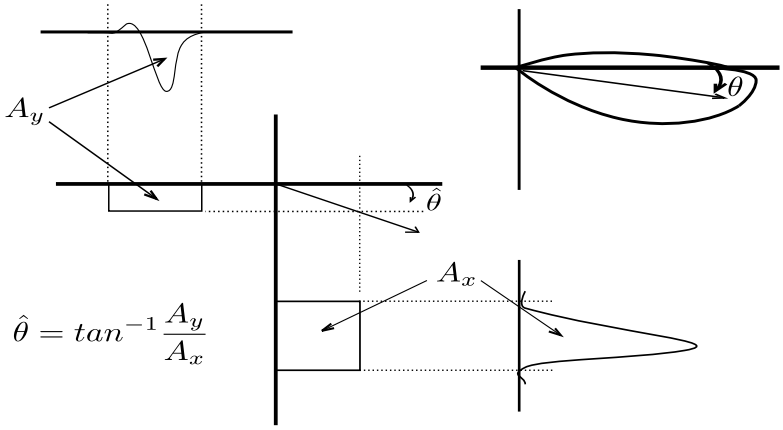

Fig. 10.2: Estimation of direction of the mean cardiac electrical axis from measurements of QRS area

The axis direction measurement during the QRS complex provides one sample of the EDR signal per cardiac cycle. Assuming that the heart rate is almost always greater than twice the respiration rate, thus the Nyquist criteria is satisfied and the respiration frequency can be estimated quite accurately with this limited set of samples. Cubic spline interpolation can be use to obtain the continuous EDR signal once its sample per cardiac cycle are estimated from the ECG signals. If small numbers of ectopic beats are present in the data they can be discarded. If a large number of similar ectopic beats are present in the data then axis direction measurement can be made for each type of ectopic beats. The measurements for beats of different morphologies will generally differ by constant angles which can be determined from the differences of the means of the measurements for each morphology [132]. After applying these constant correction angles the measurements from the ectopic beats can be merged with the measurement from the normal beats. If only one ECG lead is available, the QRS area from that lead can still be used as an approximation to the respiratory signal.

10.3. Evaluation of the implemented EDR algorithm

After the implementation, the validation of the algorithm was done using a subset of "Fantasia Database" [136]. This database contains signals from twenty young (21-34 years old) and twenty elderly (65-85 years old) healthy subjects. Each group contains equal number of males and females. The ECG and respiration signals were recorded for two hours continuously in supine resting position at the sampling rate of 250 Hz. All subjects remained in a resting state in sinus rhythm while watching the movie "*Fantasia*". The data is indexed as f1y01, f1y02, ... , f2y10 for the young healthy volunteers and as f1o01, f1o02, ... , f2o10 for the elderly volunteers. The data set starting with index (f2) also contains uncalibrated continuous non-invasive blood pressure signals along with the ECG and the respiration signals. The respiration signals were measure using a chest belt.

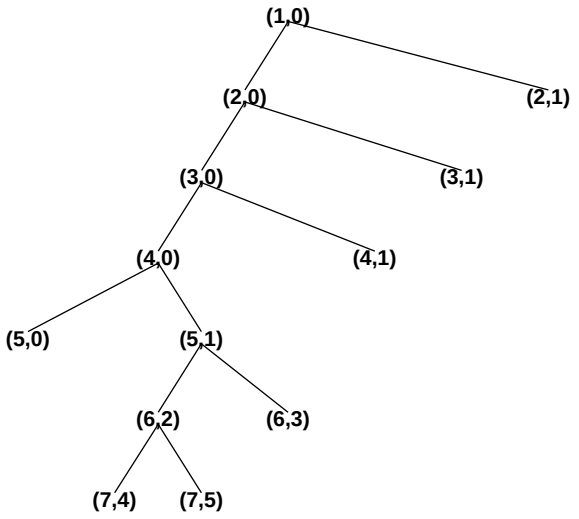

Fig. 10.3: Wavelet Packet tree used for band pass filtering the respiration signals

In our study, for validation purpose we have used ten data sets from each group (f1y01, ... , f1y10) representing the data from young volunteers and (f1o01, ... , f1o10) representing the data from elderly volunteers. Both the reference respiration signals and the respiration signals estimated using the EDR technique were decimated to a sampling rate of 4 Hz. This was done in order to analyse these signals at the same sampling rate which will be used in further analysis of heart rate variability data. The two respiratory signals were also bandpass filtered employing wavelet packet analysis, using the same principles as described in chapter 9, the bandpass filtering restricted the frequency contents of the signals to be between 9 bmp to 30 bmp. The average respiratory rate reported in a healthy adult at rest is usually given as 12 bpm ($^{12}/_{60}$ Hz) [138, 139] but estimates do vary between sources, e.g., 12–20 bpm, 10–14 bpm [140] and 16–18 bpm [141]. The range of 9 bmp to 30 bmp was used in this study so that both low and high breath rate can be taken into account. After processing the lowpass filtered signals were also compared visually with the reference signals to make sure that the respiration components were not lost due to the filtering process.

The wavelet tree used for filtering is shown in Fig. 10.3. The filtering effect was achieved by setting the coefficients coming from nodes (2,1), (3,1), (5,0) and (7,4) to zero and reconstructing the signal using the coefficients from the remaining nodes.

After filtering the reference and the estimated respiration signal the data was considered in segments of two minutes and compared using cross-correlation for similarity. Also, the PSD was used to compare the peak frequency obtained from the segments from the reference respiration signal with the peak frequency obtained from the segments of estimated respiration signal. The PSD was obtained using both Welch's method and the AR method. For Welch's method a Hamming window of 128 samples with 50% over-

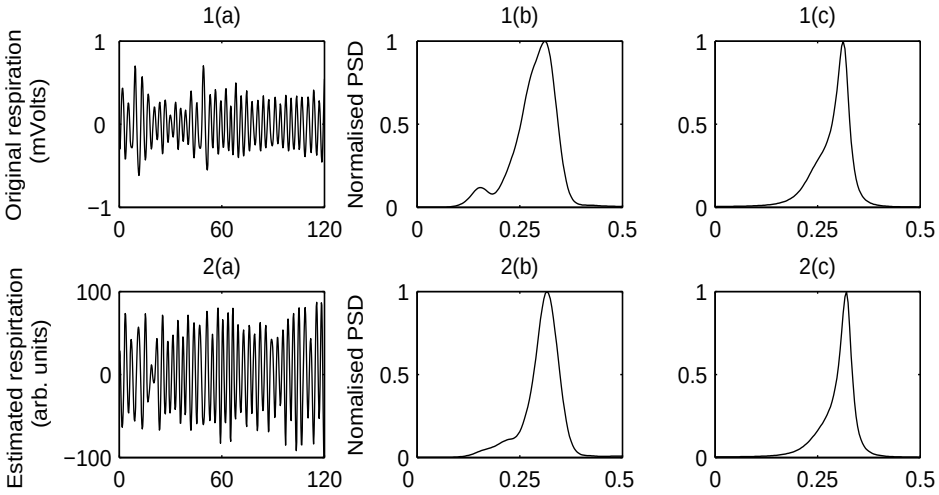

Fig. 10.4: The graphs showing reference and estimated respiration signals along with the PSD from one (f1y01) of the ten young health subject from "Fantasia Database"; top panel graphs: 1(a) reference respiration signal (signal measured using the chest belt), 1(b) PSD obtained with Welch's method, 1(c) PSD obtained from AR method; bottom panel graphs: 2(a) estimated respiration signal, 2(b) PSD obtained with Welch's method, 2(c) PSD obtained from AR method. The x-axis units for plots 1(a) and 2(a) is "seconds" while the x-axis units for rest of the plots representing PSD is "Hz"

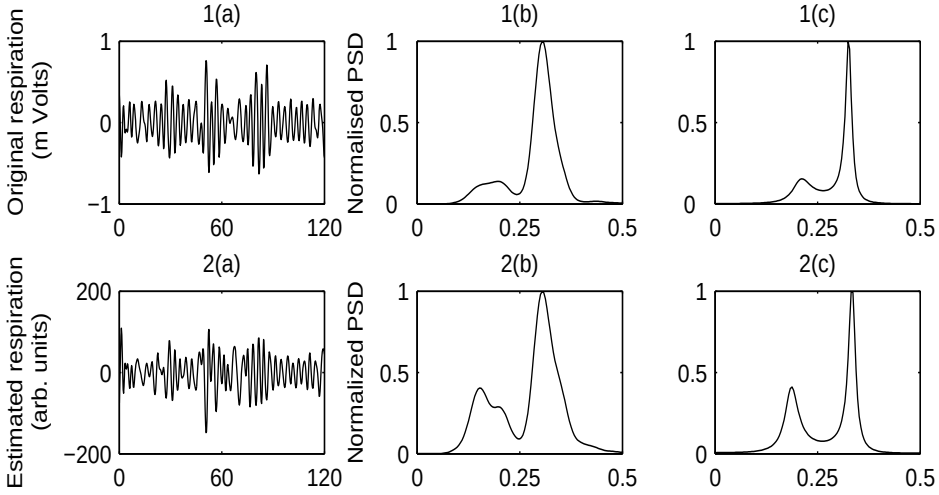

Fig. 10.5: The graphs showing reference and estimated respiration signals along with the PSD from another (f1y09) of the ten young health subject; top panel graphs: 1(a) reference respiration signal (signal measured using the chest belt), 1(b) PSD obtained with Welch's method, 1(c) PSD obtained from AR method; bottom panel graphs: 2(a) estimated respiration signal, 2(b) PSD obtained with Welch's method, 2(c) PSD obtained from AR method. The x-axis units for plots 1(a) and 2(a) is "seconds" while the x-axis units for rest of the plots representing PSD is "Hz"

lap was used while for AR method model order of 10 was used and the coefficients were estimated using the modified covariance method. The AR model order was estimated using MDL criterion (see Eq. 7.18). The reference and the estimated respiratory signals along with the spectrum for two young subjects are shown Fig. 10.4 and Fig. 10.5.

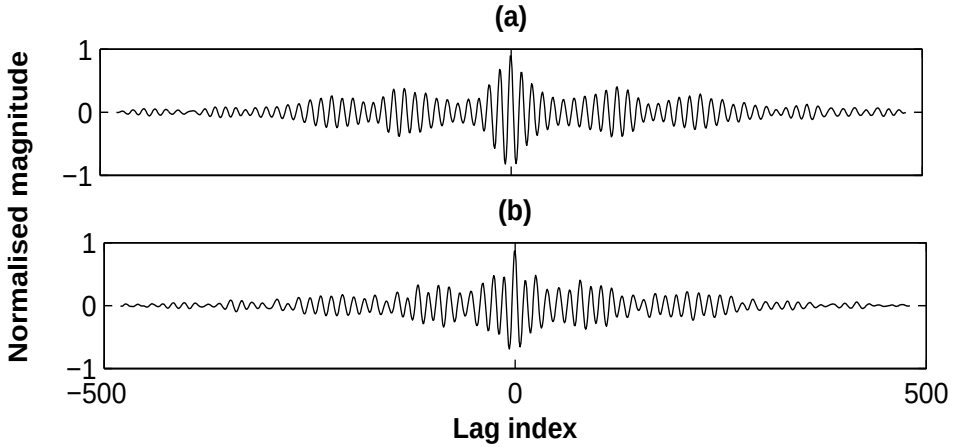

Fig. 10.6: Cross-correlation plots between; (a) reference (1(a)) and estimated (2(a)) respiration signals of Fig. 10.4, (b) reference (1(a)) and estimated (2(a)) respiration signals of Fig. 10.5

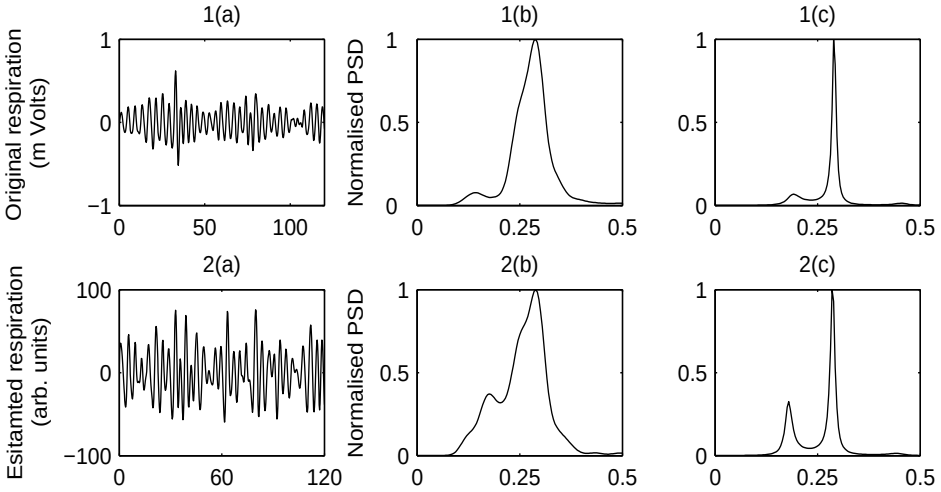

Fig. 10.7: The graphs showing reference and estimated respiration signals along with the PSD from one (f1o01) of the ten elderly health subject; top panel graphs: 1(a) reference respiration signal (signal measured using the chest belt), 1(b) PSD obtained with Welch's method, 1(c) PSD obtained from AR method; bottom panel graphs: 2(a) estimated respiration signal, 2(b) PSD obtained with Welch's method, 2(c) PSD obtained from AR method. The x-axis units for plots 1(a) and 2(a) is "seconds" while the x-axis units for rest of the plots representing PSD is "Hz"

From the PSDs shown in Fig. 10.4 and Fig. 10.5 it can be seen that the peak respiration frequency is detected quite accurately from the estimated respiration signals. As mentioned before, to check for similarity in the reference signal and the estimated signal, cross-correlation technique was used and the results obtained from the two set of respiration signals shown in Fig. 10.4 and Fig. 10.5 are presented in Fig. 10.6. The cross-correlation functions shown in Fig. 10.6 are normalised so that, if the signals being compared are exactly the same, auto-correlation case, the zero lag value will be one. The results pre-

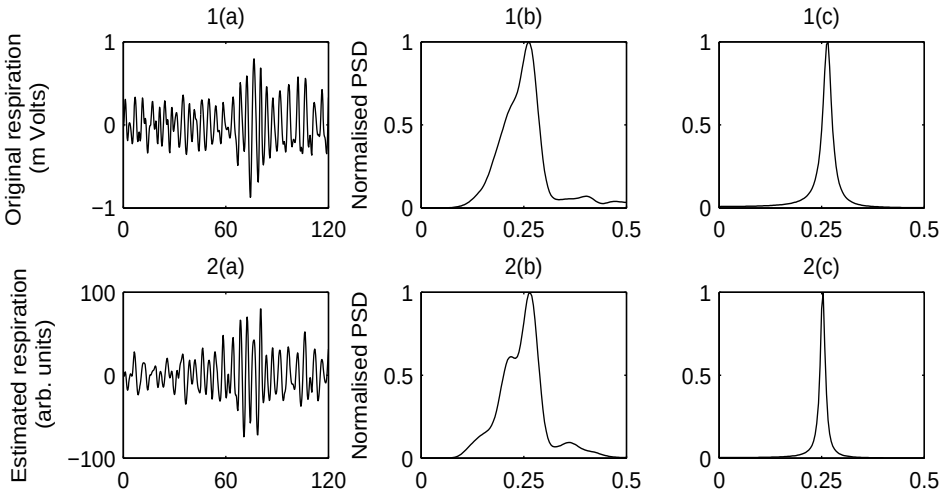

Fig. 10.8: The graphs showing reference and estimated respiration signals along with the PSD from another (f1o05) of the ten elderly health subject; top panel graphs: 1(a) reference respiration signal (signal measured using the chest belt), 1(b) PSD obtained with Welch's method, 1(c) PSD obtained from AR method; bottom panel graphs: 2(a) estimated respiration signal, 2(b) PSD obtained with Welch's method, 2(c) PSD obtained from AR method. The x-axis units for plots 1(a) and 2(a) is "seconds" while the x-axis units for rest of the plots representing PSD is "Hz"

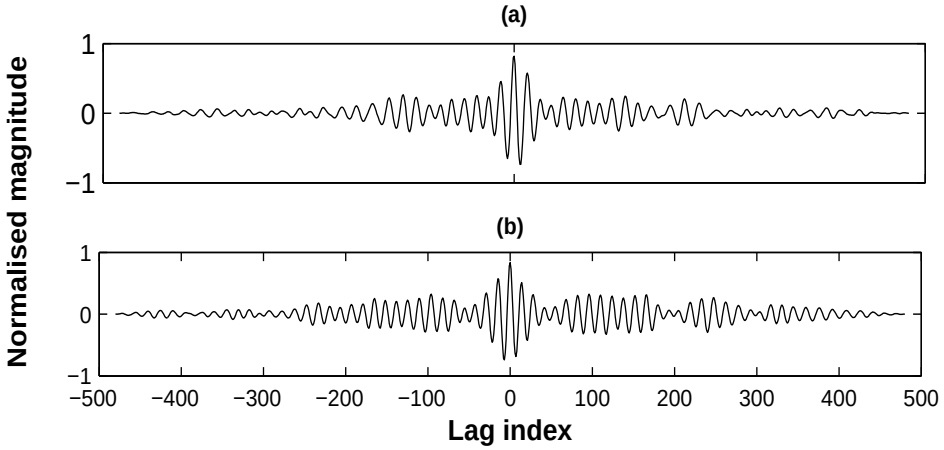

Fig. 10.9: Cross-correlation plots between; (a) reference (1(a)) and estimated (2(a)) respiration signals of Fig. 10.7, (b) reference (1(a)) and estimated (2(a)) respiration signals of Fig. 10.8

sented in Fig. 10.6 shows that the correlation of approximately 0.9 was achieved in both cases at zero lag indicating a very good match between the reference and the estimated respiration signals in both cases. Similar results for two elderly subjects are presented in Fig. 10.7, 10.8 and 10.9. The correlation values obtained by comparing the estimated and reference respiration signals from the ten young and the ten elderly healthy subjects included in this study are presented in table 10.1.

Table 10.1.: Cross-correlation values obtained by comparing segments (120 s) of the reference and the estimated respiration signals from ten young and ten elderly subjects from "Fantasia Database"

Data index	Correlation value	Data index	Correlation value
f1y01	0.89	f1o01	0.83
f1y02	0.83	f1o02	0.77
f1y03	0.75	f1o03	0.71
f1y04	0.79	f1o04	0.76
f1y05	0.85	f1o05	0.82
f1y06	0.82	f1o06	0.88
f1y07	0.80	f1o07	0.75
f1y08	0.89	f1o08	0.77
f1y09	0.87	f1o09	0.83
f1y10	0.82	f1o10	0.69

10.4. Summary and conclusion

The EDR technique of estimating signals associated with respiration was proposed and clinically validated by Moody *et. al.* [132, 133]. As this method provides an uncalibrated estimate, it is not considered suitable for tidal volume and air flow estimation. Nevertheless, it has been shown to be an effective tool for the estimation of respiratory frequency and detection of apnoea [135]. Quantitative analysis of algorithms estimating respiration using single and multi-lead ECG signals has also been presented by O'Brien and Heneghan [142]. The results presented in these studies showed that high correction (up to 0.8) existed between the respiration frequency obtained with EDR signal and the frequency measure from the reference respiration signal. O'Brien and Heneghan also highlighted the fact that as the modulation, caused by respiration, on the ECG signal varies from patient to patient and also due to the changes in the postural position, it is not possible to obtain a quantitatively interpretable tidal volume estimation using the EDR technique. Since the EDR signal is mainly used for the estimation of the respiration frequency in most studies, the reference respiration signal used for comparison with the EDR signal is obtained using indirect methods such as respiratory inductance plethysmography, PRT, etc. Direct methods such as spirometer and nasal thermocouples, measure air flow

in and out of the lungs directly, are considered the most accurate, but interfere with the normal respiration and are not suitable for ambulatory respiration monitoring. Due to these restrictions the indirect methods of respiration measurement have been used routinely for medical diagnosis of respiratory disorders such as sleep apnoea **[300]**. Therefore, comparing the respiration frequencies estimated with the EDR signal with an indirect method of respiration measurement does not represent a major drawback.

In this study in order to estimate the respiration signal, an algorithm based on EDR was written in *Matlab*. The algorithm was validated using signals from "Fantasia Database". After estimating the EDR samples from the ECG signal, spline interpolation was used to obtain regularly sampled estimated respiration signal at 4 Hz. This sampling frequency was used as the HRV signals from the locally anaesthetised patients collected during this study were analysed at the same sampling frequency. The estimated respiration signal was compared with the reference respiration signal (signal measured using the chest belt) present in the data set using the cross-correlation and the PSD. The results presented in section 10.3 indicate that in the case of both the young and elderly volunteers the estimated and measured respiration signals showed strong correlation (see Fig. 10.6, Fig. 10.9 and table 10.1). By comparing the PSD from the estimated and the measured respiration signals it was also showed that the peak respiration frequency obtained from the estimated respiration signal was quite close to the peak frequency obtained with the measured respiration signal (see Fig. 10.4, Fig. 10.5, Fig. 10.7 and Fig. 10.8).

The validated EDR method, for the estimation of the respiration signal using a single lead ECG signal, will be used for the estimation of the respiration signal from the ECG signals collected from the patients undergoing local anaesthetic procedure. The estimated respiration signal will then be included in the estimation of the parameters related to the HRV analysis.

11

Parametric and non-parametric frequency analysis of HRV data from locally anaesthetised patients

11.1. Introduction

This chapter presents the results obtained by analysing the HRV signals collected from patients undergoing local anaesthesia. The HRV signals were studied in the frequency domain using parametric (AR modelling) and non-parametric (Welch's periodogram) methods to detect any possible changes due to the local anaesthetic agents in the parameters usually estimated in HRV studies. Both the parametric and non-parametric methods were used for analysing the signal as there could be differences in the parameters estimated from the same data set using these two techniques [143]. To define the HF (respiration related) component of the signal more accurately the respiration signal was estimated using the EDR technique discussed in chapter 10.

After obtaining approval from the local research committee and informed written consent, fourteen ASA 1, 2 (American Standard of Anaesthesiology; scale 1 to 5, with 5 the most critically ill patients) patients (7 males and 7 females) aged 50.6$\pm$20.7 years (mean weight 67$\pm$15.3 Kg, mean height 1.6 $\pm$0.2 m) undergoing general elective surgery under local anaesthesia were recruited. A combination of 30 ml of 1% Lignocaine and 29 ml of 0.5% Bupivacaine with 1:200000 part Adrenaline was used as the anaesthetic agent. An AS/3 Anaesthesia Monitor (Datex-Engstrom) was used to collect lead II ECG signals from the patients. The monitoring started about 30 minutes before the start of the block and continued for approximately another 30 minutes after the surgery in the recovery ward. The ECG signal was digitised at 1000 Hz sampling frequency using a 12-bit data acquisition card (National Instruments Corporation, Austin, Texas). Further details regarding the study protocol and patients included in the study can be found in section 4.4. The results obtained from the parametric and non-parametric methods will be presented in the next section.

11.2. Results

The heart signals were pre-processed before the frequency domain analysis. The pre-processing involved the steps of *ht* signal representation, ectopic and/or missing beat correction and detrending. The *ht* signal representation and the correction procedure has been presented in chapter 8 and the detrending was carried out using the WP packet algorithm described and validated in section 9.3. The detrended signals were then employed in the spectral analysis from which the parameters related to the HRV were estimated.

11.2.1. Frequency domain HRV parameter estimation

The HRV parameters that are recommended [19] for estimation from the frequency domain analysis include the total power, power in the LF and the HF band of the signal in absolute and normalised units and the frequency related to these two bands. The total power was estimated in this study using the relationship shown in Eq. 11.1.

$$P_{total} = LF_p + HF_p = \int_{\mathrm{LF}_{\min}}^{\mathrm{LF}_{max}} P_{LF}(f)\,df \; + \int_{\mathrm{HF}_{\min}}^{\mathrm{HF}_{max}} P_{HF}(f)\,df \tag{11.1}$$

where $P(f)$ is the PSD of the signal.

In Eq. 11.1 the first integral on the right side define the power in the LF region while the second integral define the power in the HF region of the signal. The upper and lower limit of the two integral are the upper and lower boundaries associated with the two regions (LF and HF). Traditionally, the upper and lower boundaries are kept fixed in both regions with LF_{min}=0.04 Hz, LF_{max}=0.15 Hz, HF_{min}=0.15 Hz and HF_{max}=0.4 Hz.

In this study the respiration signal was estimated from the ECG signal using the EDR technique as described in chapter 10, this signal was then used in the HRV analysis for defining the HF band boundaries. The boundaries were defined using the cross-spectrum ($P_{xy} = P_x.P_y^*$, where * represent complex conjugate) between the HRV signal and the estimated respiration signal. From the cross-spectrum the Centre Frequency (CF) and the Standard Deviation Spectral Extension (SDSE) were estimated using Eq. 11.2 and Eq. 11.3 respectively.

$$\bar{f}_p = \frac{\int_{-\infty}^{\infty} f\,P(f)\,df}{\int_{-\infty}^{\infty} P(f)\,df} \tag{11.2}$$

$$\Delta f_p = \left(\frac{\int_{-\infty}^{\infty} (f - \bar{f}_p)^2\,P(f)\,df}{\int_{-\infty}^{\infty} P(f)\,df} \right)^{1/2} \tag{11.3}$$

Using the estimate of the CF and the SDSE, the range of the HF band was defined as CF$\pm$SDSE. The CF and the SDSE related to the LF region of the signal was also calculated, but in this case the estimate was carried out using the PSD of the HRV signal.

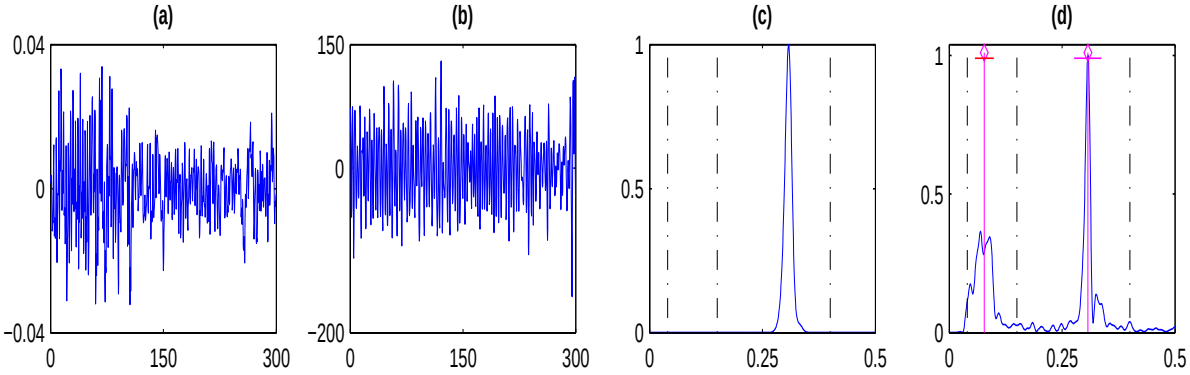

Fig. 11.1: Boundary estimation example 1; (a) HRV signal; (b) corresponding EDR estimated respiration signal; (c) cross-spectrum between HRV signal and the estimated respiration signal; (d) spectrum of the HRV signal. The dotted lines in part (c) and (d) represent the fixed boundaries of the LF and the HF region. The magenta vertical lines with a diamond marker in part (d) represent the CF of the LF and HF band while the horizontal line represent the band range as estimated by the variable boundary method (CF±SDSE). Spectral analysis is carried out using non-parametric method

In the case where the lower boundary of the HF component was below 0.15 Hz then this lower boundary was used in the estimation of the LF component CF and the boundaries otherwise the estimation was done in the frequency range of 0.04-0.15 Hz.

In order to validate the method of variable boundary estimation defined here with the help of CF and SDSE, the HRV parameters were also estimated using the fixed boundary approach. In this case the power related to both the LF and HF component was calculated directly from the HRV signal's PSD in region of 0.04 Hz to 0.15 Hz and 0.15 Hz to 0.4 Hz respectively. In both approaches (fixed and variable boundary) the frequency parameter related to the two components was estimated using Eq. 11.2. The results obtained from the non-parametric and parametric spectral analysis of the data obtained from locally anaesthetised patients will be presented in the following sections.

11.2.2. Results of non-parametric analysis of locally anaesthetised patients' data

The procedure described in section 8.5.1 and used to obtain the power spectrum of simulated signals was also used to study the signals from the locally anaesthetised patients. In this case the spectrum was calculated by overlapping the signal by 50%, so that each time 600 new samples were used.

The LF and the HF boundary estimation examples along with the corresponding HRV and the estimated respiration signals are shown Fig. 11.1 and Fig. 11.2 respectively. In both cases (Fig. 11.1 and Fig. 11.2) the estimation was carried out on five minute segments of data. In the case of Fig. 11.1 (c) the cross-spectrum shows a single well defined peak at a frequency of 0.3 Hz. This indicates that the power related to the respiration

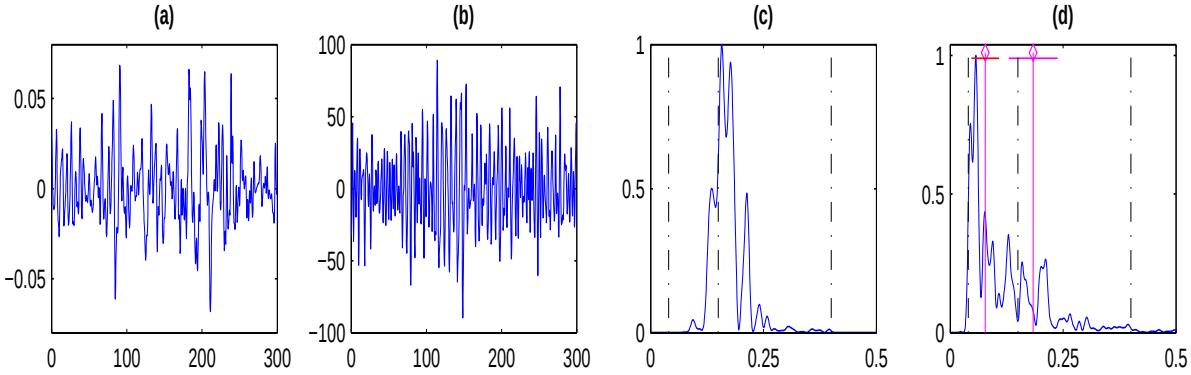

Fig. 11.2: Boundary estimation example 2; (a) HRV signal; (b) corresponding EDR estimated respiration signal; (c) cross-spectrum between HRV signal and the estimated respiration signal; (d) spectrum of the HRV signal. The dotted lines in part (c) and (d) represent the fixed boundaries of the LF and the HF region. The magenta vertical lines with a diamond marker in part (d) represent the CF of the LF and HF band while the horizontal line represent the band range as estimated by the variable boundary method (CF±SDSE). Spectral analysis is carried out using non-parametric method

component (HF) is confined to a narrow band that lies within the fixed limits defined for the HF component. Figure. 11.1 (d) (HRV signal spectrum) confirms the information represented by the cross-spectrum and shows a well defined respiration related component around 0.3 Hz. In this case the respiration component is easily distinguishable from the LF component whose CF is around 0.1 Hz. Figure. 11.1 (d) also shows that the range (CF±SDSE) of each band (LF and HF) estimated for power estimation in the variable boundary method and represented by horizontal magenta lines quite adequately covers major parts of the signal in these two regions. The situation is quite different in the second example of the boundary estimation presented in Fig. 11.2, in this case the respiration signal (see Fig. 11.2 (b)) shows more complex dynamics as compared to the respiration signal of the first example (see Fig. 11.1 (b)). Because of this reason, the cross-spectrum between the HRV signal and the estimated respiration signal shown in Fig. 11.2 (c) is spread over a larger frequency range slightly below the fixed lower boundary of the HF region and shows more than one component. By looking at the cross-spectrum shown in part (c) it can be seen that if fixed boundaries were used to calculate the power then some of the power which might be due to the respiration component would be wrongly assigned to the LF region of the signal. However, as in the variable boundary method the range of the HF component is defined by using the cross-spectrum it will be able to take into account the part of the spectrum below the fixed lower boundary of the HF region. By looking at the magenta horizontal line (in the high frequency region) in Fig. 11.1 (d) it can be seen that the boundary of the HF region as defined by the variable boundary method indeed extends below 0.15 Hz, which is considered to be the lower limit of the HF region in the fixed boundary method. Similar to the case of

first example (Fig. 11.1 (d)) even in the case of the second example (see Fig. 11.2 (d)) the major parts of the signal power are covered by the LF and the HF region as defined by the variable boundary method.

The estimated power related to the HF and the LF band was then used to estimate the $^{LF}/_{HF}$ power ratio, which is often used as a marker of sympathovagal balance. The LF and the HF power was also obtained in the normalised units, where the normalisation was done using the total power (see Eq. 11.1), similar to previous studies [144, 145]. In this case the HF and the LF power in the normalised units will have a reciprocal relationship with each other. To summarise the following parameters were estimated from the frequency domain analysis of each patients undergoing local anaesthesia.

1. Power related to the HF band of the signal in absolute units (HF_P).
2. Power related to the LF band of the signal in absolute units (LF_P).
3. Total power (PT).
4. Power related to the HF band of the signal in normalised units (HF_{Pnorm}).
5. Power related to the LF band of the signal in normalised units (LF_{Pnorm}).
6. Ratio of the power in the LF region to the power in the HF region ($^{LF}/_{HF}$ ratio).
7. CF related to the HF region of the signal (HF_f).
8. CF related to the LF region of the signal (LF_f).

The values estimated for all these parameters from one of the data sets obtained from a patient undergoing local anaesthesia are presented in Fig. 11.3. The parameters estimated using the non-parametric analysis method from the data sets of all the patients included in this study are presented in Appendix B.

The results shown in Fig. 11.3 indicates that the parameters related to the absolute value of power (PT, HF_P, LF_P) are all slightly higher in the fixed boundary method than their corresponding values obtained by using the variable boundary method. This is due to the fact that in the case of the variable boundary method there can be gaps between the boundaries of the LF and the HF region (see Fig. 11.1 and 11.2) while in the fixed boundary method these two bands covers the whole spectrum from 0.04 Hz to 0.4 Hz. But from the results it can be seen that almost similar changes are occurring in the power values most of the time. This fact can be also seen by looking at the similarities in the $^{LF}/_{HF}$ ratio values obtained from both the estimation methods (see Fig. 11.3 (a)) and more clearly by comparing the normalised power values obtained for the two bands, from the variable and the fixed boundary method (see Fig. 11.3 (e) and Fig. 11.3 (f)). This indicates that even though the variable boundary method has produced low power values in

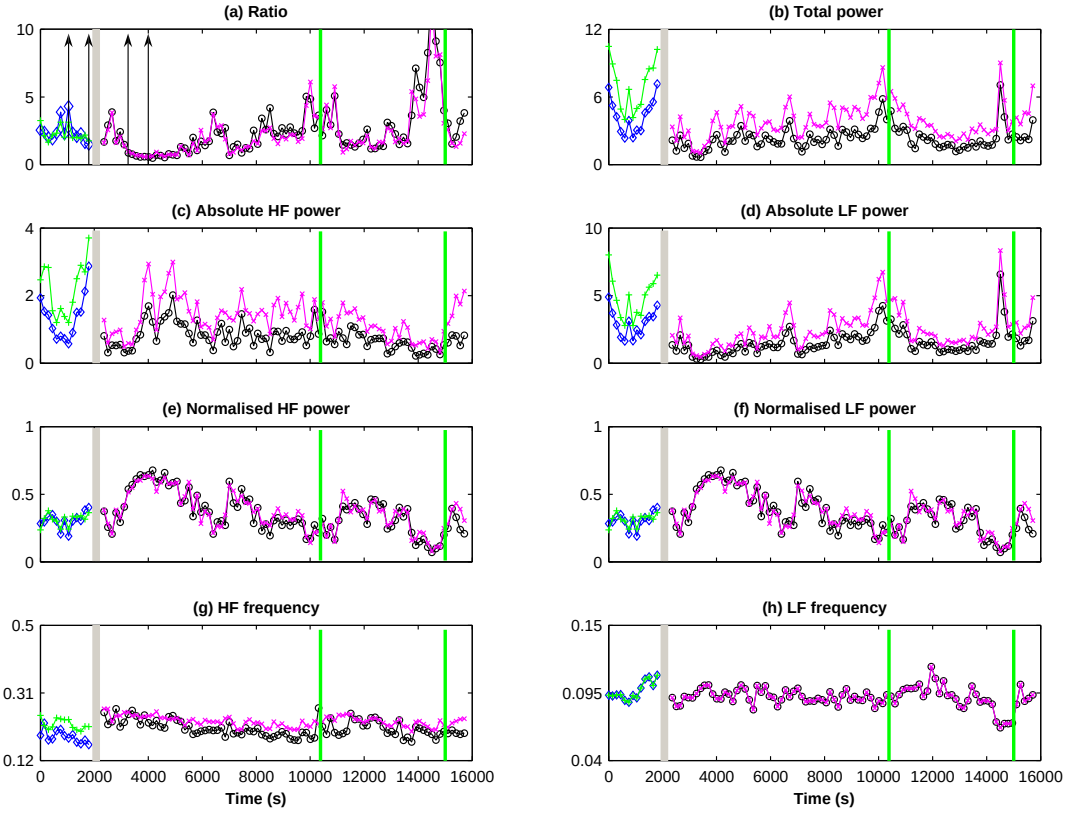

Fig. 11.3: Results obtained from the non-parametric analysis of a patient undergoing local anaesthetic procedure. In each plot the grey vertical block represents the time of block (anaesthesia) application and the green vertical lines represent start and end of the surgery. The vertical arrow pairs in part (a) show the data segment before and after the application of block which was used in statistical analysis. Each plot shows the parameter values estimated using both the fixed and the variable boundary method. Lines in green and magenta colour represent the parameter values before and after the block application estimated using fixed boundary method respectively. In the case of variable boundary method the same information is presented with blue and black colour lines respectively. The units on y-axis for the plots showing power are s^2/Hz and for the plots showing frequency values is Hz

absolute terms, it has managed to detect almost all the changes in the parameters values that are detected by fixed boundary method.

The results also indicate that the difference in the HF frequency estimated by the two method does not follow a simple pattern the values estimated by the variable boundary method is not always smaller than the values estimated by the fixed boundary method or vice versa. This is due to the fact that in the variable boundary method the HF frequency was estimated using the cross-spectrum while in the fixed boundary method the result was obtained directly from the HRV signal. If the respiration frequency is confined well within the HF band (0.15 Hz to 0.4 Hz) and measurement of respiratory signal is used for cross-spectrum rather than an estimation of the respiration signal (as used in this study) then this difference can be reduced to a minimum. But again if the respiratory signal af-

fect goes outside the fixed HF band then the values obtained from the two methods will differ. The LF frequency estimated by both methods is exactly the same (see Fig. 11.3 (h)), as in this case the respiration frequency is not low enough to significantly affect the boundary of the LF region. In cases of severely low respiratory rate or respiratory signals with wide spread frequency characteristics differences might also occurs in the LF frequency estimated by fixed and variable boundary method.

The results presented in Fig. 11.3 also show changes occurring in the HRV parameters after the application of the anaesthetic block. The $^{LF}/_{HF}$ ratio (Fig. 11.3 (a)) values increase after the application of the block (end of grey vertical block in the figure). After this increase the values have decreased and remained low for some time compared to the values before the application of the block (data values before the start of grey vertical block in the figure). By looking at these and other similar results obtained from other patients included in this study (see Appendix B) the following postulates were made.

1. The increase in the $^{LF}/_{HF}$ ratio values just after the application of the block could be due to the presence of small amount of adrenaline in the anaesthetic drug mixture (30 ml of 1% Lignocaine and 29 ml of 0.5% Bupivacaine with 1:200000 part Adrenaline) and also may be due to patient's anxiety .

2. After the application of the block there is an initial transient phase, in which the $^{LF}/_{HF}$ ratio values have increased (as mentioned in point 1), after this phase the values decrease considerably as compared to the values before the application of the block and show reduced variability for a certain amount of time. This decrease in the ratio values and the reducde variability shown by the data could be due to the anaesthetic drug indicating a shift in sympathovagal balance towards vagal enhancement.

After some time, around 6000 seconds in Fig. 11.3 (a), the ratio values have started to increase and recover the variability which was presented in the data before the application of the block. In order to verify whether the parameter values differ significantly before and after the application of the block statistical tests were performed (see section 11.3). For these tests fifteen minutes of data before and after the application of the block was used. The post-block data segment was taken after the initial transient phase (most clearly observed in the $^{LF}/_{HF}$ ratio parameter) has passed. Both pre-block and post-block data segments which were used in statistical analysis are indicated by a pair of vertical arrow lines in Fig. 11.3 (a). The arrow pair before the grey vertical block represents the pre-block data segment, while the arrow pair after the grey vertical block represents the post-block segment used in statistical analysis.

Apart from the $^{LF}/_{HF}$ ratio the total power (PT) (see Fig. 11.3 (b)) of the signal also

decreased after the application of the block. The change in the absolute values of the power in the HF and the LF band can also be seen by looking at the results presented in Fig. 11.3 (c) and Fig. 11.3 (d) respectively. The shift in power from the LF band to the HF band can be seen more clearly by comparing the power of these two bands in normalised units presented in Fig. 11.3 (e) for the HF band and Fig. 11.3 (f) for the LF band. The power of the two bands in normalised units are inversely proportional to each other therefore, as the normalised HF power is increased after the application of the block; the normalised LF power decreases after the application of the block.

Similar changes were observed in eleven of the fourteen patients for the parameters values of $^{LF}/_{HF}$ ratio values, total power, HF and LF band power in absolute and normalised units. The frequency parameter associated with the HF and the LF band, shown Fig. 11.3 (g) and Fig. 11.3 (h), have also showed some changes during the analysis. The changes in these parameters were less correlated with the application of the anaesthetic block. The timing of the decrease in the $^{LF}/_{HF}$ ratio value differed in patients, but in each case the drop occurred within an hour of the application of the block. In the remaining three patients the ratio values did not change significantly. The $^{LF}/_{HF}$ ratio and the total power values near the start and end of the surgery period shows large fluctuations which could be due to noise (artefact) generated by the patient's movement. But this is not a serious concern due to the fact that data segments taken for statistical analysis are always taken well before the patient was moved for surgery. The parameters estimated during the surgery was not included in further analysis, as in that case it might not be possible to separate the changes in the parameter values caused by the surgical procedure with the changes occurring due to the local anaesthesia.

11.2.3. Results of parametric analysis of locally anaesthetised patients data

In the case of the parametric analysis, the cross-spectrum was estimated using an AR model (see section 7.3.2). Two examples of boundary estimation for the LF and the HF component using the parametric spectral analysis method are shown Fig. 11.4 and Fig. 11.5 respectively. These figures also show the corresponding HRV and the estimated respiration signals.

Similar to the case of non-parametric analysis (see Fig. 11.1 and Fig. 11.2), the first example of boundary estimation using parametric spectral analysis represents a case where the respiration component is well defined within the fixed boundary of the HF band (0.15 Hz to 0.4 Hz), as shown by the cross-spectrum in Fig. 11.4 (c). The LF and the HF boundaries (horizontal magenta line) estimated using the variable boundary method along with the HRV signal spectrum presented in Fig. 11.4 (d) shows that the major power related to the two components is covered by these boundaries. In the second example

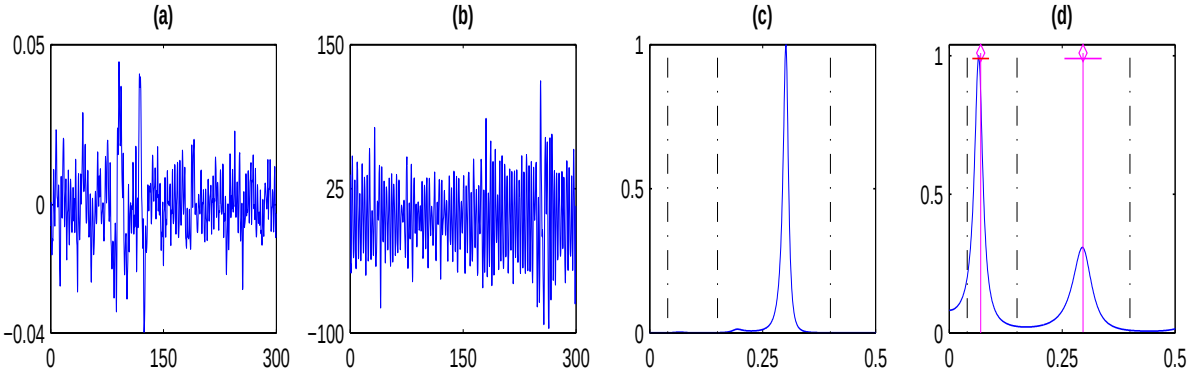

Fig. 11.4: Boundary estimation example 1; (a) HRV signal; (b) corresponding estimated respiration signal; (c) cross-spectrum between HRV signal and the estimated respiration signal; (d) spectrum of the HRV signal. The dotted lines in part (c) and (d) represent the fixed boundaries of the LF and the HF region. The magenta vertical line with a diamond in part (d) represents the CF while the horizontal line represent the band range as estimated by the variable boundary method (CF±SDSE). Spectral analysis is carried out using parametric method

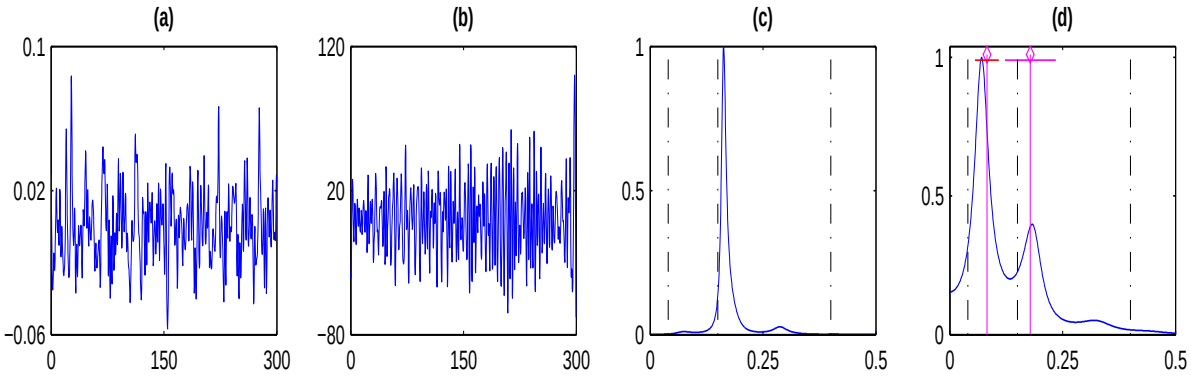

Fig. 11.5: Boundary estimation example 2; (a) HRV signal; (b) corresponding estimated respiration signal; (c) cross-spectrum between HRV signal and the estimated respiration signal; (d) spectrum of the HRV signal. The dotted lines in part (c) and (d) represent the fixed boundaries of the LF and the HF region. The magenta vertical line with a diamond in part (d) represents the CF while the horizontal line represent the band range as estimated by the variable boundary method (CF±SDSE).Spectral analysis is carried out using non-parametric method

shown in Fig. 11.5 the peak respiration frequency still lies in the HF band range but it is quite close to the lower boundary of the band (0.15 Hz) as shown by the cross-spectrum presented in Fig. 11.5 (c). The HRV spectrum shown in Fig. 11.5 (d) also shows the peak close to the fixed lower boundary of the HF component and in this case the variable HF boundary (horizontal magenta line) goes below 0.15 Hz. By looking at Fig. 11.5 (d) it can be seen that the power related to the two major components, one around 0.1 Hz and another slightly above 0.15 Hz, present in the HRV signal spectrum are adequately covered by the LF and the HF regions defined by the variable boundary method.

The *ht* signals generated from the data of the anaesthetised patients were again analysed using five minute segments with 50 % overlap. Parameters including total power,

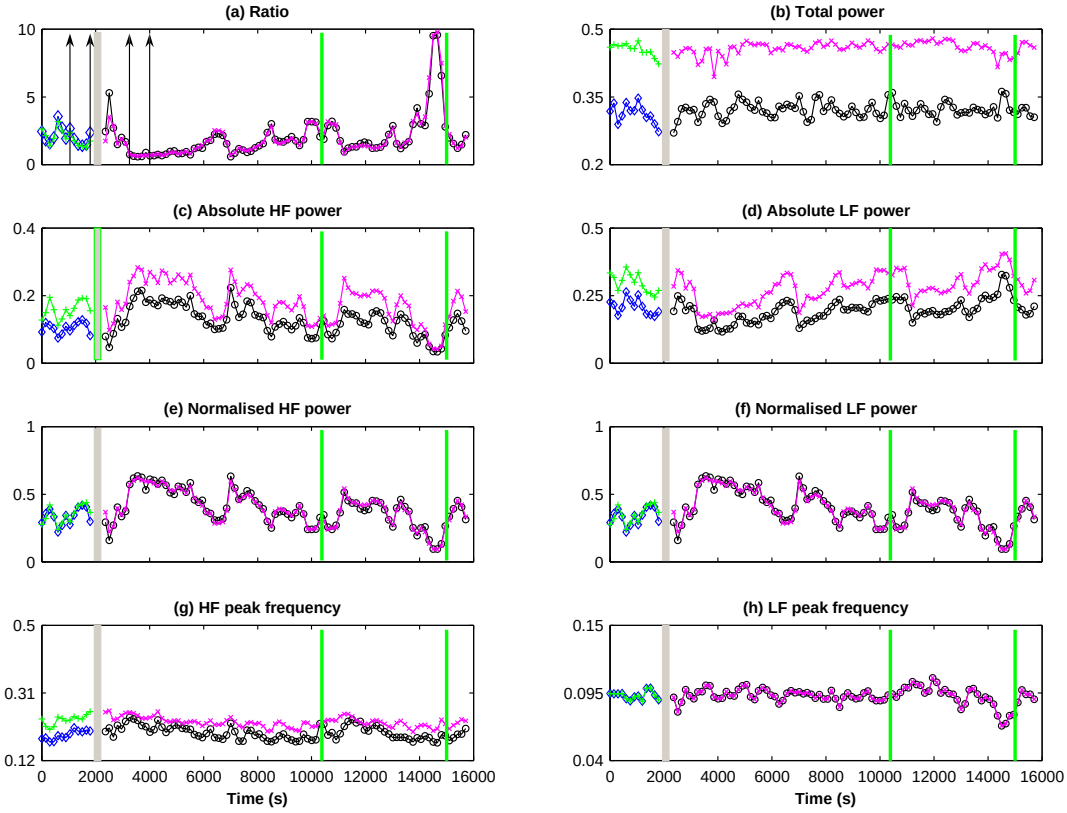

Fig. 11.6: Results obtained from the parametric analysis of a patient undergoing local anaesthetic procedure. In each plot the grey vertical block represents the time of block (anaesthesia) application and the green vertical lines represent start and end of the surgery. The vertical arrow pairs in part (a) show the data segment before and after the application of block which was used in statistical analysis. Each plot shows the parameter values estimated using both the fixed and the variable boundary method. Lines in green and magenta colour represent the parameter values before and after the block application estimated using fixed boundary method respectively. In the case of variable boundary method the same information is presented with blue and black colour lines respectively. The units on y-axis for the plots showing power are s^2/Hz and for the plots showing frequency values is Hz

power related to the HF and the LF bands in absolute and normalised units, CF related to the two frequency bands and the LF/HF power ratio which were estimated previously using non-parametric technique were estimated again this time using the parametric (AR modelling) method. All the parameters were estimated using both the variable boundary and the fixed boundary method. The results obtained from the analysis of the data obtained during this study from a patient undergoing local anaesthesia are presented in Fig. 11.6. The results obtained from parametric spectral analysis of the data from all the patient included in this study are presented in Appendix B.

From Fig. 11.6 it can be seen that the results obtained using the parametric method of spectral analysis are quite similar to the ones obtained using the Welch's (non-parametric) method presented in section 11.2.3. The absolute values of total power, HF and LF po-

wer are all higher when estimated using the fixed boundary method as compared to the variable boundary method (see Fig. 11.6 (b), (c), (d)). However, similar to the case of non-parametric analysis, in the parametric analysis the variable boundary method has been able to detect the changes that are detected by the fixed boundary method. This fact can be easily seen by looking at the close agreement between the $^{LF}/_{HF}$ ratio (Fig. 11.6 (a)), the normalised HF power (Fig. 11.6 (e)) and normalised LF power (Fig. 11.6 (f)) values estimated with the use of fixed and variable boundary methods.

In this case as well, the $^{LF}/_{HF}$ ratio shows an initial increase after the application of the block and then decreases as compared to the initial value within an hour of the application of the block. The total power of the signal decreased after the application of the block and then gradually recovered. The shift in power from the LF to HF band after the application of the block can be seen from the values of the power in the two bands presented in normalised units (see Fig. 11.6 (e) and Fig. 11.6 (f)). Similar to the non-parametric analysis case the results from the parametric analysis also indicated changes in parameter values in eleven of the fourteen patients whereas in three patients the changes in the parameter values did not correlate well with the introduction of the anaesthetic drug.

11.3. Statistical test for non-parametric and parametric analysis of HRV data from locally anaesthetised patients

As mentioned before, in the non-parametric and the parametric analysis of the data eleven out of fourteen patients showed changes in the $^{LF}/_{HF}$ ratio values after the application of the anaesthetic block. In order to quantify the results statistical tests were performed to check if the changes occurring in the parameters values after the block are significantly different than the value of the parameters before the application of the block. The parameters estimated for each patient were tested individually to check for differences before and after the block. The fifteen minutes of data segment before and after the application of the block which was used in statistical analysis are indicated by a pair of vertical arrows in each section (before and after the application of the block) of the data (see Fig. 11.3 (a) and Fig. 11.6 (a)).

The statistical analysis was carried out using *SigmaStat 2.03* (Systat Software Inc., USA). The first step in the analysis was to see whether the data was normally distributed or not. The normality test was carried out using Kolmogorov-Smirnov test with Lilliefors' correction. As most of the data included in the study was not normally distributed non-parametric test (Wilcoxon, signed rank test) was used for statistical analysis. In Wilcoxon test the difference between each set of observations (e.g. before and after exposure to a test drug) is calculated. These differences are then ranked in order of magnitude (igno-

ring the positive and negative signs), and then a positive or negative sign is attributed to these ranks, depending on the direction of the difference between the 'before and after' values. In the next step the sum of all the positive and negative ranks are calculated. Using the table of the Wilcoxon signed rank sum test along with the sum of positive and negative ranks the probability level corresponding to the data could be determined.

The results obtained for the parameters values estimated from the non-parametric analysis of the data obtained from patients undergoing local anaesthesia are presented in table 11.1.

Table 11.1.: Statistical test results obtained from non-parametric analysis of data from patients undergoing local anaesthesia. From each patient eight parameters, $^{LF}/_{HF}$ ratio, total power (PT), high and low frequency band power in absolute and normalised units (HF_P, HF_{Pnorm}, LF_P, LF_{Pnorm}) and centre frequency in high and low frequency band (HF_f, LF_f), values before and after the anaesthetic block were compared. The first row (values in black colour) for each patient indicates the p values obtained from fixed boundary method while the second row (values in blue colour) indicates p values obtained from variable boundary method. Significance level was defined as $p < 0.05$

Pat. no.	$^{LF}/_{HF}$ ratio	PT	HF_P	LF_P	LF_{Pnorm}	LF_{Pnorm}	HF_f	LF_f
1	0.008	0.008	0.016	0.008	0.008	0.008	0.008	0.195
	0.008	0.016	0.023	0.008	0.008	0.008	0.039	0.195
2	0.695	0.020	0.064	0.020	0.557	0.160	0.084	0.322
	0.432	0.027	0.027	0.037	0.375	0.432	0.695	0.322
3	0.010	0.520	0.765	0.320	0.010	0.010	0.010	0.024
	0.007	0.520	0.577	0.278	0.032	0.032	<0.001	0.024
4	<0.001	<0.001	0.273	<0.001	<0.001	<0.001	<0.001	1.00
	<0.001	<0.001	0.414	<0.001	<0.001	<0.001	<0.001	1.00
5	<0.001	0.301	0.002	0.850	<0.001	<0.001	0.204	0.339
	0.001	0.470	<0.001	0.970	<0.001	<0.001	0.470	0.339

continued on next page

Pat. no.	LF/HF ratio	PT	HF_P	LF_P	LF_{Pnorm}	LF_{Pnorm}	HF_f	LF_f
6	0.667	0.012	0.176	0.009	0.677	0.667	0.569	0.765
	0.733	0.005	0.386	0.007	0.519	0.519	0.052	0.765
7	0.232	0.004	0.004	0.027	0.275	0.275	0.084	1.00
	0.322	0.014	0.014	0.049	0.375	0.375	0196	1.00
8	0.004	0.002	0.002	0.002	0.004	0.004	0.275	0492
	0.002	0.004	0.049	0.002	0.002	0.002	0.695	0.492
9	0.016	0.047	0.938	0.047	0.016	0.016	0.109	0.078
	0.016	0.078	0.031	0.031	0.016	0.016	0.016	0.078
10	0.002	0.625	0.064	0.002	0.002	0.002	0.922	0.084
	0.002	0.770	0.037	0.002	0.002	0.002	0.922	0.084
11	0.002	0.160	0.002	0.064	0.002	0.002	0.770	0.084
	0.004	0.375	0.002	0.064	0.004	0.004	0.027	0.084
12	0.297	0.031	0.078	0.047	0.375	0.375	0.219	0.938
	0.469	0.156	0.219	0.031	0.469	0.469	0.813	0.938
13	0.002	0.002	0.004	0.002	0.002	0.002	0.004	0.160
	0.002	0.002	0.002	0.002	0.002	0.002	0.037	0.160
14	0.625	0.846	0.084	0.375	0.275	0.275	0.064	0.322
	0.557	0.770	0.131	0.375	0.232	0.232	0.820	0.322

Table 11.1 indicates that the changes in the LF/HF ratio values were significant only in nine cases. The results can be summarised as shown in table 11.2. Table 11.2 indicates that HF_{Pnorm} and LF_{Pnorm} showed best correlation with the changes in the ratio values,

Table 11.2.: Summary of the statistical test result obtained from the non-parametric analysis of the data from locally anaesthetised patients. $^{LF}/_{HF}$ ratio cell indicates the total number of cases showing significant changes after the block. For all other parameters the first value indicates the number of cases where the parameter values have shown significant changes while the second value indicates the cases where the parameter values have shown significant changes simultaneously with the $^{LF}/_{HF}$ ratio changes. The table on the left is for fixed boundary method while the one on the right is for variable boundary method

$^{LF}/_{HF}$ ratio	PT	HF_P	LF_P
9	8, 5	6, 5	9, 6
HF_{Pnorm}	LF_{Pnorm}	HF_f	LF_f
9, 9	9, 9	5, 4	1, 1

$^{LF}/_{HF}$ ratio	PT	HF_P	LF_P
9	8, 5	9, 7	9, 6
HF_{Pnorm}	LF_{Pnorm}	HF_f	LF_f
9, 9	9, 9	7, 6	1, 1

whereas the changes in the frequency values corresponding to the two bands (HF and LF) have not shown strong correlation with the changes in the ratio values. It can also be seen by looking at table 11.2 that both fixed and variable boundary methods have detected significant changes in $^{LF}/_{HF}$ ratio parameter in same number of patients. In fact, these results indicate that both techniques have produced quite similar results in all parameters except in the case of absolute power of the HF band and the CF related to this band. This difference is not unusual as this band is supposed to be the most affected by the two methods of boundary estimation.

In this study Wilcoxon signed rank test was used for statistical analysis. With this test the parameters estimated from each patient included in the study were tested for significant difference individually. This resulted in quite a long table (see table. 11.1) for the results of statistical analysis. More compact results could be obtained by using other test e.g. repeated measures ANOVA on ranks. In this way results from each patient could be combined for every parameter and comparison could be carried out to check which parameter showed significant difference after the application of the anaesthetic block. As in this study different signal processing algorithms were used for frequency analysis of the HRV signals, Wilcoxon test provided a better means of comparison. The result from this test will allow parameter wise comparison to see if significant changes were detected in the same parameters of each patient by different signal processing techniques. Also, by looking at the significance values (p values) obtained from the individual tests differentiation between these different signal processing techniques could still be made if some or all of them detected significant changes in the same number of patients and in the same parameters.

Similar analysis was carried out using the parameters values obtained by analysing the HRV signals using the parametric method. The results of the statistical testing of this data set are presented in table 11.3. Summary of the results presented in table 11.3 is presented in table 11.4. The result shown in table 11.4 indicates that the parametric analysis has also detected significant changes in $^{LF}/_{HF}$ ratio values in nine of the fourteen patients included in this study.

Table 11.3.: Statistical test results obtained from parametric analysis of data from patients undergoing local anaesthesia. From each patient eight parameters, $^{LF}/_{HF}$ ratio, total power (PT), high and low frequency band power in absolute and normalised units (HF_P, HF_{Pnorm}, LF_P, LF_{Pnorm}) and centre frequency in high and low frequency band (HF_f, LF_f), values before and after the anaesthetic block were compared. The first row (values in black colour) for each patient indicates the p values obtained from fixed boundary method while the second row (values in blue colour) indicates p values obtained from variable boundary method. Significance level was defined as $p < 0.05$

Pat. no.	$^{LF}/_{HF}$ ratio	PT	HF_P	LF_P	LF_{Pnorm}	LF_{Pnorm}	HF_f	LF_f
1	0.008	0.023	0.008	0.008	0.008	0.844	0.008	0.547
	0.008	0.023	0.016	0.008	0.008	0.844	0.008	0.547
2	1.00	0.002	0.232	0.625	0.695	0.160	0.105	0.432
	0.557	0.770	0.432	0.625	0.375	0.232	0.131	0.432
3	0.003	0.577	0.003	0.019	0.003	0.003	<0.001	0.014
	0.004	0.054	0.638	0.102	0.028	0.028	<0.001	0.014
4	<0.001	0.305	<0.001	<0.001	<0.001	<0.001	0.376	0.021
	<0.001	0.455	<0.001	<0.001	<0.001	<0.001	<0.001	0.021
5	0.002	0.002	0.005	0.001	0.003	0.003	0.092	0.850
	0.003	0.005	0.021	0.005	0.005	0.005	0.301	0.850
6	0.380	0.791	0.569	0.569	0.569	0.569	0.042	0.850
	0.380	0.791	0.569	0.569	0.569	0.569	0.042	0.850

continued on next page

Pat. no.	LF/HF ratio	PT	HF_P	LF_P	LF_{Pnorm}	LF_{Pnorm}	HF_f	LF_f
7	0.193	0.105	0.625	0.275	0.275	0.275	0.105	0.432
	0.432	0.037	0.422	0.322	0.557	0.557	0.275	0.432
8	0.002	0.002	0.002	0.002	0.002	0.002	0.695	0.322
	0.002	0.002	0.002	0.002	0.002	0.002	1.00	0.322
9	0.031	0.219	0.031	0.016	0.031	0.031	0.219	0.109
	0.031	0.061	0.031	0.016	0.031	0.031	0.031	0.109
10	0.002	0.002	0.002	0.002	0.002	0.002	1.00	1.00
	0.002	0.004	0.002	0.002	0.002	0.002	0.006	1.00
11	0.002	0.010	0.002	0.002	0.002	0.002	0.695	0.004
	0.002	0.004	0.002	0.002	0.002	0.002	0.010	0.004
12	0.156	0.297	0.109	0.219	0.156	0.156	0.078	0.469
	0.578	0.469	0.813	0.469	0.578	0.578	0.938	0.469
13	0.002	0.006	0.002	0.002	0.002	0.002	0.004	0.625
	0.006	0.002	0.010	0.004	0.006	0.006	0.006	0.625
14	0.432	0.492	0.193	0.193	0.160	0.160	0.002	0.160
	0.492	0.557	0.064	0.131	0.064	0.064	0.006	0.160

By comparing the results presented in table 11.2 and 11.4 it can be seen that the in case of parametric analysis the parameters of total power, power related to the LF and the HF band in absolute values showed better correlation with the changes occurring in the ratio values in both the fixed and the variable boundary method. But in terms of detecting changes in the sympathovagal balance (LF/HF ratio) both techniques have performed to the same level.

Table 11.4.: Summary of the statistical test result obtained from the parametric analysis of the data from locally anaesthetised patients. $^{LF}/_{HF}$ ratio cell indicates the total number of cases showing significant changes after the block. For all other parameters the first value indicates the number of cases where the parameter values have shown significant changes while the second value indicates the cases where the parameter values have shown significant changes simultaneously with the $^{LF}/_{HF}$ ratio changes. The table on the left is for fixed boundary method while the one on the right is for variable boundary method

$^{LF}/_{HF}$ ratio	PT	HF_P	LF_P
9	7, 6	9, 9	9, 9
HF_{Pnorm}	LF_{Pnorm}	HF_f	LF_f
9, 9	8, 8	6, 3	3, 3

$^{LF}/_{HF}$ ratio	PT	HF_P	LF_P
9	8, 6	9, 8	8, 8
HF_{Pnorm}	LF_{Pnorm}	HF_f	LF_f
10, 9	8, 7	10, 7	3, 3

11.4. Summary

In this chapter a new method for defining the boundaries related to the LF and the HF band of the HRV signal was proposed (see section 11.2.1). In order to accurately define the boundary related to the respiration (HF) component, the cross-spectrum between the HRV signal and the respiration signal estimated from the ECG signal was used. In this method the boundaries associated with the bands were defined as CF$\pm$SDSE. The frequency domain analysis of the HRV signal from patients under local anaesthesia was carried out using both the parametric and the non-parametric methods. By looking at the results shown in Fig. 11.3 and Fig. 11.6 it can be seen that the variable boundary method has been able to detect similar changes that were detected by the fixed boundary method.

Wilcoxon tests were used for statistical analysis. These tests were carried out on individual parameters estimated from each patient to see if there was a significant difference in the values of the parameters before and after the application of the block. The segment of data that was used for statistical analysis is shown by two pairs of vertical arrows (see Fig. 11.3 (a) and Fig. 11.6 (a)). Both methods detected significant changes in the $^{LF}/_{HF}$ ratio values in nine out of fourteen patients included in this study.

From the information available regarding the local anaesthesia drug used in this study and looking at the results obtained from the parametric and non-parametric analysis of the patients included in this study two postulates were made. Firstly, the initial increase in the $^{LF}/_{HF}$ ratio could be due to the small amount of adrenaline present in the local anaesthesia drug mixture given to the patient. Secondly, in most of the patients after this post block initial increase the $^{LF}/_{HF}$ ratio values decreases as compared to their pre-block values. This was assumed to be due to the effect of local anaesthetic drug. In this chapter

these postulates are not confirmed by comparing the results with other studies from the literature and general discussion about other possible factors that might affect the results are not presented. The reason for this is that in the next few chapters the same data will be analysed by different signal processing techniques and to avoid repeatability once the results from all the techniques are presented the general discussion and comparison of the results obtained from these techniques will be presented in a separate chapter. The validity of the postulates made about the changes occurring in the HRV parameters due to the introduction of local anaesthesia will also be discussed in that chapter by comparing the results of this study with the information available in the literature.

In the next chapter the results obtained by analysing the data from locally anaesthetised patient with continuous wavelet transform will be presented. This time-frequency analysis technique was used because of its capability to deal with non-stationary data. This ability might allow the wavelet transform to reveal more information about the dynamical changes occurring in the cardiovascular system due to the introduction of the local anaesthetic drug .

12

Wavelet (WT) analysis of HRV data from locally anaesthetised patients

12.1. Introduction

In the previous chapter the results obtained by analysing the HRV signals from the locally anaesthetised patients using the parametric (AR) modelling and non-parametric (Welch's periodogram) method were presented. Even though these methods have been extensively used in HRV studies in the past, the frequency information provided by them is averaged over the entire length of the data segment being analysed. This limitation makes these methods insufficient for the study of HRV signals which like many other biological signals are non-stationary, meaning the frequency and/or amplitude information might change during the course of the signal. The limitation of stationarity could be overcome by using methods which provide Time-Frequency Distribution (TFD) of the signal.

The TFD of the signal provides information about the energy distribution of the signal in the joint time-frequency domain. The use of such a technique enables the estimation of the instantaneous frequency (IF) and the instantaneous power (IP) by which the evolution of the signal frequency and amplitude with time could be studied. The TFD based techniques have been used previously for the estimation of the instantaneous parameters related to the HRV signals for the purpose of identifying cardiac abnormalities [146, 147, 148]. One of the techniques that can be use to obtained the TFD of the signal is the Continuous Wavelet Transform (CWT). The introductory details about this analysis technique has been presented before (see chapter 6 and chapter 9) where it has been used for ECG characterisation and detrending of the HRV signals respectively. In this chapter, scalogram (the squared modulus of the CWT), using Morlet wavelet (constructed by modulating a sinusoidal function by a Gaussian function (see Eq. 12.1)) as the mother wavelet will be used to obtained the TFD distribution of the HRV data obtained from the locally anaesthetised patients. This wavelet has been used previously in HRV studies as well [149, 150, 151].

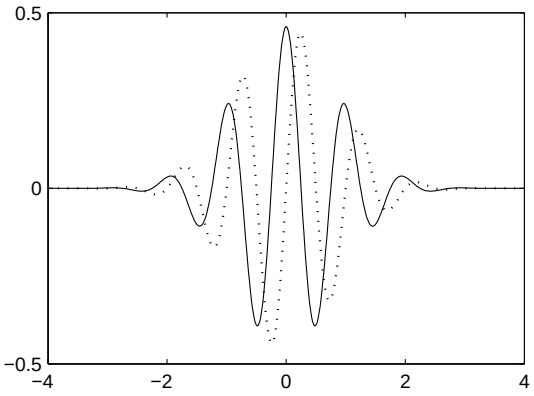

Fig. 12.1: Morlet wavelet real part (solid line) and imaginary part (dotted line)

$$\psi(x) = \pi^{-1/4} e^{i\omega_0 x} e^{-x^2/2} \tag{12.1}$$

Where $\omega_0 = 6$ was used to satisfy the admissibility condition [152]. The Morlet mother wavelet is shown in Fig. 12.1.

Before the analysis of the real patient data the CWT was used to obtain the T-F distribution of four simulated signals with known characteristics. The results obtained from the analysis of these simulated signals were used to validate the ability of CWT to track changes in the frequency and amplitude of the signals during the analysis period and also to justify the use of such a set up for analysis of HRV signals. In the following sections the details and the results obtained from the simulated signals study will be presented and discussed first followed by the results from the locally anaesthetised patients.

12.2. Results of simulated signals analysis with CWT

In this simulated study four different signals were used as the input to the IPFM model presented in Eq. 8.1. These signals consist of two components in the high and the low frequency region of the HRV signal. The threshold of the IPFM model was kept constant at one in all the simulations. The first three signals were generated for a duration of five minutes and the fourth signal was a bit longer with a duration of 500 seconds (approximately 8.3 minutes). The first simulated signal was stationary whereas the other signals simulated the non-stationary conditions, with changing amplitude and/or frequency, usually encountered in the HRV analysis.

All the signals were analysed in the analytical form. The complex valued analytical signal $x_a(t)$ associated with the real valued signal $x(t)$ can be written as shown in Eq. 12.2.

$$x_a(t) = x(t) + \imath HT(x(t)) \tag{12.2}$$

where $HT(x)$ is the Hilbert Transform (HT) of signal $x(t)$. The analytical signal can be obtained from the real signal by forcing the spectrum values associated with the nega-

tive frequencies to zero, keeping the DC value unchanged and doubling the spectrum values of the positive frequencies. The analytical signal is preferred because in this signal the bandwidth is reduced to half the bandwidth of the original (real) signal, this avoids aliasing in the useful spectral domain $[0, F_s/2]$ of this signal. Also, the use of the analytical signal presents another advantage: since the spectral domain is divided by two, the number of components in the time-frequency plane is also divided by two. Consequently, the number of interference terms that might be present in certain (quadratic) distributions (see section 13.2) will decrease significantly.

After converting the signal into its analytical form the TFD was obtained using the CWT. Using the time-frequency representation, Instantaneous Centre Frequency (ICF) and SDSE were estimated using Eq. 11.2 and Eq. 11.3. The boundaries related to the LF and the HF band of the HRV signal were estimated as described in section. 11.2.1. The ICF and the boundaries were smoothed using a median filter with a length of 10 seconds to avoid sharp fluctuations in these parameters. The instantaneous power related to each band was calculated using Eq. 12.3.

$$P_{inst.}(t) = \int_{f_{min}}^{f_{max}} tfr(t,f)\, df \tag{12.3}$$

Where $tfr(t,f)$ represents the TFD/time-frequency representation, f_{max} and f_{min} represent the maximum and minimum frequency values associated with each band.

12.2.1. Simulated signal: 1

In this case the input to the IPFM has exactly the same mathematical form as presented in Eq. 8.13. The equation is repeated here for reference (see Eq. 12.4). The input has two frequency components, one at 0.1 Hz and the other at 0.25 Hz. The only difference here is that the amplitude of the two components has been changed so that they could be differentiated.

$$m(t) = 0.2 \cdot cos(2\pi \cdot 0.1 \cdot t) + 0.3 \cdot cos(2\pi \cdot 0.25 \cdot t) \tag{12.4}$$

The first simulated signal and the T-F distribution obtained using the CWT is shown in Fig. 12.2 and Fig. 12.3 respectively. The result presented in Fig. 12.3 shows the two signal components along with their respective instantaneous frequencies and the boundaries related to the two components, which were estimated using Eq. 11.2 and Eq. 11.3. Using these boundaries the instantaneous power related to each component was also calculated and the ratio of the amplitude, square root of power, between the HF and the LF components is presented in Fig. 12.4.

From the ratio values shown in Fig. 12.4 it can be seen that the values obtained in this case

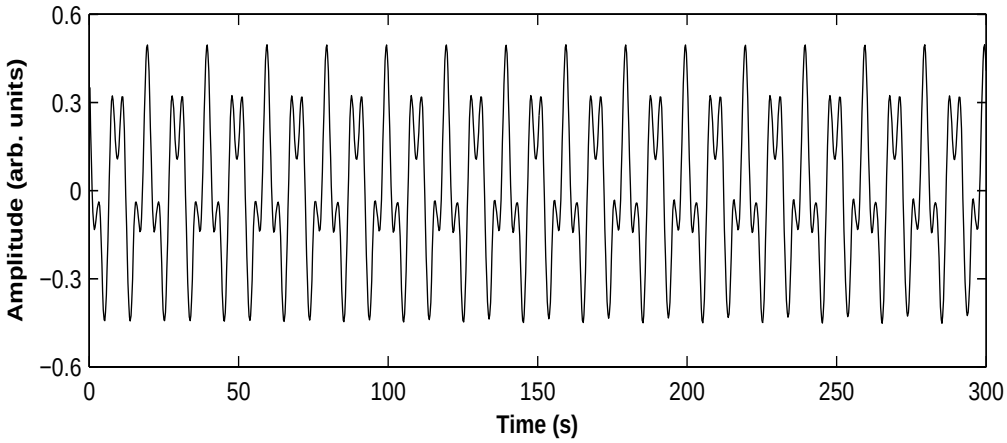

Fig. 12.2: First simulated signal consisting of two constant frequency components in the LF and HF region of the HRV signal (see Eq. 12.4)

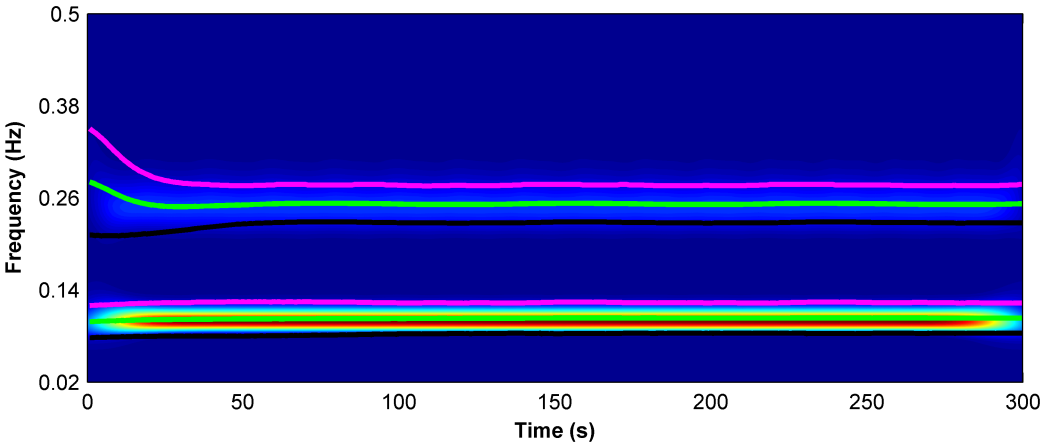

Fig. 12.3: Scalogram of the first simulated signal. The thick green lines represent the ICF for the two components present in the signal. Similarly the thick black and magenta lines represent the lower and the upper boundaries for the two components respectively. These boundaries were calculated as ICF±SDSE for each component

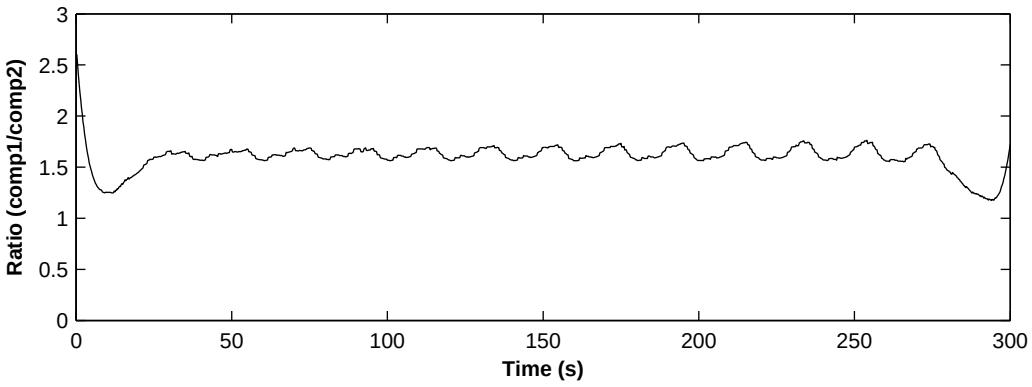

Fig. 12.4: Amplitude ratio between the two components of the first simulated signal (Eq. 12.4)

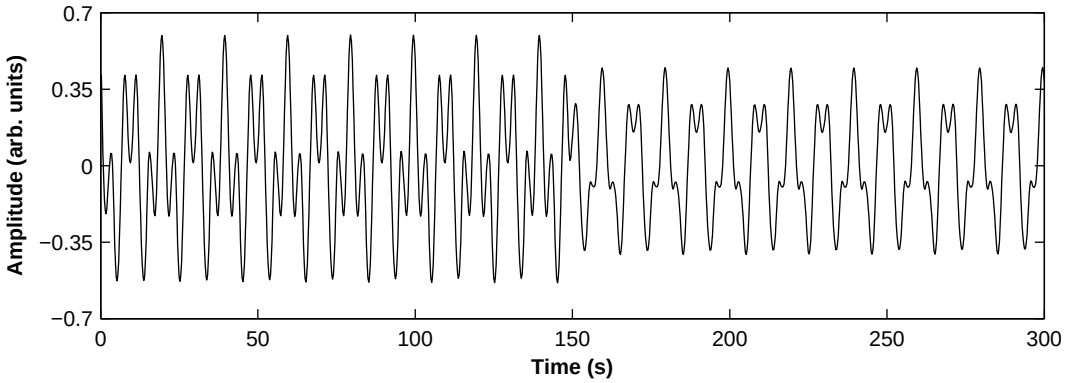

Fig. 12.5: Second simulated signal showing amplitude change in the HF component half way through the simulation

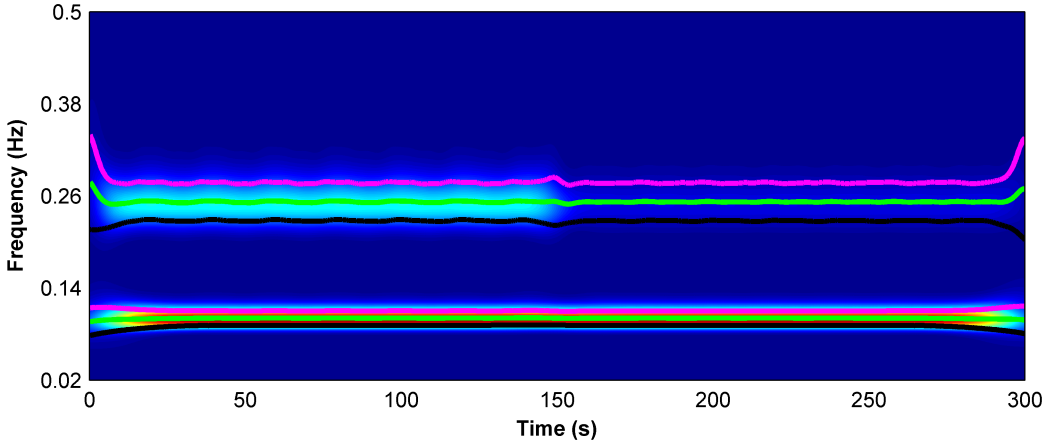

Fig. 12.6: Scalogram of the second simulated signal. The thick green lines represent the ICF for the two components present in the signal. Similarly the thick black and magenta lines represent the lower and the upper boundaries for the two components respectively. These boundaries were calculated as ICF±SDSE for each component

are quite close to the theoretical value of 1.5. From the results presented in Fig. 12.3 and Fig. 12.4 it can be seen that this technique has been successful in detecting and measuring the power related to the two frequency components presented in this simulated signal.

12.2.2. Simulated signal: 2

In order to investigate the potential of CWT to track changes in the signal during the course of time, a second simulated signal was used. This signal has the same form as given by Eq. 12.4 apart from the fact that in this case the amplitude of the high frequency component was changed from 0.3 to 0.15 half way through the IPFM simulation. The signal and the scalogram of the signal are presented in Fig. 12.5 and Fig. 12.6 respectively. The change in the amplitude of the HF component can be seen as a decrease in the intensity of this frequency component in the scalogram (see Fig. 12.6) around half way through the data. As before, the instantaneous frequencies and the boundaries of each component present in the signal are also indicated on the scalogram of Fig. 12.6.

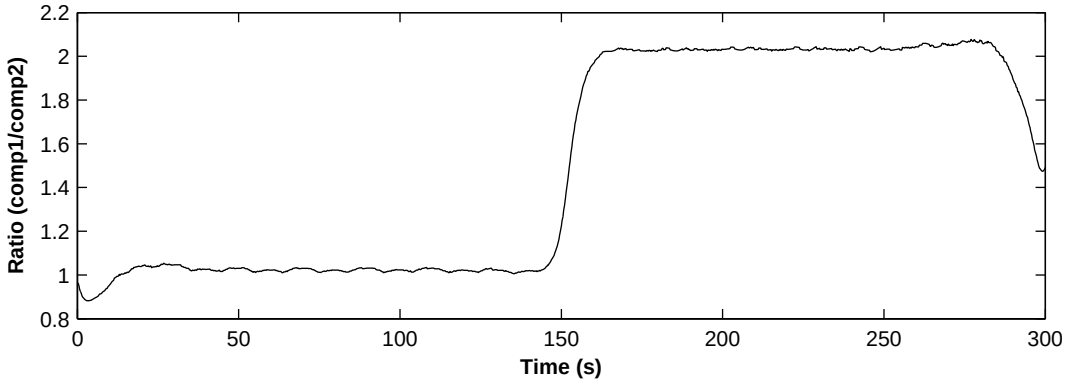

Fig. 12.7: Amplitude ratio between the two components of the second simulated signal. The change in the ratio value occurring almost at the middle of the data is in accordance with the simulation, where the amplitude of the HF component was halved mid way through the simulation

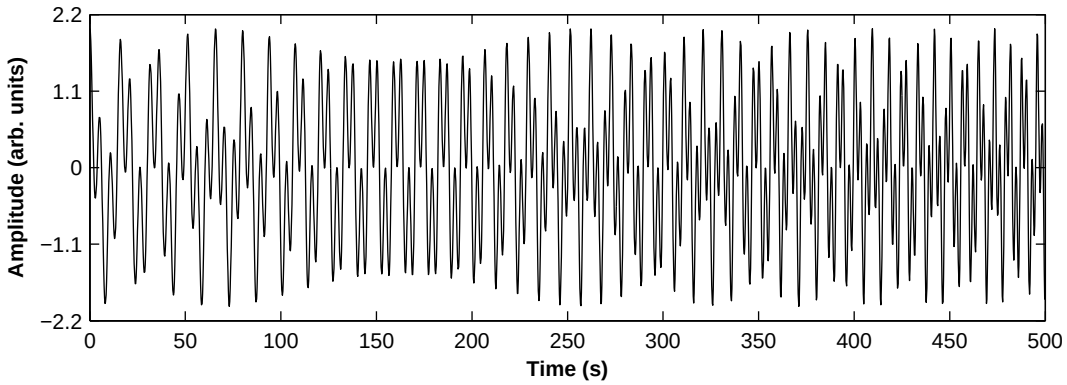

Fig. 12.8: Third simulated signal consisting of two linear chirp signals with frequencies in the LF and the HF region of the HRV signal

Using these boundaries the power related to the two components where calculated and the amplitude ratio between the LF and the HF component is presented in Fig. 12.7. From Fig. 12.7, it can be seen that the ratio values have doubled around 150 seconds, which is in accordance with the simulation. This result indicates that the CWT technique has been able to track changes in the amplitude of the signal during the course of the data.

12.2.3. Simulated signal: 3

In order to explore the frequency tracking capabilities of CWT the third simulated signal consisted of two chirp components. The amplitude of both the components was set to unity. The initial and the target frequency of both the components were selected to be in the LF and HF region of the HRV signal. The initial frequency of the first component was 0.1857 Hz and the target frequency was chosen to be 0.3643 Hz. For the second component the initial and the target frequencies were 0.0557 Hz and 0.1343 Hz respectively. This signal was simulated for 500 seconds and is shown in Fig. 12.8.

The scalogram obtained for the third simulated signal is presented in Fig. 12.9.

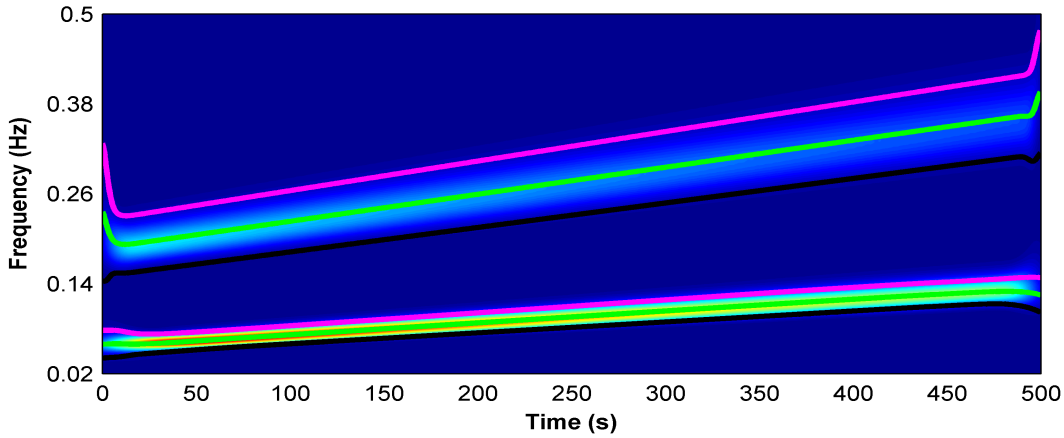

Fig. 12.9: Scalogram of the third simulated signal. The thick green lines represent the ICF for the two components present in the signal. Similarly the thick black and magenta lines represent the lower and the upper boundaries for the two components respectively. These boundaries were calculated as ICF±SDSE for each component

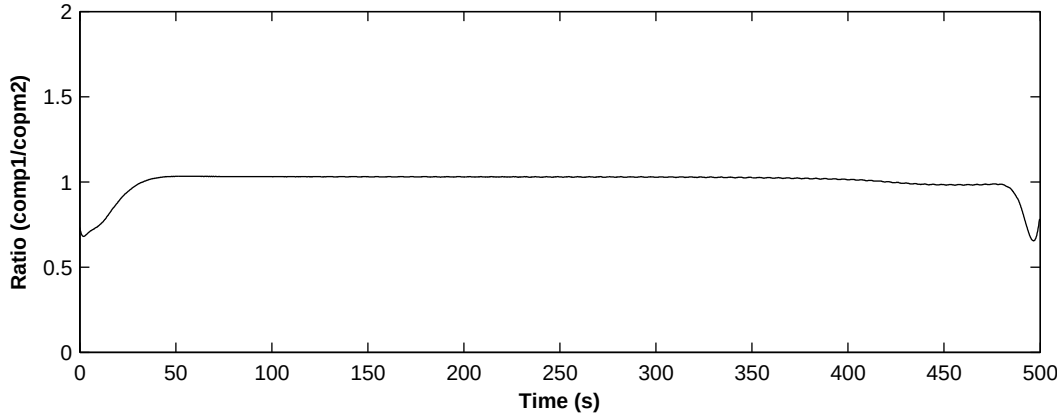

Fig. 12.10: Amplitude ratio between the two components of the third simulated signal

Figure 12.9 also shows the estimation of the ICF and the frequency boundaries for the two linear chirp components present in this simulated signal. The power of the two components was calculated using these boundaries and the ratio between the two components is presented in Fig. 12.10. From the results presented in Fig. 12.9 and Fig. 12.10 it can be seen that the scalogram is capable of tracking changes in the frequency content of the signal during the course of the analysis period.

12.2.4. Simulated signal: 4

This simulated signal was used to produce change both in the frequency and the amplitude of the modulating signal $m(t)$ used as the input to the IPFM model. In this case the amplitude of both the components at the start was set to unity and the frequencies of the LF and the HF component were set to 0.1 Hz and 0.25 Hz respectively. The amplitude and frequency parameters were changed mid way though the data. The amplitude of the LF component was dropped to half and that of the HF component was increased to two.

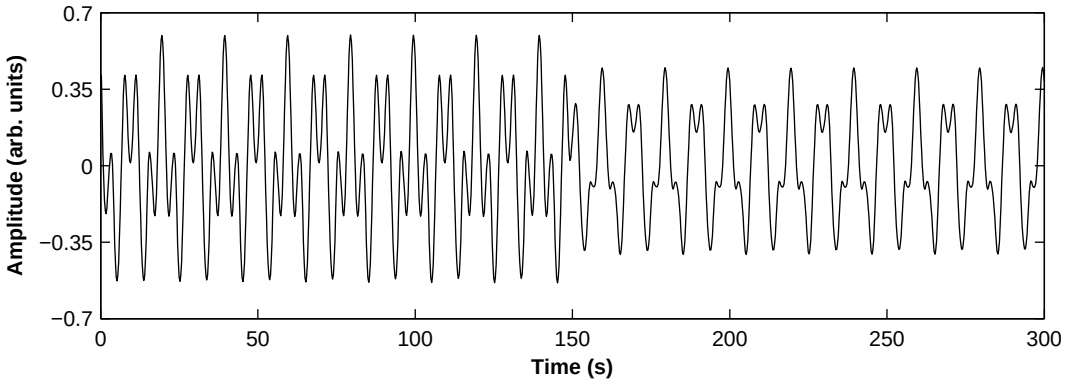

Fig. 12.11: Fourth simulated signal. In this case the amplitude and the frequencies of both the LF and the HF component were changed half way (150 s) through the simulation

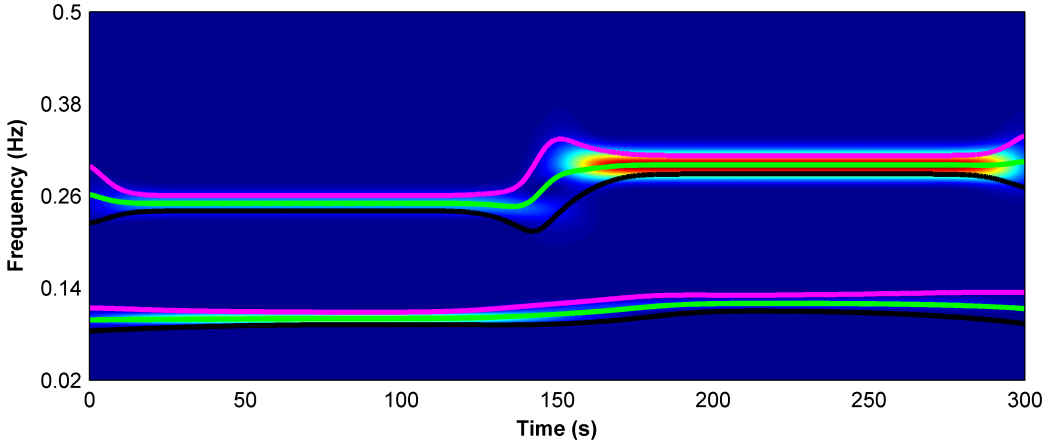

Fig. 12.12: Scalogram of the fourth simulated signal. The thick green lines represent the ICF for the two components present in the signal. Similarly the thick black and magenta lines represent the lower and the upper boundaries for the two components respectively. These boundaries were calculated as ICF$\pm$SDSE for each component

The frequencies of both the components were increased to 0.12 Hz for the LF component and to 0.3 Hz for the HF component. The signal and the corresponding scalogram are presented in Fig. 12.11 and Fig. 12.12 respectively. From the result shown in Fig. 12.12 it can be seen that the scalogram has been able to detect the change in the frequencies and the amplitudes of the two components of the signal occurring half way through the simulation. As before using the frequency boundaries presented in Fig. 12.12 for the two components, the ratio between the amplitude was calculated and is shown in Fig. 12.13. The ratio presented in Fig. 12.13 is quite close to the theoretical value of unity in the first half of the data and equal to one-fourth in the second half of the data. These results indicate that the CWT technique has been able to detect transient changes in both the amplitude and the frequency of the signal components quite effectively.

From the results obtained from the simulated signals study it can be seen that the CWT technique has been able to detect transient changes both in amplitude and the frequency of the signal. The use of this technique for the estimation of the ICF and instantaneous

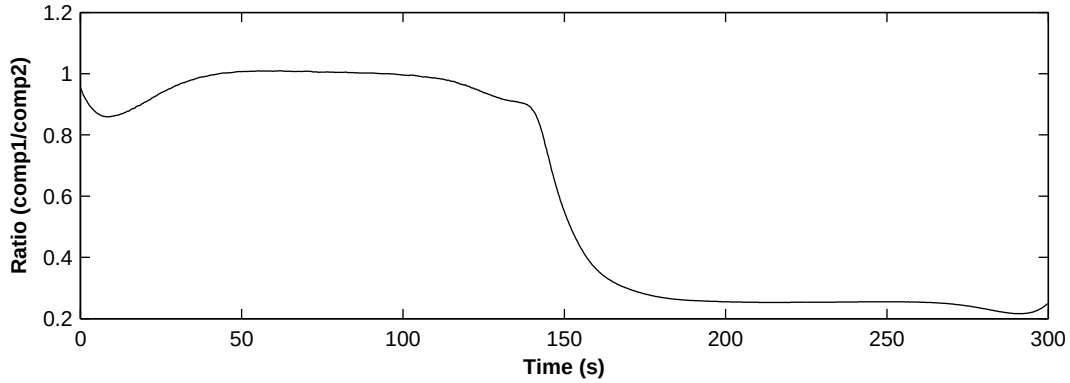

Fig. 12.13: Amplitude ratio between the two components of the fourth simulated signal

power/energy of the signal components was also demonstrated in this simulated signals study. From all the results presented here for the simulated signals it could be justified that because of its ability of tracking changes in the signal during the analysis period the CWT technique, or for that matter any other T-F distribution, might be better suited for the analysis of non-stationary physiological signals such as HRV. For this reason, in order to detect changes in the HRV signals due to local anaesthesia, the data collected from the locally anaesthetised patients during this study was further analysed using the same setup of CWT which was used in the simulated signal study.

As before the respiratory signal was included in the analysis in order to obtain a better estimate of the boundaries of the HF band of the HRV signal. For this purpose the cross-spectrum, defined in Eq. 12.5, between the CWT of the HRV signal and the respiration signal was used.

$$CWT_{xy} = CWT_x \cdot CWT_y^* \tag{12.5}$$

Where CWT_y^* represents the complex conjugate of CWT_y. The respiration (HF band) boundary and the ICF were estimated from the cross-spectrum and then this boundary was used to calculate the power in the HF band of the HRV signal. In order to validate this approach of boundary calculation and the effect of using estimated respiration signals instead of the actual measured respiration signal, tests were done using "Fantasia Database" [136] taken from *Physionet* (see chapter 10). The results obtained from the "Fantasia Database" will be presented in the next section. After the validation of the technique with this database, the results obtained by applying the same procedure for the analysis of HRV data obtained from the locally anaesthetised patients during this study will be presented.

In this case, the HRV parameters discussed in section 11.2.2 were estimated using the TFD of the data obtained with the scalogram. As in chapter 11 the results obtained with the variable boundary estimation method were compared with the results obtained from the fixed boundary method.

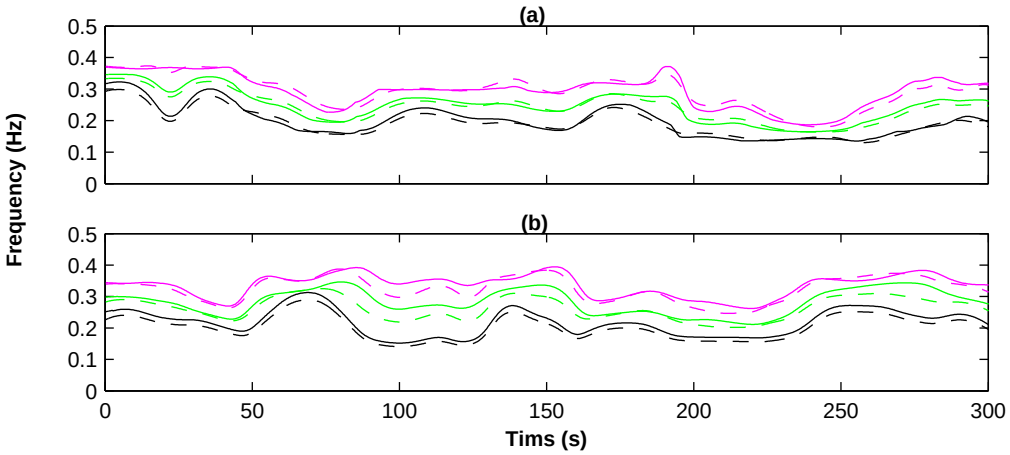

Fig. 12.14: ICF and the respiration boundaries calculated using actual respiration signal (solid lines) and respiration signal estimated from the ECG signal (dashed lines) from two young volunteers from "Fantasia Database". The ICF was calculated using Eq. 11.2 and the boundaries for the respiration component is defines as ICF$\pm$SDSE (see Eq. 11.3)

12.3. Validation of respiration boundary estimation using "Fantasia Database"

The "Fantasia Database" was used before (see chapter 10) for the validation of the algorithm for the estimation of the respiration signal from the ECG signal using the EDR method. Here the signals from the same database were used to calculate the respiration boundaries using the cross-spectrum between the CWT of the respiration signal and the HRV signal. The tests were carried out in both the young and the old volunteers included in the database, mentioned previously in chapter 10. The two important aspects which were of interest in these tests were:

- How much the boundaries calculated from the actual measured respiration signal differ from the boundaries calculated from the estimated respiration signal.
- How these respiration boundaries reflect on the TFD of the HRV signal and do they represent the major part of the HF band of the HRV signal.

The CWT representations were obtained from the heart timing (*ht*) signal, the actual measured respiration signal and the estimated respiration signal. After which the cross-spectrum between the *ht* signal and the actual and the estimated respiration signal were obtained using Eq. 12.5. From these two cross-spectrums the ICF and the boundaries related to the respiration band was obtained using Eq. 11.2 and Eq. 11.3 respectively. The ICF and the respiration boundaries calculated from the data segments from two young volunteers are presented in Fig. 12.14. From the results presented in Fig. 12.14 (a) and Fig. 12.14 (b) it can be seen that in both cases the ICF and the respiration band boundaries calculated using the estimated and actual respiration signals are quite close

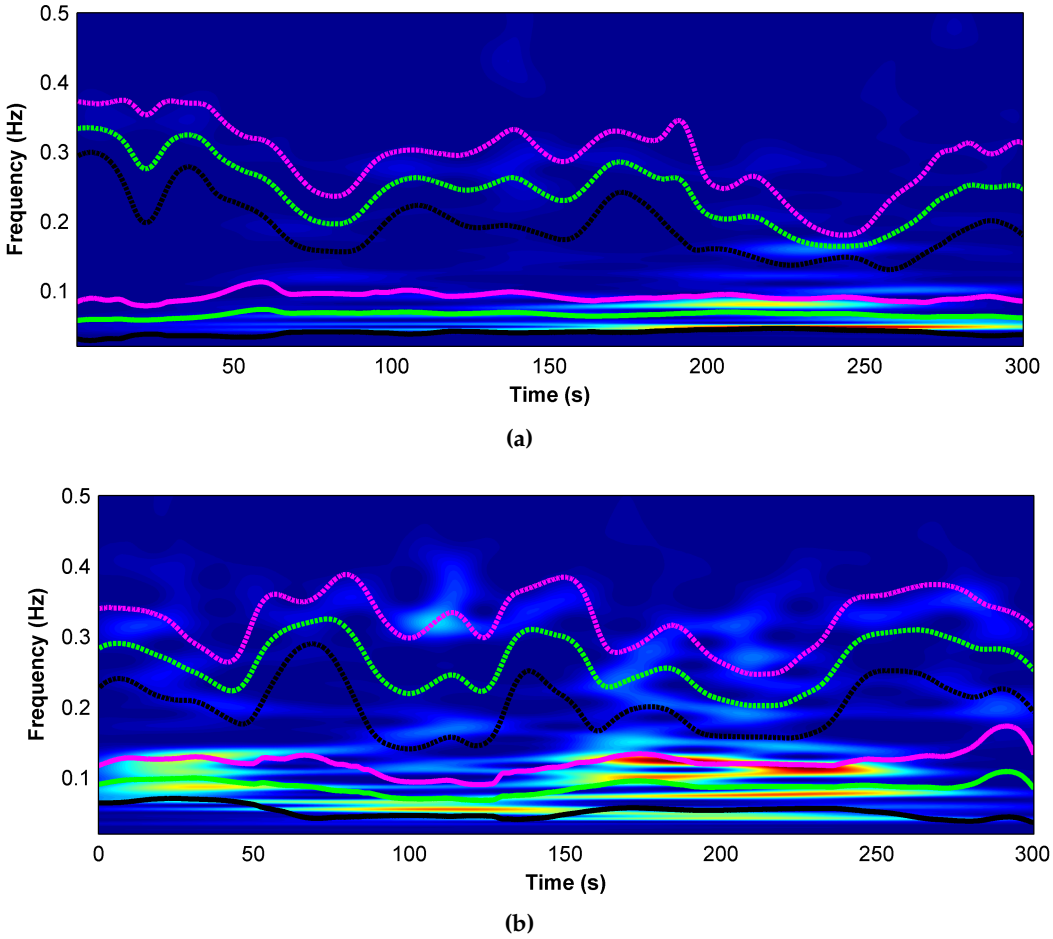

Fig. 12.15: Scalogram of the two HRV signals associated with the data segment used to generate the results of Fig. 12.14. In both cases the ICF and the boundaries related to the LF and HF band are also shown. The dashed lines represent the HF band boundaries and the ICF related to respiration and the solid lines represent the same information for the LF region of the HRV signal

to each other. After these calculations the same method was used to calculate the ICF and the boundaries associated with the LF region of the HRV signal but in this case the CWT representation of the HRV signals was used instead of the cross-spectrum between the HRV signal and the respiration signal. The scalogram of the HRV signals associated with the two data segments which are used to get the results presented in Fig. 12.14 are presented in Fig. 12.15. From the two scalograms shown in Fig. 12.15 (a) and Fig. 12.15 (b) it can be seen that the regions where the power is concentrated in the LF and the HF band of the signal are adequately covered by the boundaries calculated by the employed method. This indicates that such a technique could be used to estimate the parameters related to the HRV signals. Similar results were also obtained from the elderly volunteers data sets from the "Fantasia Database". The ICF and the boundaries of the respiration band calculated using the actual respiration signal and the estimated respiration signal were quite close to each other as shown in Fig. 12.16. As before, in the case of elderly volunteers the ICF and the boundaries of the LF region were also calculated using the CWT representation of the related HRV signals. The two scalograms with the instantaneous

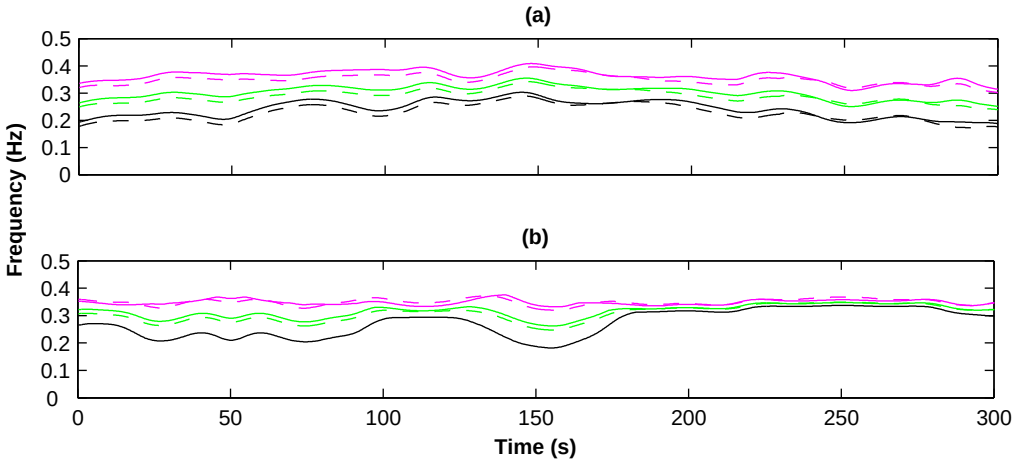

Fig. 12.16: ICF and the respiration boundaries calculated using actual respiration signal (solid lines) and respiration signal estimated from the ECG signal (dashed lines) from two elderly volunteers from "Fantasia Database". The ICF was calculated using Eq. 11.2 and the boundaries for the respiration component is defines as ICF±SDSE (see Eq. 11.3)

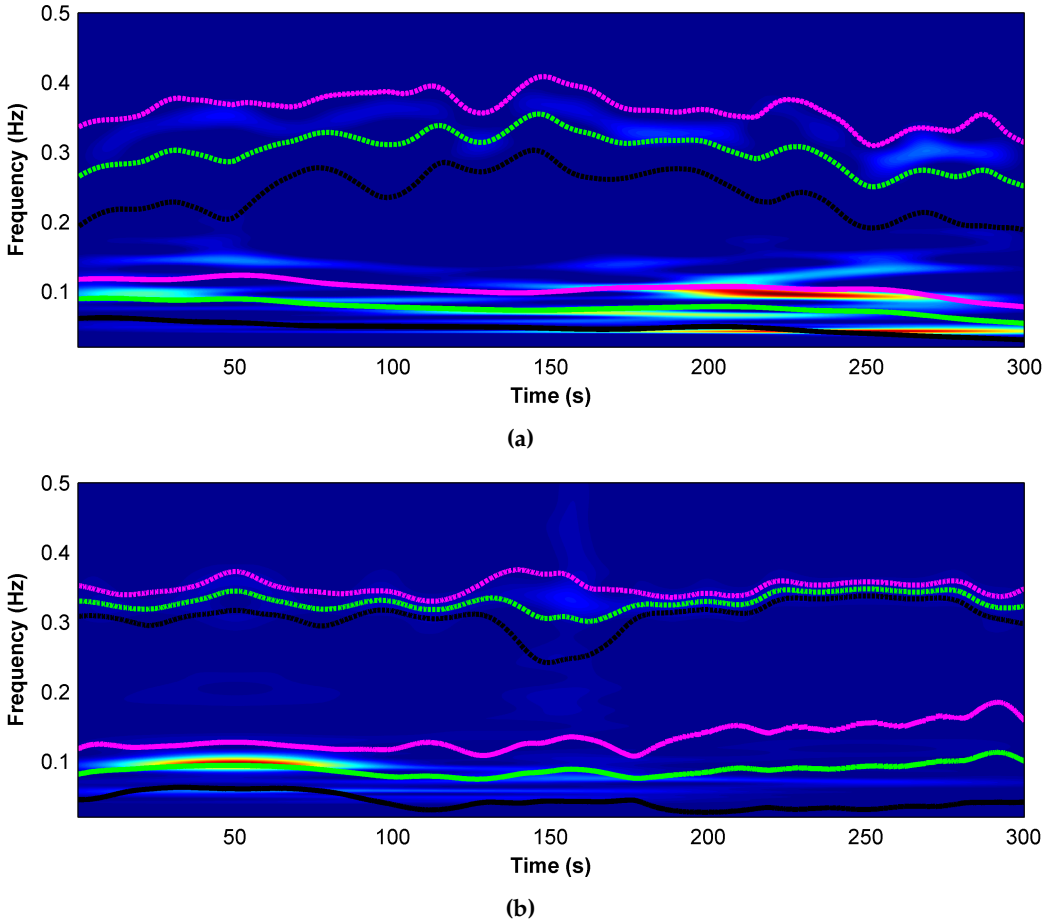

Fig. 12.17: Scalogram of the two HRV signals associated with the data segment used to generate the results of Fig. 12.16. In both cases the ICF and the boundaries related to the LF and HF band are also shown. The dashed lines represent the HF band boundaries and the ICF related to respiration and the solid lines represent the same information for the LF region of the HRV signal

frequencies and the boundaries of the LF and the HF region of the signals are presented in Fig. 12.17 (a) and Fig. 12.17 (b) respectively. The results presented in Fig. 12.17 also suggest satisfactory performance of the method for the estimation of the boundaries related

to the HF and the LF band of the HRV signal. Two important observations can be made here especially from the results presented in Fig. 12.15 and Fig. 12.17. Firstly, the lower HF boundary could extend below 0.15 Hz in some regions of the signal (see Fig. 12.15 (a) and Fig. 12.15 (b)). Secondly, the method is not 100% accurate as it has missed some of the power, possibly related to the LF region, in Fig. 12.17 (a) between 200 and 250 seconds.

The results presented in this section indicate that the method of using ICF and SDSE could be used for defining the boundaries of the LF and the HF bands of HRV signals. As the signal contents are changing with time, it makes sense that the boundaries of the LF and the HF bands also change with time rather than being kept constant. This becomes even more important when the respiration frequency is low as in this case the respiration component power might spread below 0.15 Hz. In this case the power related to the respiration component will be considered to be part of the LF band introducing error in the calculation of the parameters related to the HRV analysis. In the next section the results obtained by using CWT for the analysis of the data from the locally anaesthetised patients collected during this study will be presented. In the analysis of data from local anaesthetised patients the HRV parameters were estimated using both the fixed and the variable boundary (ICF$\pm$SDSE) methods.

12.4. Results of Wavelet (WT) analysis of locally anaesthetised patients data

After pre-processing, correcting for missing and ectopic beats and detrending, in the previous chapter the data obtained from the patients undergoing brachial plexus block (local anaesthetic) procedure were analysed in the frequency domain using the parametric (Welch's periodogram) and the non-parametric (AR modelling) method. In this section the results obtained by analysing the same data using CWT will be presented. As TFD techniques such as CWT allow the study of signal's amplitude and frequency evolution, in time this should provide better understanding of the transient changes occurring in the HRV signal during the study period.

For the analysis the CWT representation of both the HRV signal and the estimated respiration signal were obtained. The cross-spectrum between the HRV signal and the estimated respiration signal, calculated using Eq. 12.5, was used with Eq. 11.2 and Eq. 11.3 in order to obtain the ICF and the boundaries related to the respiration (HF) band of the signal. Similarly the ICF and the boundaries related to the LF band of the signal were calculated using the CWT representation of the HRV signal.

After the estimation of the boundaries related to the LF and the HF bands of the signal, the instantaneous power (see Eq. 12.3) associated with these two bands was also calcu-

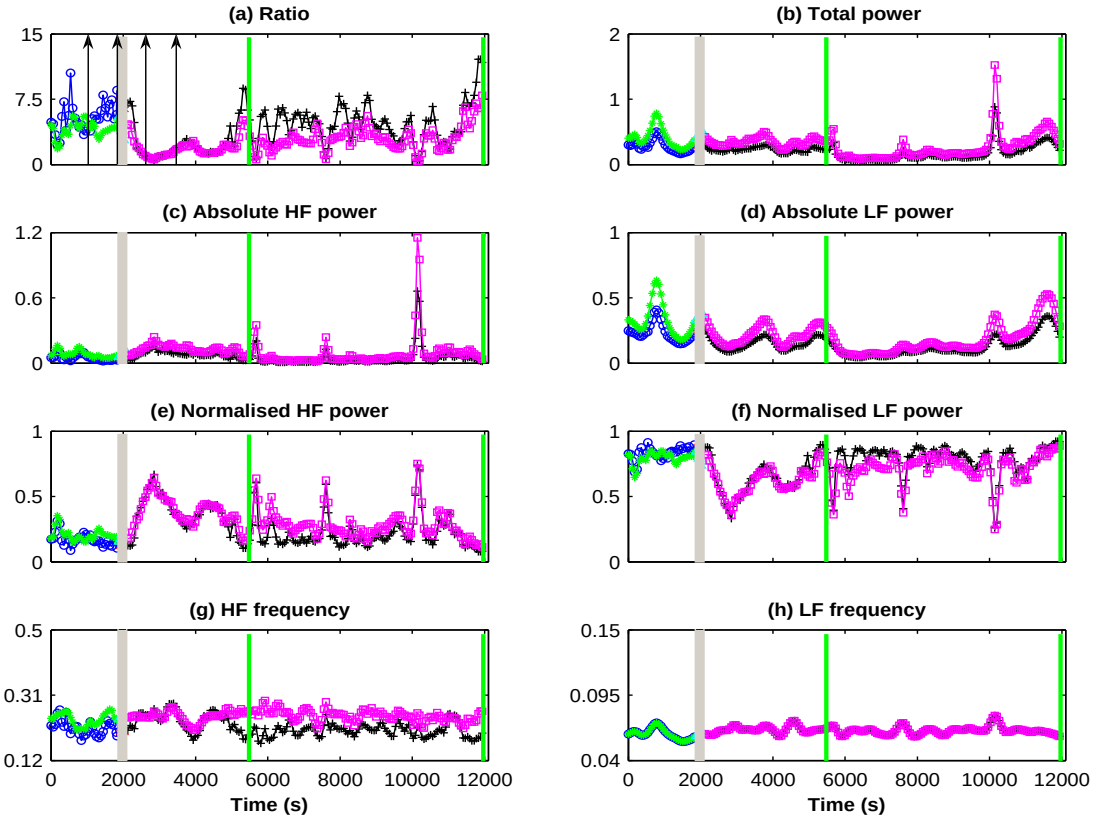

Fig. 12.18: Results obtained from the CWT analysis of a patient undergoing local anaesthetic procedure. In each plot the grey vertical block represents the time of block (anaesthesia) application and the green vertical lines represent start and end of the surgery. The vertical arrow pairs in part (a) show the data segment before and after the application of block which was used in statistical analysis. Each plot shows the parameter values estimated using both the fixed and the variable boundary method. Lines in green and magenta colour represent the parameter values before and after the block application estimated using fixed boundary method respectively. In the case of variable boundary method the same information is presented with blue and black colour lines respectively. The units on y-axis for the plots showing power are $^{s^2}/_{\text{Hz}}$ and for the plots showing frequency values is Hz

lated. Using these estimates along with the total instantaneous power, the LF and the HF power in the normalised units were also calculated. The same parameters were also estimated using the fixed boundary method. The results obtained from one of the patient data set included in this study are presented in Fig. 12.18. The results obtained from the CWT analysis of all the patients included in this study are presented in Appendix C.

Similar to the results presented in Fig. 11.3 and Fig. 11.6 it can be seen from Fig. 12.18 that the parameters related to the absolute value of power (PT (total power), HF_p (High Frequency band power), LF_p (Low Frequency band power) are all slightly higher when estimated with the fixed boundary method, shown in the figure with green (before block) and magenta (after block) colours, as compared to the values estimated with the variable boundary method and shown in the figure with blue (before block) and black (after

block) colours. But by looking at the normalised power of the two bands presented in Fig. 12.18 (e) and Fig. 12.18 (f), it can be seen that in most parts of the data similar changes are observed in the values estimated by both the fixed and the variable boundary method. However, there are incidences (e.g. around 6000 seconds) where different values of the parameters are obtain from the two methods. In all these cases the ICF estimated from the two methods shows more difference between them as compared to the other regions of the data. The use of the cross-spectrum between HRV signal and estimated respiration signal would allow the variable boundary method to consider the effect of the respiration signal below 0.15 Hz which is not possible with the fixed boundary method. Due to this difference when the respiration frequency will be close to or lower than the 0.15 Hz the parameter estimated from the two methods might be different.

The parameter values shown in Fig. 12.18 are the mean values calculated from a period of one minute. After the application of the local anaesthetic drug (data values after the grey vertical block in Fig. 12.18) the $^{LF}/_{\mathrm{HF}}$ ratio shown in Fig. 12.18 (a) increased initially and then decreased reaching a minimum value. During this decrease and some time after reaching the minimum, the ratio values showed decreased variability compared to the other sections of the data. The decrease in the ratio values was observed in each case within an hour of the application of the block. Similar changes were observed in other data sets included in this study (see Appendix D).

As expected the normalised power in the HF (Fig. 12.18 (e)) and the LF band (Fig. 12.18 (f)) show changes in the opposite direction with HF band power showing increase after the application of the block while the LF band power decreasing after the application of the block. The changes in the ICF of the LF and the HF band, shown in Fig. 12.18 (g) and Fig. 12.18 (h) respectively, seems less prominent. The changes observed in the parameter values estimated with the CWT analysis are similar to the changes observed previously with the non-parametric and the parametric analysis of the data from locally anaesthetised patients (see Fig. 11.3 and Fig. 11.6). In this case a statistical analysis was carried out as well in order to see if the values of the parameters show significant difference before and after the application of the anaesthetic block. The pre-block fifteen minutes of data segment used for statistical analysis is shown in Fig. 12.18 (a) by a pair of vertical arrows just before the start of the vertical grey box, while the pair of arrows after the grey vertical box in the same figure represents fifteen minutes of post-block data segment used for statistical analysis. The start and end of the surgery is indicated in Fig. 12.18 with a pair of green vertical lines. The parameter values during the surgery were not included in the statistical analysis as in this case it might not be possible to separately identify the changes in the HRV parameter due to the local anaesthetic drug and the changes occurring due to the surgical procedure.

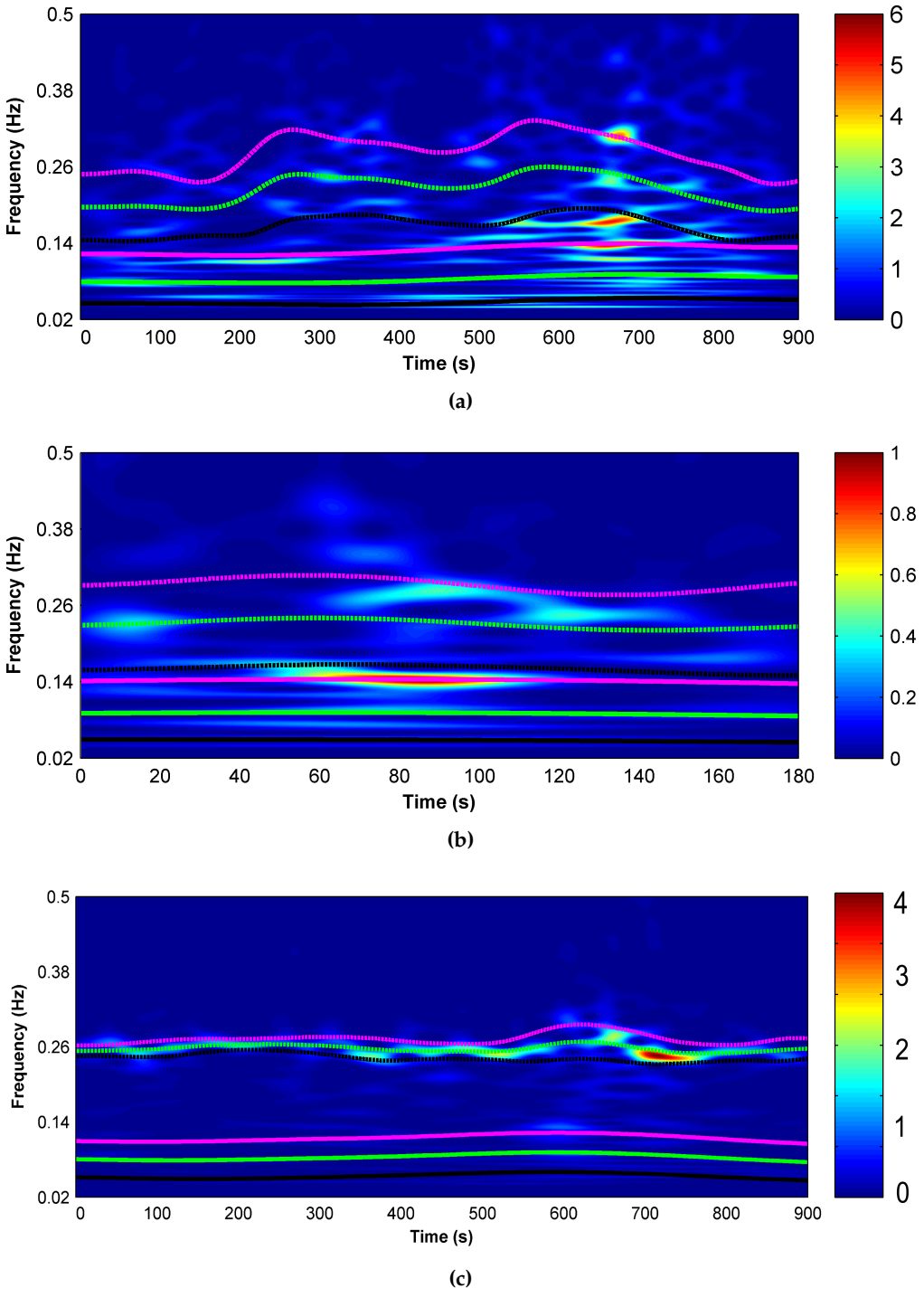

Fig. 12.19: Scalogram representation of the data obtained from a locally anaesthetised patient; (a) the representation for the data segment fifteen minutes before the application of the anaesthetic block, (b) the representation for the data obtained during the application of the block, (c) the representation of the data obtained fifteen minutes after the application of the block. In each case the ICF and the boundaries related to the HF band are represented by dashed line while boundaries and ICF related to the LF band are represented by solid lines

The scalogram representation along with the instantaneous frequencies and the boundaries related to the LF and HF band for the data set, from which the results presented in Fig. 12.18 are obtained, is presented in Fig. 12.19. Figure 12.19 (a) shows the scalogram representation obtained from the data fifteen minutes before the block (anaesthetic drug)

was applied whereas, Fig. 12.19 (b) and Fig. 12.19 (c) show the representation obtained from the data during the application of the block and from a fifteen minute data segment after the application of the block. The data segment after the application of the block is the same segment which was also used for statistical analysis. From the results shown in Fig. 12.19 it can be seen that there is a slight increase in the respiration frequency and a slight decrease in the frequency related to the LF band of the signal. A more important observation that could be made by comparing the representation for the data before the application of the block (Fig. 12.19 (a)) with the representation obtained from the data after the application of the block (Fig. 12.19 (c)), is the shift in power from the LF region to the HF region of the signal. Also, as mentioned before, after the application of the block the ratio values showed decreased variability, another view of this is presented in Fig. 12.19. Before the introduction of the anaesthetic drug into the patient's system the power is more spread out both in the LF and the HF region. After the introduction of the anaesthetic drug the spread of power has decreased in both regions this is evident by the reduction in the boundaries (ICF$\pm$SDSE) for the two regions after the application of the anaesthetic block.

12.5. Statistical test for WT analysis of HRV data from locally anaesthetised patients

Similar to the case of the non-parametric and the parametric analysis (see section 11.3) the parameters estimated with CWT analysis of the HRV data obtained from the locally anaesthetised patients were also tested to check for significant changes in the values after the application of the block as compared to the values before the application of the block. Statistical tests were carried out using the Wilcoxon signed rank sum test. The results obtained from the statistical analysis are presented in table 12.1. The results presented in table 12.1 are summarised in table 12.2. The results presented in table 12.2 indicate that the CWT analysis has been able to detect significant changes in $^{LF}/_{HF}$ ratio values in thirteen of the fourteen patients included in this study as compared to nine significant changes observed in the data from the non-parametric and the parametric analysis (see table 11.2 and 11.4). The same number of significant changes were observed in the $^{LF}/_{HF}$ ratio values from both the fixed and the variable boundary methods.

The parameters related to the power of the two bands also showed strong correlation with the changes in the $^{LF}/_{HF}$ ratio values. Another difference in the results obtained from the CWT analysis when compared to the parametric and the non-parametric method was the fact that the other parameters have shown more correlated changes with respect to the ratio value changes.

Table 12.1.: Statistical test results obtained from CWT analysis of data from patients undergoing local anaesthesia. From each patient eight parameters, $^{LF}/_{HF}$ ratio, total power (PT), high and low frequency band power in absolute and normalised units (HF_P, HF_{Pnorm}, LF_P, LF_{Pnorm}) and ICF in high and low frequency band (HF_f, LF_f), values before and after the anaesthetic block were compared. The first row (values in black colour) for each patient indicates the p values obtained from fixed boundary method while the second row (values in blue colour) indicates p values obtained from variable boundary method. Significance level was defined as $p < 0.05$

Pat. no.	$^{LF}/_{HF}$ ratio	PT	HF_P	LF_P	LF_{Pnorm}	LF_{Pnorm}	HF_f	LF_f
1	<0.001	0.002	0.389	<0.001	<0.001	0.252	0.151	0.035
	<0.001	0.003	0.679	<0.001	<0.001	0.934	0.561	0.035
2	<0.001	0.978	0.002	0.008	<0.001	<0.001	0.188	0.277
	<0.001	0.008	<0.001	0.005	<0.001	<0.001	<0.001	0.277
3	0.048	0.002	0.005	<0.001	0.083	0.083	0.003	<0.001
	0.041	<0.001	0.003	0.002	0.107	0.107	0.003	<0.001
4	<0.001	0.007	0.048	0.002	<0.001	<0.001	0.978	0.847
	<0.001	0.018	0.489	0.002	<0.001	<0.001	<0.001	0.847
5	<0.001	<0.001	<0.001	<0.001	<0.001	<0.001	<0.001	0.561
	<0.001	<0.001	<0.001	<0.001	<0.001	<0.001	0.010	0.561
6	<0.001	<0.001	<0.001	<0.001	<0.001	<0.001	<0.001	<0.001
	<0.001	<0.001	<0.001	<0.001	<0.001	<0.001	0.003	<0.001
7	0.035	0.022	0.303	0.004	0.030	0.030	0.003	0.720
	0.034	0.064	0.421	0.004	0.055	0.055	<0.001	0.720
8	<0.001	<0.001	<0.001	<0.001	<0.001	<0.001	<0.001	1.00
	<0.001	<0.001	<0.001	<0.001	<0.001	<0.001	<0.001	1.00

continued on next page

Pat. no.	LF/HF ratio	PT	HF_P	LF_P	LF_{Pnorm}	LF_{Pnorm}	HF_f	LF_f
9	<0.001	0.012	0.978	0.001	<0.001	<0.001	0.252	0.151
	0.015	<0.001	0.135	<0.001	0.035	0.035	<0.001	0.151
10	<0.001	0.454	0.003	<0.001	<0.001	<0.001	0.064	0.002
	<0.001	0.978	<0.001	<0.001	<0.001	<0.001	<0.001	0.002
11	<0.001	0.107	<0.001	<0.001	<0.001	<0.001	0.008	<0.001
	<0.001	0.208	<0.001	<0.001	<0.001	<0.001	<0.001	<0.001
12	0.489	0.002	0.008	<0.001	0.847	0.847	0.639	<0.001
	0.454	0.003	0.01	0.002	0.847	0.847	0.252	<0.001
13	<0.001	0.421	0.005	<0.001	<0.001	<0.001	0.188	<0.001
	<0.001	0.055	0.008	<0.001	<0.001	<0.001	0.489	<0.001
14	0.005	0.561	0.041	0.004	<0.001	<0.001	0.33	<0.001
	0.004	0.303	0.018	<0.001	<0.001	<0.001	0.510	<0.001

Table 12.2.: Summary of the statistical test result obtained from the CWT analysis of the data from locally anaesthetised patients. LF/HF ratio cell indicates the total number of cases showing significant changes after the block. For all other parameters the first value indicates the number of cases where the parameter values have shown significant changes while the second value indicates the cases where the parameter values have shown significant changes simultaneously with the LF/HF ratio changes. The table on the left is for fixed boundary method while the one on the right is for variable boundary method

LF/HF ratio	PT	HF_P	LF_P
13	9, 8	11, 10	14, 13
HF_{Pnorm}	LF_{Pnorm}	HF_f	LF_f
12, 12	11, 11	6, 6	8, 7

LF/HF ratio	PT	HF_P	LF_P
13	9, 8	10, 9	14, 13
HF_{Pnorm}	LF_{Pnorm}	HF_f	LF_f
11, 11	10, 10	10, 10	8, 7

Overall by comparing the results presented in table 11.2, 11.4 and 12.2 it can be said that the CWT method has been able to detect significant changes in the $^{LF}/_{HF}$ ratio values in more patients as compared to the non-parametric and the parametric method. Also, in the case of the CWT method the changes observed in other parameters were more consistent with the changes in the ratio values.

12.6. Summary

In this chapter the CWT was used for the analysis of the data obtained from locally anaesthetised patients. In the previous chapter the same data was analysed using more traditional non-parametric (Welch's periodogram) and parametric (Autoregressive modelling) methods. Due to various reasons (e.g. assumption of stationarity or estimation of correct model order) these methods are not well suited for the study of transient changes occurring during the course of the signal. CWT is one of the methods that provides signal representation in the joint time-frequency plane and hence is more suitable for the study of non-stationary data. This technique has been used extensively for the analysis of transient behaviour exhibited by many practical data sets including various physiological and biological signals. Due to its ability to track changes in the amplitude and frequency of the signal a large number of HRV studies have also employed this technique.

In this study the Morlet wavelet was used as the mother wavelet. The performance of the CWT for tracking the changes occurring in the signal was validated with the help of four simulated signals. These signals have frequency components in the LF and the HF band of the HRV signal. In the first simulated signal the amplitude and the frequency of the components were kept constant while in the other three simulated signals either the amplitude and/or the frequency of one or both the components were changed half way through the data. The use of simulated signals with known characteristics not only helped in evaluating the frequency and amplitude tracking capabilities of the CWT but also enabled the validation of the ICF and the instantaneous power calculated using the CWT representation with the variable boundary method. The boundaries of each component was defined as ICF$\pm$SDSE (see Eq. 11.3) and the power related to each component was calculated using this range. The simulated study results showed that such a definition of the boundary could be used to calculate the power related to each component quite effectively.

In order to define the boundaries related to the respiration component of the HRV signal more accurately, the cross-spectrum between the HRV signal and the respiration signal was used. To validate this and to see if the boundaries estimated with this method will adequately cover the HF component power of the HRV signal the "Fantasia

Database" from *Physionet* was used. The use of this database allowed the comparison of the HF band boundaries calculated using the cross-spectrum between the HRV signal and the original measured respiration signal with the boundaries calculated using the cross-spectrum between the HRV signal and the respiration signal estimated from the ECG signal using the EDR method (see chapter 10). The results presented in section 12.3 confirmed that the results obtained with the original measured respiration signal and that obtained with the estimated respiration signal were quite close to each other. Also these results (see Fig. 12.15 and Fig. 12.17) indicated that the boundaries defined with the help of the cross-spectrum would adequately cover the power in the HF band of the signal. The comparison between the results obtained with the measured and estimated respiration signals was important as in this study the respiration signal was estimated from the ECG data of the locally anaesthetised patients as the actual measurement of the respiration signal was not available.

For further validation HRV parameters were obtained from the data of locally anaesthetised patients using both the fixed and the variable boundary method. In this analysis the $^{LF}/_{HF}$ ratio, total instantaneous power, instantaneous power corresponding to the LF and HF bands and the ICF related to the two bands were calculated. The power in the LF and the HF band were also calculated in the normalised units. All these parameters are presented for one of the patient's data in Fig. 12.18. These results indicate that the $^{LF}/_{HF}$ ratio values showed an increase right after the block and then decreased reaching a minimum value. The variations in the ratio values were significantly low until it recovered from the minimum phase after the block, compared to the variations in other parts of the data. The results also indicated a shift in the power from the LF region to the HF region of the signal. These results were also indicated by the scalogram representation of the same data set shown in Fig. 12.19. Figure 12.19 (a) and Fig. 12.19 (c) show the representation of the signal fifteen minutes before and after the block respectively which indicates the power shift from the LF component to the HF component and also the reduction in the spread of power in both the components. The pre-block and post-block TFDs are obtained from the same data segments which were used for statistical analysis as well and are indicated in Fig. 12.18 (a) with vertical arrows. The reduction in the spread of power could be seen by the reduction in the boundaries related to the two components presented in Fig. 12.19 (c). The statistical tests carried out to test for significant difference in the parameter values obtained before and after the application of the block indicated that the CWT analysis method has been able to detect $^{LF}/_{HF}$ ratio changes in thirteen of the fourteen patients included in this study as compared to nine cases of significant changes as detected by the parametric and the non-parametric method respectively (see table 11.2, 11.4 and 12.2). The statistical test also indicated that other parameters as es-

timated in the CWT analysis seems to be more correlated to the changes in the $^{LF}/_{HF}$ ratio values as compared to the corresponding value estimated in the parametric and the non-parametric method. Also, by providing the TFD of the signal the technique has been able to provide information in a far richer context compared to the method used in the previous chapter. So in this sense alone it could be considered to present a better analysis tool.

In the next chapter other methods of time frequency analysis will be employed for the analysis of the same data sets from the locally anaesthetised patients in order to see if they can improve further the results obtained by the CWT technique.

13

Time-Frequency analysis of HRV data from locally anaesthetised patients Using Wigner Distribution

13.1. Introduction

In the previous chapter the results obtained by analysing the HRV data from the locally anaesthetised patients using the CWT were presented. By providing the TFD of the signals the CWT allowed better understanding and analysis of the transient changes occurring in the HRV signal. In this chapter another method, Wigner (Wigner-Ville) Distribution (WVD) will be employed for the analysis of the HRV signals from locally anaesthetised patients. This will provide an apportunity to compare the effect of different different time-frequency analysis method on the results obtained in this study. Before presenting the results from the data analysis a brief introduction of this method will be presented in the next section.

13.2. Introduction of quadratic transforms

The methods of constructing the TFD of the signal are generally divided into two types, linear and quadratic transforms of the signal. STFT and CWT are examples of linear transforms which decomposed the signal into elementary components, called atoms, well localised in time and in frequency. The quadratic transforms distribute the energy of the signal along time and frequency variables providing energy time-frequency distributions.

The energy of the signal can be estimated with the squared modulus of either the signal or its Fourier transform (see Eq. 13.1).

$$E_x = \int_{-\infty}^{\infty} |x(t)|^2 \, dt = \int_{-\infty}^{\infty} |X(v)|^2 \, dv \tag{13.1}$$

Where $|x(t)|^2$ and $|X(v)|^2$ can be interpreted as energy densities in time and frequency respectively.

The joint time-frequency energy density $\rho(t, v)$ can be expressed as shown in Eq. 13.2.

$$E_x = \iint_{-\infty}^{\infty} \rho(t, v)\, dt\, dv \tag{13.2}$$

As energy is a quadratic function of the signal, the time frequency energy distributions will be in a general quadratic distribution [153]. Two properties that an energy distribution should satisfy are the following marginal properties:

$$\int_{-\infty}^{\infty} \rho(t, v)\, dt = |X(v)|^2 \tag{13.3}$$

$$\int_{-\infty}^{\infty} \rho(t, v)\, dv = |x(t)|^2 \tag{13.4}$$

The marginal properties (Eq. 13.3 and Eq. 13.4) indicate that by integrating the time frequency energy density along one variable, the energy density corresponding to the other variable can be obtained.

There are many distributions that satisfy the properties presented in Eq. 13.2, 13.3 and 13.4. Additional constraints can be imposed on ρ_x so that the distribution satisfies other desirable properties. Among these desirable properties the covariance principles are of fundamental importance. Hence, the quadratic distributions are divided into two major classes. The distributions which are covariant by translations in time and frequency are representative of Cohen's class [154] while, the distributions which are covariant by translation to time and dilation are categorised as Affian class [155]. The spectrogram which is obtained by considering the squared modulus of the STFT is an example of Cohen's class while the scalogram which is obtained from the squared modulus of the CWT is as example of Affian class. However, taking the squared modulus of an atomic decomposition is only a restrictive possibility to define a quadratic representation. It has been shown that any distribution that belongs to the Cohen's class can be expressed by the general expression presented in Eq. 13.5 [156, 154].

$$C_x(t, v; f) = \iiint_{-\infty}^{\infty} e^{j2\pi\xi(s-t)} f(\xi, \tau) x(s + \tau/2) x^*(s - \tau/2) e^{-j2\pi v\tau} d\xi\, ds\, d\tau \tag{13.5}$$

Where $f(\xi, \tau)$ is a two dimensional function call the parameterisation function.

13.2.1. Winger (Wigner-Ville) Distribution (WVD)

One of the most commonly used and particularly interesting time frequency distribution is the Wigner (Wigner-Ville) distribution (WVD) defined as shown in Eq. 13.12.

$$W_x(t,v) = \int_{-\infty}^{\infty} x(t+\tau/2)\, x^*(t-\tau/2)\, e^{-j2\pi v\tau}\, d\tau \tag{13.6}$$

which can also be expressed as

$$W_x(t,v) = \int_{-\infty}^{\infty} X(v+\xi/2)\, X(v-\xi/2)\, e^{j2\pi\xi t}\, d\xi$$

This distribution is interesting because it satisfies a large number of mathematical properties. In particular, the WVD satisfies the marginal properties, it preserves time and frequency shifts and is always real valued [153]. By looking at the expression presented in Eq. 13.6 it can be seen that WVD is the FT of an acceptable form of the characteristic function for the distribution of the energy. Other main properties of the WVD can be found in the literature [153, 156].

13.2.2. Interference

All the quadratic (bilinear) representations suffer from interference. This means that the distribution of the sum of two signals is not the sum of the distribution obtained from the individual signals (quadratic superposition principle). This can be expressed as shown in Eq. 13.12.

$$y(t) = x_1(t) + x_2(t) \Rightarrow C_y(t,v) = C_{x_1}(t,v) + C_{x_2}(t,v) + 2\Re\{C_{x_1x_2}(t,v)\} \tag{13.7}$$

where $C_{x_1x_2}(t,v) = C_{x_1}(t,v)C^*_{x_2}(t,v)$ is the cross-distribution between the two signals and $\Re$ denotes the real part. Equation 13.7 represents the case when the signal consists of two components but it can be generalised for N components. The interference terms are a major drawback of the quadratic distribution as they can overlap with the auto-terms (signal terms) thus making the visual interpretation of the distribution more difficult. Also, the interference terms represent negative energy which does not have physical meaning. The structure/geometry of the interference terms depends on the signal components and the parameterisation function $f(\xi,\tau)$ of the distribution used. For the spectrogram and the scalogram the interference terms are restricted to the regions where the auto terms ($C_{x_1}(t,v)$, $C_{x_2}(t,v)$) overlap. Therefore, if the signal components are well separated in the time-frequency plane then the interference terms will nearly be zero.

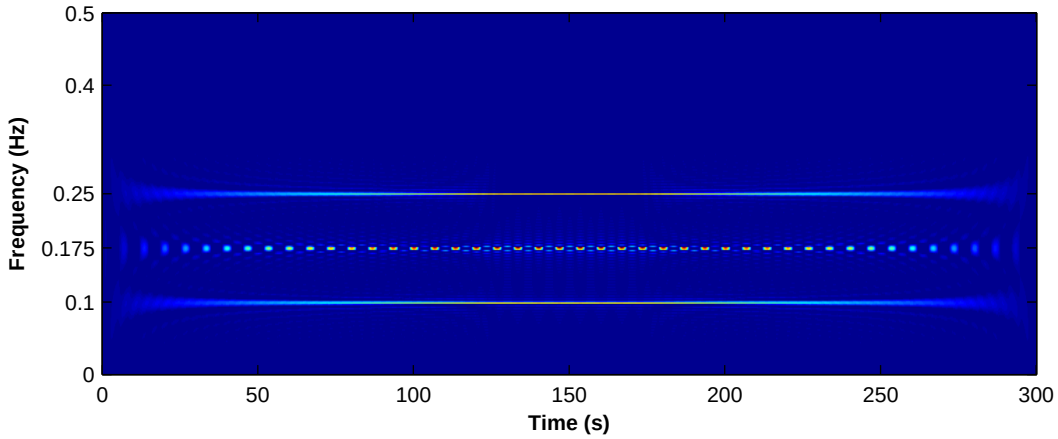

Fig. 13.1: The WVD representation of a signal consisting of two sinusoidal components of frequencies 0.15 Hz and 0.25 Hz respectively. The interference term is clearly visible at the mean of these two frequencies at 0.175 Hz

For the WVD case, the interference terms are always non zero regardless of the distance between the signal components on the time-frequency plane. If WVD is constructed for two points in the time-frequency plane then these two points will interfere to produce another point which will be located at the geometrical midpoint of these two points. These interference terms also oscillate perpendicularly to the distance between these two points. An example of the interference can be seen in Fig. 13.1, which shows the WVD obtained from a signal consisting of two sinusoidal components of 0.1 Hz and 0.25 Hz respectively. The interference term is clearly visible around 0.175 Hz which represents the mean of the two signal components.

13.2.3. Pseudo-WVD

In order to compute WVD using Eq. 13.6 the quantity $x(t+\tau/2)\,x(t-\tau/2)$ needs to be calculated from $\tau=-\infty$ to $\tau=\infty$ which is not possible with practical signals. Therefore, a window is used with the data giving rise to a new distribution which is called pseudo Wigner-Ville distribution (pseudo-WVD/PWVD) presented in Eq. 13.8.

$$PW_x(t,v)=\int_{-\infty}^{\infty} h(\tau)\,x(t+\tau/2)\,x(t-\tau/2)\,e^{-j2\pi v\tau}d\tau \tag{13.8}$$

The windowing operation is basically equivalent to a frequency smoothing of the WVD and Eq. 13.8 can also be written as shown in Eq. 13.9.

$$PW_x(t,v)=\int_{-\infty}^{\infty} H(v-\xi)W_x(t,\xi)\,d\xi \tag{13.9}$$

Where $H(v)$ is the Fourier transform of $h(t)$. Because of their oscillating nature, the interference terms will be attenuated due to this windowing in the PWVD compared to the

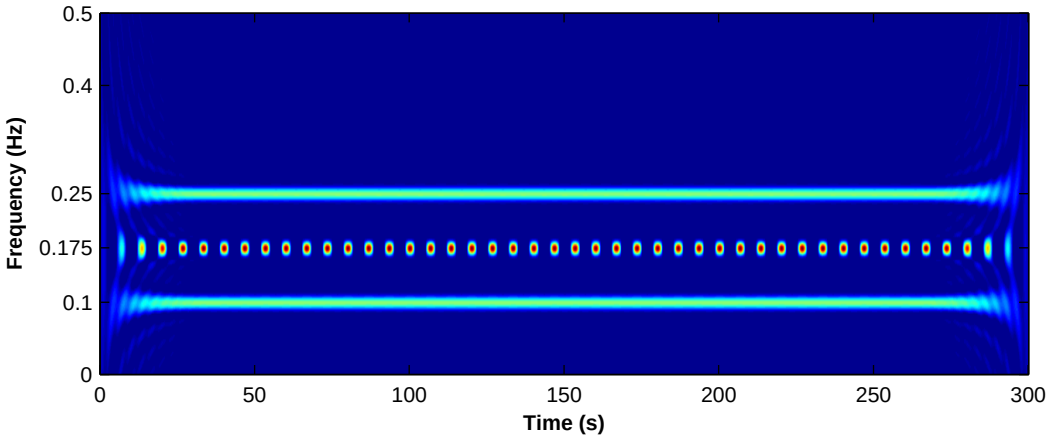

Fig. 13.2: The PWVD representation of a signal consisting of two sinusoidal components of frequencies 0.15 Hz and 0.25 Hz respectively. The interference term has reduced slightly but it is clearly visible at the mean of these two frequencies at 0.175 Hz

WVD. The disadvantage of the windowing processing is that the PWVD loses some of the important properties of WVD (marginal properties, unitarity and frequency-support conservation; the frequency-widths of the auto-terms are increased by this operation). The unitarity property as presented in Eq. 13.10 expresses the conservation of the scalar product from the time-domain to the time-frequency domain (apart from the squared modulus) [156].

$$\left| \int_{-\infty}^{+\infty} x(t)\, y^*(t)\, dt \right|^2 = \int_{-\infty}^{+\infty} \int_{-\infty}^{+\infty} W_x(t,v)\, W_y(t,v)\, dt\, dv \tag{13.10}$$

The formula presented in Eq. 13.10 is also known as Moyal's formula.

Also, because of the windowing operation, the frequency resolution of the PWVD decreases compared to WVD. The PWVD presentation of the two component signal which was used with WVD (see Fig. 13.1) is presented in Fig. 13.2. In this case frequency smoothing is done by using a Hamming window of 257 samples.

From the result presented in Fig. 13.2 it can be seen that the interference term has not been reduced that much compared to the case when the same signal was analysed with WVD. Also the frequency width of the components has been increased as compared to their widths in WVD case (see Fig. 13.1).

13.2.4. Use of analytic signal

The discrete form of the WVD can be written as shown in Eq. 13.11 [157, 158].

$$W_x[n,v] = 2T_e \sum_k x[n+k]\, x^*[n-k] e^{-j4\pi v\tau}\, d\tau \tag{13.11}$$

From Eq. 13.11 it can be seen that WVD is periodic with period $\frac{1}{2T_e}$ instead of $\frac{1}{T_e}$ as obtained in FT for a signal sampled at the Nyquist rate. This means that WVD might be affected by aliasing, especially if the signal is real valued and sampled at the Nyquist rate. In order to deal with this issue the analytical form of the signal (see Eq. 12.2) was used. The advantages of using analytical form have been mentioned before in section 12.2.

13.2.5. Smoothed-pseudo Wigner-Ville Distribution (SPWVD)

The general expression of the Cohen's class (Eq. 13.5) can also be written as (see Eq. 13.12).

$$C_x(t, v; \Pi) = \iint_{-\infty}^{\infty} \Pi(s - t, \xi - v) W_x(x, \xi)\, ds\, d\xi \tag{13.12}$$

Where

$$\Pi(t, v) = \iint_{-\infty}^{\infty} f(\xi, \tau) e^{-j2\pi(v\tau + \xi t)}\, dt\, dv$$

is the two dimensional FT of the parameterisation function $f(\xi, \tau)$. In the case where Π is a smoothing function, $C_x(t, v; \Pi)$ defined in Eq. 13.12 can be interpreted as a smoothed version of the WVD. The advantage of using this general formulation is that different distributions can be obtained by defining different parameterisation functions, which might be constructed with constraints related to particular data characteristics.

For the case of WVD the Π function is a double dirac function: $\Pi(t, v) = \delta(t)\delta(v)$ i.e. $f(\xi, \tau) = 1$. The spectrogram which is also a member of Cohen class can be seen as the smoothing of WVD with $\Pi(s, \xi)$ as the WVD of the window function h. This formulation also indicates the frequency resolution short coming of STFT. If a short window function is used, the smoothing function will be narrow in time and wide in frequency, leading to a good time resolution but bad frequency resolution; and vice versa.

The problem with STFT is that the smoothing is done in both the time and the frequency direction using the same window. Also, from the result presented in Fig. 13.2 it can be seen that frequency smoothing alone would not be able to reduce the interfering terms adequately in all signals. This problem is dealt by introducing separable smoothing function (see Eq. 13.13).

$$\Pi(t, v) = g(t)\, H(-v) \tag{13.13}$$

Where $H(v)$ is the FT of a smoothing window $h(t)$. This smoothing function allows individual control over the smoothing allowed in the time and frequency direction. The distribution obtained with this smoothing function is known as the smoothed-pseudo Wigner-Ville distribution (SPWVD) and can be written as shown in Eq. 13.14.

$$SPWV_x(t, v) = \int_{-\infty}^{\infty} h(\tau) \int_{-\infty}^{\infty} g(s - t)\, x(s + \tau/2)\, x(s - \tau/2)\, ds\, e^{-j2\pi v\tau}\, d\tau \tag{13.14}$$

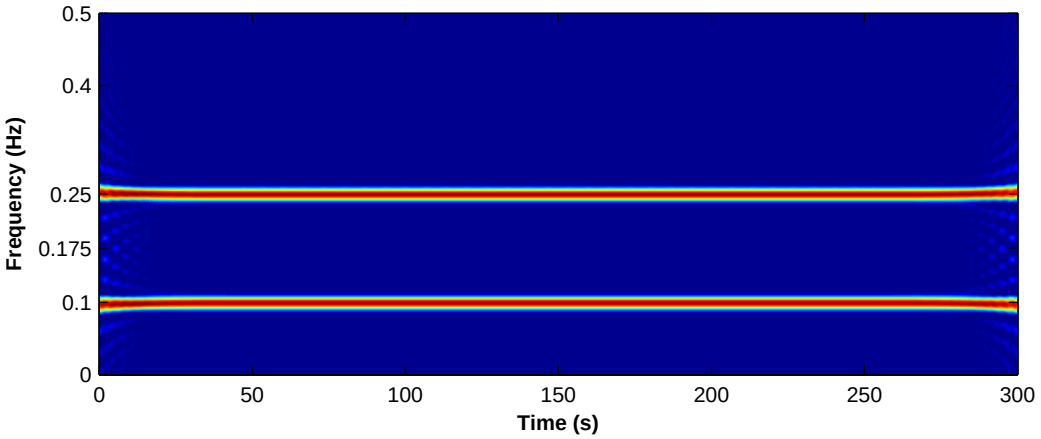

Fig. 13.3: The SPWVD representation of a signal consisting of two sinusoidal components of frequencies 0.15 Hz and 0.25 Hz respectively. The interference term has completely disappeared while the frequency spread is the same as in the case of PWVD (see Fig. 13.2)

The derivation of the discrete SPWVD is presented in detail in the literature [157, 158]. For a discrete sequence $s[n]$, the discrete SPWVD can be expressed as shown in Eq. 13.15.

$$SPWV_x[n,k] = \sum_{l=-P+1}^{P-1} h[l] \sum_{m=-Q+1}^{Q-1} g[m] \times r[n-m,l]\, e^{-j2lk\pi/M} \tag{13.15}$$

Where $r[n,l] = s[n+l]s^*[n-l]$ is the instantaneous auto correlation function. In this case the smoothing in the time direction is done using a window $g[m]$ of length $2Q-1$ and a window $h[l]$ of length $2P-1$ is used for frequency smoothing. By adjusting the length of these windows independently, much better results can be obtained than the PWVD in terms of interference reduction as seen by the result presented in Fig. 13.3. Figure 13.3 shows the SPWVD of the two component signal which has been used previously to get the results shown in Fig. 13.1 and Fig. 13.2. In this case using independent smoothing in time and frequency direction has allowed for better attenuation of the interference term than the attenuation achieved by the PWVD which only used frequency smoothing. In the case of SPWVD, a Gaussian window of 129 samples and a Hamming window of 257 samples are used for time and frequency smoothing respectively.

SPWVD is one of the most commonly used quadratic transforms which has been used in many different fields for the analysis of non-stationary data [159]. Several HRV studies have also used this quadratic distribution for the analysis of the transient changes occurring in the cardiovascular system [160, 161, 162]. In this study SPWVD was also one of the transforms that was considered for the analysis of the data collected from the patients undergoing local anaesthesia.

13.2.6. Choi-Williams Distribution (CWD)

Another distribution that has been used in HRV analysis is the Choi-Williams distribution (CWD) [163, 164, 165]. This distribution also belongs to the Cohen's class. In this case the parameterisation function depends only on the product of the variables τ and ξ and is a Gaussian function as presented in Eq 13.16.

$$f(\xi,\tau) = \exp\left[-\frac{(\pi\xi\tau)^2}{2\sigma^2}\right] \tag{13.16}$$

The corresponding distribution can be expressed as shown in Eq. 13.17.

$$CW_x(t,v) = \sqrt{\frac{2}{\pi}} \iint_{-\infty}^{\infty} \frac{\sigma}{|\tau|} e^{-2\sigma^2(s-t)^2/\tau^2} x(s+\frac{\tau}{2})\, x^*(s-\frac{\tau}{2})\, e^{-j2\pi v\tau}\, ds\, d\tau \tag{13.17}$$

The attenuation of the interference terms is controlled by varying the σ value. With $\sigma \to +\infty$ the distribution reduces to the WVD case and no interference attenuation is done. Using smaller and smaller values for σ offers more attenuation of the interference terms but it also increases the spread of the frequency components present in the signal.

Before using these distributions (SPWVD, CWD) for the analysis of the real data collected from the locally anaesthetised patients the performance of both of them was validated with the simulated signals that have been used before with the CWT analysis (see section 12.2). The results obtained from the simulated signals study will be presented in the next section.

13.3. Results of simulated signals analysis with SPWVD & CWD

The performance of the SPWVD and CWD was evaluated using the same four simulated signals, which were used previously (see section 12.2) to check the ability of the CWT to detect transient changes in the signals. These signals were used as they represented the conditions of amplitude and/or frequency changes during the course of the signal and also by using the same signal the results obtained from these methods could be compared with the results obtained in the previous chapter with CWT analysis. As before, each signal was analysed in the analytical form (see Eq. 12.2). For the SPWVD, time smoothing was done using a Gaussian window of 129 samples while frequency smoothing was done with a Hamming window of 257 samples. For the CWD transform the $\sigma = 0.01$ was used to attenuate the interference terms. This σ value was in accordance with the value suggested and used by other researchers for the analysis of the HRV signal using CWD [160, 166]. In the case of SPWVD the ICF and SDSE were calculated using Eq. 11.2 and Eq. 11.3 respectively. As before, these parameters were obtained for

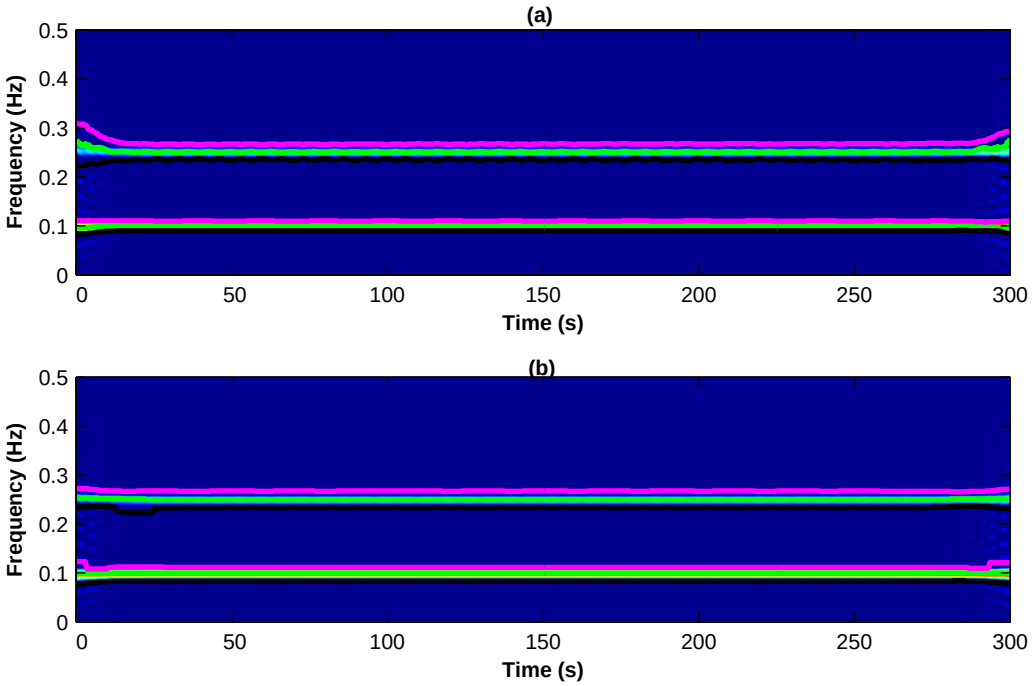

Fig. 13.4: Time-Frequency Representation (TFR) of the first simulated signal using (a) SPWVD ;(b) CWD. In each case the thick green lines represent the ICF for the two components present in the signal. Similarly the thick black and magenta lines represent the lower and the upper boundaries for the two components respectively

the HF component in the frequency range of 0.15 to 0.5 Hz and for the LF component in the frequency range of 0.04 to 0.15 Hz. ICF$\pm$SDSE was considered as the range for each band (HF and LF). However, in the case of CWD the ICF could not be estimated with Eq. 11.2 because due to "cross" shape of the parameterisation function the signal components produced strong interference. So, in this case, the ICF for the HF component was defined as the largest peak in the 0.15 to 0.5 Hz band and for the LF component the largest peak in the 0.04 to 0.15 Hz region. The first minimum on either side of the peak were taken as the boundaries related to component. The ICF and the boundaries estimated for the components in both the SPWVD and the CWD cases were smoothed using a median filter with a length of 10 seconds.

13.3.1. Simulated signal : 1

This signal consisted of two sinusoidal components in the LF (0.1 Hz) and HF (0.25 Hz) bands of the HRV signal. The amplitude of both the LF and the HF components was constant at 0.3 and 0.2 respectively. The TFDs obtained for this signal with the SPWVD and the CWD are presented in Fig. 13.4. The results in Fig. 13.4 also show the instantaneous frequencies and the boundaries related to the two components present in the signal. Using these boundaries the instantaneous power related to each component was calculated (see Eq. 12.3) and the amplitude ratio between the two components calculated

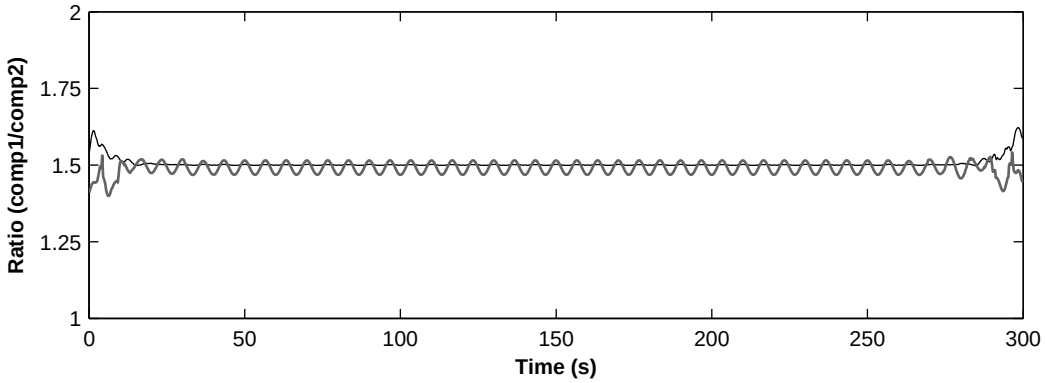

Fig. 13.5: Amplitude ratio between the two components of the first simulated signal calculated using SPWVD (thin darker line) and CWD (thick lighter line)

from both the SPWVD and CWD representations is presented in Fig. 13.5. From the results presented in Fig. 13.4 and Fig. 13.5 it can be seen that both the distributions were able to detect the components present in the signal. The ratio between the amplitude of the two components of the signal is quite close to the theoretical value of 1.5, but the ratio calculated from the CWD distribution showed larger oscillations than the one calculated with the SPWVD (see Fig. 13.5).

13.3.2. Simulated signal: 2

This signal was used to see if the TFDs were able to detect changes in the amplitude during the analysis period. Therefore, in this case the amplitude of the HF component was changed from 0.3 to 0.15. The frequency of the HF component was fixed at 0.25 Hz. The amplitude and the frequency of the LF components were the same as in the case of the first simulated signal. The TFDs obtained from this simulated signal using SPWVD and CWD are presented in Fig. 13.6. Figure 13.6 also shows the instantaneous frequencies and boundaries of the two components present in the signal. To verify that the two distributions have been able to detect the change in the amplitude of the HF component the power in the two components was calculated using the related boundaries. The ratio of the amplitude of the two components calculated from the representations obtained from the SPWVD and the CWD is presented in Fig. 13.7. Both the SPWVD and the CWD has been able to detect the change in the amplitude of the HF component of the signal as indicated by the increase in the ratio values occurring approximately at the midpoint of the data (see Fig. 13.7). The ratio values calculated with the SPWVD are more close to the theoretical values than the ones calculated using the CWD.

13.3.3. Simulated signal: 3

This signal was used to validate the frequency tracking capabilities of the SPWVD and CWD. The signal consisted of two linear chirp components one in the HF band and the

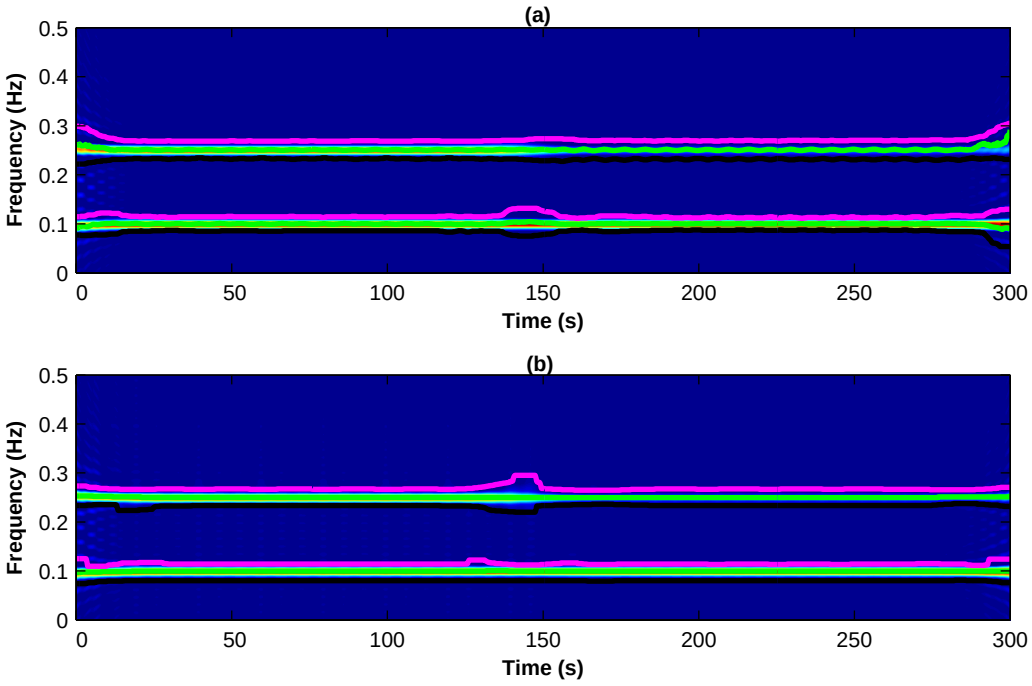

Fig. 13.6: Time-Frequency Representation (TFR) of the second simulated signal using (a) SPWVD ;(b) CWD. In each case the thick green lines represent the ICF for the two components present in the signal. Similarly the thick black and magenta lines represent the lower and the upper boundaries for the two components respectively

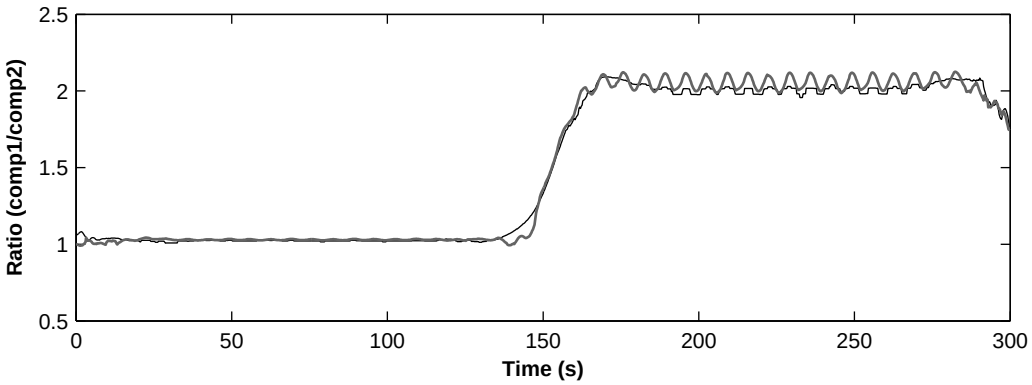

Fig. 13.7: Amplitude ratio between the two components of the second simulated signal calculated using SPWVD (thin darker line) and CWD (thick lighter line). Both these ratio have double almost at the midpoint of the data which is in accordance with the simulation

other in the LF band of the HRV signal. The amplitude of both the components was set to unity. The frequencies of both the components were increasing with time. The TFDs obtained for this simulated signal with the SPWVD and the CWD are presented in Fig. 13.8. From the results presented in Fig. 13.8 it can be seen that both the distributions have been able to detect the changes in the frequencies of the signal components. The power of the components was calculated in each case using the boundaries shows in Fig. 13.8 and the ratio of the amplitude of the two components calculated from the SPWVD and the CWD representations is presented in Fig. 13.9. The ratio values obtained from both the distribu-

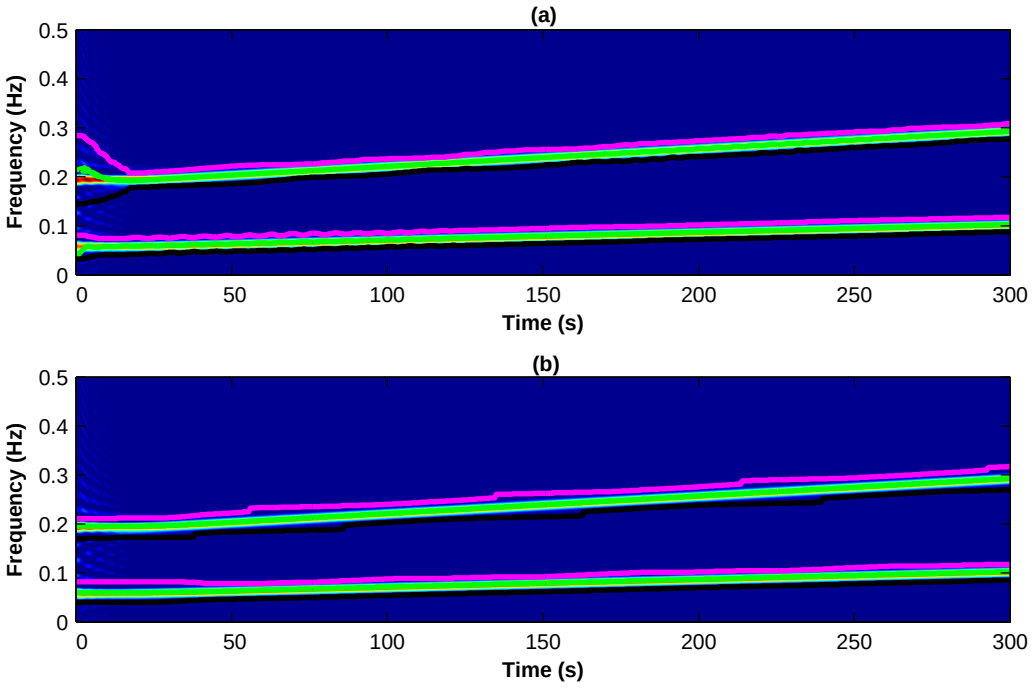

Fig. 13.8: Time-Frequency Representation (TFR) of the third simulated signal using (a) SPWVD ;(b) CWD. In each case the thick green lines represent the ICF for the two components present in the signal. Similarly the thick black and magenta lines represent the lower and the upper boundaries for the two components respectively

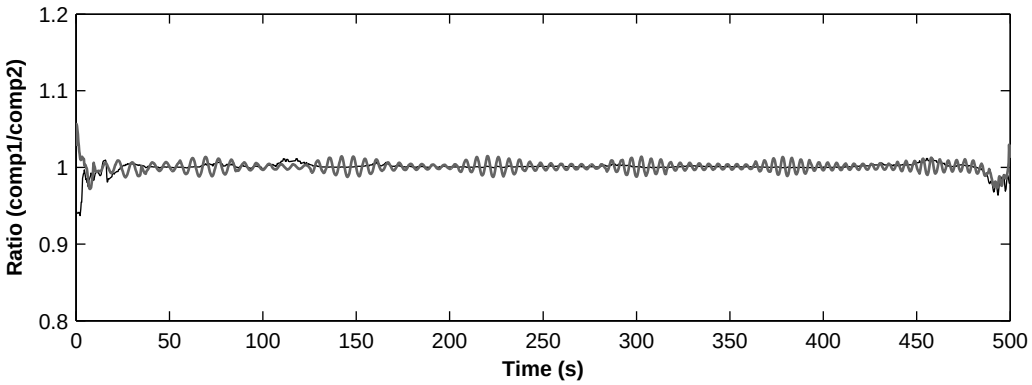

Fig. 13.9: Amplitude ratio between the two components of the third simulated signal calculated using SPWVD (thin darker line) and CWD (thick lighter line). Both the ratio values are close to one which is the theoretical value of ratio for this simulated signal

tions are close to the theoretical value of one apart from the fact that the values obtained with CWD shows more oscillations than the ratio values obtained with SPWVD.

13.3.4. Simulated signal: 4

In the fourth simulated signal the amplitude and the frequency of both the HF and the LF components were changed midway through the simulation. The frequency of the LF component frequency was increased from 0.1 to 0.12 Hz and that of the HF component was increased from 0.25 to 0.3 Hz. For the LF component the amplitude was decreased

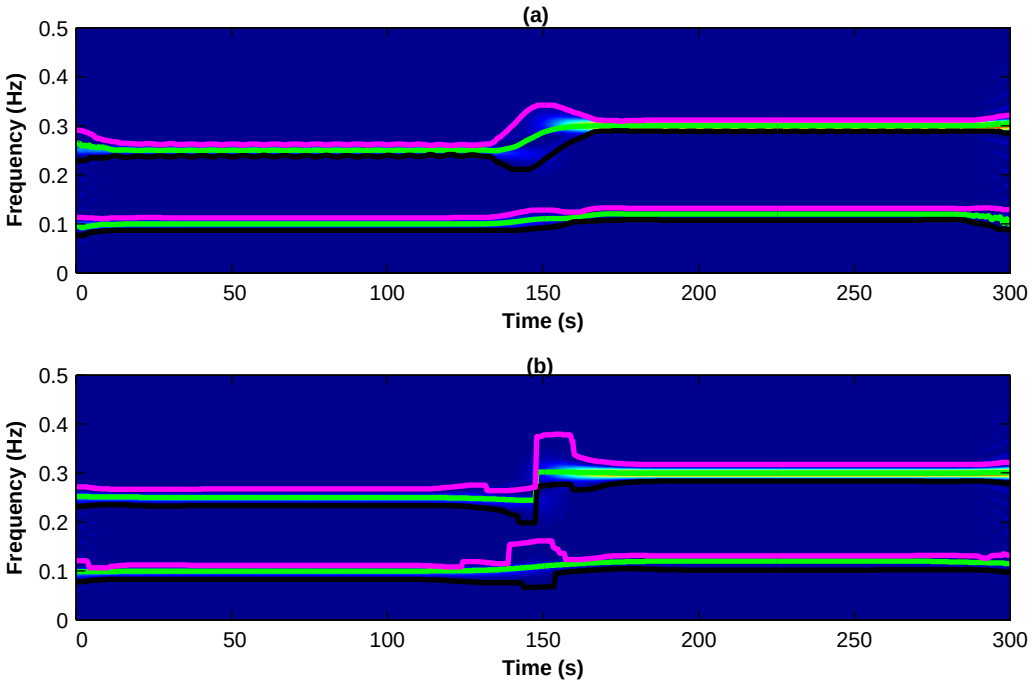

Fig. 13.10: Time-Frequency Representation (TFR) of the fourth simulated signal using (a) SPWVD ;(b) CWD. In each case the thick green lines represent the ICF for the two components present in the signal. Similarly the thick black and magenta lines represent the lower and the upper boundaries for the two components respectively

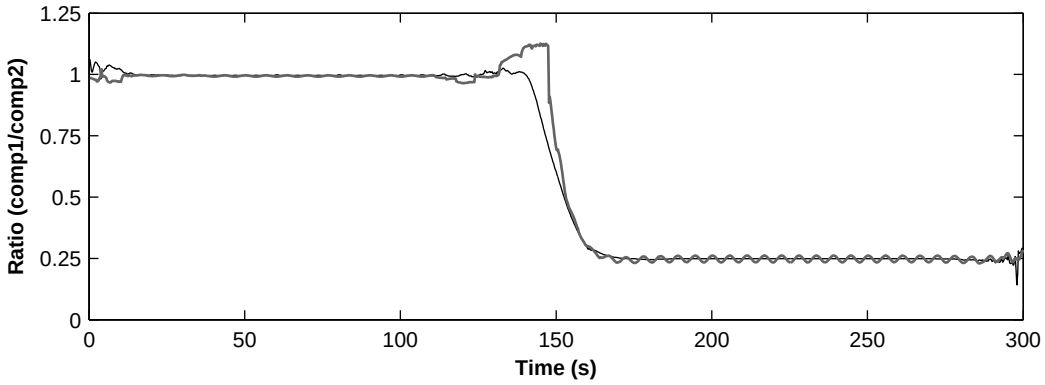

Fig. 13.11: Amplitude ratio between the two components of the fourth simulated signal calculated using SPWVD (thin darker line) and CWD (thick lighter line). Both the ratio values are close to one which is the theoretical value of ratio in the first half of the simulated signal and after the midpoint the ratio values drop to approximately one fourth which is the theoretical value in the second half of the data

from the initial value of unity to half whereas, the amplitude of the HF component was increased from the initial value of unity to two. The TFDs obtained with the SPWVD and the CWD for this simulated signal are presented in Fig. 13.10. The ratio of the two signal components calculated using the SPWVD and the CWD is presented in Fig. 13.11. From the results presented in Fig. 13.10 and Fig. 13.11 it can be seen that both the SPWVD and the CWD have been able to detect the amplitude and frequency changes occurring in the signal. The ratio values remained close to the theoretical value of unity in the first half

of the signal and in the second half when the amplitudes of the two components were changed, the ratio values drop approximately to the theoretical value of one fourth.

The results obtained from the simulated signals indicated that both techniques, the SPWVD and the CWD, were able to detect the transient changes occurring in the signal. However, by comparing the amplitude ratios calculated using the SPWVD with the ratios calculated with the CWD (see Fig. 13.5, 13.7, 13.9 and 13.11) it can be seen that in all cases the SPWVD has produced much better results than the CWD. This error in the ratio values could be due to the fact that the interference terms are more spread out in the frequency in the CWD than they are in the SPWVD. By using a higher value of σ the spread could be reduced but this would result in less attenuation of the interference terms. These findings are in conjunction with the ones presented by Pola *et. al*. [160]. In their study the authors found the CWD to be more effective when peak detection was required however, SPWVD proved to be more reliable in the calculation of the power related to the signal components.

In light of these results only the SPWVD was considered for the analysis of the data collected in this study from patients undergoing local anaesthesia. As in the case of CWT the frequency boundaries and the ICF related to the HF band of the HRV signal was calculated with the help of cross-spectrum between the HRV signal and respiration signal. This approach was again validated with the help of the "Fantasia Database" from *Physionet*. The results obtained for the respiration boundary calculation using the SPWVD on data from the "Fantasia Database" will be presented in the next section. After the validation that the boundary of the respiration defined as the ICF$\pm$SDSE could be calculated using the cross-spectrum between HRV signal and estimated respiration signal obtained with SPWVD, the results obtained by analysing the data from locally anaesthetised patients will be presented.

13.4. Validation of respiration boundary estimation using "Fantasia Database"

As in the case of CWT two important aspects were needed to be validated from this analysis. Firstly, the effect of using estimated instead of the actual respiration signal for the calculation of the ICF and the boundaries related to the HF band of the HRV signal. Secondly, to see if the boundaries calculated from the cross-spectrum does cover the HF band of the HRV signal adequately as seen by the TFD of the HRV signal provided by the SPWVD.

In this case, the TFDs of the *ht* signal, the actual and estimated respiration were calculated using the SPWVD. Using these TFDs the cross-spectrums between the *ht* signal

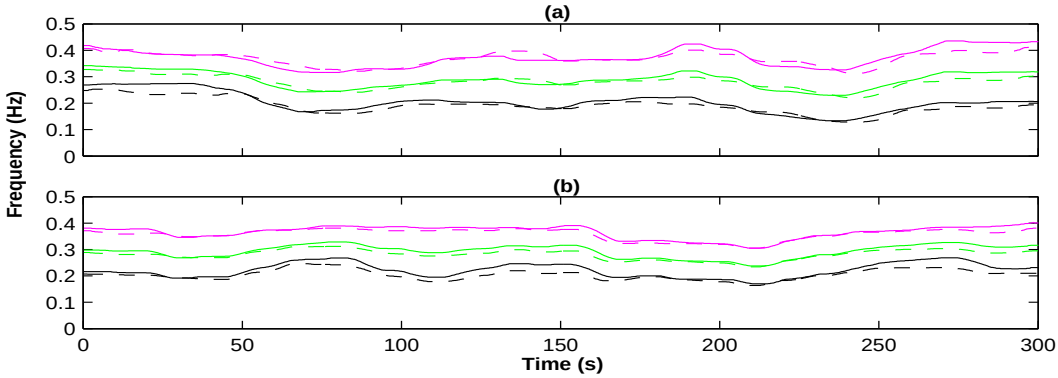

Fig. 13.12: ICF and the respiration boundaries calculated using actual respiration signal (solid lines) and respiration signal estimated from the ECG signal (dashed lines) from two young volunteers from "Fantasia Database". The ICF was calculated using Eq. 11.2 and the boundaries for the respiration component was defined as ICF±SDSE (see Eq. 11.3)

and the actual respiration signal and also between the *ht* signal and the estimated respiration signal were obtained. The ICF and the boundaries (ICF±SDSE) related to the HF band of the HRV signal was then calculated from both cross-spectrums. The results obtained from the data segments of two young volunteers from the "Fantasia Database" are presented in Fig. 13.12.

From the results presented in Fig. 13.12 it can be seen that the ICF and the boundaries calculated from both the cross-spectrums are quite close to each other in both signals. The ICF and the boundaries related to the LF band of the HRV signal was also calculated using the same approach but for this case the TFD of the HRV signal was used instead of the cross-spectrum between the HRV signal and the respiration signal. The TFDs obtained with SPWVD for the HRV data segments which are used to obtain the results presented in Fig. 13.12 are presented in Fig. 13.13. Figure 13.13 also shows the ICF and the boundaries related to the HF and the LF component of the HRV signal in both cases. By looking at the results presented in Fig. 13.13 (a) and Fig. 13.13 (b) it can be seen that in both cases the boundaries estimated for the LF and HF regions of the signal adequately cover most of the power presented in the TFD of the HRV signal in these regions. These results indicate that this method of boundary estimation could be used with SPWVD to estimate the parameters related to the HRV signals.

Similar results were obtained by analysing the elderly volunteers data sets from the "Fantasia Database". The ICF and the boundaries of the respiration band calculated using the actual respiration signal and the estimated respiration signal were quite close to each other. As an example, the results obtained from the analysis of two data sets from elderly volunteers are shown in Fig. 13.14. After these calculations the ICF and the boundaries of the LF region were also calculated using the SPWVD representation of the related HRV signals. The two TFDs obtained with SPWVD along with the instantaneous fre-

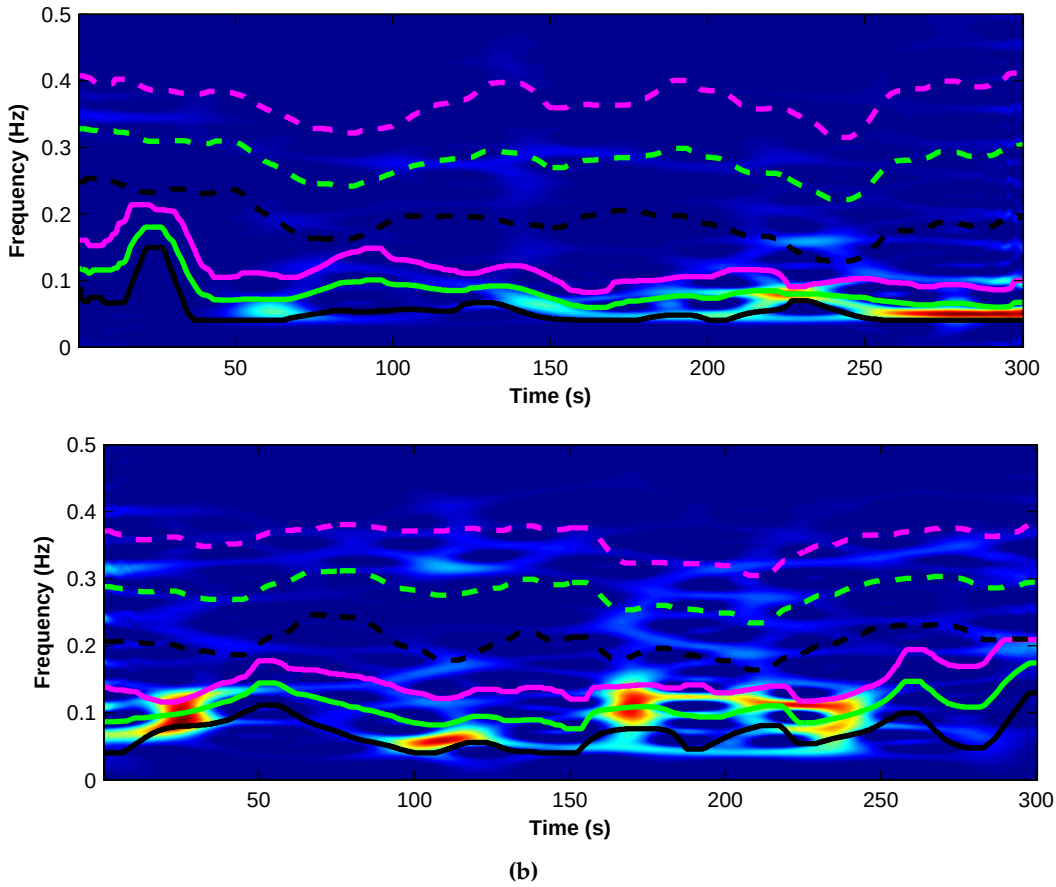

Fig. 13.13: SPWVD representation of the two HRV signals associated with the data segment used to generate the results of Fig. 13.12. In both cases the ICF and the boundaries related to the LF and HF band are also shown. The dashed lines represent the HF band boundaries and the ICF related to respiration and the solid lines represent the same information for the LF region of the HRV signal

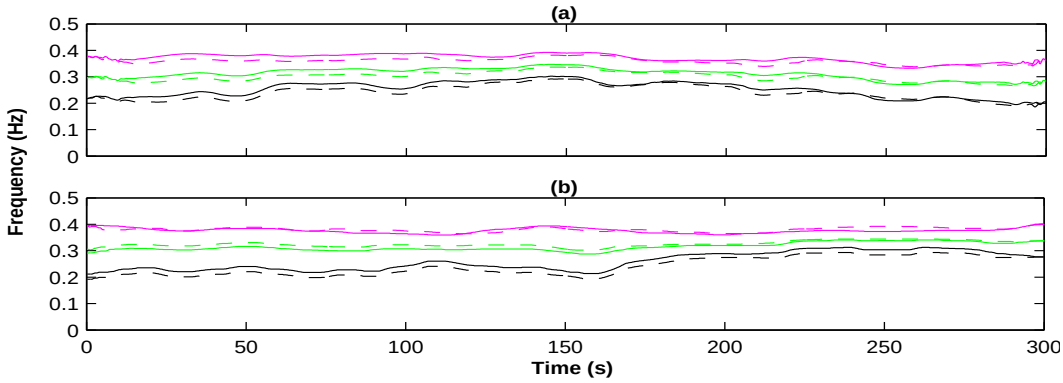

Fig. 13.14: ICF and the respiration boundaries calculated using actual respiration signal (solid lines) and respiration signal estimated from the ECG signal (dashed lines) from two elderly volunteers from "Fantasia Database". The ICF was calculated using Eq. 11.2 and the boundaries for the respiration component was defined as ICF$\pm$SDSE (see Eq. 11.3)

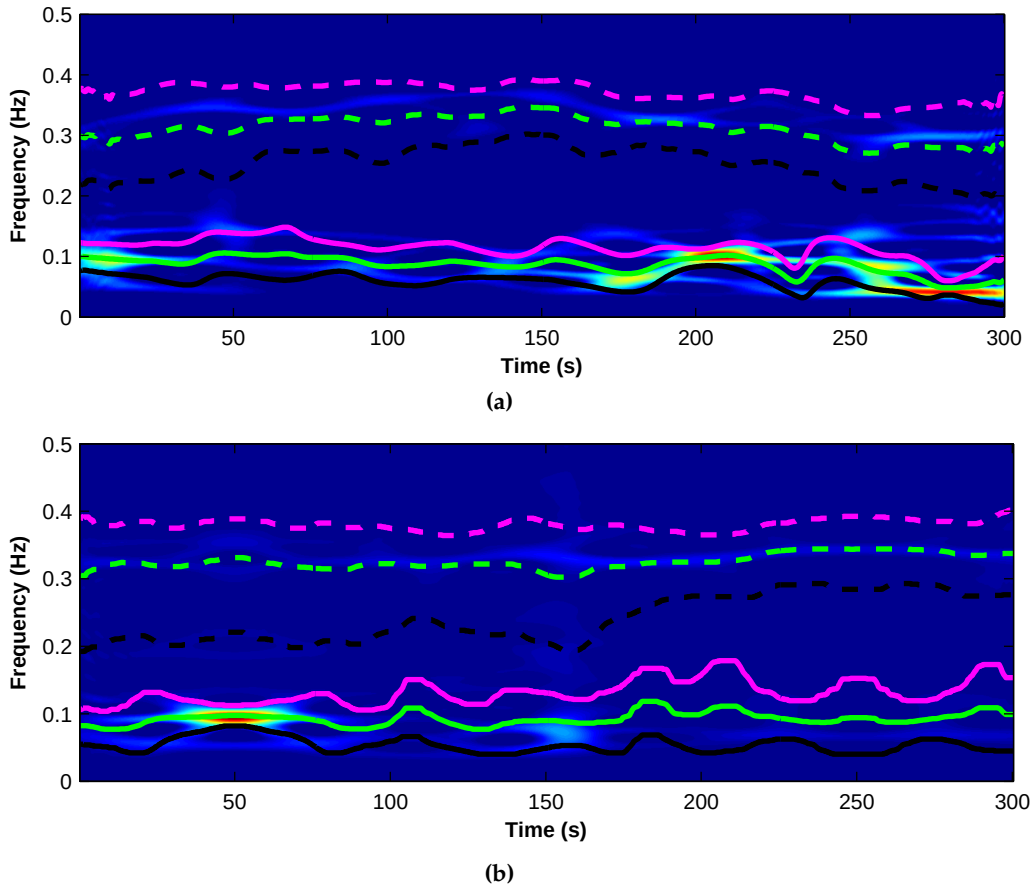

Fig. 13.15: SPWVD representation of the two HRV signals associated with the data segment used to generate the results of Fig. 13.14. In both cases the ICF and the boundaries related to the LF and HF band are also shown. The dashed lines represent the HF band boundaries and the ICF related to respiration and the solid lines represent the same information for the LF region of the HRV signal

quencies and the boundaries of the LF and the HF region of the signals are presented in Fig. 13.15 (a) and Fig. 13.15 (b) respectively. From the results presented in Fig. 13.15 it can be seen that the method for the estimation of the boundaries related to the HF and the LF band of the HRV signal has performed adequately with the SPWVD.

The results presented in this section indicate that the method of using ICF and SDSE could also be used for defining the boundaries of the LF and the HF bands of HRV signals when the TFD of the signal is obtained with SPWVD. In the next section the results obtained by using SPWVD and the boundary estimation method based on ICF and SDSE for the analysis of the data from the locally anaesthetised patients collected during this study will be presented. For validation purposes the HRV parameters from the data of locally anaesthetised patients will also be estimated using the fixed (traditional) boundaries of the LF and the HF band.

13.5. Results of Wigner (Wigner-Ville) Distribution (WVD) analysis of locally anaesthetised patients' data

In this case the pre-processed HRV data were analysed using the SPWVD. The TFDs of both the HRV signal and the estimated respiration signal were obtained with SPWVD. The cross-spectrum between the estimated respiration signal and the HRV signal was calculated using the representations obtained from the SPWVD. This cross-spectrum was then used to estimate the ICF and the boundaries related to the HF band of the HRV signal. The frequency boundaries were defined as ICF$\pm$SDSE where the ICF and the SDSE were calculated using Eq. 11.2 and Eq. 11.3 respectively. The ICF and the boundaries related to the LF component of the HRV signal was calculated using the same approach only in this case the calculation was done using the HRV signal representation instead of the cross-spectrum between the HRV signal and the estimated respiration signal.

The estimated boundaries related to the HF and the LF band of the HRV signals were then used to calculate the instantaneous power (see Eq. 12.3) of the corresponding bands. Using these estimates along with the total instantaneous power, the power related to each band was also calculated in normalised units. For comparison purposes the HRV parameters were also estimated using the fixed (traditional) boundaries for the LF and the HF components. The parameters estimated from one of the patient data included in this study are presented in Fig. 13.16. The results obtained from the SPWVD analysis of all the patients included in this study are presented in Appendix D.

In Fig. 13.16 the grey vertical box in each plot represents the timing of the application of the anaesthetic block. The parameters values estimated with the fixed boundary method are represented with green (before block) and magenta (after block) colour, as compared to the values estimated with the variable boundary method and shown in the figure with blue (before block) and black (after block) colour. As in the case of CWT analysis (see Fig. 12.18), the parameter values shown in Fig. 13.16 are the mean values calculated from a period of one minute. By comparing the results shown in Fig. 13.16 with the results obtained with other techniques previously (see Fig. 11.3, 11.6 and 12.18), it can be seen that in this case both the fixed and the variable boundary method have produced similar values for absolute total power, HF and LF power. But this could be due to the presence of interference terms which will extend the boundaries estimated in the variable boundary method with ICF$\pm$SDSE. By comparing the results obtained from all the techniques it can be seen that as compared to the spectrum obtained from non-parametric (Welch's) method and SPWVD, relatively smooth spectrum as obtained with parametric and CWT method will produce more difference in the absolute power values estimated with the variable and the fixed boundary method. This is due to the fact that in the smooth spectrum

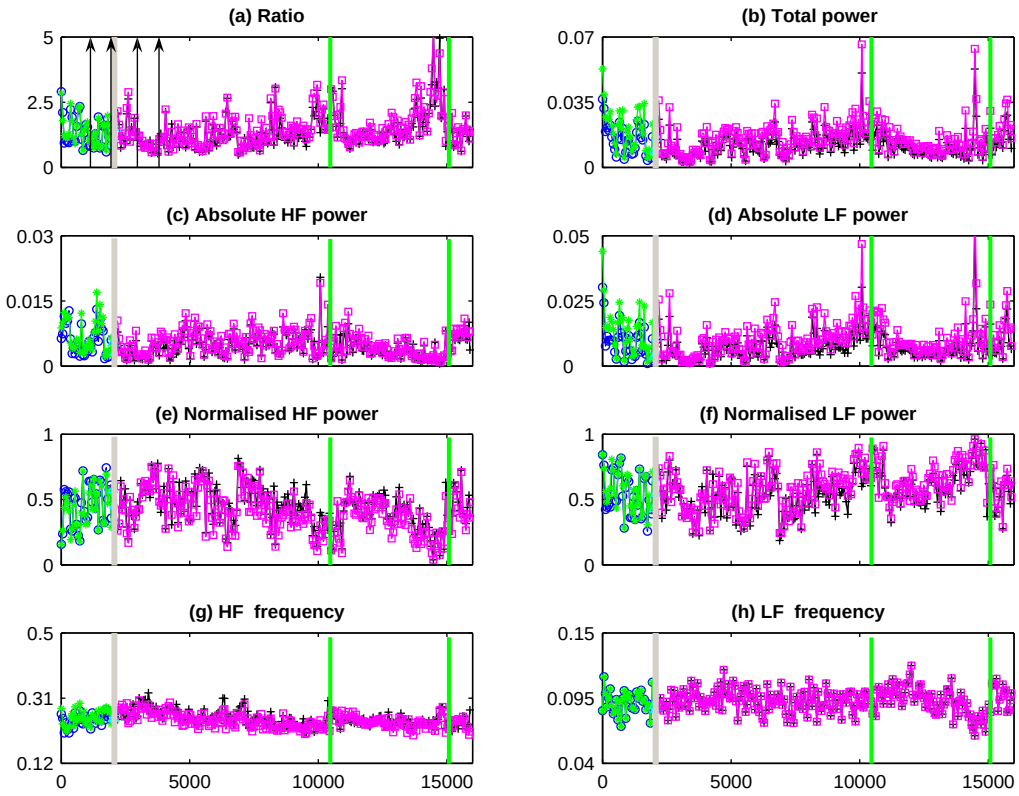

Fig. 13.16: Results obtained from the SPWVD analysis of a patient undergoing local anaesthetic procedure. In each plot the grey vertical block represents the time of block (anaesthesia) application and the green vertical lines represent start and end of the surgery. The vertical arrow pairs in part (a) shows the data segment before and after the application of block which was used in statistical analysis. Each plot shows the parameter values estimated using both the fixed and the variable boundary method. Lines in green and magenta colour represent the parameter values before and after the block application estimated using fixed boundary method respectively. In the case of variable boundary method the same information is presented with blue and black colour lines respectively. The units on y-axis for the plots showing power are s^2/Hz and for the plots showing frequency values is Hz

case the SDSE will be smaller and this will make the band related boundaries narrower.

Similar to the results obtained from other analysis techniques, the LF/HF ratio values (see Fig. 13.16 (a)) have shown an initial increase after the application of the anaesthetic block and then decreases reaching a minimum as compared to the values approximately fifteen minutes before the application of the block. Similar results were obtained from other data sets included in this study (see Appendix D). The decrease in the ratio value was observed in each case within an hour of the application of the block. The total power (Fig. 13.16 (b)) also showed a decrease after the application of the block. As expected the normalised power related to the HF and the LF band showed changes in opposite direction, with HF power (Fig. 13.16 (e)) showing an increase and LF power (Fig. 13.16 (f)) showing a decrease after the application of the block. The ICF values related to the HF

band (Fig. 13.16 (g)) of the signal showed slight changes after the application of the block while the changes in the ICF values related to the LF band (Fig. 13.16 (h)) were less significant and they did not correlated well with the changes in the $^{LF}/_{\mathrm{HF}}$ ratio values after the application of the block.

Statistical analysis was carried out using fifteen minutes of data before and after the application of the anaesthetic block to see if the HRV parameters show significant differences. The pre-block data segment used for statistical analysis is indicated in Fig. 13.16 (a) by a pair of vertical arrows before the grey vertical block while the post-block data is indicated by a pair of vertical arrows after the grey vertical box. The start and end of the surgery is indicated in Fig. 13.16 with a pair of green vertical lines. Again the parameters values after the start of the surgery were not included in the statistical analysis as in this case it will be difficult to separately identify the influence of local anaesthesia and surgery on the HRV parameters.

The SPWVD representation along with the instantaneous frequencies and the boundaries related to the LF and HF band for the data set, from which the results presented in Fig. 13.16 are obtained, is presented in Fig. 13.17. Figure 13.17 (a) and Fig. 13.17 (b) show the SPWVD representation obtained from the data fifteen minutes before the block (anaesthetic drug) was applied and during the block respectively. Similarly the representation obtained from a fifteen minute data segment after the application of the block is shown in Fig. 13.17 (c). This post-block data segment is the same which was also used for statistical analysis and is indicated in Fig. 13.16 (a) by a pair of vertical arrows after the grey vertical box.

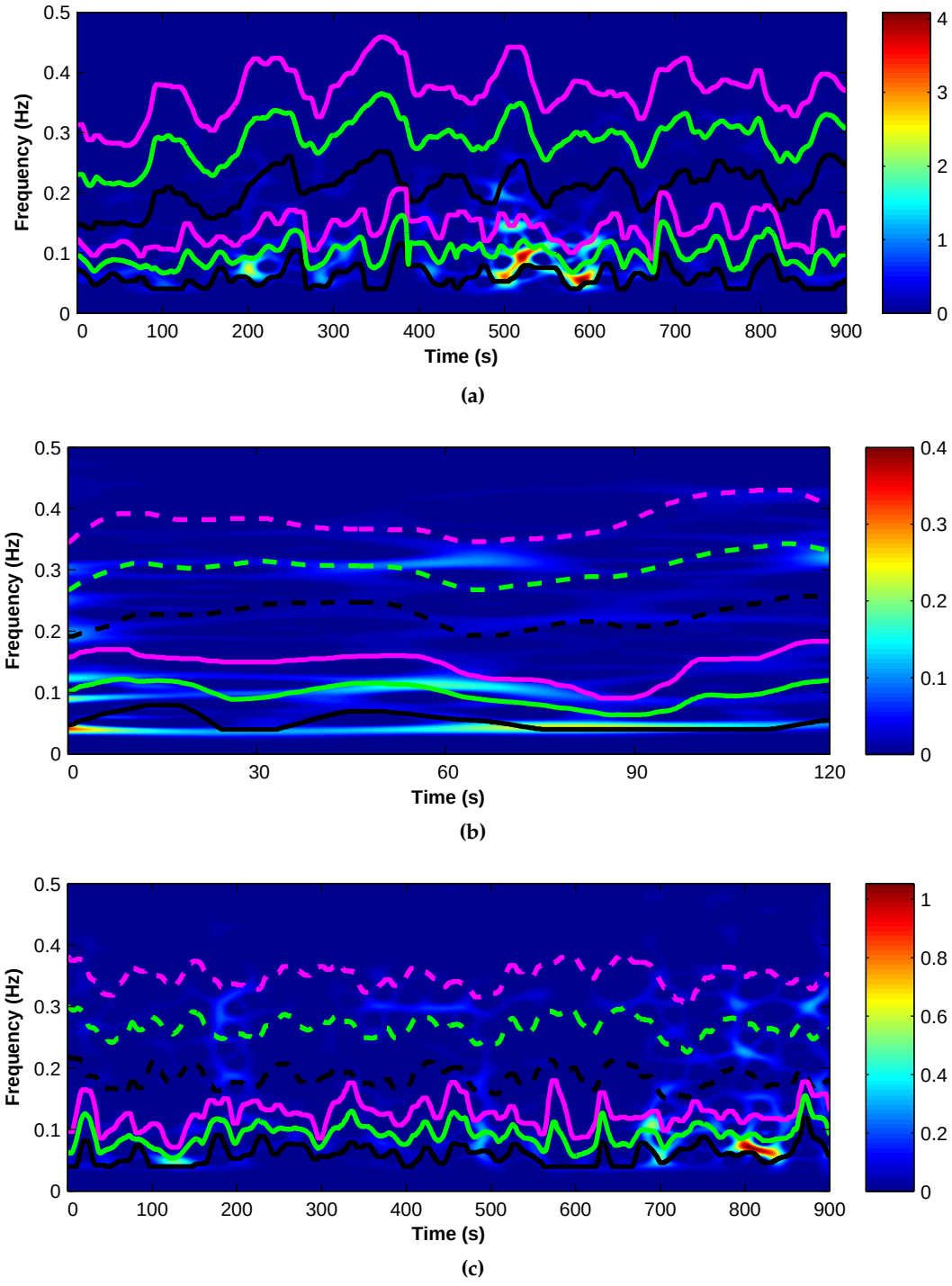

Fig. 13.17: SPWVD representation of the data obtained from a locally anaesthetised patient; (a) the representation for the data segment approximately fifteen minutes before the application of the anaesthetic block, (b) the representation for the data obtained during the application of the block, (c) the representation of a fifteen minutes data segment after the application of the block. The post-block data segment is the same which was used for statistical analysis as indicated in Fig. 13.16 (a). In each case the ICF and the boundaries related to the HF band are represented by dashed line while boundaries and ICF related to the LF band are represented by solid lines

13.6. Statistical test for SPWVD analysis of HRV data from locally anaesthetised patients

The parameters obtained from the analysis of the HRV data obtained from locally anaesthetised patients using SPWVD were also tested for statistical significant changes in the values after the application of the block by applying the Wilcoxon signed rank sum test. The statistical analysis results are presented in table 13.1.

Table 13.1.: Statistical test results obtained from SPWVD analysis of data from patients undergoing local anaesthesia. From each patient eight parameters, $^{LF}/_{HF}$ ratio, total power (PT), high and low frequency band power in absolute and normalised units (HF_P, HF_{Pnorm}, LF_P, LF_{Pnorm}) and ICF in high and low frequency band (HF_f, LF_f), values before and after the anaesthetic block were compared. The first row (values in black colour) for each patient indicates the p values obtained from fixed boundary method while the second row (values in blue colour) indicates p values obtained from variable boundary method. Significance level was defined as $p < 0.05$

Pat. no.	$^{LF}/_{HF}$ ratio	PT	HF_P	LF_P	LF_{Pnorm}	LF_{Pnorm}	HF_f	LF_f
1	0.035	0.017	0.022	0.026	0.030	0.030	0.135	0.135
	0.018	0.021	0.010	0.017	0.015	0.015	0.639	0.135
2	0.121	0.010	0.083	0.002	0.030	0.030	0.330	0.229
	0.083	0.010	0.151	0.003	0.095	0.095	0.188	0.229
3	0.026	0.095	0.083	0.064	0.073	0.073	0.188	0.934
	0.017	0.091	0.330	0.020	0.030	0.030	0.001	0.934
4	0.035	0.009	0.035	0.002	0.073	0.073	0.048	0.252
	0.035	0.011	0.030	0.002	0.107	0.107	<0.001	0.252
5	0.018	0.005	<0.001	0.893	0.026	0.026	0.639	0.679
	0.008	0.004	<0.001	0.421	0.015	0.015	0.978	0.679
6	0.022	0.005	<0.001	0.013	0.055	0.055	0.002	0.004
	0.012	0.007	<0.001	0.055	0.035	0.035	0.169	0.004

continued on next page

Pat. no.	LF/HF ratio	PT	HF_P	LF_P	LF_{Pnorm}	LF_{Pnorm}	HF_f	LF_f
7	<0.001	0.151	0.303	0.169	0.002	0.002	0.135	0.454
	0.012	0.151	0.169	0.229	0.018	0.018	0.022	0.454
8	0.002	<0.001	<0.001	<0.001	0.002	0.002	0.035	0.169
	<0.001	<0.001	0.003	<0.001	<0.001	<0.001	0.330	0.169
9	0.026	0.169	0.305	0.095	0.018	0.018	0.561	0.561
	0.041	0.110	0.742	0.058	0.030	0.030	0.561	0.561
10	<0.001	0.001	0.151	<0.001	<0.001	<0.001	0.002	0.303
	<0.001	0.007	0.847	<0.001	<0.001	<0.001	0.007	0.303
11	<0.001	0.011	<0.001	0.268	<0.001	<0.001	0.330	0.003
	<0.001	0.083	<0.001	0.359	<0.001	<0.001	0.002	0.003
12	0.489	0.002	0.008	<0.001	0.844	0.844	0.639	<0.001
	0.454	0.003	0.010	0.002	0.847	0.847	0.252	<0.001
13	0.421	0.976	0.303	0.762	0.389	0.389	0.679	0.055
	0.561	1.00	0.454	0.978	0.561	0.561	0.8847	0.055
14	0.095	0.804	0.135	0.761	0.064	0.064	0.007	0.305
	0.389	0.855	0.305	0.839	0.33	0.33	<0.001	0.305

The results presented in table 13.1 are summarised in table 13.2. Table 13.2 indicates that the LF/HF ratio values calculated using the SPWVD analysis showed significant changes after the application of the block as compared to the values before the application of the block in ten out of the fourteen data sets analysed in this study. The same number of significant changes were detected in the LF/HF ratio values by both the fixed and the variable boundary method.

Table 13.2.: Summary of the statistical test result obtained from the SPWVD analysis of the data from locally anaesthetised patients. $^{LF}/_{HF}$ ratio cell indicates the total number of cases showing significant changes after the block. For all other parameters the first value indicates the number of cases where the parameter values have shown significant changes while the second value indicates the cases where the parameter values have shown significant changes simultaneously with the $^{LF}/_{HF}$ ratio changes. The table on the left is for fixed boundary method while the one on the right is for variable boundary method

$^{LF}/_{HF}$ ratio	PT	HF_P	LF_P
10	9, 7	7, 6	7, 5
HF_{Pnorm}	LF_{Pnorm}	HF_f	LF_f
8, 7	8, 7	5, 4	3, 2

$^{LF}/_{HF}$ ratio	PT	HF_P	LF_P
10	8, 6	7, 6	7, 5
HF_{Pnorm}	LF_{Pnorm}	HF_f	LF_f
9, 9	6, 5	10, 10	3, 2

Similar to the results obtained from CWT analysis (see table 12.2) the results shown in table 13.2 for SPWVD analysis indicates that the changes in the ICF related to the HF band showed much stronger correlation with the changes in the ratio values when the estimation was carried out using variable boundary method as compared to the fixed boundary method. The difference in other parameters when estimated with the two (fixed and variable) methods was relatively smaller. The ICF of the HF band estimated using the variable boundary method could be more sensitive because in this case the respiration information was included in the analysis by estimating the boundaries of the HF component using the cross-spectrum of the HRV signal and the estimated respiration signal.

13.7. Summary

In this chapter a joint time-frequency analysis method (SPWVD) which has been used extensively in the analysis of non-stationary data including HRV studies was used for the analysis of the data collected from patients undergoing local anaesthesia.

Two energy distributions from the Cohen's class (CWD and SPWVD) which has been used before for the analysis of the HRV data were compared with the help of simulated signals (see section 13.3). From the results obtained from the simulated signal study it was shown that SPWVD performed better than the CWD method for the estimation of the power related to the signal components. For this reason in further analysis only SPWVD was used and CWD was discarded.

As previously, the use of cross-spectrum between the HRV signal and the estimated respiration signal for the calculation of the ICF and the boundaries related to the HF band of the HRV signal was validated with the help of the "Fantasia Database" from *Phy-*

sionet (see section 13.4). The results presented in section 13.4 indicate that ICF±SDSE provided a reasonable estimate of the boundaries related to the HF band of the HRV signal. After this validation the same setup was used for the analysis of the data collected during this study from patients undergoing local anaesthesia. As before, in the analysis of the real HRV data the $^{LF}/_{HF}$ ratio, total instantaneous power, instantaneous power corresponding to the LF and HF bands and the ICF related to the two bands were calculated. The power in the LF and the HF band was also calculated in the normalised units. The parameters estimated using the variable boundary method were also compared with the parameters estimated using the traditional (fixed) boundary method. These parameters calculated from one of the patients data included in this study were presented in Fig. 13.16. The results presented in Fig. 13.16 showed that the ratio and the total instantaneous power values decreased after the application of the block as compared to the values fifteen minutes before the application of the block. The results also indicated a slight shift in the power from the LF region to the HF region of the signal. The results from statistical analysis (see table 13.2) also indicated that both the fixed and the variable boundary methods detected significant changes in the $^{LF}/_{HF}$ ratio values in the same number of patients.

So far in this study two different methods, continuous wavelet transform and Wigner-Ville distribution, which could provide information about the signal in joint time frequency plane were used for the analysis of the HRV data collected from the patients undergoing local anaesthesia. In both these methods the signals are analysed using a fixed set of basis. The performance of these methods depend on the similarities between the signal and the basis used for the analysis. In the case of complex signals it is quite difficult to make an appropriate choice of the basis function based on the properties of the signal. In order to address this problem another method of joint time frequency analysis was introduced. This method known as the Empirical Mode Decomposition (EMD) can be seen as an adaptive data driven method in the sense that in this case the basis are estimated from the data itself. This method was also used for the analysis of the data collected from the locally anaesthetised patients. In the next chapter a brief introduction of the EMD method will be presented after which the results obtained from the simulated signals study and the results obtained by the analysis of the real HRV data using this method will be presented.

14

Empirical Mode Decomposition (EMD) analysis of HRV data from locally anaesthetised patients

14.1. Introduction

In the previous chapters traditional non-parametric (Welch's periodogram), parametric (AR modelling) and time-frequency analysis techniques (CWT and SPWVD) were used to analyse the HRV signals obtained from the locally anaesthetised patients (see chapter 11, 12 and 13). Even though these methods have been used extensively in HRV studies as mentioned before they have certain limitations that can be problematic when analysing signals such as the HRV signal. The Welch's periodogram (non-parametric) method requires the data to be stationary, therefore only short segments of data should be used with this technique. The shorter data lengths restrict the resolution that can be achieved by this technique. To avoid the problem of low resolution of non-parametric methods researchers usually prefer to use the parametric methods of spectral analysis. Even though these methods produce a high resolution spectrum which can be decomposed relatively easily into its components, the performance of these methods is quite dependent on the selection of correct model order to represent the data. As the HRV signal shows both inter and intra patient variability, using the same model order for the whole data set or even for the whole duration for a single patient may cause error in the results obtained through this technique. In comparison to the parametric and non-parametric techniques, Wigner distribution (a quadratic energy time-frequency distribution) can handle non-stationary data. The main drawback of this distribution is that because of its quadratic nature it contains cross-terms between the signal components. These cross-terms can produce error in the power calculated from the distribution and can even make the power values negative in some regions of the signal. As mentioned in the previous chapter due to finite signal length and to reduce the effect of cross-terms the Wigner distribution is smoothed independently in frequency and time direction using individual window functions. This implementation is referred to as *smoothed-pseudo* Wigner distribution. Even though

this smoothing operation reduces the cross-terms considerably, the introduction of longer window for providing more smoothing also reduces the resolution in that particular direction. The length of these windows, as mentioned in chapter 13 is usually defined qualitatively by observing the distribution.

In order to avoid the problems faced by the above mentioned methods, the HRV signals were analysed once again using the Empirical Mode Decomposition (EMD) method with Hilbert transform. This signal analysis technique has been used for analysing HRV signals [167, 168, 169, 170] and other biological signals [171, 172, 173] besides other applications [174, 175]. This chapter will provide a brief description of the technique, then the technique will be evaluated using simulated signals and finally the technique will be applied on the real clinical data obtained in this study from patients undergoing local anaesthesia.

14.2. Empirical Mode Decomposition (EMD)

Empirical Mode Decomposition (EMD) is an adaptive data driven method of decomposing the signals into components in such a way that Hilbert Transform (HT) can be employed to obtain the time-frequency representation of the signal. By decomposing the signal into components closely linked with the underlying physical phenomena and facilitating the use of the HT the EMD technique has the potential to be a very useful tool for the analysis of dynamical changes occurring in the signal. In the following sections some of the concepts related to this technique will be discussed briefly.

14.2.1. Instantaneous Frequency and Hilbert Transform

Due to its use of global harmonic components and linear superposition of the trigonometric functions the Fourier spectral analysis can produce spurious harmonic components when used with nonlinear and non-stationary data. These harmonic components cause energy spreading, resulting in a false energy-frequency distribution for such signals [176]. In case of nonlinear data, the production of spurious harmonics in Fourier based methods and the validity and the implication of the instantaneous frequency can be seen by considering the idealised Stokes waves in deep water. This represents a classic example of using harmonic components to represent nonlinear wave form distortion [177]. It is also the first successful application of the perturbation method to solve a nonlinear analytic equation system for a natural phenomenon [176]. To second-order, the profile can be written as shown in Eq. 14.1.

$$X(t) = \frac{1}{2}a^2k + a\,cos\omega t + \frac{1}{2}a^2k\,cos2\omega t + ..., \tag{14.1}$$

With parameters values of $a = 1$, $k = 0.2$ and frequency of $1/32$ Hz the profile is presented in Fig. 14.1 (a). By looking at the profile in Fig. 14.1 (a) it can be seen that because of the harmonic distortion, the wave form shows sharpened crests and rounded-off troughs, which make the crests and troughs asymmetric with respect to the mean surface. EMD analysis of this wave profile yields only one IMF component (see Fig. 14.1 (c)). The Stokes wave is deformed due to the harmonic distortion; it is asymmetric with respect to the mean, while the IMF is symmetric. In this case, a constant offset component, not shown in Fig. 14.1, will be the residue. Even though the wave has only one characteristic scale, the spectrum obtained from Morlet wavelet (see Fig. 14.1 (b)) shows two bands of energy, the fundamental component around 0.03 Hz and the harmonic around 0.06 Hz. The Morlet spectrum shows the second harmonic (0.06 Hz) to account for the deformity present in the signal and it has no physical meaning. In contrast, the Hilbert amplitude spectrum (see Fig. 14.1 (d)) obtained with the IMF component shown in Fig. 14.1 (d) shows only one frequency band centred around 0.03 Hz, the fundamental frequency of the wave profile. The Hilbert spectrum shows an interawave frequency modulation with a magnitude range of 0.02 to 0.04 Hz. The single component with interawave modulation represents the physical phenomena in a much better way than the harmonic representation obtained from Morlet spectrum. This interawave frequency modulation has been totally ignored in the past as the traditional definition of frequency is based on the reciprocal of periodicity [176].

Locality and adaptivity are the most important characteristics that a basis set should have in order to properly represent nonlinear and non-stationary signals. The property of locality is important especially for the non-stationary data as in these signals the frequency contents might be changing at different time instances and these events need to be identified by the time of their occurrence. The requirement of adaptivity is important for both non linear and non-stationary signals as only by adapting to the local changes in the data the decomposition will be able to fully take into account the underlying physical phenomena.

The requirements discussed here mean that the transformation correctly representing such kind of signals should have both the frequency and the amplitude (or energy) as a function of time. This can be achieved by using HT, which for an arbitrary time series $X(t)$ can be written as shown in Eq. 14.2.

$$Y(t) = \frac{1}{\pi} P \int_{-\infty}^{\infty} \frac{X(t')}{t - t'} \, dt' \tag{14.2}$$

Where P indicates the Cauchy principal value. This transform exists for all functions of class L^p [176]. With this definition, $X(t)$ and $Y(t)$ form the complex conjugate pair, so the

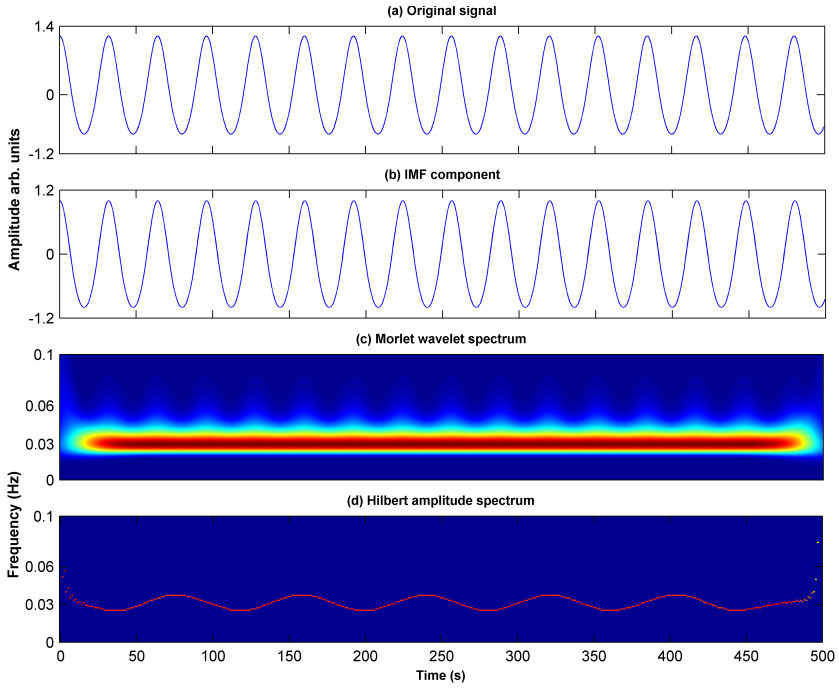

Fig. 14.1: Example of spurious harmonic component in nonlinear data; (a) The profile of a second-order Stokes waves in deep water; (b) The IMF generated by the Stokes wave, there is only one component; the constant offset is not shown; (c) Morlet wavelet spectrum for the Stokes waves; (d) Hilbert amplitude spectrum from the IMF shown in part (b)

analytical signal $Z(t)$ can be written as shown in Eq. 14.3.

$$Z(t) = X(t) + iY(t) = a(t)e^{i\theta(t)} \tag{14.3}$$

Using Eq. 14.3 the amplitude and the phase of the signal can be written as shown in Eq. 14.4 and Eq. 14.5.

$$a(t) = [X^2(t) + Y^2(t)]^{1/2} \tag{14.4}$$

$$\theta(t) = arctan\left(\frac{A}{B}\right) \tag{14.5}$$

There are infinite ways of defining the imaginary part of Eq. 14.3. The HT provides a unique way of defining the imaginary part so that the resulting signal is an analytic function. By using this analytic form of the signal the instantaneous frequency can be defined as the derivative of the phase function (see Eq. 14.6).

$$\omega = \frac{\mathrm{d}\theta(t)}{\mathrm{d}t} \tag{14.6}$$

An important point to note here is that the instantaneous frequency, as defined in Eq. 14.6, is a signal value function of time, therefore it is only valid for mono-component narrow band signals. Previous attempts of signal decomposition into narrow band components using filtering techniques have failed to give meaningful results for the estima-

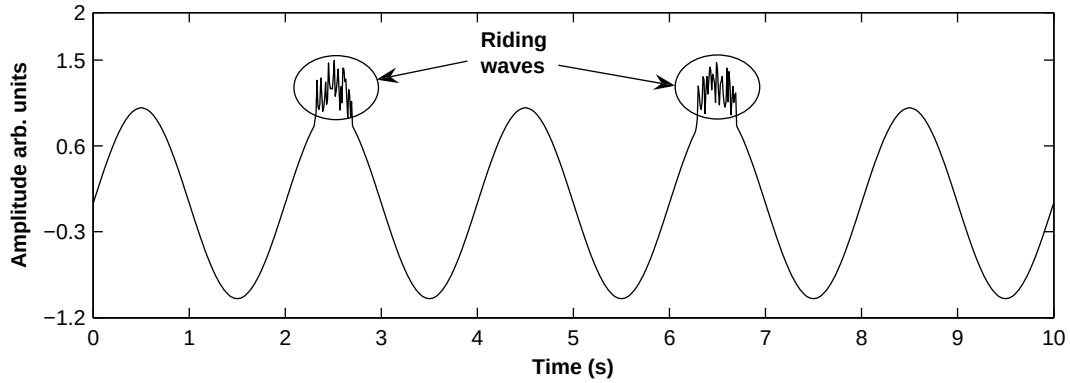

Fig. 14.2: Example of singal showing riding waves. Beacuse of these waves the signal could not be considered as an IMF component

tion of the instantaneous frequency. This inability of splitting signals into narrow band components has severely restricted the use of the HT for data analysis in the past. This exact problem is address by EMD. In this analysis method the basis functions are generated adaptively based on the characteristics of the data. The decomposition is based on the direct extraction of the energy associated with various intrinsic time scales, the most important parameter of the system [176]. The intrinsic time scale is defined as the time elapse between successive extrema. Due to the association with the intrinsic time scales these basis functions are termed as Intrinsic Mode Function (IMF). These basis functions can be linear or nonlinear as dictated by the data. The properties of the IMF functions that are presented in section 14.2.2 make it possible to obtain meaningful estimation of the instantaneous frequency and thus, a full energy-frequency-time distribution of the data can be achieved. Such a representation is designated as the Hilbert spectrum.

14.2.2. Intrinsic Mode Function (IMF) and sifting process

A function can be considered as an IMF if it satisfies the following two conditions [176]:

1. In the whole data set, the number of extrema and the number of zero crossings must either equal or differ at most by one.

2. At any point, the mean value of the envelope defined by the local maxima and the envelope defined by the local minima is zero.

Each cycle in the IMF, defined by the zero crossing should involve only one mode of oscillation, no complex riding waves (see Fig. 14.2) are allowed. With this definition, an IMF is not restricted to a narrow band signal, and it can be both amplitude and frequency modulated, in fact it can be non-stationary. This method does not always guarantee a perfect instantaneous frequency under all conditions. The method of estimating the error in instantaneous frequency estimate will be discussed later. A systematic way for extracting IMF from a complicated data set known as sifting process will be described next.

The first step is to identify all the extrema from the original data set. After this all the local maxima are connected using cubic spline to obtain the upper envelope. This procedure is repeated to form the lower envelope using the local minima. Using these lower and upper envelopes, the mean envelope designated as m_1 is calculated and subtracted from the signal (see Eq. 14.7) to obtain the first component h_1.

$$h_1 = X(t) - m_1 \tag{14.7}$$

The sifting process has two purposes, firstly to remove the riding wave from the signal and secondly, to make the wave profile more symmetric. The removal of riding waves is necessary to achieve meaningful instantaneous frequency using HT while the symmetry is important in order to avoid large disparity in the amplitude of the neighbouring waves. So if the first component given in Eq. 14.7 does not satisfy these conditions the process can be repeated up to k times to obtain the k^{th} component which can be considered as an IMF (see Eq. 14.8).

$$h_{1k} = h_{1(k-1)} - m_{1k} \tag{14.8}$$

Then it is designated as

$$c_1 = h_{1k} \tag{14.9}$$

The first IMF c_1 should contain the finest scale or the shortest period component of the signal. After obtaining the first IMF component, this is subtracted from the data as shown in Eq. 14.10.

$$r_1 = X(t) - c_1 \tag{14.10}$$

The residue signal r_1 can be subjected to the sifting process again to extract the second possible IMF component and the residue r_2. The sifting process is stopped by any of the following two criteria [176]:

1. If the amplitude of the component c_n, or the residue r_n becomes smaller than the predetermined value of substantial consequence.

2. When the residue r_n becomes a monotonic function from which no more IMF can be extracted.

3. After the full decomposition the data can be written as the summation of n IMF components and the n^{th} residue as shown in Eq. 14.11.

$$X(t) = \sum_{i=1}^{n} c_i + r_n \tag{14.11}$$

The residue could be a constant or the mean trend of the data. The completeness of the decomposition is also established by Eq. 14.11.

Another important property mentioned for a basis set is orthogonality. In the case of EMD an overall index of orthogonality (IO) can be defined by writing Eq. 14.11 as shown in Eq. 14.12.

$$X(t) = \sum_{j=1}^{n+1} C_j(t) \tag{14.12}$$

In Eq. 14.12 the residue is added as an extra component. Using Eq. 14.12 the overall index of orthogonality (IO) can be written as shown in Eq. 14.13.

$$\mathrm{IO} = \sum_{t=0}^{T} \left(\sum_{j=1}^{n+1} \sum_{k=1}^{n+1} C_j(t)\, C_k(t) \diagup X^2(t) \right) \tag{14.13}$$

Orthogonality can also be defined for any two components, C_f and C_g. The measure of orthogonality can then be written as shown in Eq. 14.14.

$$\mathrm{IO}_{fg} = \sum_{t} \frac{C_f C_g}{C_f^2 + C_g^2} \tag{14.14}$$

As the EMD process is a nonlinear decomposition method therefore it does not guarantee orthogonality which is a requirement for linear decomposition method. Fortunately, in most cases the leakage is small [176].

14.2.3. Stopping criteria

In the EMD process the basis are adaptively generated from the data itself, the properties of the IMF thus created depends to a large extent on the stopping criteria that is used in the sifting process. As mentioned before the sifting process tries to make the IMF component more symmetrical (smooth uneven amplitude) unfortunately if carried out too many times it could obliterate the physically meaningful amplitude fluctuations. This will make the IMF a pure frequency modulated signal with constant amplitude [178]. Therefore, a stopping criterion should be defined in such a way that IMF components retain enough physical sense of both the amplitude and frequency modulations.

In the literature so far, four different techniques have been used to define the stopping criteria. The first one purposed by Huang *et. al.* [176] was based on limiting the size of the standard deviation, SD, computed from the two consecutive sifting results as shown in Eq. 14.15.

$$SD_k = \frac{\sum_{t=0}^{T} |h_{k-1}(t) - h_k(t)|^2}{\sum_{t=0}^{T} h_{k-1}^2} \tag{14.15}$$

The sifting process stops when the SD value becomes smaller than a predefined value. Usually a value of 0.2-0.3 is used as a threshold. This definition has two problems, firstly there is no concrete way of choosing the threshold value. Secondly, the criterion does not depend on the definition of the IMF which means that a smaller SD value does not gua-

rantee that the function will have the same number of zero-crossing and extrema [178].

The second criterion purposed by Gabriel *et. al.* [179] is based on two thresholds θ_1 and θ_2. In this case two signals, mode amplitude and evaluation function, are computed as defined by Eq. 14.16 and Eq. 14.17.

$$a(t) = \frac{(e_{max}(t) - e_{min}(t))}{2} \tag{14.16}$$

$$\sigma(t) = \left| \frac{m(t)}{a(t)} \right| \tag{14.17}$$

Where $e_{max}(t)$ and $e_{min}(t)$ in Eq. 14.16 represent the maximum and minimum envelope respectively and $m(t)$ in Eq. 14.17 represents the mean envelope.

The sifting process is continued until $\sigma(t) < \theta_1$ for some prescribed fraction $(1 - \alpha)$ of the total duration of the data, while $\sigma(t) < \theta_2$ for the remaining fraction of the data. Typical values mentioned in Gabriel *et. al.* [179] work and used by many that are using this criterion are $\alpha \approx 0.05$, $\theta_1 \approx 0.05$ and $\theta_2 \approx 10\,\theta_2$. This criterion also suffers from the same problem as the previous one, as in this case as well the choices of α, θ_1 and θ_2 can be made independently of the data.

The third criterion is the intermittence criterion purposed by Huang *et. al.* [180]. The existence of intermittence can produce mode mixing, a phenomenon caused by having different time-scales (or spatial scales) mixed in a single IMF component, which will introduce additional, but fictitious, variations in the resulting IMFs and, hence, in the instantaneous frequency [181]. This criterion requires the selection of a number. Only waves shorter than this number of data points can be included in an IMF. If the distance between the successive extrema is larger than the selected number, the mean is used to replace that data point. The criterion requires that only when the distance between the extrema is less than the predefined number will the upper, the lower and the mean be available to extract the IMFs. This criterion is difficult to set a *priori*, unless there is a strong theoretical basis to establish a distinct scale length [181].

The fourth criterion used for stopping the sifting process is also proposed by Huang *et. al.* [180]. In this case the sifting process is stopped when the number of zero crossing and extrema remains the same for S successive sifting steps. The first task in this approach is to determine a number S. Thus, the stopping criterion provides a soft boundary for the sifting procedure; slightly different results from a given set of data can be obtained by adopting different S values [178]. As defined in the initial work of Huang *et. al.* this criterion is also not very useful in the sense that a variety of values can be considered valid for the parameter S. But using a range of valid values for this parameter Huang *et. al.* [181] were able to define a confidence limit, and using this infor-

mation a method was established for providing a range of S values that could provide stable results. This development has made this criterion the most promising so far.

In order to obtained this confidence limit the data was decomposed into IMFs components using eleven different S numbers (S = 2-10, 15 and 20). The IMFs obtained from different S settings could then be used to estimate the mean IMFs and the standard deviation for each case. The mean and standard deviation values could be used to obtain the confidence level. With the establishment of a confidence interval of the sifting process, the optimal number S could be found. In the case where the number of IMFs produced by different S values were not the same, then the IMFs mean would be meaningless. This difficulty could be overcome by averaging the Hilbert spectrum, which has the same number of bins in frequency and temporal space pre-assigned [181]. Variation of the deviation of the individual cases from the mean value could be used to find a range of stopping criteria that produces relatively stable results in either the IMFs or the Hilbert spectrum. The mean from the samples of any quantity, $V(S)$ could be calculated as a function of stopping criterion S as shown in Eq. 14.18.

$$\langle V \rangle = \frac{1}{N} \sum_{j=1}^{N} V(S_j) \tag{14.18}$$

The squared deviation of each individual case can be computed from this mean by using Eq. 14.19.

$$sd(S_j) = \left[V(S_j) - \langle V \rangle \right]^2 \tag{14.19}$$

This technique will be used to find the suitable S value for the simulated and the real HRV data that will be studied in the later sections.

14.2.4. Hilbert spectrum

After decomposing the signal into IMF components, HT is applied to each component. Now the data can be expressed as the real part $\Re$ in the form shown in Eq. 14.20.

$$x(t) = \Re \left\{ \sum_{j=1}^{n} a_j(t) \exp \left[i \int \omega_j(t) \mathrm{d}t \right] \right\} \tag{14.20}$$

By looking at Eq. 14.20 IMF could be considered as the generalised Fourier expansion. The variable amplitude and the instantaneous frequency has not only improved the efficiency of the expansion, but also enabled the expansion to accommodate the non-stationary data [176]. Equation 14.20 allows the representation of the amplitude and the instantaneous frequency as functions of time in a three-dimensional plot, in which the amplitude can be contoured on the frequency-time plane. This frequency-time distribu-

tion of the amplitude is designated as the Amplitude Hilbert-Haung Spectrum (AHHS), $H(\omega, t)$, or simply Hilbert spectrum. The energy density can be represented by using the squared values of the amplitude and this is known as the Hilbert energy spectrum.

With the Hilbert spectrum defined the marginal spectrum can also be defined as following (see Eq. 14.21).

$$h(\omega) = \int_0^T H((\omega, t)\mathrm{d}t \tag{14.21}$$

The marginal spectrum provides a way of estimating the total amplitude or energy contribution from each frequency value. It represents the accumulated amplitude over the entire data span in a probabilistic sense [176]. In addition to the marginal spectrum the instantaneous energy density level (IE) can also be defined as shown in Eq. 14.22.

$$\mathrm{IE}(t) = \int_\omega H^2(\omega, t)\mathrm{d}\omega \tag{14.22}$$

14.2.5. Normalised Hilbert spectrum

Although the HT exists for any function of L^p class, the phase function of the transformed function will not yield a physically meaningful instantaneous frequency. Obtaining IMFs satisfies only the necessary conditions; additional limitations have been summarised in two additional theorems [178].

First, the Bedrosian theorem [182] that gave the necessary conditions for obtaining a meaningful HT result of the product of functions. Using this, the HT of the envelope and the carrier can be written as shown in the Eq. 14.23.

$$H\left\{a(i)\cos\theta(t)\right\} = a(t)H\left\{\cos\theta(t)\right\} \tag{14.23}$$

According to the Bedrosian theorem, Eq. 14.23 can be valid only if the amplitude is varying slowly enough so that the frequency spectra of the envelope and the carrier waves are disjoint. This condition has made the application of the HT problematic. To satisfy this requirement, Haung and Long [183] introduced Normalised Amplitude Hilbert Transform (NAHT). In this technique the IMFs are normalised. The data is first decomposed into IMF components then each IMF is normalised by finding all the maxima of the IMF and making an envelope by a spline through all the maxima.

The normalised IMF is obtained by dividing the amplitude by the envelope. Ideally the normalised IMF will have the maximum amplitude of unity. But complications can arise from the spline fittings, and anomalies can occur especially at the point where the amplitude fluctuation is large. Whenever the amplitude goes above unity, error will occur in the representation. Even with perfect normalisation there could still be a problem es-

timating the instantaneous frequency using Eq. 14.6. This problem is highlighted by the Nuttal theorem [184].

Second, the Nuttal theorem states that the HT of a cosine is not necessarily a simple 90° phase shift, resulting in the sine function with the same phase function for an arbitrary phase function. Nuttal gave an error bound ΔE, defined as the difference between the HT and quadratur (with a phase shift of exactly 90°) of the function as (see Eq. 14.24).

$$\Delta E = \int_0^T \left| C_q(t) - C_h(t) \right|^2 dt = \int_{-\infty}^0 S_q(\omega) d\omega \tag{14.24}$$

Where $C_q(t)$, $C_h(t)$ and $S_q(\omega)$ represent the HT, the quadrature and the Fourier spectrum of the quadrature function respectively. There are two problems with this error bound which make it hardly useful. Firstly, it is expressed in terms of the spectrum of the still unknown quadrature and secondly, it gives a constant error over the whole data range. For non-stationary data, such a constant bound will not reveal the location of the error on the time axis. Using the normalisation technique Huang [183] established the time dependent error bound as well. If the HT is a perfect quadrature of the function, then its absolute value would be one. In other words if the HT and the quadrature are identical, then error should be zero. Therefore, an error index could be defined as presented in Eq. 14.25 [183].

$$E(t) = [abs(\text{Hilbert Transform}(y(t))) - 1]^2 \tag{14.25}$$

Where $y(t)$ represent the normalised IMF component.
An acceptable error index can be predefined for the process. Any instantaneous frequency with the error index above the predefined threshold should be considered incorrect.

After describing the basic EMD algorithm and some of the issues related to this technique the next section will present results obtained by analysing simulated signals when using the EMD algorithm. These results will enable a more clear and detailed understanding of the algorithm before engaging in the analysis of clinical data.

14.3. Results of Empirical Mode Decomposition (EMD) analysis of simulated signals

In this simulated study the same four simulated signals, which have been used previously for the validation of the CWT and the SPWVD techniques (see section 12.2 and 13.3), were used. The first step in the analysis of each signal was to establish the confidence interval for the EMD. The values of 2-10, 15 and 20, as mentioned before were used

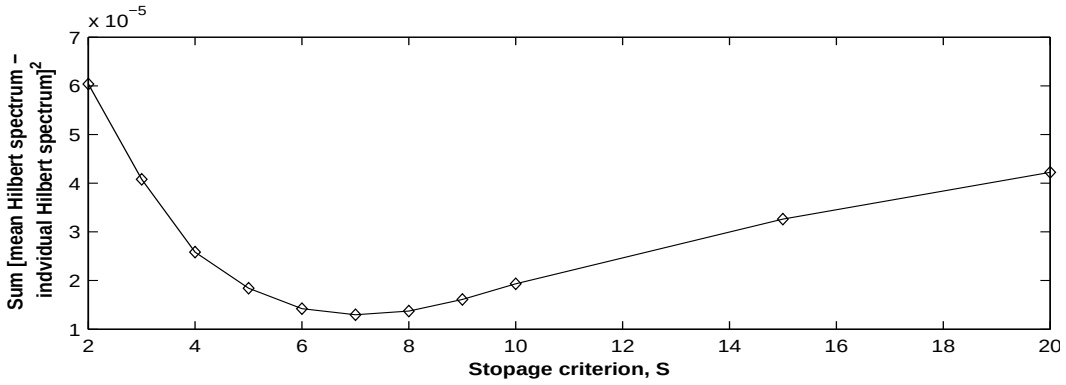

Fig. 14.3: Squared deviation obtained using the mean Hilbert spectrum and the individual Hilbert spectrum for the stoppage criterion S values of 2-10, 15 and 20 in the case of simulated signal one

for the stopping criterion S. As the number of IMF components generated by varying the S value was different therefore Hilbert spectrum was used to calculate the mean and the squared standard deviation. After calculating the mean and squared deviation for the individual values as given by Eq. 14.18 and Eq. 14.19 respectively the S value was chosen according to the minimum of the squared deviation. After decomposing the signal using the optimal S value the IMF were normalised to obtain NAHT. The HF and the LF components of the decomposition were selected based on the values obtained for the CF and the SDSE (see Eq. 11.2 and Eq. 11.3) of the individual components. These values were estimated using the marginal spectrum of the IMF components.

14.3.1. Simulated signal: 1

The first simulated signal is represented mathematically as shown in Eq. 12.4. The time domain representation of the signal is also presented in Fig. 12.2. In this case the HF component of the signal has a constant frequency of 0.25 Hz and a constant amplitude of 0.3. For the LF component of the signal the frequency and the amplitude are fixed at 0.1 Hz and 0.2 respectively.

The squared deviation obtained in this case can be seen in Fig. 14.3, which shows that the minimum value is obtained at $S = 7$. Using this value for stoppage criterion the data was decomposed into IMF components as shown in Fig. 14.4. In Fig. 14.4, the y-axis (amplitude) for each plot is kept the same which indicates that only the first two components have significant amplitude. The frequency contents of the first four IMF can be seen from the marginal spectrum shown in Fig. 14.5. Figure 14.5 also shows the CF and the SDSE calculated using Eq. 11.2 and Eq. 11.3 respectively. From Fig. 14.5, it can be seen that the CF of the first two components matches with the frequency components present in the input signal. The other two components not only have lower frequency but also their power is also quite negligible as compared to the first two components.

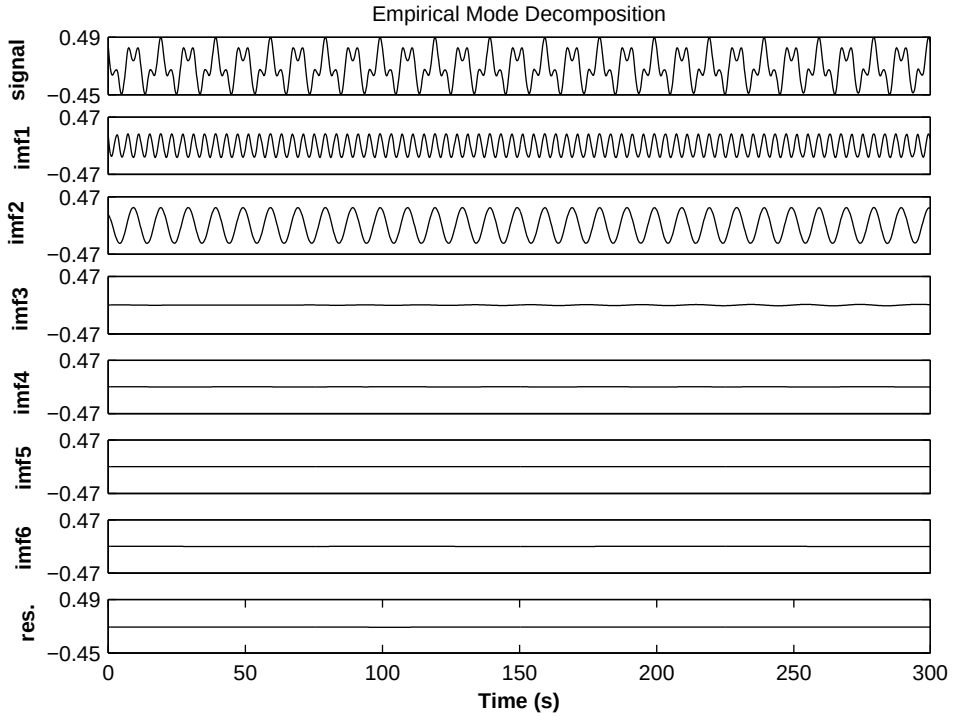

Fig. 14.4: IMF components obtained from the decomposition when the signal presented in Eq. 12.4 (simulated signal one) was used as the input to the IPFM model

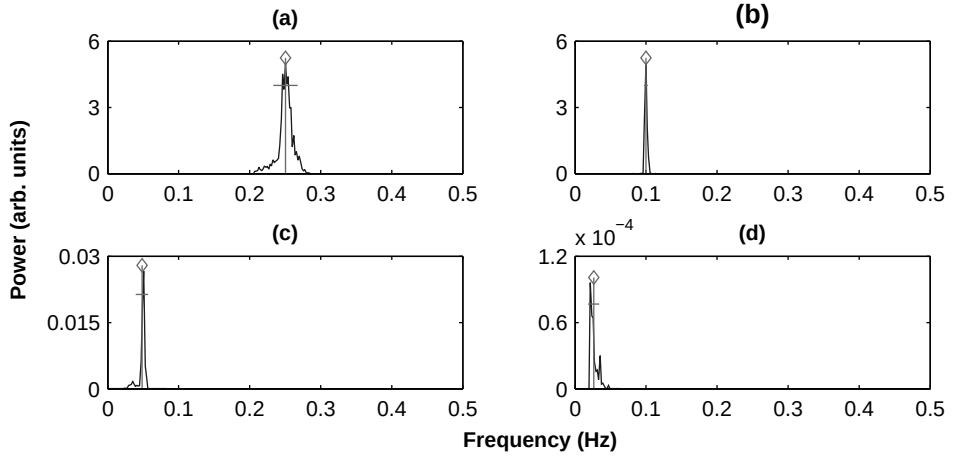

Fig. 14.5: Marginal spectrum of the first four IMF components ((a) component 1, (b) component 2, (c) component 3, (d) component 4) shown in Fig. 14.4. In each plot the diamond mark represents the CF and the horizontal line indicates the CF±SDSE. The CF and SDSE are calculated using Eq. 11.2 and Eq. 11.3 respectively

In Fig. 14.5, the marginal spectrum of IMF components five and six were not shown as these have even lower frequency and power associated with them. From the results presented in Fig. 14.4 and Fig. 14.5, it can be concluded that with the combination of the first two IMF components the input signal could be represented quite accurately.

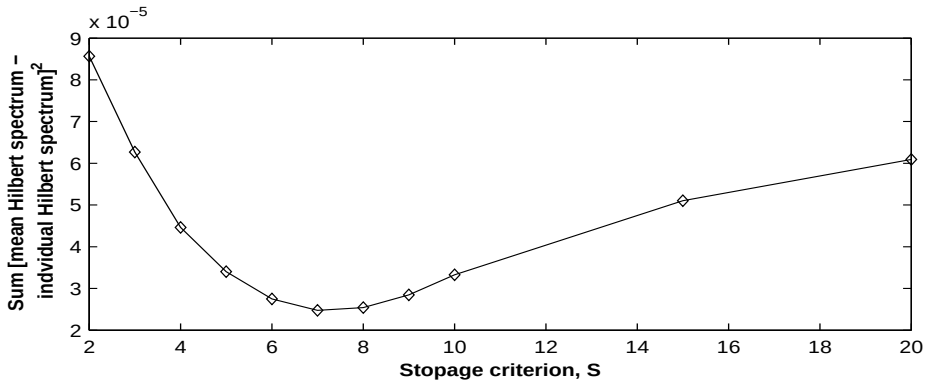

Fig. 14.6: Squared deviation obtained using the mean Hilbert spectrum and the individual Hilbert spectrum for the stoppage criterion S values of 2-10, 15 and 20 in the case of simulated signal two

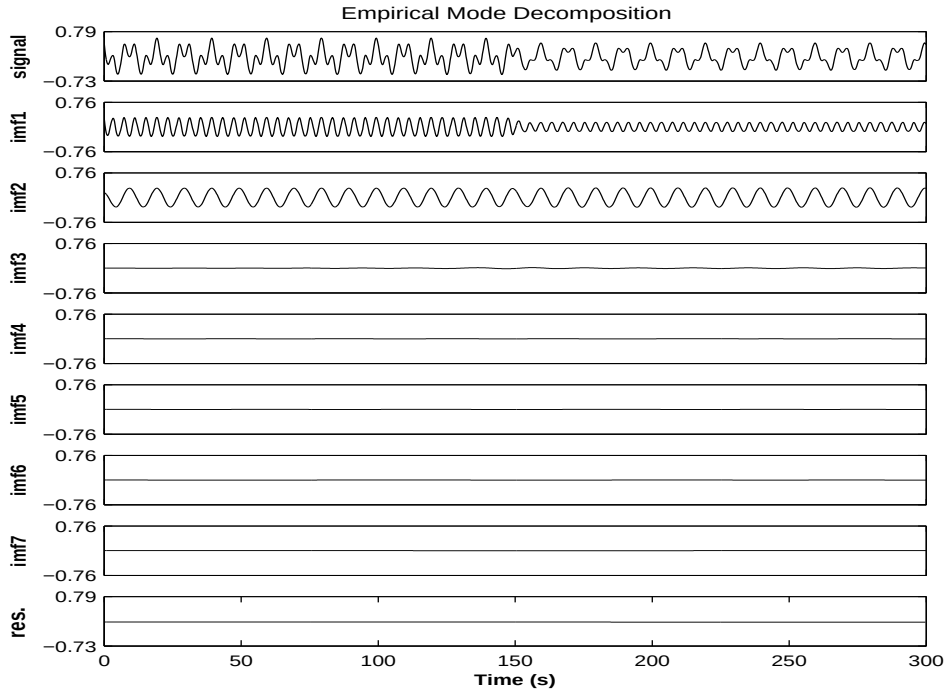

Fig. 14.7: IMF components obtained from the decomposition when the simulated signal two was used as the input to the IPFM model

14.3.2. Simulated signal: 2

The second signal was used to test the amplitude tracking capabilities of the analysis techniques. In this case the amplitude of the HF component of the signal was changed from 0.3 to 0.15 half way through the IPFM simulation. The LF component frequency and amplitude was kept constant at 0.1 Hz and 0.2 respectively. The time domain representation of the signal is presented in Fig. 12.5. First the squared deviation was calculated and the result from that is shown in Fig. 14.6. The minimum value was achieved at $S = 7$, therefore this was chosen as the stoppage criterion.

The IMF components obtained in this case are presented in Fig. 14.7. From Fig. 14.7, it can be seen that apart from the first two IMF components all other components have insi-

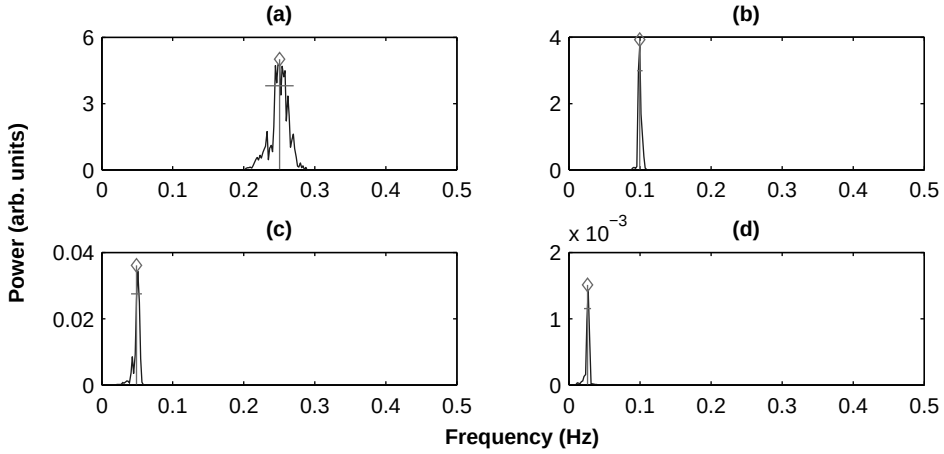

Fig. 14.8: Marginal spectrum of the first four IMF components ((a) component 1, (b) component 2, (c) component 3, (d) component 4) shown in Fig. 14.7. In each plot the diamond mark represents the CF and the horizontal line indicates the CF±SDSE. The CF and SDSE are calculated using Eq. 11.2 and Eq. 11.3 respectively

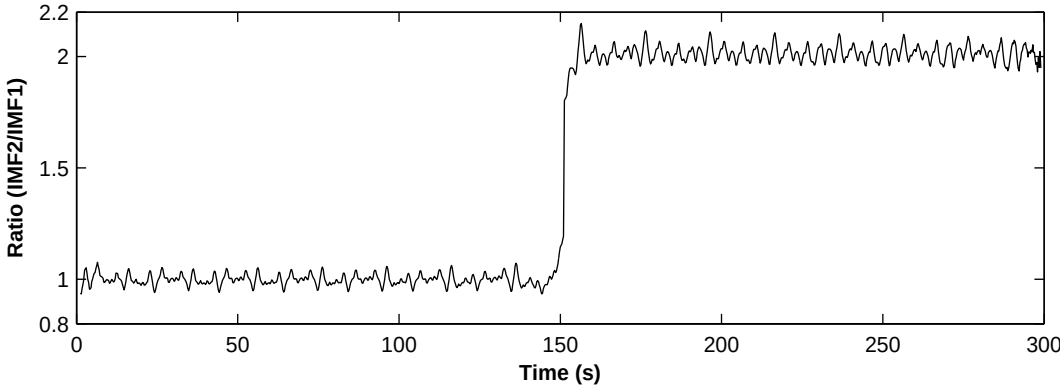

Fig. 14.9: Ratio of the first two IMF components for simulated signal two. The ratio values increase near the midpoint of the data representing a good match with the decrease in the amplitude of the high frequency component in the input signal

gnificant amplitude. The first IMF corresponds to the high frequency components of the signal and it also shows the change in the amplitude occurring at the mid way through the signal. The fact that the first two IMFs correspond to the two frequency components of the input signal can also be seen by the marginal spectrum of the first four IMFs shown in Fig. 14.8. The ratio between the amplitude of the first two IMF components is presented in Fig. 14.9 which also shows an increase near the midpoint of the data indicating a decrease in the amplitude of the first component. The amplitude Hilbert spectrum and the error index (see Eq. 14.25) related to the first two IMF components are presented in Fig. 14.10 and Fig. 14.11.

The instantaneous frequency was considered to be incorrect at positions where the error index was higher than twice the standard deviation of the error. These values were corrected by using model based interpolating scheme purposed by Paul *et. al.* [185]. But as these regions of incorrect instantaneous frequency were quite short therefore, after correction there was no significant change in the instantaneous frequency values.

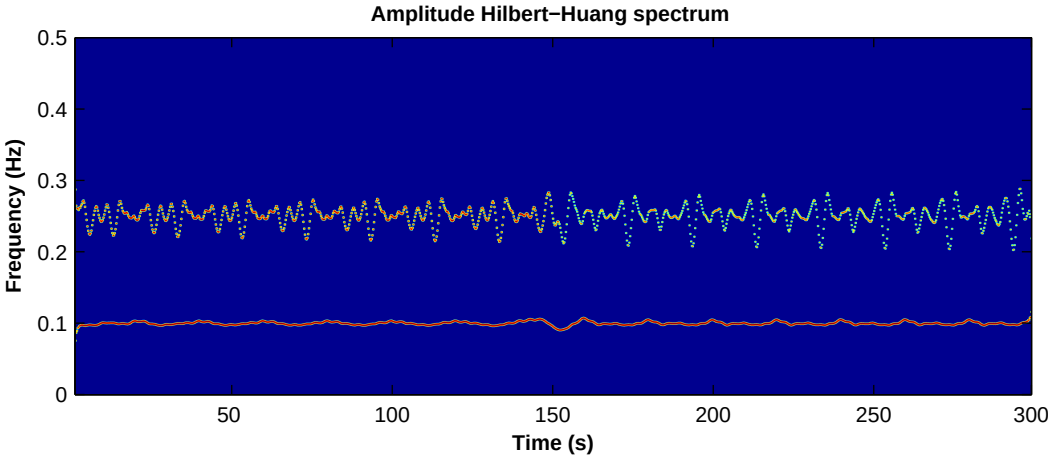

Fig. 14.10: Amplitude Hilbert Huang spectrum for the simulated signal two. The spectrum is smoothed using a 7×5 Gaussian filter for visualisation purposes

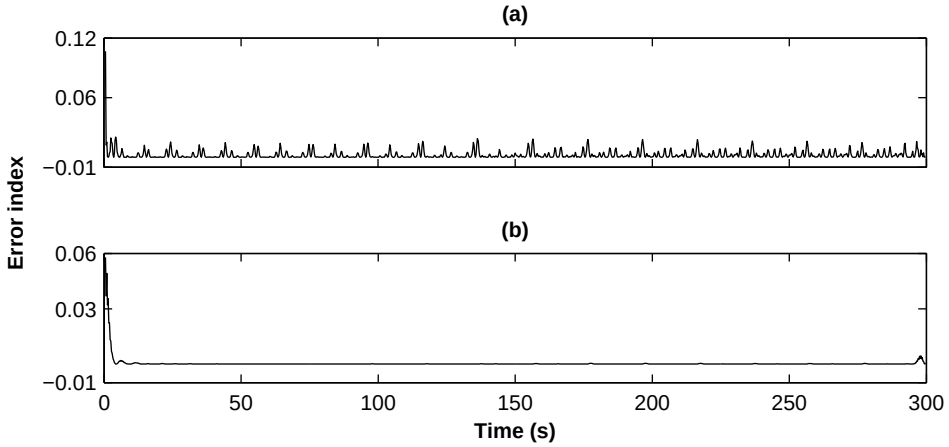

Fig. 14.11: Error index related to the instantaneous frequency; (a) error estimated for the first IMF of the simulated signal two; (b) error estimated for the second IMF component

14.3.3. Simulated signal: 3

In order to explore the frequency tracking capabilities of EMD and the Hilbert-Huang spectrum the third simulated signal consisted of two linear chrip components. The amplitude of both the components was set to unity. The initial frequency of the first component was 0.1857 Hz and the target frequency was chosen to be 0.3643 Hz. For the second component the initial and the target frequencies were 0.1343 Hz and 0.0557 Hz respectively. The time domain representation of the signal is presented in Fig. 12.8.

The squared deviation obtained by using different values of stoppage criterion S in the EMD decomposition is presented in Fig. 14.12. In this case the minimum squared deviation was achieved with the S value equal to eight. The signal was then decomposed into IMF components using this value of the stoppage criterion. The result of EMD decomposition is presented in Fig. 14.13. From Fig. 14.13 it can be seen that only the first two IMF components have significant amplitude. The fact that these two components can represent the input signal quite effectively can also be seen by looking at the mar-

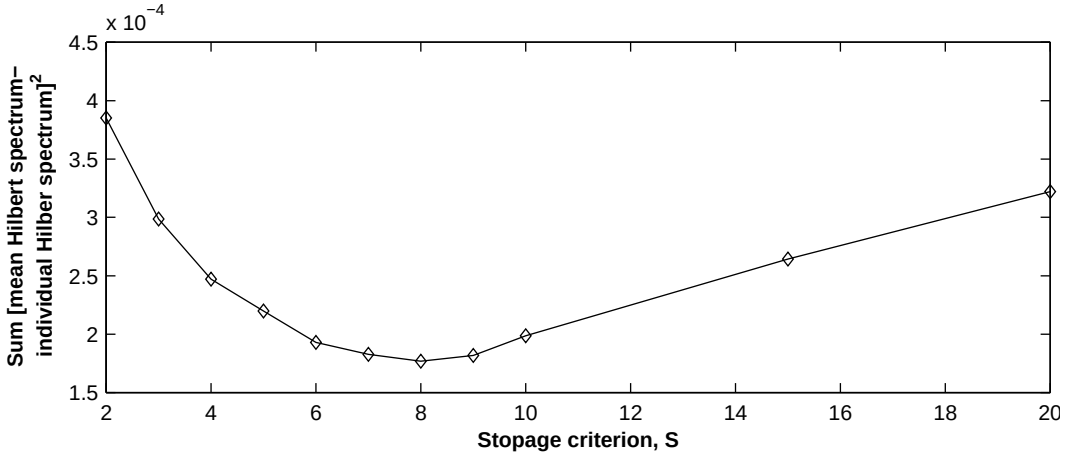

Fig. 14.12: Squared deviation obtained using the mean Hilbert spectrum and the individual Hilbert spectrum for the stoppage criterion S values of 2-10, 15 and 20 in the case of simulated signal three

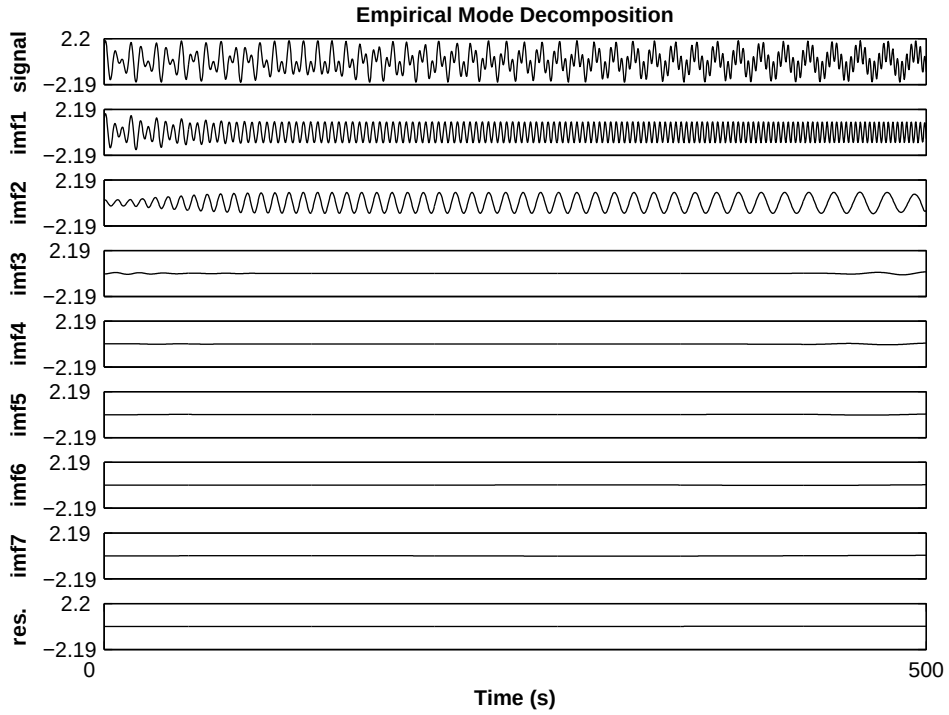

Fig. 14.13: IMF components obtained from the decomposition when the simulated signal three was used as the input to the IPFM model

ginal spectrum of the first four IMFs presented in Fig. 14.14. From the results presented in Fig. 14.14 it can be seen that IMF component three and even component four might have some contribution in the low frequency component of the input signal whose target frequency was set at 0.0557 Hz, but their contribution will be insignificant compared to that of IMF component two. Therefore, in this case as well only the first two IMFs will be used to represent the input signal. The change in the frequency of the two input signal components can be clearly seen in the amplitude Hilbert-Huang spectrum presented in Fig. 14.15. The error indexes associated with the first two IMF components calculated using Eq. 14.25 are presented in Fig. 14.16.

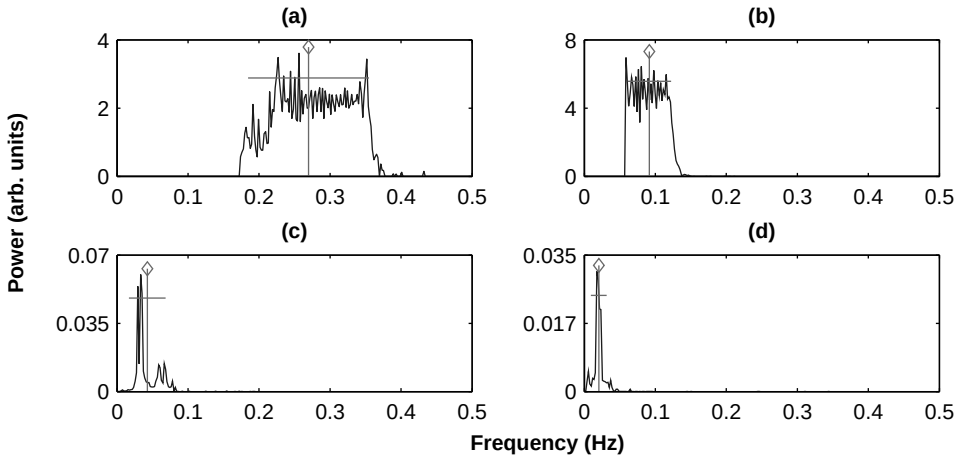

Fig. 14.14: Marginal spectrum of the first four IMF components ((a) component 1, (b) component 2, (c) component 3, (d) component 4) shown in Fig. 14.13. In each plot the diamond mark represents the CF and the horizontal line indicates the CF±SDSE. The CF and SDSE are calculated using Eq. 11.2 and Eq. 11.3 respectively

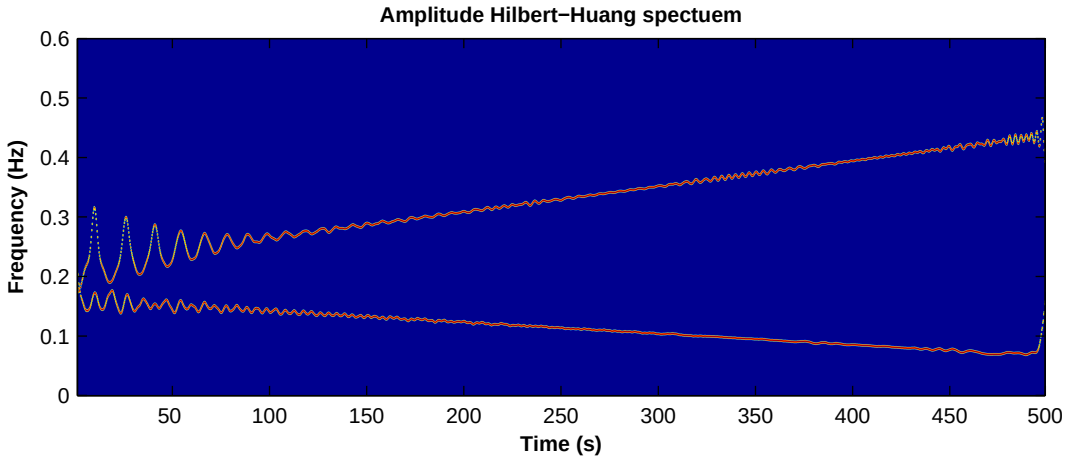

Fig. 14.15: Amplitude Hilbert Huang spectrum for the simulated signal three. The spectrum is smoothed using a 7×5 Gaussian filter for visualisation purposes

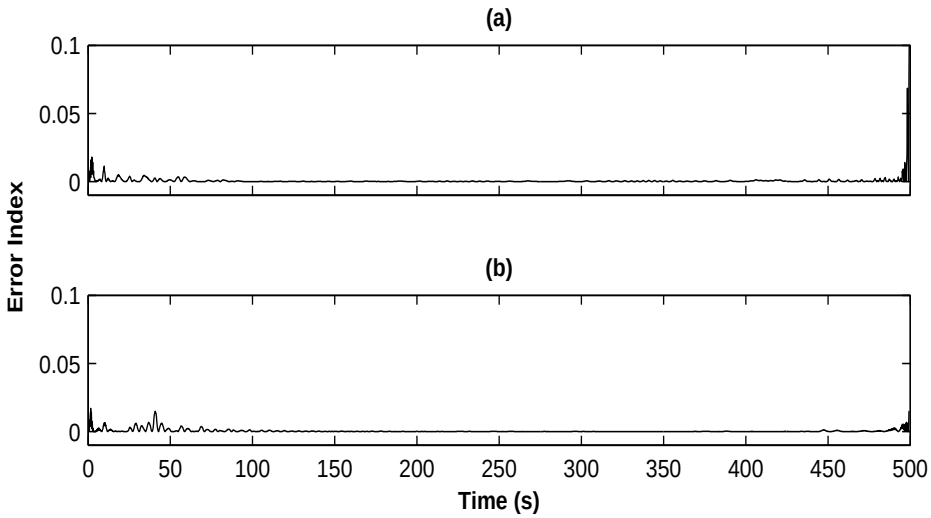

Fig. 14.16: Error index related to the instantaneous frequency; (a) error estimated for the first IMF of the simulated signal three; (b) error estimated for the second IMF component of the simulated signal three

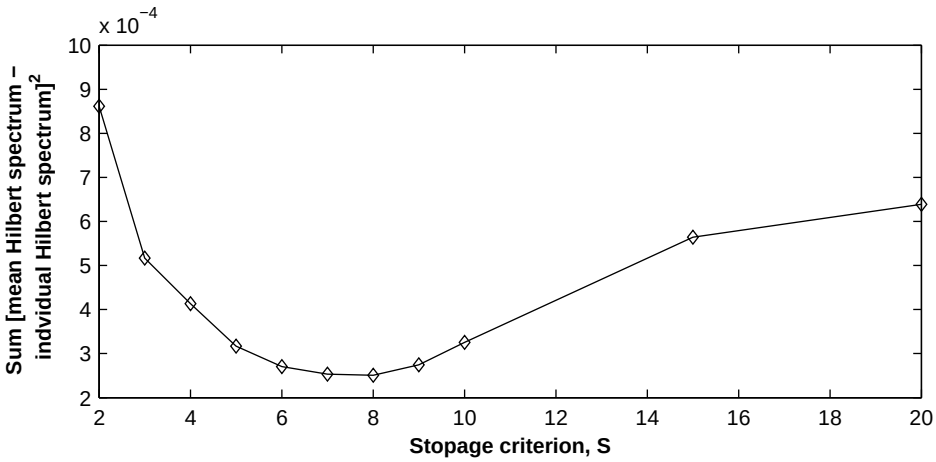

Fig. 14.17: Squared deviation obtained using the mean Hilbert spectrum and the individual Hilbert spectrum for the stoppage criterion S values of 2-10, 15 and 20 in the case of simulated signal four

From the results presented in Fig. 14.16 it can be seen that the error is quite close to zero for most of the time except at the beginning and the end where the error has increased slightly due the distortion caused by the end effect.

14.3.4. Simulated signal: 4

This simulated signal was used to validate the analysing techniques in the situation where both the frequency and amplitude of the signal components were changed simultaneously. Starting with the value of unity the amplitude of the LF component was dropped to half and that of the HF component was increased to two midway through the analysis. Similarly the frequency of the LF component was changed from 0.1 Hz to 0.12 Hz while the frequency of the HF component was changed from 0.25 Hz to 0.3 Hz. The time domain representation of this simulated signal is presented in Fig. 12.11.

The squared deviation from this case presented in Fig. 14.17 shows that the minimum value is obtained when the stoppage criterion S is equal to eight. The IMF components obtained from the decomposition of the signal are presented in Fig. 14.18. From Fig 14.18 it can be seen that the first two IMFs contains the major part of the signal this fact can also be seen by looking at the marginal spectrum of the first four IMF components presented in Fig. 14.19.

The change in the frequency of the two IMF components can also be seen from the Hilbert-Huang spectrum presented in Fig. 14.20. The error indexes related to the instantaneous frequency of the first two IMFs are shown in Fig. 14.21. The amplitude and frequency values for the two signal related components were corrected using the error index shown in Fig. 14.21. Figure 14.22 shows the ratio values calculated using the two signal related IMF components before and after the correction. The ratio values shown in Fig. 14.22 remain quite close to the theoretical value of one and one-fourth in the first

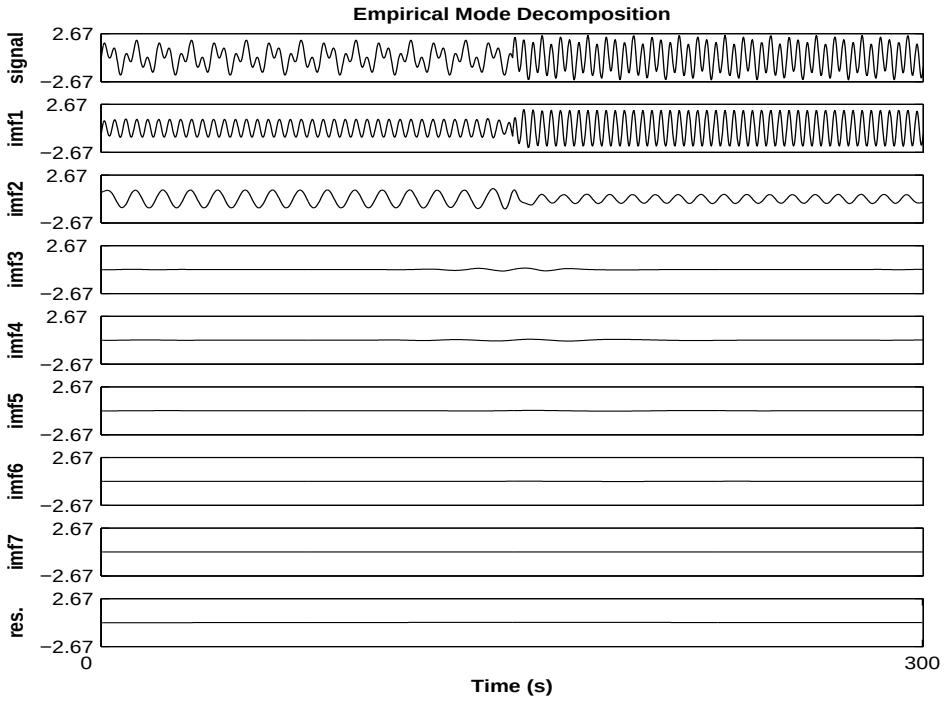

Fig. 14.18: IMF components obtained from the decomposition when the simulated signal four was used as the input to the IPFM model

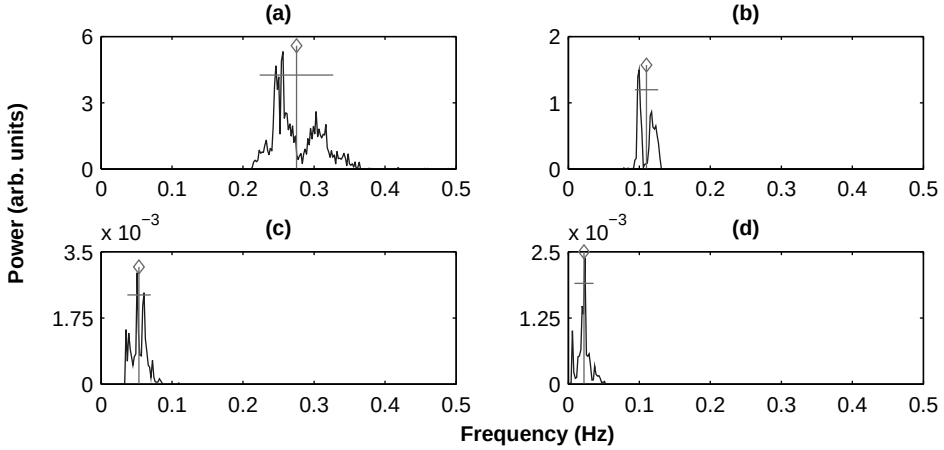

Fig. 14.19: Marginal spectrum of the first four IMF components ((a) component 1, (b) component 2, (c) component 3, (d) component 4) shown in Fig. 14.18. In each plot the diamond mark represents the CF and the horizontal line indicates the CF±SDSE. The CF and SDSE are calculated using Eq. 11.2 and Eq. 11.3 respectively

and second half of the data. The large fluctuations present in the uncorrected ratio values approximately at the midway through the data represents the time at which the amplitudes and the frequencies of the two components were changed. This rapid transition has caused more error in the calculation a fact also indicated by the large error index values obtained at the same location for the two IMF components (see Fig. 14.21). These fluctuations have been reduced considerably by correcting the amplitudes of the two IMF components using the error index values as shown by the ratio values after correction presented in Fig. 14.22.

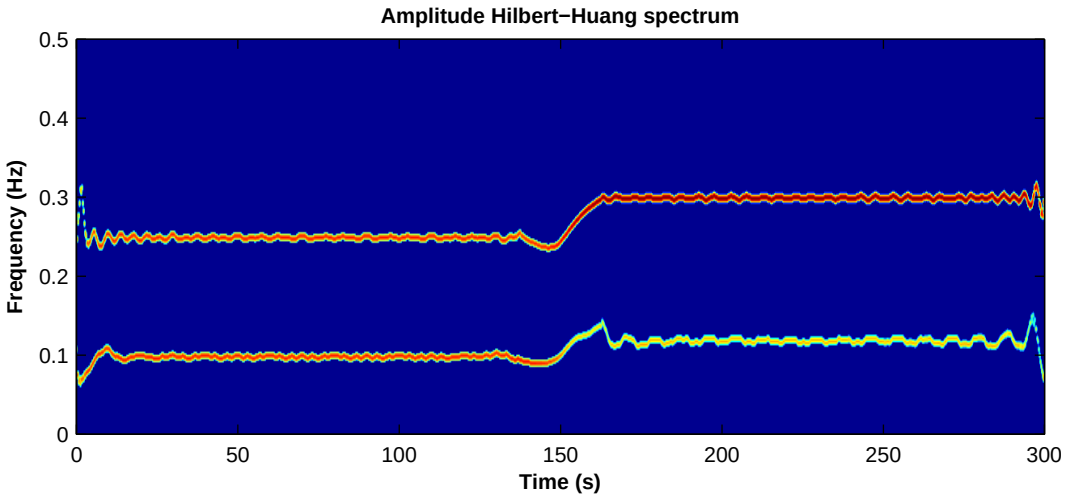

Fig. 14.20: Amplitude Hilbert Huang spectrum for the simulated signal four. The spectrum is smoothed using a 7×5 Gaussian filter for visualisation purposes

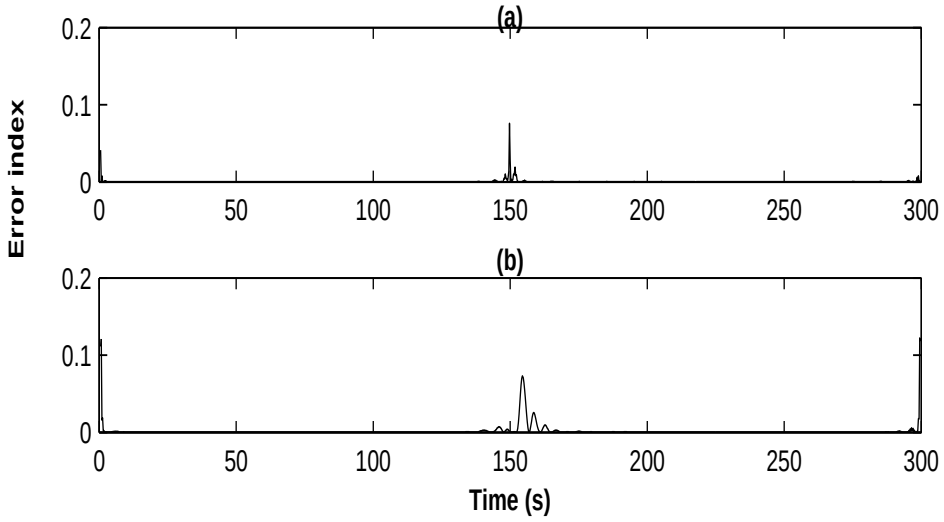

Fig. 14.21: Error index related to the instantaneous frequency; (a) error estimated for the first IMF of the fourth simulated signal; (b) error estimated for the second IMF component of the fourth simulated signal

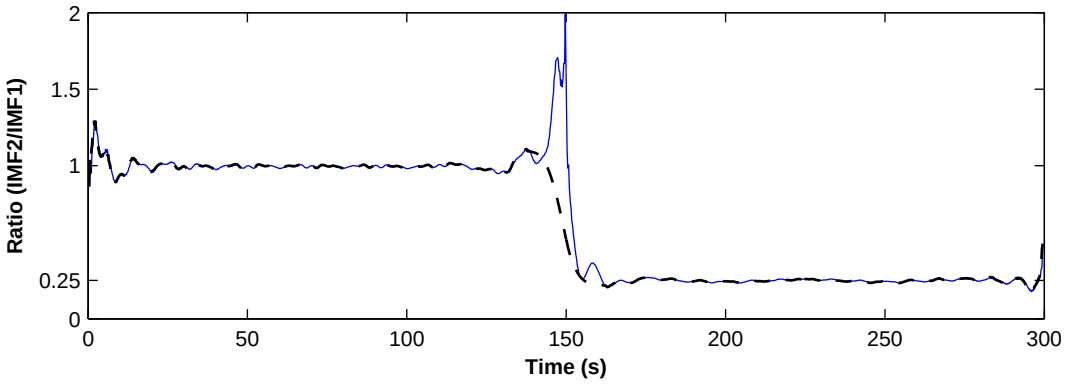

Fig. 14.22: The corrected (dashed black) and uncorrected (solid blue) ratio of the first two IMF components for the fourth simulated signal.

The results from the analysis of these simulated signals provided some evidence of the capabilities of the Hilbert-Huang spectrum in analysing stationary as well as non-stationary signals. But this study also provided another important result, as discussed before (see section 8.4.1) the HT signal provides a better representation for the HRV signals by avoiding the spurious harmonics that occurs when HR representations is used. Some evidence of this has been provided before with the use of power spectral analysis, see section 8.5.1. The lack of spurious harmonics in HT representation could also be confirmed by comparing the result of EMD decomposition for simulated signal one (see Fig. 14.4), which consisted of two constant frequency components, with the result presented by Echeverria *et. al.* [167] for EMD decomposition of a signal again with two constant frequency components. In their result Echeverria *et. al.* found three components of significant amplitude. The first two components were related to the input signal components but the third one was due to the harmonic interference component which can occur in all the possible combinations of the main input frequencies [186]. By using heart timing signal for HRV representation this harmonic component is avoided in this study which should provide more accurate representation of the original modulating signal. The other components generated by the EMD decomposition of the simulated signals have insignificant amplitude and could be considered as an artefact due to spline fittings used in the sifting process of the EMD and/or due to the leakage caused by the use of mean of the envelope instead of the local mean in defining the IMF [176].

This study of simulated signals has provided a solid frame work just before the analysis of the data that were collected from the locally anaesthetised patients during this study using the Hilbert-Huang spectrum technique. These results will be the subject of the next section.

14.4. Results of Empirical Mode Decomposition (EMD) analysis of locally anaesthetised patients data

In the analysis of HRV data from locally anaesthetised patients the first step was to obtain the confidence interval for EMD decomposition. For this purpose the signals were decomposed in the same manner as the simulated signals using values of 2-10, 15 and 20 for the stoppage criterion S. The squared deviation results obtained from all fourteen patients included in this study are presented in Fig. 14.23. Each plot in Fig. 14.23 contained results from two patients one presented in blue colour while the other one presented in black colour. The values in Fig. 14.23 have been scaled for easier visualisation but this has no effect on the general trend present in the individual data.

From the results shown in Fig. 14.23 it can be seen that the minimum value of squared

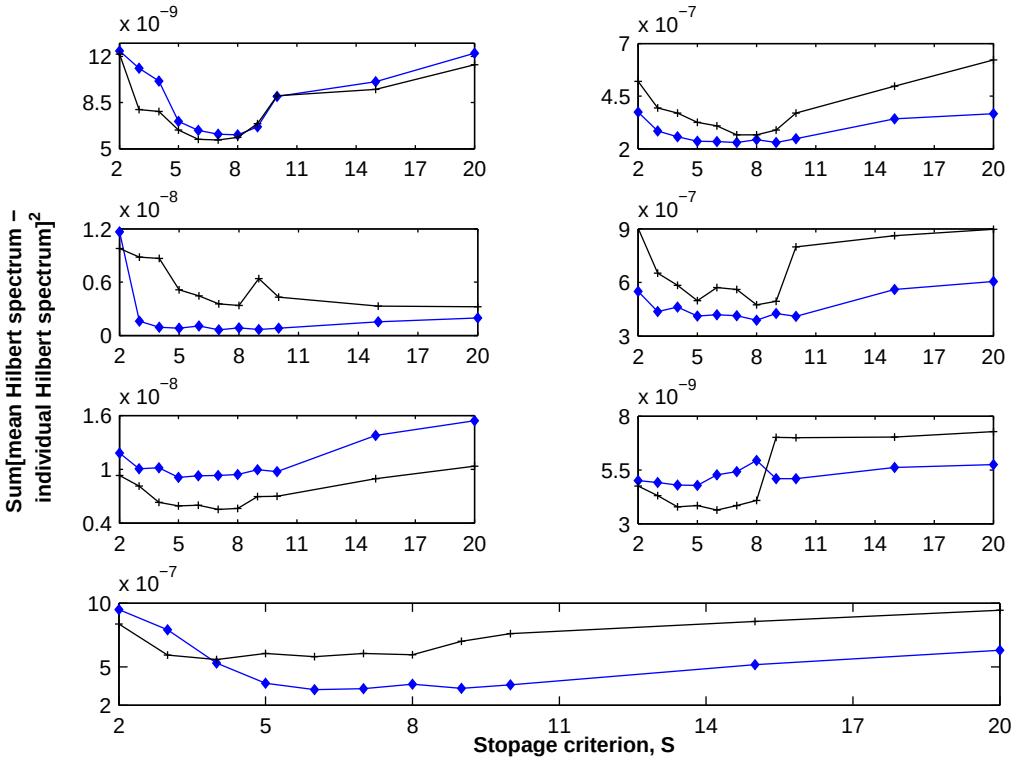

Fig. 14.23: Squared deviation obtained using the mean Hilbert spectrum and the individual Hilbert spectrum for the stoppage criterion S values of 2-10, 15 and 20 in the case of heart rate data from locally anaesthetised patients. Each plot shows the results obtained from two patients one in black colour and the other in blue colour

deviation has occurred between S values of 4 to 9 which is quite close to the interval suggested by Huang *et. al.* [181], 4 to 8. In fact only in one of our data sets the minimum has occurred at $S = 9$. For the rest of the data sets the minimum has occurred between the values of 4 to 8.

Using the information obtained from these results, each data set was decomposed using the S value which gives the minimum of the squared deviation. As an example, the first seven IMF components obtained from the HRV signal of a locally anaesthetised patient are presented in Fig. 14.24. In the case of this signal the decomposition obtained twelve IMF components in total but only the first seven are shown in Fig. 14.24 as the remaining components (IMF 8 to IMF 12) have insignificant amplitude compared to the original data. The first few IMF components can represent the major part of the signal adequately as shown in Fig. 14.25. Figure 14.25 (a) shows the difference between the original signal and the combination of the first five IMF components, while Fig. 14.25 (b) shows the difference between the original signal and the first six IMF components. Figure 14.25 uses the same y-axis scale as used for the original signal in Fig. 14.24 for comparison purposes. In both cases the residue signal is not only quite low in amplitude but also consists of very slow oscillations. After obtaining the IMF from data decomposition, normalisation of the IMF components was carried out as described before (see

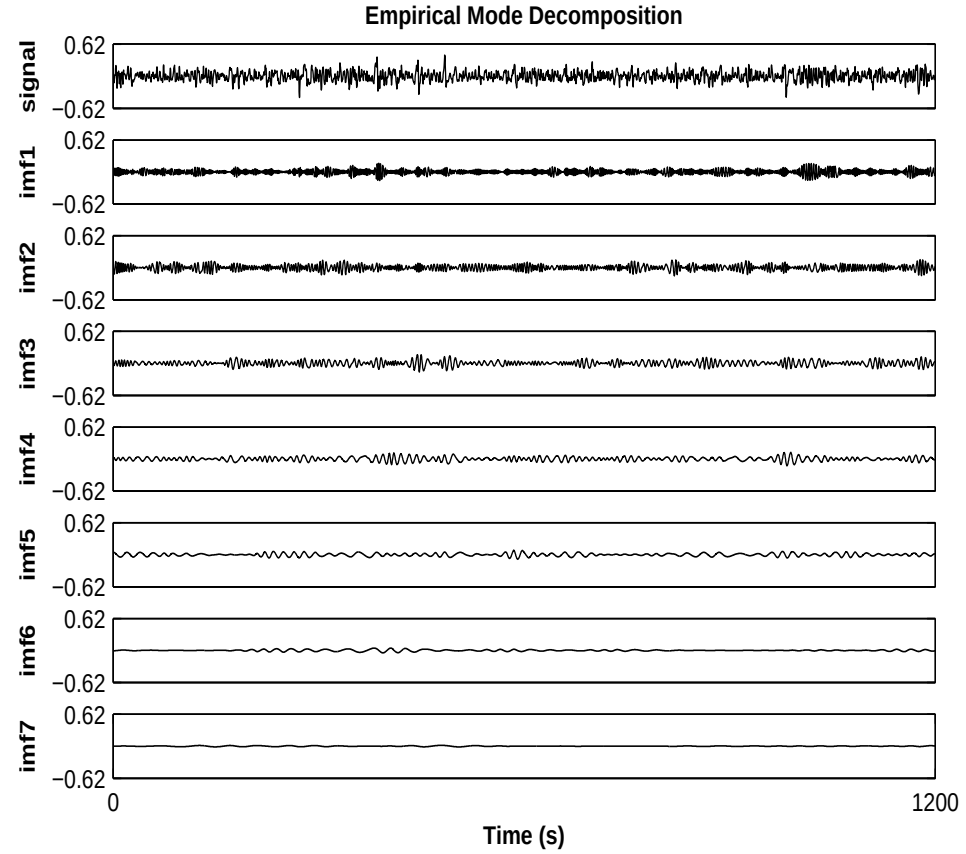

Fig. 14.24: First seven IMF components for a segment of HRV data obtained from a locally anaesthetised patient

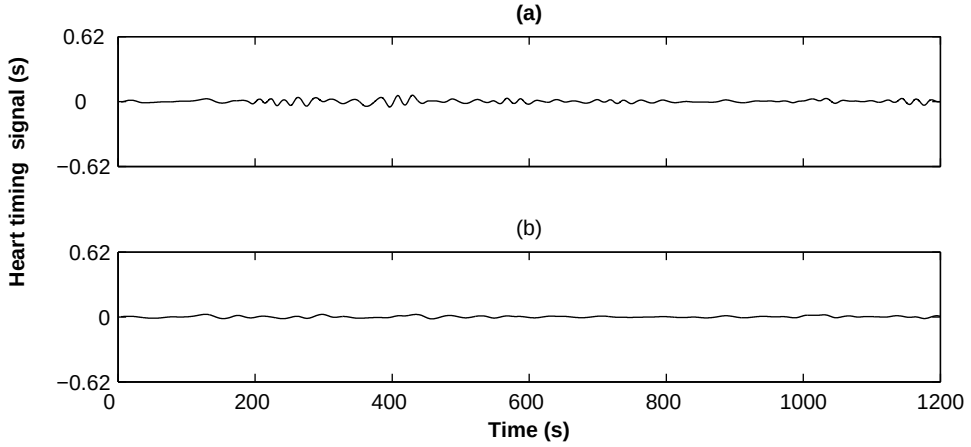

Fig. 14.25: (a) The difference between the original HRV signal and the combination of the first five IMF components; (b) The difference between the original signal and the combination of first six IMF components

section 14.2.5) and the error index associated with the instantaneous frequency was estimated using Eq. 14.25. The error index associated with the first six IMF components shown in Fig. 14.24 is presented in Fig. 14.26. From the results presented in Fig. 14.26 it can be seen that apart from the few short intervals, the error in instantaneous frequency is quite low for all the IMF components. The method mentioned above (see section 14.3.2) and used with the simulated signals for the correction of instantaneous frequency was

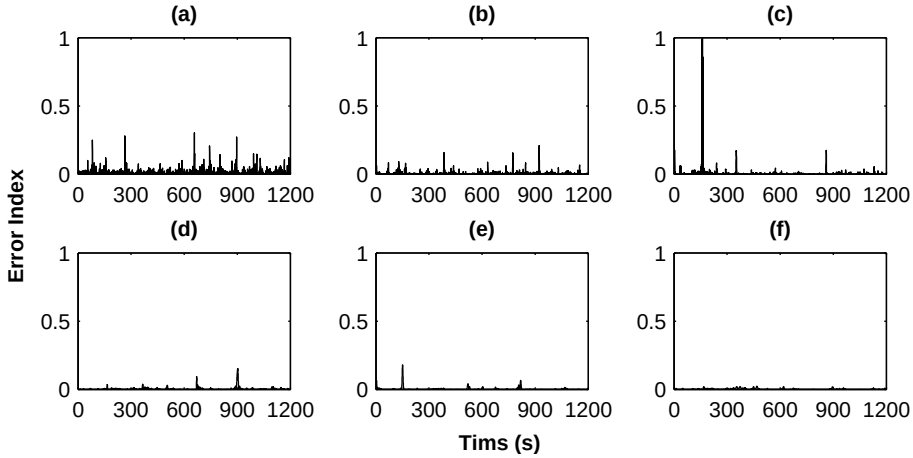

Fig. 14.26: (a)-(f) Error index related to the instantaneous frequency for the first six IMF components shown in Fig. 14.24

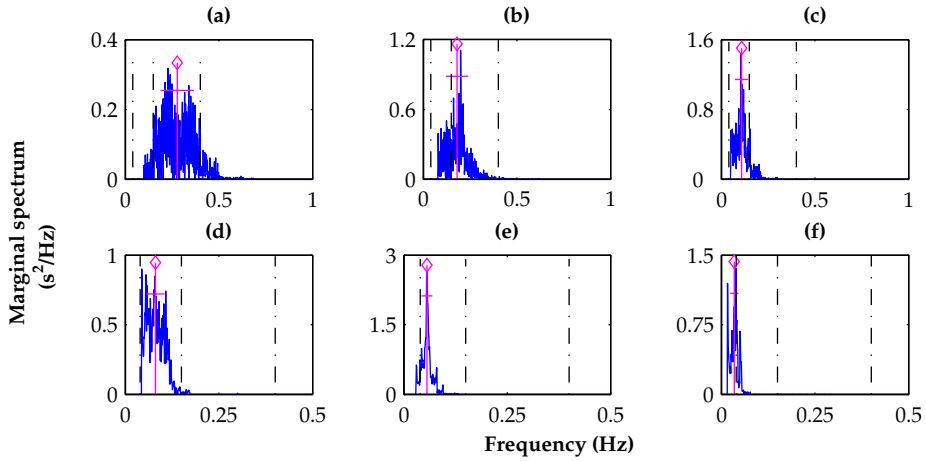

Fig. 14.27: (a)-(f) Marginal spectrum of the first six IMF components from the first five minute data segment of a locally anaesthetised patient. The blue line represents the marginal spectrum and the dash dotted black lines represent the traditional LF and HF rigid a priori frequency bands. In each plot the diamond mark represents the CF and the magenta horizontal line indicates the CF±SDSE. The CF and the SDSE are calculated using see Eq. 11.2 and Eq. 11.3

also used in these small numbers of regions where the error in the instantaneous frequency was considered to be higher than acceptable. As the regions with high error index were quite short and infrequent, the correction did not have a significant overall effect on either the instantaneous frequency or the amplitude of the IMF components.

The IMF components were assigned as the low frequency (0.04 - 0.15 Hz) or the high frequency (0.15 - 0.4 Hz) part of the signal by making use of the power spectrum and calculating the CF and the SDSE through Eq. 11.2 and Eq. 11.3 respectively. The marginal spectrum was obtained for every five minutes of data and the IMF component was assigned to a particular band if the CF lay within the band limits and the CF±SDSE value was not more than twenty percent outside the boundary of that band. The marginal spectrum of the first six IMF components from two different five minute data sets are presented in Fig. 14.27 and Fig. 14.28. The spectrum in Fig. 14.27 indicates that the first

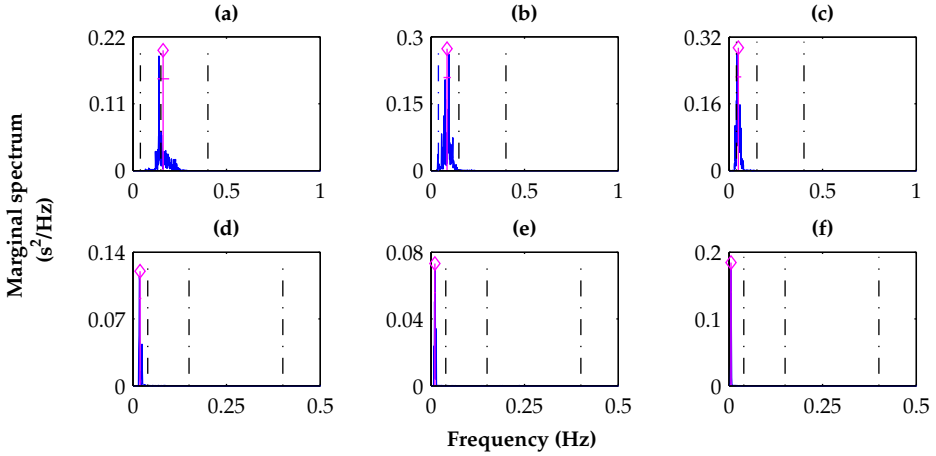

Fig. 14.28: (a)-(f) Marginal spectrum of the first six IMF components from second five minute data segment of a locally anaesthetised patient. The blue line represents the marginal spectrum and the dash dotted black lines represent the traditional LF and HF rigid a priori frequency bands. In each plot the diamond mark represents the CF and the magenta line indicates the CF±SDSE. The CF and the SDSE are calculated using see Eq. 11.2 and Eq. 11.3

two IMF components belong to the HF band and the next three belong to the LF band. The situation is different in case of Fig. 14.28 where the first component belong to the HF band and the second and third component make up the signal in the LF region.

Figure 14.29 presents the amplitude Hilbert-Huang spectrum obtained from the data of a locally anaesthetised patient. Figure 14.29 (a) represents the spectrum of the data obtained from the patient fifteen minutes before the block (application of the anaesthetic drug) whereas, part (b) represents the spectrum of the data during the block and part (c) represents the spectrum of the data obtained fifteen minutes after the block. By comparing the three spectrums shown in Fig. 14.29, it can be seen that the components show slightly less frequency deviation in the spectrum during and after the block (part (b) and part (c)) as compared to the spectrum before the block (part (a)). These spectrums also indicate a slight shift in the frequency during and after the block as compared to before the block. The change in the signal components can also be seen by comparing the marginal spectrum shown in Fig. 14.30, for the same data segments which are used to obtain the AHHS presented in Fig. 14.29. The difference in the signal energy before, during and after the block can be seen by looking at the Instantaneous Energy (IE). The IE presented in Fig. 14.31 was calculated using Eq. 14.22. The data segments from the locally anaesthetised patient which were used for the IE values presented in Fig. 14.31 were the same as the ones used for AHHS and marginal spectrum presented in Fig. 14.29 and Fig. 14.30 respectively. From Fig. 14.31 it can be seen that the IE values are quite low during and after the block as compared to the IE values calculated from the data before the application of the block. The mean values calculated from the IE for the three segments were 0.0209, 0.0156 and 0.0063 respectively.

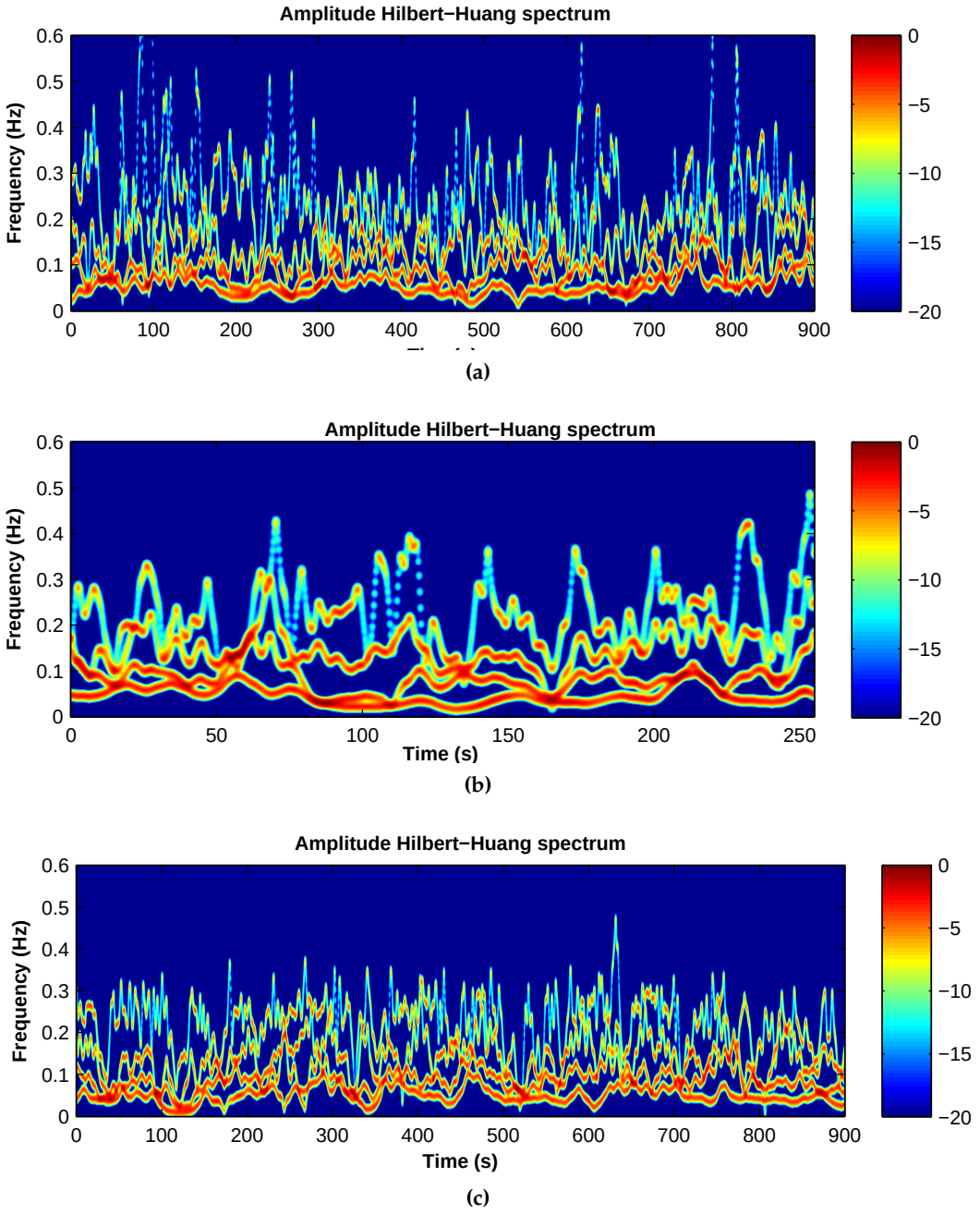

Fig. 14.29: Amplitude Hilbert-Huang spectrum for the data obtained from a locally anaesthetised patient; (a) spectrum of the data obtained from the patient 15 minutes before the application of the block; (b) spectrum of the data obtained during the block application; (c) spectrum of the data 15 minutes after the application of the block. Each spectrum presented in this figure is noramlised with respect to the maximum amplitude present in the data segment

After the assignment of the IMF components into the HF and the LF bands the HRV parameters ($^{LF}/_{HF}$ ratio and power related to the two bands in absolute and normalised units) were estimated. These values were averaged over a period of one minute. The parameters obtained from one of the locally anaesthetised patients included in this study are presented in Fig. 14.32. As before, by looking at the ratio values presented in Fig 14.32 it can be seen that after the block the ratio shows a peak and then decreases to a minimum value which is similar to the observations made in the previous chapters (see chapters 11,

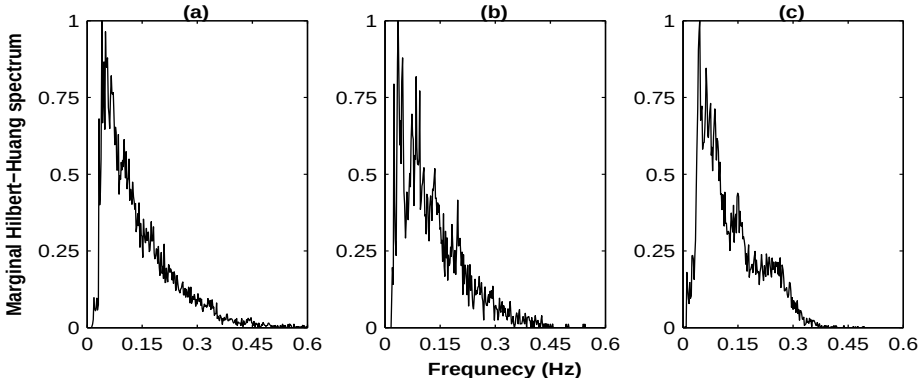

Fig. 14.30: Marginal spectrum for the data obtained from a locally anaesthetised patient; (a) spectrum for the data fifteen minutes before the block; (b) spectrum for the data between the block; (c) spectrum for the data fifteen minutes after the block

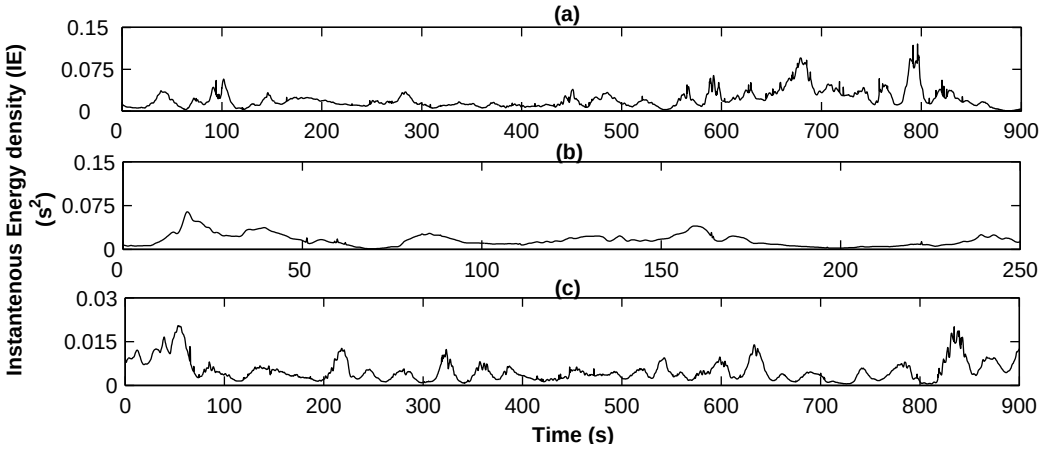

Fig. 14.31: Instantaneous Energy (IE) density level for the same three segments of data obtained from a locally anaesthetised patient which were used to generate AHHS shown in Fig. 14.29

12 and 13) using other techniques of analysis. The resolution achieved by this method was much better than that achieved by the non-parametric (Fourier based) method and being a data driven adaptive decomposition method it also avoided the problem of model order estimation as faced in the parametric method used earlier (see chapter 11). The results obtained from the EMD analysis of all the patients included in this study are presented in Appendix E. Similar to previous results the changes in the power related to the two bands is much more prominent when presented in normalised units, Fig 14.32 (e) for the HF component and Fig 14.32 (f) for the LF component. These parameters showed the expected changes with normalised HF power increasing and the normalised LF power decreasing after the application of the block. In case of EMD each five minute segment of data could have a different number of IMF components associated with the LF and the HF band (see Fig. 14.27 and Fig. 14.28) because of this reason the frequency parameters could not be compared like other power related parameters. Frequency related parameters could only be compared for individual IMF components. But this comparison will

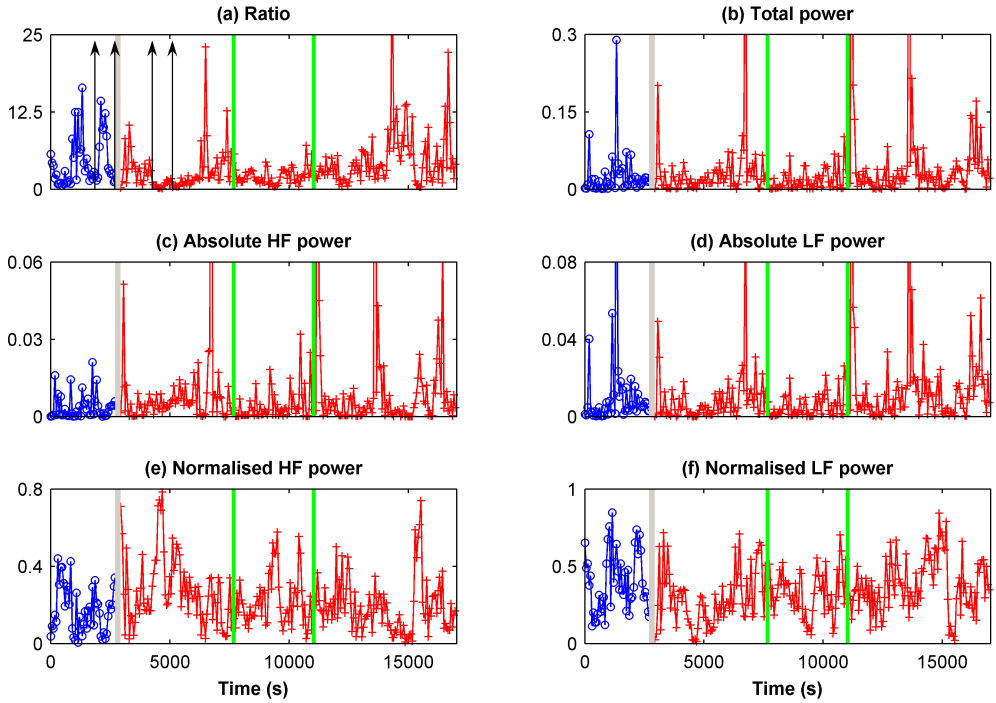

Fig. 14.32: Results obtained from the EMD analysis of a patient undergoing local anaesthetic procedure. In each plot the grey vertical block represents the time of block (anaesthesia) application and the green vertical lines represent start and end of the surgery. The pair of vertical arrows in part (a) show the data segment before and after the application of block which was used in statistical analysis. Lines in blue and red colour represent the parameter values before and after the block application respectively. The units on y-axis for the plots showing power are s^2/Hz and for the plots showing frequency values is Hz

make sense only if physiological interpretation of each IMF component could be found. This difficulty could also be noted from the fact that all the HRV studies, using EMD analysis [167, 170, 168], that were found in the literature have made no quantitative comparison of frequency parameters.

14.5. Statistical test for EMD analysis of HRV data from locally anaesthetised patients

Statistical tests were also carried out on the parameters estimated using the EMD analysis technique. As before, Wilcoxon signed rank sum test was used to check if the values after the block were significantly different than the values before the application of the block. In the case of the EMD analysis there was more than one frequency value associated with both the HF and the LF band of the signal therefore, in this case only the parameters related to the power of the signal *i.e.* LF/HF ratio, total power (PT), power related to the HF band of the signal (HF_p), the LF band amplitude (LF_p) and the HF and LF normalised power (HF_{Pnorm},LF_{Pnorm}) were compared to see if their values differ significantly after the

Table 14.1.: Statistical test results obtained from EMD analysis of data from patients undergoing local anaesthesia. From each patient six parameters, $^{LF}/_{HF}$ ratio, total power (PT) and high and low frequency band power in absolute and normalised units (HF_P, HF_{Pnorm}, LF_P, LF_{Pnorm}), values before and after the anaesthetic block were compared. Significance level was defined as $p < 0.05$

Patno.	$^{LF}/_{HF}$ ratio	PT	HF_P	LF_P	HF_{Pnorm}	LF_{Pnorm}
1	<0.001	0.008	0.008	<0.001	<0.001	<0.001
2	0.026	0.048	0.847	0.018	0.083	0.041
3	<0.001	0.004	<0.001	0.135	<0.001	<0.001
4	<0.001	<0.001	0.847	<0.001	0.002	0.001
5	0.037	0.002	0.012	0.296	0.103	0.034
6	<0.001	0.808	<0.001	0.015	<0.001	<0.001
7	<0.001	0.015	0.208	<0.001	<0.001	<0.001
8	<0.001	0.002	0.041	<0.001	<0.001	<0.001
9	0.978	0.855	0.380	0.806	0.524	0.599
10	<0.001	0.004	0.389	<0.001	<0.001	<0.001
11	<0.001	0.421	<0.001	<0.001	<0.001	<0.001
12	0.005	0.095	0.359	0.022	0.005	0.007
13	<0.001	0.454	0.055	0.107	0.007	0.005
14	0.007	<0.001	0.350	<0.001	0.003	0.003

introduction of the anaesthetic drug. The results obtained from the statistical analysis of these parameters are presented in table 14.1. The statistical results presented in table 14.1 are summarised in table 14.2. From the results presented in table 14.2 it can be seen that the EMD analysis has been able to detect significant changes in the ratio values after the application of the anaesthetic drug in thirteen out of the fourteen patients included in this study. These results indicate that the EMD method has been able to detect dynamical changes occurring in the HRV signals in more patients than the parametric, the non-parametric and the SPWVD method. The number of significant changes observed in the

Table 14.2.: Summary of the statistical test results obtained from the EMD analysis of the data from locally anaesthetised patients. $^{LF}/_{HF}$ ratio cell indicates the total number of cases showing significant changes after the block. For all other parameters the first value indicates the number of cases where the parameter values have shown significant changes while the second value indicates the cases where the parameter values have shown significant changes simultaneously with the $^{LF}/_{HF}$ ratio changes

LF_{amp}/HF_{amp}	PT	HF_P
13	9, 9	6, 6
LF_P	HF_{Pnorm}	LF_{Pnorm}
10, 10	11, 11	13, 13

$^{LF}/_{HF}$ ratio values are same as detected by the CWT method (see table 12.2).

The EMD technique could be preferred over other methods of analysis because by using data driven basis it produces much more compact representation of the signal as compared to the other analysis methods which uses fixed basis for signal decomposition. Also, the components produced by EMD method could provide better understanding of the physical phenomena being studied as compared to the representation obtained from other analysis methods. Another advantage of EMD technique is that it is computationally more efficient than the other time-frequency analysis method used in this study.

14.6. Summary

In this chapter the EMD decomposition technique along with the Hilbert transform was used to obtain the time-frequency distribution of the data obtained from the locally anaesthetised patients. This technique is unique from the other methods of time-frequency analysis as it is adaptive in nature and uses the characteristics of the data being analysed to obtained the components rather than the fixed basis that are usually employed in other techniques. This results in more compact and usually more physically meaningful components. In the literature this technique has shown to provide much better results especially in analysis of non-stationary and nonlinear data [176]. These characteristics are usually encountered in the HRV signal analysis, therefore EMD was used in this study as well. EMD analysis has been able to detect changes in the $^{LF}/_{HF}$ ratio (often used as a marker of sympathovagal balance) after the application of anaesthetic block in more patients (thirteen out of fourteen) as compared to parametric, nonparametric (nine out of fourteen see table 11.2 and 11.4) and SPWVD (ten out of fourteen see table 13.2) analysis. The results obtained by EMD, in terms of $^{LF}/_{HF}$ ratio changes, are the same as those obtai-

ned by the CWT method (see table 12.2). EMD provides better resolution than the other methods which is quite beneficial in the analysis of transient changes occurring during the course of the study.

However, a major drawback in this case is the lack of well defined theoretical base of the technique itself. This means it is not straight forward to justify the goodness of the decomposition. In this study a systematic approach was used to perform the analysis step by step in order to obtain a reasonable data representation. Simulated signals with well known characteristics were used to validate the method of decomposition and the extraction of information from the decomposed signal components.

15

Comparison and discussion

15.1. Introduction

In this chapter discussion regarding the main aspects of the analysis methods used in this study will be presented.. The method used for defining the variable boundaries related to the LF and the HF band of the HRV signal and the different frequency domain analysis methods will be compared with other relevant studies published in the literature. Also, general discussion and comparison of the results obtained from the analysis of the HRV data acquired from locally anaesthetised patients will be presented. The assumptions made regarding the changes in the HRV parameters after the application of the block will be validated against other published results.

15.2. Variable boundary definition

In many studies the HRV parameters for the LF and HF region are obtained directly from the HRV signal without taking any kind of respiration estimation into account [131]. Even though the traditional (fixed) boundaries of the two components (LF and HF) are define based on the fact that the physiological mechanisms related to the LF and the HF band confined to these ranges in normal health people most of the time. It is well documented that respiratory effect does not necessarily be confounded to the fixed limits defined for the HF band of the signal. For instance, in resting condition the breathing rate could becomes lower then 0.15 Hz, under certain activity such as verbal conversation the respiration pattern could becomes highly irregular [187] or during exercise the respiration rate could becomes higher than 0.4 Hz [188]. In such situations the parameters estimated from the HRV signal alone, would not be able to provide correct estimate of the physiological phenomena being studied. Therefore is it strongly recommended that respiration information should be taken into account during HRV analysis [42, 189].

In literature different approaches have been proposed for the estimation of boundaries related to the HF band of the HRV signal using information obtained from the respira-

tion signal. However, because of the way these methods are defined they could not be considered to represent a general solution. Some of these approaches are:

- Bailón *et. al*. [190] have used smoothed-pseudo Wigner-Ville distribution (see section 13.2.5) for time-frequency analysis of HRV signals and used the rate of change in respiration frequency to control the length of time smoothing window that is used in this analysis technique. The main drawback of this technique is that it might not be applicable with other frequency analysis methods.

- Other authors have centred the HF band on the highest peak in the spectrum of either the estimated or the measured respiration signal and the range of the HF band was defined as peak frequency$\pm$0.05 Hz [144], peak frequency$\pm$0.125 Hz [188], frequency$\pm$0.1 Hz [191] and 0.65*peakfrequency to 1.35*peak frequency [192]. All these definitions lack strict mathematical justification and represents author's choice for a particular analysis. For instance, peak frequency$\pm$0.125 Hz has been used in stress testing using HRV. The 0.125 Hz on both side of the peak frequency was chosen to match the bandwidth of the variable HF component to the bandwidth of the standard/fixed HF component. The LF component was defined using the standard range (0.04-0.015 Hz). In this study in most cases the respiration frequency was quite high, which allows the application of this particular definition of HF range but if the peak respiration frequency goes below 0.275 Hz then the lower boundary of the HF band will be below the upper boundary defined for the LF region. This will means that under normal breathing rate the HF band will mostly extend below 0.15 Hz and maybe even cover most of the LF region. The other definitions mentioned here will have similar problems as they all take only the peak frequency of the respiration signal into account but the boundaries are defined without considering any other aspect (e.g. signal frequency spread) of the respiration signal.

- In another approach the range of the HF band was defined by using the respiration time-frequency representation [193]. In this case the peak frequency (maximum value) of respiration was searched in the frequency range of 0.15 Hz to 0.6 Hz and the boundaries of the HF band was defined by locating the minima surrounding the peak value. The LF bandwidth was defined in a similar manner but in this case the HRV signal spectrum was used to find the maximum and minimum values in the frequency range of 0.02 Hz to 0.15 Hz. There are two major problems with this method firstly, the respiration rate could be below 0.15 Hz and secondly, respiration signal might exhibit bimodal behaviour and in this case defining the boundaries of the HF region with the first minimum on either side of the maximum value will give inaccurate results.

The boundary estimation method presented in this study relies on the cross-spectrum between the HRV signal and the respiration signal. The cross-spectrum provides an indication of the frequency range in which both signals have significant amount of power. Magnitude coherence, which provides the same information as the cross-spectrum in normalised units has been used previously to include the effect of respiration in HRV analysis [61, 194]. The method proposed in this study uses centre frequency$\pm$SDSE for the definition of the boundaries of the component. The boundaries related to the HF band of the signal are estimated using the cross-spectrum between the HRV signal and the estimated respiration signal whereas, the boundaries related to the LF band of the signal are directly estimated from the spectrum of the HRV signal. This definition is based on mathematics as compared to all the other methods mentioned before therefore, its value will depends on the characteristics of the signal being analysed. This represents a major advantage and from the results shown in previous chapters it can be seen that this method should be able to take into account the considerable variations present in the respiration signals.

By comparing the results obtained from locally anaesthetised patients (see Fig. 11.3, 11.6, 12.18 and 13.16) it can be seen that when the respiration component is in the range of 0.15 Hz to 0.4 Hz the variable boundary method has been able to detect similar changes in the HRV signal parameters that were detected by the fixed (traditional) boundary method. In the case when the respiration frequency is lower than 0.15 Hz or the respiration pattern is such that it effects the signal in much lower frequency than 0.15 Hz one would expect the results obtained from the fixed and the variable boundary method to differ. In this study respiration rates well below 0.15 Hz have not been observed. Only on few occasions the respiration rate is low enough that the lower boundary of the HF band (defined by the variable method) has gone below 0.15 Hz. Besides the rare occurrence of these events the phenomena under investigation (effect of local anaesthesia on HRV) might not represents the best possibility of validating the effectiveness of variable boundary method under low breathing rates. Simpler tests, such as orthostatic tilt test whose effect on the sympathovagal balance is better understood should be performed with controlled low and high breathing rates, so that more rigorous validation of variable boundary method could be achieved.

15.3. Parametric and non-parametric frequency analysis

In this study apart from the different time-frequency analysis techniques the data from locally anaesthetised patients was also analysed with the two most commonly (traditional) frequency domain analysis methods (parametric and non-parametric). The Welch's

periodogram was used for non-parametric analysis, while the parametric analysis was carried out using the autoregressive modelling technique. Both these methods have their advantages and disadvantages. The non-parametric method uses simples FFT based algorithm and have high processing speed. But this method requires the data to be stationary and in case of limited data results in poor frequency resolution. The main advantage of parametric methods such as autoregressive (AR) method is that the smoother spectral components can be distinguished independently of the selected frequency bands. Consequently, they allow an accurate estimation of power spectral density with automatic calculation of the LF and HF power components [19]. Also by deriving the spectrum from a best-fitted model the parametric method achieved better frequency resolution as compared to the non-parametric method. All these advantages of parametric spectral analysis largely depend on the selection of the appropriate model order. As there is no standard criterion that could be used to estimate model order accurately, some of the advantages of the parametric spectrum might be lost. Another important aspect that is largely ignored, is the fact that even if the model order can be estimated accurately, the HR signal could change considerably with time, which raises the question of the feasibility of using the same model order throughout the whole signal. On the other hand, it is also difficult if not impossible to compare the spectrum generated using model of different orders. In short, it is quite important to choose a suitable method for spectral analysis and the spectrum generated using the parametric method should always be checked against the spectrum obtained by the non-parametric method.

Although FFT and AR spectral analyses are supposed to provide comparable results in most physiological conditions, recently it has been shown that although these two spectral analysis methods produce similar trends in HRV indices in sitting, supine and standing position they are not interchangeable at rest in healthy subjects [143]. Pichon *et. al* [143] have shown that FFT analysis overestimate the power associated with the LF and the HF bands of the signal as compared to the AR analysis. Several explanations could be proposed for this overestimation. Firstly, the wide-band noise that is isolated and suppressed with AR constitutes a part of the total power spectrum with FFT analysis [195, 196]. Secondly, Badilini *et. al* [197] proposed that differences observed between FFT and AR results may be the consequence of a tail effect. Indeed, with FFT, the component calculated between one frequency band includes the power corresponding to the tail of the neighbouring component, whereas with AR analysis, spectral power corresponds only to a specific oscillatory pattern representing one HRV component.

Due to these differences that could be present in the HRV parameters estimated by the parametric and the non-parametric methods, in this study the data from locally anaesthetised patients were analysed with both the methods. The results obtained in this study

indicated that similar trends were detected by these two analysis methods. Detecting similar trends means that in both cases significant differences were found in the $^{LF}/_{HF}$ ratio values in nine out of fourteen patients. However, as purposed by Pichon *et. al* [143] all other parameters showed difference among the two frequency analysis methods. The total power, the power associated with the HF band in normalised and absolute units, the power of the LF band in absolute units and the frequency associated with the two bands all showed better correlation with the changes in ratio values in the results obtained from parametric analysis as compared to the non-parametric analysis (see table 11.2 and 11.4). Only the LF power in the normalised units have shown better correlation with the ratio values in non-parametric analysis. The differences in the HRV parameters obtained from the non-parametric and parametric analysis in this study are in accordance with the results published by other authors as mentioned here. These results suggests that even though similar trend could be obtained from these two analysis methods they might not always be interchangeable under certain conditions.

15.4. Time-Frequency analysis

Apart from the traditional parametric and non-parametric method and data from the locally anaesthetised patients was also analysed using time-frequency analysis approach. The time-frequency analysis was carried out using the continuous wavelet analysis, Cohen's class distribution and Empirical mode decomposition techniques.

In case of Cohen's class, Smoothed-pseudo Wigner-Ville Distribution (SPWVD) and Choi-Williams Distribution (CWD) were considered for the analysis of the HRV signals. In CWD case the parametrisation function is a Gaussian function (see Eq. 13.16) and interference terms are reduced by using smaller values for σ. But very small value of σ also decrease the time resolution. In this study $\sigma = 0.01$ was used to attenuate the interference terms. This σ value was in accordance with the value suggested and used by other researchers for the analysis of the HRV signal using CWD [160, 166].

In case of SPWVD, the time and frequency smoothing are controlled by two independent windows. As there is no standard way of defining the optimal length of these windows a huge variety of options has been used in different studies presented in the literature. In some cases [198, 199] the time smoothing is carried out using rectangular window of nine samples. From the experience of analysing signals with SPWVD during this study we believed that the length purposed in these study for time smoothing window is quite small and it will not be able to reduce the interference terms effectively. Also, rectangular window is not generally considered to be ideal for data smoothing. In another study [200] a simulated signal consisting of two frequency components around

0.1 Hz and 0.25 Hz is used and the optimal length of the time and the frequency smoothing windows is chosen so that the root mean square error between the theoretical and estimated $^{LF}/_{HF}$ ratio value is minimum. In this case the optimal window lengths were found to be 54 and 57 samples for the time and frequency smoothing respectively. Both time and frequency smoothing was carried out using Hamming window. The problem in this case is that there is not much of a difference between the length of time and frequency smoothing windows which means that the results obtained from this setup will be almost the same as those obtained from STFT where the same window is used for both time and frequency smoothing. Therefore, in this case the main advantage of SPWVD of having different time and frequency resolution is almost lost.

In this study the length for the time and frequency smoothing windows were chosen by looking at the results obtained from the simulated signals. As mentioned before (see section 13.3) a Hamming window of 257 samples and a Gaussian window of 129 samples were used for frequency and time smoothing respectively. The length of the windows were chosen so that the power related to the LF and the HF band of the signal remains positive. The absence of negative power is a good indication that the interference terms has been removed sufficiently.

The simulated signal study was also used to see the differences between the SPWVD and CWD. The results obtained in this case (see Fig. 13.5, 13.7, 13.9 and 13.11) indicated that the SPWVD has managed to estimate the power related to the LF and the HF band of the signal more accurately than the CWD. As mentioned before, these results are similar to the findings of Pola *et. al*. [160] where they found CWD to be better in peak detection while, the SPWVD was found to be more suitable for the estimation of the power related to the component of the signal. For this reason the data from the locally anaesthetised was only analysed using the SPWVD method. The statistical analysis carried out on the HRV parameters obtained from the SPWVD analysis of the data indicated that the $^{LF}/_{HF}$ ratio showed significant changes in ten out of fourteen patients (see table 13.2). This represented a slight improvement from the results obtained with parametric and non-parametric analysis where significant changes were observed in only nine patients. The correlation of other parameters with the changes in the ratio values did not improved with SPWVD method. The slight improvement achieved with this method as compared to the traditional non-parametric and parametric method was not justifiable considering the extra computational requirement of this analysis method. Therefore, it order to see the effect of analysis method on the results another time-frequency analysis method (CWT) was applied for the analysis of the data.

In case of CWT the scalogram was obtained with Morlet wavelet which has been used in many other HRV studies for spectral analysis [149, 150, 151]. This technique did not

suffer from cross-interference terms. From the results obtained from the statistical analysis (see table 12.2) in this case significant changes were detected in the $^{LF}/_{HF}$ ratio values in thirteen out of fourteen patients. Also, in comparison to other analysis methods in this case the changes in other parameters showed better correlation with the changes in the ratio values. The improvement in the number of significant changes detected by the CWT method could be due its superior capability of detecting transient changes occurring in the signals. The better performance of the CWT method over the SPWVD method in detecting the transient changes occurring in the signal has also been reported by other researchers [149, 201]. D A Newandee [201] tested four different bilinear distributions (STFT, SPWVD, CWD and Born-Jordan-Cohen Distribution) and five different wavelets (Morlet, Mayer, Daubechies 4, Mexican Hat and Har) for the analysis of HRV, respiration and blood pressure variability signals in investigation of normal and chronic obstruction pulmonary disease. The results of this study indicated that Morlet wavelet produces the best results among all the methods tested. Faust *et. al.* [149] have also reported better performance of Morlet wavelet as compared to SPWVD in detection of different cardiac disfunctions using HRV analysis. From these studies presented in the literature and the results obtained in this study it could be said that the presence of interference terms could severally effect the results obtained from the time-frequency analysis method. In case of simulated signals, where the interference was almost completely removed, the SPWVD method has produced better estimate of the power related to the signal components as compared to the CWT method. But as there is no standard way of defining the optimal length of the windows therefore in case of real physiological signals it becomes quite difficult to remove the interference terms effectively.

Another method that was used for the analysis of HRV signal from locally anaesthetised patients is EMD. Unlike other analysis methods which uses fixed basis for analysis this method is completely data driven and basis are extracted directly from the signal. It has been shown that this method could achieved much better resolution than the other time-frequency analysis methods [176]. The results obtained from statistical analysis of the parameters obtained from the EMD analysis (see table 14.2) indicated that in this case as well significant changes in the $^{LF}/_{HF}$ ratio values were detected in thirteen out of fourteen patients. The other parameters also showed good correlation with the changes in the ratio values. The correlation was slightly less than the CWT method but it was better than the correlation obtained by all the other method employed for the analysis of the signals in this study. One major problem with this method is the fact that in this case different number of IMF components could be associated with the two bands (LF and HF) of the signal, so a single frequency value could not be associated with each band. For this reason, just like other studies [167, 168, 169, 170] which have used EMD method

for HRV analysis, in this study as well only parameters associated with the power of the two bands were analysed. Further relatively simple studies in which the changes in the sympathovagal will be more predictable should be carried out so that IMF components generated by EMD could possibly be associated with different physiological phenomenas. This would help in analysing the frequency related parameters for individual IMF components.

15.5. Results obtained from analysis of locally anaesthetised patients

In this study the data obtained from patients undergoing brachial plexus block using the axillary approach was analysed. A combination of 30 ml of 1% Lignocaine and 29 ml of 0.5% Bupivacaine with 1:200000 part Adrenaline (epinephrine) was used as anaesthetic agent. The rate of systemic absorption of local anaesthetics is dependent upon the total dose and concentration of drug administered, the route of administration, the vascularity of the administration site, and the presence or absence of epinephrine in the anaesthetic solution. In order to take advantage of rapid onset of the block as achieved by Lignocaine and the longer lasting effect of Bupivacaine the two drugs were used in combination. Adrenaline in dilute concentration (1:200,000 or 5 $\mu g/ml$) is used as it usually reduces the rate of absorption and peak plasma concentration, permitting the use of moderately larger total doses and sometimes prolonging the duration of action.

The potential effect of local anaesthetic on cardiac rhythm has also been reported in the literature [202, 203, 204]. Moreover, the anxiety associated with both minor surgery and the injection of local anaesthetic may induce a catecholamine surge which could increase myocardial oxygen demand and may be arrhythmogenic [205, 206]. Thus, overly anxious patients often exhibit signs of vasodepression, pallor, tachycardia and palpitation. The dose of local anaesthetic agent employed for most surgical procedures is not in general associated with a cardio-depressant effect, although some cardiovascular depression may also occur following extensive use of local anaesthesia [207, 208].

As mentioned before (see section 11.2.2) by looking at the results obtained from the frequency domain analysis of the signals obtained during this study the following postulates were made.

1. The increase in the LF/HF ratio values just after the application of the block could be due to the presence of small amount of Adrenaline in the anaesthetic drug mixture and also may be due to patient's anxiety .

2. After the application of the block there is an initial transient phase in which the

$^{LF}/_{HF}$ ratio values have increased (as mentioned in point 1). After this phase the values decrease considerably as compared to the values before the application of the block and show reduced variability for a certain amount of time. This decrease in the ratio values and the reduced variability shown by the data could be due to the anaesthetic drug indicating a shift in sympathovagal balance towards vagal enhancement.

In this section these results will be discussed and validated with the help some of the relevant studies presented in the literature. The first aspect in this comparison is to see the hemodynamic effect of Adrenaline present in the anaesthetic drug. Kudret *et. al.* [209] compared the hemodynamic and blockade effects of low (25 μg) and high (200 μg) epinephrine during axillary brachial plexus blockade with 1.5% Lidocaine. In this study sixty ASA I and II patients were divided into three groups. Patients in group 1 received 5 ml of saline containing 25 μg epinephrine and then 35 ml of 1.5% Lidocaine; patients in group 2 received 5 ml of saline alone and then 200 μg of epinephrine mixed with 35 ml of 1.5% Lidocaine; patients in group 3 received 5 ml of saline alone and then 35 ml of 1.5% Lidocaine. Hemodynamic data were measured for 1 to 10 minutes at 1-minute intervals after axillary injection. The authors found a higher heart rate and blood pressure in the high dose epinephrine group within the first 6 minutes after drug administration. Even though, this study showed heart rate and blood pressure changes due to high concentration of epinephrine (Adrenaline) the authors have not provided any information as to how the heart rate was monitor. In this case it could be assume that the heart rate reading were taken from a commercial ECG monitoring system usually used in the hospitals. This represents an average value which might be less sensitive. Instantaneous heart rate estimated from the ECG signal might have provided better information about the dynamical changes occurring in the analysis period due to epinephrine. In another study Ueda *et. al.* [210] study the effect of Adrenaline in fourth ASA I and II patients. In this study the ECG and arterial pressure waves were recorded continuously. The patients were divided into four groups, and each group received one of the following anaesthetic solution through cutaneous injection.

1. 1:200,000 epinephrine in normal saline solution (group E, n=8).
2. 1:200,000 epinephrine with 0.5% Lidocaine in normal saline solution (group LE, n=9).
3. 1:200,000 epinephrine with 10% low-molecular-weight dextran in normal saline solution (group ED, n=11).
4. 1:200,000 epinephrine with 0.5% Lidocaine and 10% low-molecular-weight dextran

in normal saline solution (group LED, n=12).

Arterial blood for analysis of the epinephrine concentration was obtained six times, *i.e.*, before the injection and 1, 5, 10, 20 and 30 minutes after the completion of the injection. In 33 out of 40 patients the peak concentration of epinephrine was obtained 5 minutes after the completion of the injection. In seven remaining patients, one in LED group and two in each of the other three groups, the concentration of epinephrine peaked at one minute after the injection. No relationship was found between the age or the body weight and the plasma epinephrine level. The solutions containing Lidocaine showed significantly higher plasma epinephrine level than the solutions without Lidocaine. The authors concluded that epinephrine when added to local anaesthetic drugs such as Lidocaine could cause elevation in the heart rate and blood pressure.

The effect of epinephrine concentration on Lidocaine disposition during epidural anaesthesia was also studied by Ohno *et. al.* [211]. In this study forty ASA I female patients were divided in four groups of ten patients each. Group 1, 2, 3 and 4 received 15 ml of 2% Lidocaine solution, with 1:200,000 epinephrine, with 1:400,000 epinephrine and with 1:600,000 epinephrine. Apart from the 1:600,000 dose all the other doses of epinephrine caused changes in the HR and mean arterial blood pressure. From these results the authors recommended that the appropriate epinephrine concentration of 1:600,000 or less should be added to Lidocaine for the reduction of systemic toxicity during epidural anaesthesia. Unfortunately, again in this case no information is given as to how the heart rate was measured.

Several authors have also studied the effect of Adrenaline presents in the local anaesthetic mixture used in dental surgery. Salonen *et. al.* [212] observed significant increase in heart rate when 1:80,000 Adrenaline mixed with 2% Lidocaine mixture was used as anaesthetic agent during minor oral surgery. The systolic and the diastolic blood pressure were not affected by Adrenaline. The concentration of Adrenaline in plasma was increased more than 10-fold, mostly due to the exogenous Adrenaline. The heart rate did not change significantly when Lidocaine alone was used for anaesthesia. Based on their results authors concluded that the increase in sympathetic activation associated with minor oral surgery seems to be negligible as compared to the effects of Adrenaline in the local anaesthetic. Cioffi *et. al.* [213] in a study of hemodynamic and plasma catecholamine responses to amalgam restoration of a single tooth with local anaesthesia (1.8 ml of 2% Lidocaine with 1:100,000 epinephrine), found plasma epinephrine to increase from a baseline of 28 ± 8 pg/ml 5 minutes after the injection. Heart rate increased in parallel with the epinephrine concentration, but mean arterial pressure was unaltered. However, there are also some contradicting results presented in the literature. For instance, Meechan and Rawlins [214] conducted studies on volunteers (n=10) and patients (n=16, 8 were

given anaesthetic drug with Adrenaline and 8 were injected with local anaesthesia without Adrenaline) awaiting minor oral surgery. They observed no significant changes in heart rate and blood pressure immediately after and ten minutes following the injection of epinephrine-containing local anaesthesia. Volunteers received 4 ml of 2% Lidocaine containing 50 μg Adrenaline and the patients received 4.2 ml of Lidocaine with 1:80,000 Adrenaline.

Some of the studies mentioned here were not related to Brachial plexus block. These studies were mentioned here to reflect the fact that Adrenaline present in the local anaesthesia applied to other parts of the body could also cause cardiovascular changes. Since, the amount of Adrenaline (1:80,000 or 1:100,0000) mostly used in dental surgery is quite high as compared to the amount (1:200,000) used in this study and due to the difference in vascularity of the injection sites it could be said that these results might not be comparable to the results obtained in the present study. Nevertheless, they highlight some important facts. Firstly, due to the lack of standardisation and proper guidelines it becomes quite difficult to compared the results from different studies. It might be more obvious that differences in drugs concentration, anaesthetic block technique and different measurement devices might influence the results. But also minor difference in the studies could produce completely different results. For instance, it could be argued that Meechan and Rawlins [214] did not observed significant changes in heart rate simply because they compared the baseline readings (before the injection) with values immediately after the injection and then 10 minutes after the injection. In other studies significant changes in the heart rate were observed approximately 5 minutes after the anaesthetic injection and the authors reported that the effect was short lived. So it is quite possible that the changes in heart rate values were not significant around and after 10 minutes mark. Other important point, that most of the studies mentioned previously, indicated was the fact that even though patient's anxiety due to the anticipation of having minor surgery or having the local anaesthetic injection might produce some Adrenaline in the system, the Adrenaline present in the local anaesthetic mixture was the major cause of increase in plasma concentration of a Adrenaline and hence the increase in heart rate.

As mentioned before, the second observation made from the results obtained during this study was the decrease in the $^{LF}/_{HF}$ ratio values after the initial transient phase. This drop was considered to be due to the sympathetic blockage effect of local anaesthesia drug. The axillary approach to the brachial plexus continues to be the most popular technique selected by anaesthesiologists for forearm and hand surgery. The main reasons that the axillary approach is so popular are that it is easy to perform, easy to teach, and the risk of complications is lower than the supraclavicular approach [215]. In a retrospective analysis of 346 records of ASA I-IV patients who underwent elective unilateral ortho-

paedic upper limb surgery with transarterial plexus anaesthesia overall success rate of 94% has been reported [216]. These results were obtained with a 70 ml dose of local anaesthetic. In this study 1% Lidocaine without Adrenaline, 2% Lidocaine with Adrenaline 10 μg/ml, and 1% prilocaine is separate syringes were primarily used as anaesthetic solution. Local anaesthetic toxicity, nerve injury, failure, hematoma formation are the most common complications but most of these could be avoided by proper preparation and application of block. Due to high success rate and low potential of serious medical complications there are not many studies present in the literature that have analysed the effect of axillary approach of brachial plexus block on cardiovascular dynamics. In most studies, different formulation of local anaesthetic agents or different enhancement methods such as multiple injections, use of nerve simulator or ultrasound for locating the relevant structures, has been compared to see if they could help in achieving better anaesthetic blocks. These studies are usually concerned with the plasma concentration of the drugs, onset of motor and sensory blocks and unfortunately heart rate and/or blood pressure values are only discussed if they showed medically significant changes which might require medical intervention.

Another problem in comparing results obtained from different studies is the fact that due to the lack of standardisation their are various signal processing methods that are used for HRV analysis. It is quite possible to obtained different results from the same data set by applying different signal processing techniques for the steps (peak detection, detrending, ectopic/missed beat correction and parameter estimation) involved in HRV analysis. In a lot of published work information regarding the methods used for detrending and ectopic/missed beat correction are completely missing and this alone could have a major impact on comparing results from different studies. Another example of the ambiguity caused by the use of different analysis techniques is the study presented by Deschamps *et. al*. [217]. In this work authors have used wavelet transform to analyse heart rate and blood pressure variability in thirteen laboring patients undergoing epidural anaesthesia with 20 ml of 0.125% Bupivacaine and 50 μg of fentanly. They compared the values obtained five minutes before the application of the block with the values obtained 10 minutes after the application of the block. The authors observed no changes in the heart rate and blood pressure values due to the anaesthesia. However, high frequency power increased and the $^{LF}/_{HF}$ ratio of the HRV signal decrease after the epidural. The high and low frequency power related to blood pressure variability also decreased after the epidural. These finding suggests an increase in parasympathetic drive and decrease in sympathetic outflow. The major problem with this study is the fact that in this case the wavelet transform was done on the irregularly spaced tachogram (RR-interval) time series. In Fourier based techniques the data is required to be regularly sampled therefore,

it is difficult to predict as to how much the results of this study were effect by this particular choice of analysis method. Apart from some the studies done by this particular group of authors, wavelet analysis was never used to analysed irregularly sample HRV signal in any other publish work found during literature review in this study.

In another study [218] the effect of Brachial plexus block was studied by analysing the Laser Doppler Flowmetry (LDF) signals with the help of wavelet transform (Morlet wavelet). The study included thirteen ASA I healthy patients undergoing hand surgery (aged 22-66 years) and ten healthy nonsmokers in the control group. Brachial plexus block was performed by transarterial technique using 2.5 $^{mg}/_{ml}$ of Bupivacaine, 10 $^{mg}/_{ml}$ of Lidocaine and 6.25 $^{\mu g}/_{ml}$ of epinephrine. The LDF was recorded from the arm subjected to anaesthesia, and also from the contralateral arm. The first recording was obtained for an interval of 30 minutes before the Brachial plexus block. After the block was complete, there was an interval of 50 minutes. The second recording was then obtained for an interval of 30 min. Blood pressure was measured before and after the registrations. Respiration frequency, heart rate, and skin temperature were measured during both recordings. Both groups (patients and control) followed the same protocol in the control group the block was not performed. Heart rate and systolic blood pressure showed significant increase after the block. However, there was no significant difference in the mean arterial blood pressure, diastolic pressure, respiration frequency and the temperature difference between the two arms. In the control group these parameters did not show any significant changes.

The spectrum obtained from the wavelet analysis of the LDF signal was divided into five bands (0.0095-0.021, 0.021-0.052, 0.052-0.145, 0.145-0.6 and 0.6-2 Hz). After Brachial block there were highly significant reductions in relative amplitude in the 0.021-0.052 Hz ($P<0.001$) and the 0.0095-0.02 Hz ($P<0.001$) frequency intervals. Significant increase was also observed in the 0.15-0.6 Hz ($P=0.002$) frequency interval. In the contralateral arm, there were no significant changes in the frequency intervals, except for a reduction in the 0.6-2 Hz frequency interval ($P=0.006$). In the control group, there were no significant differences in relative amplitude between the two registrations.

It has been demonstrated in previous studies that 0.0095-0.021 Hz and 0.021-0.052 Hz frequency intervals represent endothelium and neurogenic activities respectively [219, 220]. The reduction of the endothelial related oscillations could be a direct effect of the local anaesthetic on the endothelium, as has been described by several investigators [221, 222, 223]. Another explanation could be that alterations in sympathetic activity during brachial plexus block have a direct influence on endothelial function [224].The overall results for this study indicates an inhibitory effect of the Brachial plexus block on the sympathetic and the endothelial activity.

The studies mentioned in this section provide some evidence in support of the two postulates that were made from the results obtained during this study. Namely, the presence of Adrenaline in the local anaesthesia mixture could cause a transient short live increase in the heart rate. The presence of Adrenaline in the local anaesthetic mixture and patient's anxiety could result in the transient increase in the $^{LF}/_{HF}$ ratio which was observed in almost all the patients included in this study.

Unfortunately, due as mentioned before due to high success rate of the axillary block and the lack of standardisation in terms of appropriate signal processing that should be used in HRV analysis, it was not possible to directly validate the second postulate (Lidocaine and Bupivacaine present in the anaesthetic mixture cause a shift in the sympathovagal balance toward vagal enhancement). Deschamps *et. al*. [217] results are quite similar to the results obtained during this study. But in this case there are two problems. Firstly, they have analysed data from laboring patients undergoing epidural anaesthesia as compared to patients included in this study which received Brachial plexus block for hand surgery. Secondly, the used of wavelet analysis with irregularly sample signal (tachogram) might not yield appropriate results. However, the results obtained with the analysis of LDF signal [218] provide some evidence suggesting the inhibitation of sympathetic activity due to Brachial block. Using LDF signal sympathetic impairment due to Brachial plexus block was also reported in two other studies [225, 226]. There are some differences in results obtained from the LDF signal study and the results reported here. The 0.0095-0.021 Hz and 0.021-0.052 Hz frequency intervals which showed significant decrease after block approximately represent the VLF band of the HRV signal. In the present study the signal component corresponding to this band was removed before the analysis as per the recommended guidelines [19] for HRV analysis. In future inclusion of this component in the analysis could provide more information regarding the dynamical changes occurring in the cardiovascular system due to anaesthesia. In the present study apposite changes were observed in the LF (decrease) and the HF (increase) bands of the HRV signal. However, in the LDF signal analysis [218] the band approximately equal to the LF band of the HRV did not show any changes. While, the respiratory related band showed a significant increase. This case would also results in a decrease in the $^{LF}/_{HF}$ ratio indicating a shift of sympathovagal balance toward vagal enhancement. Another possible explanation of this difference could be due to the fact that in present study parameter where estimated continuously after the application of the block while, Landsverk *et. al*. [218] started the post-block measurement of the LDF signal 50 minutes after the application of the block.

With the literature discussed here it could be said that the two postulates made from the results obtained during this study are not completely unrealistic. These results in-

dicates that by appropriate and structured analysis of HRV data it might be possible to detect changes in the sympathovagal balance occurring due to the application of axillary Brachial plexus block in patients undergoing minor upper limb surgery.

One limitation of the current study is the fact that two of the included patients were smokers. Cigarette smoking has been associated with increased activity of the sympathetic nervous system. Hence, in resting condition smokers exhibit higher $^{LF}/_{HF}$ ratio values as compared to nonsmokers [227, 228]. It is difficult to predict the effect of smoking on the results obtained from these patients. Using the traditional parametric and non-parametric method no significant changes were observed in the $^{LF}/_{HF}$ ratio values. But when the same data was analysed with the time-frequency analysis techniques all of them (CWT, SPWVD and EMD) were able to detect significant changes in the ratio values after the application of the block. Possible explanation of this difference could be the fact that in these patients the inhibitation of sympathetic activity was less as compared to non-smokers or the changes that occurs in these cases were some what more complex nature, which could only be detected with the help of time-frequency analysis method.

Another interesting observation from the results obtained during this study was the fact that apart from the EMD technique non of the other analysis techniques detected significant changes in the $^{LF}/_{HF}$ ratio values after the application of the block in patient twelve. This was the only patient that was classified as anxious before the procedure by the medical staff. At present it is not possible to explain whether the EMD analysis was able to detect significant changes in this patients data due to it higher resolution compared to the other techniques or this was due to some other reason. We can not simply assume that this result was because of the higher resolution of the EMD method as this method was unable to detect significant changes in patient number nine whereas the other methods have been able to detect changes in this patients. Overall, by comparing the number of significant changes detected in $^{LF}/_{HF}$ ratio values after the application of the block it could be said that CWT and EMD gave similar performance. In this sence these two method were better than the other utilised methods but they are not interchangeable with each other.

16

Conclusions

Information about the autonomic neural regulation of the heart and the circulatory system can be obtained by analysing the variability in the cardiovascular signals. Neural regulation due to the sympathetic and parasympathetic divisions of the autonomic nervous system involves responses to respiration, blood pressure regulation and thermoregulation. The degree of neural regulation could be altered by many cardiovascular diseases, medications and physical and mental stress. Several factors can have an indirect effect on cardiovascular signals. Artefacts and other types of noises are also present with the useful information. Heart rate variability (HRV), the beat to beat fluctuation in the heart rate, is a non-invasive technique used with an aim in gaining information about the cardiovascular function. Although there are generally accepted standards for the calculation of HRV metrics and some agreement concerning the clinical application of these metrics, the field of HRV analysis contains many contradictory studies and there exists no clear consensus on the clinical value of HRV metrics.

The aim of this study was to utilise the technique of HRV for the first time in a group of fourteen locally anaesthetised patients undergoing brachial plexus block. The focus of the study was to investigate the effect of the local anaesthetics drugs on the parameters estimated during HRV analysis. In order to achieve the goal of this study a systematic HRV analysis of the ECG signals acquired from the clinical study was performed using different techniques of spectral analysis.

The first step in the analysis of HRV is the detection of the R-wave from the ECG signal. In this study, the ECG signal was acquired at a sampling rate of 1000 Hz to minimise the error in the RR time series. For the detection of the R-wave two algorithms, one based on digital filtering technique and the other utilising wavelet transform were implemented. Both these algorithms were validated using simulated ECG signals corrupted with known levels of artefacts which are generally present in the ECG recordings (see section 5.3 and 6.4). The results from these simulated signals provided information on the effect of varying levels of different artefacts on the performance of the two ECG R-wave

detection algorithms. The two algorithms were also validated offline by using Normal Sinus Rhythm (NSR) database from *Physionet* and on-line on volunteers and patients undergoing local anaesthesia. In most cases both the peak detection algorithms have performed reasonably achieving sensitivity and accuracy of over 95%. In the digital filter algorithm the peaks were searched in a single filtered signal while the wavelet algorithm used signals at four different scales for peak detection. By using more than one signal the wavelet algorithm was able to detect peaks more reliably than the digital filter algorithm in cases when the signals were contaminated with artefacts with wide spread frequency characteristics. An example of such a signal is presented in Fig. 5.14. The sawtooth wave (artefact) shown in Fig. 5.14 was present in the beginning of the three signals in the NSR database and caused large amount of error in peak detection when the digital filter algorithm was used. However, the wavelet analysis algorithm was able to detect peaks in the ECG signals containing these artefacts quite accurately. Because of its ability to deal with these kinds of artefacts better than the digital filter algorithm, the wavelet peak detection algorithm was used in further analysis to detect the R-waves of the ECG signals collected from patients undergoing local anaesthesia.

After the successful detection of the R-wave the next step was to choose the signal representation for spectral analysis. Usually the HR or the heart period signal is used for this purpose but in this work, the heart timing (*ht*) signal was used. Using simulated signals consisting of two sinusoidal components one in the LF band and the other in the HF band region it was shown that the signal was able to avoid both the low pass filtering effect and the spurious peaks present in the spectrum obtained using the HR signal representation as shown in Fig. 8.10. The absence of spurious peaks in the ht representation was also confirmed by comparing the results obtained in this study through the EMD analysis of simulated signals consisting of two components with the results obtained by Echeverria *et. al* [167].

The ectopic beat correction is another important aspect of the HRV study that was also addressed in this study. Usually missing peaks and ectopic beats are replaced by calculating the mean of the few normal beats before and after the ectopic beat or the missing peak. This method can provide acceptable results when used for missing peaks but in the case of ectopic beats the error in the power spectrum remains largely unchanged (see section 8.4.1 and [116]). In order to reduce the error introduced by ectopic beats the algorithm presented by Mateo *et. al.* [116] was used. The algorithm's performance was validated with the help of simulated signals in both the parametric and non-parametric spectral analysis. The signals were corrupted by removing or moving five beats from a simulated signal of five minutes. The results presented in section 8.5.1 and 8.5.2 indicate that even this small amount of ectopic/missing beats can cause enormous errors in the

spectral estimation of the HRV signals. By comparing the spectrum of the original uncorrupted signal with the spectrum obtained after beat correction it was also shown that the ectopic beat correction algorithm has performed satisfactorily in reducing the error caused by the ectopic/missing beats. The study with the simulated signal in a way provided the upper limit of the performance of the beat correcting algorithm. Since the simulated signals were much simpler than the real HRV signals the improvement achieved by the algorithm was expected to be reduced in the case of the real signals. Therefore, tests similar to the ones carried out with simulated signals were also performed with real HRV signals. The results obtained from this beat correction analysis in the case of real HRV signals (see section 8.6) showed that this method was able to reduce the error introduced by missing and/or ectopic beats quite considerably.

For the analysis of short segments of HRV signal, the slow varying (VLF) component has to be removed before estimating the HRV parameters. For this purpose two algorithms were implemented. One of the algorithms was based on *Smoothness Prior Approach* (SPA) and the other was implemented using wavelet packet analysis. The performance of the two algorithms was evaluated using simulated signals and real HRV data (see section 9.2.1 and 9.3.2). The results presented in section 9.2.1 and 9.3.2 and Fig. 9.16 indicated the superior performance of the wavelet packet algorithm. This algorithm performed better than the detrending algorithm based on SPA not only in terms of attenuation of the VLF component of the signal but also in terms of computational efficiency. For this reason the wavelet packet algorithm was used for detrending the HRV signals before the spectral analysis.

The EDR algorithm was implemented for the estimation of the respiration signal from a single lead ECG signal. This algorithm was validated using signals from "Fantasia Database" available from *Physionet* [136]. The high correlation results obtained between the estimated and original respiration signal and the spectral results presented in section 10.3 indicated satisfactory performance of the algorithm in estimating the respiration signal from single lead ECG signal. This algorithm was then used to obtain the estimation of the respiration signal from the ECG data of the patients undergoing local anaesthesia included in this study.

After all the necessary pre-processing, the data was analysed in the frequency domain using the non-parametric (Welch's periodogram) and parametric (AR modelling) spectral analysis method. The boundaries related to the HF component of the signal were estimated using cross-spectrum estimated using the HRV signal and the respiration signal. The boundaries related to the LF and the HF components were defined as centre frequency $\pm$ the standard deviation spectral extension (Eq. 11.2 and 11.3). The frequency domain parameters of $^{LF}/_{HF}$ ratio, total power, power related to the HF and the LF band in absolute

and normalised units and centre frequency related to the two bands were estimated from the data of each patient included in this study (see Fig. 11.3 and 11.6). In order to validate the use of the variable boundary method for estimation of the HRV parameters the same parameters were also calculated using the traditional (fixed) boundary method. The parameters values before and after the application of the anaesthetic block were statistically compared using the Wilcoxon signed rank test with the results summarised in table 11.2 and 11.4. These results indicated that the ratio values showed significant changes in nine out of the fourteen patients included in this study when the data was analysed using the non-parametric and the parametric method. The same number of changes in the $^{LF}/_{HF}$ ratio values were obtained from the fixed and variable boundary method. This shows that the results were not significantly affected by the definition used in the variable boundary method. But as this method takes the respiration signal into consideration by the cross-spectrum, it might prove beneficial in HRV analysis in cases when the respiration frequency is quite low or the respiration effect spread over a large frequency band.

In order to further analyse the dynamical changes occurring in the HRV signals, time-frequency analysis methods were also employed. In this case, the continuous wavelet transform (CWT) was the method used for the analysis of the HRV signals. The analysis was carried out using Morlet wavelet. Before the analysis of the HRV signals the ability of the CWT to detect transient changes in the signal was validated using simulated signals with changes in the amplitude and/or frequency (see section 12.2). The variable boundary method was validated with the help of signals from the "Fantasia Database" resulting in satisfactory results presented in section 12.3. Following the successful performance of the variable boundary method on simulated signals and on data from the "Fantasia Database" the method was then used for the analysis of the HRV signal from the locally anaesthetised patients. The parameters related to the two bands were estimated using both the variable boundary method and also the traditional (fixed) boundary method. The HRV parameters of $^{LF}/_{HF}$ ratio, instantaneous total power, instantaneous power in the HF and the LF band both in absolute and normalised units and instantaneous frequency related to the HF and the LF band were estimated from each data set included in this study. An example of these parameters estimated from the data of one of the patients included in this study is presented in Fig. 12.18. These parameter values were also tested to find out if there was any statistical difference in the values before and after the application of the anaesthetic drug (block). The results of the statistical tests are presented in table table 12.2. These results indicated that in the case of the CWT analysis the $^{LF}/_{HF}$ ratio values showed significant differences in thirteen out of fourteen patients included in this study. The changes in the normalised power of the two bands showed strong correlation with the changes in the ratio values. Similar results were obtained

from the variable and the fixed boundary method. The results obtained from the CWT analysis of the data indicated quite an improvement as compared to the results obtained from the non-parametric and the parametric analysis. The improvement could be due to the ability of the CWT to provide the time-frequency distribution of the signal from which the dynamical changes occurring in the signal could be analysed more precisely.

Even though the CWT provided better results than the non-parametric and the parametric method, another method of time frequency analysis was employed for the study of HRV signals with an aim to explore the possibility of even further improvement. In this case two quadratic distributions (smoothed-pseudo Wigner distribution (SPWVD) and Choi-Williams distribution (CWD)) from the Cohen's class were tested for their feasibility in the analysis of the HRV signals. The results from the simulated signals shown in section 13.3 indicated that SPWVD was much better suited for the analysis of the HRV signal than the CWD. On the basis of these results only SPWVD was employed for further analysis of the data. The inclusion of the respiration signal by using cross-spectrum was also validated again using signals from the "Fantasia Database". The results from this analysis are presented in section 13.4. After getting satisfactory results from the simulated signals and validating the use of cross-spectrum between the respiration and the HRV signal for the estimation of the boundaries related to the HF band of the signal the same setup was used for the analysis of the HRV signal from the locally anaesthetised patients. The parameters estimated with the variable boundary method were again validated with the help of parameters estimated with the fixed boundary method. The parameters estimated from one of the patients included in this study are presented in Fig. 13.17. Statistical tests (Wilcoxon, signed rank test) were carried out on the parameters estimated using SPWVD to check if there was any statistical significant difference in the HRV parameters before and after the block. The results of these statistical tests are summarised in table 13.2. These results indicated that for the SPWVD case significant changes in the ratio values were observed in eleven of the fourteen patients. Both the variable and the fixed boundary method detected changes in the ratio values in the same number of patients. The normalised power of the two bands and the total power also showed significant changes which were correlated with the changes in the ratio values. The SPWVD performed poorly as compared to the CWT in analysing the HRV signals. This could be due to the presence of the interference terms which causes error in the estimation of the instantaneous power. The use of smoothing windows helps in attenuating these interference terms but determination of the optimal window length is difficult. Using a longer window will certainly reduce the interference terms but this also reduces the time resolution, thus reducing the capability of the analysis technique to detect transient changes in the signal.

Lastly, the HRV signals were analysed using the Empirical Mode Decomposition (EMD) method. As in this method the basis was computed from the data set, it produced a much more compact representation of the signal. This method has been shown to produce much better results in the analysis of non-stationary data therefore; it was included as one of the analysis method in this study. The method was tested vigorously again on the simulated signals (see section 14.3) before analysis of the HRV signals. First the confidence interval of the stopping criteria was established and all the signals were decomposed using the value that gave the minimum of the squared deviation (Eq. 14.19). The index error associated with each component was calculated using the normalisation procedure explained in section 14.2.5. Using the error index, correction was done for the instantaneous frequency and amplitude values in the region where the error was higher than twice the standard deviation. The signal components were then assigned to either the HF or the LF region of the signal depending on the centre frequency and the standard deviation spectral extension calculated from the marginal spectrum of each component. This assignment was done on five minute segments of the data. After the assignment of the components the ratio between the HF and the LF components and total power was calculated for each of the data sets included in this study. The ratio and the power values calculated from one of the data sets are presented in Fig. **??**. These results indicate a drop in both the ratio and the total amplitude after the application of the anaesthetic drug.

The statistical analysis results, summarised in table 14.2, indicate that this technique has been able to detect changes in thirteen out of the fourteen patients included in this study. The changes in the normalised amplitude of the HF and the LF band of the signal also showed strong correlation with the changes in the ratio values. In terms of detecting changes in the ratio values, the EMD method has performed similar to the CWT method. As mentioned before there was one patient included in this study which was categorised as anxious by the medical staff. Apart from the EMD technique none of the other techniques were able to detect significant changes in this patient. However, due to the lack of other similar cases it is not possible to say whether the EMD analysis was able to detect changes in these patients because of its higher resolution or there are some other unknown factors affecting the analysis of this patients' data by EMD technique. An argument against the high resolution claim could be made because this method has not detected significant changes in another patient (pat #9) where as the all the other methods has been able to detect changes in this patient.

In conclusion, a systematic approach for the analysis of HRV data from locally anaesthetised patients undergoing Brachial plexus block was applied in this study. Effort was made to validate the performance and optimise each step involved in the analysis with the help of simulated signals with known characteristics. After obtaining encouraging

results from the traditional parametric and non-parametric analysis, the HRV data were analysed further using time-frequency analysis techniques such as CWT, SPWVD and EMD. The ability of these methods in tracking the dynamical changes occurring in the amplitude and/or frequency of the signal components was also tested using the simulated signals, which showed transient behaviour during the analysis period. These simulated studies also provided the basic frame work for each technique which was then employed in the analysis the real HRV signal from anaesthetic patients. The CWT and the EMD methods were able to detect ratio changes, before and after the application of the anaesthetic block, in thirteen out of fourteen patients included in this study. However, the SPWVD detected changes only in eleven of the fourteen patients. The lower performance achieved by the SPWVD method as compared to the CWT and the EMD methods could be due to the presence of interference terms which causes error in the estimation of the instantaneous power of the signal components. The analysis showed that time-frequency methods which were able to deal with the non-stationary characteristics of the data has the capability to reveal much more information about the dynamical changes occurring in the signal as compared to the traditional parametric and non-parametric methods.

Finally the results obtained in this study provide evidence that it could be possible to detect changes in the sympathovagal balance caused by the application of the local anaesthesia (axillary Brachial plexus block) through appropriate analysis of HRV. The results show that due to anxiety and/or adrenaline present in the local anaesthesia mixture the $^{LF}/_{HF}$ ratio values show a transient increase shortly after the application of the block. After this transient increase the ratio values decrease considerably and remain low as compared to the values before the application of the block. This decrease could represent the shift of the sympathovagal balance towards parasympathetic predominance and/or inhabitation of sympathetic activity due to local anaesthesia. Such results might enable the clinicians to optimise and manage better the administration of local anaesthesia. Also, the clinicians involved in the study suggested that the HRV results may act as an indicative of blood toxicity due to the administration of local anaesthetic drugs. However, such claims need more rigorous investigation.

In future this work could be improved further by extending the clinical trial including a larger group of patients plus increasing the physiological parameters recorded (i.e. include respirations, temperature, blood pressure etc). This will enable a more rigorous investigation.

Also, a pilot animal study will be very useful as it will give us the opportunity to have more control in the protocol and therefore being able to make more accurate and perhaps consistent observations.

These studies will help in the development of signal processing techniques which

could possibly be used for the modelling/prediction of HRV. This could be a very useful tool in many HRV applications. By comparing the predicted values with the actual values effect of external stimuli such as the application of anaesthetic drug could be studied more effectively.

A

Non-parametric analysis results

Results obtained from the non-parametric analysis of data from patients undergoing local anaesthetic procedure. In each plot the grey vertical block represents the time of block (anaesthesia) application and the green vertical lines represent start and end of the surgery. The vertical arrow pairs in part (a) show the data segment before and after the application of block which was used in statistical analysis. Each plot shows the parameter values estimated using both the fixed and the variable boundary method. Lines in green and magenta colour represent the parameter values before and after the block application estimated using fixed boundary method respectively. In the case of variable boundary method the same information is presented with blue and black colour lines respectively. The units on y-axis for the plots showing power are s^2/Hz and for the plots showing frequency values is Hz.

Patient 1

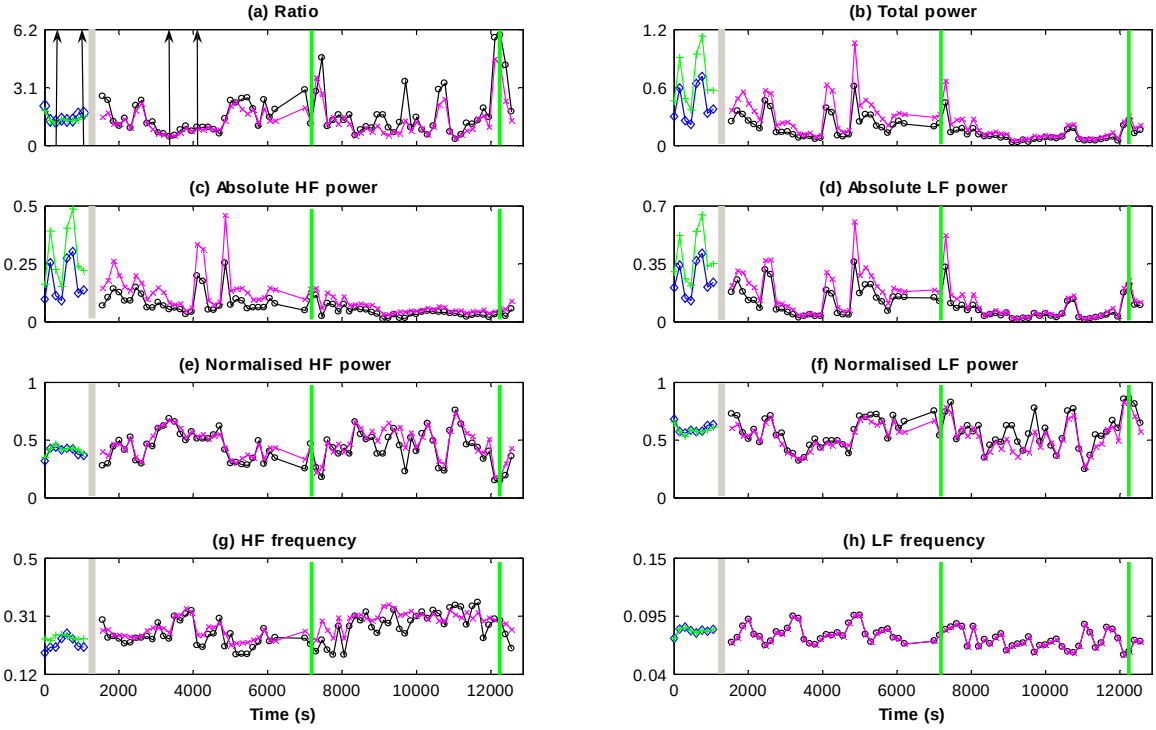

Patient 2

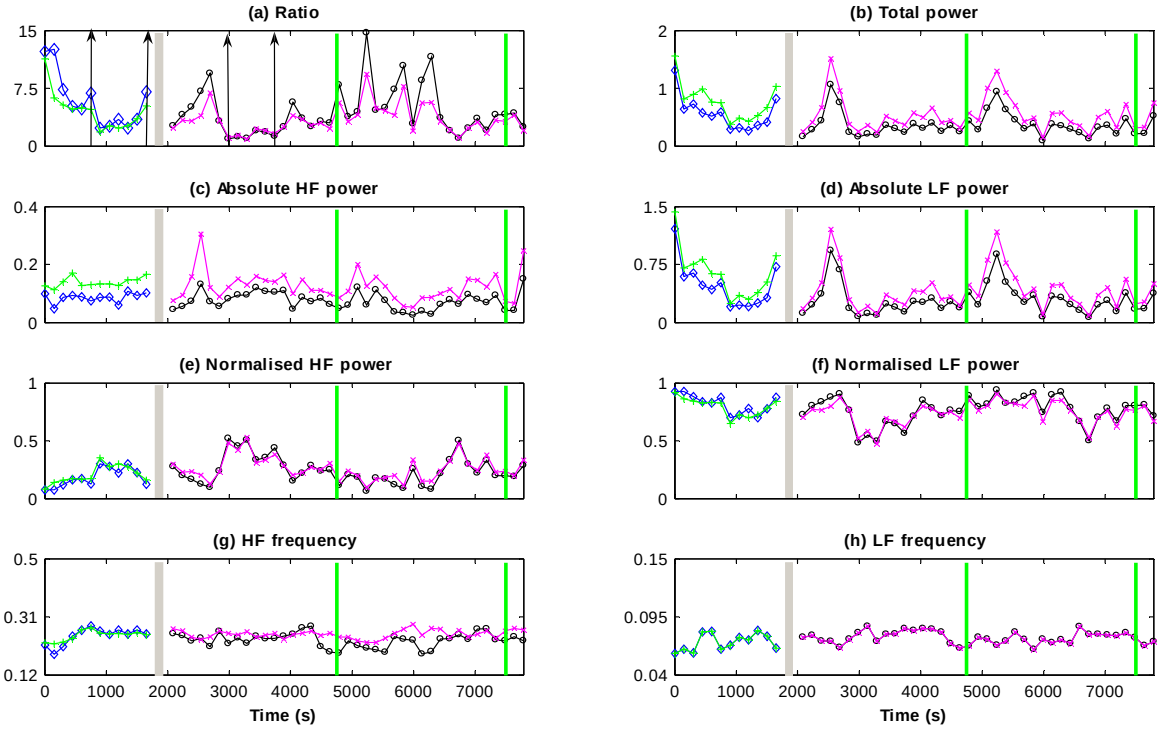

Patient 3

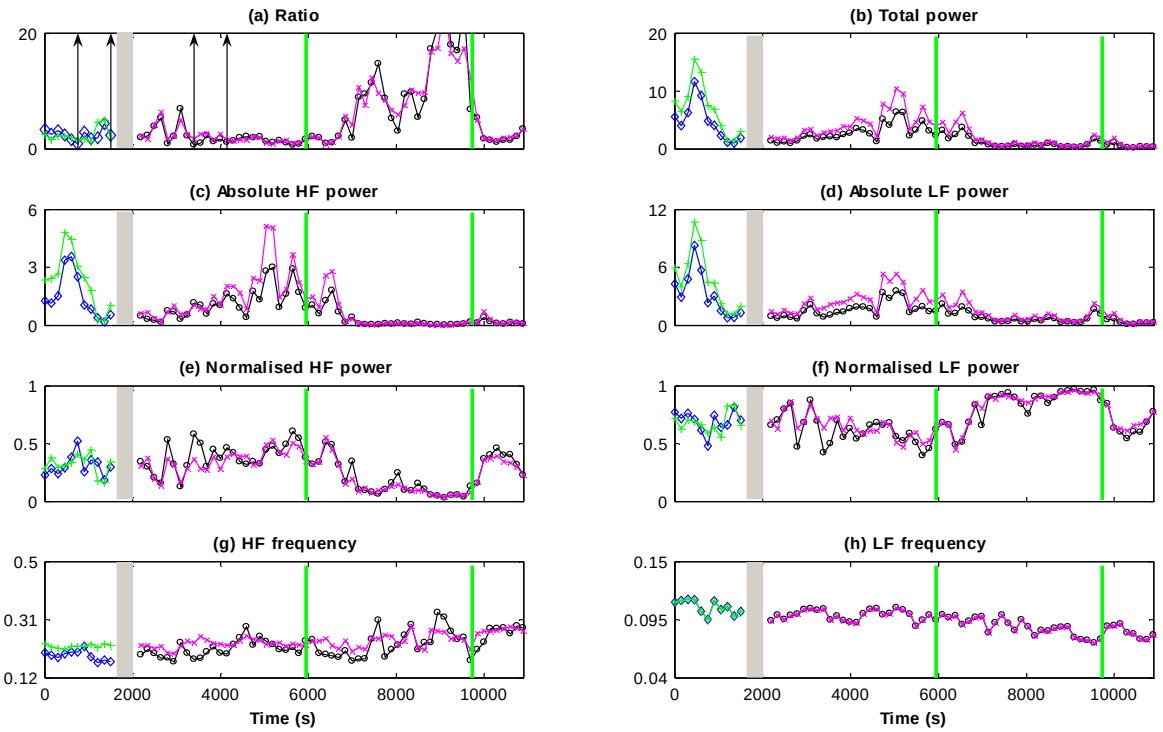

Patient 4

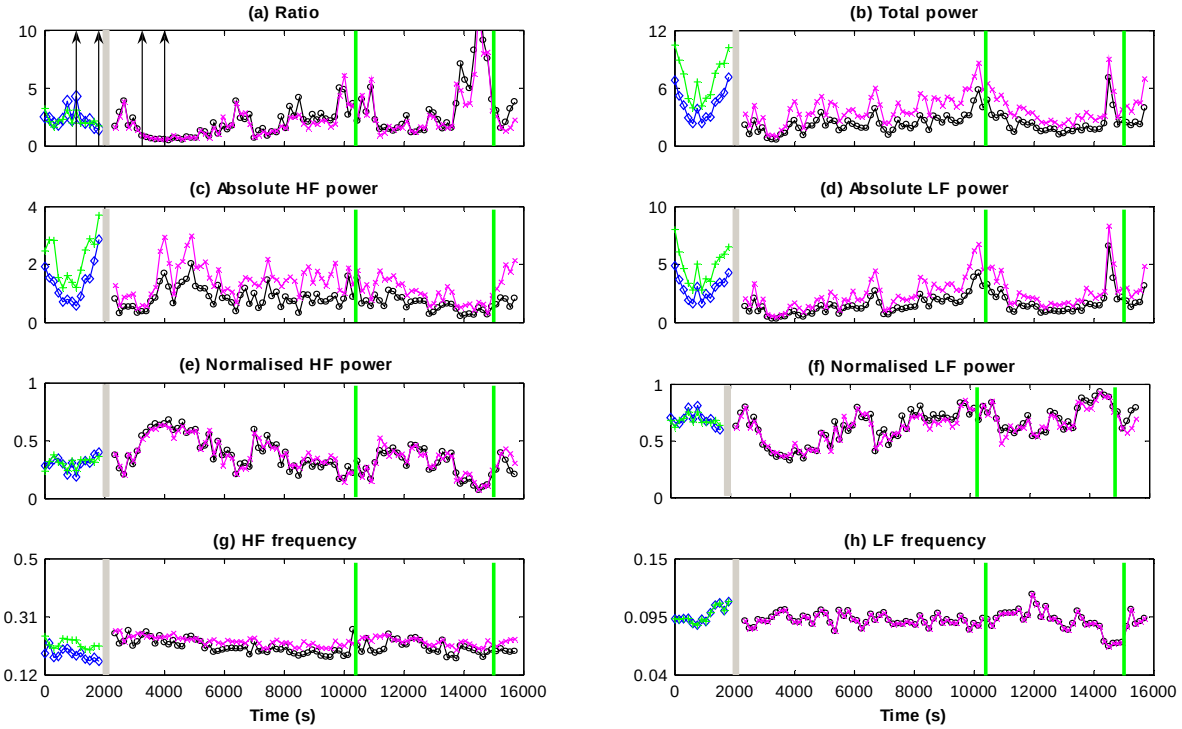

Patient 5

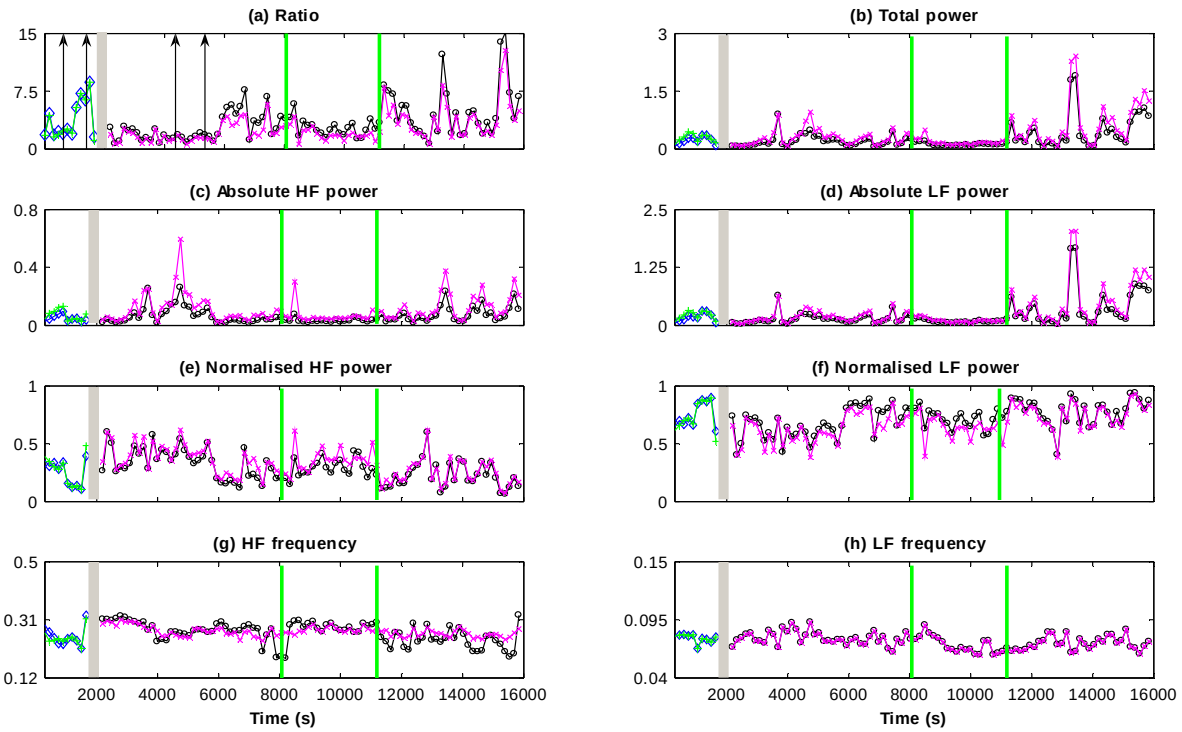

Patient 6

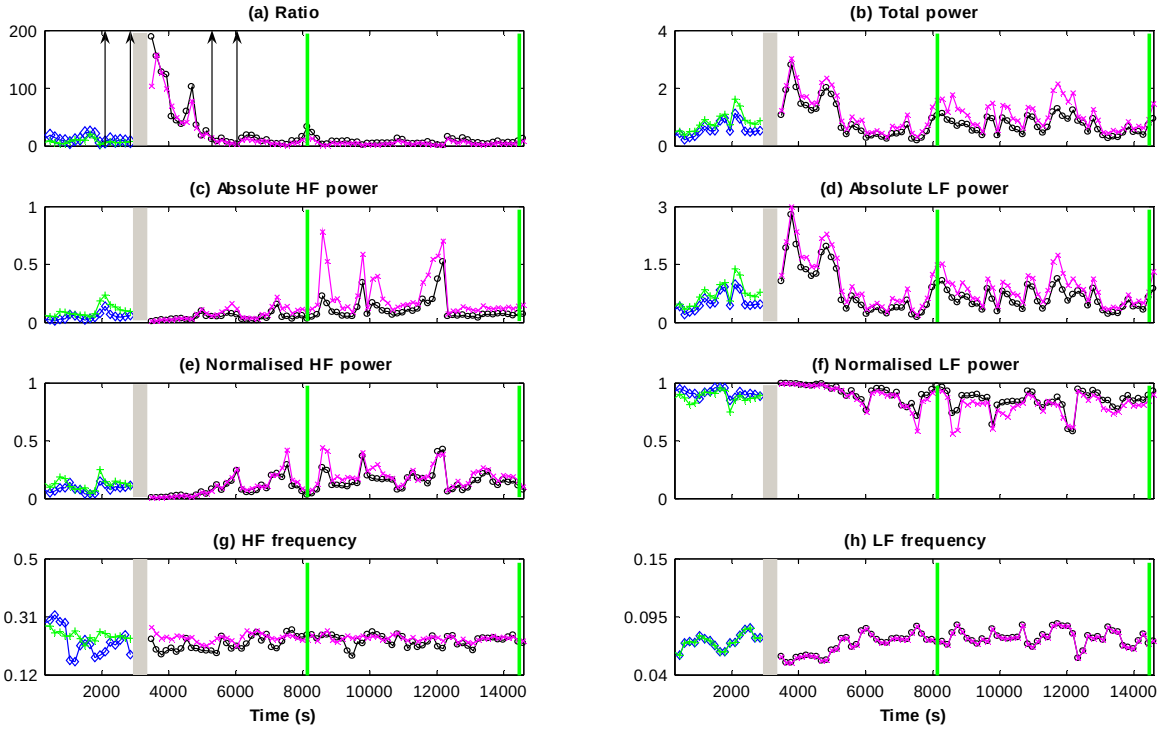

Patient 7

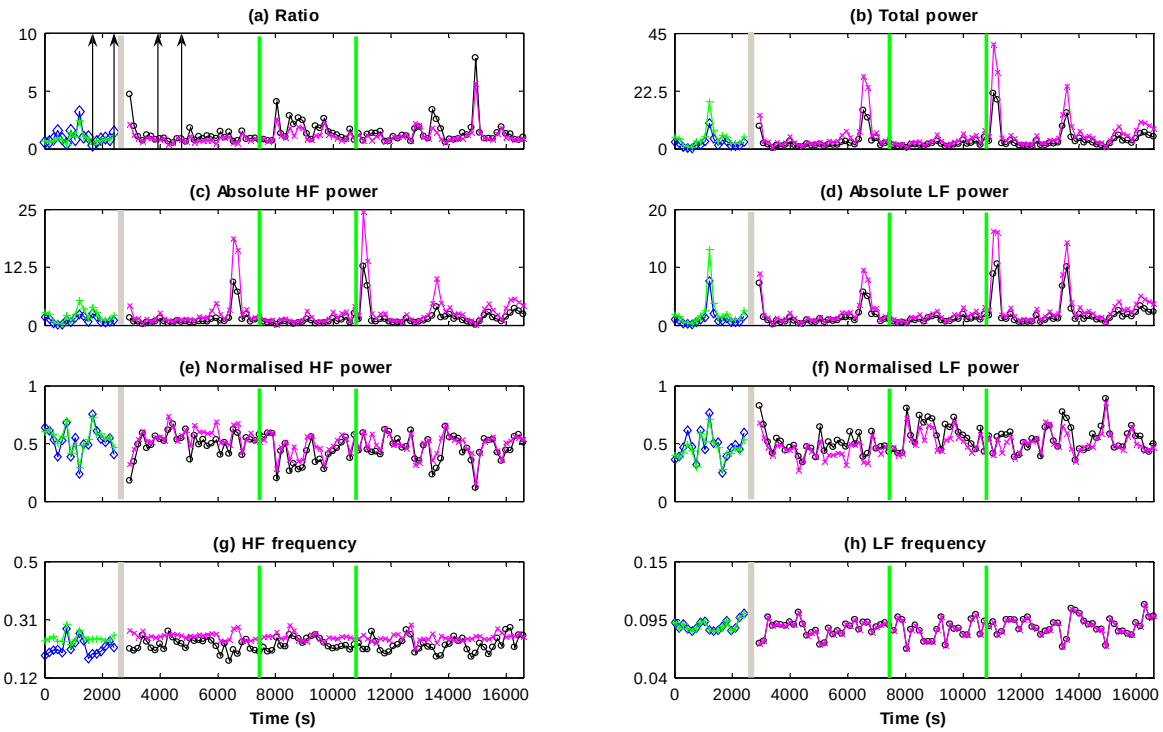

Patient 8

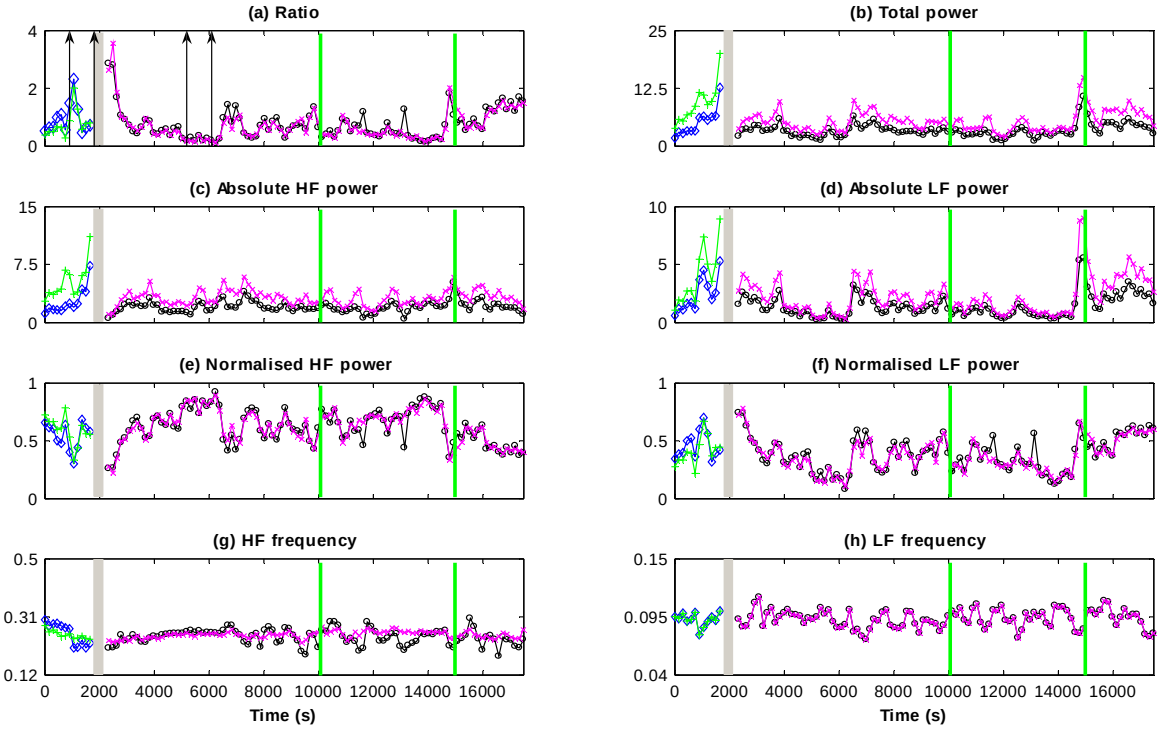

Patient 9

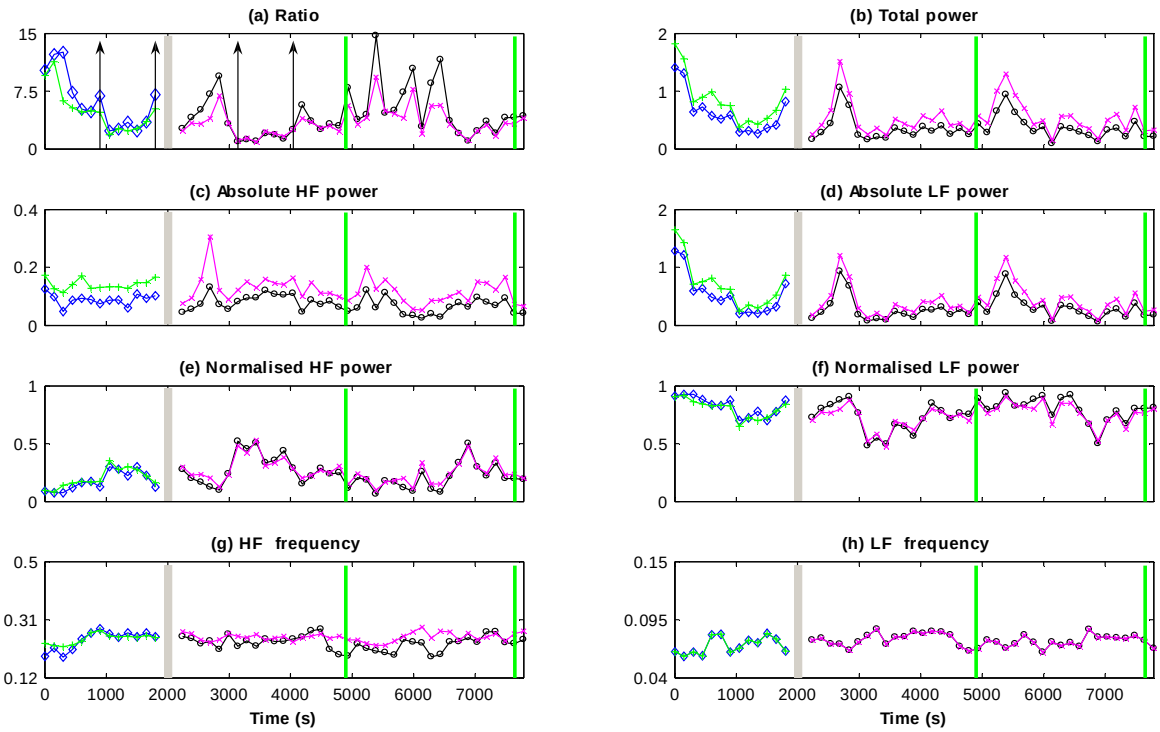

Patient 10

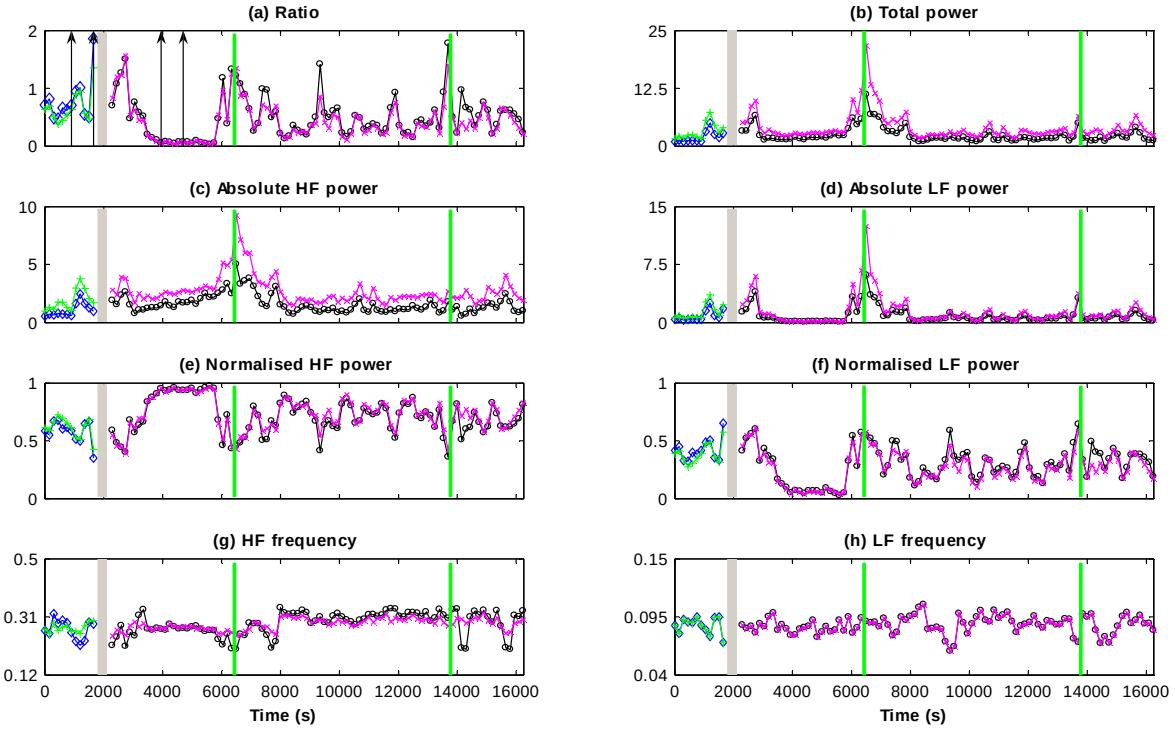

Patient 11

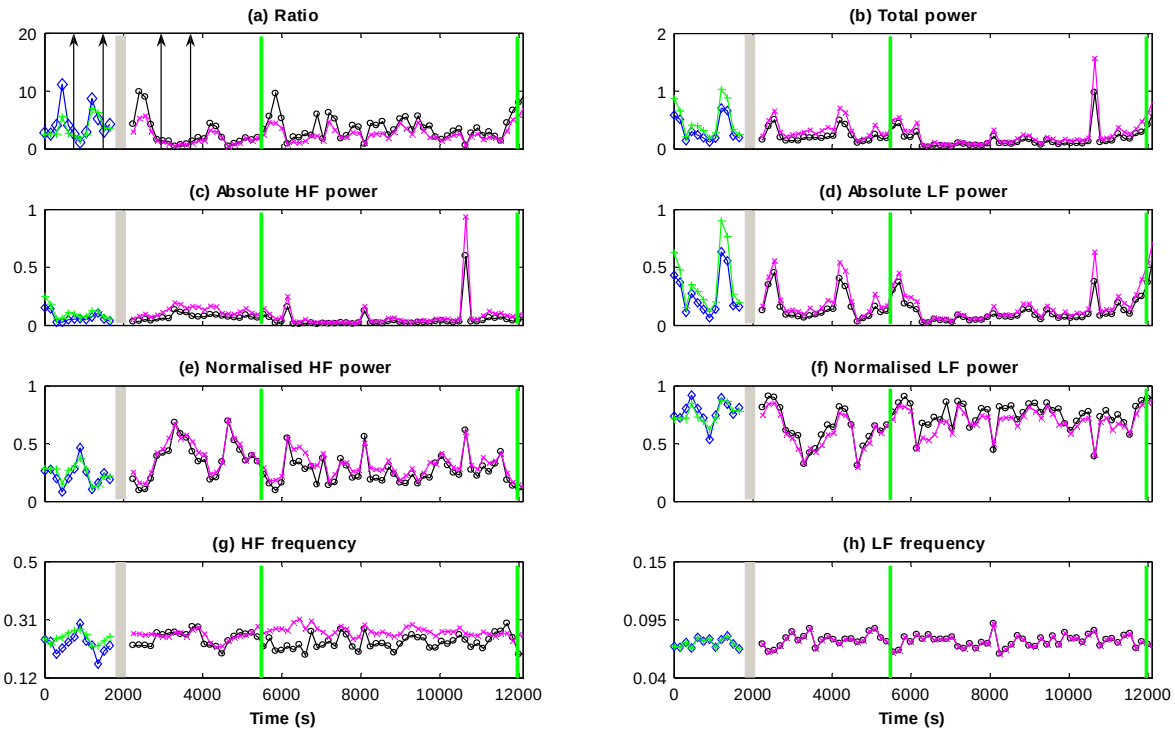

Patient 12

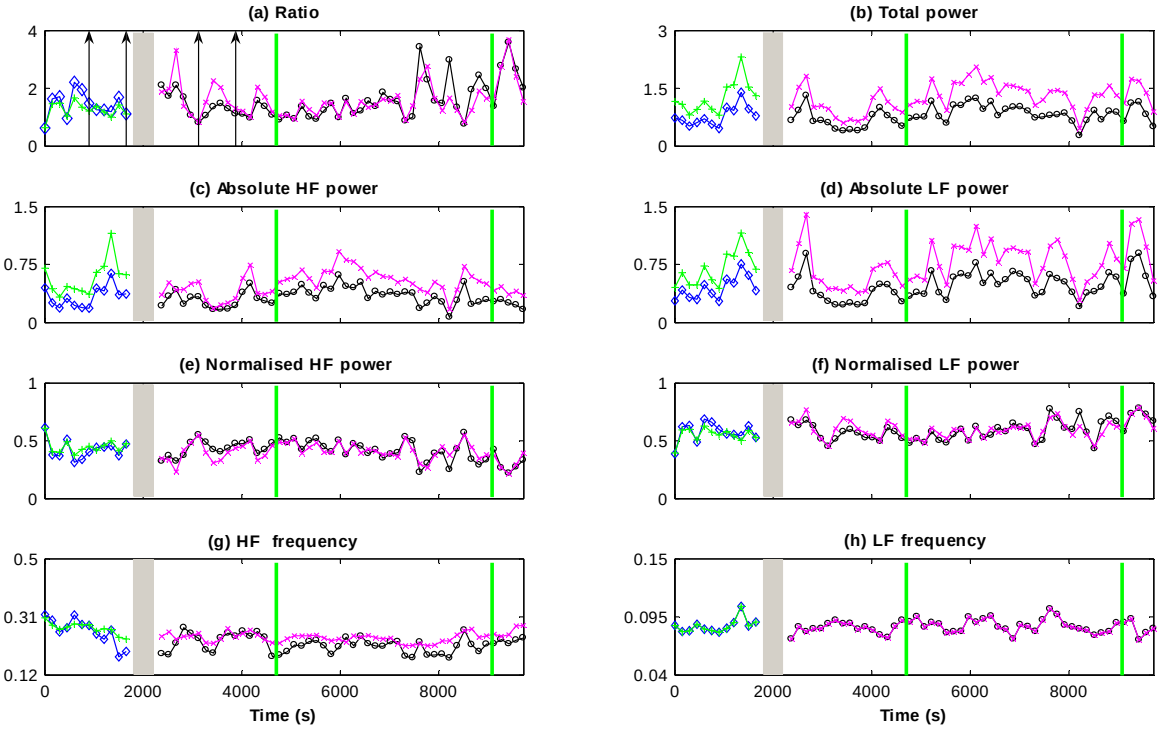

Patient 13

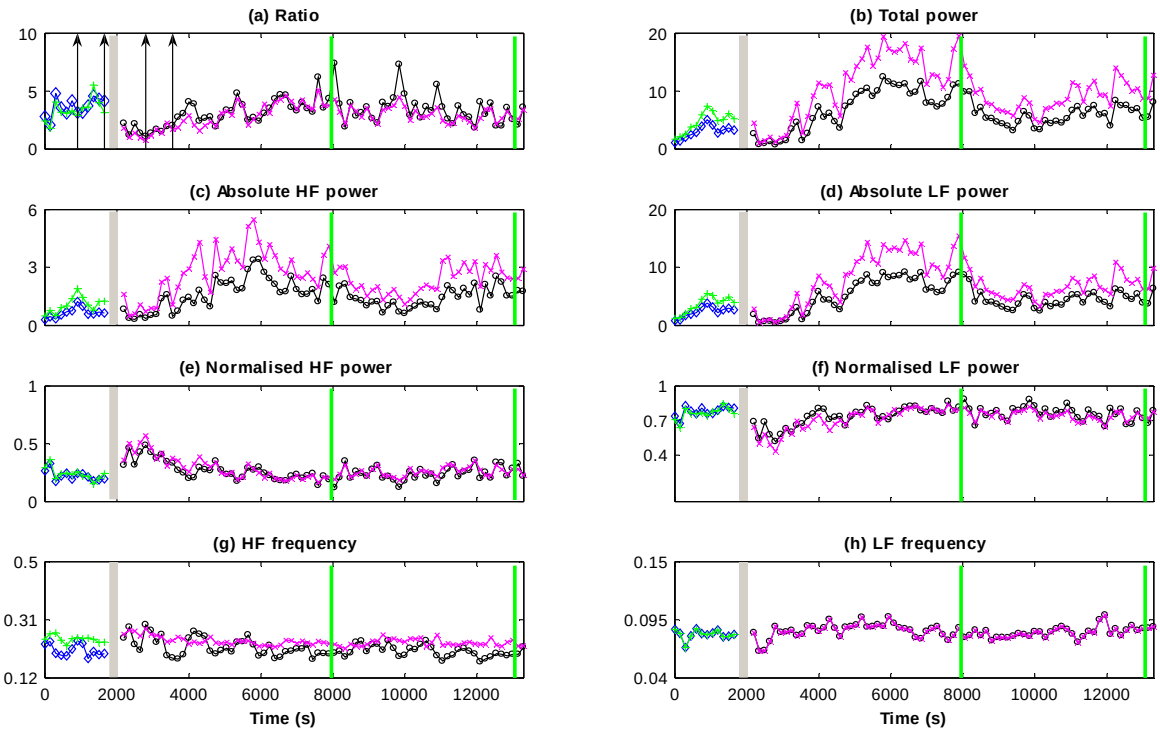

Patient 14

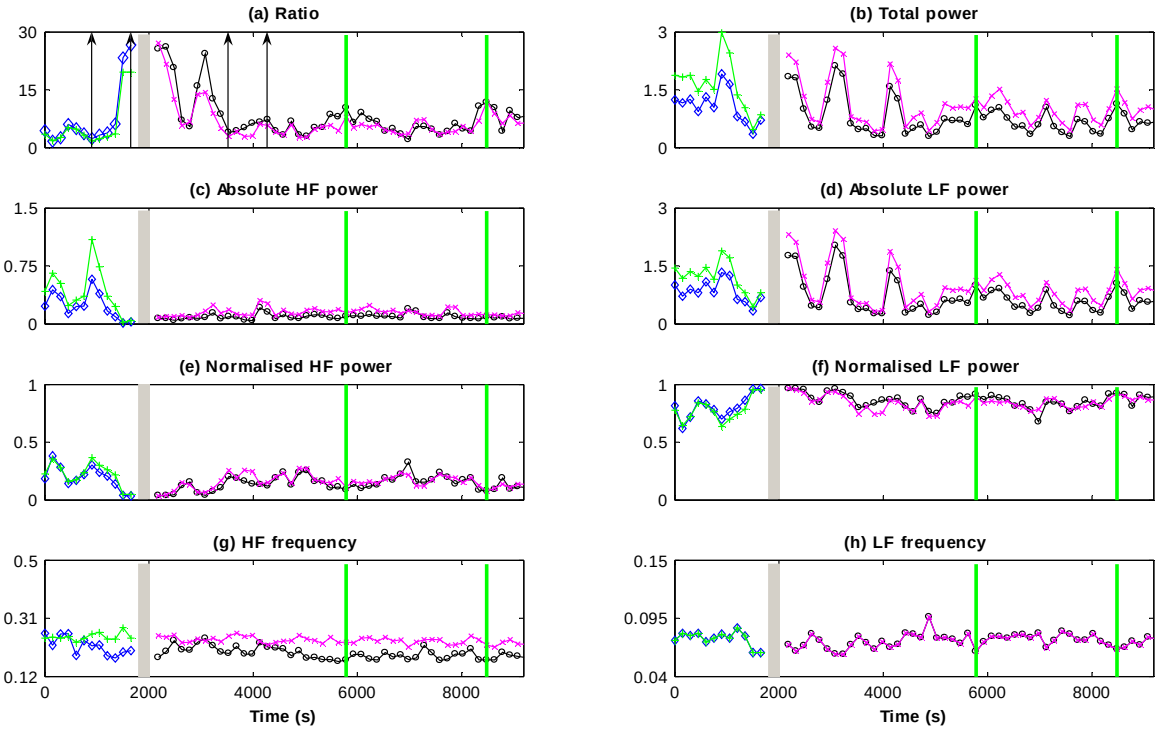
(a) Ratio
(b) Total power
(c) Absolute HF power
(d) Absolute LF power
(e) Normalised HF power
(f) Normalised LF power
(g) HF frequency
(h) LF frequency
Time (s)
Time (s)

B

Parametric analysis results

Results obtained from the parametric analysis of data from patients undergoing local anaesthetic procedure. In each plot the grey vertical block represents the time of block (anaesthesia) application and the green vertical lines represent start and end of the surgery. The vertical arrow pairs in part (a) show the data segment before and after the application of block which was used in statistical analysis. Each plot shows the parameter values estimated using both the fixed and the variable boundary method. Lines in green and magenta colour represent the parameter values before and after the block application estimated using fixed boundary method respectively. In the case of variable boundary method the same information is presented with blue and black colour lines respectively. The units on y-axis for the plots showing power are s^2/Hz and for the plots showing frequency values is Hz.

Patient 1

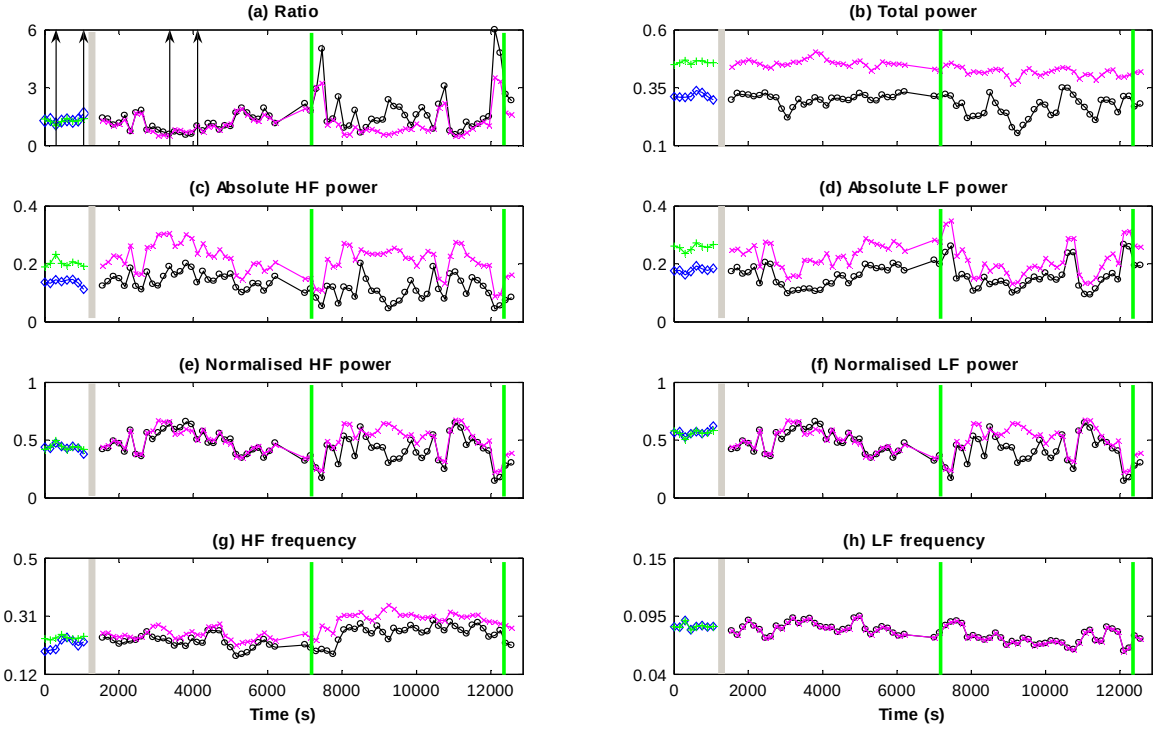

Patient 2

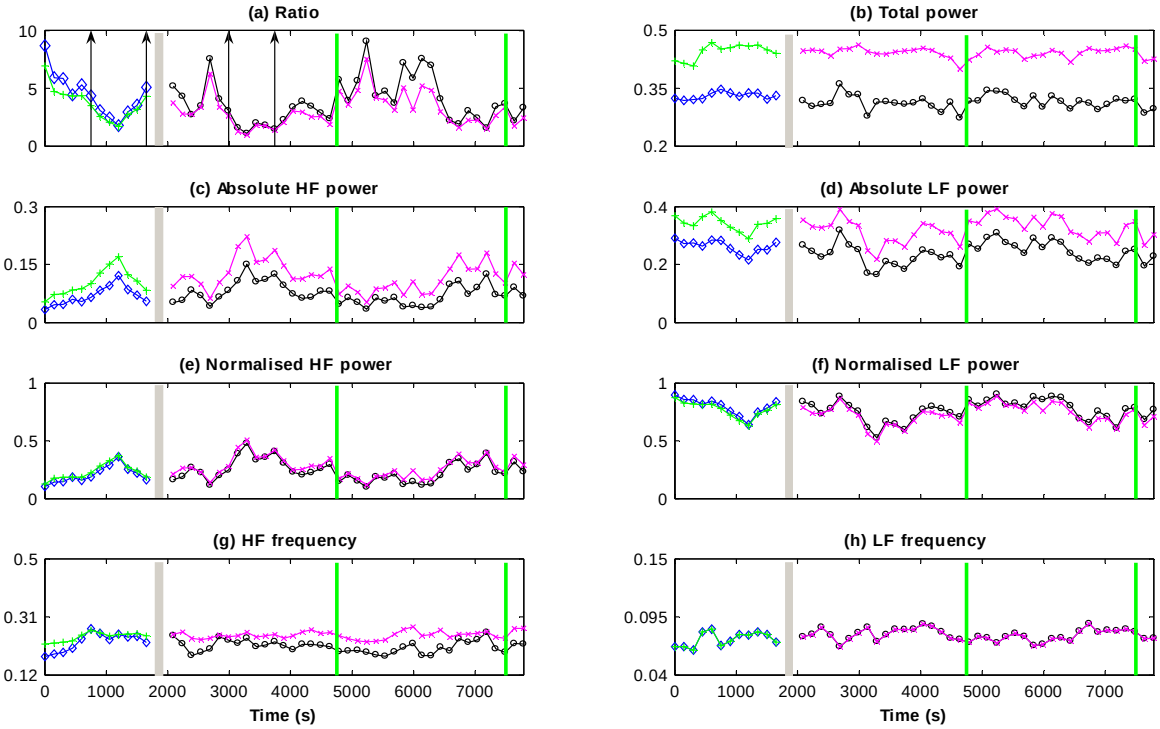

Patient 3

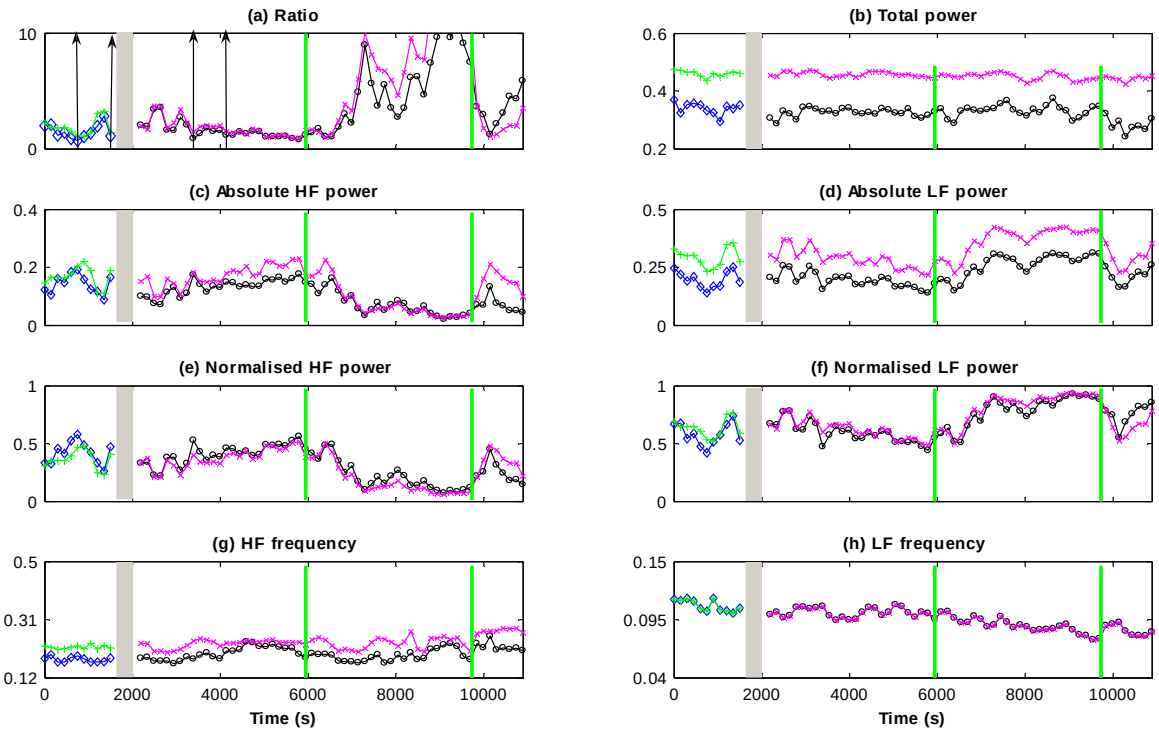

Patient 4

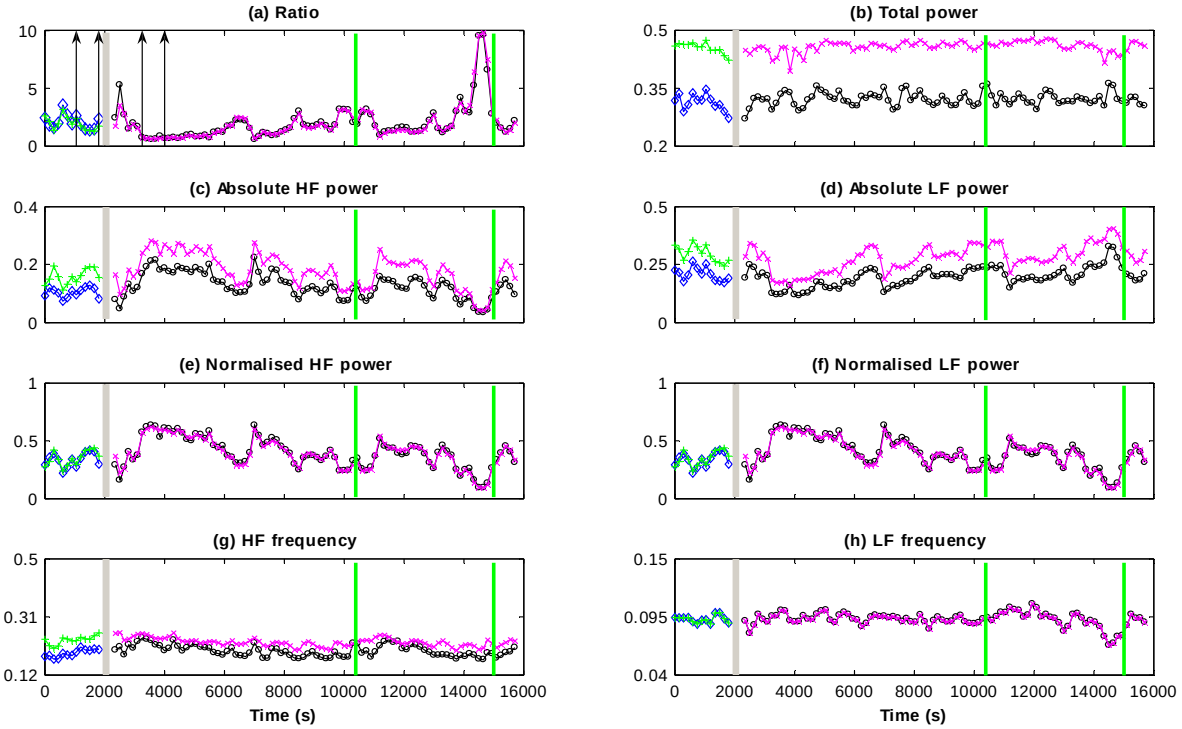

Patient 5

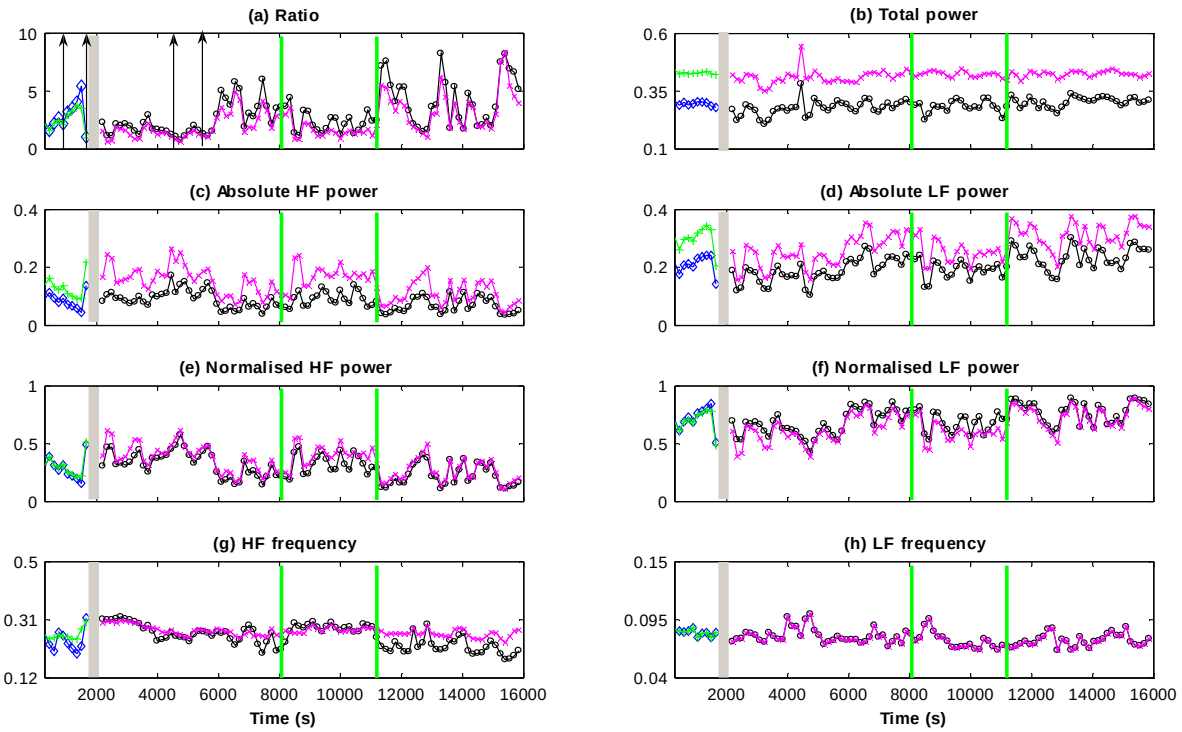

Patient 6

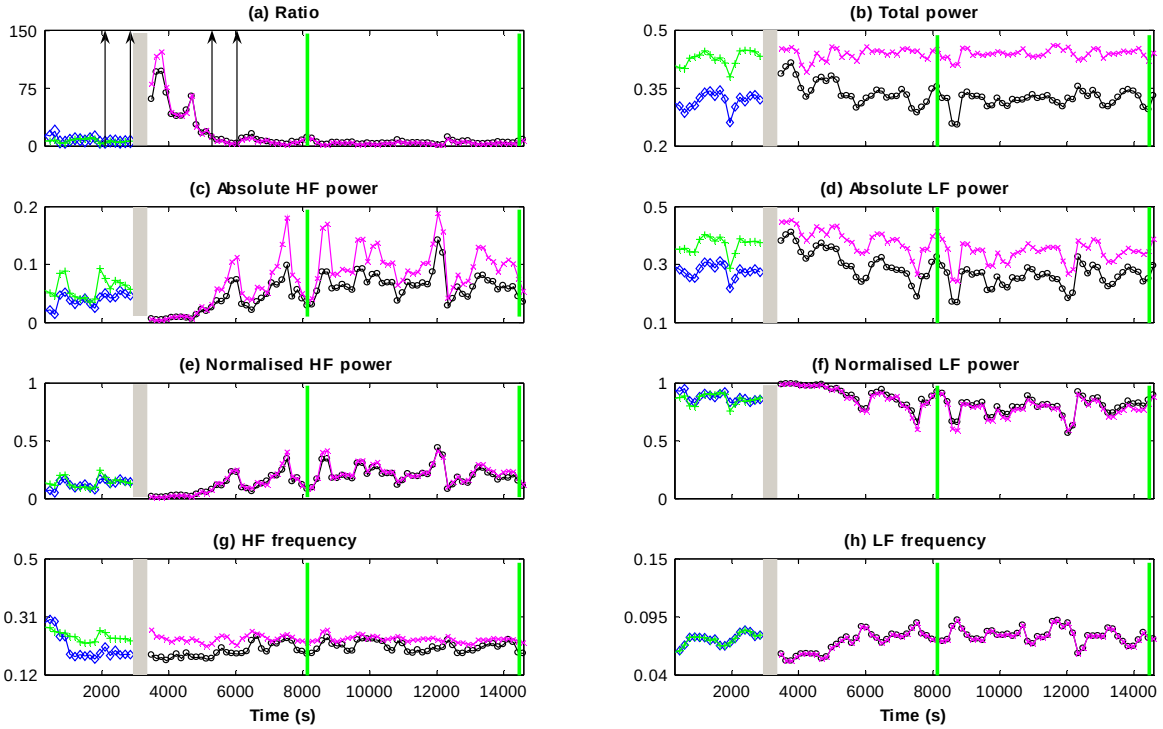

Patient 7

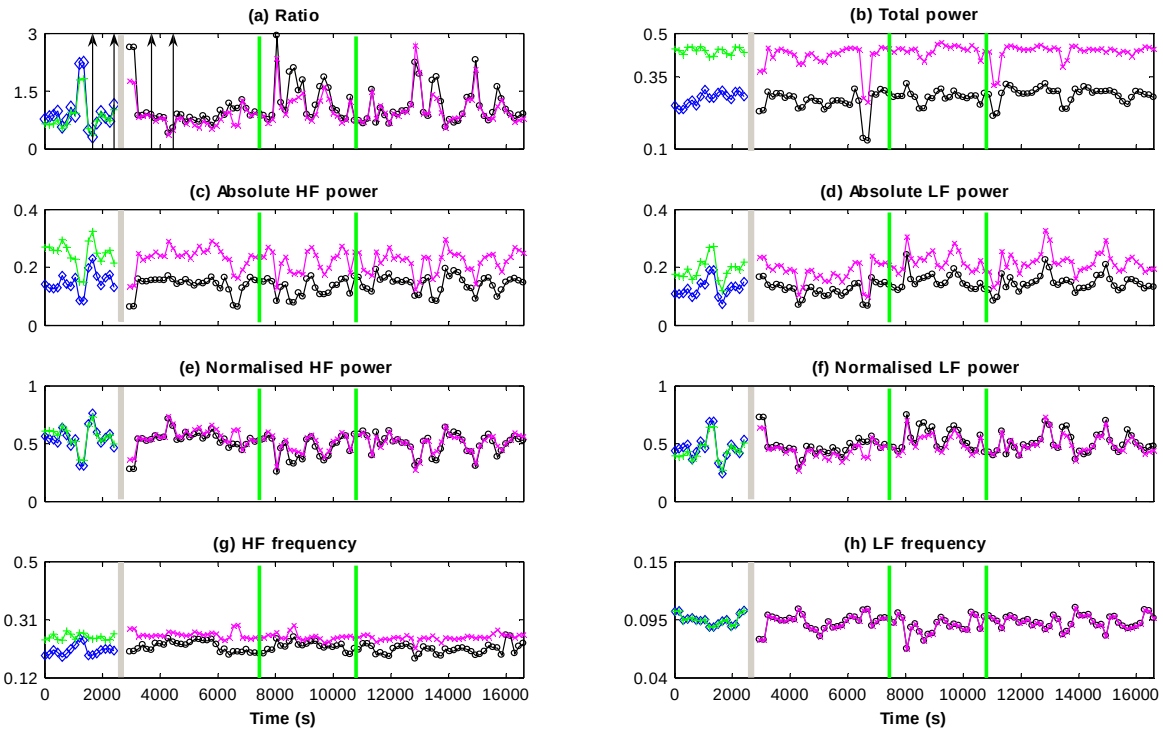

Patient 8

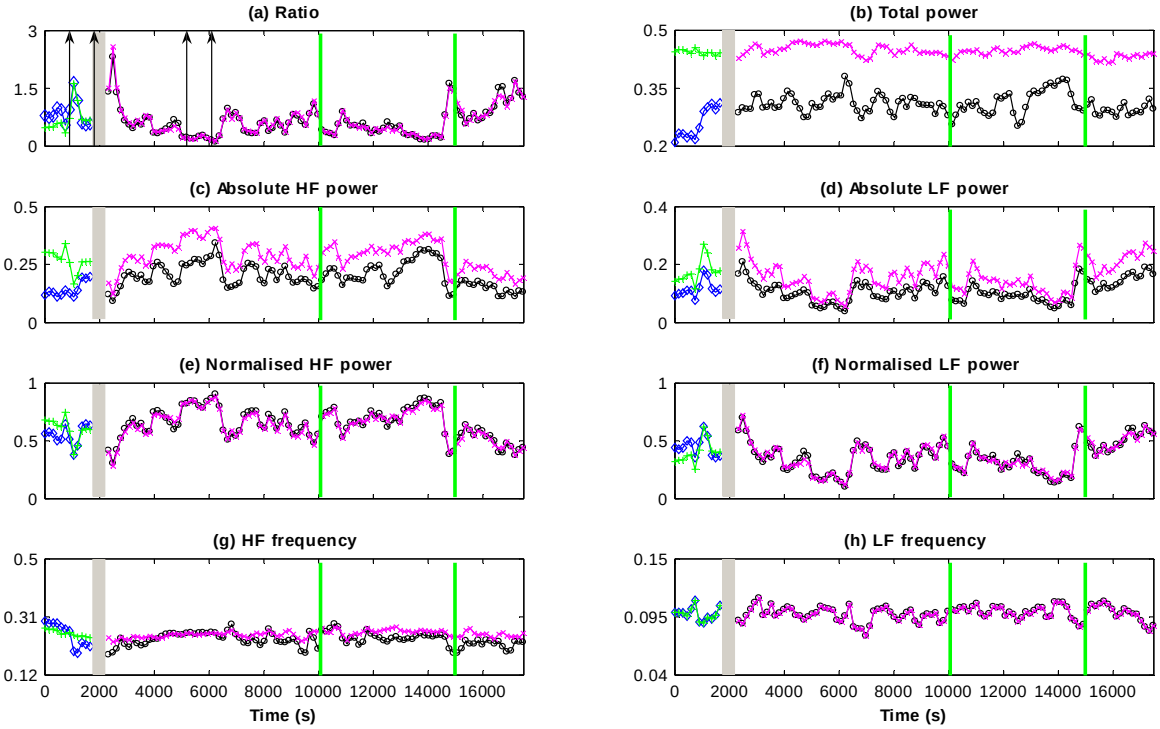

Patient 9

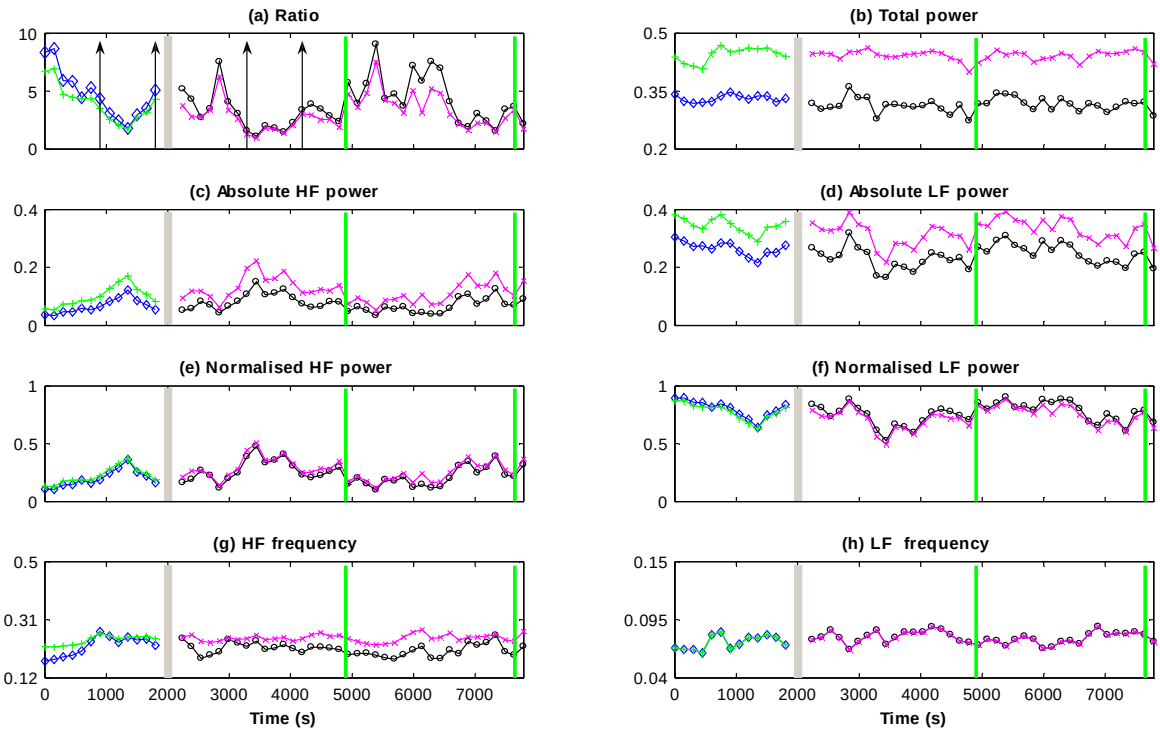

Patient 10

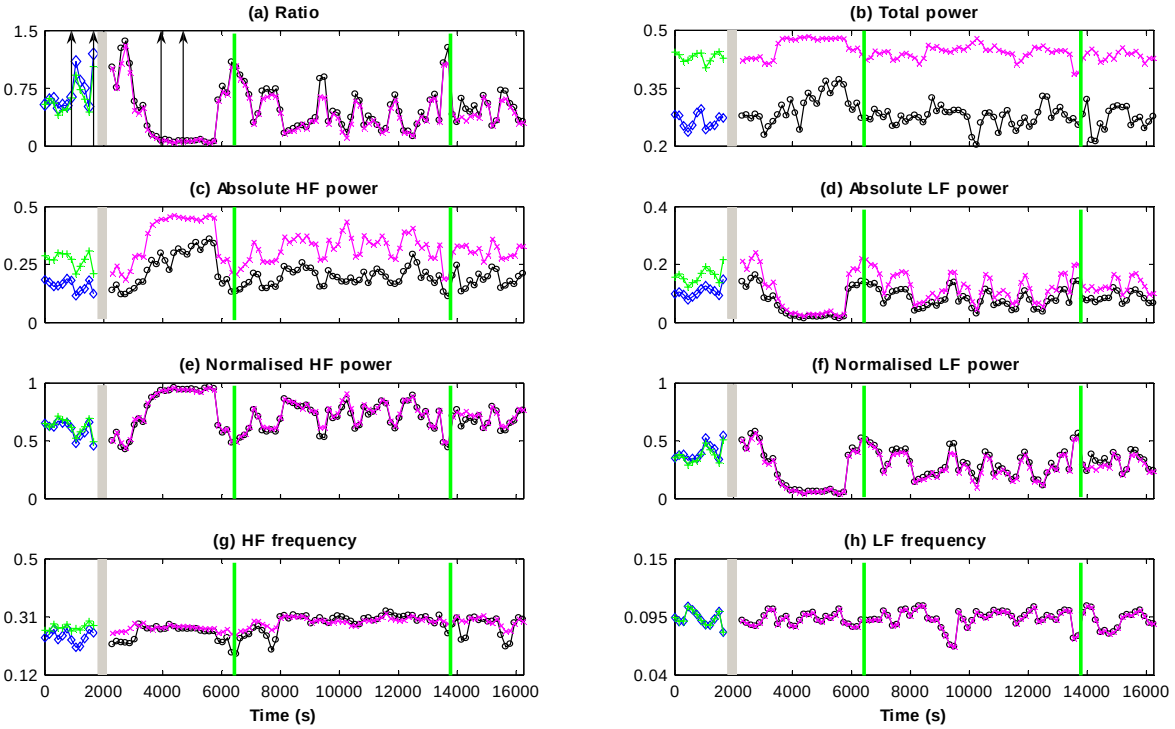

Patient 11

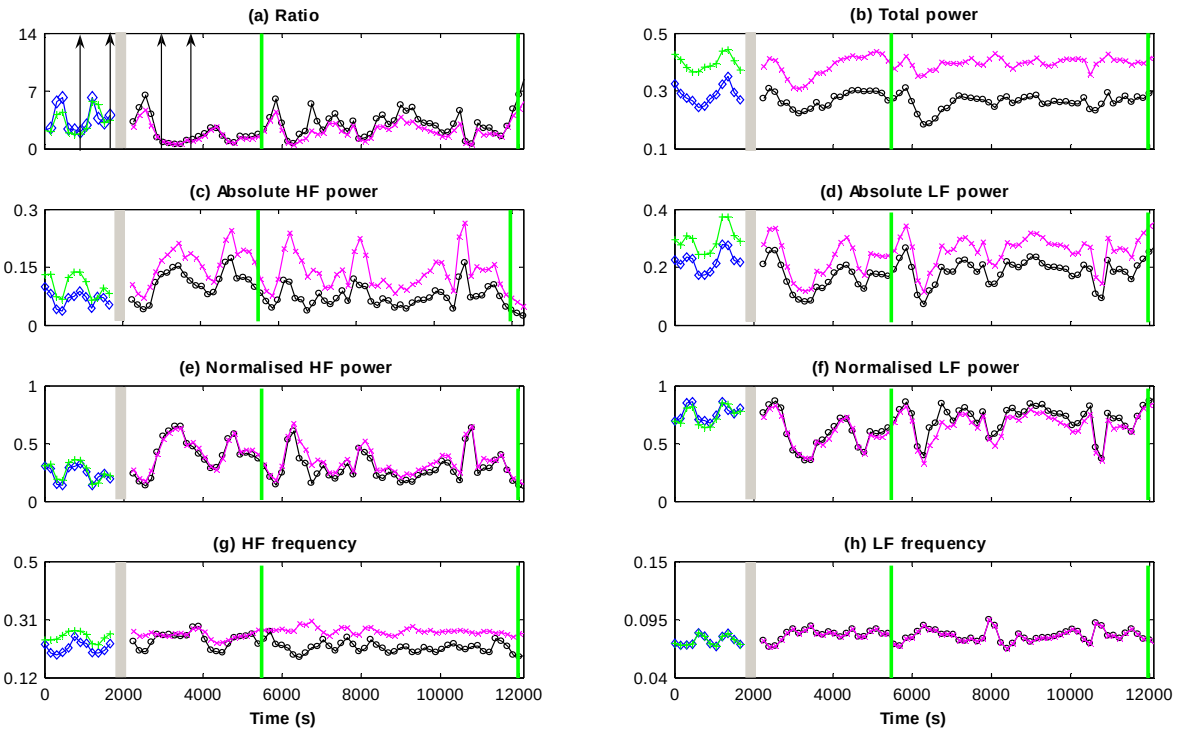

Patient 12

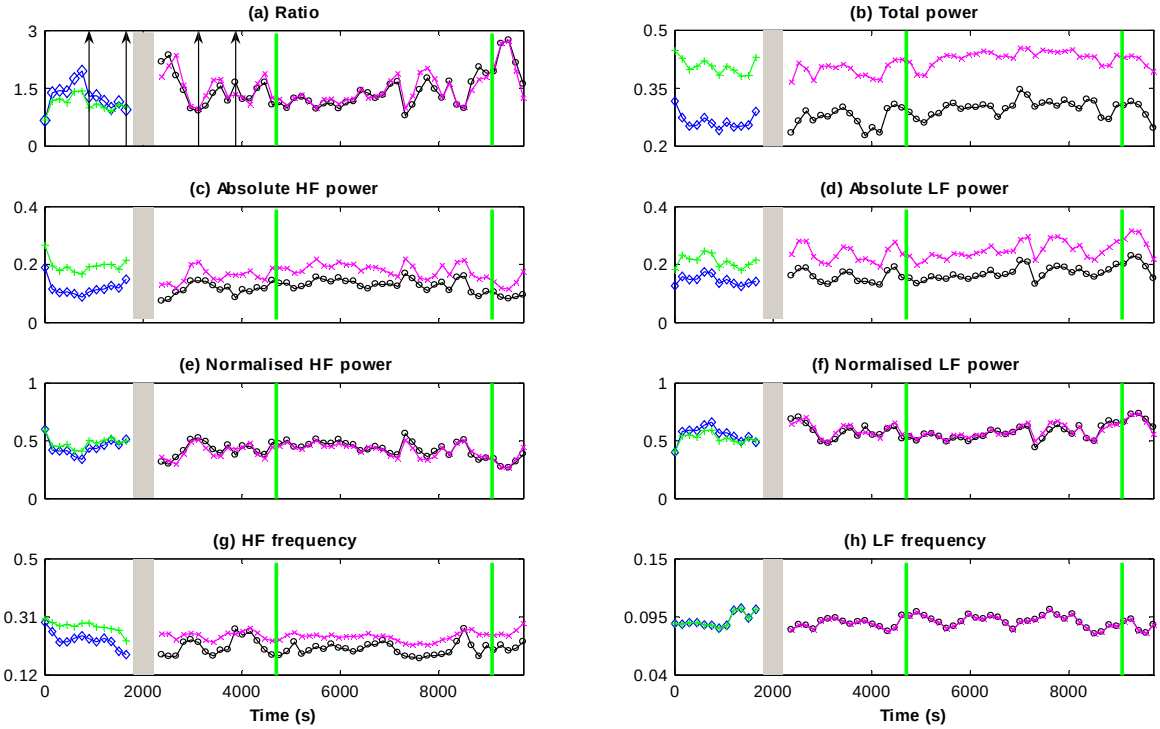

Patient 13

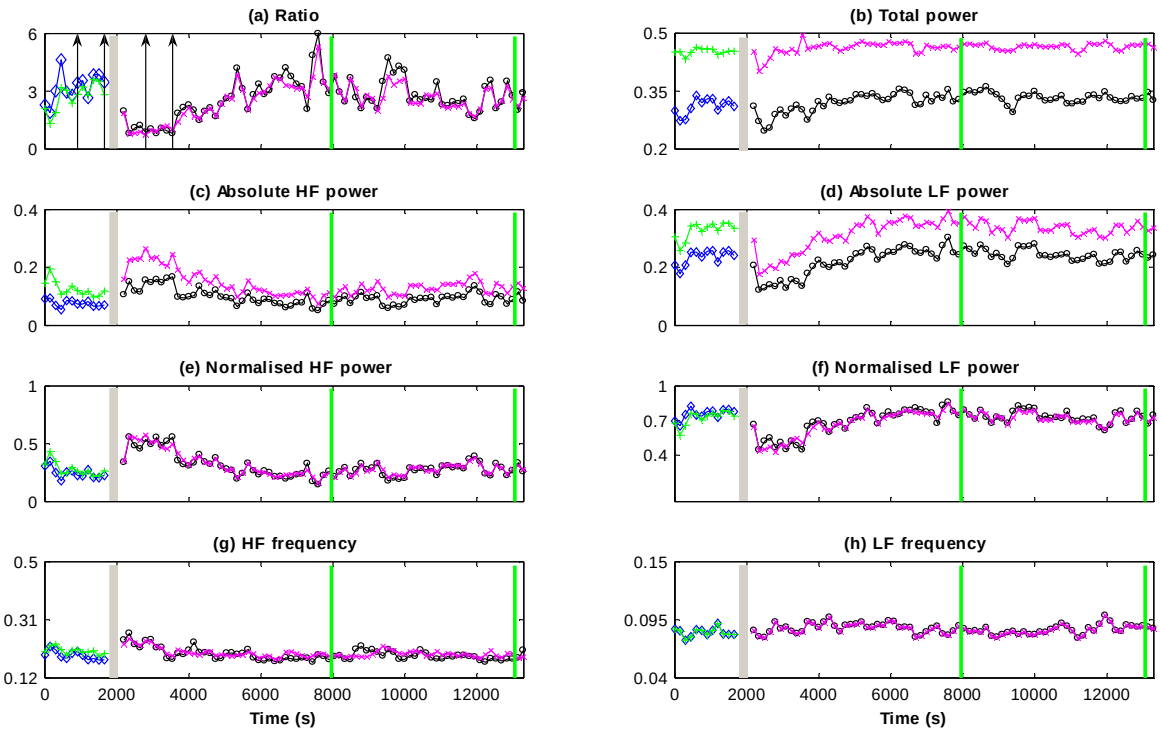

Patient 14

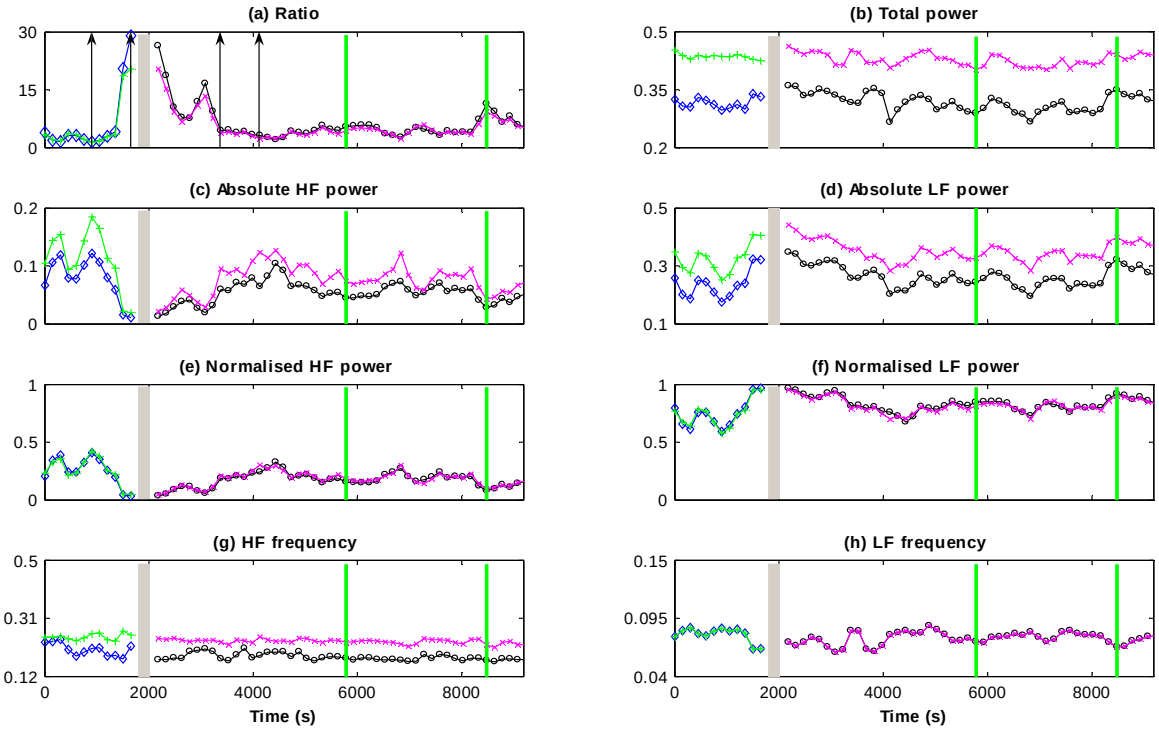
(a) Ratio
30
15
0
(b) Total power
0.5
0.35
0.2
(c) Absolute HF power
0.2
0.1
0
(d) Absolute LF power
0.5
0.3
0.1
(e) Normalised HF power
1
0.5
0
(f) Normalised LF power
1
0.5
0
(g) HF frequency
0.5
0.31
0.12
(h) LF frequency
0.15
0.095
0.04
0
2000
4000
6000
8000
Time (s)

C

Continous wavelet anlysis results

Results obtained from the continous wavelet analysis of data from patients undergoing local anaesthetic procedure. In each plot the grey vertical block represents the time of block (anaesthesia) application and the green vertical lines represent start and end of the surgery. The vertical arrow pairs in part (a) show the data segment before and after the application of block which was used in statistical analysis. Each plot shows the parameter values estimated using both the fixed and the variable boundary method. Lines in green and magenta colour represent the parameter values before and after the block application estimated using fixed boundary method respectively. In the case of variable boundary method the same information is presented with blue and black colour lines respectively. The parameter values are the mean values calculated from a period of one minute. The units on y-axis for the plots showing power are s^2/Hz and for the plots showing frequency values is Hz.

Patient 1

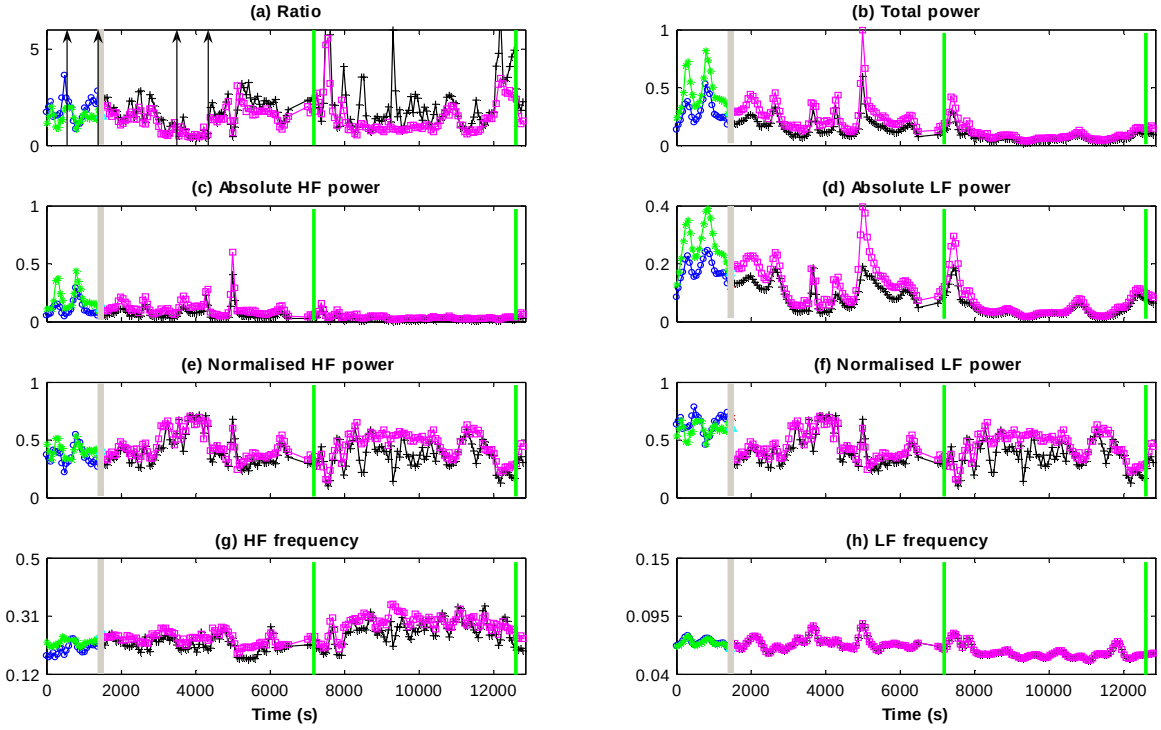

Patient 2

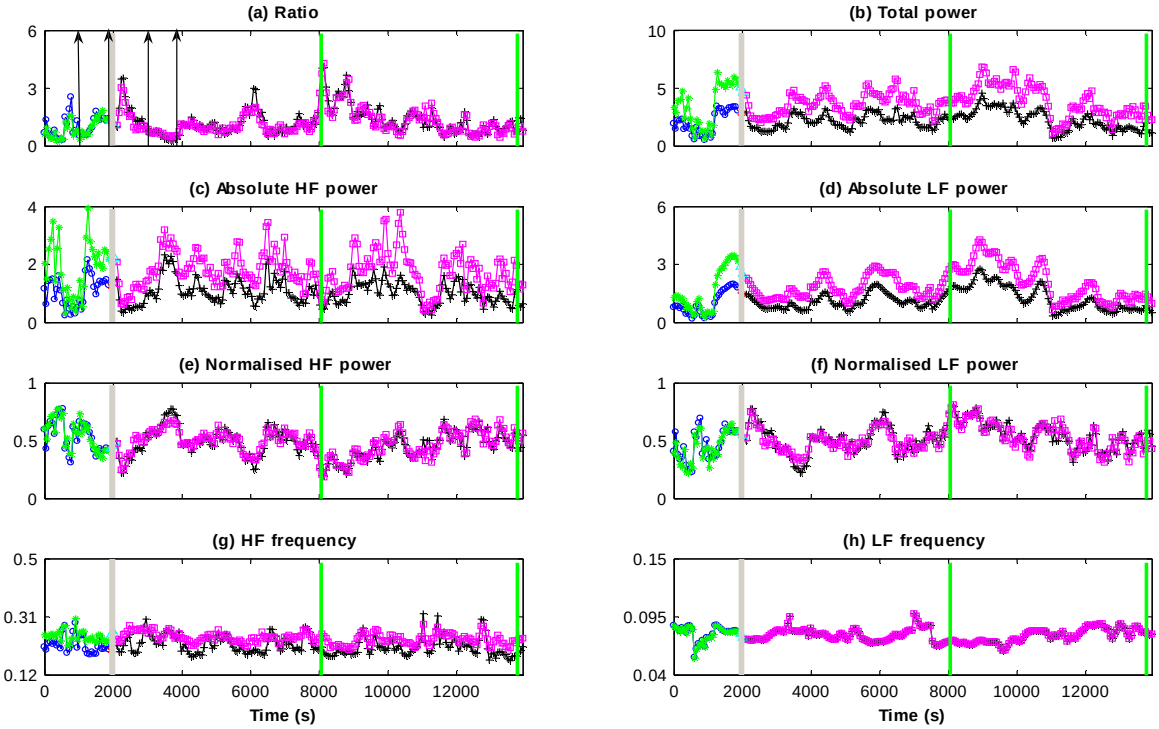

Patient 3

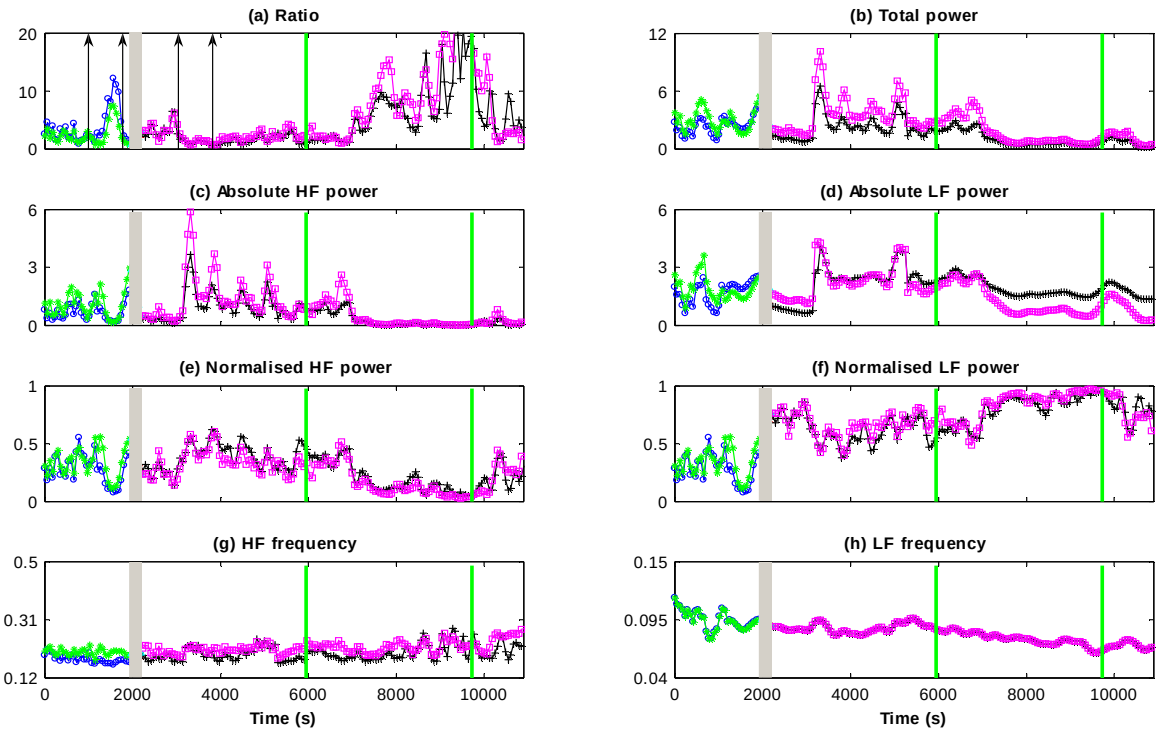

Patient 4

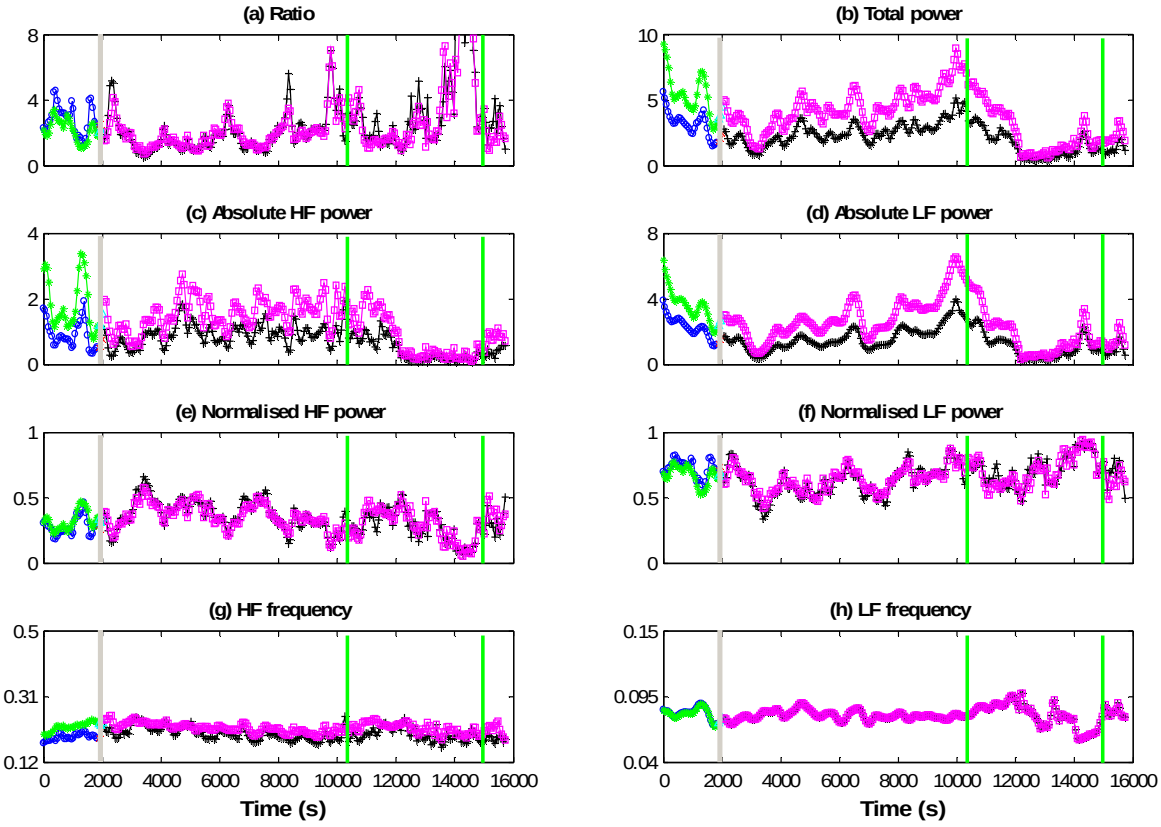

Patient 5

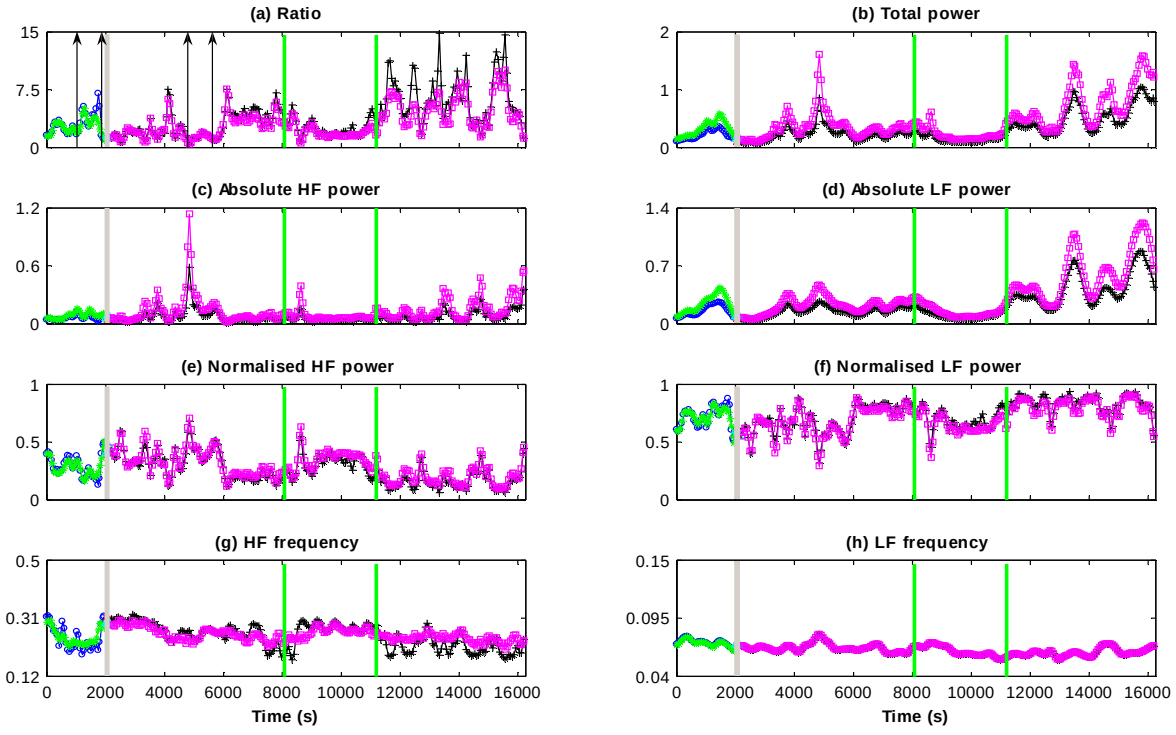

Patient 6

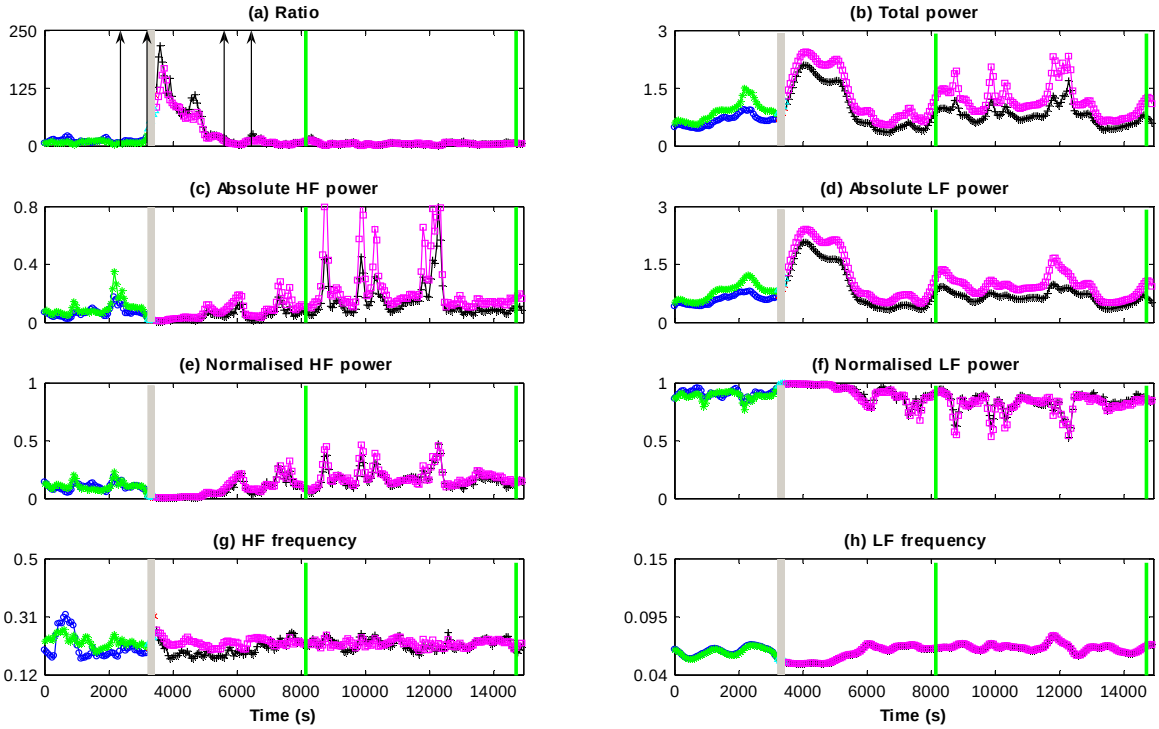

Patient 7

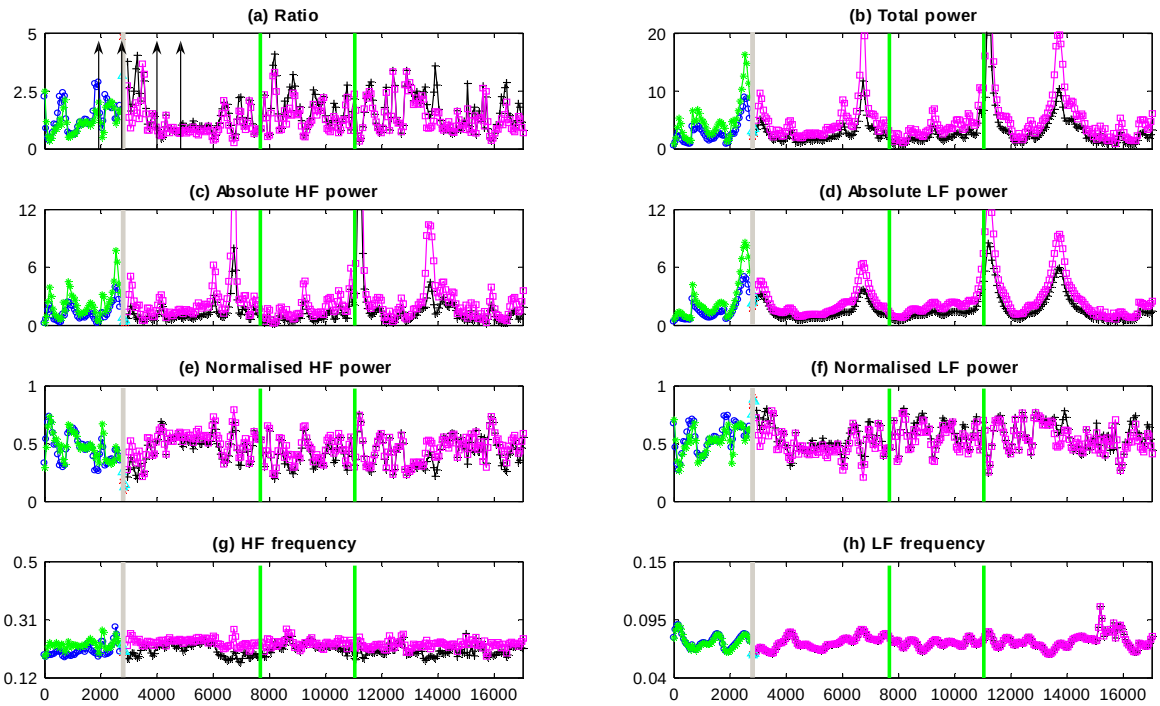

Patient 8

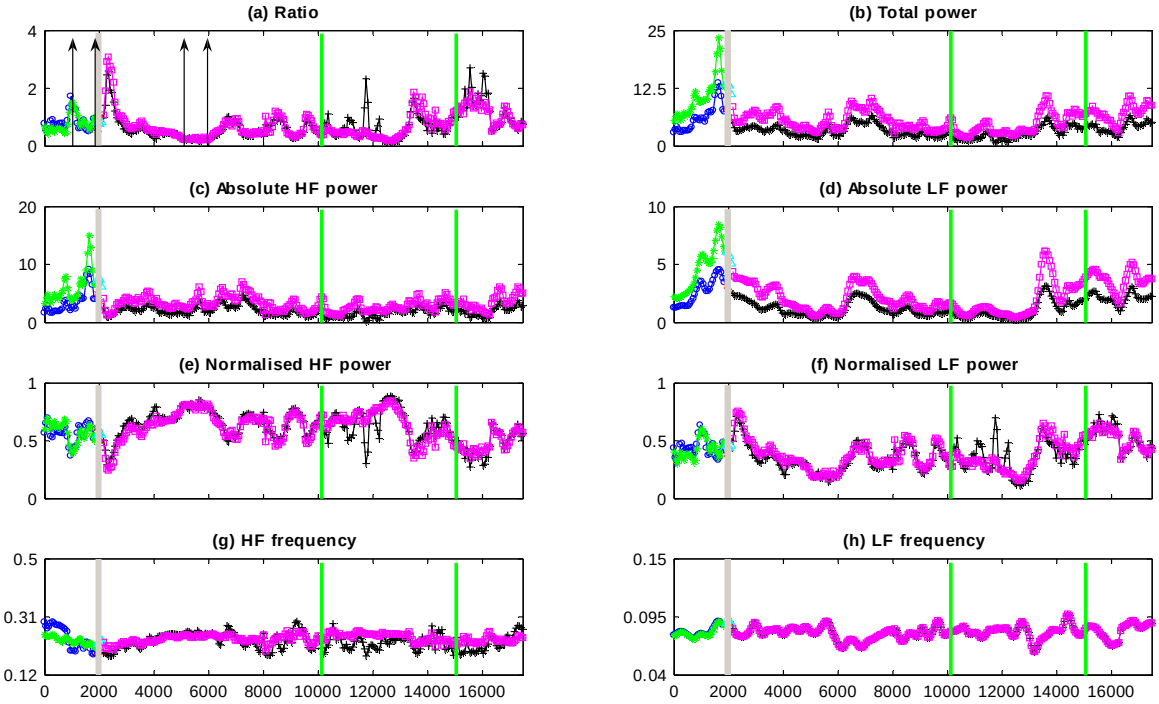

Patient 9

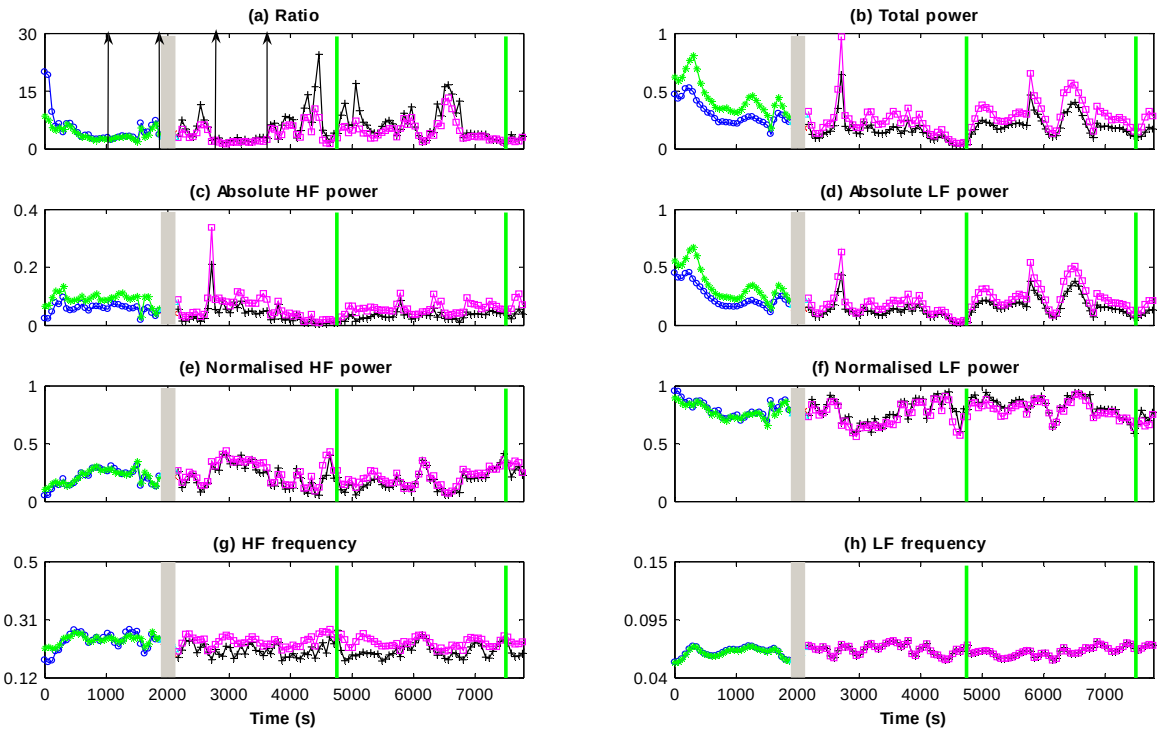

Patient 10

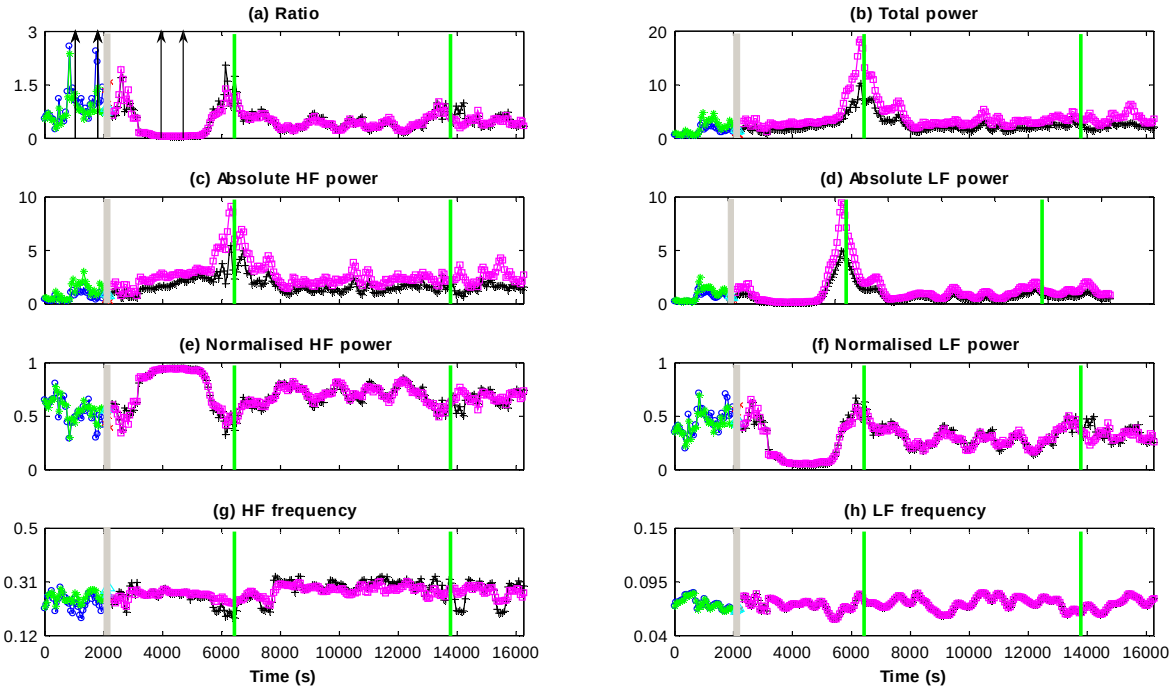

Patient 11

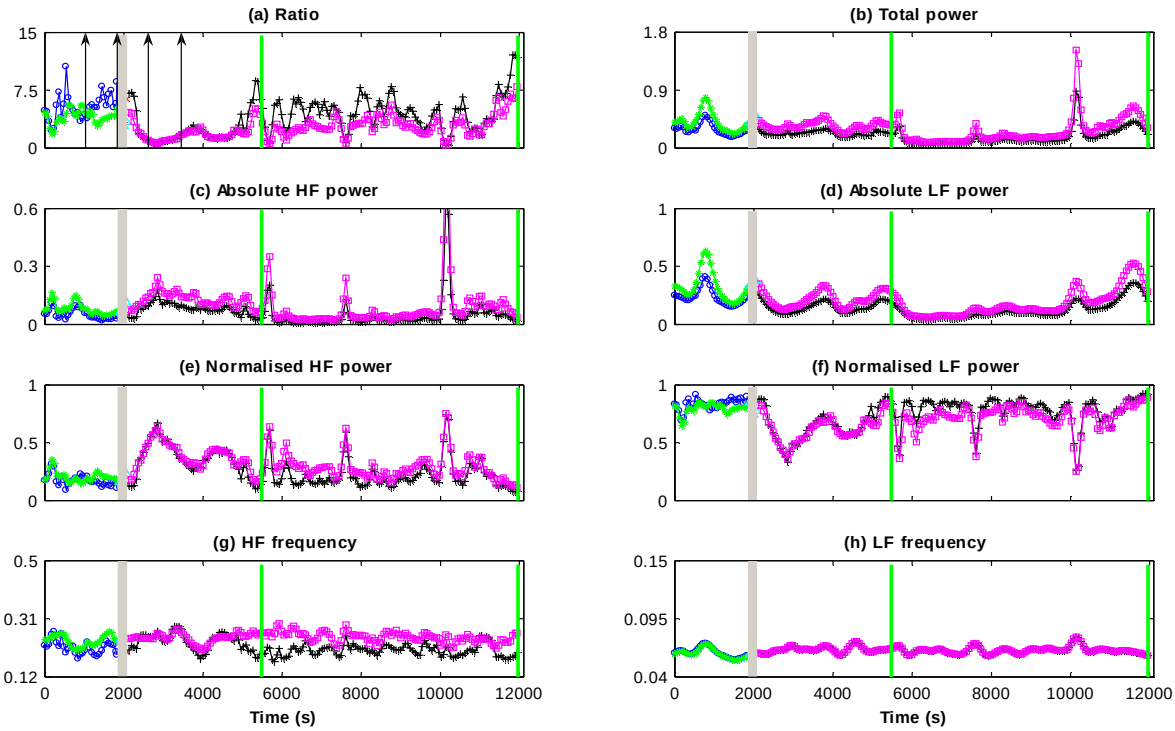

Patient 12

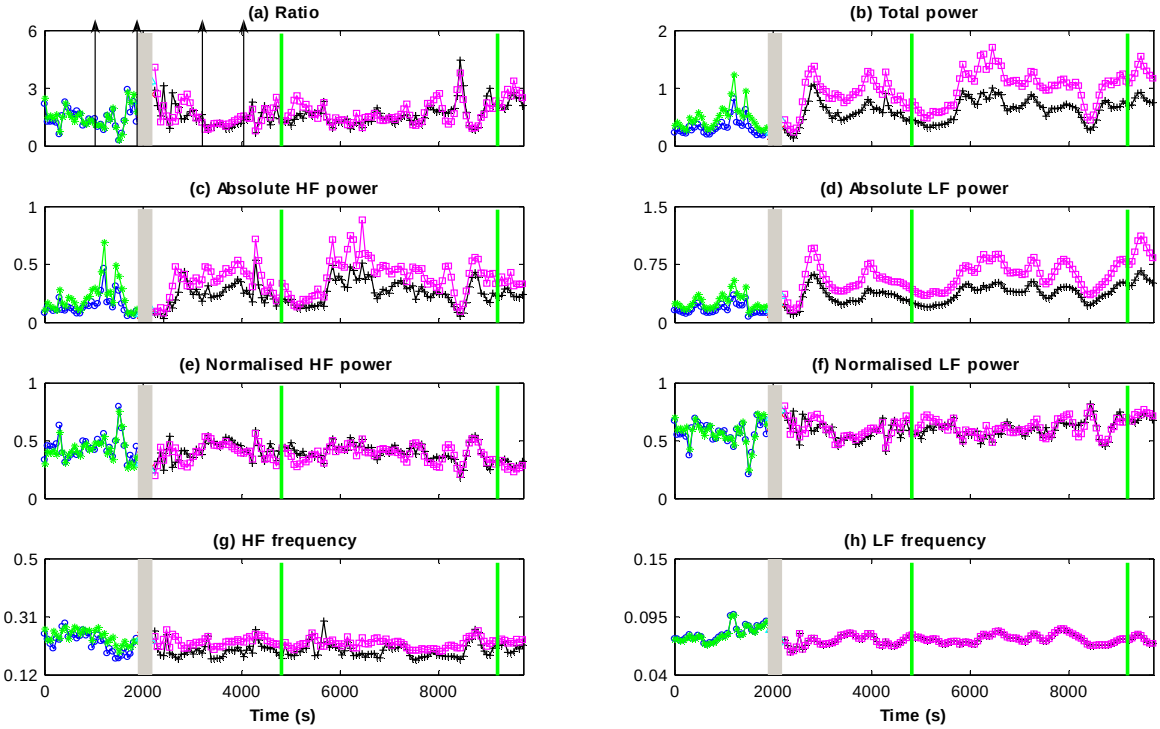

Patient 13

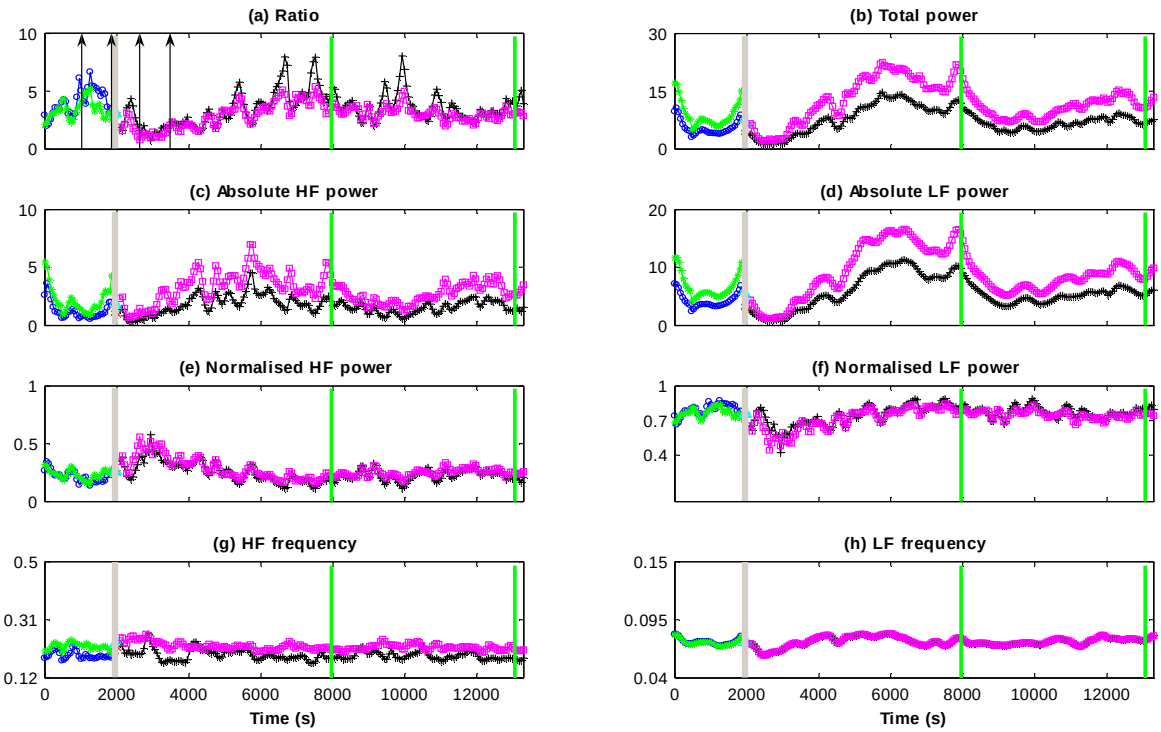

Patient 14

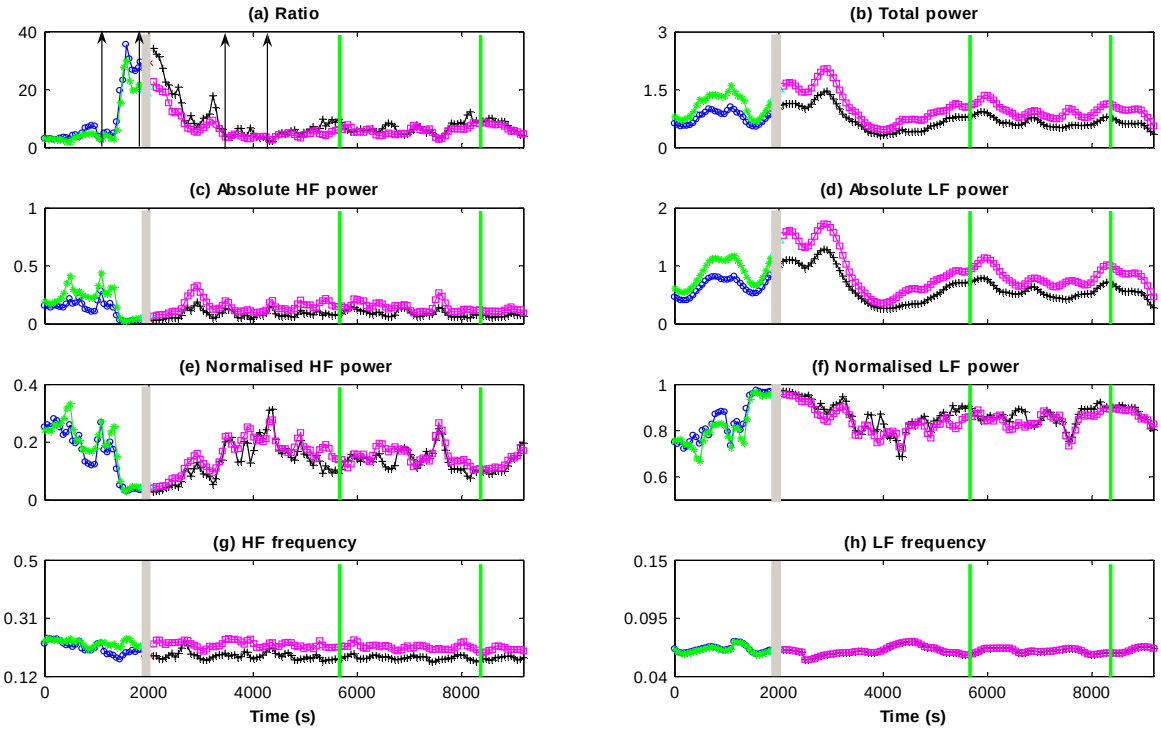
(a) Ratio
(b) Total power
(c) Absolute HF power
(d) Absolute LF power
(e) Normalised HF power
(f) Normalised LF power
(g) HF frequency
(h) LF frequency
Time (s)
Time (s)

D

Smoothed-pseudo Wigner-Ville Distribution anlysis results

Results obtained from the Smoothed-pseudo Wigner-Ville Distribution analysis of data from patients undergoing local anaesthetic procedure. In each plot the grey vertical block represents the time of block (anaesthesia) application and the green vertical lines represent start and end of the surgery. The vertical arrow pairs in part (a) show the data segment before and after the application of block which was used in statistical analysis. Each plot shows the parameter values estimated using both the fixed and the variable boundary method. Lines in green and magenta colour represent the parameter values before and after the block application estimated using fixed boundary method respectively. In the case of variable boundary method the same information is presented with blue and black colour lines respectively. The parameter values are the mean values calculated from a period of one minute. The units on y-axis for the plots showing power are s^2/Hz and for the plots showing frequency values is Hz.

Patient 1

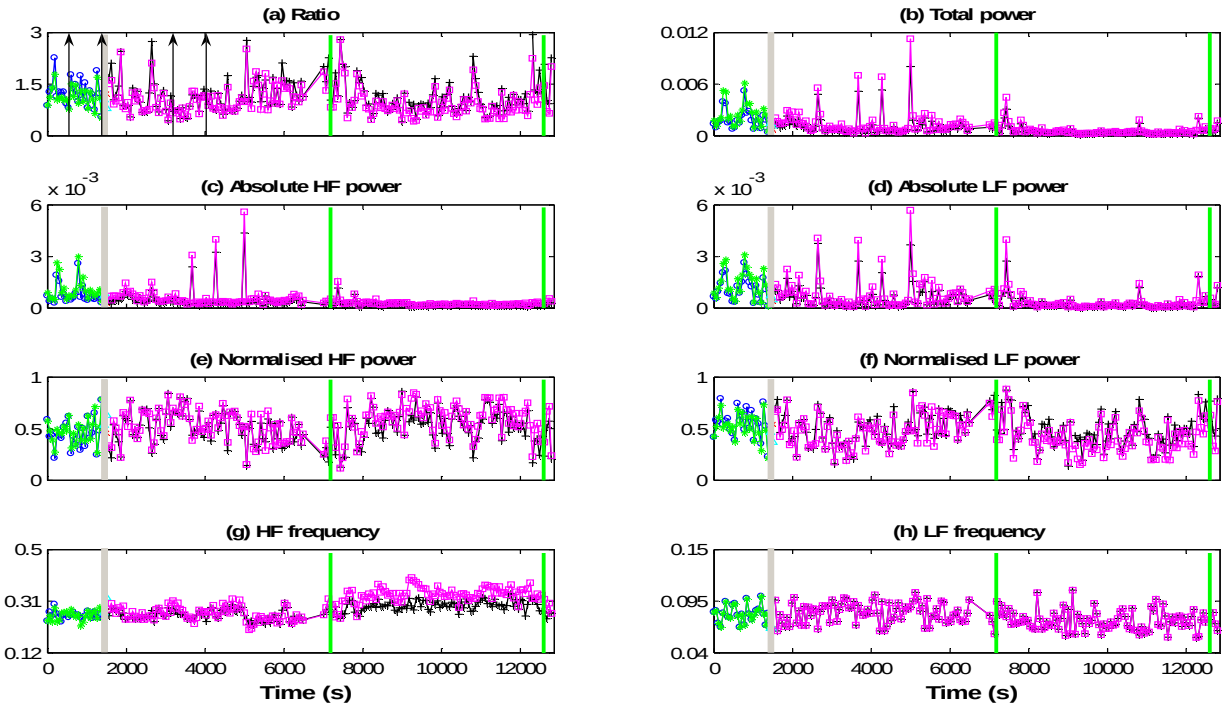

Patient 2

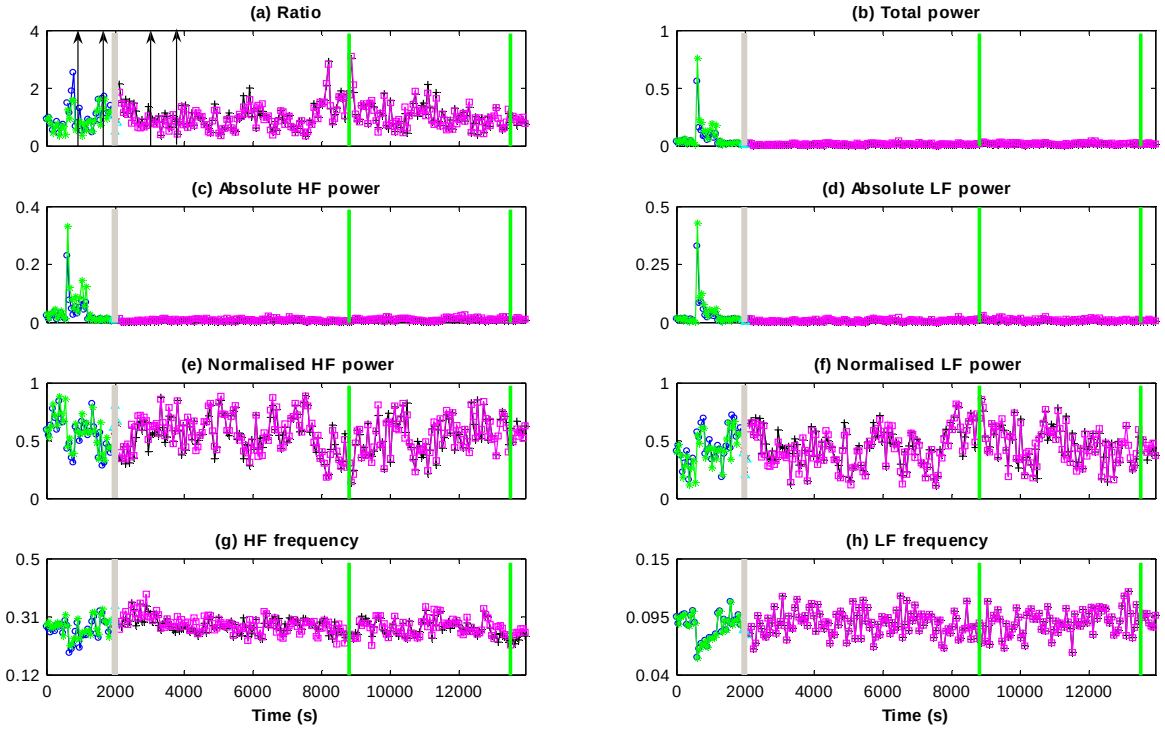

Patient 3

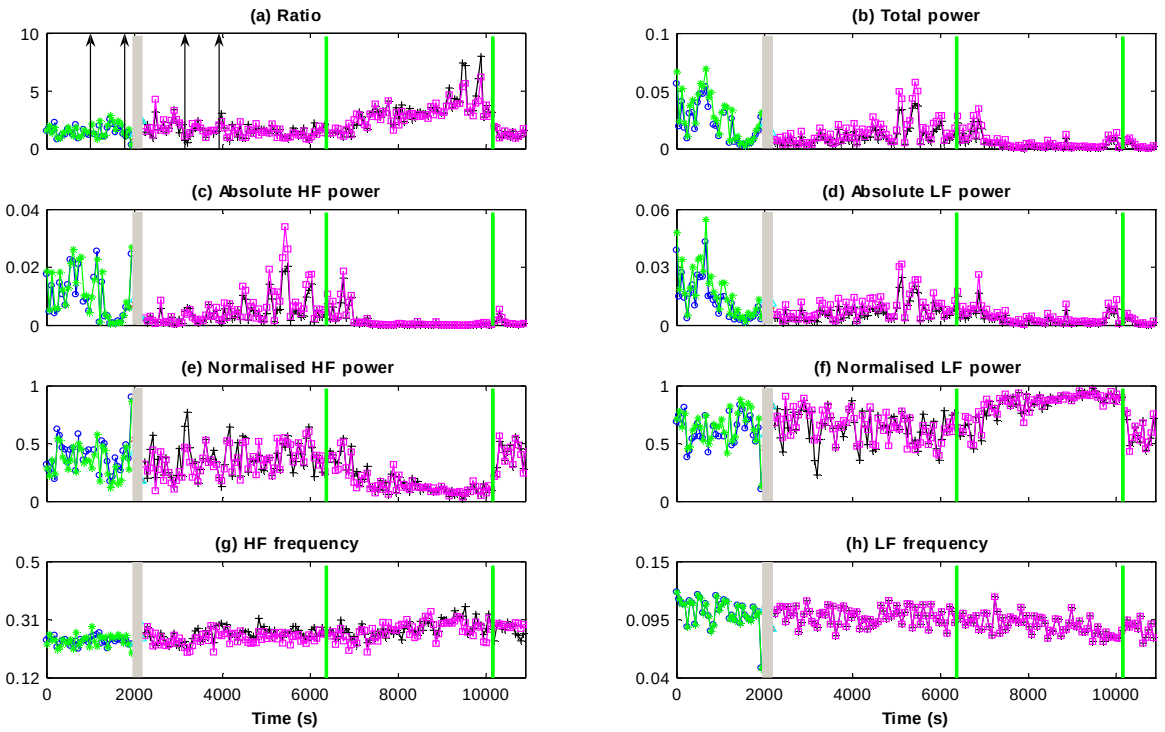

Patient 4

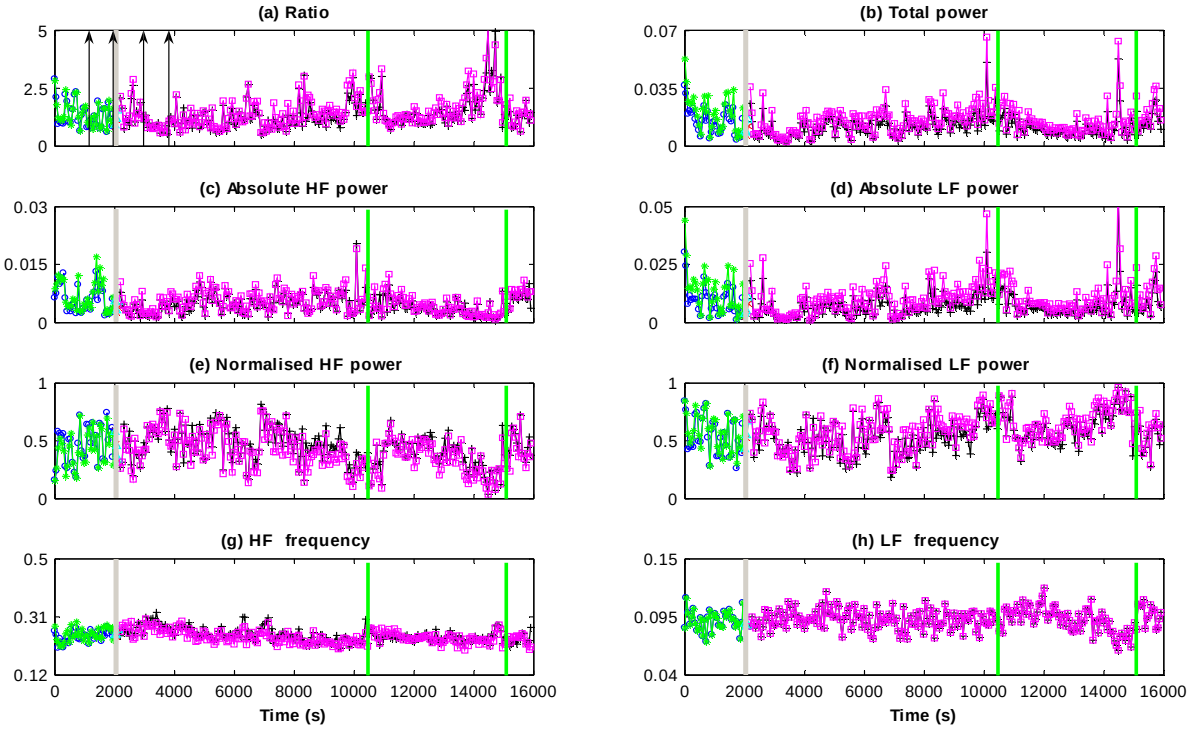

Patient 5

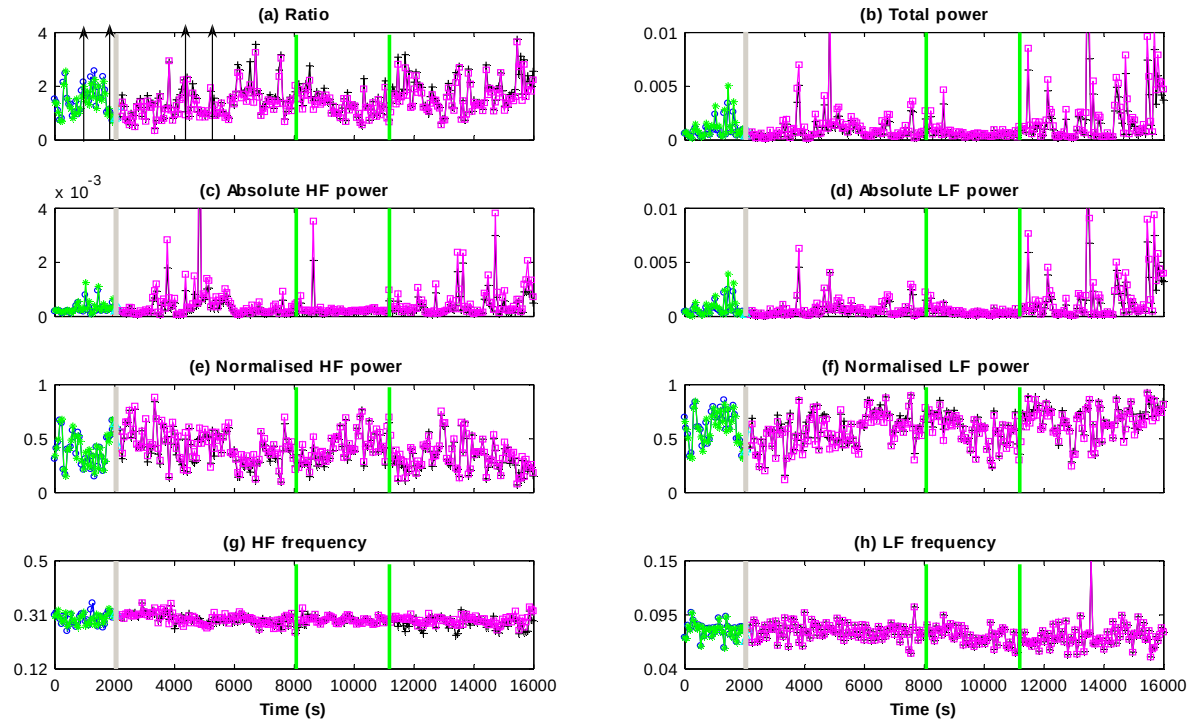

Patient 6

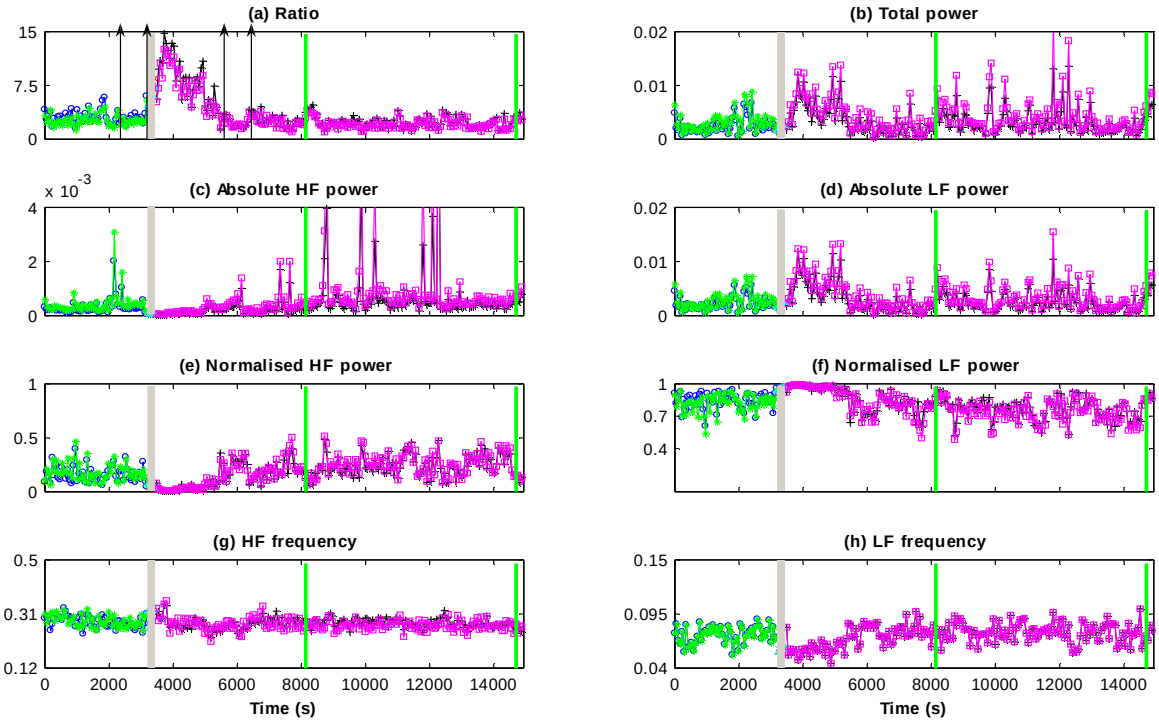

Patient 7

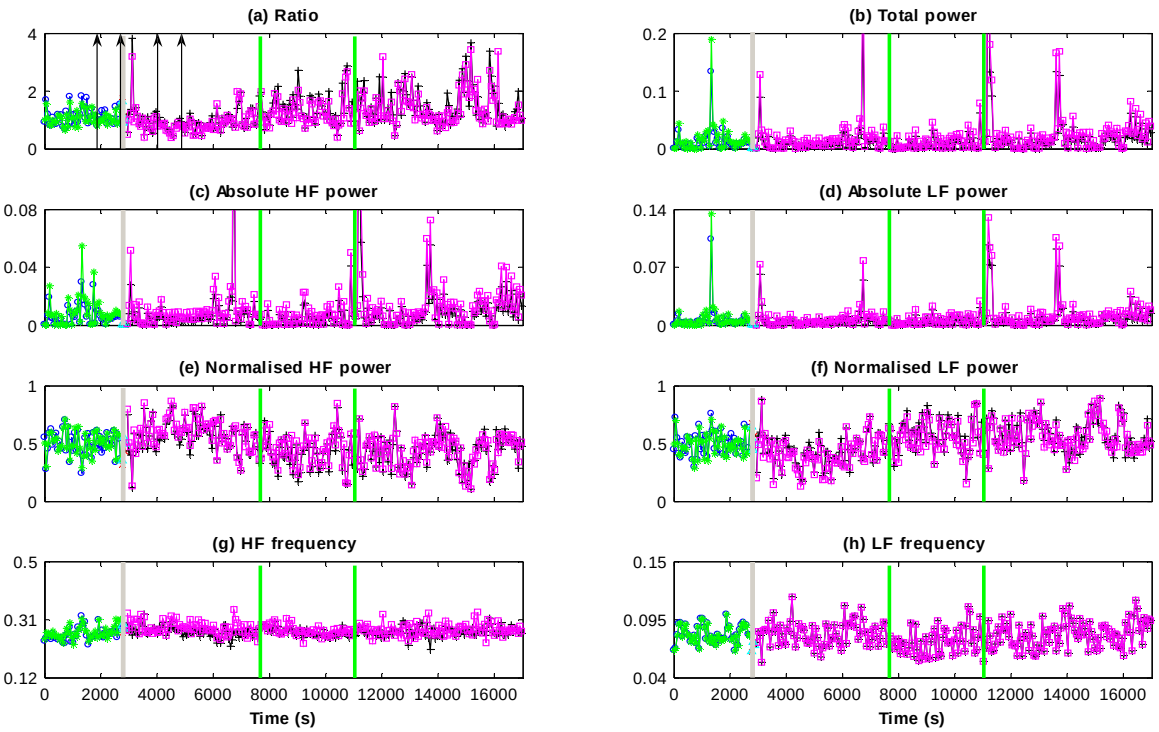

Patient 8

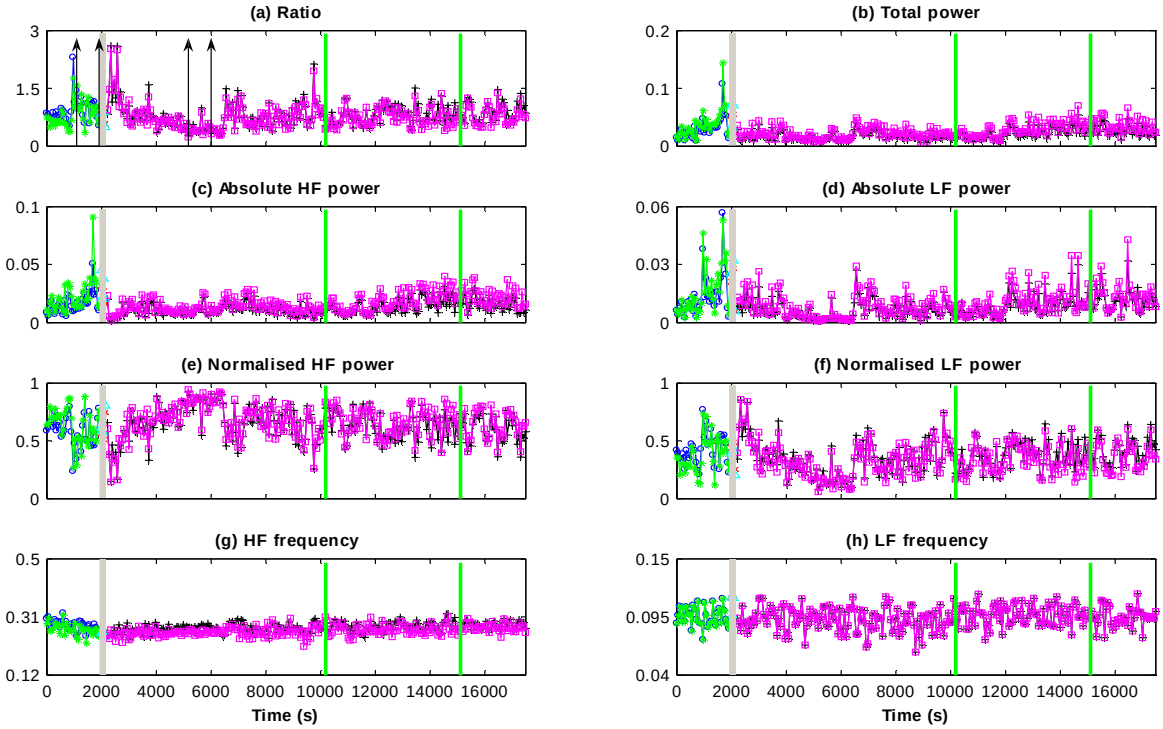

Patient 9

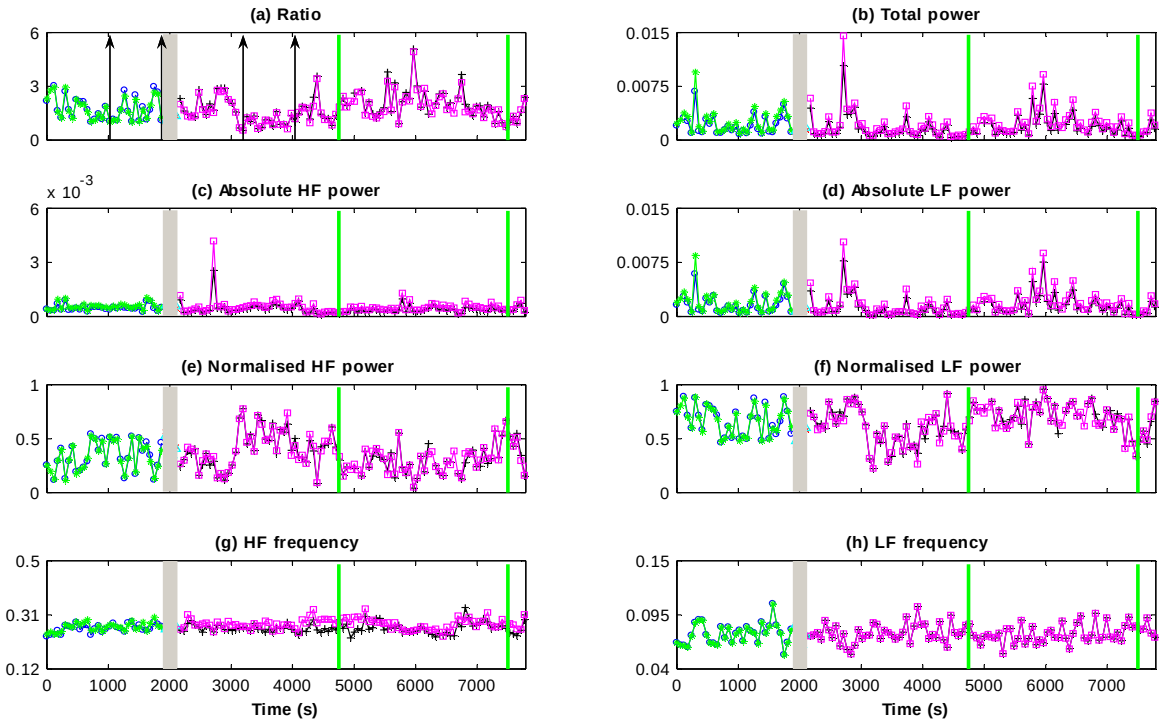

Patient 10

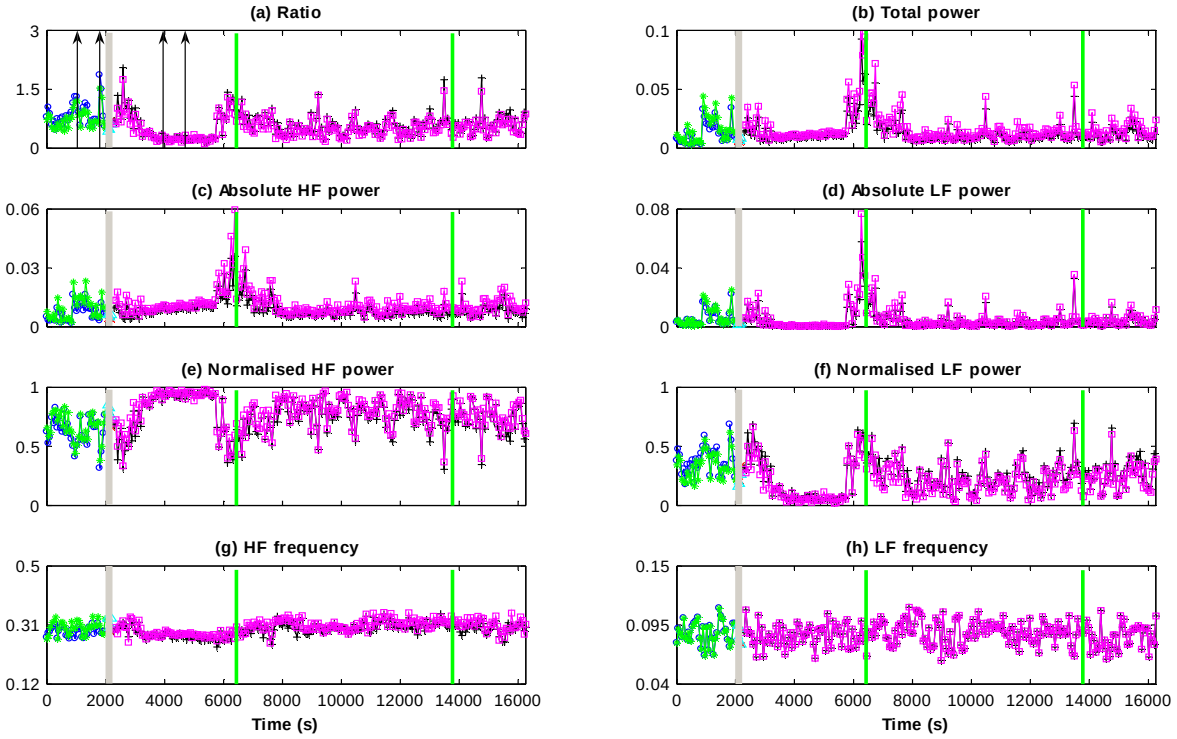

Patient 11

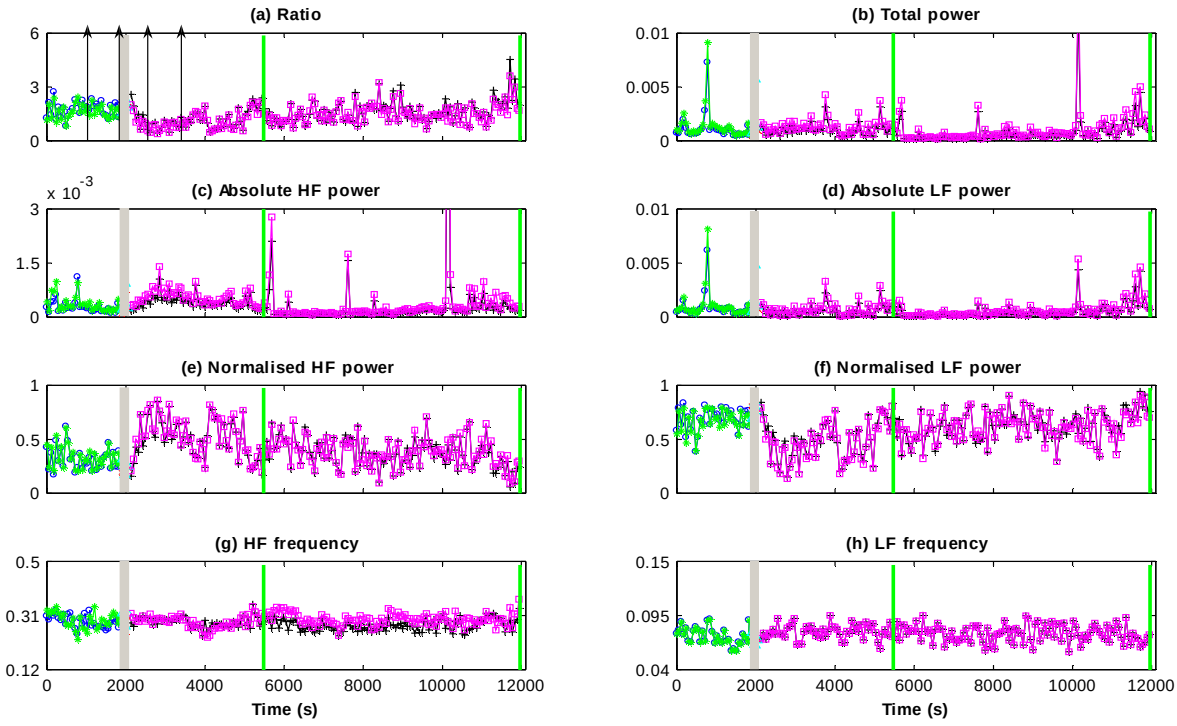

Patient 12

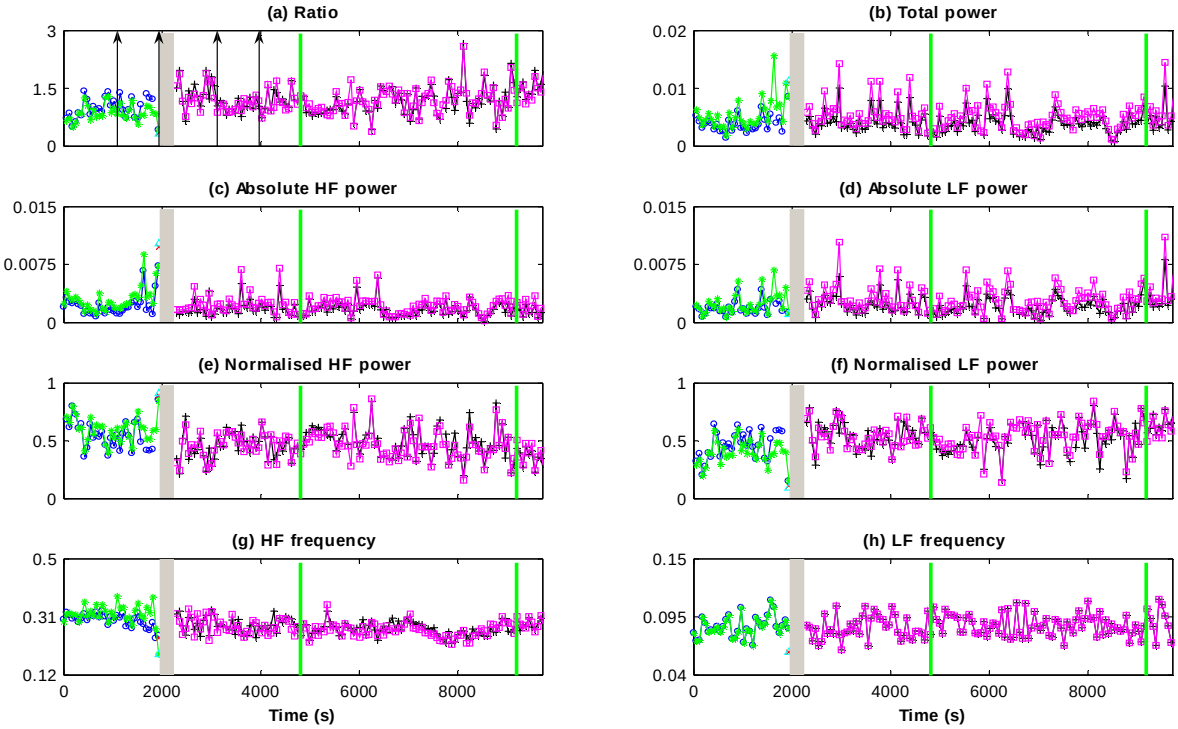

Patient 13

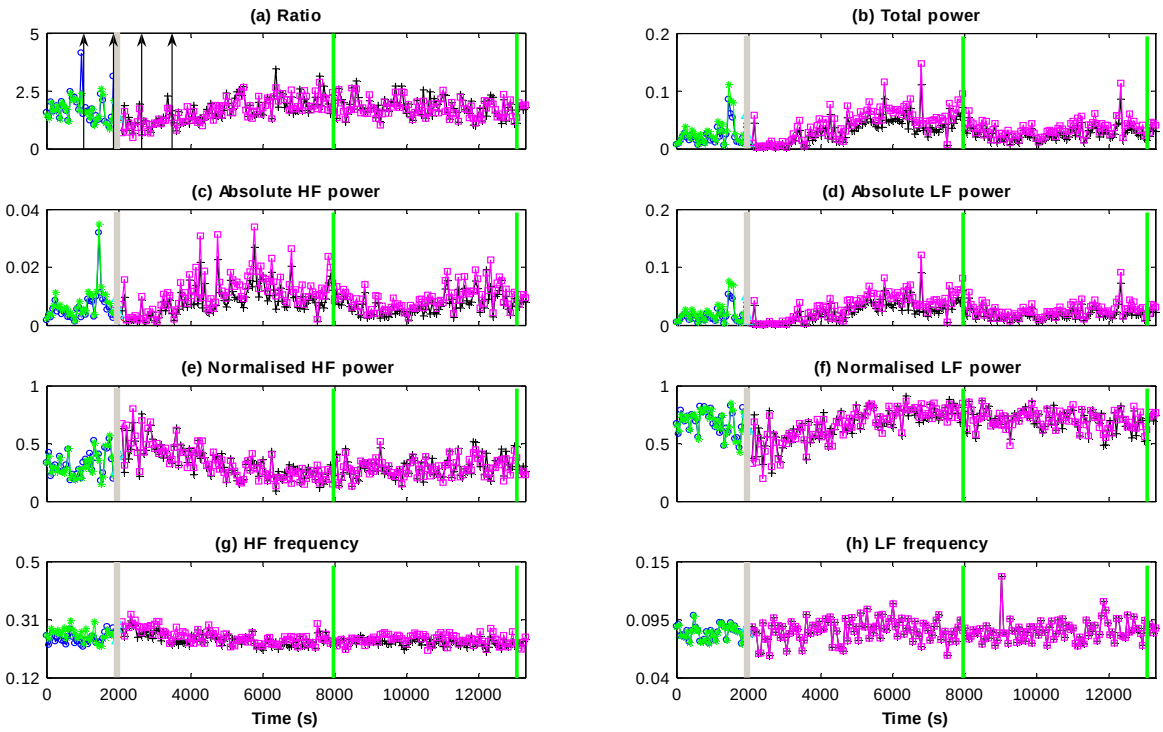

Patient 14

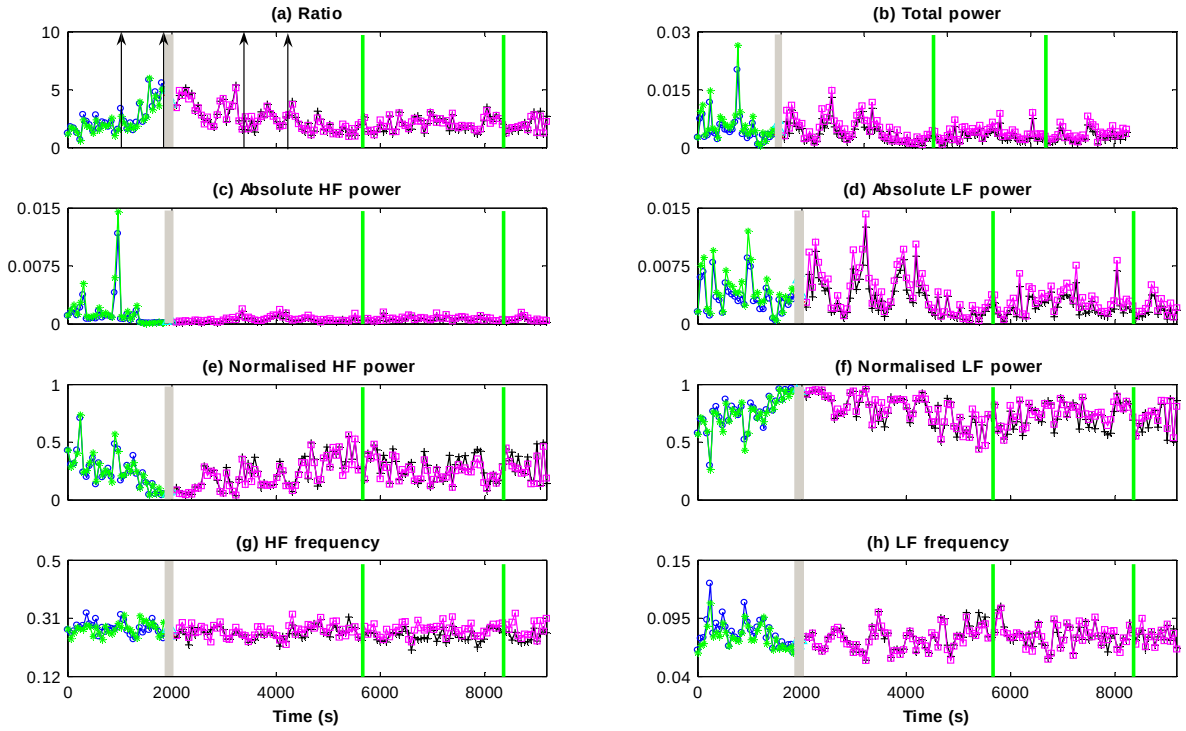
(a) Ratio
10
5
0
(b) Total power
0.03
0.015
0
(c) Absolute HF power
0.015
0.0075
0
(d) Absolute LF power
0.015
0.0075
0
(e) Normalised HF power
1
0.5
0
(f) Normalised LF power
1
0.5
0
(g) HF frequency
0.5
0.31
0.12
(h) LF frequency
0.15
0.095
0.04
0
2000
4000
6000
8000
Time (s)

E

Empirical Mode Decomposition anlysis results

Results obtained from the Empirical Mode Decomposition (EMD) analysis of a patient undergoing local anaesthetic procedure. In each plot the grey vertical block represents the time of block (anaesthesia) application and the green vertical lines represent start and end of the surgery. The vertical arrow pairs in part (a) show the data segment before and after the application of block which was used in statistical analysis. Lines in blue and red colour represent the parameter values before and after the block application respectively. The units on y-axis for the plots showing power are s^2/Hz and for the plots showing frequency values is Hz.

Patient 1

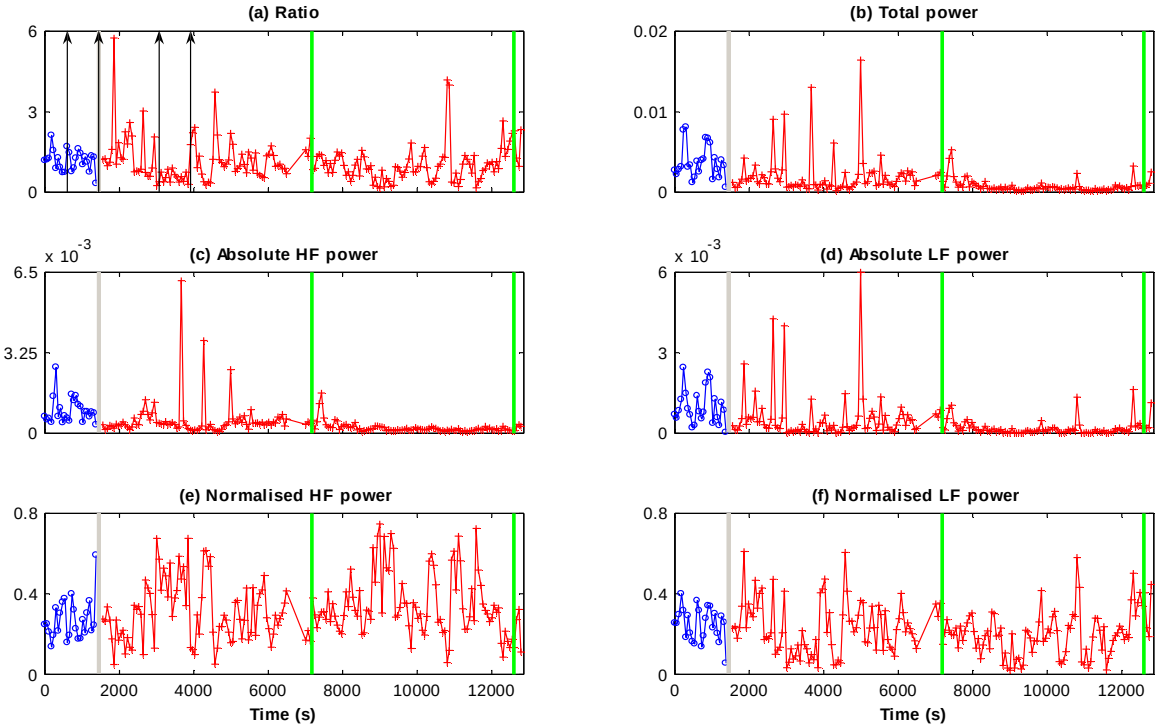

Patient 2

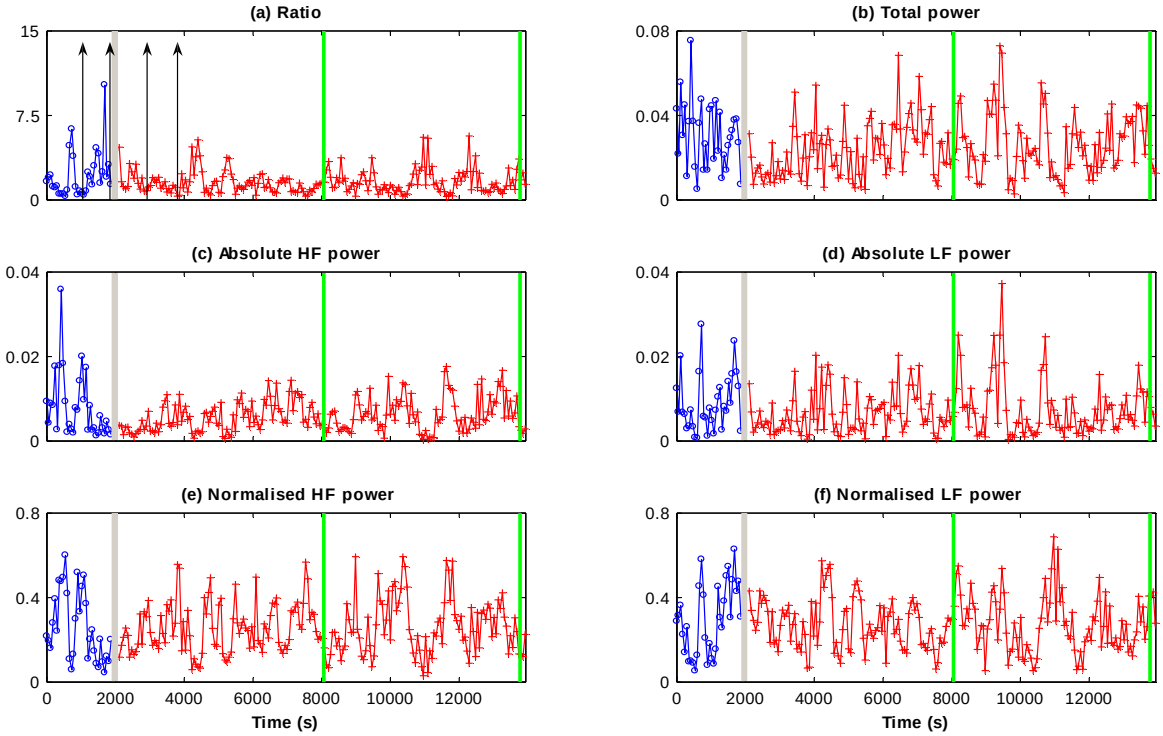

Patient 3

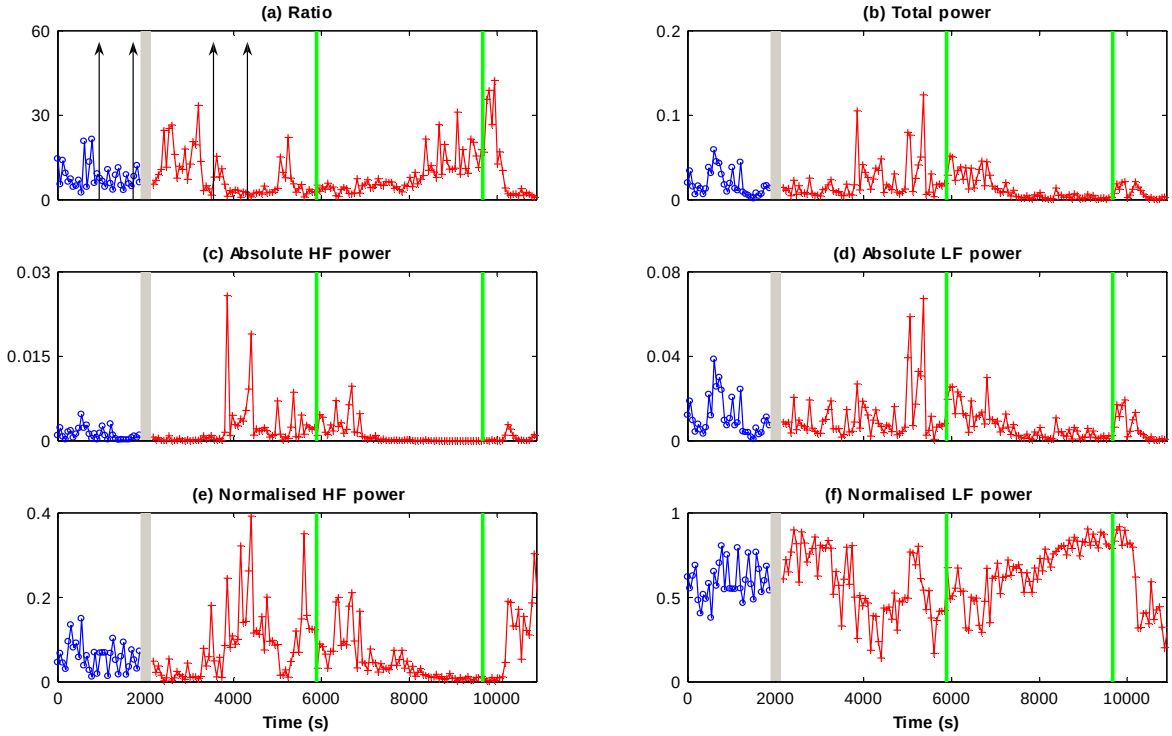

Patient 4

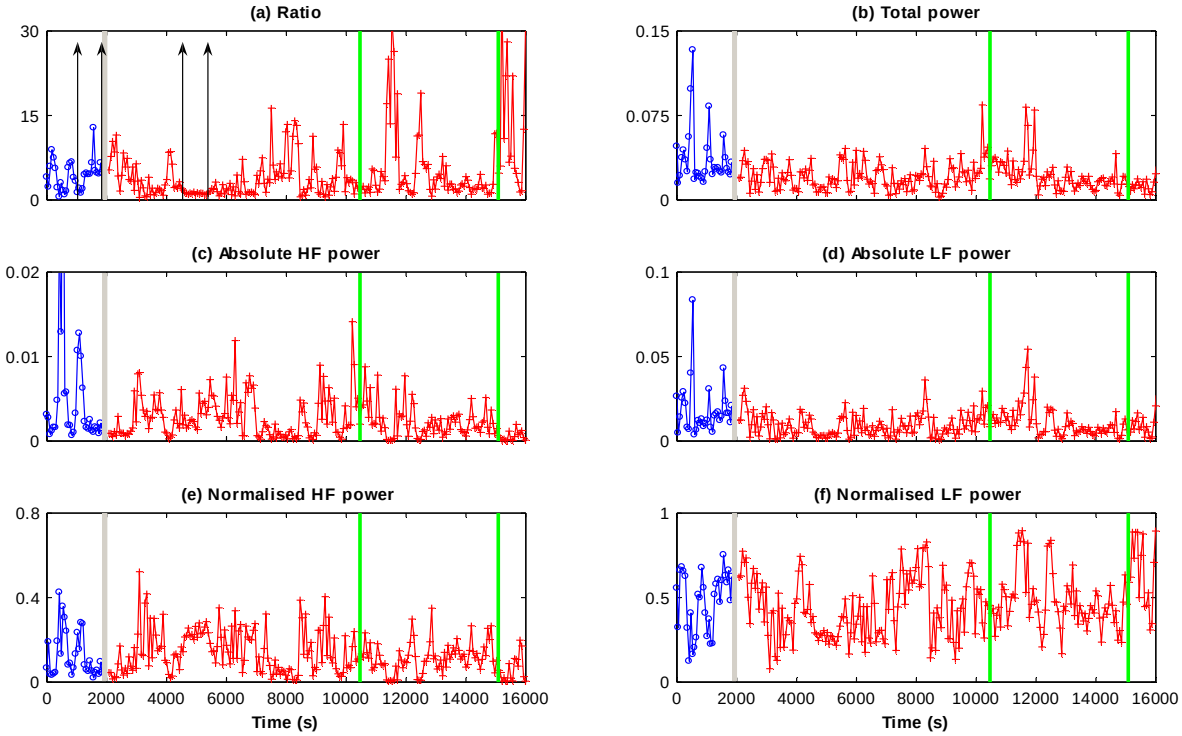

Patient 5

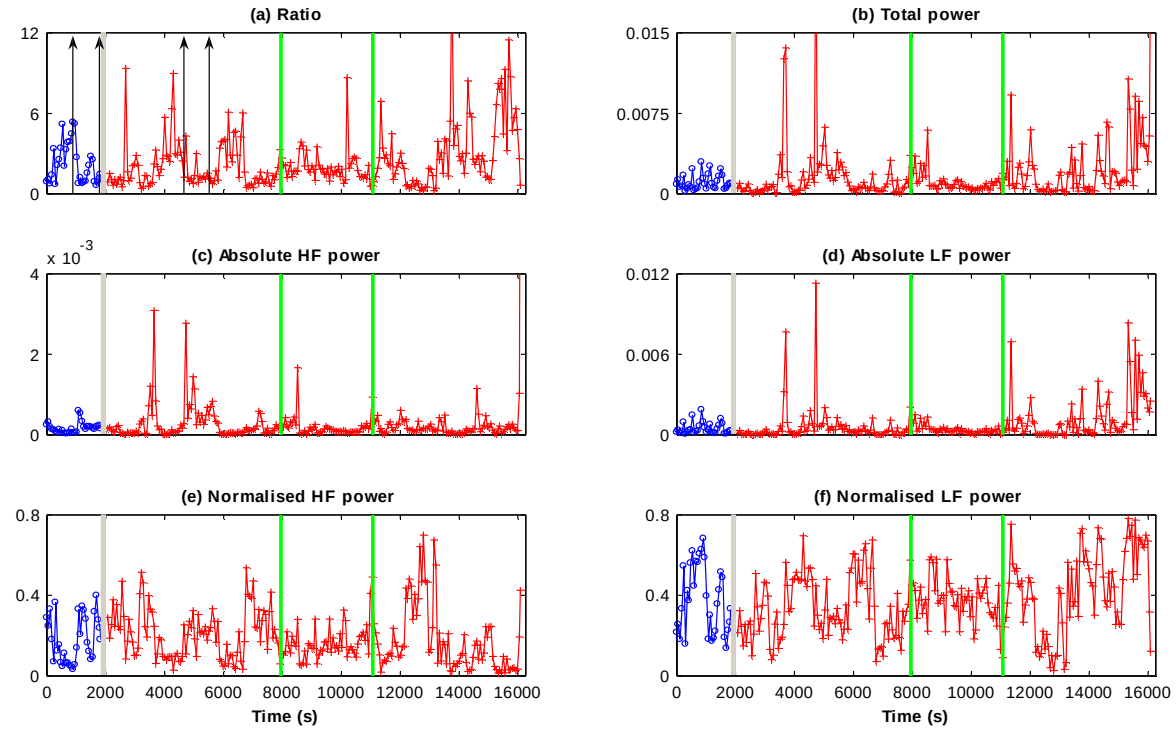

Patient 6

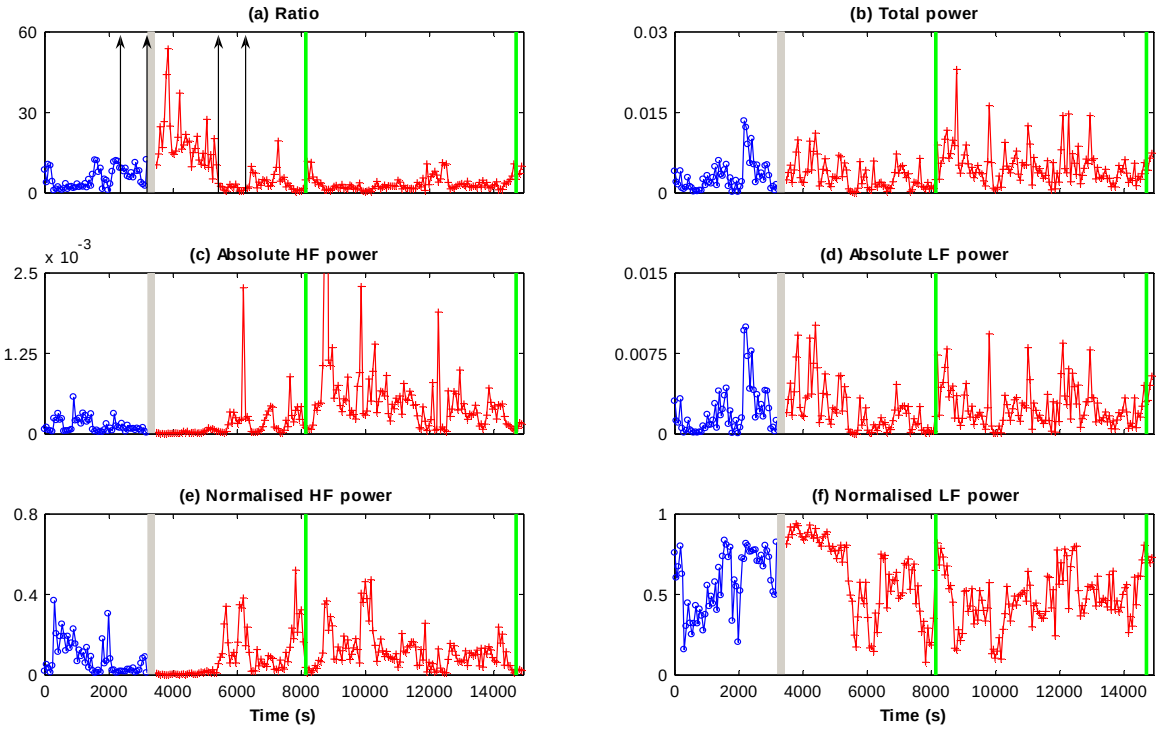

Patient 7

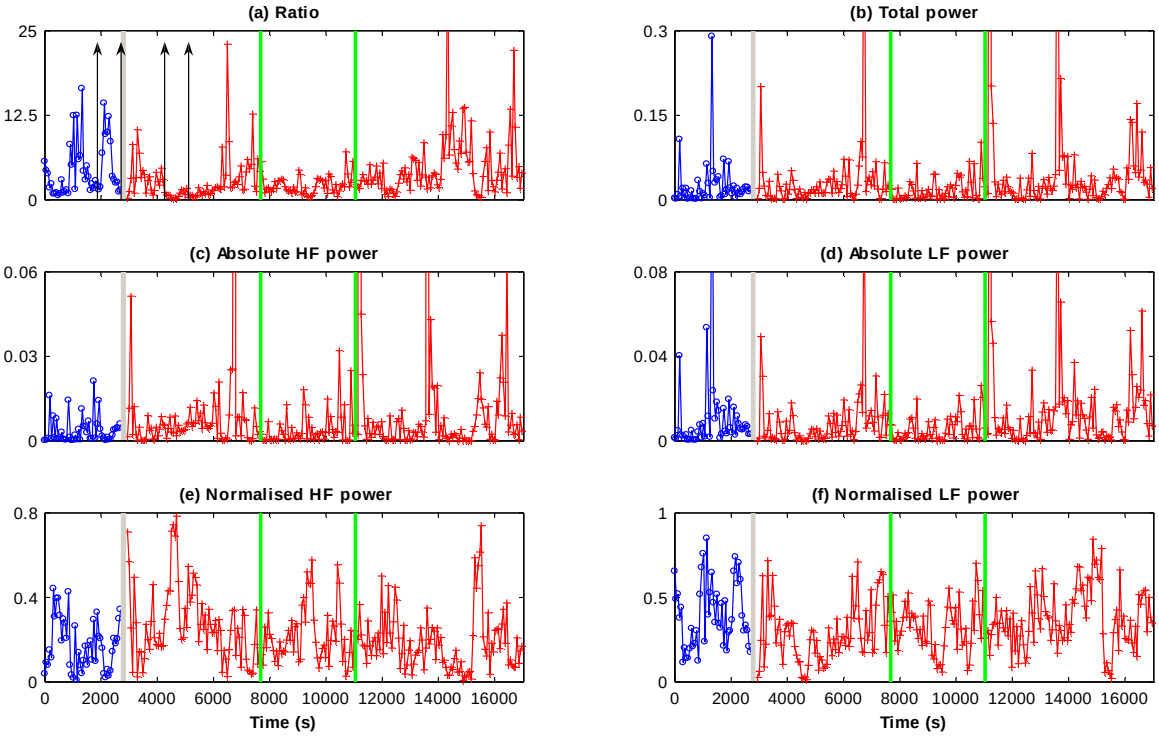

Patient 8

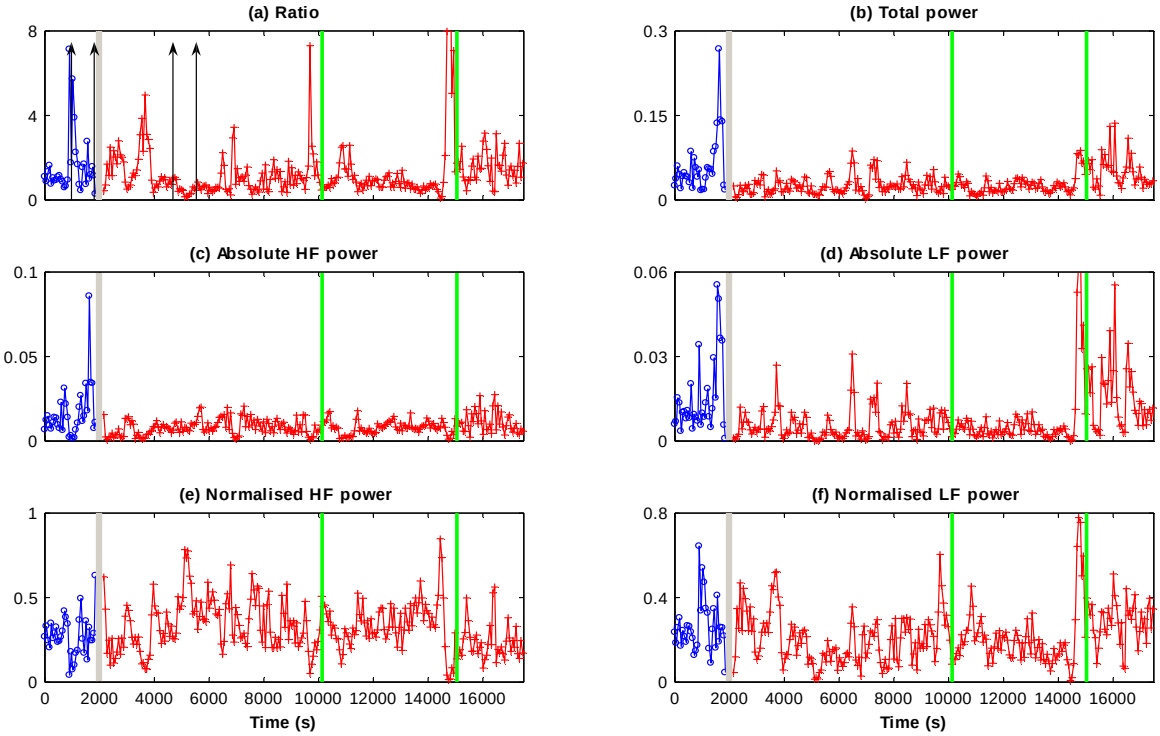

Patient 9

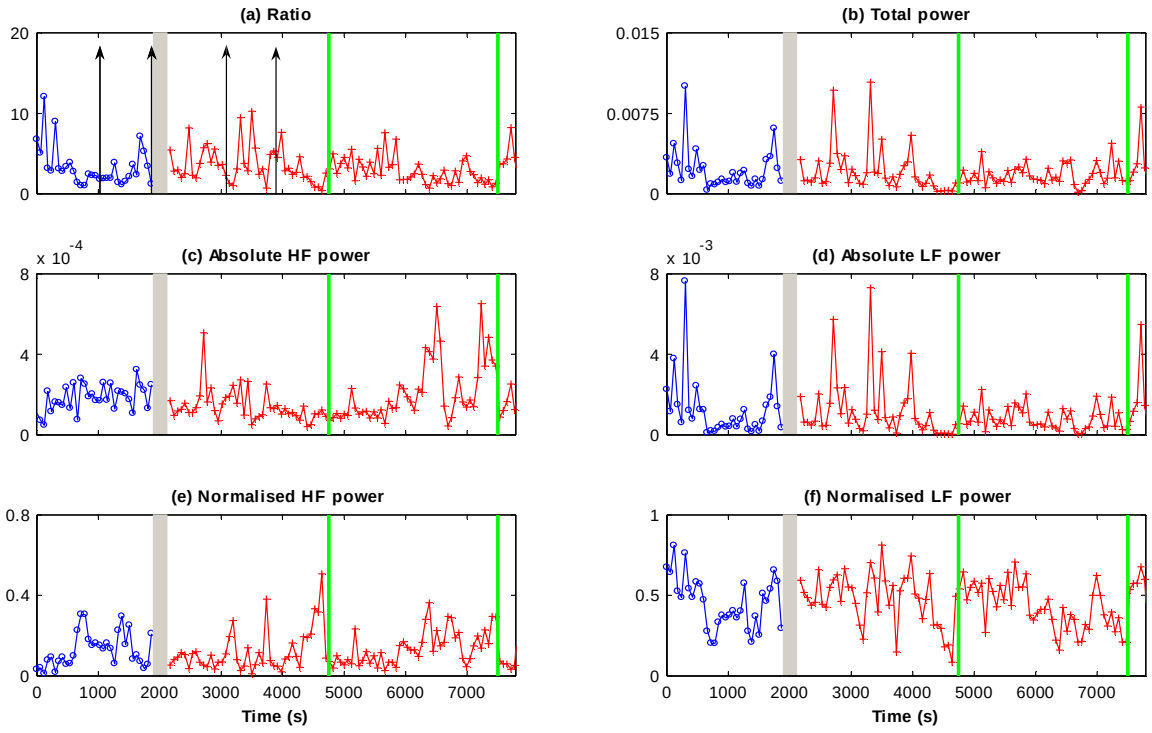

Patient 10

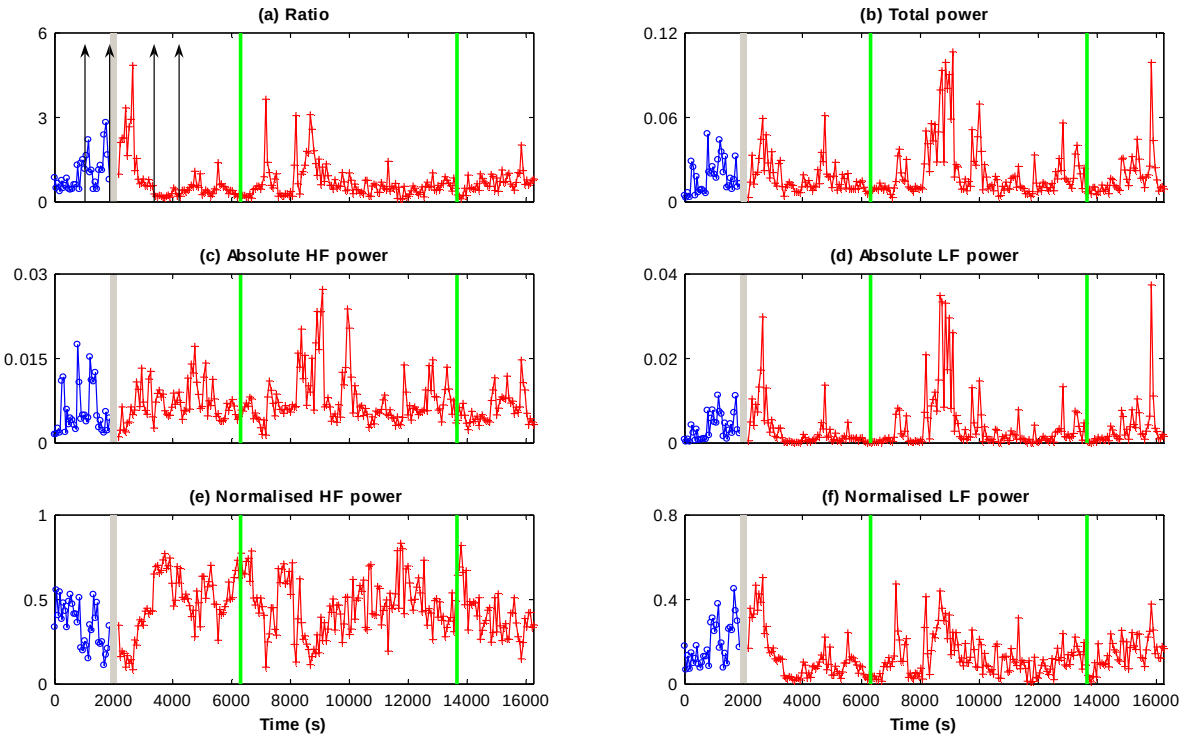

Patient 11

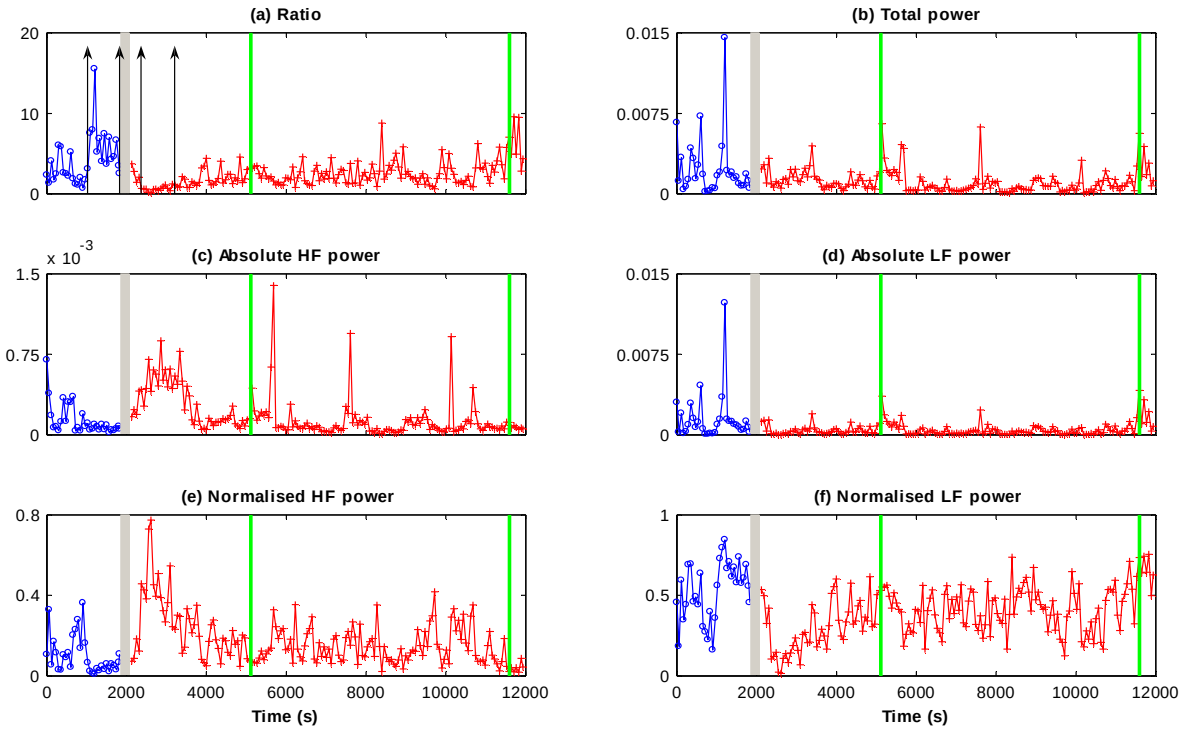

Patient 12

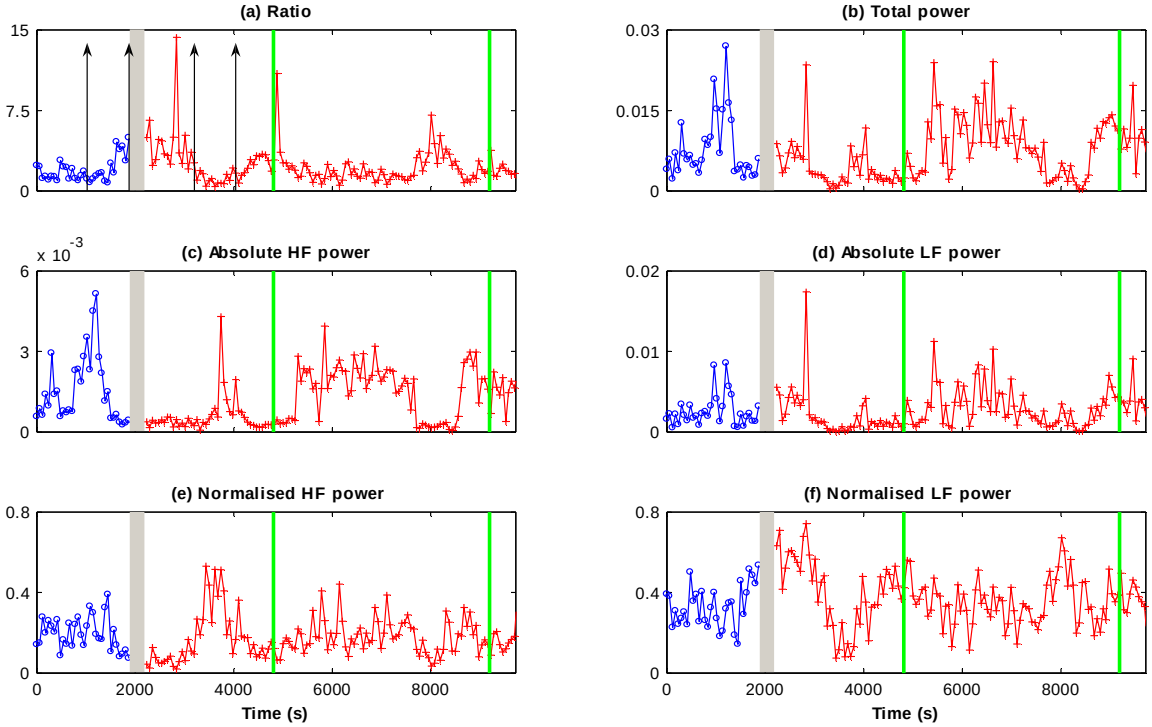

Patient 13

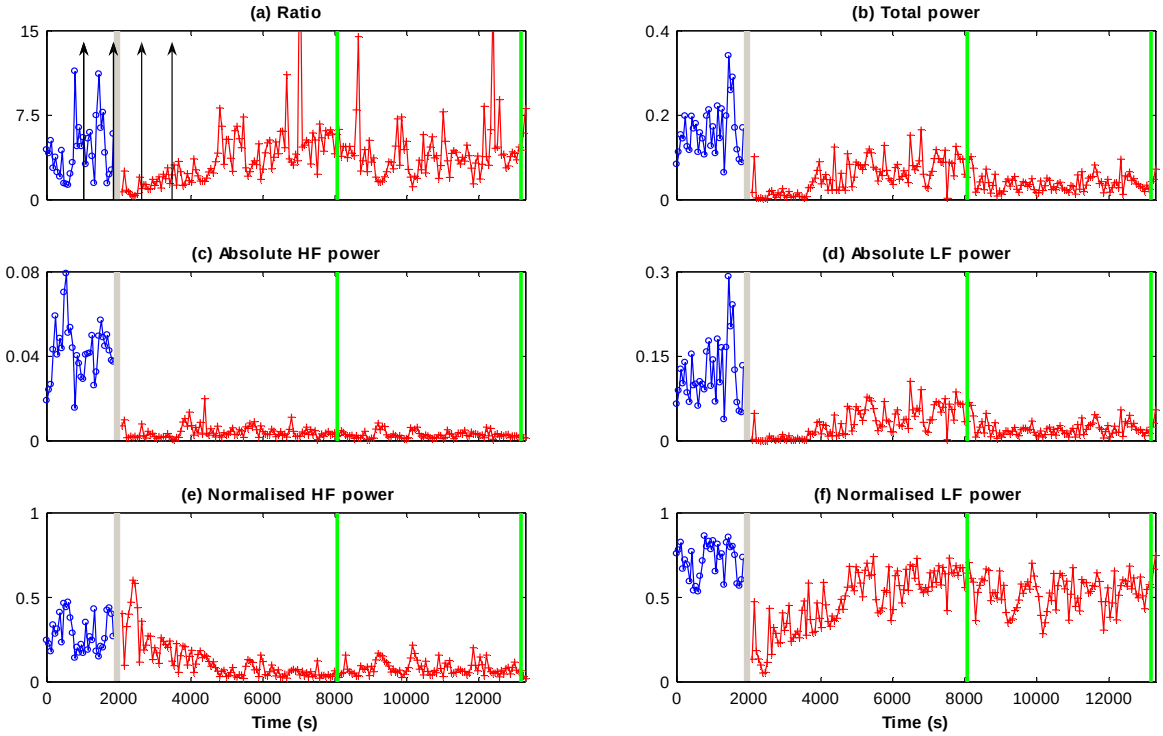

Patient 14

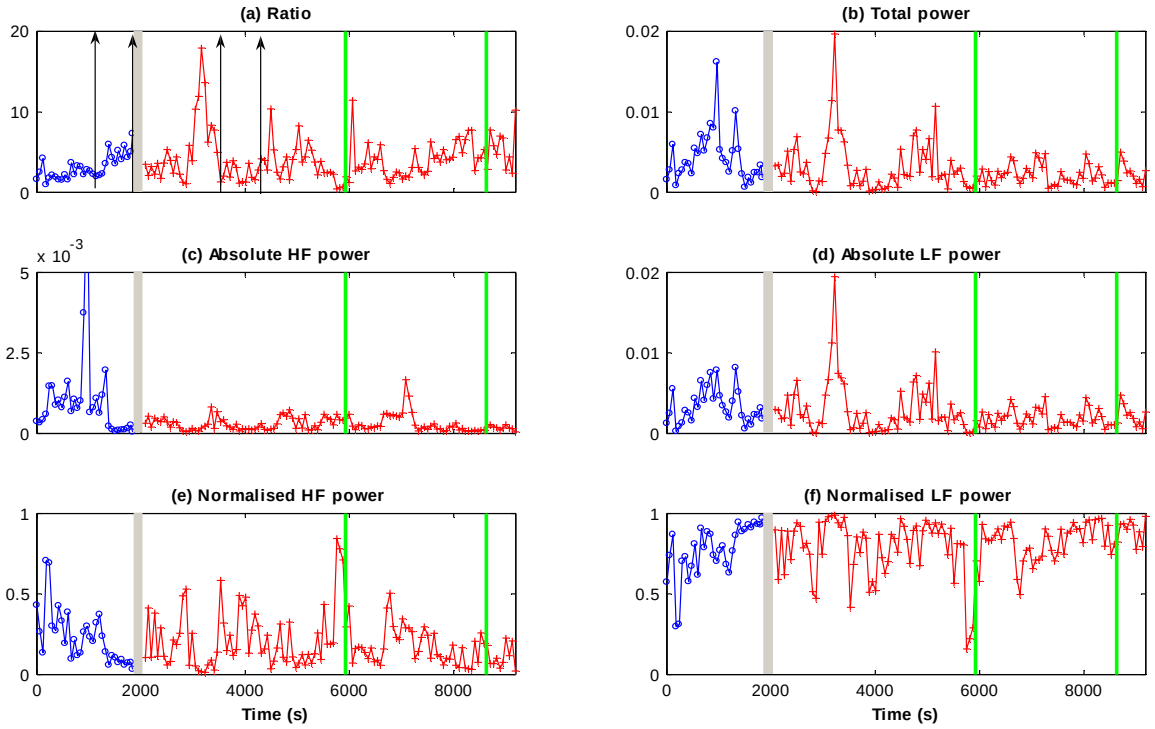
(a) Ratio
(b) Total power
(c) Absolute HF power
x 10^-3
(d) Absolute LF power
(e) Normalised HF power
(f) Normalised LF power
Time (s)
Time (s)

F

Publications List

[1] K. Shafqat, S. K. Pal, S. Kumari, and P. A. Kyriacou, "Empirical mode decomposition (emd) analysis of hrv data from locally anesthetized patients." *Conf Proc IEEE Eng Med Biol Soc*, vol. 1, pp. 2244–2247, 2009. [Online]. Available: http://dx.doi.org/10.1109/IEMBS.2009.5335000

[2] ——, "Time-frequency analysis of hrv data from locally anesthetized patients." *Conf Proc IEEE Eng Med Biol Soc*, vol. 1, pp. 1824–1827, 2009.
[Online]. Available: http://dx.doi.org/10.1109/IEMBS.2009.5332604

[3] ——, "Wavelet analysis of hrv data from locally anesthetized patients," in *Annual National Conference of the Institute of Physics and Engineering in Medicine (IPEM)*, 2009.

[4] K. Shafqat, S. K. Pal, and P. A. Kyriacou, "Evaluation of two detrending techniques for application in heart rate variability." *Conf Proc IEEE Eng Med Biol Soc*, vol. 2007, pp. 267–270, 2007. [Online]. Available: http://dx.doi.org/10.1109/IEMBS.2007.4352275

[5] K. Shafqat, S. K. Pal, S. Kumari, and P. A. Kyriacou, "Changes in heart rate variability in patients under local anesthesia." *Conf Proc IEEE Eng Med Biol Soc*, vol. 2007, pp. 299–302, 2007. [Online]. Available: http://dx.doi.org/10.1109/IEMBS.2007.4352283

[6] S. Kumari, K. Shafqat, P. A. Kyriacou, and S. K. Pal, "Investigation of heart rate variability in patients undergoing hand surgery under axillary plexus block," *British Journal of Anaesthesia*, vol. 98(2), p. 282, 2007.

[7] K. Shafqat, P. A. Kyriacou, S. K. Pal, and S. Kumari, "Investigation of heart rate variability in patients under local anaesthesia," in *Proceedings of the fifth IASTED International Conference: biomedical engineering*. Anaheim, CA, USA: ACTA Press, 2007, pp. 231–237. [Online]. Available: http://portal.acm.org/citation.cfm? id=1295494.1295535

Bibliography

[1] M. Malik, *Heart Rate Variability*, A. J. Camm, Ed. Futura Publishing Company, 1995.
(Cited on pages 1, 6, 8, 15, 17, 18, 20, 22, 25, 31, 32, 34, and 36.)

[2] S. Lauralee, *Human Physiology: From Cells to Systems*, 3rd ed. Brooks \ Cole Publishing Pacific Grove, 2001.
(Cited on pages 6 and 7.)

[3] J. Malmivuo and R. Plonsey, *Bioelectromagnetism: Principles and Applications of Bioelectric and Biomagnetic Fields*. Oxford University Press, New York, 1995.
(Cited on page 7.)

[4] A. Vander, *Human physiology : the mechanisms of body function*, 10th ed. McGraw-Hill New York, 1990.
(Cited on page 7.)

[5] R. H. Mehta, E. Bossone, and K. A. Eagle, "Current concepts in secondary prevention after acute myocardial infarction," *Herz*, vol. 25(1), pp. 47–60, 2000.
(Cited on page 7.)

[6] [Online]. Available: http://www.riversideonline.com/source/images/image_popup/ch7_theheart.jpg
(Cited on page 8.)

[7] E. N. Marieb and K. Hoehn, *Human Anatomy & Physiology*, 7th ed. Pearson Higher Education, Mar 2006.
(Cited on pages 9 and 14.)

[8] A. Biggs, L. Daniel, E. P. Ortleb, P. Rillero, and D. Zike, *Life Science*. Glencoe/McGraw-Hill, 2005.
(Cited on page 9.)

[9] E. N. Marieb, *Human Anatomy & Physiology*, 6th ed. Benjamin Cummings, 2003.
(Cited on pages 9 and 10.)

[10] [Online]. Available: http://images.med.cornell.edu/body/greystone/em_0018.jpg
(Cited on page 10.)

[11] J. G. Webster, Ed., *Medical Instrumentation: Application and Design*, 3rd ed. John Wiley and Sons Ltd, 1998.
(Cited on pages 11 and 16.)

[12] F. H. Netter, *CIBA Collection of Medical Illustrations*, R. T. Woodburne, E. S. Crelin, and F. S. Kaplan, Eds. N J Summit : Ciba, 1953-1997., vol. 5.
(Cited on page 12.)

[13] http://www.lond.ambulance.freeuk.com/ecg/1t2.jpg.
(Cited on page 12.)

[14] K. I. Panoulas, L. J. Hadjileontiadis, and S. M. Panas, "Engineering in medicine and biology society," in *Proceeding of the 23rd Annual International Conference of the IEEE*, vol. 1, 2001, pp. 344–347.
(Cited on page 13.)

[15] [Online]. Available: http://www.nottingham.ac.uk/nursing/practice/resources/cardiology/function/5_12_lead_placement.php
(Cited on page 13.)

[16] L. Cromwell, F. Weibell, and E. Pfeiffer, *Biomedical Instrumentation and Measurements*. Prentice-Hall, 1996.
(Cited on page 13.)

[17] A. Houghton and D. Gray, *Making Sense of the ECG*, 2nd ed. OUP, 1997.
(Cited on page 14.)

[18] E. R. Klabunde, "Cardiovascular physiology concepts." [Online]. Available: www.cyphysiology.com/Arrhythmias/A009.htm
(Cited on pages 14 and 15.)

[19] T. F. of the Euro. Society of Cardiology the N. American Society of Pacing Electrophysiology, "Heart Rate Variability Standards of Measurement, Physiological Interpretation, and Clinical Use," *European Heart Journal*, vol. 17, p. 354, 1996.
(Cited on pages 15, 25, 26, 27, 28, 30, 31, 32, 34, 35, 120, 145, 244, and 254.)

[20] A. C. Wilson and J. B. Kostis, "The prognostic significance of very low frequency ventricular ectopic activity in survivors of acute myocardial infarction. bhat study group," *Chest*, vol. 102(3), pp. 732–736, 1992.
(Cited on page 15.)

[21] H. Henneveld, P. Hutter, M. Bink-Boelkens, and N. Sreerama, "Junctional ectopic tachycardia evolving into complete heart block," *Heart*, vol. 80, pp. 627–628, 1998.
(Cited on page 15.)

[22] E. H. Hon and S. T. Lee, "Electronic evaluation of the fetal heart rate patterns preceding fetal death," *Am. J. Obstet. Gynecol .*, vol. 84, pp. 814–826, 1965.
(Cited on page 17.)

[23] http://bioliscious.blogspot.com/2008/04/compendium-chapters-13-14.html.
(Cited on page 19.)

[24] J. E. Dowling, *Creating Mind (How The Brain Works)*. W.W. Norton & Co. New York, 1998.
(Cited on page 18.)

[25] M. N. Levy and P. J. Martin, *Handbook of Physiology*. Bethesda, Md: Am. Physiol. Soc., 1979, vol. 1, no. section 2.
(Cited on pages 19 and 20.)

[26] R. Hainsworth, *Heart Rate Variability*. Armonk,N.Y. Futura Pub. Co. Inc., 1995, ch. The Control and Physiological Importance of Heart Rate, pp. 3–19.
(Cited on pages 20 and 21.)

[27] S. Akselrod, *Heart Rate Variability*. Armonk, N.Y. Futura Pub. Co., 1995, ch. Components of Heart Rate Variability, pp. 147–163.
(Cited on pages 22 and 29.)

[28] M. T. L. Rovere, A. Mortara, G. D. Pinna, and L. Bernardi, *Heart Rate Variability*. Armonk, N.Y. Futura Pub. Co., 1995, ch. Baroreflex Sensitivity and Heart Rate Variability in the Assessment of the Autonomic Status, pp. 147–163.
(Cited on page 22.)

[29] P. Sleight and B. Casadei, *Heart Rate Variability*. Armonk, N.Y. Futura Pub. Co., 1995, ch. Relationships between Heart Rate, Respiration and Blood Pressure, pp. 311–330.
(Cited on page 22.)

[30] P. Lavie, *The enchanted world of sleep*. Yale Uninversity Press, New Haven, 1996.
(Cited on page 24.)

[31] C. J. M. amd M Alam, *Heart Rate Variability*. Armonk, N.Y. Futura Pub. Co., 1995, ch. Circadian Changes of the Cardiovascular System and the Autonomic Nervous System, pp. 21–30.
(Cited on page 24.)

[32] E. Barrett-Connor and K. Khaw, "Family history of heart attack as an independent predictor of death due to cardiovascular disease," *Circulation*, vol. 69, pp. 1065–1069, 1984.
(Cited on page 24.)

[33] M. T. Keating, "Genetic approaches to cardiovascular disease supravalvular aortic stenosis, williams syndrome, and long-qt syndrome," *Circulation*, vol. 92, pp. 142–147, 1995.
(Cited on page 24.)

[34] R. Sinnreich, J. D. Kark, Y. Friedlander, D. Sapoznikov, and M. H. Luria, "Five minute recordings of heart rate variability for population studies: repeatability and age-sex characteristics," *Heart*, vol. 80, pp. 156–162, 1998.
(Cited on page 24.)

[35] R. E. Kleiger, P. K. Stein, M. S. Bosner, and J. N. Rottman, *Heart Rate Variability*. Armonk, N.Y. Futura Pub. Co., 1995, ch. Time Domain Measurements of Heart Rate Variability, pp. 33–45.
(Cited on page 26.)

[36] M. P. Griffin and J. R. Moorman, "Toward the early diagnosis of neonatal sepsis and sepsis-like illness using novel heart rate analysis," *Pediatrics*, vol. 2001, pp. 97–104, 107(1).
(Cited on page 27.)

[37] S. Akselrod, D. Gordon, F. A. Ubel, D. C. Shannon, A. C. Berger, and R. J. Cohen, "Power spectrum analysis of heart rate fluctuation: a quantitative probe of beat-to-beat cardiovascular control," *Science*, vol. 213, pp. 220–222, 1981.
(Cited on pages 28 and 86.)

[38] S. Cerutti, A. M. Bianchi, and L. T. Mainardi, *Heart Rate Variability*. Armonk, N.Y. Futura Pub. Co., 1995, ch. Spectral Analysis of Heart Rate Variability Signal, pp. 63–74.
(Cited on page 29.)

[39] J. A. Taylor, D. L. Carr, C. W. Myers, and D. L. Eckberg, "Mechanisms underlying very-low-frequency rr-interval oscillations in humans," *Circulation*, vol. 98, pp. 547–555, 1998.
(Cited on page 29.)

[40] J. M. Serrador, H. G. Finlayson, and R. L. Hughson, "Physical activity is a major contributor to the ultra-low frequency components of heart rate variability," *Heart*, vol. 82, p. e9, 1999.
(Cited on page 29.)

[41] D. L. Eckberg, "Sympathovagal balance," *Circulation*, vol. 96, pp. 3224–3232, 1997.
(Cited on pages 29, 30, and 31.)

[42] J. A. Hirsch and B. Bishop, "Respiratory sinus arrhythmia in humans: how breathing pattern modulates the heart rate," *Am. J. Physiol.*, vol. 241, pp. 11 620–11 629, 1981.
(Cited on pages 29 and 241.)

[43] M. V. Kamath and E. L. Fallen, "Power spectral analysis of hrv: a noninasive signature of cardiac autonomic functions," *Crit. Rev. Biomed. Eng.*, vol. 21(3), pp. 245–311, 1993.
(Cited on page 29.)

[44] T. Laitinen, J. Hartikainen, L. Niskanen, G. Ghilaine, and E. Lansimies, "Sympathovagal balance is a major determinant of short-term blood pressure varaibility in healthy subjects," *Am. Physiol. Soc.*, vol. 276(4 Pt 2), pp. H1245–H1252, 1999.
(Cited on page 29.)

[45] S. Y. Kim and D. E. Euler, "Baroreflex sensitivity assessed by complex demodulation of cardiovascular variability," *Hypertension*, vol. 29, pp. 1119–1125, 1997.
(Cited on page 30.)

[46] N. S. D. Mironov, P. W. Armstrong, A. M. Ross, and A. Langer, "Heart rate variability assessment early after acute myocardial infarction: Pathophysiological and prognostic correlates - for the gusto ecg substud," *Circulation*, vol. 93, pp. 1388–1395, 1996.
(Cited on pages 30 and 31.)

[47] J. O. Valkama, H. V. Huikuri, K. E. Airaksinen, M. L. L. M.L, and J. T. Takkunen, "Determinants of frequency domain measures of heart rate variability in the acute and convalesccent phases of myocardial infarction," *Cardiovasc. Res.*, vol. 28(8), pp. 1273–1276, 1994.
(Cited on pages 30 and 31.)

[48] M. G. Signorini, S. Guzzetti, C. Manzoni, S. Milani, and S. Cerutti, "Multiparametric analysis of hrv signal by linear and nonlinear methods in heart faliure patient population," in *Proc of 20th Int. Conf. IEEE Eng. Med. Biol. Soc.*, vol. 20(1), 1998.
(Cited on page 31.)

[49] M. C. Teich, S. B. Lowen, B. M. J. K. Vibe-Rheymer, and C. Heneghan, *Nonlinear Biomedical Signal Processing Vol. II: Dynamic Analysis and Modeling*. IEEE Press, Piscataway, NJ, 2000, ch. Heart Rate Variability: Measures and Models.
(Cited on page 31.)

[50] M. T. L. Rovere, J. T. Bigger, F. I. M. Jr., A. Mortara, and P. J. Schwartz, "Baroreflex sensitivity and heart rate variability in prediction of total cardiac mortality after myocardial infarction. the results of atrami (autonomic tone and reflexes after myocardial infarction)," *Lancet*, vol. 351, pp. 478–484, 1998.
(Cited on page 31.)

[51] B. M. McClements and A. A. Adgey, "Value of signal-averaged electrocardiography, radionuclide ventriculography, holter monitoring and clinical variables for prediction of arrhythmic events in survivors of acute myocardial infarction in the thrombolytic era," *J.Am.Coll.Cardiol.*, vol. 12(6), pp. 1419–1427, 1993.
(Cited on page 31.)

[52] A. B. Cooper, K. S. Thornley, G. B. Young, A. S. Slutsky, T. E. Stewart, and P. J. Hanly, "Sleep in critically ill patients requiring mechanical ventilation," *Chest*, vol. 117, pp. 809–818, 2000.
(Cited on page 31.)

[53] J. Nolan, P. D. Batin, R. Andrews, S. J. Lindsay, P. Brooksby, M. Mullen, W. Baig, A. D. Flapan, A. Cowley, R. J. Prescott, J. M. M. Neilson, and K. A. A. Fox, "Clinical investigation and reports: Prospective study of heart rate variability and mortality in chronic heart failure - results of the united kingdom heart failure evaluation and assessment of risk trial (uk-heart)," *Circulation*, vol. 98, pp. 1510– 1516, 1998.
(Cited on page 32.)

[54] J. Haaksma, W. A. Dijk, J. Brouwer, M. P. van den Berg, W. R. M. Dassen, B. Mulder, and H. J. G. M. Crijns, "The influence of recording length on time and frequency domain analysis of heart rate variablity," *IEEE, Computers in Cardiology*, vol. 25, pp. 377–380, 1998.
(Cited on page 33.)

[55] S. Abboud and O. Barnea, "Errors due to sampling frequency of electrocardiogram in spectral analysis of heart rate signals with low variability," *Computers in Cardiology*, pp. 461–463, 1995.
(Cited on page 34.)

[56] A. C. Wilson and J. B. Kostis, "The prognostic significance of very low frequency ventricular ectopicactivity in survivors of acute myocardial infarction. bhat study group," *Chest*, vol. 102(3), pp. 732–736, 1992.
(Cited on page 34.)

[57] O. Odemuyiwa, M. Malik, T. Farrell, Y. Bashir, J. Poloniecki, and J. Camm, "Comparison of the predictive characteristics of heart rate variability index and left ventricular ejection fraction for all-cause mortality, arrhythmic events and sudden death after acute myocardial infarction," *Am J Cardiol.*, vol. 67, pp. 434–439, 1991.
(Cited on page 34.)

[58] J. A. Arrowood, A. J. Minisi, E. Goudreau, A. B. Davis, and A. L. King, "Absence of parasympatheticcontrol of heart rate after human orthotopic cardiac transplantation," *Circulation*, vol. 96, pp. 3492–3498, 1997.
(Cited on page 34.)

[59] E. L. Fallen, M. V. Kamath, D. N. Ghista, and D. Fitchett, "Spectral analysis of heart rate variabilityfollowing human heart transplantation: evidence for functional reinnervation," *J. Auton. Nerv. Syst.*, vol. 23, pp. 199–206, 1998.
(Cited on page 34.)

[60] M. L. Smith, K. A. Ellenbogen, D. L. Eckberg, S. Szentpetery, and M. D. Thames, "Subnormal heart periodvariability in heart failure: effect of cardiac transplantation," *J. Am. Coll. Cardiol.*, vol. 14, pp. 106–111, 1989.
(Cited on page 34.)

[61] L. Bernardi, B. Bianchini, G. Spadacini, S. Leuzzi, F. V. F, E. Marchesi, C. Passino, A. Calciati, M. Vigano, and M. Rinaldi, "Demonstrable cardiac reinnervation after human heart transplantation by carotid baroreflex modulation of rr interval," *Circulation*, vol. 92, pp. 2895–2903, 1995.
(Cited on pages 34 and 243.)

[62] A. P. Statement, "Heart rate variability for risk stratification of life- threatening arrhythmias," *J. Am. Coll. Cardiol.*, pp. 948–950, 1993.
(Cited on page 36.)

[63] K. Allman and I. Wilson, Eds., *Oxford Handbook of Anaesthesia*, 2nd ed. Oxford university press, 2006.
(Cited on pages 38 and 39.)

[64] http://www.nerveblocks.net/tutorium/.
(Cited on pages 39 and 40.)

[65] [Online]. Available: http://en.wikipedia.org/wiki/Local_anesthetic
(Cited on page 39.)

[66] http://www.anaesthesiauk.com/article.aspx?articleid=100446.
(Cited on page 41.)

[67] H. G. Goovaerts, H. H. Ros, T. H. vanden Akker, and H. Schnedier, "A digital QRS detector based on the principle of contour limiting," *IEEE Trans. Biomed. Eng*, vol. BME-23, p. 154, 1976.
(Cited on page 45.)

[68] N. V. Thakor, J. G. Webster, and W. J. Tompkins, "Optimal QRS Detector," *Med. Biol. Eng. Comput*, vol. 21, pp. 343–350, 1983.
(Cited on page 45.)

[69] ——, "Estimation of QRS complex power spectrum for the design of a QRS filter," *IEEE Trans. Biomed. Eng*, vol. 31, pp. 702–706, 1984.
(Cited on page 45.)

[70] T. Saramäki, *Handbook for Digital Signal Processing*, M. S. K and K. J. F, Eds. New York: J. Wiley & Sons, 1993.
(Cited on page 45.)

[71] P. E. McSharry, G. D. Clifford, L. Tarassenko, and L. A. Smith, "A dynamical model for generating synthetic electrocardiogram signals." *IEEE Trans Biomed Eng*, vol. 50, no. 3, pp. 289–294, Mar 2003. [Online]. Available: http://dx.doi.org/10.1109/TBME.2003.808805
(Cited on page 47.)

[72] R. Sameni, M. B. Shamsollahi, C. Jutten, and G. D. Clifford, "A nonlinear bayesian filtering framework for ecg denoising." *IEEE Trans Biomed Eng*, vol. 54, no. 12, pp. 2172–2185, Dec 2007.
(Cited on pages 48, 50, and 74.)

[73] The MIT-BIH Noise Stress Test Database. [Online]. Available: http://www.physionet.org/physiobank/database/nstdb/
(Cited on page 48.)

[74] [Online]. Available: http://en.wikipedia.org/wiki/White_noise
(Cited on page 48.)

[75] [Online]. Available: http://en.wikipedia.org/wiki/Colors_of_noise
(Cited on page 49.)

[76] J. B. Allen and L. R. Rabiner, "A unified approach to short-time Fourier analysis and synthesis," *Proceedings of IEEE*, vol. 65(11), pp. 1558–1564, 65, No.1977.
(Cited on page 62.)

[77] M. R. Portnoff, "Time-frequency representation of digital signals and systems based on short-time Fourier analysis," *IEEE Trans. on Acoustic, Speech, and Signal Processing*, vol. 28, pp. 55–69, 1980.
(Cited on page 62.)

[78] P. Dupuis and C. Eugene, "Combined detection of respiratory and cardiac rhythm disorders by high-resolution differential cuff pressure measurement," *IEEE Transactions on Instrumentation and Measurement*, vol. 49(3), pp. 498–502, 2000.
(Cited on page 63.)

[79] L. J. Hadjileontiadis and S. M. Panas, "Separation of discontinuous adventitious sounds from vesicular sounds using a wavelet-based filter," *IEEE Transactions on Biomedical Engineering*, vol. 44(12), pp. 1269–1281, 1997.
(Cited on page 63.)

[80] A. Marrone, A. D. Polosa, G. Scioscia, S. Stramaglia, and A. Zenzola, "Wavelet analysis of blood pressure waves in vasovagal syncope," *Physica A*, vol. 271, pp. 458–469, 1999.
(Cited on page 63.)

[81] M. Khalil and J. Duchene, "Uterine emg analysis: a dunamic approach for change detection and classification," *IEEE Transactions on Biomedical Engineering*, vol. 47(6), pp. 748–755, 2000.
(Cited on page 63.)

[82] A. Petrosian, D. Prokhorov, R. Homan, R. Dasheiff, and D. Wunsch, "Recurrent neural network based prediction of epileptic seizures in intra- and extracranial EEG," *Neurocomputing*, vol. 30, pp. 201–218, 2000.
(Cited on page 63.)

[83] A. Arneodo, Y. d'Auberton Carafa, B. Audit, E. Bacry, J. F. Muzy, and C. Thermes, "Nucleotide composition effects on the long-range correlations in human genes," *The European Physical Journal B*, vol. 1, pp. 259–263, 1998.
(Cited on page 63.)

[84] S. Qain, *Introduction to Time-Frequency and Wavelet Transforms*. Prentice Hall Upper Saddle River, NJ 07458, 2002.
(Cited on page 63.)

[85] I. Daubechies, "Ten Lectures on Wavelets," in *CBMS-NSF Regional Conference Series in Applied Mathematics, SIAM, Philadelphia*, 1992.
(Cited on pages 66 and 69.)

[86] S. G. Mallat, "A theory of multiresolution signal decomposition: The wavelet representation," *IEEE Transactions on Pattern Analysis and Machine Intelligence*, vol. 11(7), pp. 674–693, 1989.
(Cited on pages 67, 68, and 69.)

[87] P. S. Addison, "Wavelet transforms and the ECG: A Review," *Physiological Measurement*, vol. 26, pp. R155–R199, 2005.
(Cited on page 67.)

[88] ——, *The Illustrated Wavelet Transform Handbook: Introductory Theory and Applications in Science Engineering, Medicine and Finance*. Institute of Physics Publishing, Bristol, 2002.
(Cited on page 69.)

[89] J. S. Sahambi, S. N. Tandon, and R. K. Bhatt, "Using wavelet transforms for ECG characterization. An on-line digital signal processing system," *IEEE Eng Med Biol Mag*, vol. 16(1), pp. 77–83, 1997.
(Cited on page 69.)

[90] ——, "Wavelet based ST-segment analysis," *Med Biol Eng Comput.*, vol. 36(5), pp. 568–572, 1998.
(Cited on page 70.)

[91] C. Li, C. Zheng, and C. Tai, "Detection of ECG characteristic points using Wavelet Transforms," *IEEE Trans. Biomed. Eng*, vol. 42(1), pp. 21–28, 1995.
(Cited on page 72.)

[92] B. U. Kohler, C. Hennig, and R. Orglmeister, "The principles of software qrs detection," *IEEE EMB*, vol. 21, no. 1, pp. 42–57, Jan.–Feb. 2002.
(Cited on pages 84 and 85.)

[93] D. Singh, K. Vinod, S. C. Saxena, and K. K. Deepak, "Effects of rr segment duration on hrv spectrum estimation," *Physiological Measurement*, vol. 25, no. 3, pp. 721–735, 2004. [Online]. Available: http://stacks.iop.org/0967-3334/25/721
(Cited on page 86.)

[94] S. Akselrod, D. Gordon, J. B. Madwed, N. C. Snidman, D. C. Shannon, and R. J. Cohen, "Hemodynamic regulation: investigation by spectral analysis," *American Journal of Physiology*, vol. 249(4Pt 2), pp. H867–875, 1985.
(Cited on page 86.)

[95] B. Pomeranz, R. J. B. Macaulay, M. A. Caudill, I. Kutz, D. Adam, D. Gordon, K. M. Kilborn, A. C. Barger, D. C. Shannon, R. J. Cohen, and H. Benson, "Assessment of autonomic function in humans by heart rate spectral analysis," *American Journal of Physiology*, vol. 248, pp. H151–H153, 1985.
(Cited on page 86.)

[96] M. Pagani, F. Lombardi, S. Guzzetti, O. Rimoldi, R. Furlan, P. Pizzinelli, G. Sandrone, G. Malfatto, S. DellÓrto, E. Piccaluga, M. Turiel, G. Baselli, S. Cerutti, and A. Malliani, "Power spectral analysis of heart rate and arterial pressure variabilities as a marker of sympatho-vagal interaction in man and conscious dog," *Circulation Research*, vol. 59, pp. 178–193, 1986.
(Cited on page 86.)

[97] S. L. Marple, *Digital spectral analysis: with applications*. Prentice-Hall, Inc. Upper Saddle River, NJ, USA, 1986.
(Cited on pages 87, 88, 90, and 91.)

[98] M. H. Hayes, *Statistical Digital Signal Processing and Modeling*, S. Elliot, Ed. John Wiley & Sons, 1996.
(Cited on page 87.)

[99] G. Baselli, S. Cerutti, S. Civardi, D. Liberati, F. Lombardi, A. Malliani, and M. Pagani, "Spectral and cross-spectral analysis of heart rate and arterial blood pressure variability signals." *Comput Biomed Res*, vol. 19, no. 6, pp. 520–534, Dec 1986.
(Cited on page 91.)

[100] H. Akaike, "Power spectrum estimation through autoregression model fitting," *Ann. Inst. Stat.l Math.*, vol. 21, pp. 407–419, 1969.
(Cited on page 91.)

[101] ——, "A new look at the statistical model identification," *IEEE Trans. Autom. Control*, vol. AC-19(6), pp. 716–723, 1974.
(Cited on page 91.)

[102] J. A. Rissanen, "Universal prior for the integers and estimation by minimum description length," *Ann. Stat.*, vol. 11, pp. 417–431, 1983.
(Cited on page 91.)

[103] H. Akaike, "A bayesian analysis of the minimum aic procedure," *Ann. Inst. Statist. Math.*, vol. 30 (A), pp. 9–14, 1978.
(Cited on page 91.)

[104] ——, "On entropy maximization principle," *Applications of Statistics Proceedings*, pp. 27–41, 1997.
(Cited on page 91.)

[105] G. Schwartz, "Estimating the dimension of a mode," *The Ann. of Stat.*, vol. 6(2), pp. 461–464, 1978.
(Cited on page 91.)

[106] E. Parzen, "Some recent advances in time series modeling," *IEEE Trans. Autom. Control*, vol. AC-19, pp. 723–730, 1974.
(Cited on page 91.)

[107] J. G. Proakis and D. G. Manolakis, *Digital signal processing (3rd ed.): principles, algorithms, and applications*. Upper Saddle River, NJ, USA: Prentice-Hall, Inc., 1996.
(Cited on page 92.)

[108] A. Boardman, F. S. Schlindwein, A. P. Rocha, and A. Leite, "A study on the optimum order of autoregressive models for heart rate variability," *Physiological Measurement*, vol. 23, pp. 325–336, 2002.
(Cited on page 92.)

[109] J. L. A. Carvalho, A. F. Rocha, I. Santos, C. Itiki, L. F. J. Jr, and F. A. O. Nascimento, "Study on the optimal order for the auto-regressive time-frequency analysis of heart rate variability," in *25th Annual International Conference of the IEEE Engineering in Medicine and Biology Society*, 2003 pp 2621-2624, pp. 2574–2577.
(Cited on page 92.)

[110] J. Mateo and P. Laguna, "Improved heart rate variability signal analysis from the beat occurrence times according to the IPFM," *IEEE Trans. Biomed. Eng.*, vol. 47(8), pp. 985–996, 2000.
(Cited on pages 93, 94, 98, 102, and 109.)

[111] R. D. Berger, S. Akselrod, D. Gordon, and R. Cohen, "An efficient algorithm for spectral analysis of HRV," *IEEE Trans. Biomed. Eng.*, vol. 33(9), pp. 900–904, 1986.
(Cited on pages 94, 95, 96, and 120.)

[112] B. W. Hyndman and P. K. Mohn, "A pulse modulator model for pace maker activity," in *10th Int. Conf. Med. Biol. Eng.*, 1973 pp. 223.
(Cited on page 95.)

[113] M. Ebden, "A Comparison of HRV Techniques: The Lomb Periodogram versus The Smoothed Pseudo Wigner-Ville Distribution," University of Oxford, http://www.robots.ox.ac.uk/ mebden/reports/reports.html, Tech. Rep., 2002.
(Cited on page 96.)

[114] D. Kaplan, "Software for heart rate variability," http://www.macalester.edu/%7Ekaplan/hrv/doc/index.html, Mathematics & Computer Science,Macalester College.
(Cited on page 97.)

[115] http://biosig.sourceforge.net/.
(Cited on page 97.)

[116] J. Mateo and P. Laguna, "Analysis of heart rate variability in the presence of ectopic beats using the heart timing signal," *IEEE Trans. Biomed. Eng.*, vol. 50(3), pp. 334–343, 2003.
(Cited on pages 98, 100, 101, 102, and 257.)

[117] N. Strock, M. Ericson, L. Lindblad, and M. Jensen-Urstad, "Automatic computerized analysis of heart rate variability with digital filtering of ectopic beats," *Clinical Physilogy*, vol. 21(1), pp. 15–24, 2001.
(Cited on page 98.)

[118] D. Litvack, T. Oberlandern, L. Carney, and J. Sau, "Time and frequency domain methods for heart rate variability analysis: A methodological comparison," *Psychophysiol.*, vol. 32, pp. 492–504, 1995.
(Cited on page 119.)

[119] I. Mitov, "A method for assessment and processing of biomedical signals containing trend and periodic components," *Med. Eng. Phys.*, vol. 20, pp. 660–668, 1998.
(Cited on page 119.)

[120] S. Porges and R. Bohrer, *The analysis of periodic processes in psychophysiological research Principles of Psychophysiology: Physical Social and Inferential Elements*, 2000.
(Cited on pages 119 and 120.)

[121] P. M. Tarvainen, O. P. Ranta-aho, and P. A. Karjalainen, "An advanced detrending method with application to HRV analysis," *IEEE Trans. Biomed. Eng.*, vol. 49(2), pp. 172–175, 2002.
(Cited on pages 120 and 121.)

[122] U. Wiklund, M. Akay, and U. Niklasson, "Short-Term Analysis of Heart-Rate Variability by Adapted Wavelet Transforms," *IEEE Engineering in Medicine and Biology*, vol. 16(5), pp. 113–118, 1997.
(Cited on pages 120, 126, 127, and 133.)

[123] A. Jensen and A. la Cour-Harbo, *Ripples in Mathematics The Discrete Wavelet Transform*, 1st ed. Springer, 2001.
(Cited on page 126.)

[124] A. Schlogl, J. Fortin, W. Habenbacher, and M. Akay, "Adaptive mean and trend removal of heart rate variability using kalman filtering," in *Proc. 23rd Annual International Conference of the IEEE Engineering in Medicine and Biology Society*, vol. 1, 2001, pp. 571–573 vol.1.
(Cited on page 133.)

[125] P. Flandrin, P Gonçalvès, and G. Rilling, "Detrending and denoising with empirical mode decompositions," in *Eusipco, 12th European Signal Processing Conference, September 6-10 Vienna, Austria*, 2004.
(Cited on page 133.)

[126] L. J. Badra, W. H. Cooke, J. B. Hoag, A. A. Crossman, T. A. Kuusela, K. U. Tahvanainen, and D. L. Eckberg, "Respiratory modulation of human autonomic rhythms." *Am J Physiol Heart Circ Physiol*, vol. 280, no. 6, pp. H2674–H2688, Jun 2001.
(Cited on page 135.)

[127] T. E. Brown, L. A. Beightol, J. Koh, and D. L. Eckberg, "Important influence of respiration on human R-R interval power spectra is largely ignored," *J Appl Physiol*, vol. 75, no. 5, pp. 2310–2317, 1993. [Online]. Available: http://jap.physiology.org/cgi/content/abstract/75/5/2310
(Cited on page 135.)

[128] V. Novak, P. Novak, J. de Champlain, A. R. L. Blanc, R. Martin, and R. Nadeau, "Influence of respiration on heart rate and blood pressure fluctuations." *J Appl Physiol*, vol. 74, no. 2, pp. 617–626, Feb 1993.
(Cited on page 135.)

[129] M. V. Pitzalis, F. Mastropasqua, F. Massari, A. Passantino, R. Colombo, A. Mannarini, C. Forleo, and P. Rizzon, "Effect of respiratory rate on the relationships between rr interval and systolic blood pressure fluctuations: a frequency-dependent phenomenon." *Cardiovasc Res*, vol. 38, no. 2, pp. 332–339, May 1998.
(Cited on page 135.)

[130] J. E. Sanderson, L. Y. Yeung, D. T. Yeung, R. L. Kay, B. Tomlinson, J. A. Critchley, K. S. Woo, and L. Bernardi, "Impact of changes in respiratory frequency and posture on power spectral analysis of heart rate and systolic blood pressure variability in normal subjects and patients with heart failure." *Clin Sci (Lond)*, vol. 91, no. 1, pp. 35–43, Jul 1996.
(Cited on page 135.)

[131] S. JD, A. G, and P. M, "Effect of respiration rate on short-term heart rate variability," *Journal of Clinical and Basic Cardiology*, vol. 2(1), pp. 92–95, 1999.
(Cited on pages 135 and 241.)

[132] G. B. Moody, R. G. Mark, A. Zoccola, and S. Mantero, "Derivation of respiratory signals from Multi-lead ECGs," *Computers in Cardiology*, vol. 12, pp. 113–116, 1985.
(Cited on pages 135, 136, 137, and 142.)

[133] G. B. Moody, R. G. Mark, M. A. Bump, J. S. Weinstein, A. D. Berman, J. E. Mietus, and A. L. Goldberger, "Clinical validation of the ECG-Derived Respiration (EDR) technique," *Computers in Cardiology*, vol. 13, pp. 507–510, 1986.
(Cited on pages 135 and 142.)

[134] L. A. Lipsitz, F. Hashimoto, L. P. Lubowsky, J. Mietus, G. B. Moody, O. Appenzeller, and A. L. Goldberger, "Heart rate and respiratory rhythm dynamics on ascent to high altitude," *British Heart Journal*, vol. 74 (4), pp. 390–396, 1995.
(Cited on page 135.)

[135] P. de Chazal, C. Heneghan, E. Sheridan, R. Reilly, P. Nolan, and M. O'Malley, "Automated processing of the single-lead electrocardiogram for the detection of obstructive sleep apnoea," *IEEE Trans. Biomed. Eng.*, vol. 50, no. 6, pp. 686–696, June 2003.
(Cited on pages 135 and 142.)

[136] [Online]. Available: http://www.physionet.org/physiobank/database/fantasia/
(Cited on pages 135, 137, 170, and 258.)

[137] A. Pellegrini, F. Pinciroli, R. Rossi, and L. Vergani, "Virtual leads for ambulatory ECG monitoring: Remarks on the persistency of their direction," *Computers in Biomedical Research*, vol. 18, pp. 62–78, 1985.
(Cited on page 136.)

[138] G. J. T. N. P. Anagnostakos, *Principles of Anatomy and Physiology*, 6th ed. Harper-Collins, New York, 1990.
(Cited on page 138.)

[139] L. Sherwood, *Fundamentals of Physiology: A Human Perspective*. Thomson Brooks/Cole, 2006.
(Cited on page 138.)

[140] [Online]. Available: http://www.meddean.luc.edu/lumen/MedEd/MEDICINE/pulmonar/PD/pstep73.htm
(Cited on page 138.)

[141] B. S. Beckett, *Illustrated Human and Social Biology*. Oxford University Press, 1995.
(Cited on page 138.)

[142] C. O'Brien and C. Heneghan, "A comparison of algorithms for estimation of a respiratory signal from the surface electrocardiogram." *Comput Biol Med*, vol. 37, no. 3, pp. 305–314, Mar 2007. [Online]. Available: http://dx.doi.org/10.1016/j.compbiomed.2006.02.002
(Cited on page 142.)

[143] A. Pichon, M. Roulaud, S. Antoine-Jonville, C. de Bisschop, and A. Denjean, "Spectral analysis of heart rate variability: interchangeability between autoregressive analysis and fast fourier transform." *J Electrocardiol*, vol. 39, no. 1, pp. 31–37, Jan 2006. [Online]. Available: http://dx.doi.org/10.1016/j.jelectrocard.2005.08.001
(Cited on pages 144, 244, and 245.)

[144] S. Jasson, C. Médigue, P. Maison-Blanche, N. Montano, L. Meyer, C. Vermeiren, P. Mansier, P. Coumel, A. Malliani, and B. Swynghedauw, "Instant power spectrum analysis of heart rate variability during orthostatic tilt using a time-/frequency-domain method." *Circulation*, vol. 96, no. 10, pp. 3521–3526, Nov 1997.
(Cited on pages 148 and 242.)

[145] N. Montano, T. G. Ruscone, A. Porta, F. Lombardi, M. Pagani, and A. Malliani, "Power spectrum analysis of heart rate variability to assess the changes in sympathovagal balance during graded orthostatic tilt." *Circulation*, vol. 90, no. 4, pp. 1826–1831, Oct 1994.
(Cited on page 148.)

[146] A. Monti, C. Medigue, and L. Mangin, "Instantaneous parameter estimation in cardiovascular time series by harmonic and time-frequency analysis," vol. 49, no. 12, pp. 1547–1556, 2002.
(Cited on page 162.)

[147] H. van Steenis, M. WLJ, and J. Tulen, "Time-frequency parameters of heart-rate variability," vol. 21, no. 4, pp. 46–58, July–Aug. 2002.
(Cited on page 162.)

[148] J. Vila, F. Palacios, J. Presedo, M. Fernandez-Delgado, P. Felix, and S. Barro, "Time-frequency analysis of heart-rate variability," vol. 16, no. 5, pp. 119–126, Sept.–Oct. 1997.
(Cited on page 162.)

[149] O. Faust, R. Acharya U, S. Krishnan, and L. Min, "Analysis of cardiac signals using spatial filling index and time-frequency domain," *BioMedical Engineering OnLine*, vol. 3, no. 1, p. 30, 2004. [Online]. Available: http://www.biomedical-engineering-online.com/content/3/1/30
(Cited on pages 162, 246, and 247.)

[150] V. P. S. Naidu, "Time-variant analysis of heart rate time series by morlet transform technique," *Institution of Engineers (India) Journal*, vol. 85, pp. 37–40, 2004.
(Cited on pages 162 and 246.)

[151] R. Acharya, B. M. Hegde, S. B. P, A. Rao, and N. U. Cholayya, "Wavelet analysis of heart rate variability: New method of studying the heart's function," *Kuwait medical journal*, vol. 34(3), pp. 195–200, 2002.
(Cited on pages 162 and 246.)

[152] F. M, "Wavelet transforms and their applications to turbulence," *Annu. Rev. Fluid Mech.*, vol. 24, pp. 395–457, 1992.
(Cited on page 163.)

[153] http://tftb.nongnu.org/tutorial.pdf.
(Cited on pages 185 and 186.)

[154] L. Cohen, "Time-frequency distributions-a review," vol. 77, no. 7, pp. 941–981, 1989.
(Cited on page 185.)

[155] O. Rioul and P. Flandrin, "Time-scale energy distributions: a general class extending wavelet transforms," vol. 40, no. 7, pp. 1746–1757, 1992.
(Cited on page 185.)

[156] P. Flandrin, *TIME-FREQUENCY/TIME-SCALE ANALYSIS*. Acadamic press, 1998.
(Cited on pages 185, 186, and 188.)

[157] M. Richman, T. Parks, and R. Shenoy, "Discrete-time, discrete-frequency, time-frequency analysis," vol. 46, no. 6, pp. 1517–1527, 1998.
(Cited on pages 188 and 190.)

[158] J. O'Neill, P. Flandrin, and W. Williams, "On the existence of discrete wigner distributions," vol. 6, no. 12, pp. 304–306, 1999.
(Cited on pages 188 and 190.)

[159] D. Dragoman, "Applications of the wigner distribution function in signal processing," *EURASIP Journal on Applied Signal Processing*, vol. 1, pp. 1520 – 1534, 2005.
(Cited on page 190.)

[160] S. Pola, A. Macerata, M. Emdin, and C. Marchesi, "Estimation of the power spectral density in nonstationary cardiovascular time series: assessing the role of the time-frequency representations (tfr)," vol. 43, no. 1, pp. 46–59, 1996.
(Cited on pages 190, 191, 197, 245, and 246.)

[161] L. Spicuzza, L. Bernardi, A. Calciati, and G. U. D. Maria, "Autonomic modulation of heart rate during obstructive versus central apneas in patients with sleep-disordered breathing." *Am J Respir Crit Care Med*, vol. 167, no. 6, pp. 902–910, Mar 2003. [Online]. Available: http://dx.doi.org/10.1164/rccm.200201-006OC
(Cited on page 190.)

[162] H.-L. Chan, M.-A. Lin, P.-K. Chao, and C.-H. Lin, "Correlates of the shift in heart rate variability with postures and walking by time-frequency analysis." *Comput Methods Programs Biomed*, vol. 86, no. 2, pp. 124–130, May 2007. [Online]. Available: http://dx.doi.org/10.1016/j.cmpb.2007.02.003
(Cited on page 190.)

[163] F. Claria, M. Vallverdu, M. Reyna, R. Jane, and P. Carninal, "Time-frequency analysis of heart rate variability as an aid to diagnose pathologies," in *Proc. 18th Annual International Conference of the IEEE Bridging Disciplines for Biomedicine Engineering in Medicine and Biology Society*, vol. 4, 1996, pp. 1604–1605 vol.4.
(Cited on page 191.)

[164] M. Dehkordi, A. Erfanian, and A. Foroutan, "Time-frequency analysis of the heart-rate variability during physical and physical-pharmacological tests," in *Proc. First Joint [Engineering in Medicine and Biology 21st Annual Conf. and the 1999 Annual Fall Meeting of the Biomedical Engineering Soc.] BMES/EMBS Conference*, vol. 1, 1999, pp. 261 vol.1–.
(Cited on page 191.)

[165] H. L. Chan, H. H. Huang, and J. L. Lin, "Time-frequency analysis of heart rate variability during transient segments." *Ann Biomed Eng*, vol. 29, no. 11, pp. 983–996, Nov 2001.
(Cited on page 191.)

[166] F. Clariá, M. Vallverdú, R. Baranowski, L. Chojnowska, and P. Caminal, "Heart rate variability analysis based on time-frequency representation and entropies in hypertrophic cardiomyopathy patients." *Physiol Meas*, vol. 29, no. 3, pp. 401–416, Mar 2008. [Online]. Available: http://dx.doi.org/10.1088/0967-3334/29/3/010
(Cited on pages 191 and 245.)

[167] J. C. Echeverría, J. A. Crowe, M. S. Woolfson, and B. R. Hayes-Gill, "Application of empirical mode decomposition to heart rate variability analysis." *Med Biol Eng Comput*, vol. 39, no. 4, pp. 471–479, Jul 2001.
(Cited on pages 210, 230, 237, 247, and 257.)

[168] E. P. S. Neto, M. A. Custaud, J. C. Cejka, P. Abry, J. Frutoso, C. Gharib, and P. Flandrin, "Assessment of cardiovascular autonomic control by the empirical mode decomposition." *Methods Inf Med*, vol. 43, no. 1, pp. 60–65, 2004. [Online]. Available: http://dx.doi.org/10.1267/METH04010060
(Cited on pages 210, 237, and 247.)

[169] M. Ortiz, E. Bojorges, S. Aguilar, J. Echeverria, R. Gonzalez-Camarena, S. Carrasco, M. Gaitan, and A. Martinez, "Analysis of high frequency fetal heart rate variability using empirical mode decomposition," in *Proc. Computers in Cardiology*, 2005, pp. 675–678.
(Cited on pages 210 and 247.)

[170] E. P. de Souza Neto, P. Abry, P. Loiseau, J. C. Cejka, M. A. Custaud, J. Frutoso, C. Gharib, and P. Flandrin, "Empirical mode decomposition to assess cardiovascular autonomic control in rats." *Fundam Clin Pharmacol*, vol. 21, no. 5, pp. 481–496, Oct 2007. [Online]. Available: http://dx.doi.org/10.1111/j.1472-8206.2007.00508.x
(Cited on pages 210, 237, and 247.)

[171] A. O. Andrade, S. Nasuto, P. Kyberd, C. M. Sweeney-Reed, and F. Van Kanijn, "Emg signal filtering based on empirical mode decomposition," *Biomedical Signal Processing and Control*, vol. 1, no. 1, pp. 44–55, Jan. 2006. [Online]. Available: http://www.sciencedirect.com/science/article/B7XMN-4K66FC7-1/2/d7a89c3dc03c0c85b6e3d0723e09212b
(Cited on page 210.)

[172] R. Balocchi, D. Menicucci, E. Santarcangelo, L. Sebastiani, A. Gemignani, B. Ghelarducci, and M. Varanini, "Deriving the respiratory sinus arrhythmia from the heartbeat time series using empirical mode decomposition," *Chaos, Solitons & Fractals*, vol. 20, no. 1, pp. 171–177, Apr. 2004. [Online]. Available: http://www.sciencedirect.com/science/article/B6TJ4-49HSTC3-2/2/7bf3eab5b09e3e51ed8e844905edaf72
(Cited on page 210.)

[173] A. Torres, J. A. Fiz, R. Jané, J. B. Galdiz, J. Gea, and J. Morera, "Application of the empirical mode decomposition method to the analysis of respiratory mechanomyographic signals." *Conf Proc IEEE Eng Med Biol Soc*, vol. 2007, pp. 1566–1569, 2007. [Online]. Available: http://dx.doi.org/10.1109/IEMBS.2007.4352603
(Cited on page 210.)

[174] N. E. Huang, "Empirical mode decomposition for analysing acoustical signal," US patent, 6862558 B2, March 2005.
(Cited on page 210.)

[175] K. Huang, "Structur sfatey test," US patent, 6192758 B1, Feb 2001.
(Cited on page 210.)

[176] N. E. Huang, Z. Shen, S. R. Long, M. C. Wu, H. H. Shih, Q. Zheng, Nai-Chyuan Yen, C. C. Tung, and H. H. Liu, "The empirical mode decomposition and the hilbert spectrum for nonlinear and non-stationary time series analysis," *Proc. R. Soc. London A.*, vol. 454, pp. 903–995, 1998.
(Cited on pages 210, 211, 213, 214, 215, 217, 218, 230, 239, and 247.)

[177] L. H, *Hydrodynamics*. Cambridge University Press., 1932.
(Cited on page 210.)

[178] N. E. Huang and S. S. Shen, *Hilbert-Huang Transform and Its Applications*. World Scientific, 2005.
(Cited on pages 215, 216, and 218.)

[179] G. Rilling, P. Flandrin, and P. Gonçalve, "On empirical mode decomposition and its algorithms," in *IEEE-EURASIP Workshop on Nonlinear Signal and Image processing*, 2003.
(Cited on page 216.)

[180] N. E. Huang, Z. Shen, and S. R. Long, "A new view of nonlinear water waves: The hilbert spectrum," *Annual Review of Fluid Mechanics*, vol. 31, no. 1, pp. 417–457, 1999. [Online]. Available: http://arjournals.annualreviews.org/doi/abs/10.1146/annurev.fluid.31.1.417
(Cited on page 216.)

[181] N. E. Huang, M.-L. C. Wu, S. R. Long, S. S. P. Shen, W. Qu, P. Gloersen, and K. L. Fan, "A confidence limit for the empirical mode decomposition and hilbert spectral analysis," *The Royal Society Proceedings: Mathematical, Physical and Engineering Sciences*, vol. Vol. 459, No. 2037, pp. 2317–2345, 2003.
(Cited on pages 216, 217, and 231.)

[182] E. Bedrosian, "A product theorem for hilbert transforms," *IEEE J. Proc.*, vol. 51, no. 5, pp. 868–869, 1963.
(Cited on page 218.)

[183] N. E. Haung, "Computing instantaneous frequency by normalising Hilbert Transform," US patient, 6901353 B1, 2005.
(Cited on pages 218 and 219.)

[184] A. Nuttall and E. Bedrosian, "On the quadrature approximation to the hilbert transform of modulated signals," *IEEE J. Proc.*, vol. 54, no. 10, pp. 1458–1459, 1966.
(Cited on page 219.)

[185] P. A. A. Esquef and V. Välimäki, "Interpolation of long gaps in audio signals using the warped burg's method," in *Proceedings of the 6th Int. Conference on Digital Audio Effects (DAFx-03)*, 2003. [Online]. Available: http://www.elec.qmul.ac.uk/dafx03/proceedings/pdfs/dafx10.pdf
(Cited on page 223.)

[186] M. Nakao, M. Norimatsu, Y. Mizutani, and M. Yamamoto, "Spectral distortion properties of the integral pulse frequency modulation model," vol. 44, no. 5, pp. 419–426, 1997.
(Cited on page 230.)

[187] A. Beda, F. C. Jandre, D. I. W. Phillips, A. Giannella-Neto, and D. M. Simpson, "Heart-rate and blood-pressure variability during psychophysiological tasks involving speech: influence of respiration." *Psychophysiology*, vol. 44, no. 5, pp. 767–778, Sep 2007. [Online]. Available: http://dx.doi.org/10.1111/j.1469-8986.2007.00542.x
(Cited on page 241.)

[188] R. Bailon, P. Laguna, L. Mainardi, and L. Sornmo, "Analysis of heart rate variability using time-varying frequency bands based on respiratory frequency," in *Proc. 29th Annual International Conference of the IEEE Engineering in Medicine and Biology Society EMBS 2007*, 2007, pp. 6674–6677.
(Cited on pages 241 and 242.)

[189] J. Hayano, S. Mukai, M. Sakakibara, A. Okada, K. Takata, and T. Fujinami, "Effects of respiratory interval on vagal modulation of heart rate." *Am J Physiol*, vol. 267, no. 1 Pt 2, pp. H33–H40, Jul 1994.
(Cited on page 241.)

[190] R. Bailon, L. T. Mainardi, and P. Laguna, "Time-frequency analysis of heart rate variability during stress testing using "a priori" information of respiratory frequency," in *Proc. Computers in Cardiology*, 2006, pp. 169–172.
(Cited on page 242.)

[191] L. Keselbrener and S. Akselrod, "Selective discrete fourier transform algorithm for time-frequency analysis: method and application on simulated and cardiovascular signals," vol. 43, no. 8, pp. 789–802, 1996.
(Cited on page 242.)

[192] B. Aysin and E. Aysin, "Effect of respiration in heart rate variability (hrv) analysis." *Conf Proc IEEE Eng Med Biol Soc*, vol. 1, pp. 1776–1779, 2006. [Online]. Available: http://dx.doi.org/10.1109/IEMBS.2006.260773
(Cited on page 242.)

[193] Y. Goren, L. R. Davrath, I. Pinhas, E. Toledo, and S. Akselrod, "Individual time-dependent spectral boundaries for improved accuracy in time-frequency analysis of heart rate variability," vol. 53, no. 1, pp. 35–42, 2006.
(Cited on page 242.)

[194] A. Bianchi, B. Bontempi, S. Cerutti, P. Gianoglio, G. Comi, and M. G. N. Sora, "Spectral analysis of heart rate variability signal and respiration in diabetic subjects." *Med Biol Eng Comput*, vol. 28, no. 3, pp. 205–211, May 1990.
(Cited on page 243.)

[195] R. H. Fagard, K. Pardaens, J. A. Staessen, and L. Thijs, "Power spectral analysis of heart rate variability by autoregressive modelling and fast fourier transform: a comparative study." *Acta Cardiol*, vol. 53, no. 4, pp. 211–218, 1998.
(Cited on page 244.)

[196] A. Malliani, M. Pagani, F. Lombardi, and S. Cerutti, "Cardiovascular neural regulation explored in the frequency domain." *Circulation*, vol. 84, no. 2, pp. 482–492, Aug 1991.
(Cited on page 244.)

[197] F. Badilini, P. Maison-Blanche, and P. Coumel, "Heart rate variability in passive tilt test: comparative evaluation of autoregressive and fft spectral analyses." *Pacing Clin Electrophysiol*, vol. 21, no. 5, pp. 1122–1132, May 1998.
(Cited on page 244.)

[198] P. Novak and V. Novak, "Time/frequency mapping of the heart rate, blood pressure and respiratory signals." *Med Biol Eng Comput*, vol. 31, no. 2, pp. 103–110, Mar 1993.
(Cited on page 245.)

[199] H. H. Huang, H. L. Chan, P. L. Lin, C. P. Wu, and C. H. Huang, "Time-frequency spectral analysis of heart rate variability during induction of general anaesthesia." *Br J Anaesth*, vol. 79, no. 6, pp. 754–758, Dec 1997.
(Cited on page 245.)

[200] M. J. Ebden, L. Tarassenko, S. J. Payne, A. Darowski, and J. D. Price, "Time-frequency analysis of the ecg in the diagnosis of vasovagal syndrome in older people." *Conf Proc IEEE Eng Med Biol Soc*, vol. 1, pp. 290–293, 2004. [Online]. Available: http://dx.doi.org/10.1109/IEMBS.2004.1403149
(Cited on page 245.)

[201] D. A. Newandee, "Time-Frequency investigation of Heart Rate Variability and Cardiovascular system modeling of normal and chronic obstructive pulmonary disease (COPD) subjects," Ph.D. dissertation, New Jersey Institute of Technology, 2003.
(Cited on page 247.)

[202] R. M. WILLIAMS, M. KEYES, D. J. BECKER, R. A. WILLIAMS, and F. WASSERMAN, "Electrocardiographic changes during oral surgical procedures under local anesthesia." *Oral Surg Oral Med Oral Pathol*, vol. 16, pp. 1270–1275, Oct 1963.
(Cited on page 248.)

[203] C. L. Hughes, J. K. Leach, R. E. Allen, and G. O. Lambson, "Cardiac arrhythmias during oral surgery with local anesthesia." *J Am Dent Assoc*, vol. 73, no. 5, pp. 1095–1102, Nov 1966.
(Cited on page 248.)

[204] W. Ryder, "The electrocardiogram in dental anaesthesia." *Anaesthesia*, vol. 25, no. 1, pp. 46–62, Jan 1970.
(Cited on page 248.)

[205] B. Chernow, H. R. Alexander, R. C. Smallridge, W. R. Thompson, D. Cook, D. Beardsley, M. P. Fink, C. R. Lake, and J. R. Fletcher, "Hormonal responses to graded surgical stress." *Arch Intern Med*, vol. 147, no. 7, pp. 1273–1278, Jul 1987.
(Cited on page 248.)

[206] Editorial, "Analgesia and the metabolic response to surgery," *Lancet*, vol. 1, p. 1018, 1985.
(Cited on page 248.)

[207] M. R. Blair, "Cardiovascular pharmacology of local anaesthetics." *Br J Anaesth*, vol. 47 suppl, pp. 247–252, Feb 1975.
(Cited on page 248.)

[208] S. D. B, "Toxicity caused by local anaesthetic drug," *Br J Anaesth*, vol. 58, pp. 353–554, 1981.
(Cited on page 248.)

[209] K. Dogru, F. Duygulu, K. Yildiz, M. S. Kotanoglu, H. Madenoglu, and A. Boyaci, "Hemodynamic and blockade effects of high/low epinephrine doses during axillary brachial plexus blockade with lidocaine 1.5%: A randomized, double-blinded study," *Reg Anesth Pain Med*, vol. 28, no. 5, pp. 401–405, 2003.
(Cited on page 249.)

[210] W. Ueda, M. Hirakawa, and K. Mori, "Acceleration of epinephrine absorption by lidocaine." *Anesthesiology*, vol. 63, no. 6, pp. 717–720, Dec 1985.
(Cited on page 249.)

[211] H. Ohno, M. Watanabe, J. Saitoh, Y. Saegusa, Y. Hasegawa, and T. Yonezawa, "Effect of epinephrine concentration on lidocaine disposition during epidural anesthesia." *Anesthesiology*, vol. 68, no. 4, pp. 625–628, Apr 1988.
(Cited on page 250.)

[212] M. Salonen, H. Forssell, and M. Scheinin, "Local dental anaesthesia with lidocaine and adrenaline. effects on plasma catecholamines, heart rate and blood pressure." *Int J Oral Maxillofac Surg*, vol. 17, no. 6, pp. 392–394, Dec 1988.
(Cited on page 250.)

[213] G. A. Cioffi, B. Chernow, R. P. Glahn, G. T. Terezhalmy, and C. R. Lake, "The hemodynamic and plasma catecholamine responses to routine restorative dental care." *J Am Dent Assoc*, vol. 111, no. 1, pp. 67–70, Jul 1985.
(Cited on page 250.)

[214] J. G. Meechan and M. D. Rawlins, "The effects of two different local anaesthetic solutions administered for oral surgery on plasma potassium levels in patients taking kaliuretic diuretics." *Eur J Clin Pharmacol*, vol. 42, no. 2, pp. 155–158, 1992.
(Cited on pages 250 and 251.)

[215] B. T. Finucane, Ed., *Complications of Regional Anesthesia*, 2nd ed. Springer, 2007.
(Cited on page 251.)

[216] R. Aantaa, O. Kirvelä, A. Lahdenperä, and S. Nieminen, "Transarterial brachial plexus anesthesia for hand surgery: a retrospective analysis of 346 cases." *J Clin Anesth*, vol. 6, no. 3, pp. 189–192, 1994.
(Cited on page 252.)

[217] A. Deschamps, I. Kaufman, S. B. Backman, and G. Plourde, "Autonomic nervous system response to epidural analgesia in laboring patients by wavelet transform of heart rate and blood pressure variability." *Anesthesiology*, vol. 101, no. 1, pp. 21–27, Jul 2004.
(Cited on pages 252 and 254.)

[218] S. A. Landsverk, P. Kvandal, T. Kjelstrup, U. Benko, A. Bernjak, A. Stefanovska, H. Kvernmo, and K. A. Kirkeboen, "Human skin microcirculation after brachial plexus block evaluated by wavelet transform of the laser doppler flowmetry signal." *Anesthesiology*, vol. 105, no. 3, pp. 478–484, Sep 2006.
(Cited on pages 253 and 254.)

[219] H. D. Kvernmo, A. Stefanovska, K. A. Kirkeboen, and K. Kvernebo, "Oscillations in the human cutaneous blood perfusion signal modified by endothelium-dependent and endothelium-independent vasodilators." *Microvasc Res*, vol. 57, no. 3, pp. 298–309, May 1999. [Online]. Available: http://dx.doi.org/10.1006/mvre.1998.2139
(Cited on page 253.)

[220] J. Kastrup, J. Bülow, and N. A. Lassen, "Vasomotion in human skin before and after local heating recorded with laser doppler flowmetry. a method for induction of vasomotion." *Int J Microcirc Clin Exp*, vol. 8, no. 2, pp. 205–215, Apr 1989.
(Cited on page 253.)

[221] R. A. Johns, "Local anesthetics inhibit endothelium-dependent vasodilation." *Anesthesiology*, vol. 70, no. 5, pp. 805–811, May 1989.
(Cited on page 253.)

[222] Y. Minamoto, K. Nakamura, H. Toda, I. Miyawaki, R. Kitamura, V. H. Vinh, Y. Hatano, and K. Mori, "Suppression of acetylcholine-induced relaxation by local anesthetics and vascular no-cyclic gmp system." *Acta Anaesthesiol Scand*, vol. 41, no. 8, pp. 1054–1060, Sep 1997.
(Cited on page 253.)

[223] N. N. Turan, A. T. Demiryürek, and H. Celebi, "Effects of lidocaine on rabbit isolated thoracic aorta." *Pharmacol Res*, vol. 42, no. 5, pp. 453–458, Nov 2000. [Online]. Available: http://dx.doi.org/10.1006/phrs.2000.0729
(Cited on page 253.)

[224] J. H. Eisenach, E. S. Clark, N. Charkoudian, F. A. Dinenno, J. L. D. Atkinson, R. D. Fealey, N. M. Dietz, and M. J. Joyner, "Effects of chronic sympathectomy on vascular function in the human forearm." *J Appl Physiol*, vol. 92, no. 5, pp. 2019–2025, May 2002. [Online]. Available: http://dx.doi.org/10.1152/japplphysiol.01025.2001
(Cited on page 253.)

[225] S. Lehtipalo, O. Winsö, L. O. Koskinen, G. Johansson, and B. Biber, "Cutaneous sympathetic vasoconstrictor reflexes for the evaluation of interscalene brachial plexus block." *Acta Anaesthesiol Scand*, vol. 44, no. 8, pp. 946–952, Sep 2000.
(Cited on page 254.)

[226] T. Szili-Torok, D. Paprika, Z. Peto, B. Babik, F. Bari, P. Barzo, and L. Rudas, "Effect of axillary brachial plexus blockade on baroreflex-induced skin vasomotor responses: assessing the effectiveness of sympathetic blockade." *Acta Anaesthesiol Scand*, vol. 46, no. 7, pp. 815–820, Aug 2002.
(Cited on page 254.)

[227] O. Karakaya, I. Barutcu, D. Kaya, A. M. Esen, M. Saglam, M. Melek, E. Onrat, M. Turkmen, O. B. Esen, and C. Kaymaz, "Acute effect of cigarette smoking on heart rate variability." *Angiology*, vol. 58, no. 5, pp. 620–624, 2007. [Online]. Available: http://dx.doi.org/10.1177/0003319706294555
(Cited on page 255.)

[228] I. Barutcu, A. M. Esen, D. Kaya, M. Turkmen, O. Karakaya, M. Melek, O. B. Esen, and Y. Basaran, "Cigarette smoking and heart rate variability: dynamic influence of parasympathetic and sympathetic maneuvers." *Ann Noninvasive Electrocardiol*, vol. 10, no. 3, pp. 324–329, Jul 2005. [Online]. Available: http://dx.doi.org/10.1111/j.1542-474X.2005.00636.x
(Cited on page 255.)